Halide Perovskites

Halide Perovskites

Photovoltaics, Light Emitting Devices, and Beyond

Edited by Tze-Chien Sum and Nripan Mathews

WILEY-VCH

The Editors

Prof. Tze-Chien Sum
Nanyang Technological University
Physical and Mathematiccal Sciences
21 Nanyang Link
SPMS-PAP-03-05
637371 Singapore
Singapore

Prof. Nripan Mathews
Nanyang Technological University
Materials Science & Engineering
Block N4.1, Nanyang Avenue
N4.1-02-35
639798 Singapore
Singapore

Library of Congress Card No.: applied for

British Library Cataloguing-in-Publication Data
A catalogue record for this book is available from the British Library.

Bibliographic information published by the Deutsche Nationalbibliothek
The Deutsche Nationalbibliothek lists this publication in the Deutsche Nationalbibliografie; detailed bibliographic data are available on the Internet at <http://dnb.d-nb.de>.

Print ISBN: 978-3-527-34111-5
ePDF ISBN: 978-3-527-80075-9
ePub ISBN: 978-3-527-80078-0
oBook ISBN: 978-3-527-80076-6

Cover Design Tata Consulting Services
Typesetting SPi Global, Chennai, India
Printing and Binding

Printed on acid-free paper

10 9 8 7 6 5 4 3 2 1

G.C. Papavassiliou (31st Oct. 1940 to 11th Feb. 2018) was born in Lepiana, a small remote village near Arta in Greece, two days after the beginning of the Italian-Greek war. Despite the humble underprivileged location of his village, which suddenly transformed into a war zone including that of the civil war, he managed to set up a small chemistry laboratory in his parent's basement which included homemade electronic circuits and also self-taught English and French through radio-provided Linguaphone lessons. He graduated from the Chemistry Department (University of Athens) in 1968 after fulfilling his military service. Since then he was employed by the National Hellenic Research Foundation (Theoretical and Physical Chemistry Institute, TPCI). His Ph.D. was awarded in 1972 titled "Laser-Raman Spectra of Adsorbed Materials." After a successful career and multiple assessments/elections, he became Director of Research as well as served twice as director of TPCI. Finally, after his retirement in 2009, he was named Researcher Emeritus until his passing.

His published research work focused on a broad set of topics such as metallic nanoparticles, TCNQ-based metals, mixed valence metal complexes, semiconducting nanoparticles, organometallic conductors, charge-transfer complexes as well as hybrid organic–inorganic low-dimensional materials with semiconducting, conducting, and superconducting properties.

Some of his pioneer works are in the fields of quantum dots, organic superconductors, and hybrid organic inorganic semiconductors (known as perovskites). Specifically, he published the first-ever research in observing and explaining the quantum size effect (blueshift), which mostly goes unnoticed, in the Journal of Solid State Chemistry 40, 330–335 (1981) titled "Luminescence Spectra and Raman Excitation Profiles in Small CdS Particles." Later he published the first asymmetrical TTF-based organic superconductor in 1988 in two publications in Synthetic Metals, 27, 373–378 and 379–383 (1988) titled "Conducting Solids Based on Some New Unsymmetrical Tetraheterofulvalenes" and "Low Temperature Measurements of the Electrical Conductivities of Some Charge Transfer Salts with the Asymmetric Donors MDT-TTF, EDT-TTF and EDT-DSDTF $(MDT\text{-}TTF)_2AuI_2$, a new superconductor ($T_c = 3.5$ K at ambient pressure)," respectively. In the field of perovskites, his early pioneering works date precede by 12 years the majority of the current related publications. Their novelty included, in some cases, crucial details regarding synthesis, the use of colloidal suspensions, the novel excitonic energy transfer phenomena observed in mixtures of quasi-2D (q2D) perovskites, and, finally, the first effort for fabricating room temperature energy transfer q2D-perovskite-based LED, beyond the 2011 reported 2D perovskite-based LED. Overall, his published work counts 177 articles, receiving approximately 3000 citations.

He has been a beloved, humble, modest and low-profile researcher, a mentor to his students as well as many colleagues to whom he effortlessly communicated his knowledge. Finally, throughout the years his laboratory and infrastructure were freely and kindly provided to anyone who needed those.

Contents

Part IV Beyond Perovskite Photovoltaics *249*

Part I

Basic Properties and Early Works in Organic–Inorganic Perovskites

1.1

Structural, Optical, and Related Properties of Some Perovskites Based on Lead and Tin Halides: The Effects on Going from Bulk to Small Particles

George C. Papavassiliou[1], *George A. Mousdis*[1], *and Ioannis Koutselas*[2]

[1] *Theoretical and Physical Chemistry Institute, National Hellenic Research Foundation, 48, Vasileos Constantinou Avenue, 11635 Athens, Greece*
[2] *University of Patras, Department of Materials Science, Patras 26504, Greece*

1.1.1 Introduction

The preparation or/and investigation of perovskites, based on PbX_y and SnX_y ($X = Cl$, Br, I) units, was the subject of publications in a number of papers (see, for instance, [1–63]). The majority of these compounds consist either of a small cation (SC) group, such as K^+, Cs^+, and $CH_3NH_3{}^+$, or of a big cation (BC) group, such as $C_{10}H_{21}NH_3{}^+$, $CH_3C_6H_4CH_2NH_3{}^+$, and $C_{10}H_7CH_2NH_3{}^+$, or both of them (SC, BC). Several combinations of the PbX_y or/and SnX_y units give a large number of frameworks; when these are combined with the numerous possibilities of SC and BC compounds, a large number of final compounds can be synthesized. Some of them, having the general formula $(SC)_{n-1}(BC)_2M_nX_{3n+1}$, exhibit a variety of structural, optical, and other properties. They can be prepared from simple starting materials, for example, PbX_2, SnX_2, CH_3NH_2, $C_{10}H_{21}NH_2$, $CH_3C_6H_4CH_2NH_2$, and $C_{10}H_7CH_2NH_2$, according to the following reactions:

$$(SC)X + MX_2 = (SC)MX_3 \tag{1.1.1}$$

$$2(BC)X + MX_2 = (BC)_2MX_4 \tag{1.1.2}$$

or generally,

$$(n-1)(SC)MX_3 + (BC)_2MX_4 = (SC)_{n-1}(BC)_2M_nX_{3n+1} \tag{1.1.3}$$

where $n = 1,2, \ldots, \infty$, the number of inorganic layers.

A number of observations (grinding effects, behavior of suspensions, etc.) showed that these reactions are reversible [30–41]. In this chapter, some important findings concerning the structural, optical, and related properties of semiconducting perovskites of the type $(SC)_{n-1}(BC)_2M_nX_{3n+1}$ $n = 1, 2, \ldots, \infty$, when they are in the bulk (e.g. single-crystal, polycrystalline pellets) and/or in the particulate forms, are briefly reviewed. In these materials, the organic part could be a saturated molecule (or a weakly conjugated molecule) or non-saturated, while the inorganic part consists of an infinite number of interacting units in a three-dimensional (3D) framework, or a finite number of interacting MX_y

Halide Perovskites: Photovoltaics, Light Emitting Devices, and Beyond, First Edition.
Edited by Tze-Chien Sum and Nripan Mathews.

units in a 3D framework, or an infinite number of interacting MX_y units in a two-dimensional (2D) framework, or in similar patterns for lower dimensional cases. In these materials, the organic moiety possesses the role of a barrier. In a second series of perovskites, the organic moiety consists of non-saturated molecules.

1.1.2 Materials Based on Saturated Organic Moiety

1.1.2.1 Bulk Perovskites (SC)MX_3

These are the products of reaction (1.1.1) or that of reaction (1.1.3) with $n = \infty$. The crystals of (SC)MX_3 perovskites consist of an infinitive number of interacting MX_y units, which form a 3D framework [4, 9, 11]. The published papers [1–5] concerning the preparation as well as the structural, optical, and related properties of $CH_3NH_3PbI_3$ (and similar compounds) led the authors of Ref. [42] to use these compounds as the light sensitizer components of solar cells. Moreover, it has been found that the compounds of the type (SC)MX_3 exhibit a variety of properties. Crystals of compounds with MI_3 group are black, crystals with MBr_3 group are red, and crystals with MCl_3 group are yellowish [1, 2, 11, 40–52]. The stability in air is on the order of $MI_3 < MBr_3 < MCl_3$. Figure 1.1.1A shows a simplified picture of the structure of (SC)MX_3 (3D). The X–Pb–X distance is c. 6.4, 5.8, and 5.4 Å for X = I, Br, and Cl, respectively [11]. In the past years, a number of 3D perovskites with several different structures (cubic, tetragonal, and orthorhombic) have been prepared and studied [11, 39, 40, 43, 44, 48, 52, 61, 62]. It has been found that the bulk (SC)PbI_3 possesses the tetragonal structure as the most stable form at room temperature [43]. Also, Figure 1.1.1B shows typical

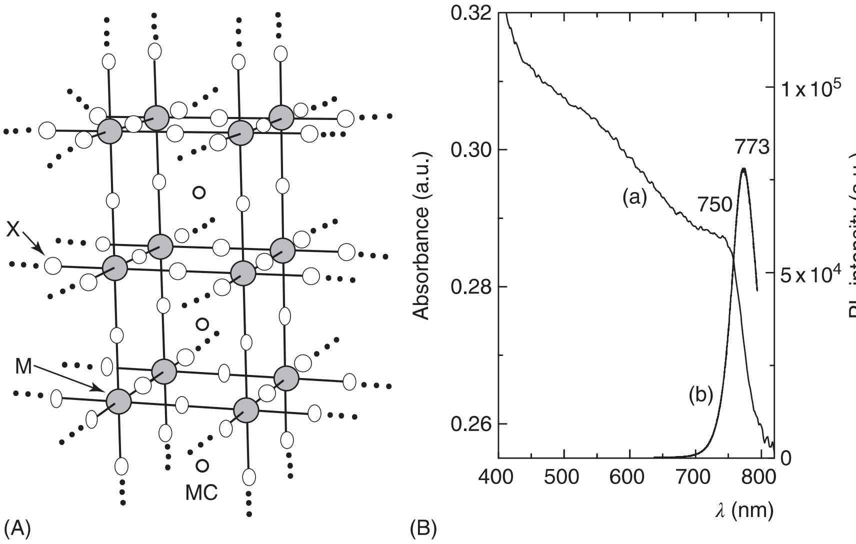

Figure 1.1.1 (A) Simplified crystal structure depiction of (SC)MX_3. (B) Typical OA (a) and corresponding PL (b) spectra of a $CH_3NH_3PbI_3$ single crystal.

optical absorption (OA) and photoluminescence (PL) spectra of a $CH_3NH_3PbI_3$ single crystal. There are some similarities with the spectra of CdS, of which one phase is an anisotropic 3D semiconductor [11]. The bands in the OA spectra of a SnX_3-based compound occur at longer wavelengths than in those of PbX_3, respectively. Attempts were made to obtain materials with high PL yield. The UV–vis diffuse reflectance spectra of (SC)PbX_3 from films were described in [48]. The composition tuning of the samples enabled the band gap to display absorption, PL, etc. over a wide range of 400–850 nm (see [3, 48]).

1.1.2.2 Particulate Perovskites (SC)MX_3

The particulate materials obtained from (SC)MX_3 consist of a finite number of interacting MX_n units in a 3D framework. Some years ago, it was found that by intensive grinding crystals of 3D perovskites, the OA and PL spectra change [18, 40]. In the case of $CH_3NH_3PbI_3$, $CH_3NH_3PbBr_3$, and $CH_3NH_3PbCl_3$, for example, the initial color is black, red, and yellow; and it turns to red, green, and white, respectively, after intensive grinding. Figure 1.1.2A shows the PL spectra of the $CH_3NH_3PbBr_3$ before (a) and after (b) grinding [18]. One can observe that

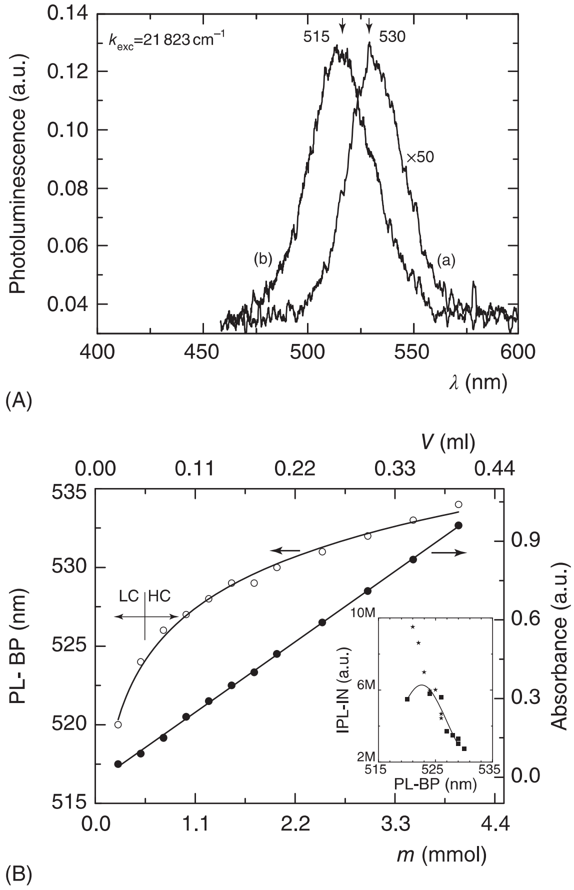

Figure 1.1.2 (A): PL spectra of $CH_3NH_3PbBr_3$ before (a) and after (b) intensive grinding. Source: Reproduced from [18a] with permission from Springer Verlag. (B): PL-BP and the OA values of the emitters, obtained from $CH_3NH_3PbBr_3$ in toluene (15 ml), as a function of the corresponding mass of the compound and the corresponding volume of its DMF solution. The inset shows the IPL-IN versus the PL-BP for two samples: in toluene (tetragonals) and in toluene–PMMA (stars). Solid lines are trend lines added to guide the eyes. Source: Papavassiliou et al. 2012 [29]. Reproduced with permission of Royal Society of Chemistry.

a blueshift of the peak occurs after intensive grinding (quantum dots). These two low-frequency bands are attributed to free excitons. The large particles exhibit PL spectra which occur close to those obtained from the respective single crystals. Similar results were obtained from other (3D) compounds, such as $CH_3NH_3PbI_3$ and $CH_3NH_3PbCl_3$ [1, 5].

The OA and PL spectra and related properties of particulate (nanocrystalline/microcrystalline) materials based on $Pb(Br_xCl_{1-x})_3$, $Pb(Br_xI_{1-x})_3$, and $Pb(Cl_xI_{1-x})_3$ ($x = 0$–1) units, in several macroscopic forms, have been reported in [30]. The spectra of the material, in the form of a suspension in toluene or in toluene containing a polymer, such as polymethyl methacrylate (PMMA) were observed from the corresponding $(SC)MX_3$ (or its precursors), mainly, by a titration-like method [24, 29, 31, 44]. This is the injection of solutions of the corresponding compound based on $Pb_n(Br_xCl_{1-x})_{3n+1}$, $Pb_n(Br_xI_{1-x})_{3n+1}$, and $Pb_n(Cl_xI_{1-x})_{3n+1}$ ($n \geq 1$) units, respectively, into net toluene or toluene–PMMA, with parallel observation of the PL spectra. With this method, the mass of the lead–halide is controlled and the position of the low-frequency PL band could be tuned in a wide spectral range, i.e. from c. 400–750 nm. Figure 1.1.2B shows the PL band position (PL-BP) and the corresponding OA values of the emitters versus the mass value of $CH_3NH_3PbBr_3$ suspended in toluene, as well as versus the corresponding volume value of its dimethylformamide (DMF) solution. It was observed that there is a Stokes shift of the PL bands in comparison to those of the OA bands. The inset presents the integrated photoluminescence intensity (IPL-IN) versus PL-BP in toluene and in toluene–PMMA [29]. Other stabilizing molecules such as oleylamine were not added to the solutions in order to avoid the generation of 2D and quasi-two-dimensional (q-2D) lead halide variants. The preparation and investigation of related structures can be found in [46b, 52–55].

Based on the amounts of mass and the properties of the aforementioned suspensions, the region of Figure 1.1.2 containing the data was divided into two discrete regions: the low-content (LC) and high-content (HC) regions. Suspensions of the LC region are stable upon aging (do not precipitate) for several days. Dilution of suspensions of the LC region with toluene–PMMA leads to the decrease of PL intensity, but does not cause any considerable change in the PL band position. In the LC region, there is almost a linear increase of the IPL-IN against the position of the bands as well as against the mass of the emitters. In other words, in the LC region on going from HC to LC emitters, the PL intensity decreases and the PL bands are blueshifted. Using q-2D instead of 3D compounds, the results are more pronounced (see subsequent text). Figure 1.1.3A shows the evolution of the PL spectrum of a number of emitters based on $CH_3NH_3PbBr_3$ [29]. The inset shows a typical OA spectrum of a $CH_3NH_3PbBr_3$ suspension.

The particle size dependence of the OA and PL spectra of several perovskite compounds have been reported in [2, 11, 43, 44, 48, 52]. Figure 1.1.3B shows the mean value of the PL-BP of $CsPbBr_3$ particles in the spectral region X (c. 460–510 nm) versus the particle diameter of colloidal $CsPbBr_3$ particles [52], as well as the PL-BP of $CH_3NH_3PbBr_3$ suspension in the spectral region Y (c. 510–535 nm) and in the region with longer wavelengths [29]. Recent investigations show that the suspensions are aggregates consisting of particles at least

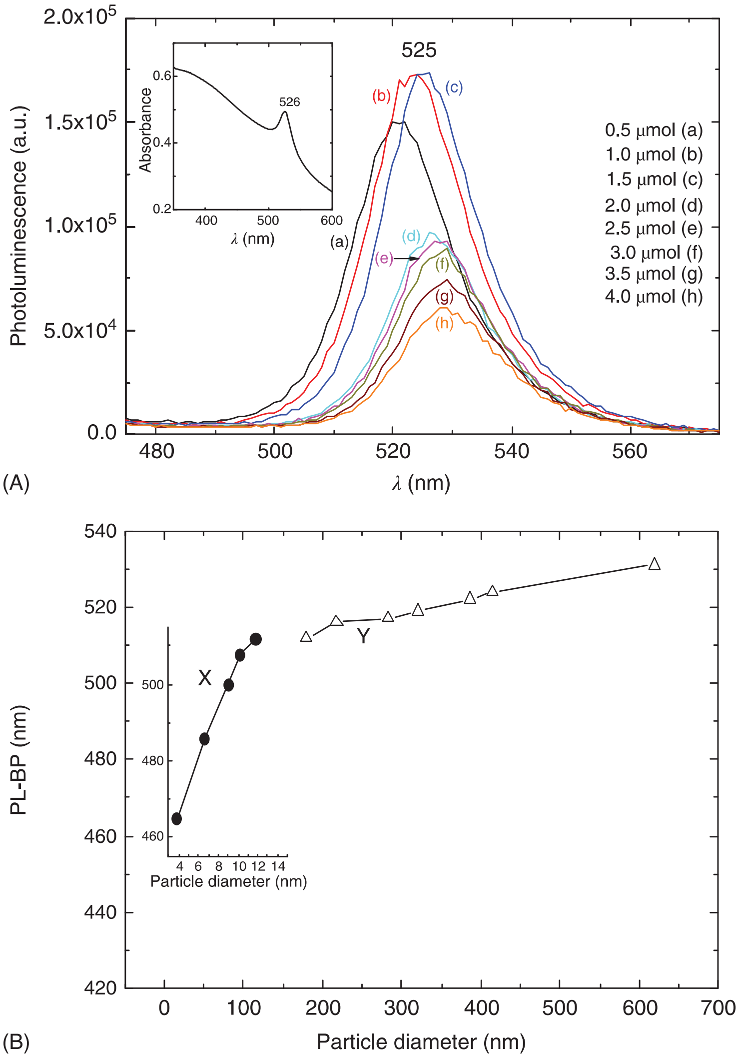

Figure 1.1.3 (A) Evolution of the PL spectra in a number of emitters based on $CH_3NH_3PbBr_3$ after addition of the compound DMF solution in fixed toluene volume. The inset shows a typical OA spectrum of the suspension. Source: Papavassiliou et al. 2012 [29]. Reproduced with permission of Royal Society of Chemistry. (B) Particle size dependence of the band position in the PL spectra of $CsPbBr_3$ (X) and $CH_3NH_3PbBr_3$ (Y and longer wavelengths).

50 times smaller than the aggregate sizes, e.g. 6 nm [35] and 5 nm [48] (see also [44, 46b, 52, 55]. It has been observed that samples with a particle size of 6 nm exhibit OA and PL bands at c. 517 and 526 nm, respectively [35]. One can see that there are some similarities in the spectra of $PbBr_3$ and those of CdS particles [11a], as these were first experimentally observed in Ref. [11b]. For example, the particle size effect in the spectral region X obeys the Bohr equation (quantum confinement effect) [11].

The increase of the emitter PL band's intensity, mainly of those in the LC region which redshift, with increasing mass (or size of the particles) could be attributed to the increase of the superradiance-enhanced radiative decay rate, an effect observed in the microcrystalline state ($R \gg$ Bohr radius) of high-quality materials only [39, 40]. Superradiance effects have been observed, for example, from $CsPbCl_3$ and $CsPbBr_3$ particles (4–20 nm) in CsCl and CsBr matrices, respectively, at low temperatures [36]. Results similar to those obtained from $CsMX_3$ have been reported in [29].

1.1.2.3 Bulk Perovskites of the Type $(BC)_2MX_4$

These perovskites are the reaction (1.1.2) products. These compounds consist of an infinitive number of interacting MX_4 units, which form a 2D framework in a form of infinite equidistant planes, of c. 0.6 nm thickness, separated by the organic part. The investigation of the perovskites or the materials of the type $(BC)_2MX_4$ (where M is Pb or Sn; X is Cl, Br, I) was the subject of the papers published in the 1990s [2–8]. The compounds were prepared in single-crystal form, or in epitaxial films, or in the form of suspensions in different solvents, etc. Their 2D semiconducting behavior is similar to that obtained from artificial quantum wells based, for example, on GaAs or GaN [11]. The crystal structure and the properties of 2D perovskites vary from compound to compound and depend mainly on the nature of BC, the metal (M), and halogen (X) [13]. From the plethora of results obtained from this kind of materials, those based on $H_3N(CH_2)_6NH_3PbX_4$, $(C_6H_5CH_2NH_3)_2PbI_4$, $(C_{10}H_{21}SC\text{-}(NH_2)_2)_2PbI_4$, and $(CH_3C_6H_4CH_2NH_3)_2PbX_4$, as well as the Sn analogs [2, 4] were selected and are discussed herein (see also [13]). Figure 1.1.4 shows the crystal structure as well as the OA and PL spectra of $(CH_3C_6H_4CH_2NH_3)_2PbI_4$. Figure 1.1.5 shows the OA and PL spectra of $(C_{10}H_{21}SC\text{-}(NH_2)_2)_2PbI_4$ (a, b), respectively [20], as well as the OA and PL spectra of $H_3N(CH_2)_6NH_3PbX_4$ ($X = I$, Br, Cl) at room temperature [15].

More information could be obtained from measurements at low temperatures. The results from a selection of several papers concerning excitons and bi-excitons in 2D semiconductors are reported [15, 19, 26]. As an example, the results obtained from a single crystal of $H_3N(CH_2)_6NH_3PbI_4$ are discussed in [19]. The broad PL band observed at room temperature is divided into narrow lines at low temperature (~4 K). The lines are due to the free excitons, with an emitting binding energy of 0.33 meV for $H_3N(CH_2)_6NH_3PbI_4$ [19]. Extremely large bi-exciton energy of 40 meV was estimated for $(CH_3C_6H_4CH_2NH_3)_2PbI_4$ [25]. For some more information concerning optical and related properties of such 2D materials, see [11, 13, 14, 20, 23, 46].

1.1.2.4 Particulate Perovskites of the Type $(BC)_2MX_4$

The OA and PL spectra of $(RNH_3)_2PbBr_4$ in the particulate form are reported in [13]. The size of particles, (200–500 nm), is large compared to the Bohr exciton radius (c. 0.82–1.7 nm) [13, 19]. All observations led to the conclusion that the optical characteristics of materials do not depend on their size. There is no

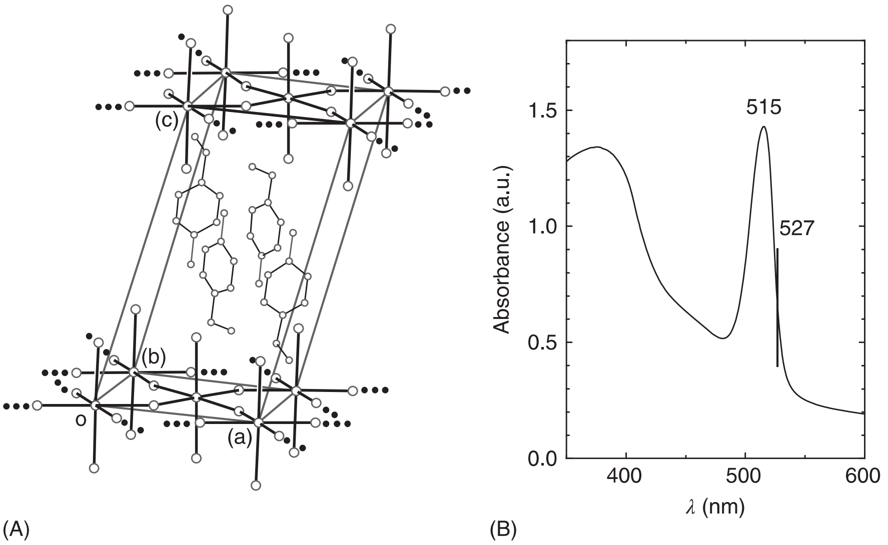

Figure 1.1.4 (A) Crystal structure and (B) OA spectrum of $(CH_3C_6H_4CH_2NH_3)_2PbI_4$ at room temperature. Vertical line indicates the PL band position. Source: Papavassiliou et al. 2000 [16]. Reproduced with permission of Walter De Gruyter.

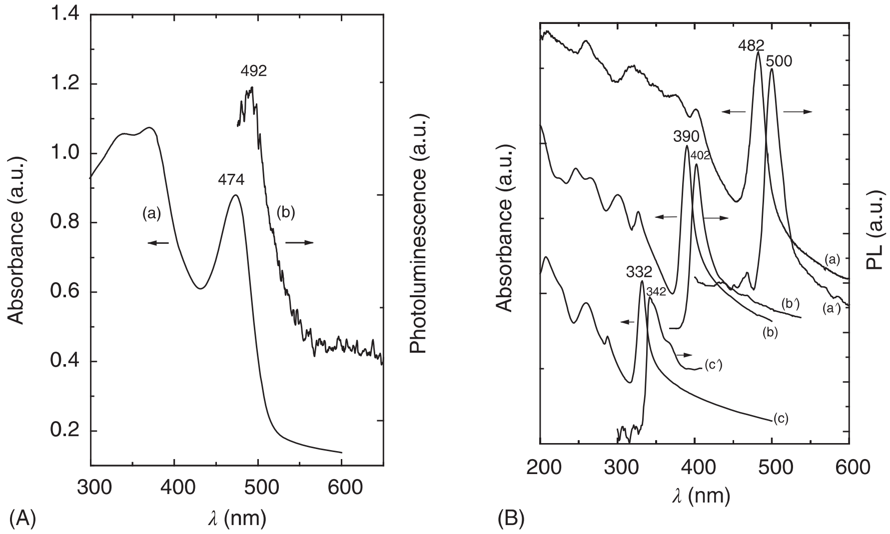

Figure 1.1.5 (A) OA and PL spectra of $[C_{10}H_{21}SC\text{-}(NH_2)_2]_2PbI_4$. Source: Papavassiliou et al. 2001 [20]. Reproduced with permission of Walter De Gruyter. (B) OA (a, b, c) and PL (a′, b′, c′) spectra of $(C_6)PbI_4$ (a, a′), $(C_6)PbBr_4$ (b, b′), and $(C_6)PbCl_4$ (c, c′), where C_6 is $H_3N(CH_2)_6NH_3$. Source: Mousdis et al. 2000 [15]. Reproduced with permission from Royal Society of Chemistry.

information on the behavior of particles with size smaller than 50 nm. The thin films of the compound $(C_6H_5CH_2NH_3)_2SnI_4$ was found to be very good material for a component of field-effect transistors (FETs) [37].

1.1.2.5 Bulk Perovskites of the Type $(SC)_{n-1}(BC)_2M_nX_{3n+1}$

These are the products of reaction (1.1.3) (where n is 2, 3, 4, etc., the number of layers). These are crystalline compounds and they are characterized as q-2D semiconductors [11]. Figure 1.1.6 shows a photograph of a polycrystalline block of parallel-oriented single $(CH_3NH_3)(CH_3C_6H_4CH_2NH_3)_2Pb_2I_7$ crystals and that of the Pb_3Br_{10} analog. Also, it shows the crystal structure of $(CH_3NH_3)(CH_3C_6H_4CH_2NH_3)_2Pb_2I_7$. It consists of corner-sharing PbI_x, forming a bilayer framework [62b]. The corresponding powders of randomly oriented single crystals of materials have the same color. The first is a reddish compound, of which the PL band occurs at c. 530 nm. The Pb_2Br_7 analog is yellow, with a PL band at c. 460 nm [11]. It has been observed that there is no considerable difference between the color of crystalline (bulk) materials and that of the corresponding polycrystalline powders. The OA and PL spectra occur at longer wavelength than those of Pb-X analogs [11]. The OA and PL spectra of Sn analogs occur at longer wavelengths [4].

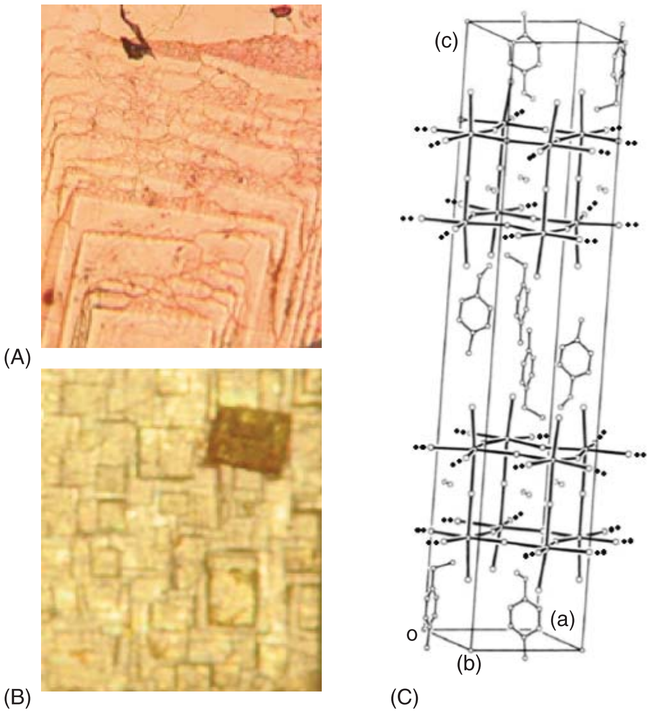

Figure 1.1.6 Photographs of (A) $(CH_3NH_3)(CH_3C_6H_4CH_2NH_3)_2Pb_2I_7$ and the (B) Pb_2Br_7 analog. (C) Crystal structure of $(CH_3NH_3)(CH_3C_6H_4CH_2NH_3)_2Pb_2I_7$. Source: Papavassiliou et al. 2000 [16]. Reproduced with permission of Walter De Gruyter.

1.1.2.6 Particulate Perovskites of the Type $(SC)_{n-1}(BC)_2M_nX_{3n+1}$

Microscopic and spectroscopic investigations of grinding $(SC)_{n-1}(BC)_2M_nX_{3n+1}$ materials and the materials in the form of suspensions showed that they consist of nanocrystalline/microcrystalline particles of $(SC)MX_3$, $(BC)_2MX_4$, etc., in accordance with the reversible reactions [1–4, 10]. This observation leads to the assumption that a small particle has a structure close to that shown in Figure 1.1.7. On the other hand, the emission of quantum well M_nX_{3n+1} $n = 1, 2, 3$ (donor) spectrally overlaps with the OA of $(SC)MX_3$ particles (acceptor).

In these cases, the donor M_nX_{3n+1} interacts with the acceptor (MX_3), and energy transfer (ET) from the donor to acceptor takes place, leading to the enhancement of the PL intensity of MX_3 (see Figure 1.1.8B). The effect is similar to that observed from an artificial system (conventional system), like InGaN, GaN/CdSe, ZnSe [64], namely, a quantum well/quantum dot system [11, 29, 64]. In this case, the PL behavior varies from sample to sample [11, 16, 27]. Figure 1.1.8 shows the OA and PL spectra of particulates $(CH_3C_6H_4CH_2NH_3)_2PbI_4$ and $(CH_3NH_3)(CH_3C_6H_4CH_2NH_3)_2Pb_2I_7$.

The OA excitonic peak of $(CH_3C_6H_4CH_2NH_3)_2PbI_4$ and the corresponding PL peak occur at c. 515 and 527 nm, respectively, while the OA and PL spectra of a crystal $(CH_3NH_3)(CH_3C_6H_4CH_2NH_3)_2Pb_2I_7$ exhibit strong excitonic bands at c. 565 and 580 nm, respectively [16, 27]. Intensive grinding and rubbing of those q-2D samples on quartz plates (or even paper) leads to very thin deposits with a strong PL band at c. 710 nm. Also, it was observed that thin deposits of the 3D semiconductor system $CH_3NH_3PbI_3$ on quartz plates exhibit a PL band at c. 750 nm, which is shifted at c. 720 nm and becomes more intense after intensive grinding and rubbing. This is a confirmation of the existence of

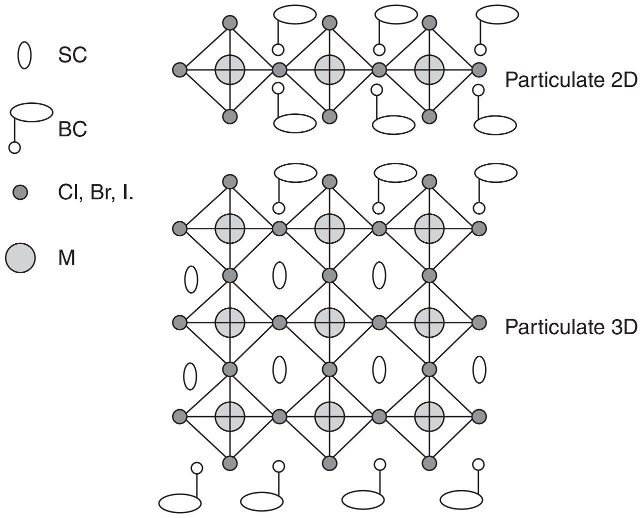

Figure 1.1.7 Suggested schematic presentation of the structure of $(SC)(BC)_2M_2X_7$ particulates (i.e. parts of $PbBr_4$ and $PbBr_3$) based on the crystal structure of individual $(SC)MX_3$ and $(BC)_2MX_4$.

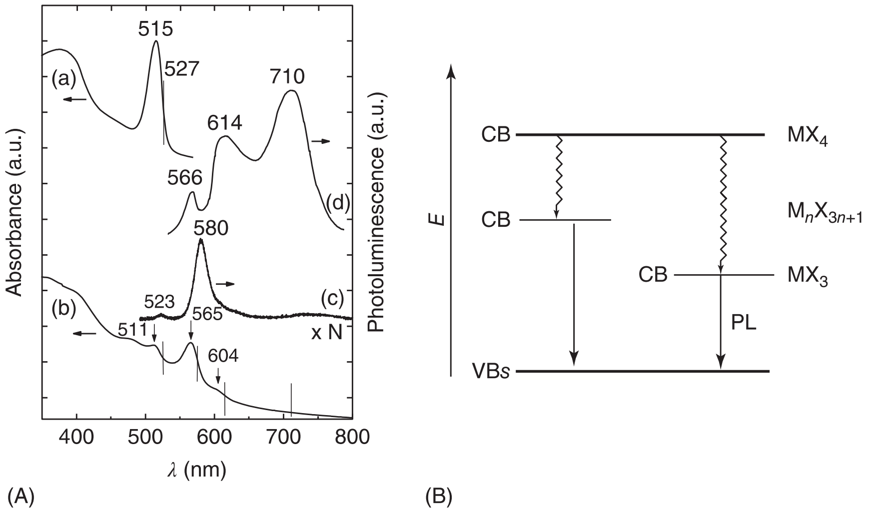

Figure 1.1.8 (A) OA (a, b) and PL (c, d) spectra of $(CH_3C_6H_4CH_2NH_3)_2PbI_4$ (a) and $(CH_3NH_3)(CH_3C_6H_4CH_2NH_3)_2Pb_2I_7$ (b–d) thin deposits on quartz plates (a, b, d) and of a single crystal (c); spectrum (c) before/spectra (a, b, d) after grinding and rubbing; $\lambda_{exc} = 457.9$ nm. Vertical bars indicate the PL peak positions with the same excitation; $N \geq 20$. Source: Papavassiliou et al. 2000 [16]. Reproduced with permission of Walter De Gruyter. (B) Diagram of energy levels and energy-transfer mechanism for the donor–acceptor system.

2D and 3D species in the particulates $(CH_3NH_3)(CH_3C_6H_4CH_2NH_3)_2Pb_2I_7$. In some samples of particulate q-2D intensity, enhancement of PL bands of shorter wavelengths, e.g. 614 nm in Figure 1.1.8A was attributed to $Pb_nX_{3n+}1$. Figure 1.1.8B shows the diagram of energy levels and the ET mechanism. Similar results have been obtained from $(CH_3NH_3)_{n-1}(CH_3C_6H_4CH_2NH_3)_2Pb_nBr_{3n+1}$ [16, 27, 29]. In these compounds, OA and PL spectra with ($n \geq 2$) exhibit excitonic peaks at longer wavelengths than those of $(CH_3C_6H_4CH_2NH_3)_2PbBr_4$. The PL spectrum of $(CH_3NH_3)_2(CH_3C_6H_4CH_2NH_3)_2Pb_3Br_{10}$ single crystal exhibits an excitonic peak at c. 471 nm. After intensive grinding and rubbing of $(CH_3NH_3)_2(CH_3C_6H_4CH_2NH_3)_2Pb_3Br_{10}$ or $CH_3NH_3PbBr_3$ single crystals on quartz plates (or paper), very thin deposits are obtained. They exhibit a strong blue–green PL with a maximum at c. 513 nm. The greater enhancement of band intensity is observed from MX_3 emitters, in contact with M_nX_{3n+1} ($n \geq 2$) species (obtained mainly with 350 and 400 nm excitation [29]), could be attributed to Förster ET from M_nX_{3n+1} species to MX_3 species, as in the case of artificial systems [11, 64]. Similar results were obtained from the corresponding suspensions. In these cases, the PL spectra show strong bands attributed to MX_3 frameworks [29]. Figure 1.1.9 summarizes the data obtained by applying the titration-like method for the preparation of suspension of $(CH_3NH_3)(CH_3C_6H_4CH_2NH_3)_2Pb_2Br_7$ in toluene–PMMA. There are some similarities as well as considerable differences between the data of Figure 1.1.2B and Figure 1.1.9. For example, the PL-IN is at least 10 times higher and is blueshifted in the sample of Figure 1.1.2B. The inset of Figure 1.1.9 shows the IPL-IN versus the PL-BP values and the mass of a series of injections. As in

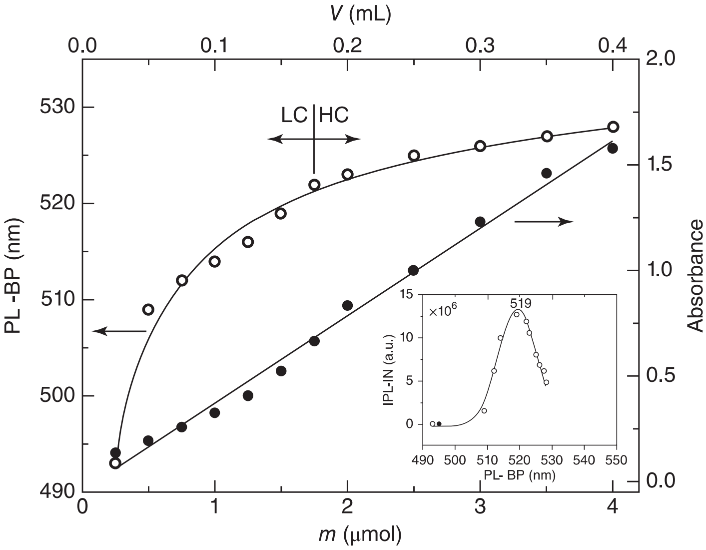

Figure 1.1.9 PL-BP and the corresponding values of optical absorption (OA) of emitters obtained from $(CH_3NH_3)(CH_3C_6H_4CH_2NH_3)_2Pb_2Br_7$ in toluene–PMMA (15 ml) as a function of the corresponding mass of the compound and the corresponding volume of its DMF solution. The inset shows the IPL-IN versus the PL-BP in toluene–PMMA. Solid lines are trend lines added to guide the eyes. Source: Papavassiliou et al. 2012 [29]. Reproduced with permission of Royal Society of Chemistry.

Figure 1.1.2B, there is a Stokes shift in the PL bands in comparison to that of OA bands.

In Figure 1.1.9 one can see that as the mass of Pb_2Br_7 increases from 0.25 to 4 μmol, the position of the emitters' PL band is shifted to longer wavelengths, from c. 495 to 530 nm. In other words, the degree of redshift could be controlled by choosing the appropriate amount of injecting material. All emitters exhibit narrow PL bands, which have full width at half maximum (FWHM) values close to 30 nm. This is an indication of the homogeneous growth of emitters; in particular, the OA bands follow the PL bands. Using these methodologies we can prepare materials with required emission in the spectral region c. 300–750 nm [29; see also 66].

Evolution of the PL spectra of $(SC)_{n-1}(BC)_2M_nX_{3n+1}$ ($n \geq 2$) was obtained, similar to those of Figure 1.1.3A. For example, Figure 1.1.10 shows the evolution of the PL spectra of emitters based on $(SC)_2(BC)_2M_3X_{10}$. Again, as in Figure 1.1.3A, in Ref. [29], this behavior is attributed to superradiance effects.

1.1.2.7 Some Common Features in the Properties of 3D and q-2D Systems

It has been discussed before that the spectra of 2D compounds do not exhibit particle size effects. Also, as in the case of MX_4, the enhancement of intensity of low-frequency PL bands of $(SC)_{n-1}(BC)_2Pb_nX_{3n+1}$ (q-2D) materials is a result of intermolecular interactions of 2D and 3D layers [44, 52, 61, 62]. From the crystal

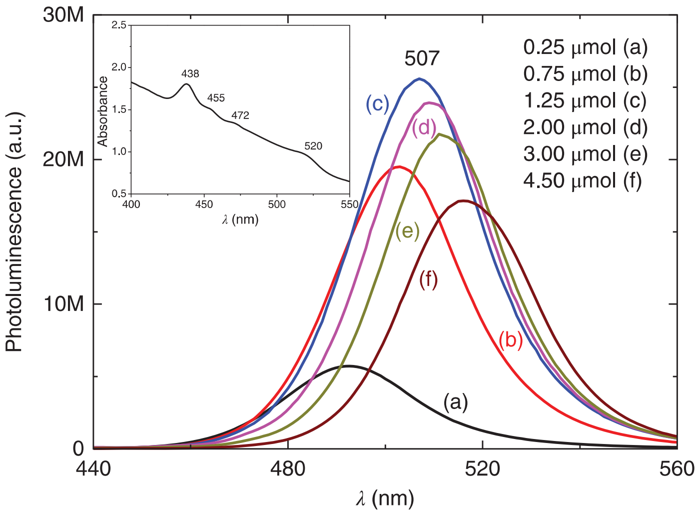

Figure 1.1.10 As in Figure 1.1.3A, but for $(SC)_2(BC)_2M_3X_{10}$ [29].

structure solution on the Pb-based compounds, the layer thicknesses of I–Pb–I, Br–Pb–Br, and Cl–Pb–Cl are c. 0.64, 0.58, and 0.54 nm, respectively [11, 14]. Using these data and the OA and PL-BP values of q-2D compounds [11, 62b], one can obtain the diagrams (a, b, c,) of Figure 1.1.11. Also, some experimental data obtained from particulate samples of $CsPbBr_3$ [52] and $CH_3NH_3PbBr_3$ [46b, 55] have been included for comparison. One can say that for the spectra

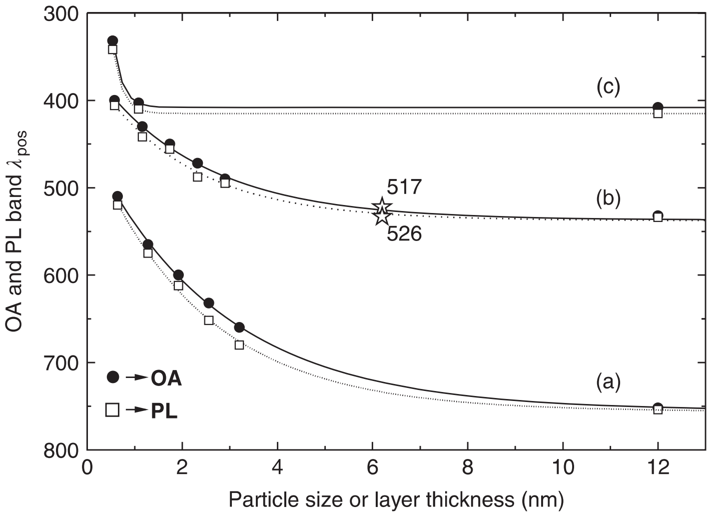

Figure 1.1.11 OA and PL band position values of $(SC)_{n-1}(BC)_2Pb_nX_{3n+1}$ versus the inorganic layer thickness (a, b, c, stand for I, Br, Cl, respectively). Experimental data obtained from $CsPbBr_3$ (points 1, 2, 3, 4, 5) [52] and $CH_3NH_3PbBr_3$ (point 6) [55a] are given for comparison. Solid lines are only to connect the points.

of these series of materials (iodides, bromides, chlorides), there is a common feature, namely, the layer thickness and the particle size dependence obey the same law. The same results are expected for alloys, as well as in SnX-based compounds [11, 37, 59]. The results obtained from clusters of the type $(SC)_xPb_xI_{3x}$ [11, 37, 49] have been reported recently. In a sample of $CH_3NH_3PbBr_3$ consisting of spherical particles of size 6.2 nm, there is a common feature with that of OA and PL spectral bands of bulk q-2D compounds at 517 and 526 nm, respectively. In other words, from the OA and PL spectra of $(SC)_{n-1}(BC)_2Pb_nX_{3n+1}$ with $n = 6$, the same bands of $CH_3NH_3PbBr_3$ particles of size c. 6 nm are expected. Similar results are expected for Pb–I, and Sn analogs, for alloys and clusters [47]. The results are similar to those reported for particles of the type $Cd_xS_y(SPH)_2$ of diameter c. 1–5 nm, together with those for larger CdS particles [11, 64].

1.1.2.8 Low-Dimensional (LD) Perovskites

In recent literature, one finds that there are a number of papers concerning low-dimensional (LD) materials [15, 17, 22]. For example, they consist of an infinite number of interacting MX_y units in a 1D framework (quantum wires) [15, 17, 22] or finite number of interacting MX_y units. Z-scan measurements indicate that some of these compounds are good candidates for optical semiconducting nonlinear optical (NLO) materials.

1.1.2.9 Related Properties

Conductivity measurements in a number of 3D, 2D, 1D, and some q-2D perovskites and in a wide temperature region showed that the 3D materials show semiconducting behavior from room temperature down to 50 K. The iodides are more conductive than the bromides, and the Sn-based materials are more conductive than the Pb analogs [11]. Measurements of the mobility under conditions of FET showed high value, varied 0.2–0.6 $cm^2\ V^{-1}\ s^{-1}$ for $(C_6H_5CH_2NH_3)_2SnI_4$, which is, compared to that observed from FETs, based on porous silicon [31, 37]. The photoconductivity (PC) measures showed behavior similar to that of PL. Figure 1.1.12 shows the PC spectra of $CH_3NH_3PbI_3$ (3D), $(CH_3NH_3)(CH_3C_6H_4CH_2NH_3)_2Pb_2I_7$ (double layer: q-2D), $(CH_3C_6H_4CH_2NH_3)_2PbI_4$ (single layer: 2D), and $(H_2NC(I){=}NH_2)_3PbI_5$(1D) [17]. One can see that the position of the low-frequency PC band is shifted to shorter wavelengths as the dimensionality (or the size) of the inorganic network is decreased. The PC peaks are redshifted, in comparison to the excitonic OA peaks. The PL peaks occur almost between the OA and PC peaks. The PC peaks are more intense in the 2D than in the 1D systems. The PC spectrum of the q-2D system $(CH_3NH_3)(CH_3C_6H_4CH_2NH_3)_2Pb_2I_7$ exhibits a broad band at c. 585 nm. The broadening may be due to contamination from other species, e.g. $(CH_3NH_3)_{n-1}(CH_3C_6H_4CH_2NH_3)_2Pb_nI_{3n+1}$ (here, $n = 1, 3, 4, 5,\ldots$).

The observed electroluminescence (EL) spectra are similar to the corresponding PL spectra (see, e.g. [28]). The EL bands occur close to the OA onset of materials. Their external quantum efficiency closes to 9% and further can be good candidate materials for fabrication of light-emitting diodes (LEDs) and

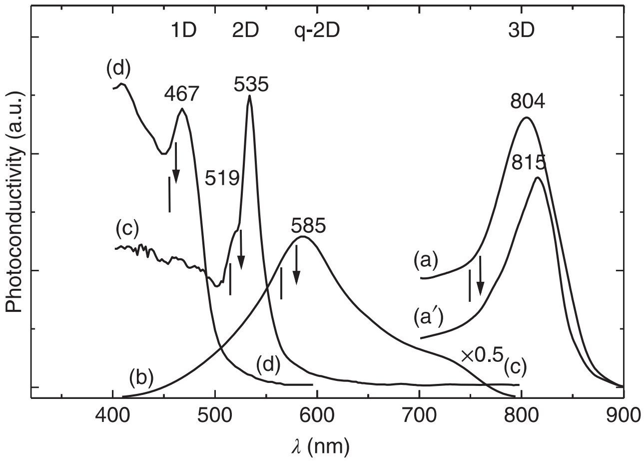

Figure 1.1.12 PC spectra of $CH_3NH_3PbI_3$ (a, a′: two samples), $(CH_3NH_3)(CH_3C_6H_4CH_2NH_3)_2Pb_2I_7$ (b), $(CH_3C_6H_4CH_2NH_3)_2PbI_4$ (c), and $(H_2NC(I){=}NH_2)_3PbI_5$ (d). Arrows indicate the peak position of the PL spectra and vertical bars the OA spectra. Source: Papavassiliou et al. 2001 [17]. Reproduced with permission of World Scientific Publishing Company.

displays (see, for example, [8, 28, 39, 52]). These perovskites can also be inserted in mesoporous matrices, which also provide strong EL signals, due to ET effects, and are yet protected from degradation by virtue of the glass host (see, e.g. [28d]). Similarly, it is possible to entrap q-2D perovskites within mesoporous polymer–silica hybrid matrices that exhibit excitonic EL and can form flexible, free-standing durable films [28e]. Simple blends of q-2D perovskites can form ET LEDs in a single-layer device on an indium tin oxide (ITO) substrate with Ga/In contact, which can function in air for a period of months without degrading [28f] (Figure 1.1.13).

1.1.3 Perovskites Consisting of Non-saturated Organic Moiety BC

Depending on the nature of two compounds, i.e. the vibronic and electronic structure of organic moiety, a number of effects have been reported [28–32, 34]. Using the appropriate amine as starting material (with a non-saturated organic moiety) and applying several techniques (titration, precipitation, etc.), a number of materials with a broad band in the PL spectra have been obtained. For example, a broad phosphorescence band, with three main maxima at c. 500, 536, and 577 nm, was observed at room temperature, either from a mixture of (1-naphthylmethyl ammonium)$_2$$PbCl_4$ and $CH_3NH_3PbCl_3$ or from (CH_3NH_3)(1-naphthylmethyl ammonium)$_2$$Pb_2Cl_7$, or some Cl/Br analogs, in the form of suspensions in toluene or in the form of grinding deposits on quartz plates (see Figure 1.1.14A). It should be noticed that suspensions of $(C_{10}H_7CH_2NH_3)_2PbCl_4$ do not exhibit any PL bands in the region

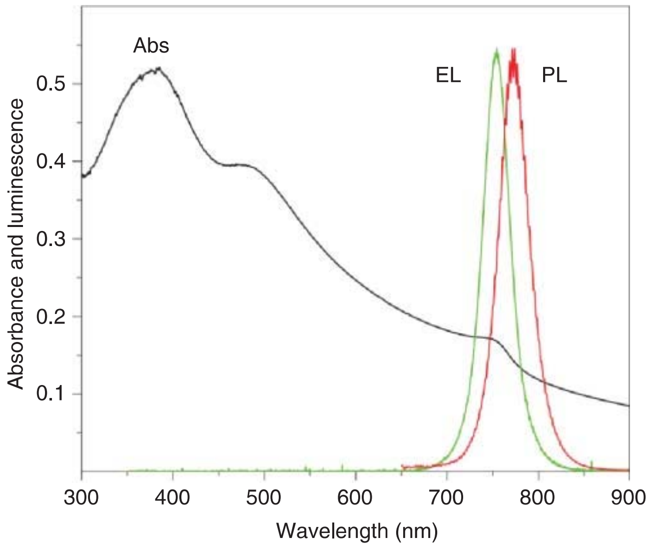

Figure 1.1.13 OA spectrum of $CH_3NH_3PbI_3$ (onset at 780 nm), EL ($\lambda_{max} = 754$ nm), and PL ($\lambda_{max} = 773$ nm). Source: Tan et al. 2014 [28c]. Reprinted with permission of Macmillan Publishers Ltd.

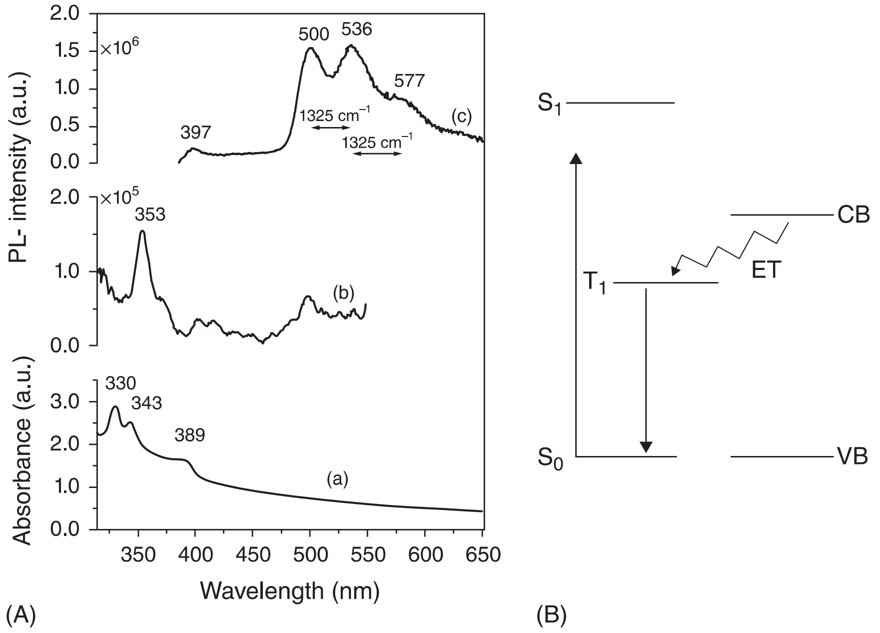

Figure 1.1.14 (A): OA (a) and PL (b, c) spectra for suspension obtained from a mixture of equimolar amounts of $(C_{10}H_7CH_2NH_3)_2PbCl_4$ and $CH_3NH_3PbCl_3$. Excitation 280 nm (b) and 350 nm (c). Source: Papavassiliou et al. 2013 [31]. Reproduced with permission of Elsevier. (B): Diagram of energy levels and energy transfer for this mixture.

350–600 nm, while $CH_3NH_3PbCl_3$ shows an excitonic band at c. 400 nm [31]. The phosphorescence band disappears when the excitation wavelength is 450 nm, and a broad and weak band at c. 500 nm that is due to trapped states is observed [24, 30]. This new effect discussed before is a case of perovskites, where the Wannier excitonic band of inorganic moiety lies energetically in between the energy levels S_1 and T_1 of the organic moiety (Figure 1.1.14B). Then, ET takes place from the conduction band (CB) of inorganic ($PbCl_3$) to the organic moiety and enhancement of the phosphorescence band has been observed.

Several effects have been observed from perovskites based on naphthyl methyl amine, anthracene methyl amine, and pyrene methyl amine [30, 31]. In short, it has been showed that the perovskites with non-saturated BC exhibit broad phosphorescence bands, arising from the organic moiety, while perovskites with saturated BC exhibit narrow excitonic PL bands arising from the inorganic moiety.

1.1.4 Other Perovskite Structures

Recently, a number of structures regarding some different perovskites have been published [65, 66], two examples of which are provided here. In Ref. [65], a perovskite structure is found consisting of interacting MX_3 units forming a 2D framework of the formula $(SC)MX_3$. In Ref. [66], a perovskite structure consisting of interacting MX_4 octahedra units forms a 1D network of the formula $(BC)_2MX_4$. In this way, it is possible to choose the semiconductor with appropriate properties covering the region from c. 350–750 nm.

References

1. Papavassiliou, G.C., Patsis, A.P., Lagouvardos, D.J., and Koutselas, I.B. (1993). Spectroscopic studies of $(C_{10}H_{21}NH_3)_2PbI_4$, $(CH_3NH_3)PbI_3$, and similar compounds. *Synth. Met.* 55–57 (1): 3889–3894.
2. Papavassiliou, G.C., Koutselas, I.B., and Lagouvardos, D.J. (1993). Preparation and characterization of $(C_6H_5CH_2CH_2NH_3)_2SnI_4$ and $(C_6H_5CH_2CH_2NH_3)_2SnBr_4$. *Z. Naturforsch. B: Chem. Sci.* 48 (7): 1013–1014.
3. Papavassiliou, G.C., Koutselas, I.B., Lagouvardos, D.J. et al. (1994). Optical and related properties of some natural three and lower dimensional semiconductor systems. *Mol. Cryst. Liq. Cryst.* 253 (1): 103–112.
4. Papavassiliou, G.C., Koutselas, I.B., Terzis, A., and Whangbo, M.-H. (1994). Structural and electronic properties of the natural quantum-well system $(C_6H_5CH_2CH_2NH_3)_2SnI_4$. *Solid State Commun.* 91 (9): 695–698.
5. Papavassiliou, G.C. and Koutselas, I.B. (1995). Structural optical and related properties of some natural three- and lower-dimensional semiconductors systems. *Synth. Met.* 71 (1–3): 1713–1714.
6. Papavassiliou, G.C., Koutselas, I.B., Terzis, A., and Raptopoulou, C.P. (1995). Some natural three- and lower-dimensional semiconductor systems with metal-halide units. *Mater. Res. Soc. Symp. Proc.* 358: 283–288.

7 Kashiwamura, S. and Kitazawa, N. (1998). Thin films of microcrystalline $(CH_3NH_3)(C_6H_5C_2H_4NH_3)_2Pb_2Br_7$ and related compounds: fabrication and optical properties. *Synth. Met.* 96 (2): 133–136.

8 (a) Koutselas, I.B., Ducasse, L., and Papavassiliou, G.C. (1996). Electronic properties of three- and low-dimensional semiconducting materials with Pb-halide and Sn-halide units. *J. Phys. Condens. Matter* 8 (9): 1217–1227. (b) Even, J., Pedesseau, L., and Katan, C. (2014). Understanding quantum confinement of charge carriers in layered 2D hybrid Perovskites. *ChemPhysChem* 15: 3733–3741. doi: 10.1002/cphc.201402428.

9 Papavassiliou, G.C. (1996). Synthetic three-and lower dimensional semiconductors based on inorganic units. *Mol. Cryst. Liq. Cryst.* 286 (1): 231–238.

10 Koutselas, I.B., Mitzi, D.B., Papavassiliou, G.C. et al. (1997). Optical and related properties of natural one-dimensional semiconductors based on PbI and SnI units. *Synth. Met.* 86 (1–3): 2171–2172.

11 (a) Papavassiliou, G.C. (1997). Three- and low-dimensional inorganic semiconductors. *Prog. Solid State Chem.* 25 (3): 125–270. (b) Papavassiliou, G.C. (1981). Luminescence spectra and Raman excitation profiles in small CdS particles. *J. Solid State Chem.* 40: 330–335.

12 Papavassiliou, G.C., Mousdis, G.A., Koutselas, I.B. et al. (1998). Synthetic low-dimensional semiconductors based on inorganic units. *Adv. Mater. Opt. Electron.* 8 (5): 263–267.

13 (a) Papavassiliou, G.C., Mousdis, G.A., Raptopoulou, C.P., and Terzis, A. (1999). Preparation and characterization of $[C_6H_5CH_2NH_3]_2PbI_4$, $[C_6H_5CH_2CH_2SC(NH_2)_2]_3PbI_5$ and $[C_{10}H_7CH_2NH_3]PbI_3$ organic–inorganic hybrid compounds. *Z. Naturforsch.B: Chem. Sci.* 54 (11): 1405–1409. (b) Zhang, S., Audebert, P., Wei, Y. et al. (2010). Preparations and characterizations of luminescent two dimensional organic–inorganic perovskite semiconductors. *Materials* 3 (5): 3385–3406. (c) Dammak, H., Triki, S., Mlayah, A. et al. (2016). Excitonic luminescence in the self-assembled organic–inorganic quantum well crystal: $(C_4H_3SC_2H_4\text{-}NH_3)_2[PbI_4]$. *J. Lumin.* 173: 203–207. (d) Kawano, N., Koshimizu, M., Sun, Y. et al. (2014). Effects of organic moieties on luminescence properties of organic–inorganic layered perovskite-type compounds. *J. Phys. Chem. C* 118 (17): 9101–9106. (e) Audebert, P., Clavier, G., Alain-Rizzo, V. et al. (2009). Synthesis of new perovskite luminescent nanoparticles in the visible range. *Chem. Mater.* 21 (2): 210–214.

14 Papavassiliou, G.C., Mousdis, G.A., and Koutselas, I.B. (1999). Some new organic–inorganic hybrid semiconductors based on metal-halide units: structural, optical and related properties. *Adv. Mater. Opt. Electron.* 9 (6): 265–271.

15 Mousdis, G.A., Papavassiliou, G.C., Raptopoulou, C.P., and Terzis, A. (2000). Preparation and characterization of $[H_3N(CH_2)_6NH_3]PbI_4$ and similar compounds with layered perovskite structure. *J. Mater. Chem.* 10 (2): 515–518.

16 Papavassiliou, G.C., Mousdis, G.A., Raptopoulou, C.P., and Terzis, A. (2000). Some new luminescent compounds based on 4-methylbenzylamine and lead halides. *Z. Naturforsch., B: Chem. Sci.* 55 (6): 536–540.

17 Papavassiliou, G.C., Mousdis, G.A., Koutselas, I.B., and Papaioannou, G.J. (2001). Excitonic bands in the photoconductivity spectra of some

organic–inorganic EL hybrid compounds based on metal-halide units. *Int. J. Mod. Phys. B* 15 (28–30): 3727–3731.

18 (a) Papavassiliou, G.C., Mousdis, G.A., and Koutselas, I.B. (2001). Excitonic bands in the spectra of some organic–inorganic hybrid compounds based on metal halide units. *Chem. Monthly* 132 (1): 113–119. (b) Papavassiliou, G.C., Mousdis, G.A., and Anyfantis, G.C. (2010). Organic–inorganic hybrid compounds based on lead-halide units: preparation from melts and grinding effects. *Z. Naturforsch., B: Chem. Sci.* 65 (4): 516–520.

19 Goto, T., Ohshima, N., Mousdis, G.A., and Papavassiliou, G.C. (2001). Excitons in single crystals of the two-dimensional semiconductor $H_3N(CH_2)_6NH_3PbI_4$. *Solid State Commun.* 117 (1): 13–16.

20 Papavassiliou, G.C., Mousdis, G.A., and Koutselas, I.B. (2001). Some organic–inorganic hybrid compounds based on iso-thiuronium cations and metal halide anions. *Z. Naturforsch., B: Chem. Sci.* 56 (1): 57–61.

21 Papavassiliou, G.C., Mousdis, G.A., and Koutselas, I.B. (2001). Excitonic bands in the spectra of some organic–inorganic hybrid compounds based on metal halide units. *Synth. Met.* 121 (1–3): 1339–1340.

22 Raptopoulou, C.P., Terzis, A., Mousdis, G.A., and Papavassiliou, G.C. (2002). Preparation, structure and optical properties of $[CH_3SC(NH_2)_2]_3SnI_5$, $[CH_3SC(NH_2)_2]_2[HSC(NH_2)_2]SnBr_4$, $[CH_3C_5H_4NCH_3]PbBr_3$ and $[C_6H_5CH_2SC(NH_2)_2]_4Pb_3I_{10}$. *Z. Naturforsch., B: Chem. Sci.* 57 (6): 645–650.

23 Papavassiliou, G.C., Koutselas, I.B., Mousdis, G.A., and Papaioannou, G.J. (2002). Some organic–inorganic hybrid semiconductors obtained from melts. In: *Molecular Low-Dimensional and Nanostructured Materials. For Advanced Applications* (ed. A. Graja, B.R. Bułka and F. Kajzar), 319–322. the Netherlands: Kluwer Academic Publishers.

24 Goto, T., Oshima, N., Mousdis, G.A., and Papavassiliou, G.C. (2002). Exciton dynamics in synthetic one dimensional semiconductor $C_{10}H_7CH_2NH_3PbI_3$. *Nonlinear Opt.* 29 (7–9): 379–384.

25 Makino, H., Goto, T., Yao, T. et al. (2005). Induced absorption and spontaneous emission due to biexciton in two-dimensional semiconductor $(CH_3C_6H_4CH_2NH_3)_2PbBr_4$ single crystal. *J. Lumin.* 112 (1–4): 54–57.

26 Goto, T., Makino, H., Yao, T. et al. (2006). Localization of triplet excitons and biexcitons in the two-dimensional semiconductor $(CH_3C_6H_4CH_2NH_3)_2PbBr_4$. *Phys. Rev. B* 73 (11): 115206.

27 Papavassiliou, G.C., Mousdis, G.A., and Anyfantis, G.C. (2010). Strong photoluminescence from thin deposits of organic–inorganic hybrid compounds based on metal-halide units. *Luminescence* 25 (3): 218–219.

28 (a) Koutselas, I., Bampoulis, P., Maratou, E. et al. (2011). Some unconventional organic–inorganic hybrid low-dimensional semiconductors and related light-emitting devices. *J. Phys. Chem. C* 115 (17): 8475–8483. (b) Li, G., Tan, Z.-K., Di, D. et al. (2015). Efficient light-emitting diodes based on nanocrystalline perovskite in a dielectric polymer matrix. *Nano Lett.* 15 (4): 2640–2644. (c) Tan, Z.-K., Moghaddam, R.S., Lai, M.L. et al. (2014). Bright light-emitting diodes based on organometal halide perovskite. *Nat. Nanotechnol.* 9: 687–692. (d) Vassilakopoulou, A., Papadatos, D., and Koutselas,

I. (2017). Light emitting diodes based on blends of quasi-2D lead halide perovskites stabilized within mesoporous silica matrix. *Microporous Mesoporous Mater.* 249: 165–175. (e) Vassilakopoulou, A., Papadatos, D., and Koutselas, I. (2017). Flexible, cathodoluminescent and free standing mesoporous silica films with entrapped quasi-2D perovskites. *Appl. Surf. Sci.* 400: 434–439. (f) Vassilakopoulou, A., Papadatos, D., Zakouras, I., and Koutselas, I. (2016). Mixtures of quasi-two and three dimensional hybrid organic–inorganic semiconducting perovskites for single layer LED. *J. Alloys Compd.* 692: 589–598.

29 Papavassiliou, G.C., Pagona, G., Karousis, N. et al. (2012). Nanocrystalline/microcrystalline materials based on lead-halide units. *J. Mater. Chem.* 22 (17): 8271–8280.

30 (a) Papavassiliou, G.C., Mousdis, G.A., Pagona, G. et al. (2014). Room temperature enhanced blue-green, yellow-orange and red phosphorescence from some compounds of the type $(CH_3NH_3)_{n\text{-}1}$(1-naphthylmethyl ammonium)$_2$Pbn$(Cl_xBr_{1\text{-}x})_{3n+1}$ (with $n = 1{,}2$ and $0 \leq x \leq 1$) and related observations from similar compounds. *J. Lumin.* 149: 287–291. (b) Papavassiliou, G.C., Vidali, M.-S., Pagona, G. et al. (2015). Effects of organic moieties on the photoluminescence spectra of perovskite-type tin bromide based compounds. *J. Phys. Chem. Solids* 79: 1–6.

31 Papavassiliou, G.C., Pagona, G., Mousdis, G.A., and Karousis, N. (2013). Enhanced phosphorescence from nanocrystalline/microcrystalline materials based on (CH_3NH_3)(1-naphthylmethyl ammonium)$_2Pb_2Cl_7$ and similar compounds. *Chem. Phys. Lett.* 570: 80–84.

32 Era, M., Maeda, K., and Tsutsui, T. (1998). Enhanced phosphorescence from naphthalene-chromophore incorporated into lead bromide-based layered perovskite having organic–inorganic superlattice structure. *Chem. Phys. Lett.* 296: 417–420.

33 Ema, K., Inomata, M., Kato, Y. et al. (2008). Nearly perfect triplet–triplet energy transfer from Wannier excitons to naphthalene in organic–inorganic hybrid quantum-well materials. *Phys. Rev. Lett.* 100: 257401.

34 (a) Braun, M., Tuffentsammer, W., Wachtel, H., and Wolf, H.C. (1999). Pyrene as emitting chromophore in organic–inorganic lead halide-based layered perovskites with different halides. *Chem. Phys. Lett.* 307: 373–378. (b) Braun, M., Tuffentsammer, W., Wachtel, H., and Wolf, H.C. (1999). Tailoring of energy levels in lead chloride based layered perovskites and energy transfer between the organic and inorganic planes. *Chem. Phys. Lett.* 303: 157–164.

35 (a)Ishihara, T., Hirasawa, M., and Goto, T. (1995). Optical properties and electronic structures of self-organized quantum well $(C_nH_{2n+1}NH_3)_2PbX_4$ (X = I, Br, cl). *Jpn. J. Appl. Phys.* 34: 71–73. (b) Ishihara, T. (1995). *Optical Properties of Low-Dimensional Materials* (ed. T. Ogawa and Y. Kanemitsu), 288. Singapore: World Scientific Publishing Co.

36 (a) Kondo, S., Saito, T., Asada, H., and Nakagawa, H. (2007). Stimulated emission from microcrystalline $CsPbBr_3$ films: edge emission versus surface emission. *Mater. Sci. Eng., B* 137: 156–161. (b) Kondo, S. and Saito, T. (2010). Dramatic improvement of excitonic photoluminescence in metal halide films. *J. Lumin.* 130 (2): 191–205. (c) Kondo, S., Nakagawa, H., Saito, T., and Asada,

H. (2003). Photoluminescence of $CsPbCl_3$ films prepared by quench deposition and subsequent heat treatments. *J. Phys. Condens. Matter* 15: 1247–1257. (d) Babin, V., Fabeni, P., Nikl, M. et al. (1999). Polarized luminescence of $CsPbBr_3$ nanocrystals (quantum dots) in CsBr:Pb single crystal. *Chem. Phys. Lett.* 314 (1–2): 31–36.

37 (a) Mitzi, D.B., Dimitrakopoulos, C.D., and Kosbar, L.L. (2001). Structurally tailored organic–inorganic perovskites: optical properties and solution-processed channel materials for thin-film transistors. *Chem. Mater.* 13: 3728–3740. (b) Mitzi, D.B., Wang, S., Field, C.A. et al. (1995). Conducting layered organic–inorganic halides containing <110> oriented perovskite sheets. *Science* 267: 1473–1476.

38 Trigui, A., Abid, H., Mlayah, A., and Abid, Y. (2012). Optical properties and vibrational studies of a new self-assembled organic–inorganic nanowire crystal $(C_6H_{13}N_3)_2Pb_3I_{10}$. *Synth. Met.* 162: 1731–1736.

39 (a) Nikl, M., Mihokova, E., Nitsch, K. et al. (1994). Photoluminescence and decay kinetics of $CsPbCl_3$ single crystal. *Chem. Phys. Lett.* 220: 14–18. (b) Kitazawa, N., Watanabe, Y., and Nakamura, Y. (2002). Optical properties of $CH_3NH_3PbX_3$ (X = halogen) and their mixed-halide crystals. *J. Mater. Sci.* 37 (17): 3585–3587. (c) Heidrich, K., Ktinzel, H., and Treusch, J. (1978). Optical properties and electronic structure of $CsPbCl_3$ and $CsPbBr_3$. *Solid State Commun.* 25: 887–889. (d) Haupt, H.J., Heidrich, K., Künzel, H., and Mauersberger, P. (1978). Kristallzucht Strukturübersicht und optische Eigenschaften der Alkali trihalogeno plumbate $M[PbX_3]$. *Z. Phys. Chem.* 110 (1): 63–73.

40 Tanaka, K., Takahashi, T., Ban, T. et al. (2003). Comparative study on the excitons in lead-halide-based perovskite-type crystals $CH_3NH_3PbBr_3$ $CH_3NH_3PbI_3$. *Solid State Commun.* 127: 619–623.

41 Calabrese, J., Jones, N.L., Harlow, R.L. et al. (1991). Preparation and characterization of layered lead halide compounds. *J. Am. Chem. Soc.* 113: 2328–2330.

42 Kojima, A., Teshima, K., Shiral, Y., and Miyasaka, T. (2009). Organometal halide perovskites as visible-light sensitizers for photovoltaic cells. *J. Am. Chem. Soc.* 131: 6050–6051.

43 Buin, A., Comin, R., Ip, A.H., and Sargent, E.H. (2015). Perovskite quantum dots modelled using ab initio and replica exchange molecular dynamics. *J. Phys. Chem. C* 119 (24): 13965–13971.

44 (a) Chilvery, A.K., Guggilla, P., Batra, A.K. et al. (2015). Efficient planar perovskite solar cell by spray and brush solution-processing methods. *J. Photonics Energy* 5: 053093. (b) Ding, X.-K., Li, X.-M., Gao, X.-D. et al. (2015). Optical and electrical properties of $CH_3NH_3Pbl_3$ perovskite thin films transformed from PbO-Pbl_2 hybrid films. *Acta Phys. Chim. Sin.* 31: 576–582. (c) Dirin, D.N., Dreyfuss, S., Bodnarchuk, M.I. et al. (2014). Lead halide perovskites and other metal halide complexes as inorganic capping ligands for colloidal nanocrystals. *J. Am. Chem. Soc.* 136 (18): 6550–6553.

45 (a) Eperon, G.E., Bryant, D., Troughton, J. et al. (2015). Efficient, semitransparent neutral-colored solar cells based on microstructured formamidinium lead trihalide perovskite. *J. Phys. Chem. Lett.* 6 (1): 129–138. (b) Etgar, L., Gao, P., Qin, P. et al. (2014). A hybrid lead iodide perovskite and lead sulfide QD heterojunction solar cell to obtain a panchromatic response. *J. Mater. Chem. A* 2 (30): 11586–11590.

46 (a) Gottesman, R., Gouda, L., Kalanoor, B.S. et al. (2015). Photoinduced reversible structural transformations in free-standing $CH_3NH_3PbI_3$ perovskite films. *J. Phys. Chem. Lett.* 6 (12): 2332–2338. (b) Gonzalez-Carrero, S., Espallargas, G.M., Galian, R.E., and Pérez-Prieto, J. (2015). Blue-luminescent organic lead bromide perovskites: highly dispersible and photostable materials. *J. Mater. Chem. A* 3 (26): 14039–14045.

47 Horvath, E., Spina, M., Szekrényes, Z. et al. (2014). Nanowires of methylammonium lead iodide ($CH_3NH_3PbI_3$) prepared by low temperature solution-mediated crystallization. *Nano Lett.* 14 (12): 6761–6766.

48 Jang, D.M., Park, K., Kim, D.H. et al. (2015). Reversible halide exchange reaction of organometal trihalide perovskite colloidal nanocrystals for full-range band gap tuning. *Nano Lett.* 15 (8): 5191–5199.

49 Mitzi, D.B., Field, C.A., Harrison, W.T.A., and Guloy, A.M. (1994). Conducting tin halides with a layered organic-based perovskite structure. *Nature* 369: 467–469.

50 (a) Li, Y., Zhu, J., Wei, J. et al. (2015). Efficient inorganic solid solar cells composed of perovskite and PbS quantum dots. *Nanoscale* 7 (21): 9902–9907.

51 Nie, W., Tsai, H., Asadpour, R. et al. (2015). High-efficiency solution-processed perovskite solar cells with millimeter-scale grains. *Science* 347 (6221): 522–525.

52 (a) Protesescu, L., Yakunin, S., Bodnarchuk, M.I. et al. (2015). Nanocrystals of cesium lead halide perovskites ($CsPbX_3$, X = Cl, Br, and I): novel optoelectronic materials showing bright emission with wide color gamut. *Nano Lett.* 15 (6): 3692–3696. (b) Bekenstein, Y., Koscher, B.A., Eaton, S.W. et al. (2015). Highly luminescent colloidal nanoplates of perovskite cesium lead halide and their oriented assemblies. *J. Am. Chem. Soc.* 137 (51): 16008–16011.

53 Rhee, J.H., Chung, C.-C., and Diau, E.W.-G. (2013). A perspective of mesoscopic solar cells based on metal chalcogenide quantum dots and organometal-halide perovskites. *NPG Asia Mater.* 5: e68. doi: 10.1038/am.2013.53.

54 Rong, Y., Tang, Z., Zhao, Y. et al. (2015). Solvent engineering towards controlled grain growth in perovskite planar heterojunction solar cells. *Nanoscale* 7 (24): 10595–10599.

55 Schmidt, L.C., Pertegas, A., González-Carrero, S. et al. (2014). Nontemplate synthesis of $CH_3NH_3PbBr_3$ perovskite nanoparticles. *J. Am. Chem. Soc.* 136 (3): 850–853.

56 Tsai, H., Nie, W., Cheruku, P. et al. (2015). Optimizing composition and morphology for large-grain perovskite solar cells via chemical control. *Chem. Mater.* 27 (16): 5570–5576.

57 Tyagi, P., Arveson, S.M., and Tisdale, W.A. (2015). Colloidal organohalide perovskite nanoplatelets exhibiting quantum confinement. *J. Phys. Chem. Lett.* 6 (10): 1911–1916.

58 Wu, K.-L., Kogo, A., Sakai, N. et al. (2015). High efficiency and robust performance of organo lead perovskite solar cells with large grain absorbers prepared in ambient air conditions. *Chem. Lett.* 44 (3): 321–323.

59 Yakunin, S., Protesescu, L., Krieg, F. et al. (2015). Low-threshold amplified spontaneous emission and lasing from colloidal nanocrystals of caesium lead halide perovskites. *Nat. Commun.* 6: 8056.

60 Zhang, W., Saliba, M., Stranks, S.D. et al. (2013). Enhancement of perovskite-based solar cells employing core-shell metal nanoparticles. *Nano Lett.* 13 (9): 4505–4510.

61 Zhu, F., Men, L., Guo, Y. et al. (2015). Shape evolution and single particle luminescence of organometalhalide perovskite nanocrystals. *ACS Nano* 9 (3): 2948–2959.

62 (a) Stoumpos, C.C., Malliakas, C.D., and Kanatzidis, M.G. (2013). Semiconducting tin and lead iodide perovskites with organic cations: phase transitions, high mobilities, and near-infrared photoluminescent properties. *Inorg. Chem.* 52 (15): 9019–9038. (b) Stoumpos, C.C., Cao, D.H., Clark, D.J. et al. (2016). Ruddlesden–popper hybrid lead iodide perovskite 2D homologous semiconductors. *Chem. Mater.* 28 (8): 2852–2867.

63 Choi, J.J., Yang, X., Norman, Z.M. et al. (2014). Structure of methylammonium lead iodide within mesoporous titanium dioxide: active material in high-performance perovskite solar cells. *Nano Lett.* 14 (1): 127–133.

64 (a) Acherman, M., Petruska, A.M., Kos, S. et al. (2004). Energy-transfer pumping of semiconductor nanocrystals using an epitaxial quantum well. *Nature* 429 (10): 642–646. (b) Kopylov, O., Huck, A., Shirazi, R. et al. (2013). Design and geometry of hybrid white light-emitted diodes for efficient energy transfer from the quantum well to the nanocrystals. Proc. SPIE 8625, Gallium Nitride Materials and Devices VIII, 862524. (c) Vasiliev, R.B., Dirin, D.N., and Gaskov, A.M. (2011). Semiconducting nanoparticles with spatial separation of charge carriers: synthesis and optical properties. *Russ. Chem. Rev.* 80 (12): 1139–1158.

65 Hintermayr, V.A., Richter, A.F., Ehrat, F. et al. (2016). Perovskite nanoplatelets: tuning the optical properties of perovskite nanoplatelets through composition and thickness by ligand-assisted exfoliation. *Adv. Mater.* 28 (43): 9478–9485.

66 Yuan, Z., Zhou, C., Tian, Y. et al. (2017). One-dimensional organic lead halide perovskites with efficient bluish white-light emission. *Nat. Commun.* 8: 14051.

1.2

Ab Initio and First Principles Studies of Halide Perovskites

Jacky Even[1] *and Claudine Katan*[2]

[1] *Univ Rennes, INSA Rennes, CNRS, Institut FOTON – UMR 6082, 35000 Rennes, France*
[2] *Univ Rennes, ENSCR, INSA Rennes, CNRS, ISCR (Institut des Sciences Chimiques de Rennes) – UMR 6226, 35000 Rennes, France*

1.2.1 Introduction to Ab Initio and DFT Studies of All-inorganic, 3D and Layered Hybrid Organic Metal Halide Perovskites

Before the emergence of halide perovskites in the field of photovoltaics [1–10], layered hybrid organic perovskites (HOPs) already exhibited promising optoelectronic properties for applications in optoelectronics and microelectronics [11–16]. Nowadays, 3D lead-halide-based HOP of general formulae $CH_3NH_3PbX_3$ (X = I, Br, Cl) are the most popular due to their breakthrough for solar cells. Their crystal structures, including for other metal dications Sn^{2+} or Ge^{2+}, reveal a three-dimensional lattice, related to the reference cubic perovskite lattice with corner-shared BX_6 octahedra, B, denoting the metal (Figure 1.2.1). Replacement of the organic methylammonium (MA: $[CH_3NH_3]^+$) cation has already been implemented, for example, with formamidinium (FA: $[HC(NH_2)_2]^+$) or guanidinium (GA: $[C(NH_2)_3]^+$) cations. However, few alternative solutions are compatible with a 3D lattice. Analog all-inorganic perovskites (AIPs) do also exist within the class of ABX_3 perovskites (Figure 1.2.1), such as $A = Cs^+$ or Rb^+ [10]. The quest for new 3D materials has become an active field, and recently 3D alternative structures gained renewed interest [17, 18]. In fact, considering larger organic cations or a mixture of them offers extended possibilities for chemical engineering, and leads to crystal packing with other dimensionalities that may be controlled by the stoichiometric ratio. Ruddlesden–Popper (RP) halide perovskites, a general crystal structure of the form $A_{n-1}A'_2B_nX_{3n+1}$, where $n = 1$ correspond to a 2D monolayered perovskite and $n = \infty$ to a 3D perovskite [19–24] are also promising for various applications [25–30]. The structures range from layered inorganic sheets (2D) up to isolated inorganic octahedrons (0D) and may share corners, edges, and/or faces [31–34].

It turns out that prior to the perovskite boom for solar cells, the 2D HOP had witnessed significant attention from the scientific community, including theoretical investigations based on first-principles approaches, particularly density

Halide Perovskites: Photovoltaics, Light Emitting Devices, and Beyond, First Edition.
Edited by Tze-Chien Sum and Nripan Mathews.

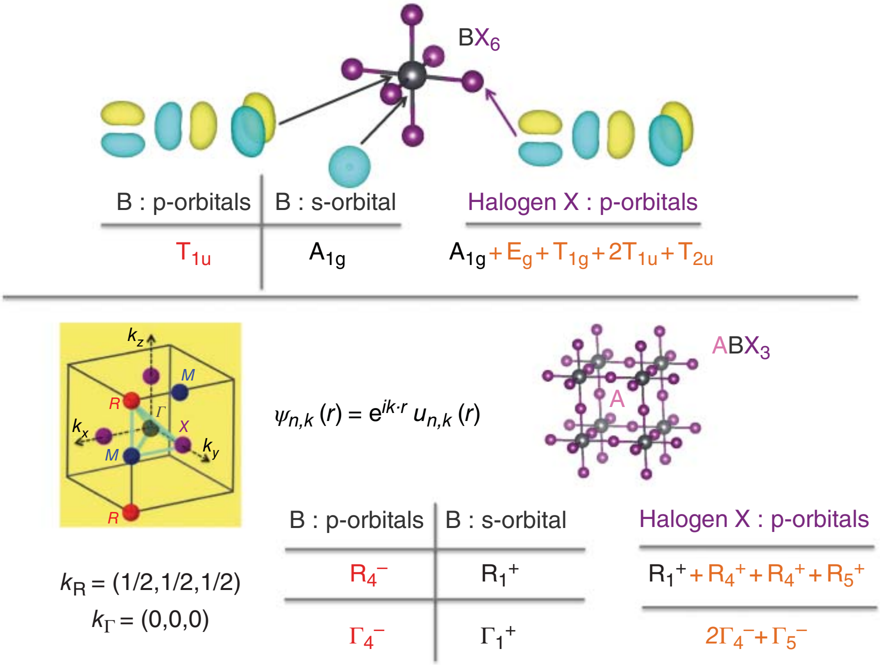

Figure 1.2.1 (Top) Irreducible representations (IRREPs) of the Oh point group corresponding to symmetrized linear combinations of atomic orbitals (SLCAO) for an isolated BX_6^{4-} octahedron. s- and p-orbitals of the metal B and p-orbitals of halogen X are considered. Two A_{1g} IRREPs are hybridized combinations of s(B) and p(X) orbitals and three triply degenerated T_{1u} vectorial states are hybridized combinations of p(B) and p(X) orbitals. (Bottom) Reciprocal space 3D view showing the first BZ of the $Pm\bar{3}m$ space group. Points of high symmetry in the cubic Brillouin Zone (BZ) are indicated by conventional letters: Γ denotes the origin of the BZ; *X* is the center of a square face at the BZ boundary, *M* is a center of a cube edge; and *R* are vertices of the cube. SLCAO includes translational symmetries of the cubic perovskite lattice at Γ and *R* points of the BZ. Spin–orbit coupling (SOC) is not considered.

functional theory (DFT) [35–38]. For instance, as predicted by Papavassiliou et al. in the 1980s [35] based on extended Hückel tight-binding model of a single $(SnI_4)^{2-}$ layer, these early DFT calculations revealed the main features of the band structures of HOP: (i) semiconductors with a direct bandgap, (ii) valence band (VB) mainly composed of p-orbitals of the halogens that undergo antibonding hybridization with the s-orbitals of the metal, (iii) conduction band (CB) essentially made of p-orbitals of the metal. They also demonstrated that the molecular orbitals of the organic molecule do not contribute near the bandgap, except in a few cases. As such, the organic cation could be safely replaced by either a background charge density or by an inorganic ion such as Na^+ [37, 38]. It is noteworthy that it allows recovering an accurate band structure in the vicinity of the bandgap, but should not be used for a too wide energy range or whenever relaxations of atomic positions and/or unit cell parameters are needed.

This trick may be particularly useful for DFT calculations to save computational resources but also to investigate the properties of structures in which the symmetry of the organic cation does not fit with the site symmetry of the crystal. This applies, in particular, to the room and high-temperature phases of ABX_3 compounds, which are tetragonal and cubic, respectively, when A = MA. This leads us to consider several issues that have to be carefully taken into account before performing DFT calculations on 3D [35–49] or layered [50–54] HOP. The starting point of a DFT calculation with periodic boundary conditions is a unit cell (which may or not be primitive, depending on the software) and the atomic positions. By fixing arbitrarily the orientation of the A cations in the tetragonal or cubic cell, one introduces spurious static dipolar interactions (e.g. ferroelectricity) and elastic strain. In reality, the cations undergo dynamic stochastic reorientational motion that can be addressed using ab initio molecular dynamics (MD) with supercells of appropriate size. Then, it could be envisaged to optimize the atomic positions and maybe the parameters defining the unit cell using DFT. In this case, it should be recalled that DFT does not account for temperature effects and can at best lead to the structure relevant to 0 K. For instance, comparison of a DFT-optimized structure with that recorded at room temperature may lead to sizeable differences, especially regarding the tilt angles of the perovskite octahedra, which may or not be a consequence of phase transitions. Such structural changes have a direct impact on the computed properties, especially on the bandgap as stated initially by Mitzi and coworkers [36].

This leads us to stress another well-known intrinsic limitation of DFT, namely, the numerical evaluation of the optical bandgap that is especially important for photovoltaic and other optoelectronic applications. Even though the DFT-computed bandgap of $MAPbI_3$ matches nicely with experimental optical bandgaps, it should be stressed that this results from fortuitous error compensation. DFT is a ground-state theory. One needs, in principle, to implement many-body corrections to DFT ground-state energies, such as GW self-energy corrections, to cure for charged excitations corresponding to the addition or removal of an electron [42, 55–58]. Then, to account for electron–hole interactions, further corrections can be made on the basis of Bethe–Salpeter equation (BSE). This is currently the state-of-the-art level of theory to compute optical spectra of solids, but it is beyond reach for systems having large unit cells such as layered HOP. In addition, it does not account for atomic/molecular motion that may affect exciton binding energies. Besides, another important factor influences dramatically the DFT-computed bandgaps of HOP, in this instance, the relativistic effects. In the case of lead-based HOP, both spin–orbit coupling (SOC) and many-body effects are huge (c.a. 1 eV) and act in opposite directions [38, 42]. Of note, time-dependent density functional theory (TD-DFT) including SOC might also be an option that has still to be checked. Alternatively, hybrid exchange-correlation functionals specifically designed to recover semiconductor bandgaps within DFT may also be an option.

Last but not least, the results of DFT electronic structure calculations as well as those of ab initio MD simulations may be seemingly complex to analyze. Symmetry considerations can help circumvent this issue, as might introduction of a reference crystal structure such as the cubic structure for ABX_3 perovskites [47, 59, 60].

In this chapter we illustrate through a few examples that, despite all these pitfalls, first-principles studies have contributed greatly to our present understanding of the physical properties of HOP and may further contribute and provide guidance for improving the operation and performances of related optoelectronic devices. DFT-based technics offer a powerful simulation tool whenever carefully used. Besides, semi-empirical and symmetry-based tight-binding or multiband $\mathbf{k}\cdot\mathbf{p}$ approaches also afford complementary tools to DFT simulations [61–64]. In fact, such methods parameterized on accurate DFT and precise experimental data of reference HOP bulk materials also open new opportunities to tackle larger systems and nanostructures, which are beyond reach due to limited computational resources.

1.2.2 Brillouin Zone Folding, Lattice Strain, and Topology of the Electronic Structure

Performing basic DFT simulations of halide perovskite materials are relatively easy tasks with available DFT simulation codes, but reliable theoretical predictions may be hampered by several factors. The complexity of the available halide perovskite crystallographic structures may lead to the conclusion that the various situations should be treated one by one without connections between them. More, the thermally activated stochastic rotations of the organic cations are not easily taken into account without using MD. It is thus tempting to perform a structure relaxation without constraints from the perovskite lattice symmetry, before computing the electronic structure. This may lead to wrong conclusions, if the resulting structure significantly deviates from the experimental one and does not fulfill its symmetry requirements. One may choose, alternatively, to perform a DFT study for a low-temperature crystallographic structure where the cation positions are frozen, but at the price of an increasing computational cost. More, one may wonder how the conclusions drawn for low-temperature structures can be transferred to the room temperature or higher temperatures, where most of the real halide perovskite devices are operating.

For classical IV, III–V, or II–VI semiconductors like Si, GaAs, CdTe, a fruitful methodology consists in considering a reference structure (diamond, zinc-blende, würtzite, etc.) and taking advantage of its high symmetry to treat many problems as perturbations to it. Such an approach is possible for halide perovskites, and the $Pm\overline{3}m$ perovskite cubic phase is a natural choice for that purpose. In fact, it corresponds to the most commonly accepted high-temperature crystal structure of 3D HOP and AIP. Then, most of the low-temperature crystal structures can be understood as structural distortions of this phase. For instance, $CH_3NH_3BI_3$ are suspected to support a non-centrosymmetric tetragonal space group $P4mm$, close to room temperature, and known to exhibit, at lower temperatures, phase transitions to a tetragonal $I4cm$ or $I4/mcm$ phase, as well as to an orthorhombic $Pnma$ phase. All these space groups are associated with a group–subgroup relationship with the $Pm\overline{3}m$ reference space group, which eases the analyses and allows introducing the concept of Brillouin zone (BZ) folding [48, 49].

To introduce the concept of BZ folding, a key example is the low-temperature orthorhombic phases (*Pnma*) of the $CH_3NH_3PbX_3$ 3D HOP ($Z = 4$ for X = I or Br and $Z = 8$ for X = Cl). In fact, it allows conducting a rigorous DFT computation including all atoms in an ordered lattice. The electronic bandgap is direct and shows up at the Γ point of the BZ (Figure 1.2.2). The electronic band structure of the *Pnma* phase of $CH_3NH_3PbI_3$ appears very complicated. In order to compute that of the reference cubic phase, for comparison purposes, we need to use a trick, as the cations cannot be fixed (Section 1.2.1). The tactic of replacing the MA cations by Cs^+ cations located at nitrogen positions of the *Pnma* crystal structure leaves the electronic band diagram close to the bandgap unchanged [42, 47–49]. Then, the same tactic can be implemented for the $Pm\bar{3}m$ reference structure, while placing the Cs^+ at the center of the cube to observe the principles of symmetry. At first sight, the band structure of the *Pnma* phase appears very different from that computed for the reference cubic phase (Figure 1.2.2). For instance, the gap moves off the BZ center toward the *R*-point. Moreover, for

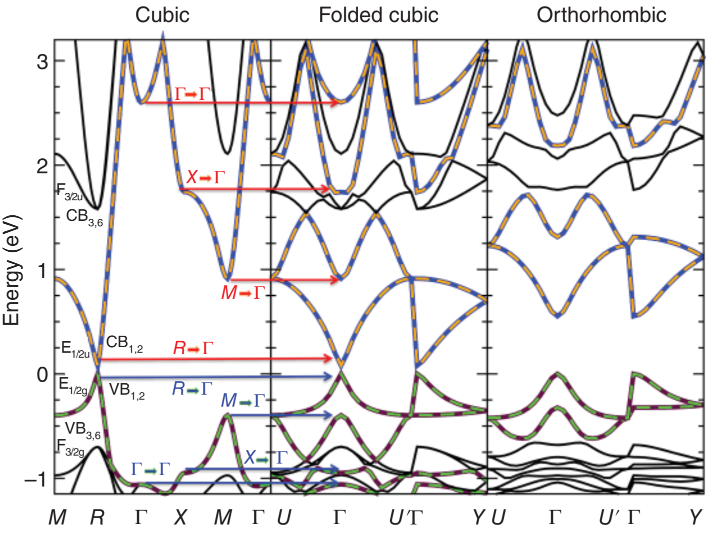

Figure 1.2.2 Band folding in the Brillouin zone (BZ) shown for $CH_3NH_3PbI_3$ with DFT calculations including SOC. (Left) Electronic band diagram calculated for the reference cubic $Pm\bar{3}m$ (space group no. 221, $Z = 1$) crystal structure and represented along principal directions of the first BZ (Figure 1.2.1) with irreducible representations of the double group. (Middle) The very same band structure represented along principal directions of the first BZ of the orthorhombic *Pnma* unit cell (space group n° 62, $Z = 4$) evidencing the band folding from *R*, *M*, and *X* to Γ, which results in an apparent fourfold increase of the number of bands. (Right) Electronic band diagram calculated for the real low-temperature orthorhombic *Pnma* crystal structure shown along principal directions of its first BZ. It highlights effects of structural distortions on the band structure, namely, the increased bandgap and the change in effective masses at VBM and CBM. Of note, the band mixing remains moderate as a direct consequence of the large splitting of $CB_{1,2}$ and $CB_{3,6}$ (left) induced by SOC, whereas such mixing would have been largely overestimated without SOC. Source: Katan et al. 2015 [48]. Reproduced with permission of Royal Society of Chemistry.

$CH_3NH_3PbX_3$, the number of bands is multiplied by a factor of 4–8 ($Z = 4$ or 8) with respect to the cubic lattice.

To rationalize this apparent complexity, the effect of the $Pm\overline{3}m$ to $Pnma$ cell transformation can be explored considering the supercell ($\vec{a} + \vec{b}, 2\vec{c}, \vec{a} - \vec{b}$) of the cubic cell ($\vec{a}, \vec{b}, \vec{c}$) while keeping the atoms at the special positions of the $Pm\overline{3}m$ phase. This leads to the folded-cubic band structure also shown in Figure 1.2.2. As the cell size undergoes a fourfold increase, it leads to a reduction of the BZ volume by the same amount. Electronic states close to the bandgap are folded from R of the $Pm\overline{3}m$ BZ to Γ of the $Pnma$ supercell BZ. In addition, electronic states from M also fold back to Γ and get mixed with R-states at the Γ point of the BZ of the supercell. This band folding clarifies the seeming complexity of the band diagram in the low-temperature phase.

This procedure also reveals that, besides electronic band folding, the most important transformation of the band diagram is due to atomic displacements [47, 61]. Thus, it becomes clear that the bandgap increase stems from lattice distortions that are mainly related to tilts of the inorganic octahedra (vide infra) and space group symmetry reduction. Similar band folding helps understand the main features of the electronic band diagram of the $Pm\overline{3}m$ to $I4mcm$ cell transformation, or other transformations [48, 49].

Change of the lattice lifts also the conduction band minimum (CBM) degeneracy. This is consistent with the group–subgroup relationship between cubic and orthorhombic phases. A detailed understanding of the influence of strain (ε_{ij} tensor) and degeneracy lifting can be afforded by empirical or semiempirical approaches. Among the simplest way, one could start with a $\mathbf{k}\cdot\mathbf{p}$ Hamiltonian, and then add a strain perturbation Hamiltonian within the $|\boldsymbol{X}\rangle$, $|\boldsymbol{Y}\rangle$, $|\boldsymbol{Z}\rangle$ bases functions of the simple group at the R-point of the BZ [61].

Moreover, the concept of BZ folding and reference phase can be further extended to layered structures [14, 54]. Figure 1.2.4 highlights the BZ folding using and artificially designed 2D HOP: Cs_2PbCl_4. It corresponds to D_{4h} point group. But layered HOPs often present a high-temperature phase that shows a cell doubling within the inorganic plane (perpendicular to the stacking axis), as a result of antiferrodistorsive tilts of the octahedra. Such a distortion of the lattice results in the reduction of point group symmetry to D_{2h} and a folding of the BZ, as illustrated in Figure 1.2.4. As an example, Bz_2PbCl_4 ($Bz = C_7H_7NH_3$) is reported to undergo such a structural transformation, with a ferroelectric phase transition from centrosymmetric $Cmca$ space group at high temperature to the non-centrosymmetric $Cmc2_1$ group below 478 K [65–67].

Layered structure (Figure 1.2.3a,b) can be further used to streamline the effect of octahedral tilting on the optical bandgap [54]. For that purpose, we define two angles denoted β and δ, characteristic of in-plane rotation and out-of-plane tilt of the BX_6 octahedra, respectively (Figure 1.2.5a). Thus, β corresponds to the in-plane projection of the B-B-M angle (the metal atoms obtained by periodic replication along $\vec{a}$ and $\vec{b}$ define the plane), and δ to the B-B-M angle along the stacking direction (two B atoms derived the one from the other by a vertical translation $\vec{c}$). For an undistorted structure, $\beta = \delta = 0$. Figure 1.2.5b highlights the variation of the computed electronic bandgap with respect to β and δ angles

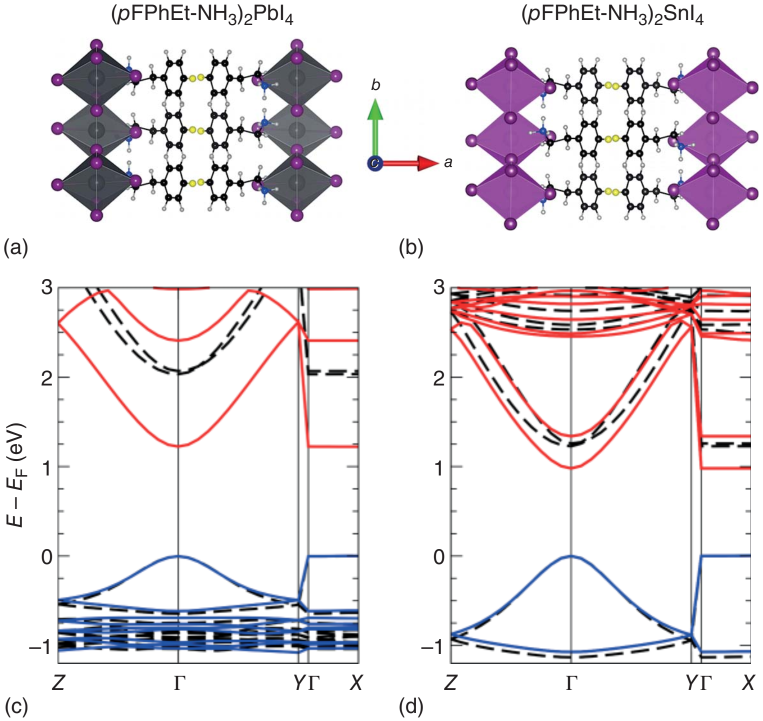

Figure 1.2.3 (a, b) Structure and (c, d) corresponding DFT-computed electronic band structures of $(C_6H_4FC_2H_4NH_3)_2PbI_4$ and $(C_6H_4FC_2H_4NH_3)_2SnI_4$, respectively, computed without (dashed line) and with (straight line) SOC. The zero energy is referenced to the valence band maximum. Source: Pedesseau et al. 2016 [54]. Adapted with permission of American Chemical Society.

for a Cs_2PbI_4 model, keeping the Pb–I distances fixed. Bandgaps calculated for several real layered HOPs are reported on the same color map. The nice agreement with the prediction of the model emphasizes the relevance of β and δ angles as key parameters that control the bandgap in 2D HOPs. For the investigated experimental structures, it appears that the bandgap changes between high- and low-temperature phases are mainly related to the out-of-plane tilt angle δ. Of note, similar deformations of the octahedron also occur along the tetragonal to *Pnma* phase transition in 3D HOPs.

A classical chemical analysis of the atomic bonding for the electronic states close to the band edges was proposed several years ago for halide perovskites, without making explicit reference to the symmetry properties of the perovskite lattice. But it is possible to reconcile chemistry- and physics-based descriptions, through tight binding analyses of the DFT results [48, 64]. Figure 1.2.1 helps to understand why the translational symmetries of the perovskite lattice are important to describe the electronic properties of the halide perovskites close to the bandgap. The symmetrized linear combinations of atomic orbitals (SLCAO) for an isolated BX_6^{4-} octahedron are related to s- and p-orbitals of the metal B and

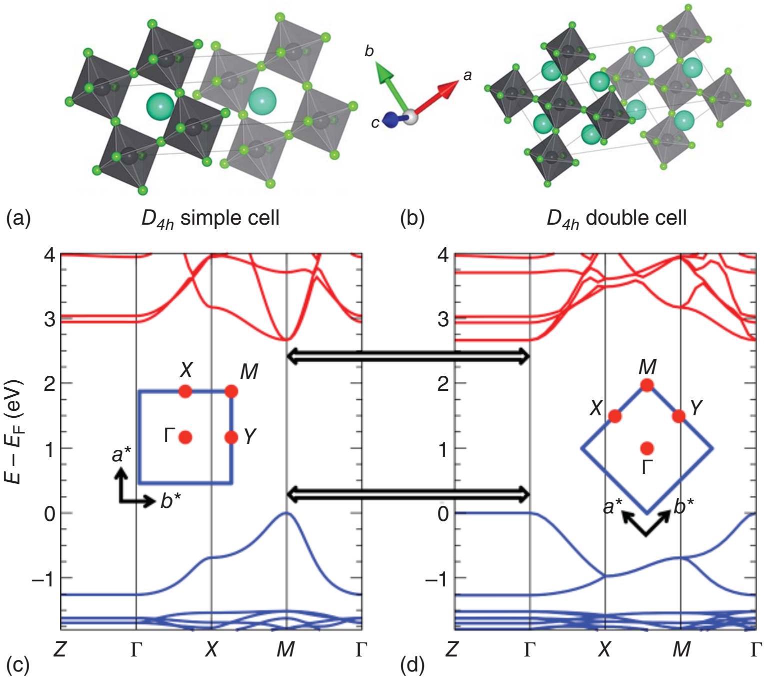

Figure 1.2.4 (a) Artificially designed highly symmetric D_{4h} layered structure of $(Cs)_2PbCl_4$ and (b) the same structure doubled in the (*x*,*y*) plane. (c) Electronic band diagram without SOC for the initial structure. (d) Same band diagram using the BZ of the expanded structure. The band folding from the *M* point to the Γ point is indicated by arrows for CBM and VBM states. Source: Pedesseau et al. 2016 [54]. Adapted with permission of American Chemical Society.

p-orbitals of halogen X. For example, from the inspection of the irreducible representations (IRREPs) of the Oh point group, it becomes straightforward to deduce that hybridization of s(B) and p(X) are allowed by symmetry (A_{1g} IRREP) [59].

Now, when considering a halide perovskite cubic crystal, a similar bonding state involving the same atoms and orbitals at the BZ center Γ is no more possible. Indeed, at Γ, B atoms located along the long diagonal of the cubic cell are expected to have the same local bonding configuration with the surrounding halogen atoms, but this condition cannot be met by considering hybridizations between s(B) and p(X) [48, 59, 60]. On the other hand, a bonding state involving both s(B) and p(X) orbitals is possible at the *R* point of the BZ. This is due to the translational symmetries and to the formation of Bloch electronic states $\Psi_{n,k}(r)$ with a strict dependence on periodic $u_{n,k}(r)$ functions. Thanks to the phase factor of $\Psi_{n,k}(r)$, appropriate antibonding orbital overlap can be recovered.

In terms of symmetry properties of the $Pm\bar{3}m$ space group, s(B) and p(X) orbitals share the same representation R_1^+ at the *R* point. A DFT computation will correctly yield the IRREP decompositions of the $Pm\bar{3}m$ Bloch states, if the cations are compatible with the site symmetries. High-temperature experimental structures of HOP materials are compatible with the $Pm\bar{3}m$ space group, only because the positions of individual atoms of the organic cation are dynamically

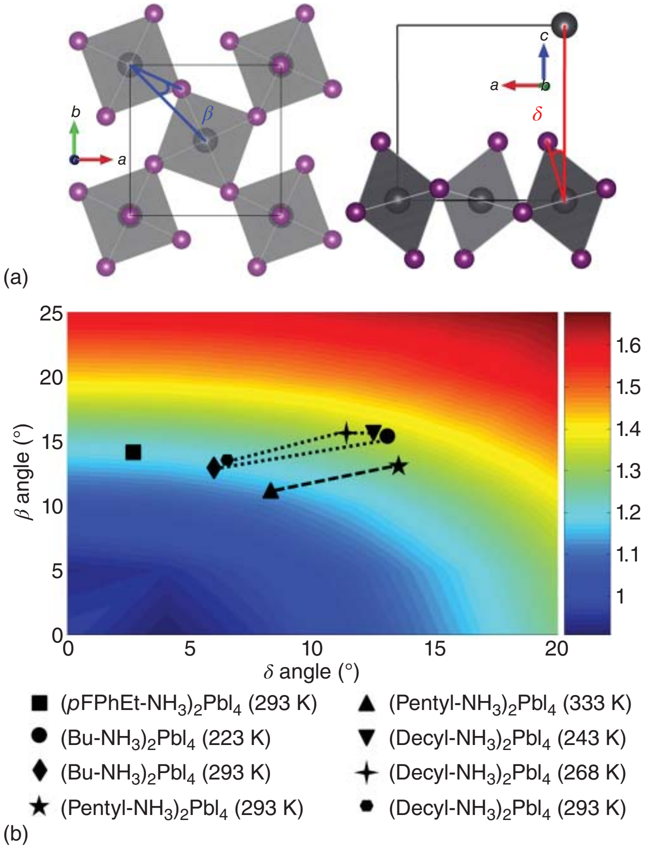

Figure 1.2.5 (a) Schematic representations of the β and δ angles chosen to characterize the in-plane and out-of-plane octahedral tilting. (b) Color map of the computed electronic bandgap including SOC for a distorted $(Cs)_2PbI_4$ reference structure (Figure 1.2.4) as a function of β and δ octahedral tilting angles, with axial d^{ax}_{Pb-I} and equatorial d^{eq}_{Pb-I} distances fixed to 3.18 Å. The β and δ octahedral tilting angles for several experimental structures of layered perovskites are also reported on the color map. Values in the color bar are given in eV. Source: Pedesseau et al. 2016 [55]. Adapted with permission of American Chemical Society.

averaged. Therefore, to mimic this effect one needs to replace the organic cation by an atomic cation (e.g. Cs^+ or Na^+) occupying the same special Wickoff position at the center of the cubic cell.

1.2.3 Importance of Spin–Orbit Coupling (SOC)

Despite an early symmetry analysis highlighting the band splitting due to SOC at the R-edge of the BZ [39], the importance of relativistic effects in halide perovskites have long been obscured by the fortuitous match of the experimental and DFT-computed bandgap of lead iodide perovskites. The situation has improved only recently, almost concomitantly for AIPs [41] 2D [38], and 3D

[42] HOPs. In fact, regardless of the crystal structure, a giant SOC operates on the CB of lead-based AIPs and HOPs. This is illustrated in Figure 1.2.3c for a layered HOP. Even though three times smaller, it remains sizeable in tin-based perovskites, as shown in Figure 1.2.3d. Analysis of the computed band structures of $CH_3NH_3BCl_3$, with B = Pb, Sn, Ge, shows that SOC splittings are consistent with metal atomic energy–level tables with an increase of the splitting down group-14 of the periodic table [48]. Of note, SOC interactions stemming from halogens may also be sizable, especially for iodine-based perovskites, consistently with atomic data [48].

The degeneracy lifting due to SOC contributes to increase the seeming complexity of the band structure. Then, one can turn to symmetry considerations. Considering electron spin effects (e.g. SOC) requires double groups, instead of simple groups whenever such effects can be neglected [42, 47, 59, 60]. Double-space group IRREPs are deduced from the products of the $D_{1/2} = \mathrm{E}_{1/2g}$ electron spin IRREP with the simple space group IRREPs. Bloch functions transform as IRREPs of the double-space group, based on the character table of the space group relevant to the crystal structure of interest. For the $Pm\overline{3}m$ reference phase, they can be analyzed, at Γ and R, using the double-point group IRREPs of Oh. Time-reversal symmetry is also important for spin effects, whether it is combined or not with inversion symmetry close to high symmetry points [59, 61, 65].

More specifically, for the reference cubic phase of 3D HOPs, a good starting point at R are $|\boldsymbol{X}\rangle$, $|\boldsymbol{Y}\rangle$, $|\boldsymbol{Z}\rangle$ bases functions of the simple group R_4^- vectorial IRREPs of the CBM and the corresponding energy E^0_{CBM}. The spinor state basis transforms into $|\boldsymbol{X}\uparrow\rangle$, $|\boldsymbol{Y}\uparrow\rangle$, $|\boldsymbol{Z}\uparrow\rangle$, $|\boldsymbol{X}\downarrow\rangle$, $|\boldsymbol{Y}\downarrow\rangle$, $|\boldsymbol{Z}\downarrow\rangle$. CBM becomes a twofold degenerate spin–orbit split-off (SO) state of energy $E_{(\mathrm{so})} = E^0_{\mathrm{CBM}} - 2\Delta_{\mathrm{SO}}/3$, with Δ_{SO} the energy splitting resulting from SOC. The remaining fourfold degenerate CB states undergo a positive energy shift, $E = E^0_{\mathrm{CBM}} + \Delta_{\mathrm{so}}/3$. Thus, at R, the simple group R_4^- vectorial representation of the CBM splits in a doubly degenerated R_6^- ($\mathrm{E}_{1/2u}$) SO state and a fourfold degenerated R_8^- ($\mathrm{F}_{3/2u}$) light electron (LE) and heavy electron (HE) state (Figure 1.2.6). In this case, the ground-state isotropic optical transition stems from the transition between the doubly degenerated R_6^+ valence band maximum (VBM) and R_6^- CBM states. At R, a series of other transitions are optically allowed. The lowest in energy corresponds to two secondary transitions, $R_8^+ \rightarrow R_6^-$ and $R_6^+ \rightarrow R_8^-$. Isotropic optical activity is also found at M, given that for a pseudocubic phase the star of $\mathbf{k}_{\mathrm{M}}$ contains three arms (Figure 1.2.6) [47]. Besides, SOC leads to a dramatic reduction of oscillator strengths or, alternatively, Kane energy. For instance, in $CH_3NH_3PbI_3$ the latter drops to c.a. 6 eV, i.e. about four times smaller than that of GaAs. This in addition to a reverse band ordering are among the main differences between conventional semiconductors and halide perovskites.

The impact of SOC can be empirically or semiempirically rationalized by considering the spinor state basis and adding a perturbation Hamiltonian accounting for SOC [61, 64]. For instance, the lattice distortion at the cubic-tetragonal phase transition in 3D AIPs and HOPs combined with SOC leads to a complete splitting of the vectorial representation, whereas only a partial splitting is predicted when SOC is not taken into account. For such a tetragonal lattice distortion, the three

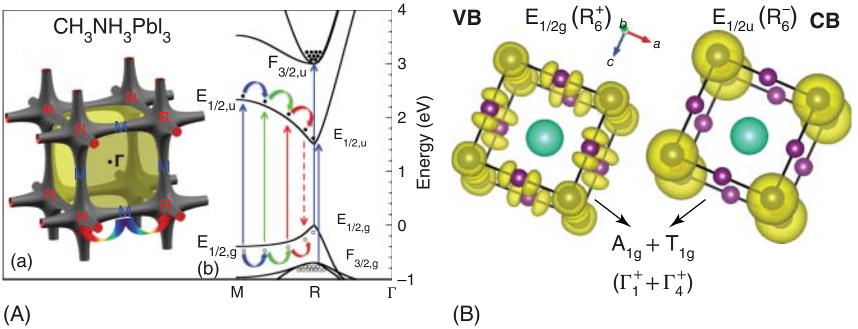

Figure 1.2.6 (A) (a) Fermi surface ($E = -0.5$ eV) in the first BZ. The points R and M of the BZ are connected along the edges, highlighting the saddle point nature of M. (b) Electronic band structure for the high-temperature cubic $Pm\overline{3}m$ phase of $CH_3NH_3PbI_3$ with SOC at the LDA (local density approximation) level of theory. An upward energy shift of 1.4 eV has been applied to match the experimental band gap value at R. Labels of double-group irreducible representations (IRREP) are given at R and M for electronic states close to the bandgap. Vertical arrows show various possible optical transitions close to the bandgap energy. Optical transitions along the M–R line generate carriers that can relax easily toward R. Source: Even et al. 2014 [47]. Copyright 2014. Adapted with permission of American Chemical Society. (B) The electronic densities for both the valence band (VB) and the conduction band (CB) lead to the same IRREP decomposition at the Γ point, when the SOC is taken into account.

eigenvalues of the Hamiltonian are doubly degenerated and can be analytically calculated at the critical point of the BZ, e.g. the R point in the cubic phase:

$$E_0 = E^0_{\mathrm{CB}} + (l + m)\varepsilon_{xx} + m\varepsilon_{zz} + \Delta_{\mathrm{SO}}/3$$

$$E_\pm = E_0 \frac{\delta E + \Delta_{\mathrm{SO}}}{2} \pm \sqrt{\left(\frac{\delta E - \Delta_{\mathrm{SO}}/3}{2}\right)^2 + 2\Delta^2_{\mathrm{SO}}/9}$$

where l, m, and n are deformation potentials and $\delta E = (l - m)(\varepsilon_{xx} - \varepsilon_{zz})$, and ε_{ij} are the components of the lattice strain tensors, which can be derived from experimental or DFT data. In lead halide perovskites, the effect of strain is systematically smaller than that induced by SOC. Close to the $Pm\overline{3}m/I4mcm$ phase transition, strain tensor components should exhibit a quadratic dependence with octahedra rotation. Thus, at least for small angles, the bandgap should show a quadratic variation with the rotation angle and, indeed, DFT simulations evidenced a $[(T_c - T)^{0.25}]^2$ behavior [60].

Now, when taking SOC into account in DFT, the calculated bandgaps of AIPs and HOPs appear substantially underestimated as illustrated in Figure 1.2.2 for the $Pm\overline{3}m$ phase of $CH_3NH_3PbI_3$ with a computed bandgap <0.1 eV, whereas the experimental optical bandgap amounts to c.a. 1.6 eV [41, 44]. This well-known limitation of DFT can be cured by including many-body effects. These afford more accurate effective masses of the carrier, both for conventional semiconductors and metal-halide perovskites. In HOPs, substantial increase of the bandgap has already been achieved by performing a one-shot GW correction on the DFT + SOC energies [42, 53, 61]. The quasi-particle corrections to the bandgap are large and in a direction opposite to that of SOC, whatever the metal

(B = Pb, Sn or Ge) [48]. Further improvement is obtained using self-consistent GW corrections for the bandgap [55–58]. Even though calculated bandgaps come closer to the experimental ones, differences may remain sizeable. In fact, several parameters have been shown to influence the computed properties in 3D HOPs, especially bandgaps and effective hole and electron masses: (i) SOC effects and GW corrections are nonadditive, (ii) they depend on the starting Kohn–Sham orbitals, (iii) the crystal structure in use should be relevant to experimental conditions, for instance, the P_C space group should be used for $CH_3NH_3SnCl_3$ at room temperature and the replacement of MA by Cs^+ to afford appropriate site symmetry constitutes an approximation.

1.2.4 Interplay of SOC and Loss of Inversion Symmetry: Rashba and Dresselhaus Effects

The large SOC occurring in the CB of lead-based HOPs and AIPs makes them promising candidates for spin-based applications. In that prospect, Rashba and Dresselhaus effects play a central role. They originally correspond to spin splittings occurring in zinc-blende and würtzite structures, respectively. Later, evidence of Rashba and Dresselhaus effects have been observed in various compounds, such as quasi-2D or heterostructures, nanowires, or quantum wells. In the case of HOPs, **k**-dependent spin-splitting was first predicted for $CH_3NH_3BI_3$ [61] and since confirmed by numerous theoretical studies [57, 63, 65, 68, 69].

Theoretical investigation of Rashba and Dresselhaus effects needs to consider both time reversal and inversion symmetries [61, 65]. The first yields the general conditions for conjugated spinor states: $\varepsilon_{n\uparrow}(\mathbf{k}) = \underline{\varepsilon_{n}}_{\downarrow}(-\mathbf{k})$ and $\varepsilon_{n\downarrow}(\mathbf{k}) = \varepsilon_{n\uparrow}(-\mathbf{k})$, where $\varepsilon_{n\downarrow}$ and $\varepsilon_{n\uparrow}$ are the eigenvalues of the spinor states for $s = -1/2$ and $+1/2$, respectively. Inversion symmetry yields additional conditions: $\varepsilon_{n\uparrow}(\mathbf{k}) = \varepsilon_{n\uparrow}(-\mathbf{k})$ and $\varepsilon_{n\downarrow}(\mathbf{k}) = \varepsilon_{n\downarrow}(-\mathbf{k})$. Considering both symmetries lead to a double-spin degeneracy across all the dispersion diagram within the BZ, $\varepsilon_{n\uparrow}(\mathbf{k}) = \varepsilon_{n\downarrow}(\mathbf{k})$. When inversion symmetry is lost, this spin degeneracy condition can be lost for a general wave vector, except for special high-symmetry points. For instance, in zinc-blende and würtzite structures, the loss of inversion symmetry combined with SOC induces a splitting of the spinor bands away from Γ.

Distinction between Rashba and Dresselhaus effects can be envisioned by considering a quasi-2D structure (in-plane: (x, y)) having C_{2v} symmetry and limiting the expression of the linear terms. Then, the Rashba–Dresselhaus Hamiltonian reads [65]:

$$H_{\mathrm{RD}}(\boldsymbol{k}_{\parallel}) = \lambda_{\mathrm{R}}(k_x\sigma_y - k_y\sigma_x) + \lambda_{\mathrm{D}}(k_x\sigma_x - k_y\sigma_y)$$

where $\boldsymbol{k}_{\parallel} = (\boldsymbol{k}_x, \boldsymbol{k}_y)$, σ_x and σ_y are the in-plane components of the Pauli spin matrices, λ_{R} and λ_{D} the Rashba and Dresselhaus parameters, characteristic of the strength of respective effects. When $\lambda_{\mathrm{D}} = 0$, one recovers the pure Rashba effect that is related to site inversion asymmetry (SIA). When $\lambda_{\mathrm{R}} = 0$, one retrieves the term related to bulk inversion asymmetry (BIA) that is usually found in zinc-blende structures. Computing the expectation value of the Pauli operator

$\langle \sigma \rangle_{\pm}$ allows deducing the relative strength of each effect (spin texture). While for C_{2v} symmetry the spin distribution remains in-plane up to the cubic terms, for point groups such as C_{3v} or D_{2d} the latter may contain contributions involving σ_z. To theoretically evidence Rashba–Dresselhaus effects, one has to compute both the band structure and the spin texture close to the relevant high-symmetry point of the BZ and take care to appropriately define $\boldsymbol{k}_{\parallel}$ based on the symmetry of the crystal structure of interest.

Theoretical prediction of Rashba–Dresselhaus effects was first exemplified for hybrid ABX_3 bulk structures. Starting from the reference highly symmetrical cubic phase of the $Pm\bar{3}m$ space group, one can follow the different phase transitions possible and select the ones leading to loss of inversion symmetry. Figure 1.2.7 provides examples of hybrid ABX_3 bulk structures belonging to $P4mm$, $R3m$, and $Amm2$ space groups. The first corresponds to a translation of the ions along the z direction. It is exemplified using $CH_3NH_3PbI_3$ in the $P4mm$ phase (Figure 1.2.7a). The C_4 axis naturally defines the perpendicular direction. Thus, $\boldsymbol{k}_{\parallel}$ can be defined by the two vectors $\boldsymbol{k}_x = [100]$ and $\boldsymbol{y}_x = [100]$ and A $(1/2, 1/2, 1/2)$ corresponds to the critical point of interest. SOC has three effects on the band structure: the bandgap is significantly reduced (Section 1.2.3), VBM and CBM are displaced away from the high-symmetry point A and split. For all four bands, the spin textures reveal spins orthogonal to the crystal momenta (Figure 1.2.7d). This corresponds to the pure Rashba effect. The strength of the Rashba effect is given by $\lambda_R = \Delta E/2k_R$, where ΔE is the the energy splitting and k_R the momentum shift. The Rashba splitting of VBM and CBM amount to c.a. 3.7 eV Å and are thus comparable to the largest splittings experimentally measured in bulk materials.

Translating simultaneously the ions along the three crystallographic axes enables to go from the $Pm\bar{3}m$ to the $R3m$ space group, which has C_{3v} point group symmetry. The effect of such a transformation is illustrated in Figure 1.2.7b, taking as an example $CH_3NH_3GeI_3$. The quantization axis, that is C_3, is parallel to $[1, 1, 1]$. Thus, the appropriate plane to investigate the spin splitting is defined from the $[1, \bar{1}, 0]$ and $[1, 1, \bar{2}]$ directions, and the relevant critical point is L $(-1/2, 1/2, 1/2)$. Except for a more pronounced splitting in the CB ($\lambda_R = 0.89$ eV Å) as compared to the VB ($\lambda_R = 0.45$ eV Å), the overall features are weaker (consistently with atomic SOC splittings) but similar to that obtained for $CH_3NH_3PbI_3$ with $P4mm$ space group, with spin textures characteristic of the pure Rashba effect (Figure 1.2.7e).

By implementing twin translations of ions along the x and y crystallographic axes, the crystal structure changes from the $Pm\bar{3}m$ to the $Amm2$ space group, which has C_{2v} point group symmetry and a C_2 axis in the $[0, 1, 1]$ direction. The resulting band structure and spin textures are illustrated in Figure 1.2.7c,f taking $CH(NH_2)_2SnI_3$ as an example and probing the $[1, 0, 0]$ and $[0, 1, \bar{1}]$ directions around R $(1/2, 1/2, 1/2)$. The spin textures shown in Figure 1.2.7f significantly differ from the two previous examples, evidencing simultaneous Rashba and Dresselhaus effects, with $\lambda_R = 0.5$ eV Å and $\lambda_D = 2.6$ eV Å in the CBM. The effect is much weaker in the VBM.

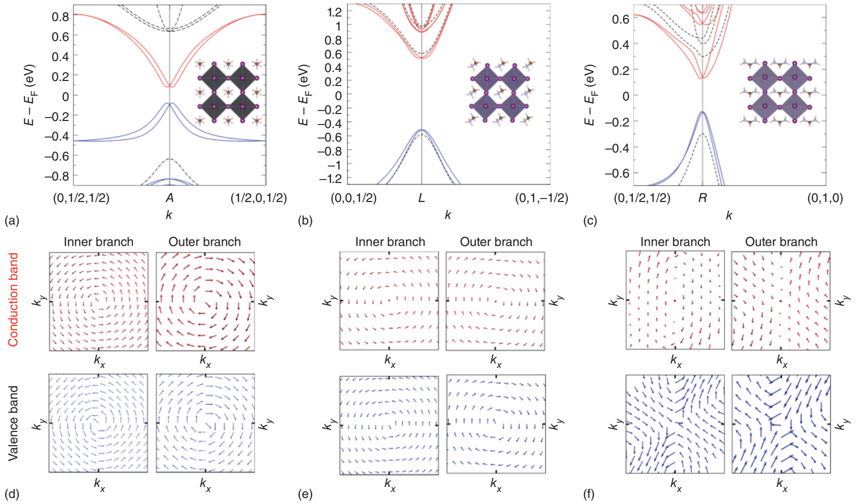

Figure 1.2.7 Hybrid organic inorganic halide perovskites crystallized in phases corresponding to a ferroelectric phase transition from $Pm\bar{3}m$. (a) Band structure and structure (inset) of $CH_3NH_3PbI_3$ in the *P4mm* phase. Straight and dashed lines are the results with and without SOC, respectively. (b) Same in the case for $CH_3NH_3GeI_3$ in the *R3m* phase. (c) Same in the case for $CH(NH_2)_2SnI_3$ crystallized in the *Amm*2 group. (d–f) Spin textures for the inner and outer branches for both occupied and unoccupied bands of $CH_3NH_3PbI_3$, $CH_3NH_3GeI_3$, and $CH(NH_2)_2SnI_3$, respectively. Source: Kepenekian et al. 2015 [65]. Copyright 2015. Reprinted with permission of American Chemical Society.

Rashba–Dresselhaus effects have also been predicted for layered perovskites [65]. This is illustrated with Bz_2PbCl_4, already mentioned in Section 1.2.2 [66, 67] and shown as an inset in Figure 1.2.8a. Its high-temperature phase is reported to belong to the *Cmca* space group with D_{2h} point symmetry. Thus, it does not present any spin-splitting and related Rashba–Dresselhaus effect. Contrarily, at low temperature ($Cmc2_1$ space group), the band structure reveals clear spin splitting along $\Gamma \rightarrow Y$ (Figure 1.2.8a). No spin splitting occurs along $\Gamma \rightarrow Z$ because the C_2 quantization axis is along the [0, 0, 1] direction. Of note, there is no dispersion along $\Gamma \rightarrow X$ as it corresponds in real space to the stacking axis ([1, 0, 0]) where the inorganic sheets are well separated from each other thanks to the benzylammonium organic cations. This situation differs notably from that observed in

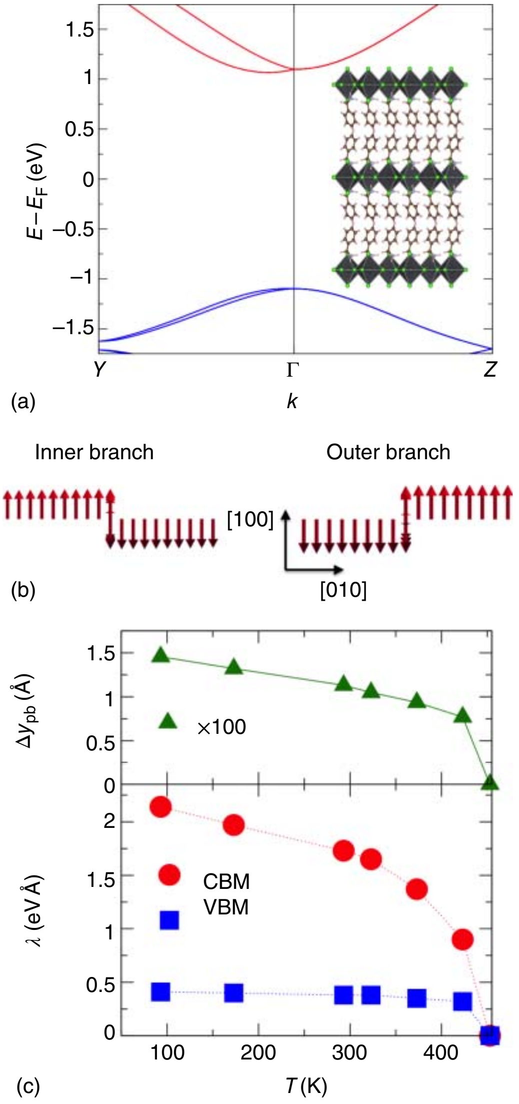

Figure 1.2.8 (a) Band structure of $(C_7H_7NH_3)_2PbCl_4$ in the low-temperature $Cmc2_1$ phase, computed with SOC. (b) Spin textures for the inner and outer branches of the conduction band. (c) Temperature dependence of the Pb displacement along *y* (see text) and computed Rashba parameters for the conduction and valence bands. Source: Kepenekian et al. 2015 [65]. Copyright 2015. Reprinted with permission of American Chemical Society.

conventional semiconductors, because the quantization and stacking axes do not coincide. The strength of the Rashba–Dresselhaus effect can be analyzed on the basis of a 1D model, which involves only k_y. No observable (e.g. $\langle\sigma\rangle_{\pm} \propto \mp k_y/|k_y|$, Figure 1.2.8b) allows making the distinction between Rashba- or Dresselhaus-like nature of the spin splitting, which strength can be quantified by

$$\lambda = \frac{\Delta E_{\mathrm{RD}}(k_y)}{2k_y}$$

Figure 1.2.8c shows the corresponding amplitudes as a function of temperature in the VBM and CBM, which correlate nicely with the displacement of the Pb atoms along the y-axis. In fact, besides the order–disorder character related to the disordered orientations of the organic cations in the *Cmca* phase, the phase transition to $Cmc2_1$ corresponds to displacive distortions with atomic displacements in the inorganic layers with an order parameter belonging to the $\mathrm{B_{1u}}$ IRREP of the D_{2h} point group. Analysis of the phonon modes in the *Cmca* space group reveals that the $\mathrm{B_{1u}}$ IRREP shows up in the mechanical representations of both the Pb and Cl atoms: it involves an antiparallel motion of two lead (or chlorine) atoms along the y axis and parallel motion along z. A similar study can be performed for another layered HOP $(\mathrm{CH_3NH_3})_2\mathrm{Pb(SCN)_2I_2}$ [70–72], where the "incomplete" Rashba-like effect is due to the alignment of the high-symmetry axis perpendicular to the stacking axis in the crystallographic structure [54].

1.2.5 Collective Vibrations, Stochastic Cation Reorientations, and Molecular Dynamics

Most applications of halide perovskite materials such as photovoltaic cells, photodetectors, or light-emitting diodes require room temperature or above room temperature operation. It is thus important to understand the origin of the stability of the crystallographic phases at high temperature, using energetic but also entropy considerations. Halide perovskite crystals very often present structural instabilities. Investigation of the structural phase transitions in halide perovskites may thus yield useful information. The predictions of the structural instabilities in these materials are severe tests for any attempt of a theoretical description of these phenomena. Of note, the metastability of the perovskite phase of various halide materials and alloys is a well-known issue for photovoltaic device stability. In 3D HOPs such as $\mathrm{FAPbI_3}$, this specific phenomenon is related to a transition from the perovskite phase to a so-called yellow non-perovskite phase.

Besides, in conventional semiconductors, various collision processes with the lattice phonons, which represent the structural excitations of the crystal, affect charge carrier (electrons and holes) mobilities. A precise description of these processes is still lacking for halide perovskites, but several theoretical approaches have been proposed recently to clarify this aspect. The optical absorption and, more generally, the optoelectronic properties of HOPs close to the electronic bandgap, also exhibit excitonic contributions. These excitonic features are screened in 3D materials at high temperature, leading to carrier mobilities dominated by free carriers [47]. Screening mechanisms can be ascribed to variations of the dielectric constant. These variations, which are related to various contributions from the polar structural excitations of the system, are not yet completely understood in HOPs.

The phonons are collective vibrational excitations, which can lead to structural instabilities. The phonons are classically represented by energy dispersions in the BZ. Despite the practical importance of HOPs, a complete experimental description of the phonon spectrum is still lacking, although some progress has been made recently using various phonon spectroscopy techniques [73]. The vibrations of the halide perovskite lattice are highly damped in most cases at high temperature [60]. Moreover, from Debye Waller factor measurements by diffraction techniques, it has been shown experimentally that the motion of halide atoms is strongly anharmonic [74]. When considering the vibrational properties of the cubic perovskite lattice, the symmetry analysis of the lattice modes at the Γ point yield $3\Gamma_4^- + \Gamma_5^-$ [59, 60]. The three acoustic modes belong to Γ_4^-. Some of the Γ_4^- optical phonons are active in infrared spectroscopy, while the Γ_5^- optical phonon mode is neither active in Raman scattering nor in infrared spectroscopy.

The inspection of the optical modes and symmetries at the edge of the BZ may yield some guidance for the prediction of structural instabilities from DFT-based studies. For instance, a triply degenerated R_4^+ phonon mode, involving only motions of the halide atoms and rotations of the octahedra, is expected to be involved in the structural instabilities of $\mathrm{MAPbX_3}$ compounds in a displacive picture. From the point of view of first-principles simulations, a first approach consists in computing the phonon spectrum from a dynamical matrix in the harmonic approximation. The interatomic forces are either obtained from a finite difference method or from a density functional perturbation theory (DFPT) implementation available in several softwares. The description of the full phonon spectrum can be used to extract complex quantities such as the electron–phonon coupling matrix elements relevant for the description of the relaxation and mobility of charge carriers [75]. The complexity and high computational cost of such approaches may explain the slow progress made for HOPs in this respect.

Tackling the contribution of the anharmonicity of phonons in HOPs is also a difficult issue. However, for the reference cubic lattice, a symmetry analysis of the possible electron–phonon coupling mechanisms shows that the collision processes with acoustic and optical phonons should be dominated by deformation potential and Fröhlich polar mechanisms, respectively [8, 76]. A second alternative suited for systems exhibiting strong structural fluctuations is the use of MD simulations, which have been essentially implemented at the DFT level [60, 77–81] and, more rarely, using classical force fields [82]. The phonon spectrum can be extracted via the Fourier transform of the velocity–velocity autocorrelation functions of the atoms.

Meanwhile, MD has also been intensively used in the past years to describe the relaxational motions in HOPs. These motions are related either to the migration of various ionic species and defects in the perovskite lattice or to stochastic reorientations of the organic cations in HOPs. The first case is important, since processes involving ion migration have been proposed to explain several experimental observations, such as hysteresis in perovskite photovoltaic devices, degradation mechanisms, or additional contributions to the dielectric constant at very low frequency. The second case corresponds to thermally activated molecular reorientations operating in 3D HOPs containing small cations such as MA or FA. In fact, interpretation of early millimeter wave spectroscopy, NMR, and dielectric measurements performed at high temperature on MA-based HOPs [83–86] relied on a simple picture: the MA cations were expected to tumble between various discrete dipole orientations. This simplified description can be connected to the concept of pseudospins that accounts for the symmetry properties of the lattice [59, 60]. This framework allows computing the entropy contribution to the structural phase transition. Order–disorder mechanisms were indeed proposed to drive the structural instabilities in 3D HOPs, in contrast to displacive processes that are related classically to phonon softening [60]. When such plastic crystals are cooled, the rotational motion may freeze, leading to an orientational order at low temperature. Recent experimental studies of phase transitions in halide perovskites show that the picture can be even more complex, because translation–rotation coupling processes may correspond to mixed order–disorder and displacive mechanisms for the phase transitions [60, 73, 87]. Using discrete pseudospins also led to simple framework to model relaxation processes [60, 84]. The latter were also investigated recently by inelastic incoherent and coherent neutron scattering on $MAPbI_3$ and $MAPbBr_3$ [73, 87–89]. Molecular relaxational processes in MA-based compounds correspond at least to two different dynamics, the first one being attributed to the reorientation of the C–N molecular axis and the second to the rotation around the same axis. The first motion is expected to be frozen at low temperature, but experimental evidences point toward a dynamics around the C–N axis remaining active at low temperature [89–91].

DFT-based MD simulations proved efficient to investigate these complex phenomena. For instance, they revealed that the discrete pseudospin picture may be an oversimplification. In fact, as highlighted in Figure 1.2.9a, the probability distribution functions are rather continuous, as compared to KCN or NaCN [60]. Nevertheless, it remains possible to systematically account for the symmetry properties of the perovskite lattice by introducing symmetry-based cubic harmonics [60, 81]. Compared to MA, the specific symmetry of the FA cation leads to the definition of and additional orientation variable perpendicular to the polar axis that can also be described through specific orientational maps. The dynamics of the various relaxation mechanisms can be extracted by computing the autocorrelation functions [60, 81]. Ab initio MD simulations show that the relaxation is faster perpendicular to the polar axis of the FA cations. The relaxation of the individual MA and FA molecules allows investigating the heterogeneity of the dynamical processes in the crystal. A large distribution of relaxation times is obtained from the simulation and may result from frustrated interactions (Figure 1.2.9b) [60]. The absence of long-range spatial correlations between the molecular orientations combined with a freezing of the orientations at low temperature may lead to a glassy state. Indeed, from MD simulations an orientational glass behavior has been predicted to take place in 3D HOPs [60].

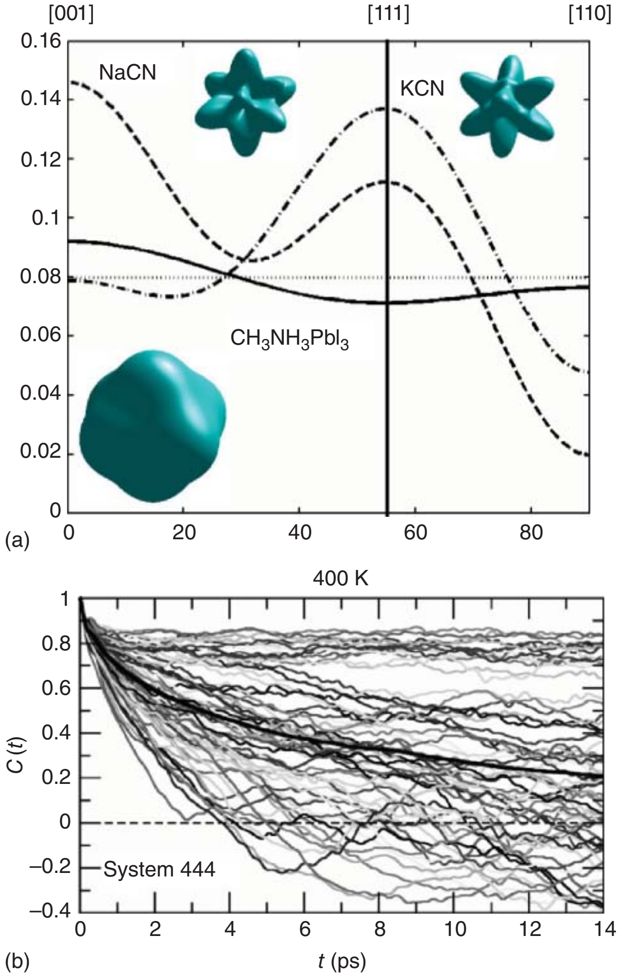

Figure 1.2.9 (a) Angular dependence ($\varphi = 45°$ and $\theta = [0 : 90°]$) of the probability distribution functions relevant for Γ_1^+ for molecular orientation in NaCN (dashed line) and KCN (dashed-dotted line) and for $CH_3NH_3PbI_3$ (solid line) obtained from MD simulation at 450 K. 3D representations of the corresponding rotator functions are also inserted. It corresponds to symmetry-adapted cubic harmonic expansions. (b) Time dependence of the autocorrelation function of the Γ_4^- vectorial representation for all molecules within a 444 supercell of $CH_3NH_3PbI_3$ extracted from MD simulation at $T = 400$ K. The average time dependence is plotted in bold dark for comparison. Source: Even et al. 2016 [60]. Reproduced with permission of Royal Society of Chemistry.

Recent experimental results are consistent with this hypothesis [90, 91], but it deserves further investigations.

DFT-based MD also revealed an odd/even effect on calculated properties, related to the supercell size considered to perform the simulation [60, 81]. Comparison of MA- and FA-based 3D HOPs helped determine the origin of this odd/even effect, i.e. to distinguish between (i) effect of improper BZ sampling (Figure 1.2.10a) or (ii) frustrated dipolar coupling of molecular cations belonging to neighboring cells (Figure 1.2.10b) [48]. Considering that FA has an almost vanishing electric dipole moment and that both the FA- and MA-based HOPs present similar trends, it can be concluded that the main origin of this odd/even effect stems from the inadequate description of the phase factor of the electronic wave function introduced from the sole Γ-point sampling combined with an odd number of cell replicas in at least one direction of the supercell (Figure 1.2.10a). In other words, the ability of an MD simulation to properly

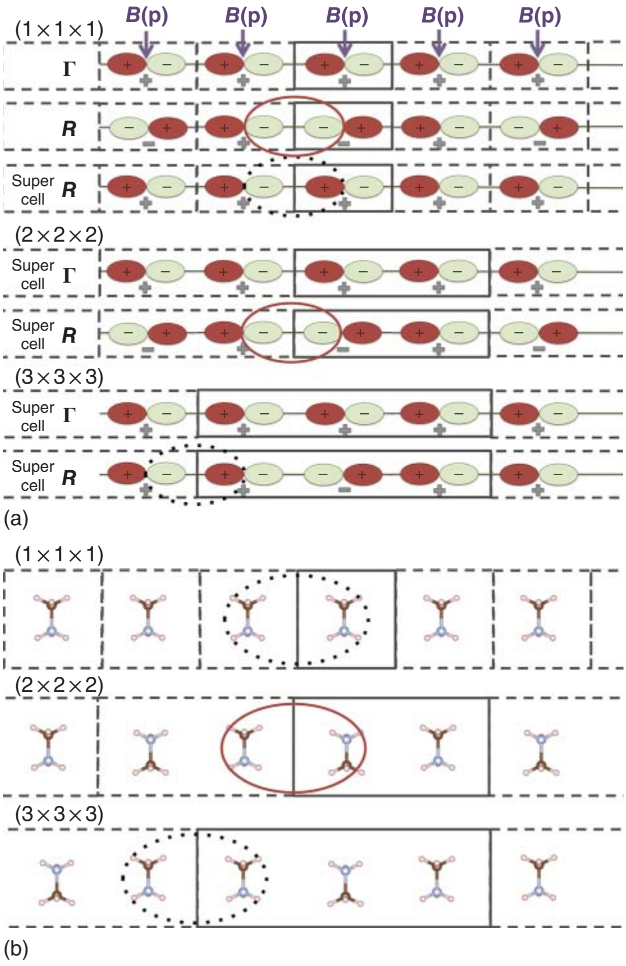

Figure 1.2.10 (a) Schematic view based on a linear chain of p-atomic orbitals of the metal, labeled *B*(p), illustrating proper (straight line oval) and improper (dotted line oval) account of the wavefunction phase factor at the BZ center (Γ) and boundary (*R*). (b) Effect of odd and even numbers of unit cells on molecular interactions exemplified with a linear chain of CH_3NH_3 molecules highlighting the presence of unphysical ferroelectric dipole–dipole interaction (dotted line oval). Source: Even et al. 2016 [60]. Reproduced with permission of Royal Society of Chemistry.

predict the structural properties of HOPs strongly depends on its ability to capture the bonding/antibonding character of the electronic wave function defined by the perovskite inorganic lattice. It is also indicative of a strong coupling between the structural and the electronic excitations, which cannot be easily captured by classical MD approaches [82].

The contributions of stochastic molecular relaxations and polar phonons to the frequency-dependent dielectric constant $\varepsilon(\omega)$ of 3D halide perovskites are schematically plotted in Figure 1.2.11 [47]. At high temperature and low frequency, $\varepsilon(\omega)$ undergoes a further increase in HOPs. This dielectric increment is attributed to the tumbling of the C–N axis of the MA cations in $CH_3NH_3PbX_3$, which is activated above the orthorhombic to tetragonal phase transition. Unfortunately, DFT simulations of such molecular relaxation contributions to the dielectric constant are still lacking.

For layered halide perovskites, the enhanced exciton binding energy of layered HOPs has been attributed to dielectric confinement effects [11–13, 20, 36]. Such effects can be investigated thanks to an original computational scheme allowing for DFT-computed dielectric profiles [52] i.e. beyond phenomenological approximation of abrupt dielectric-constant changes at the organic–inorganic interfaces [36]. This is illustrated in Figure 1.2.12 by computing the infinite and static dielectric constant profiles for slabs of 3D, 2D, as well as 2D/3D RP HOPs. The latter have a general crystal structure of the form $A_{n-1}A'_2B_nX_{3n+1}$, where $n = 1$ correspond to a 2D monolayered perovskite and $n = \infty$ to a 3D perovskite. A and A′ are small and large organic cations, respectively. In the case of layered HOPs, the profile of the high-frequency dielectric constant presents a clear dielectric contrast between the low dielectric constant of the organic part and the high dielectric

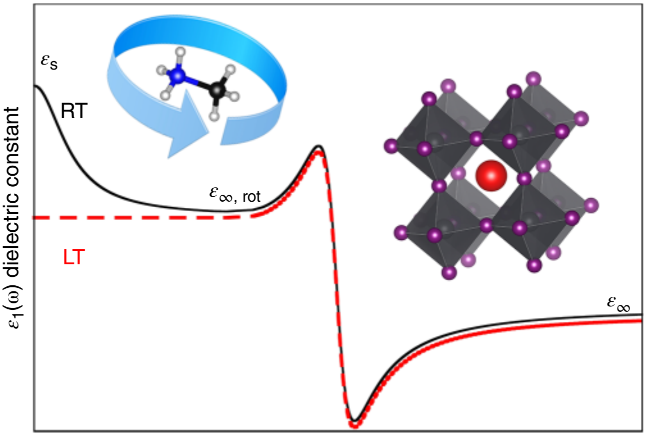

Figure 1.2.11 Frequency dependence of the dielectric constant of $CH_3NH_3PbX_3$ as derived from available experimental data. The high-frequency response is related to vibrational polar phonons stemming from modes of the perovskite lattice (right-hand side). The low-frequency region (left-hand side) shows significant differences for the low (LT, dashed line) and room (RT, straight line) temperature phases. The static dielectric constant (ε_S) increase at RT is primarily attributed to rotational motion of $CH_3NH_3^+$ cations. Source: Even et al. 2014 [47]. Copyright 2014. Reprinted with permission of American Chemical Society.

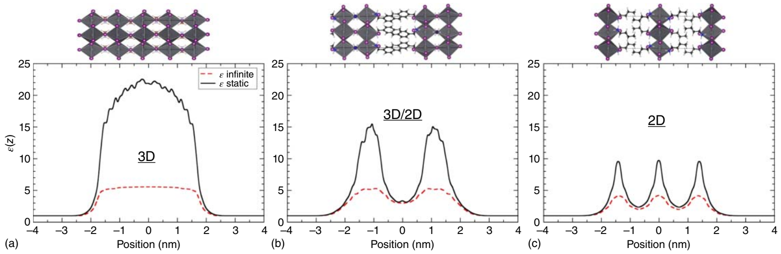

Figure 1.2.12 Infinite (dashed lines) and static (straight lines) dielectric profiles for slabs of $CH_3NH_3PbI_3$ (a), of the 3D/2D hybrid perovskite $(C_{10}H_{24}N)_2PbI_3CH_3NH_3PbI_4$ (b), and of the 2D hybrid perovskite $(C_4H_{12}N)_2PbI_4$ (c).

constant of the inorganic part. For all 2D materials with $n = 1$, the computed value for the inorganic part is about 4. This value is lower than the bulk value of 3D materials. The dielectric constant obtained for aromatic cation A′ amounts to about 3, while that of aliphatic chains A′ is closer to 2. These values are in agreement with the experimental high-frequency dielectric constants reported in the literature for such organic molecules. The difference explains the enhancement of the exciton binding energy in RP phases made of aliphatic chains.

Of note, such an ab initio determination of the dielectric profile can be combined with an empirical implementation of the BSE to compute the Green's function of the exciton, and subsequently the full absorption spectrum [54]. Besides, at low excitation frequency, atoms can move and participate in the polarization of the lattice and yield additional contributions to the dielectric constant profiles [52]. Changes are particularly important in the inorganic region, as illustrated in Figure 1.2.12. For instance, in layered perovskites, the static profiles reveal clear additional contributions to the dielectric constant stemming from polar phonons. Unfortunately, and contrary to what is known for 3D halide perovskites, in layered RP HOPs, neither experimental nor theoretical information on phonons is available and this clearly deserves further investigations by DFT approaches.

References

1 Kojima, A., Teshima, K., Shirai, T., and Miyasaka, T. (2009). Organometal halide perovskites as visible-light sensitizers for photovoltaic cells. *J. Am. Chem. Soc.* 131: 6050–6051.

2 Lee, M.M., Teuscher, J., Miyasaka, T. et al. (2012). Efficient hybrid solar cells based on meso-superstructured organometal halide perovskites. *Science* 338: 643–647.

3 Kim, H.-S., Lee, C.-R., Im, J.-H. et al. (2012). Lead iodide perovskite sensitized all-solid-state submicron thin film mesoscopic solar cell with efficiency exceeding 9%. *Sci. Rep.* 2: 591.

4 Burschka, J., Pellet, N., Moon, S.-J. et al. (2013). Sequential deposition as a route to high-performance perovskite-sensitized solar cells. *Nature* 499: 316–319.

5 Liu, M., Johnston, M.B., and Snaith, H.J. (2013). Efficient planar heterojunction perovskite solar cells by vapour deposition. *Nature* 501: 395–398.

6 Green, M.A., Ho-Baillie, A., and Snaith, H.J. (2014). The emergence of perovskite solar cells. *Nat. Photonics* 8: 506–514.

7 Nie, W., Tsai, H., Asadpour, R. et al. (2015). High-efficiency solution-processed perovskite solar cells with millimeter-scale grains. *Science* 347: 522.

8 Nie, W., Blancon, J.-C., Neukirch, A.J. et al. (2016). Light-activated photocurrent degradation and self-healing in perovskite solar cells. *Nat. Commun.* 7: 11574.

9 Bi, D., Tress, W., Dar, M.I. et al. (2016). Efficient luminescent solar cells based on tailored mixed-cation perovskites. *Sci. Adv.* 2: e1501170.

10 Saliba, M., Matsui, T., Domanski, K. et al. (2016). Incorporation of rubidium cations into perovskite solar cells improves photovoltaic performance. *Science* 354: 206.

11 Ishihara, T., Takahashi, J., and Goto, T. (1990). Optical properties due to electronic transitions in two-dimensional semiconductors $(C_nH_{2n+1}NH_3)_2PbI_4$. *Phys. Rev. B* 42: 11099–11107.

12 Koutselas, I.B., Ducasse, L., and Papavassiliou, G.C. (1996). Electronic properties of three- and low-dimensional semiconducting materials with Pb halide and Sn halide units. *J. Phys. Condens. Matter* 8: 1217–1227.

13 Papavassiliou, G.C. (1997). Three- and low-dimensional inorganic semiconductors. *Prog. Solid State Chem.* 25: 125–270.

14 Kagan, C.R., Mitzi, D.B., and Dimitrakopoulos, C.D. (1999). Organic–inorganic hybrid materials as semiconducting channels in thin-film field-effect transistors. *Science* 286: 945–947.

15 Mitzi, D.B., Chondoudris, K., and Kagan, C. (2001). Organic–inorganic electronics. *IBM J. Res. Dev.* 45: 29–45.

16 Saparov, B. and Mitzi, D.B. (2016). Organic–inorganic perovskites: structural versatility for functional materials design. *Chem. Rev.* 116: 4558–4596.

17 Slavney, A.H., Hu, T., Lindenberg, A.M., and Karunadasa, H.I. (2016). A bismuth-halide double perovskite with long carrier recombination lifetime for photovoltaic applications. *J. Am. Chem. Soc.* 138: 2138–2141.

18 Volonakis, G., Filip, M.R., Haghighirad, A.A. et al. (2016). Lead-free halide double perovskites via heterovalent substitution of noble metals. *J. Phys. Chem. Lett.* 7: 1254–1259.

19 Calabrese, J., Jones, N., Harlow, R. et al. (1991). Preparation and characterization of layered lead halide compounds. *J. Am. Chem. Soc.* 113: 2328–2330.

20 Hong, X., Ishihara, T., and Nurmikko, A.U.P. (1992). Dielectric confinement effect on excitons in PbI_4-based layered semiconductors. *Phys. Rev. B* 45: 6961–6964.

21 Papavassiliou, G.C., Patsis, A.P., Lagouvardos, D.J., and Koutselas, I.B. (1993). Spectroscopic studies of $(C_{10}H_{21}NH_3)_2PbI_4$, $(CH_3NH_3)(C_{10}H_{21}NH_3)_2Pb_2I_7$, (CH_3NH_3) PbI_3, and similar compounds. *Synth. Met.* 57: 3889–3894.

22 Kataoka, T., Kondo, T., Ito, R. et al. (1994). Magneto-optical effects of excitons in the layered perovskite-type material $(C_6H_{13}NH_3)_2(CH_3NH_3)Pb_2I_7$. *Physica B* 201: 423–426.

23 Tabuchi, Y., Asaia, K., Rikukawa, M. et al. (2000). Preparation and characterization of natural lower dimensional layered perovskite-type compounds. *J. Phys. Chem. Solids* 61: 837–845.

24 Wu, X., Tuan Trinh, M., Niesner, D. et al. (2015). Trap states in lead iodide perovskites. *J. Am. Chem. Soc.* 137: 2089–2096.

25 Smith, I.C., Hoke, E.T., Solis-Ibarra, D. et al. (2014). A layered hybrid perovskite solar-cell absorber with enhanced moisture stability. *Angew. Chem. Int. Ed.* 53: 11232–11235.

26 Cao, D.H., Stoumpos, C.C., Farha, O.K. et al. (2015). 2D homologous perovskites as light-absorbing materials for solar cell applications. *J. Am. Chem. Soc.* 137: 7843–7850.

27 Stoumpos, C.C., Cao, D.H., Clark, D.J. et al. (2016). Ruddlesden–Popper hybrid lead iodide perovskite 2D homologous semiconductors. *Chem. Mater.* 28: 2852–2867.

28 Tsai, H., Nie, W., Blancon, J.-C. et al. (2016). High-efficiency two-dimensional Ruddlesden–Popper perovskite solar cells. *Nature* 536: 312–317.

29 Yuan, M., Quan, L.N., Comin, R. et al. (2016). Perovskite energy funnels for efficient light-emitting diodes. *Nat. Nanotechnol.* 11: 872–877.

30 Koh, T.H., Shanmugam, V., Schlipf, J. et al. (2016). Nanostructuring mixed-dimensional perovskites: a route toward tunable, efficient photovoltaics. *Adv. Mater.* 28: 3653–3661.

31 Dou, L., Wong, A.B., Yu, Y. et al. (2015). Atomically thin two-dimensional organic–inorganic hybrid perovskites. *Science* 349: 1518–1521.

32 Yaffe, O., Chernikov, A., Norman, Z.M. et al. (2015). Excitons in ultrathin organic–inorganic perovskite crystals. *Phys. Rev. B* 92: 045414.

33 Tyagi, P., Arveson, S.M., and Tisdale, W.A. (2015). Colloidal organohalide perovskite nanoplatelets exhibiting quantum confinement. *J. Phys. Chem. Lett.* 6: 1911–1916.

34 Protesescu, L., Yakunin, S., Bodnarchuk, M.I. et al. (2015). Nanocrystals of cesium lead halide perovskites ($CsPbX_3$, X = Cl, Br, and I): novel optoelectronic materials showing bright emission with wide color gamut. *Nano Lett.* 15: 3692–3696.

35 Papavassiliou, G.C., Koutselas, I.B., Terzis, A., and Whangbo, M.-H. (1994). Structural and electronic-properties of the natural quantum-well system $(C_6H_5CH_2CH_2NH_3)_2SnI_4$. *Solid State Commun.* 91: 695–698.

36 (a) Muljarov, E.A., Tikhodeev, S.G., Gippius, N.A., and Ishihara, T. (1995). Excitons in self-organized semiconductor/insulator superlattices: PbI-based perovskite compounds. *Phys. Rev. B* 51: 14370–14378; (b) Knutson, J.L., Martin, J.D., and Mitzi, D.B. (2005). Tuning the band gap in hybrid tin iodide perovskite semiconductors using structural templating. *Inorg. Chem.* 44: 4699–4705.

37 Sourisseau, S., Louvain, N., Bi, W. et al. (2007). Reduced band gap hybrid perovskites resulting from combined hydrogen and halogen bonding at the organic—inorganic interface. *Chem. Mater.* 19: 600–607.

38 Even, J., Pedesseau, L., Dupertuis, M.-A. et al. (2012). Electronic model for self-assembled hybrid organic/perovskite semiconductors: reverse band edge electronic states ordering and spin–orbit coupling. *Phys. Rev. B* 86: 205301.

39 Tanaka, K., Takahashi, T., Ban, T. et al. (2003). Bandgap and exciton binding energies in lead-iodide-based natural quantum-well crystals. *Solid State Commun.* 127: 619–623.

40 Borriello, I., Cantele, G., and Ninno, D. (2008). Ab initio investigation of hybrid organic–inorganic perovskites based on tin halides. *Phys. Rev. B* 77: 235214.

41 Chung, I., Song, J.-H., Im, J. et al. (2012). $CsSnI_3$: semiconductor or metal? High electrical conductivity and strong near-infrared photoluminescence from a single material. High hole mobility and phase-transitions. *J. Am. Chem. Soc.* 134: 8579–8587.

42 Even, J., Pedesseau, L., Jancu, J.-M., and Katan, C. (2013). Importance of spin–orbit coupling in hybrid organic/inorganic perovskites for photovoltaic applications. *J. Phys. Chem. Lett.* 4: 2999–3005.

43 Mosconi, E., Amat, A., Nazeeruddin, M.K. et al. (2013). First-principles modeling of mixed halide organometal perovskites for photovoltaic applications. *J. Phys. Chem. C* 117: 13902–13913.

44 Brivio, F., Walker, A.B., and Walsh, A. (2013). Structural and electronic properties of hybrid perovskites for high-efficiency thin-film photovoltaics from first-principles. *APL Mater.* 1: 042111.

45 Giorgi, G., Fujisawa, J.-I., Segawa, H., and Yamashita, K. (2013). Small photocarrier effective masses featuring ambipolar transport in methylammonium lead iodide perovskite: a density functional analysis. *J. Phys. Chem. Lett.* 4: 4213–4216.

46 Du, M.H. (2014). Efficient carrier transport in halide perovskites: theoretical perspectives. *J. Mater. Chem. A* 2: 9091–9098.

47 Even, J., Pedesseau, L., and Katan, C. (2014). Analysis of multivalley and multibandgap absorption and enhancement of free carriers related to exciton screening in hybrid perovskites. *J. Phys. Chem. C* 118: 11566–11572.

48 Katan, C., Pedesseau, L., Kepenekian, M. et al. (2015). Interplay of spin–orbit coupling and lattice distortion in metal substituted 3D tri-chloride hybrid perovskites. *J. Mater. Chem. A* 3: 9232–9240.

49 Even, J., Pedesseau, L., Katan, C. et al. (2015). Solid-state physics perspective on hybrid perovskite semiconductors. *J. Phys. Chem. C* 119: 10161–10177.

50 Pedesseau, L., Jancu, J.-M., Rolland, A. et al. (2014). Electronic properties of 2D and 3D hybrid organic/inorganic perovskites for optoelectronic and photovoltaic applications. *Opt. Quantum Electron.* 46: 1225–1232.

51 Even, J., Pedesseau, L., and Katan, C. (2014). Understanding quantum confinement of charge carriers in layered 2D hybrid perovskites. *ChemPhysChem* 15: 3733–3741.

52 Sapori, D., Kepenekian, M., Pedesseau, L. et al. (2016). Quantum confinement and dielectric profiles of colloidal nanoplatelets of halide inorganic and hybrid organic–inorganic perovskites. *Nanoscale* 8: 6369–6378.

53 Fraccarollo, A., Cantatore, V., Boschetto, G. et al. (2016). Ab initio modeling of 2D layered organohalide lead perovskites. *J. Chem. Phys.* 144: 164701.

54 Pedesseau, L., Sapori, D., Traore, B. et al. (2016). Advances and promises of layered halide hybrid perovskite semiconductors. *ACS Nano* 10: 9776–9786.

55 Umari, P., Mosconi, E., and De Angelis, F. (2014). Relativistic GW calculations on $CH_3NH_3PbI_3$ and $CH_3NH_3SnI_3$ perovskites for solar cell applications. *Sci. Rep.* 4: 4467.

56 Menéndez-Proupin, E., Palacios, P., Wahnón, P., and Conesa, J.C. (2014). Self-consistent relativistic band structure of the $CH_3NH_3PbI_3$ perovskite. *Phys. Rev. B* 90: 045207.

57 Brivio, F., Butler, K.T., Walsh, A., and van Schilfgaarde, M. (2014). Relativistic quasiparticle self-consistent electronic structure of hybrid halide perovskite photovoltaic absorbers. *Phys. Rev. B* 89: 155204.

58 Bokdam, M., Sander, T., Stroppa, A. et al. (2016). Role of polar phonons in the photo excited state of metal halide perovskites. *Sci. Rep.* 6: 28618.

59 Even, J. (2015). Pedestrian guide to symmetry properties of the reference cubic structure of 3D all-inorganic and hybrid perovskites. *J. Phys. Chem. Lett.* 4: 2999–3005.

60 Even, J., Carignano, M., and Katan, C. (2016). Molecular disorder and translation/rotation coupling in the plastic crystal phase of hybrid perovskites. *Nanoscale* 8: 6222–6236.

61 Even, J., Pedesseau, L., Jancu, J.-M., and Katan, C. (2014). DFT and $k{\cdot}p$ modelling of the phase transitions of lead and tin halide perovskites for photovoltaic cells. *Phys. Status Solidi RRL* 8: 31–35.

62 Yu, Z.G. (2016). Effective-mass model and magneto-optical properties in hybrid perovskites. *Sci. Rep.* 6: 28576.

63 Kim, M., Im, J., Freeman, A.J. et al. (2014). Switchable $S=1/2$ and $J=1/2$ Rashba bands in ferroelectric halide perovskites. *Proc. Natl. Acad. Sci. U.S.A.* 111: 6900–6904.

64 Boyer-Richard, S., Katan, C., Traore, B. et al. (2016). Symmetry-based tight binding modeling of halide perovskite semiconductors. *J. Phys. Chem. Lett.* 7: 3833–3840.

65 Kepenekian, M., Robles, R., Katan, C. et al. (2015). Rashba and Dresselhaus effects in hybrid organic–inorganic perovskites: from basics to devices. *ACS Nano* (12): 11557–11567.

66 Braun, M. and Frey, W. (1999). Crystal structure of bis(benzylammonium)lead tetrachloride, $(C_7H_7NH_3)_2PbCl_4$. *Z. Kristallogr. – New Cryst. Struct.* 214: 331–332.

67 Liao, W.-Q., Zhang, Y., Hu, C.-L. et al. (2015). A lead-halide perovskite molecular ferroelectric semiconductor. *Nat. Commun.* 6: 7338.

68 Amat, A., Mosconi, E., Ronca, E. et al. (2014). Cation-induced band-gap tuning in organohalide perovskites: interplay of spin–orbit coupling and octahedra tilting. *Nano Lett.* 14: 3608–3616.

69 Stroppa, A., Di Sante, D., Barone, P. et al. (2014). Tunable ferroelectric polarization and its interplay with spin–orbit coupling in tin iodide perovskites. *Nat. Commun.* 5: 5900.

70 Daub, M. and Hillebrecht, H. (2015). Synthesis, single-crystal structure and characterization of $(CH_3NH_3)_2$ $Pb(SCN)_2$ I_2. *Angew. Chem. Int. Ed.* 54: 11016–11017.

71 Ganose, A.M., Savory, C.N., and Scanlon, D.O. (2015). $(CH_3NH_3)_2$ $Pb(SCN)_2I_2$: a more stable structural motif for hybrid halide photovoltaics? *J. Phys. Chem. Lett.* 6: 4594–4598.

72 Xiao, Z., Meng, W., Saparov, B. et al. (2016). Photovoltaic properties of two-dimensional $(CH_3NH_3)_2Pb(SCN)_2I_2$ perovskite: a combined experimental and density functional theory study. *J. Phys. Chem. Lett.* 7: 1213–1218.

73 Létoublon, A., Paofai, S., Rufflé, B. et al. (2016). Elastic constants, optical phonons, and molecular relaxations in the high temperature plastic phase of the $CH_3NH_3PbBr_3$ hybrid perovskite. *J. Phys. Chem. Lett.* 7: 3776–3784.

74 Baikie, T., Barrow, N.S., Fang, Y. et al. (2015). A combined single crystal neutron/X-ray diffraction and solid-state nuclear magnetic resonance study of the hybrid perovskites $CH_3NH_3PbX_3$ (X = I, Br and Cl). *J. Mater. Chem. A* 3: 9298–9307.

75 Kawai, H., Giorgi, G., Marini, A., and Yamashita, K. (2015). The mechanism of slow hot-hole cooling in lead-iodide perovskite: first-principles calculation on carrier lifetime from electron–phonon interaction. *Nano Lett.* 15: 3103–3108.

76 Neukirch, A.J., Nie, W., Blancon, J.-C. et al. (2016). Polaron stabilization by cooperative lattice distortion and cation rotations in hybrid perovskite materials. *Nano Lett.* 16: 3809–3816.

77 Mosconi, E., Quarti, C., Ivanovska, T. et al. (2014). Structural and electronic properties of organo-halide lead perovskites: a combined IR-spectroscopy and ab initio molecular dynamics investigation. *Phys. Chem. Chem. Phys.* 16: 16137–16144.

78 Lindblad, R., Bi, D., Park, B.-W. et al. (2014). Electronic structure of $TiO_2/CH_3NH_3PbI_3$ perovskite solar cell interfaces. *J. Phys. Chem. Lett.* 5: 648–653.

79 Frost, J.M., Butler, K.T., and Walsh, A. (2014). Molecular ferroelectric contributions to anomalous hysteresis in hybrid perovskite solar cells. *APL Mater.* 2: 081506.

80 Carignano, M.A., Kachmar, A., and Hutter, J. (2015). Thermal effects on $CH_3NH_3PbI_3$ perovskite from ab initio molecular dynamics simulations. *J. Phys. Chem. C* 119: 8991–8997.

81 Carignano, M.A., Saeed, Y., Aravindh, S.A. et al. (2016). A close examination of the structure and dynamics of $HC(NH_2)_2PbI_3$ by MD simulations and group theory. *Phys. Chem. Chem. Phys.* 18: 27109–27118.

82 Mattoni, A., Filippetti, A., Saba, M.I., and Delugas, P. (2015). Methylammonium rotational dynamics in lead halide perovskite by classical molecular dynamics: the role of temperature. *J. Phys. Chem. C* 119: 17421–17428.

83 Wasylishen, R.E., Knop, O., and Macdonald, J.B. (1985). Cation rotation in methylammonium lead halides. *Solid State Commun.* 56: 581–582.

84 Poglitsch, A. and Weber, D. (1987). Dynamic disorder in methylammoniumtrihalogenoplumbates(II) observed by millimeter-wave spectroscopy. *J. Chem. Phys.* 87: 6373–6378.

85 Onoda-Yamamuro, N., Matsuo, T., and Suga, H. (1990). Calorimetric and IR spectroscopic studies of phase transitions in methylammonium trihalogenoplumbates(II). *J. Phys. Chem. Solids* 51: 1383–1392.

86 Onoda-Yamamuro, N., Matsuo, T., and Suga, H. (1992). Dielectric study of $CH_3NH_3PbX_3$ (X = Cl, Br, I). *J. Phys. Chem. Solids* 53: 935–939.

87 Swainson, I.P., Stock, C., Parker, S.F. et al. (2015). From soft harmonic phonons to fast relaxational dynamics in $CH_3NH_3PbBr_3$. *Phys. Rev. B* 92: 100303(R).

88 Leguy, A.M.A., Frost, J.M., McMahon, A.P. et al. (2015). The dynamics of methylammonium ions in hybrid organic–inorganic perovskite solar cells. *Nat. Commun.* 6: 7124.

89 Chen, T., Foley, B.J., Ipek, B. et al. (2015). Rotational dynamics of organic cations in the $CH_3NH_3PbI_3$ perovskite. *Phys. Chem. Chem. Phys.* 17: 31278–31286.

90 Fabini, D.H., Hogan, T., Evans, H.A. et al. (2016). Dielectric and thermodynamic signatures of low-temperature glassy dynamics in the hybrid perovskites $CH_3NH_3PbI_3$ and $HC(NH_2)_2PbI_3$. *J. Phys. Chem. Lett.* 7: 376–381.

91 Roiland, C., Trippé-Allard, G., Jemli, K. et al. (2016). Multinuclear NMR as a tool for studying local order and dynamics in $CH_3NH_3PbX_3$ ($X = Cl, Br, I$) hybrid perovskites. *Phys. Chem. Chem. Phys.* 18: 27133–27142.

1.3

Excitonics in 2D Perovskites

Wee Kiang Chong, David Giovanni, and Tze-Chien Sum

Division of Physics and Applied Physics, School of Physical and Mathematical Sciences, Nanyang Technological University, 21 Nanyang Link, SPMS-PAP-03-05, Singapore 637371, Singapore

1.3.1 Introduction to Two-dimensional Perovskites

Traditionally, the term “perovskite” refers to the calcium titanium oxide mineral (or calcium titanate), which has the formula $CaTiO_3$ and its structure is broadly known as the perovskite structure. Since then, “perovskite” is associated with compounds having a general ABX_3 chemical formula. Most recently, “three-dimensional organic–inorganic hybrid perovskites (3D-OIHPs)” has emerged as a new player in the scientific arena due to their exceptional optoelectronic properties. Henceforth, they have found applications in solar cells [1–3], light-emitting diodes (LEDs) [4–6], lasers [7–9], photodetectors [10, 11], and field-effect transistor applications [12]. While 3D-OIHPs are often in the limelight of these applications, there has also been an increasing number of reports for 2D-OIHPs, which also possess favorable optoelectronic properties [13–15]. These OIHPs consist of two basic constituents: organic cation (A^+) and inorganic octahedron (BX_6^{4-}). While 3D-OIHP is formed by repeating units of six corner-sharing BX_6^{4-} octahedron with individual A^+ embedded within (Figure 1.3.1a), 2D-OIHP (having a general chemical formula of A_2BX_4) comprises alternating organic and inorganic layers. The inorganic network in these 2D-OIHPs is made up of repeating units of four corner-sharing BX_6^{4-} octahedron layers (Figure 1.3.1b). Because of the layered arrangement between two layers with different bandgaps and dielectric constants, a type-I quantum well configuration with an inorganic well and an organic barrier can be achieved in 2D-OIHPs. Likewise, a configuration with an organic well and an inorganic barrier could also be achieved through careful choice of organic perovskite constituents [20].

In these 2D-OIHPs, excitonic properties become very prominent as a result of quantum and dielectric confinement in their self-assembled structures. This is in contrast to 3D-OIHPs where optical properties are dominated by free carriers. The dimensions of these quantum well and barrier are in the order of subnanometer to a few nanometers [21]. Thin films [22], single crystals [23], and microdisk 2D-OIHPs [24] can be self-assembled using facile solution

Halide Perovskites: Photovoltaics, Light Emitting Devices, and Beyond, First Edition.
Edited by Tze-Chien Sum and Nripan Mathews.

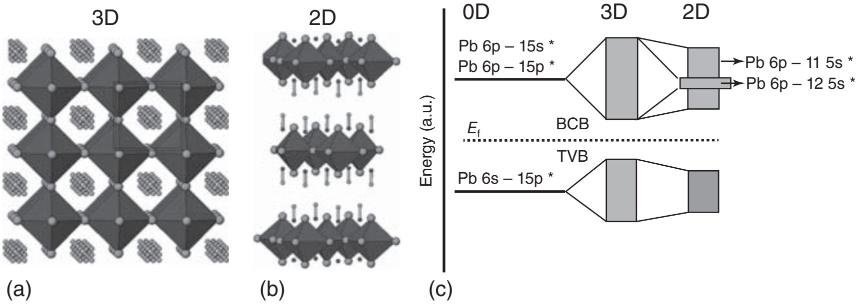

Figure 1.3.1 Crystal structures of (a) $CH_3NH_3PbI_3$ [16], and (b) $(CH_3NH_3)_2PbI_4$ [17], corresponding to 3D and 2D networks. (c) Bonding diagram of 2D crystal $(C_4H_9NH_3)_2PbI_4$ at the top of the valence band and the bottom of the conduction band. Source: (a,b): Sum and Mathews 2014 [18]. http://pubs.rsc.org/-/content/articlehtml/2014/ee/c4ee00673a. Licensed Under CC BY 3.0. (c) Umebayashi et al. 2003 [19]. Copyright 2003. Reprinted with permission of American Physical Society.

processing. Other fabrication processes include mechanical exfoliation [25], single-source thermal ablation [26], and thermal evaporation [27]. These fabrication processes result in the growth of 2D-OIHPs orientated in the ⟨001⟩ or ⟨110⟩ direction [28], which is also generally more moisture insensitive compared to their 3D counterparts [29, 30]. The excitonic nature of 2D-OIHPs together with their versatile fabrication methods hold great promise for high-stability solar cells, LEDs, photodiodes and potentially polariton-laser applications. In addition, the pronounced excitonic behavior in 2D-OIHPs also gives rise to significant quasi-particle interactions, such as exciton–phonon [31–33] and exciton–photon interactions [34–36]. These quasi-particle interactions have potential applications for white LEDs and polariton lasers, which would otherwise be very difficult to achieve using the 3D-OIHPs systems. In this chapter, an overview of 2D-OIHP excitonic properties and their optical transitions, quasi-particle interactions, and their emerging applications in the recent years are discussed.

1.3.2 Excitonic Properties and Optical Transitions in 2D-OIHPs

The exciton binding energies of these 2D-OIHPs are in the order of hundreds of meV [14, 37–40], which is equivalent to ~1000 K. The large exciton binding energy gives rise to pronounced room temperature excitonic effects. This also results in enhanced exciton oscillator strength from the larger spatial overlap between electrons and holes in 2D-OIHPs. In contrast to weakly bound excitons in 3D-OHIPs (exciton binding energies a few to tens of meV [18]), the strongly bound excitons in 2D-OIHPs exhibit pronounced excitonic absorption (with an excitonic absorption coefficient of $\sim 10^5$ cm^{-1} [41, 42] in $(C_6H_5C_2H_4NH_3)_2PbI_4$) and emission [21, 43]. Similar to 3D-OHIPs, the valence band of most 2D-OIHPs consist of hybridizations between B *n*s orbital and X $(n-1)$p orbitals, while their conduction band consists of hybridizations between B *n*p and X (*n* − 1)s orbitals (e.g. B = Pb, X = I, and *n* = 6) (Figure 1.3.1c) [19]. However, there also exist exceptions where organic molecules are responsible for optical properties in 2D-OIHPs through the formation of an organic well and inorganic barrier configuration [20]. This contrasts with 3D-OHIPs systems where optical transitions are dominated by the inorganic lattice. These strong excitonic properties, therefore, allow the realization of bright LEDs [14].

1.3.3 White Light Emission (WLE) from 2D-OIHPs

Broadband visible emission is an interesting and technologically important optical phenomenon that was reported in several 2D-OIHPs. This phenomenon is mostly exclusive to these low-dimensional 2D perovskites, such as those in Figure 1.3.2, even though some reports have demonstrated white light emission (WLE) from 1D-$C_4N_2H_{14}PbBr_4$ [45] and 3D-$CH_3NH_3PbBr_3$ nanoclusters [46]. Examples of such 2D-OHIPs and their respective broad emission spectra are shown in Figure 1.3.3a–e. In addition, the CIE 1931 coordinates for some of these

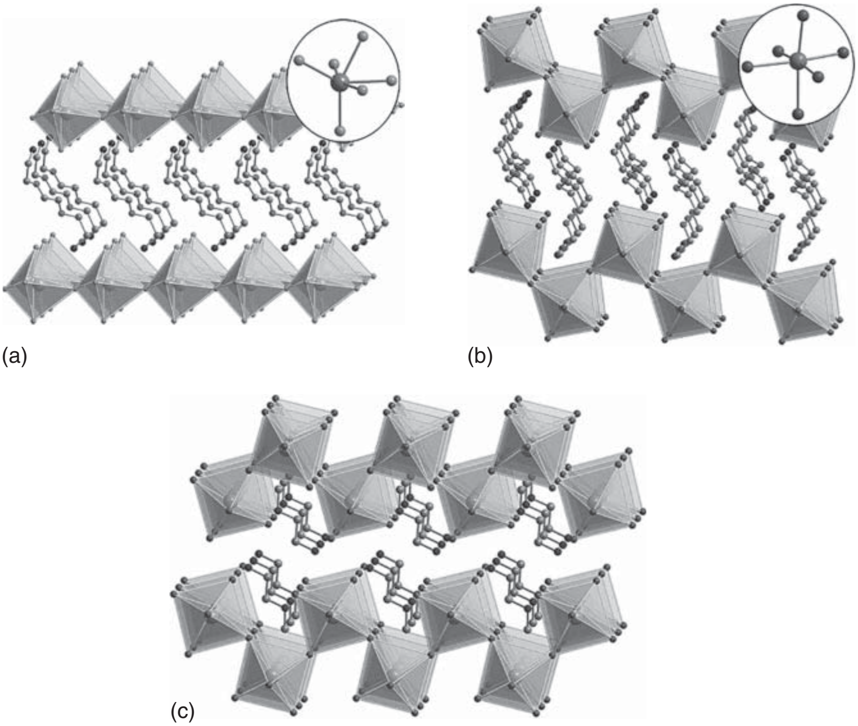

Figure 1.3.2 Structure of 2D-OHIP broadband visible emitters: (a) (EDBE)[$PbCl_4$] [31], (b) (EDBE)[$PbBr_4$] [31], and (c) (N-MEDA)[$PbBr_4$] [44]. N-MEDA and EDBE refer to *N*¹-methylethane-1,2-diammonium and (ethylenedioxy)bis(ethylammonium), respectively. Source: Panel (a) and (b): Adapted with permission from ref. [31], copyright 2014 ACS. (c) Adapted with permission from ref. [44], copyright 2014 ACS.

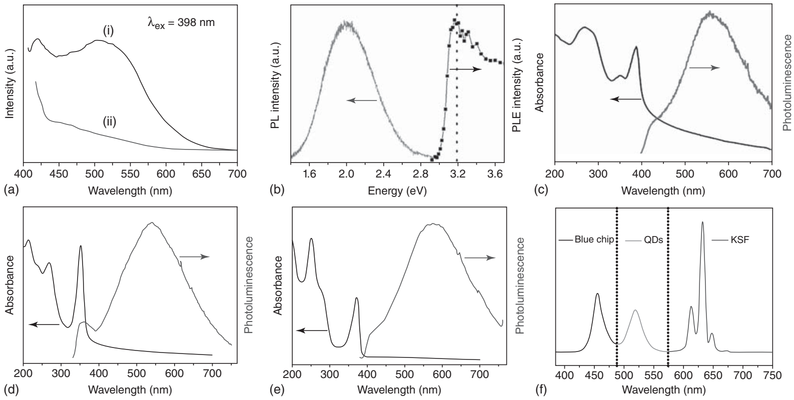

Figure 1.3.3 Photoluminescence (PL) spectra showing broadband visible emission from (a) $(C_6H_{13}N_3)PbBr_4$ - spectrum (i). (Spectrum (ii) is for the organic component $C_6H_{11}N_3$).2HBr) (b) $(C_6H_{11}NH_3)_2PbBr_4$ (c) (N-MEDA)$[PbBr_4]$ (d) (EDBE)$PbCl_4$, and (e) (EDBE)$PbBr_4$ 2D-OIHPs. (f) White emission from a stack consisting of a blue chip, $CH_3NH_3PbBr_3$ quantum dots, and K_2SiF_6:Mn^{4+} (KSF). Source: (a) is adapted with permission from ref. [20], copyright 2006 American Chemical Society (ACS). (b) is adapted with permission from ref. [33], copyright 2015 ACS. (c) is adapted with permission from ref. [44], copyright 2014 ACS. (d) and (e) are adapted with permission from ref. [31], copyright 2014 ACS. (f) is adapted with permission from ref. [47], copyright 2015 ACS.

materials ((N-MEDA)[$PbBr_4$], (EDBE)$PbCl_4$, and (EDBE)$PbBr_4$) have also been reported to lie in the white region that are attractive for white LED applications. In contrast to WLE achieved using a series of different phosphors (Figure 1.3.3f), a single white-emitting material would eliminate any self-absorption arising from absorption overlap between the phosphors. Consequently, this WLE phenomenon has driven several photophysical studies focusing on the origins of broadband emission in 2D-OIHPs [20, 31–33, 44]. To date, several origins have been proposed to explain the broadband emission (Figure 1.3.4). These include (i) energy transfer mechanism, (ii) deep-level defect emission, and (iii) self-trapped excitons. In the following sections, the evidence supporting these mechanisms is discussed in detail.

1.3.3.1 Energy Transfer Mechanism

The energy transfer mechanism responsible for WLE in ($C_6H_{13}N_3$)$PbBr_4$ perovskite was investigated in detail by Li et al. [20]. In particular, the energy transfer takes place from the inorganic to organic layer (Figure 1.3.4a). This

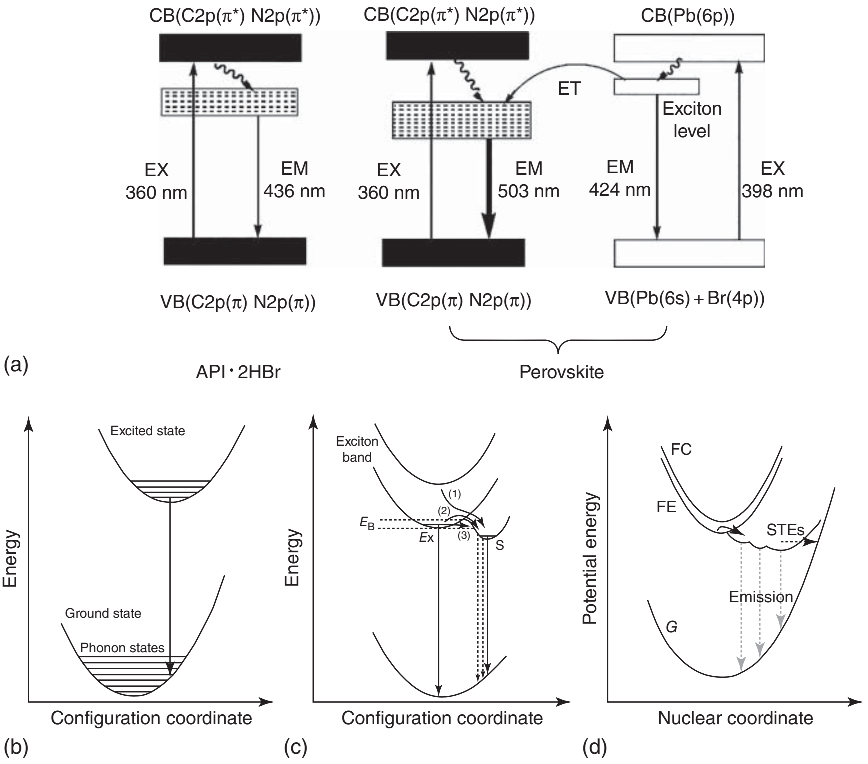

Figure 1.3.4 Proposed mechanisms for white emission in 2D-OIHPs include (a) energy transfer mechanism, (b) deep-level defect emission, and (c, d) self-trapped excitons. Source: Mechanism (a) is adapted with permission from ref. [20], copyright 2006 ACS. Mechanisms (b) and (c) are adapted with permission from ref. [33], copyright 2015 ACS. Mechanism (d) is adapted with permission from ref. [32], copyright 2016, ACS.

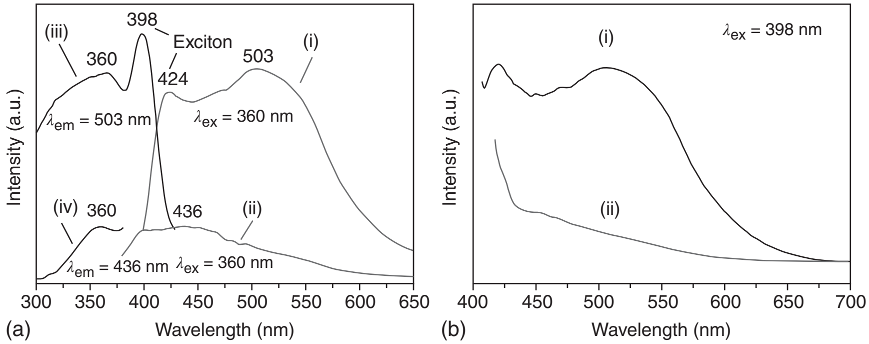

Figure 1.3.5 Broadband emission from an optically active organic component in $(C_6H_{13}N_3)PbBr_4$ perovskite. (a) PL emission (i and ii) and excitation (iii and iv) spectra for $(C_6H_{11}N_3)\cdot 2HBr$ (i, ii) and the perovskite compound 1 (iii, iv) under the same instrumental conditions. An excitation wavelength of 360 nm is used for PL emission measurements. (b) PL emission spectrum of perovskite (i) $(C_6H_{13}N_3)PbBr_4$, and (ii) $(C_6H_{11}N_3)\cdot 2HBr$ excited at 398 nm. Source: Li et al. 2006 [20]. Copyright 2006. Adapted with permission of American Chemical Society.

conclusion was derived from excitation-wavelength-dependent PL measurements of $(C_6H_{13}N_3)PbBr_4$ and its organic component $(C_6H_{11}N_3)\cdot 2HBr$. Upon exciting both samples with 360 nm, $(C_6H_{13}N_3)PbBr_4$ was found to emit broadly, peaking at 424 and 503 nm, across the visible wavelength (Figure 1.3.5a(i)). On the contrary, the emission of $(C_6H_{11}N_3)\cdot 2HBr$, peaking at 436 nm, is weaker (Figure 1.3.5a(ii)). Photoluminescence (PL) excitation spectra of $(C_6H_{13}N_3)PbBr_4$ perovskite measured at 503 nm revealed two states (peaks at 398 and 360 nm) associated with its emission (Figure 1.3.5a(iii)). The former is due to the excitonic state in the inorganic layers, while the latter is due to the contribution from the organic layers (Figure 1.3.5a(iv)). This suggests that the organic layers play a role in the broad emission. Furthermore, upon exciting the samples with 398 nm, the emission of $(C_6H_{11}N_3)\cdot 2HBr$ quenches significantly, while the broad emission of $(C_6H_{13}N_3)PbBr_4$ remains invariant (Figure 1.3.5b). This suggests the presence of an energy transfer process from inorganic to organic layers in $(C_6H_{13}N_3)PbBr_4$, which is responsible for the broad emission. In addition, this suggests that direct excitation of the organic framework is not a prerequisite for the broad emission in $(C_6H_{13}N_3)PbBr_4$. A similar energy transfer process from inorganic to organic layers leading to a triplet emission has also been observed in naphthalene-based 2D perovskite [48].

1.3.3.2 Broadband Defect Emission

Defect-related broadband emission could also be another origin for WLE in 2D perovskites. The intensity and profile of such emission are typically very dependent on defect concentrations. At higher excitation intensity, these defects become filled by the photoexcited charge carriers and emission intensity is expected to saturate. In addition, the emission profile should also show a strong

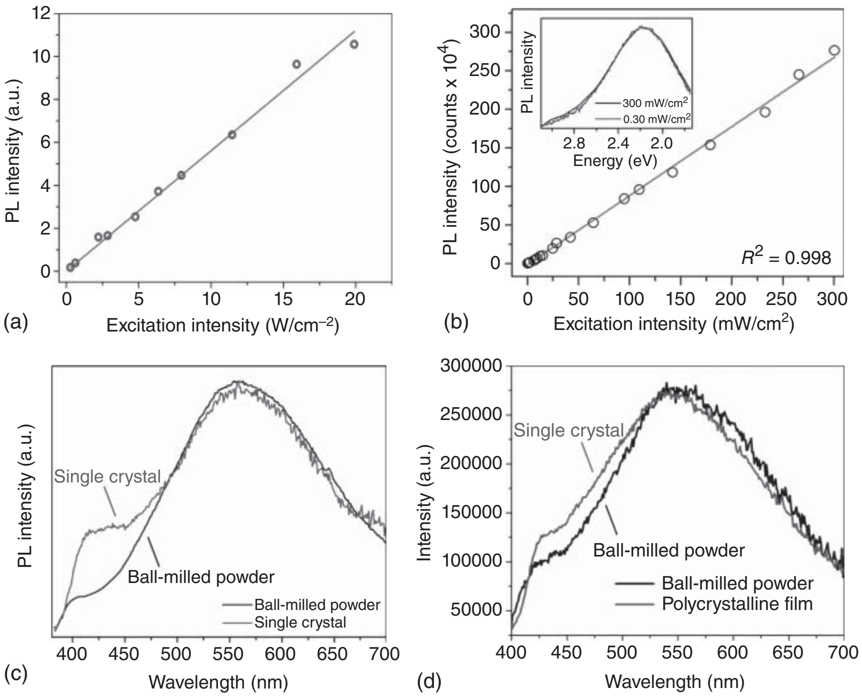

Figure 1.3.6 Non-trap-related broadband emission. A plot of PL intensity with excitation intensity of (a) (EDBE)$PbBr_4$ and (b) $(C_6H_{11}NH_3)_2PbBr_4$, showing a linear relationship without saturation. Comparison of PL spectrum between ball-milled powder and a single crystal of (c) (EDBE)$PbBr_4$ and (d) (N-MEDA)$PbBr_4$. Source: (a) and (c) are adapted with permission from ref. [31], copyright 2014 ACS. (b) is adapted with permission from ref. [33], copyright 2015 ACS. (d) is adapted with permission from ref. [44], copyright 2014 ACS.

dependence on particle size [49]. These signatures of defect-related emission have not been observed in several white-emitting 2D perovskite. Dohner et al. [31] have shown that the PL intensity of (EDBE)$PbBr_4$ is linear, without saturation, with excitation intensity (Figure 1.3.6a). This linear behavior has also been observed in $(C_6H_{11}NH_3)_2PbBr_4$ by Yangui et al. [33] (Figure 1.3.6b). In addition, the particle size of these perovskites has also been shown to have little influence on the broadband emission, with identical PL spectra reported for ball-milled powder and single-crystal samples [31, 44] (Figure 1.3.6c,d). These evidence suggest that defects in 2D-OIHPs are unlikely to be the origin of the broadband emission. This is in contrast to 3D-$CH_3NH_3PbBr_3$ nanoclusters [46], where saturation of broadband PL emission (trap-state-related emission) is observed at higher laser fluences.

1.3.3.3 Self-trapped Excitons

The presence of self-trapped excitons (STEs) in white-emitting 2D-OIHPs were confirmed by Karunadasa and coworkers [31, 32]. There are four pieces of

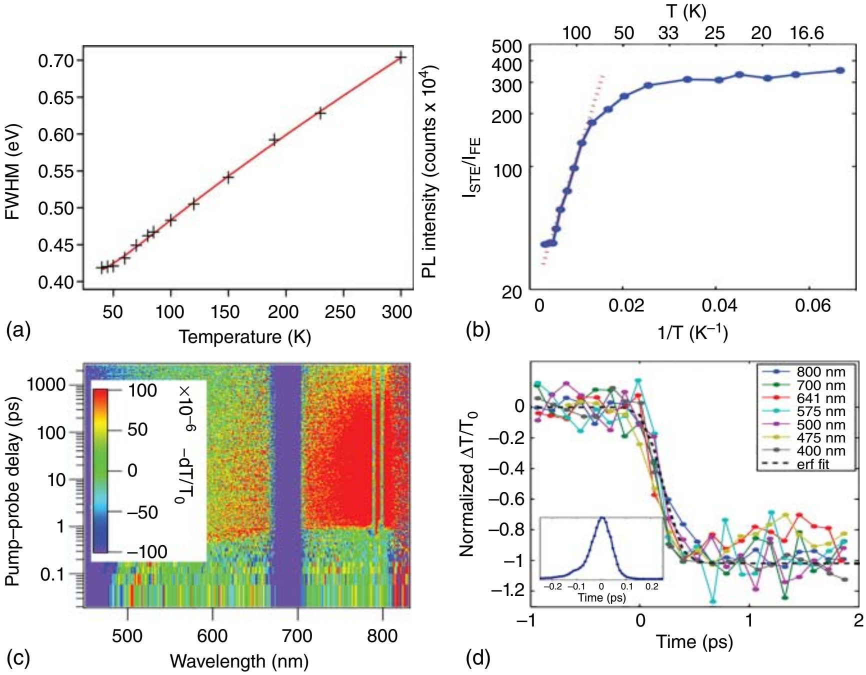

Figure 1.3.7 Evidence of self-trapped excitons. (a) Temperature dependence of the main emission bandwidth in (EDBE)PbBr$_4$ and a fit to a model that includes contributions from vibronic coupling and inhomogeneous broadening due to defect sites. A large exciton–phonon coupling of 130 ± 7 meV was obtained from the fitting. (b) Intensity ratio of STE and free exciton luminescence (I_{STE}/I_{FE}) in (N-MEDA)PbBr$_4$ as a function of temperature under 343 nm photoexcitation. (c) Two-dimensional pseudocolor ($-\Delta T/T_0$) plot of the TA spectrum as a function of probe wavelength and pump–probe delay for (N-MEDA)PbBr$_4$. (d) Normalized TA onsets probed at below-gap wavelengths under 387 nm resonant photoexcitation at room temperature for (N-MEDA)PbBr$_4$. Source: (a) is adapted with permission from ref. [31], copyright 2014 ACS. (b), (c) and (d) are adapted with permission from ref. [32], copyright 2016 ACS.

evidence suggesting the presence of STEs in these materials. The first evidence is the large exciton–phonon coupling strength (Γ_{phonon}) in (EDBE)PbBr$_4$. A large Γ_{phonon} value increases the probability of STE formation [50]. A value of $\Gamma_{\text{phonon}} = 130 \pm 7$ meV has been extracted from the temperature-dependent full-width at half maximum (FWHM) plot of (EDBE)PbBr$_4$ (Figure 1.3.7a) via fitting using the expression:

$$\Gamma(T) = \Gamma_0 + \Gamma_{\text{phonon}}(e^{E_{\text{LO}}/k_B T} - 1)^{-1} + \Gamma_{\text{inhomo}} e^{-E_b/k_B T} \tag{1.3.1}$$

where Γ_0 is the emission FWHM at $T = 0$ K, E_{LO} is the energy of the longitudinal optical phonon mode energy, E_b is the average binding energy of emissive defect states and Γ_{phonon} and Γ_{inhomo} are the electron–phonon coupling and inhomogeneous broadening constant. The fitted value of Γ_{phonon} is also comparable to ZnO multi-quantum well systems [51], which are known for their large exciton–phonon coupling strength. The fitting also yields a value of $E_{\mathrm{LO}} = 12 \pm 1\,\mathrm{meV}$, which corresponds well to the stretching frequency of Pb—Br bond and suggests self-trapping of excitons at the inorganic framework.

The second evidence is the presence of a self-trapping barrier. Its presence in (N-MEDA)$PbBr_4$ can be derived from Figure 1.3.7b where the PL intensity ratio of STE (I_{STE}) and free excitons (I_{FE}) decreases with temperature. This trend can be interpreted as due to an increased thermally driven back transfer of STE to the free exciton states at higher temperature, which leads to smaller $I_{\mathrm{STE}}/I_{\mathrm{FE}}$ ratio at higher temperature. The presence of such a barrier has also been observed in $(C_6H_{11}NH_3)_2PbBr_4$ broadband emitting system [33]. The third evidence can be seen from the presence of a photo-induced absorption signal, i.e. lack of photo-bleaching signal, in the transient absorption spectrum (Figure 1.3.7c,d) in (N-MEDA)$PbBr_4$. Since STEs are formed from free exciton trapping, optical transition from ground state to STE state should occur with a very low probability. This results in an absence of a photo-bleaching signal at the visible wavelength, consistent with Figure 1.3.7c. This is evident from the good correspondence between the transient absorption rise time of ~400 fs (Figure 1.3.7d) and period of Pb—Br stretching mode of ~300 fs. These are characteristic signatures of STEs being the underlying mechanism for broadband emission in 2D-OIHPs.

1.3.3.4 Role of Organic Framework in Broadband 2D-OIHP Emitters

Self-trapping at the inorganic framework has been widely assigned to the origins of broad emission in 2D-OIHPs. However, the influence of the organic framework on white emission cannot be ruled out given the close proximity between the organic and inorganic layers. To date, studies have found that the organic framework plays two roles for white emission. Firstly, excitons generated in the inorganic halide layers can also undergo self-trapping at the organic framework. The direct contribution of the organic framework to white emission has been demonstrated experimentally in $(C_6H_5C_2H_4NH_3)_2PbCl_4$ 2D-OIHPs [52]. A similar temperature-dependent PL FWHM analysis was carried out using Eq. (1.3.1) and the fitting revealed Γ_{LO} and E_{LO} to be $265 \pm 80\,\mathrm{meV}$ and $54 \pm 6\,\mathrm{meV}$, respectively. The large value of Γ_{LO} is indicative of strong exciton–phonon coupling and suggests the presence of self-trapped excitons. The value of E_{LO} is also in good agreement with a phonon mode in $C_6H_5C_2H_4NH_3Cl$. These evidence suggest the self-trapping of excitons at the organic framework. Secondly, there is another report suggesting an alternative role of the organic cation–inorganic cage interaction in broadband emission. Specifically, certain organic cations could lead to a stronger lead halide bond distortion [53]. The distorted inorganic cage could, therefore, give rise to charge self-trapping, resulting in broad emission from the inorganic framework.

Despite the different roles of the organic framework for the broadband emitter, both reports convey one important message: the organic framework is equally important as the inorganic framework for broadband emission. As such, these findings highlight that judicious selection of both organic and inorganic components presents new opportunities for tuning white emission from 2D-OIHP.

1.3.4 Strong Exciton–Photon Coupling in 2D-OIHPs

The large exciton oscillator strength and binding energy in 2D-OIHPs also give rise to strong exciton–photon coupling. This strong interaction offers us new opportunities to unlock new physics and applications. In fact, fundamental studies of strong exciton–photon coupling in other semiconductor systems have been an active research area for decades. This quest for novel technologies was first pioneered by inorganics and then extended to organics. Promising results have been achieved for both systems, e.g. realization of a new type of coherent light source called as *polariton lasers* [54–62], each with its own advantages and drawbacks. Organic–inorganic hybrid halide perovskites, which possesses the best of both systems (i.e. excellent electrical and optical properties of inorganic system, with the low-cost, chemical flexibility and versatility of organic system) are therefore exciting new systems to further explore these possibilities. However, these systems have only been recently investigated and just been realized in the UV bandgap 3D lead halide perovskite system [63], but are yet to be demonstrated for the 2D system with stronger excitonic behavior and visible emission. In this section, the early works on investigating the fundamentals of strong exciton–photon coupling in 2D perovskites systems are reviewed.

1.3.4.1 Jaynes–Cummings Model

One of the simplest theoretical models to describe the exciton–photon coupling phenomenon is the *Jaynes–Cummings* model. This model assumes a two-level exciton/atom with ground state $|a\rangle$ and excited state $|b\rangle$ with energy $E_b - E_a = \hbar\omega_0 > 0$ in the presence of a single-mode radiation field with energy $\hbar\omega$. Given the total energy of the system $E = E_a + (n + 1)\hbar\omega$, by conservation of energy there are only two possible quantum states available for the system: $|a, n + 1\rangle$ (i.e. ground state $|a\rangle$ with $(n + 1)$ photons) and $|b, n\rangle$ (i.e. excited state $|b\rangle$ with n photon). These states are known as *bare states*, which do not include the interaction energy. The total Hamiltonian with interaction is given by

$$H = \frac{1}{2}\hbar\omega_0(|b\rangle\langle b| + |a\rangle\langle a|) + \hbar\omega\left(\hat{c}^\dagger\hat{c} + \frac{1}{2}\right) + \hbar\omega_\mathrm{R}(|b\rangle\langle a|\hat{c} + |a\rangle\langle b|\hat{c}^\dagger). \tag{1.3.2}$$

The third term corresponds to the interaction between the photon and exciton, which includes absorption and stimulated emission. Here, $\hat{c}^\dagger$ and $\hat{c}$ are the creation and annihilation operators of the photon, respectively, (i.e. $\hat{c}^\dagger|n\rangle = \sqrt{n+1}|n+1\rangle$ and $\hat{c}|n\rangle = \sqrt{n}|n-1\rangle$); ω_R is the *vacuum Rabi frequency*, which parameterizes the coupling strength between the exciton/atom and photon; and $E_a = -\hbar\omega_0/2$ and $E_b = +\hbar\omega_0/2$ are taken as the energy reference. Note that the spontaneous emission term is omitted, which is valid when the spontaneous emission rate Γ is much slower than the field oscillation frequency ω (i.e. $\Gamma \ll \omega$). For algebraic simplification, the *Rabi energy* $\hbar\Omega_\mathrm{R} = 2\hbar\omega_\mathrm{R}\sqrt{n+1}$ and detuning energy $\Delta = \hbar\omega_0 - \hbar\omega$ are defined. The eigenstates of this

Hamiltonian in Eq. (1.3.2) is given by

$$|+\rangle = -\sin\theta|a, n+1\rangle + \cos\theta|b, n\rangle \tag{1.3.3}$$

$$|-\rangle = \cos\theta|a, n+1\rangle + \sin\theta|b, n\rangle \tag{1.3.4}$$

where

$$\tan\theta = \hbar\Omega_R/(\sqrt{(\hbar\Omega_R)^2 + \Delta^2} - \Delta) \tag{1.3.5}$$

The eigenenergies of the above eigenstates are

$$E_\pm = \hbar\omega(n+1) \pm \frac{1}{2}\sqrt{(\hbar\Omega_R)^2 + \Delta^2} \tag{1.3.6}$$

It is clear that the eigenenergies are no longer pure photon states or excited exciton/atom states, but are a quantum mixture of both, which is termed as *photon-dressed states*. In the case of the exciton, it is also known as *exciton–polariton*. The signature of this interaction is the energy shift from the bare states and the anti-crossing of the eigenenergies at zero detuning – see Figure 1.3.8.

1.3.4.2 Exciton–Photon Coupling in 2D Perovskites Thin Films: Optical Stark Effect

From the Jaynes–Cummings model, strong exciton–photon coupling results in the shift of the energy as compared to the bare states. When the frequency of a light pulse is red-detuned with respect to the excitonic resonance ($\Delta > 0$), the eigenenergy of the system (i.e. absorption) will be blueshifted as much as

$$\Delta E = \frac{1}{2}(\sqrt{(\hbar\Omega_R)^2 + \Delta^2} - \Delta) \approx \frac{(\hbar\Omega_R)^2}{4\Delta} \propto \text{Intensity} \tag{1.3.7}$$

which is the shift from $|b, n\rangle$ to $|+\rangle$. This effect is also known as the *optical Stark effect* (OSE). It is a useful phenomenon to investigate the strength of light-matter coupling in a material system. Recently, T.C. Sum and coworkers reported

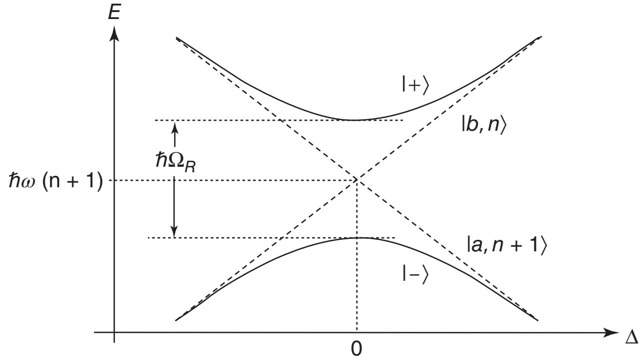

Figure 1.3.8 The eigenenergies of the dressed states as a function of detuning Δ. The eigenenergies show anti-crossing behavior, as compared to crossing behavior of the non-interacting bare states.

a study of strong exciton–photon coupling in several solution-processed 2D perovskite thin films via OSE: $(C_6H_5C_2H_4NH_3)_2PbBr_4$, $(C_6H_5C_2H_4NH_3)_2PbI_4$, and $(C_6H_4FC_2H_4NH_3)_2PbI_4$ (called PEPB, PEPI, and FPEPI, respectively) [64]. In these films, ultrafast spin-selective OSE was observed at room temperature using transient absorption spectroscopy (TAS). The illustrated and the experimental spectral OSE signature from TAS is shown in Figure 1.3.9a,b, respectively, from which the energy shift can be estimated. Furthermore, Figure 1.3.9b,c shows the spin selectivity of this process, represented by the dependence on the pump and probe circular polarization. The OSE spectral signature can only be observed when the pump and probe are co-circular during the duration of the pump. Meanwhile, the counter-circular pump and probe polarization results in a state-filling TA signal, which arises from two-photon absorption. This is confirmed by the linear and quadratic behavior of the co-circular and counter-circular signal, respectively – Figure 1.3.9d. This study uncovers an energy shift of ~4.5 meV on PEPI thin film with linear absorption spectrum peaked at ~2.39 eV, by pump laser with photon energy of 2.16 eV and fluence of 1.66 mJ cm^{-2}.

From the energy shift, Rabi energy $\hbar\Omega_R$ of ~33 meV, ~47 meV and ~63 meV were estimated under such pump fluence on PEPB, PEPI, and FPEPI thin films, respectively. The Rabi energy by these 2D perovskites system at room temperature was found to be about four times higher than that for a classic inorganic semiconductor system GaAs/AlGaAs multi-quantum well (MQW) at cryogenic temperature excited under similar pump fluence. This result is also consistent with other studies, which had found the vacuum Rabi energy of PEPI (in a cavity) to be one order of magnitude higher than GaAs-based cavity system [65–67] (this will be discussed later). While one reason could be the higher oscillator strength of the 2D perovskites as compared to GaAs [65–67], this recent work (Ref. [64]) surprisingly revealed that it is the strength of Rabi energy normalized with respect to square root of fluence (and thus fluence independent) that is proportional to the dielectric contrast of the organic and inorganic layers, rather than simply due to the oscillator strength (see Figure 1.3.9e). Although this result provides a pragmatic straightforward strategy for tuning the exciton–photon coupling strength in 2D perovskites material system, further studies are warranted to clearly understand these dependencies.

1.3.4.3 Exciton–Photon Coupling in 2D Perovskite Microcavities: Exciton–Polariton

As described by the Jaynes–Cummings model, the strong interaction between the exciton and the photon will result in new eigenstates which are admixtures of both the exciton and the photon states. This interaction is parameterized by the vacuum Rabi frequency ω_R:

$$\omega_R = |p_{ab}|\sqrt{\frac{\hbar\omega}{2V_m}} \tag{1.3.8}$$

where $|p_{ab}| = \langle a|\hat{p}|b\rangle$ is the transition dipole moment of the exciton, and V_m is the photon confinement volume. From the abovementioned relation, optical

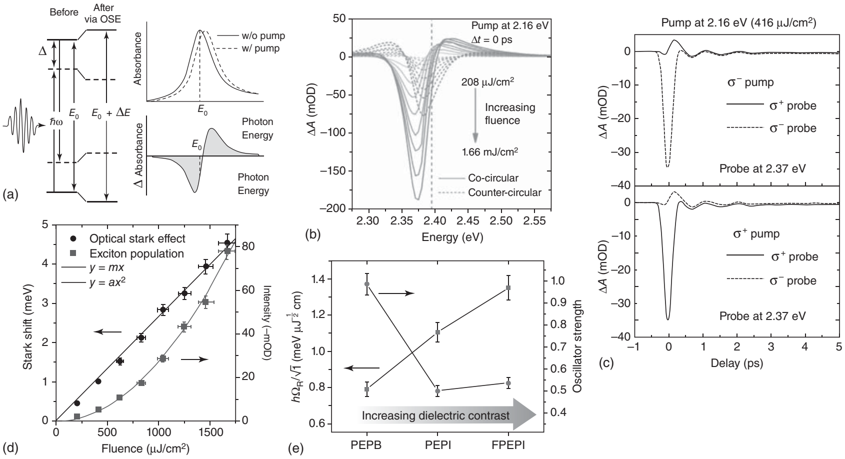

Figure 1.3.9 (a) The illustration of OSE and its spectral signature. The circular polarization dependence (b) spectral, and (c) temporal signature of OSE signal. (d) Linear behavior of the estimated energy shift from OSE with respect to pump fluence. The signal from counter-circular polarization shows a quadratic behavior, consistent with a two-photon absorption process. (e) The normalized Rabi energy shows a direct correspondence to the dielectric contrast of the organic and inorganic layer, but not to the oscillator strength. Source: Giovanni et al. 2016 [64]. Adapted with permission of AAAS.

confinement of the system (e.g. by using optical cavity) will strongly reduce V_m and thus enhance the exciton–photon coupling strength. In this so-called *strong coupling regime*, the new eigenstates form a new quasi-particle with a distinct anti-crossing dispersion relation, known as the *exciton–polariton*. The main proof of the presence of this strong coupling regime is the anti-crossing between the new eigenenergies, typically called the *upper polariton branch* (UPB) and *lower polariton branch* (LPB). Exciton–polariton exhibits many exotic physical phenomena such as Bose–Einstein condensation (BEC). BEC is basically the macroscopic occupation of the polariton ground state. The ability to condense and manipulate these exciton–polaritons will lead to new technologies that include polariton lasers, optical-spin switches for transistors and IC [68–72], logic gates [70, 71], etc.

To achieve BEC, these exciton–polaritons should thermalize to the ground state. However, this thermalization process is nontrivial. The early stage involves the relaxation via acoustic phonons from the higher states toward the inflection point of the LPB (i.e. around the anti-crossing point between LPB and UPB). Nonetheless, beyond the inflection point, the LPB dispersion becomes too steep for any relaxation via scattering with acoustic phonons. This results in a significant slowing of the polariton relaxation to the ground state, known as the *polariton bottleneck effect*, which is a major challenge toward achieving BEC [60, 62]. One proposed approach to achieve BEC is through a *parametric scattering* of the exciton–polaritons, where two exciton–polaritons scatter with each other, resulting in one polariton in the ground state and the other at a higher energy state, conserving total energy and momentum in the process. Due to the bosonic properties of exciton–polaritons, a small population in the ground state will stimulate more parametric scattering events to occur. This process is known as *stimulated scattering*. Another mechanism which has also been suggested to enhance polariton relaxation is via polariton-free carrier scattering [73, 74].

The investigation of the presence of strong coupling regime in 2D perovskites was pioneered by Ishihara and coworkers [65]. The experiment was performed on a patterned quartz substrate coated with PEPI, forming a distributed feedback (DFB) cavity at room temperature. The polaritonic behavior in the strong coupling regime of this system was evident from the observed anti-crossing behavior of the dips position as a function of the grating periodicities (photon mode detuning) from the absorption spectra. This anti-crossing energy splitting (also known as *Rabi splitting*) was found to be ~100 meV in room temperature, which is much higher than the ~9 meV splitting in the GaAs system. Another evidence of the strong coupling in this system is from the energy-momentum dispersion relation in the system, which could be investigated using the angle-resolved transmissivity measurements (i.e. by changing photon incident angle, hence changing photon momentum projection on sample plane). The observed anti-crossing behavior in momentum space validated the presence of exciton–polariton in this simple system. However, there was no discussion on achieving BEC in this work.

Following Ishihara's pioneering study, the work on exciton–polaritons in 2D perovskite cavity was further advanced mainly by Deleporte and coworkers, which focused on PEPI in Fabry–Perot (FP) cavity architecture at room temperature [34, 36, 66, 67, 75–77]. In the FP cavity, light is confined in one direction (taken as z-axis), which forms a standing wave. Depending on the thickness, the cavity photon acquires a minimum standing wave energy of $E_0 = hc'/m\lambda_0$, where $m = 1, 2, 3, \ldots$; $c' = c/n_{\text{eff}}$ is the speed of light in the microcavity with n_{eff} as the effective refractive index; and $\lambda_0 = n_{\text{eff}}d/2$ is the minimum standing wave wavelength allowed with d as cavity thickness. The cavity photon momentum wave vector k is defined along the x–y plane. The energy dispersion of the FP cavity is therefore given by

$$E_{\pm}(k) = \frac{E_{\text{x}} + E_{\text{ph}}(k)}{2} \pm \frac{1}{2}\sqrt{(\hbar\Omega_{\text{R}})^2 + (E_{\text{x}} - E_{\text{ph}}(k))^2} \tag{1.3.9}$$

where E_{x} is the exciton energy; and $E_{\text{ph}}(k) = \sqrt{E_0^2 + (\hbar c'k)^2}$ is the momentum-dependent energy of the cavity photon.

Figure 1.3.10a shows the typical FP cavity system containing 2D perovskites. The fabrication of such cavity includes spin coating the 2D perovskite precursor solution as the active material, spin coating of the PMMA layer as the spacer, and, lastly, evaporation of silver as the top reflector layer. In this type of cavity,

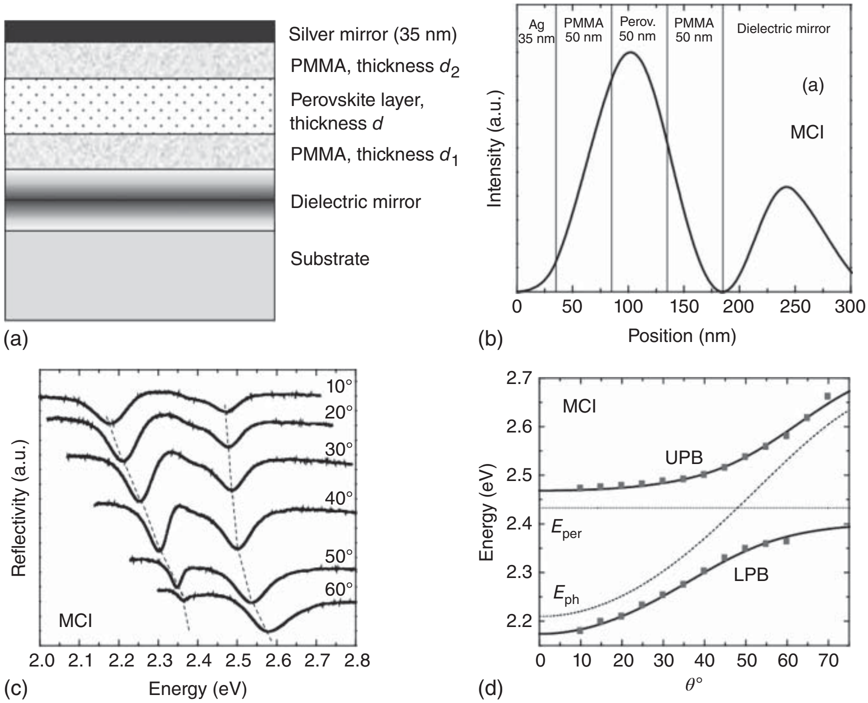

Figure 1.3.10 (a) Fabry–Perot cavity system employing 2D perovskites as the active material. (b) Angle-resolved reflectivity measurements on the cavity showing dips which correspond to the UPB and the LPB. (c) Theoretical simulation on the light field intensity inside the cavity. (d) A plot of UPB and LPB dispersion of the 2D perovskite FP cavity. Source: This figure is adapted with permission from ref. [67], copyright 2016 IOP Publishing.

depending on the refractive index, the thickness of each material layer can be adjusted to maximize the light electric field "experienced" by the active material. Figure 1.3.10b shows the simulated electric field intensity distribution in one such example of the 2D perovskite FP cavity architecture, where the perovskite layer is designed to yield the maximum intensity and hence strengthen the interaction. The tuning of layer thickness in this architecture also allows the relative detuning between the 2D perovskite exciton mode and the cavity mode [67]. The exciton–polariton dispersion relation in the FP cavity can then be inferred from the angle-resolved reflectivity measurement (Figure 1.3.10c), where the dips in the reflectivity spectra indicate the energy dispersion of the polariton states. Figure 1.3.10d shows the plot of energy dips as a function of the angle. A clear anti-crossing behavior with Rabi splitting in order of 100 meV is observed, which indicates the presence of a strong coupling regime in this cavity system. Anti-crossing behavior and Rabi splitting with a similar order of magnitude are also found in FPEPI-based FP cavity [36].

However, regardless of the presence of the strong coupling regime, the observation of BEC in 2D perovskites cavity remains elusive. While emission from the LPB has been observed, the polariton bottleneck effect was found to be the major challenge for realizing BEC in the 2D perovskite cavity, signified by strong emission at large angle [36, 67]. Another factor which contributes to the problem is the relatively low-quality FP cavity fabricated using such solution-processed and metal evaporation techniques. The fabricated FP cavity only has a Q-factor of ~25 [66], much lower than typical high-quality cavity system with Q-factor ≥ 1000. Another attempt to improve the Q-factor was also performed by Deleporte and coworkers, using separate growth of the *distributed Bragg reflectors* (DBR) and the assembly technique based on the liquid migration on the top of the dielectric mirror [34]. This microcavity architecture is depicted in Figure 1.3.11a. The top DBR, which consisted of eight pairs of YF3/ZnS $\lambda/4$-layers with stop-band centered at PEPI PL peak (2.37 eV), was first evaporated at low temperature (<100 °C) on a Si substrate coated with a polymer sacrificial layer with thin Ti/Ni top bilayer as compensator for the internal stress of the multilayer pile. Meanwhile, the bottom DBR (stop-band centered at 2.37 eV), which consisted of 11 pairs of SiN_x/SiO_2 $\lambda/4$-layers, were deposited on a fused silica substrate by plasma-enhanced chemical vapor deposition. The PEPI layer with a thickness of ~60 nm was then spin coated on top of the bottom DBR, continued by sputtering SiN_x layer, which acts as a spacer. The top DBR was then immersed in a solvent which dissolved the sacrificial polymer layer, which therefore released it from the Si substrate. By gradually exchanging the initial solvent with toluene (does not dissolve PEPI), the released top DBR floated on toluene, which was then positioned onto the designated substrate of SiN_x/perovskites/bottom DBR. The toluene solution was then gradually evacuated and annealed at 90 °C. This results in the adsorption of the top DBR by the surface of the SiN_x layer via van der Waals force with a good mechanical contact.

From the reflectivity spectrum, three polariton branches, labeled as LPB, MPB, and HPB (correspond to low, middle, and high polariton branch, respectively)

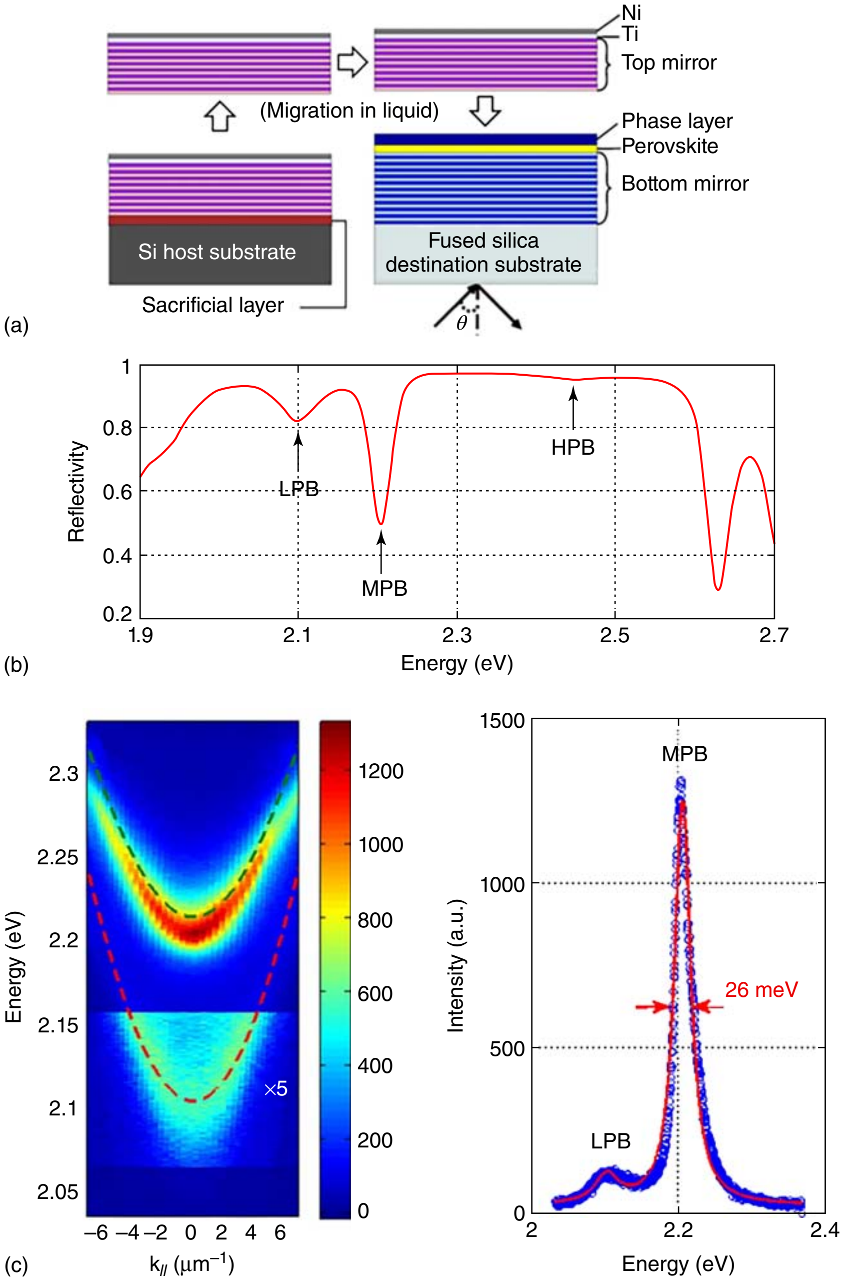

Figure 1.3.11 (a) Fabrication technique of the high-*Q* planar cavity. (b) Reflectivity spectra at normal incidence. (c) Emission of high *Q*-factor 2D perovskite-based cavity. Source: Han et al. 2012 [34]. Copyright 2012.Adapted with permission of The Optical Society.

were observed in the cavity (Figure 1.3.11b), which arose from the coupling of the perovskite exciton to both the cavity mode and the Bragg mode just at the lower energy edge of the SiO_2/SiN_x DBR stop-band. Meanwhile, the emission spectra exhibit well-resolved polariton branches without any significant emission from the uncoupled perovskite exciton (contrary to previously reported low Q-factor samples [36, 67, 76]). Efficient polariton relaxation toward the bottom of the MPB was also observed. The Q-factor of the DBR is 86, which was an improvement by a factor of >3 from the previous metal-based top mirror layer (Figure 1.3.11c). However, room temperature BEC 2D perovskite remained elusive.

More recently, there was another report by Deleporte's group for the PEPI perovskite system embedded in the FP cavity made by similar migration in liquid technique [77]. In this latest study, the measurement was performed on a ~900-nm-diameter sphere-like defect site, which provides extra zero dimension (0D)-like confinement on the perovskite system. The strong coupling regime in such system was marked by observations of the discrete PL of the LPB. While the polariton bottleneck issue has yet been tackled, the measured emission Q-factor was ~750, which was almost an order of magnitude improvement over the previous system. This work demonstrated the feasibility of further improvements for realizing room temperature BEC with the 2D-OIHP system.

Strong coupling is not limited to occurrences between the exciton and photon. More recently, Niu et al. [78] reported observations of strong interaction between photons, excitons, and surface plasmons in Ag-based DFB grating coated with 2D perovskite $(C_6H_9C_2H_4NH_3)_2PbI_4$ (or CHPI), with coupling strengths that are one order larger than for III–V quantum wells at room temperature (Figure 1.3.12a). This study was mainly done by incident polar (θ) and azimuthal (φ) angle-resolved reflectivity measurement with transverse electric (TE) and transverse magnetic (TM) modes. Under TM mode excitation (Figure 1.3.12b), the presence of an additional ~100 meV redshifted exciton dip was observed, which was assigned to the excitation of the *surface plasmon polariton* (SPP). This effect was absent in TE mode measurements (Figure 1.3.12c) and CHPI-coated planar Ag-film (Figure 1.3.12d). This redshift of ~100 meV could be well explained by the *method of images*, where the exciton in CHPI coupled via Coulomb interaction with its own image on the metal surface, forming a "biexciton." The magnitude of the redshift observed agrees very well with the well-established model in Ref. [79]. Further tunability of this "biexciton" redshift was also demonstrated up to 185 meV by simply changing the azimuthal angle of the incident light. This "biexciton" holds an interesting potential application for light-emission devices, since its decay channel via emission to SPP (Figure 1.3.12e) has been previously used to improve the luminescence efficiency of LEDs [80, 81]. The strong interaction of the exciton, bi-exciton, and the grating mode could be well explained using the three coupled-oscillators model (Figure 1.3.12f), where large Rabi splitting of 156 and 125 meV were obtained for the exciton and biexciton interaction with SPP, respectively. These values are comparable to those with J-aggregates. These results, therefore, open up an exciting new direction for optoelectronic applications through coupling SPP with exciton–photon interaction in 2D perovskites.

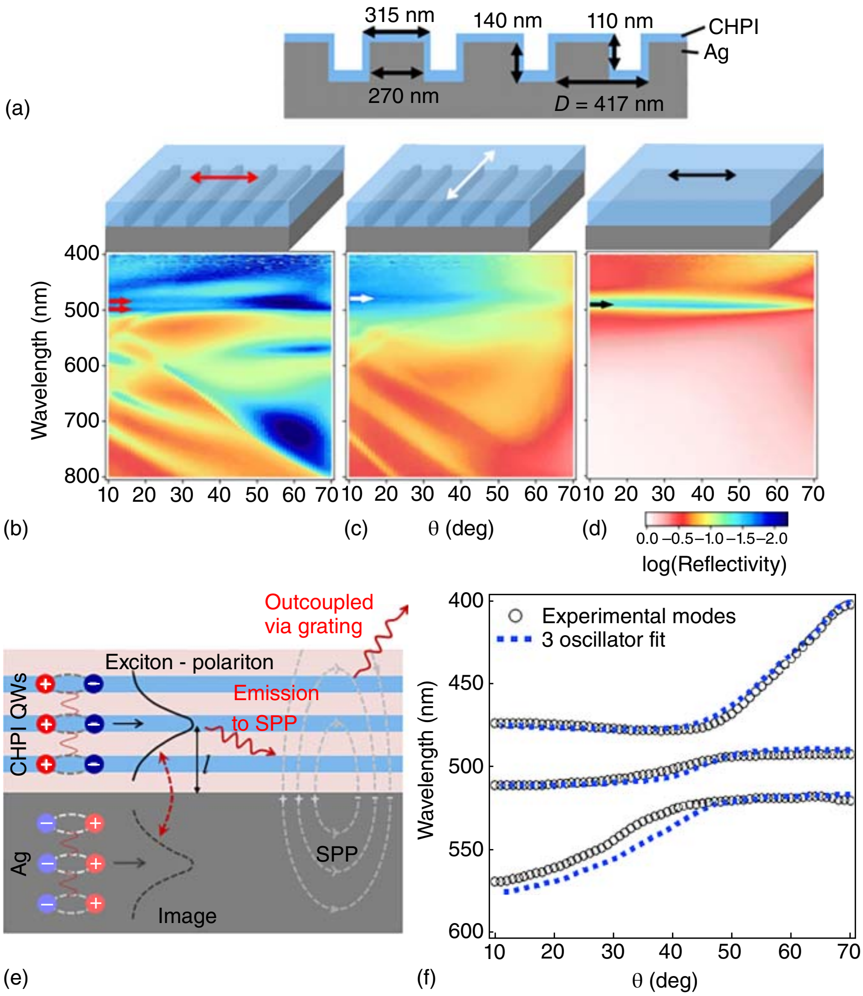

Figure 1.3.12 (a) CHPI/Ag-based DFB grating, which is the system under study in Ref. [78]. Angle-resolved reflectivity spectra of the sample with (b) TM (c) TE, and (d) planar mode measurements. The arrows indicate the observed exciton mode. (e) A schematic mechanism for SPP-mediated emission of the image biexciton. (f) Extracted spectral mode positions reflection dips (open circles) with $\varphi = 90°$, fitted with three coupled-oscillators model (dashed lines). Source: Niu et al. 2015 [78]. Copyright 2015. Adapted with permission of American Physical Society.

1.3.5 Concluding Remarks

In conclusion, 2D-OIHPs possess novel electronic properties, akin to their 3D counterparts. Quantum and dielectric confinement effect in 2D-OIHPs strongly enhanced its excitonic binding energy and oscillator strength, hence endowing it with great potential for exciton-based applications. 2D-OIHPs are especially interesting due to their much stronger interactions with phonons and photons compared to other conventional systems. In this chapter, we highlighted some of the most recent studies which aimed to uncover the fundamental understanding and implications of these strong interactions. While there has been some success in qualitative modeling to partially explain experimental observations on the phenomenological level, the detailed photophysical mechanisms and origins of the strong interaction are still not fully understood. Furthermore, issues such as lower mobility than traditional semiconductors, polariton bottleneck, etc. remain unresolved. Importantly, the holy grail of achieving BEC with these 2D perovskite systems remains elusive. Most recently, another family of perovskites known as Ruddlesden–Popper (RP) perovskites, possessing self-assembled MQW structure similar to 2D perovskites but with tunable well thickness, has entered the field. Due to their better ambient moisture resilience as compared to 3D and relatively strong excitonic properties [13], efficient LEDs [6] and photovoltaic devices [13] have been demonstrated using this novel system. Further research into understanding these interactions is key to the realization of applications of white-light LEDs, polariton lasers, or plasmonic devices based on 2D OIHPs. The future of perovskite LEDs continues to shine brightly.

References

1 Saliba, M., Matsui, T., Seo, J.-Y. et al. (2016). Cesium-containing triple cation perovskite solar cells: improved stability, reproducibility and high efficiency. *Energy Environ. Sci.* 9 (6): 1989–1997.

2 Bi, D., Tress, W., Dar, M.I. et al. (2016). Efficient luminescent solar cells based on tailored mixed-cation perovskites. *Sci. Adv.* 2 (1): e1501170.

3 NREL: Efficiency Chart (2017). Best research-cell efficiencies. https://www.nrel.gov/pv/assets/images/efficiency-chart.png (accessed 10 September 2017).

4 Tan, Z.-K., Moghaddam, R.S., Lai, M.L. et al. (2014). Bright light-emitting diodes based on organometal halide perovskite. *Nat. Nanotechnol.* 9 (9): 687–692.

5 Cho, H., Jeong, S.-H., Park, M.-H. et al. (2015). Overcoming the electroluminescence efficiency limitations of perovskite light-emitting diodes. *Science* 350 (6265): 1222–1225.

6 Yuan, M., Quan, L.N., Comin, R. et al. (2016). Perovskite energy funnels for efficient light-emitting diodes. *Nat. Nanotechnol.* 11 (10): 872–877.

7 Xing, G., Mathews, N., Lim, S.S. et al. (2014). Low-temperature solution-processed wavelength-tunable perovskites for lasing. *Nat. Mater.* 13 (5): 476–480.

8 Zhu, H., Fu, Y., Meng, F. et al. (2015). Lead halide perovskite nanowire lasers with low lasing thresholds and high quality factors. *Nat. Mater.* 14 (6): 636–642.

9 Yakunin, S., Protesescu, L., Krieg, F. et al. (2015). Low-threshold amplified spontaneous emission and lasing from colloidal nanocrystals of caesium lead halide perovskites. *Nat. Commun.* 6: 8056.

10 Dou, L., Yang, Y., You, J. et al. (2014). Solution-processed hybrid perovskite photodetectors with high detectivity. *Nat. Commun.* 5: 5404.

11 Fang, Y., Dong, Q., Shao, Y. et al. (2015). Highly narrowband perovskite single-crystal photodetectors enabled by surface-charge recombination. *Nat. Photonics* 9 (10): 679–686.

12 Chin, X.Y., Cortecchia, D., Yin, J. et al. (2015). Lead iodide perovskite light-emitting field-effect transistor. *Nat. Commun.* 6: 7383.

13 Tsai, H., Nie, W., Blancon, J.-C. et al. (2016). High-efficiency two-dimensional Ruddlesden–Popper perovskite solar cells. *Nature* 536 (7616): 312–316.

14 Koutselas, I., Bampoulis, P., Maratou, E. et al. (2011). Some unconventional organic–inorganic hybrid low-dimensional semiconductors and related light-emitting devices. *J. Phys. Chem. C* 115 (17): 8475–8483.

15 Ahmad, S., Kanaujia, P.K., Beeson, H.J. et al. (2015). Strong photocurrent from two-dimensional excitons in solution-processed stacked perovskite semiconductor sheets. *ACS Appl. Mater. Interfaces* 7 (45): 25227–25236.

16 Kawamura, Y., Mashiyama, H., and Hasebe, K. (2002). Structural study on cubic–tetragonal transition of $CH_3NH_3PbI_3$. *J. Phys. Soc. Jpn.* 71 (7): 1694–1697.

17 Papavassiliou, G.C. (1997). Three- and low-dimensional inorganic semiconductors. *Prog. Solid State Chem.* 25 (3): 125–270.

18 Sum, T.C. and Mathews, N. (2014). Advancements in perovskite solar cells: photophysics behind the photovoltaics. *Energy Environ. Sci.* 7 (8): 2518–2534.

19 Umebayashi, T., Asai, K., Kondo, T., and Nakao, A. (2003). Electronic structures of lead iodide based low-dimensional crystals. *Phys. Rev. B* 67 (15): 155405.

20 Li, Y.Y., Lin, C.K., Zheng, G.L. et al. (2006). Novel ⟨110⟩-oriented organic–inorganic perovskite compound stabilized by *N*-(3-aminopropyl)imidazole with improved optical properties. *Chem. Mater.* 18 (15): 3463–3469.

21 Pradeesh, K., Nageswara Rao, K., and Vijaya Prakash, G. (2013). Synthesis, structural, thermal and optical studies of inorganic–organic hybrid semiconductors, R-PbI4. *J. Appl. Phys.* 113 (8): 083523.

22 Ahmad, S., Hanmandlu, C., Kanaujia, P.K., and Prakash, G.V. (2014). Direct deposition strategy for highly ordered inorganic organic perovskite thin films and their optoelectronic applications. *Opt. Mater. Express* 4 (7): 1313–1323.

23 Dang, Y., Ju, D., Wang, L., and Tao, X. (2016). Recent progress in the synthesis of hybrid halide perovskite single crystals. *CrystEngComm* 18 (24): 4476–4484.

24 Yuan, Z., Shu, Y., Tian, Y. et al. (2015). A facile one-pot synthesis of deep blue luminescent lead bromide perovskite microdisks. *Chem. Commun.* 51 (91): 16385–16388.

25 Niu, W., Eiden, A., Vijaya Prakash, G., and Baumberg, J.J. (2014). Exfoliation of self-assembled 2D organic–inorganic perovskite semiconductors. *Appl. Phys. Lett.* 104 (17): 171111.

26 Mitzi, D.B., Prikas, M.T., and Chondroudis, K. (1999). Thin film deposition of organic–inorganic hybrid materials using a single source thermal ablation technique. *Chem. Mater.* 11 (3): 542–544.

27 Era, M., Hattori, T., Taira, T., and Tsutsui, T. (1997). Self-organized growth of PbI-based layered perovskite quantum well by dual-source vapor deposition. *Chem. Mater.* 9 (1): 8–10.

28 Cheng, Z. and Lin, J. (2010). Layered organic–inorganic hybrid perovskites: structure, optical properties, film preparation, patterning and templating engineering. *CrystEngComm* 12 (10): 2646–2662.

29 Cao, D.H., Stoumpos, C.C., Farha, O.K. et al. (2015). 2D homologous perovskites as light-absorbing materials for solar cell applications. *J. Am. Chem. Soc.* 137 (24): 7843–7850.

30 Smith, I.C., Hoke, E.T., Solis-Ibarra, D. et al. (2014). A layered hybrid perovskite solar-cell absorber with enhanced moisture stability. *Angew. Chem. Int. Ed.* 53 (42): 11232–11235.

31 Dohner, E.R., Jaffe, A., Bradshaw, L.R., and Karunadasa, H.I. (2014). Intrinsic white-light emission from layered hybrid perovskites. *J. Am. Chem. Soc.* 136 (38): 13154–13157.

32 Hu, T., Smith, M.D., Dohner, E.R. et al. (2016). Mechanism for broadband white-light emission from two-dimensional (110) hybrid perovskites. *J. Phys. Chem. Lett.* 7 (12): 2258–2263.

33 Yangui, A., Garrot, D., Lauret, J.S. et al. (2015). Optical investigation of broadband white-light emission in self-assembled organic–inorganic perovskite $(C_6H_{11}NH_3)_2PbBr_4$. *J. Phys. Chem. C* 119 (41): 23638–23647.

34 Han, Z., Nguyen, H.-S., Boitier, F. et al. (2012). High-Q planar organic–inorganic perovskite-based microcavity. *Opt. Lett.* 37 (24): 5061–5063.

35 Lanty, G., Zhang, S., Lauret, J.S. et al. (2011). Hybrid cavity polaritons in a ZnO-perovskite microcavity. *Phys. Rev. B* 84 (19): 195449.

36 Wei, Y., Lauret, J.S., Galmiche, L. et al. (2012). Strong exciton–photon coupling in microcavities containing new fluorophenethylamine based perovskite compounds. *Opt. Express* 20 (9): 10399–10405.

37 Ishihara, T., Takahashi, J., and Goto, T. (1990). Optical properties due to electronic transitions in two-dimensional semiconductors $(C_nH_{2n+1}NH_3)_2PbI_4$. *Phys. Rev. B* 42 (17): 11099–11107.

38 Kitazawa, N., Aono, M., and Watanabe, Y. (2012). Temperature-dependent time-resolved photoluminescence of $(C_6H_5C_2H_4NH_3)_2PbX_4$ (X = Br and I). *Mater. Chem. Phys.* 134 (2–3): 875–880.

39 Tanaka, K., Sano, F., Takahashi, T. et al. (2002). Two-dimensional Wannier excitons in a layered-perovskite-type crystal $(C_6H_{13}NH_3)_2PbI_4$. *Solid State Commun.* 122 (5): 249–252.

40 Papavassiliou, G.C. (1996). Synthetic three- and lower-dimensional semiconductors based on inorganic units. *Mol. Cryst. Liq. Cryst. Sci. Technol., Sect. A* 286 (1): 231–238.

41 Ishihara, T., Hong, X., Ding, J., and Nurmikko, A.V. (1992). Dielectric confinement effect for exciton and biexciton states in PbI_4-based two-dimensional semiconductor structures. *Surf. Sci.* 267 (1): 323–326.

42 Shimizu, M., Fujisawa, J.-I., and Ishi-Hayase, J. (2005). Influence of dielectric confinement on excitonic nonlinearity in inorganic–organic layered semiconductors. *Phys. Rev. B* 71 (20): 205306.

43 Zhang, S., Audebert, P., Wei, Y. et al. (2011). Synthesis and optical properties of novel organic-inorganic hybrid UV (R-$NH_3)_2PbCl_4$ semiconductors. *J. Mater. Chem.* 21 (2): 466–474.

44 Dohner, E.R., Hoke, E.T., and Karunadasa, H.I. (2014). Self-assembly of broadband white-light emitters. *J. Am. Chem. Soc.* 136 (5): 1718–1721.

45 Yuan, Z., Zhou, C., Tian, Y. et al. (2017). One-dimensional organic lead halide perovskites with efficient bluish white-light emission. *Nat. Commun.* 8: 14051.

46 Teunis, M.B., Lawrence, K.N., Dutta, P. et al. (2016). Pure white-light emitting ultrasmall organic–inorganic hybrid perovskite nanoclusters. *Nanoscale* 8 (40): 17433–17439.

47 Zhang, F., Zhong, H., Chen, C. et al. (2015). Brightly luminescent and color-tunable colloidal $CH_3NH_3PbX_3$ (X = Br, I, Cl) quantum dots: potential alternatives for display technology. *ACS Nano* 9 (4): 4533–4542.

48 Ema, K., Inomata, M., Kato, Y. et al. (2008). Nearly perfect triplet-triplet energy transfer from Wannier excitons to naphthalene in organic–inorganic hybrid quantum-well materials. *Phys. Rev. Lett.* 100 (25): 257401.

49 Bowers, M.J., McBride, J.R., and Rosenthal, S.J. (2005). White-light emission from magic-sized cadmium selenide nanocrystals. *J. Am. Chem. Soc.* 127 (44): 15378–15379.

50 Gardens, O.G. (2007). *Trends in Optical Materials Research*. Nova Publishers.

51 Makino, T., Segawa, Y., and Kawasaki, M. (2005). Analytical study on exciton-longitudinal-optical-phonon coupling and comparison with experiment for ZnO quantum wells. *J. Appl. Phys.* 97 (10): 106111.

52 Thirumal, K., Chong, W.K., Xie, W. et al. (2017). Morphology-independent stable white-light emission from self-assembled two-dimensional perovskites driven by strong exciton–phonon coupling to the organic framework. *Chem. Mater.* 29 (9): 3947–3953.

53 Cortecchia, D., Neutzner, S., Srimath Kandada, A.R. et al. (2017). Broadband emission in two-dimensional hybrid perovskites: the role of structural deformation. *J. Am. Chem. Soc.* 139 (1): 39–42.

54 Das, A., Bhattacharya, P., Heo, J. et al. (2013). Polariton Bose–Einstein condensate at room temperature in an Al(Ga)N nanowire–dielectric microcavity with a spatial potential trap. *Proc. Natl. Acad. Sci. USA* 110 (8): 2735–2740.

55 Kena Cohen, S. and Forrest, S.R. (2010). Room-temperature polariton lasing in an organic single-crystal microcavity. *Nat. Photonics* 4 (6): 371–375.

56 Kim, S., Zhang, B., Wang, Z. et al. (2016). Coherent polariton laser. *Phys. Rev. X* 6 (1): 011026.

57 Schneider, C., Rahimi-Iman, A., Kim, N.Y. et al. (2013). An electrically pumped polariton laser. *Nature* 497 (7449): 348–352.

58 Deng, H., Weihs, G., Snoke, D. et al. (2003). Polariton lasing vs. photon lasing in a semiconductor microcavity. *Proc. Natl. Acad. Sci. USA* 100 (26): 15318–15323.

59 Kavokin, A., Malpuech, G., and Laussy, F.P. (2003). Polariton laser and polariton superfluidity in microcavities. *Phys. Lett. A* 306 (4): 187–199.

60 Byrnes, T., Kim, N.Y., and Yamamoto, Y. (2014). Exciton–polariton condensates. *Nat. Phys.* 10 (11): 803–813.

61 Deng, H., Weihs, G., Santori, C. et al. (2002). Condensation of semiconductor microcavity Exciton polaritons. *Science* 298 (5591): 199–202.

62 Kavokin, A. and Malpuech, G. (2003). Frequently asked questions. In: *Thin Films and Nanostructures*, vol. 32 (ed. K. Alexey and M. Guillaume), 13–26. Academic Press.

63 Su, R., Diederichs, C., Wang, J. et al. (2017). Room-temperature polariton lasing in all-inorganic perovskite nanoplatelets. *Nano Lett.* 17 (6): 3982–3988.

64 Giovanni, D., Chong, W.K., Dewi, H.A. et al. (2016). Tunable room-temperature spin-selective optical stark effect in solution-processed layered halide perovskites. *Sci. Adv.* 2 (6): 1600477.

65 Fujita, T., Sato, Y., Kuitani, T., and Ishihara, T. (1998). Tunable polariton absorption of distributed feedback microcavities at room temperature. *Phys. Rev. B* 57 (19): 12428–12434.

66 Brehier, A., Parashkov, R., Lauret, J.S., and Deleporte, E. (2006). Strong exciton–photon coupling in a microcavity containing layered perovskite semiconductors. *Appl. Phys. Lett.* 89 (17): 171110.

67 Lanty, G., Bréhier, A., Parashkov, R. et al. (2008). Strong exciton–photon coupling at room temperature in microcavities containing two-dimensional layered perovskite compounds. *New J. Phys.* 10 (6): 065007.

68 Li, G., Liew, T.C.H., Egorov, O.A., and Ostrovskaya, E.A. (2015). Incoherent excitation and switching of spin states in exciton–polariton condensates. *Phys. Rev. B* 92 (6): 064304.

69 Liew, T.C.H., Kavokin, A.V., Ostatnický, T. et al. (2010). Exciton–polariton integrated circuits. *Phys. Rev. B* 82 (3): 033302.

70 Ballarini, D., De Giorgi, M., Cancellieri, E. et al. (2013). All-optical polariton transistor. *Nat. Commun.* 4: 1778.

71 Gao, T., Eldridge, P.S., Liew, T.C.H. et al. (2012). Polariton condensate transistor switch. *Phys. Rev. B* 85 (23): 235102.

72 Amo, A., Liew, T.C.H., Adrados, C. et al. (2010). Exciton–polariton spin switches. *Nat. Photonics* 4 (6): 361–366.

73 Tartakovskii, A.I., Krizhanovskii, D.N., Malpuech, G. et al. (2003). Giant enhancement of polariton relaxation in semiconductor microcavities by polariton-free carrier interaction: experimental evidence and theory. *Phys. Rev. B* 67 (16): 165302.

74 Lagoudakis, P.G., Martin, M.D., Baumberg, J.J. et al. (2003). Electron–polariton scattering in semiconductor microcavities. *Phys. Rev. Lett.* 90 (20): 206401.

75 Wenus, J., Parashkov, R., Ceccarelli, S. et al. (2006). Hybrid organic–inorganic exciton–polaritons in a strongly coupled microcavity. *Phys. Rev. B* 74 (23): 235212.

76 Lanty, G., Lauret, J.S., Deleporte, E. et al. (2008). UV polaritonic emission from a perovskite-based microcavity. *Appl. Phys. Lett.* 93 (8): 081101.

77 Nguyen, H.S., Han, Z., Abdel-Baki, K. et al. (2014). Quantum confinement of zero-dimensional hybrid organic–inorganic polaritons at room temperature. *Appl. Phys. Lett.* 104 (8): 081103.

78 Niu, W., Ibbotson, L.A., Leipold, D. et al. (2015). Image excitons and plasmon-exciton strong coupling in two-dimensional perovskite semiconductors. *Phys. Rev. B* 91 (16): 161303.

79 Chance, R.R., Prock, A., and Silbey, R. (1975). Frequency shifts of an electric-dipole transition near a partially reflecting surface. *Phys. Rev. A* 12 (4): 1448–1452.

80 Frischeisen, J., Niu, Q., Abdellah, A. et al. (2011). Light extraction from surface plasmons and waveguide modes in an organic light-emitting layer by nanoimprinted gratings. *Opt. Express* 19 (S1): A7–A19.

81 Kumar, A., Srivastava, R., Tyagi, P. et al. (2012). Efficiency enhancement of organic light emitting diode via surface energy transfer between exciton and surface plasmon. *Org. Electron.* 13 (1): 159–165.

Part II

Organic–Inorganic Perovskite Solar Cells

2.1

Working Principles of Perovskite Solar Cells

Pablo P. Boix[1], *Sonia R. Raga*[2], *and Nripan Mathews*[3,4]

[1] *Universidad de Valencia, Instituto de Ciencia Molecular, C/J. Beltrań 2, Paterna 46980, Spain*
[2] *Monash University, ARC Centre of Excellence in Exciton Science, Department of Chemical Engineering, Clayton, VIC, 3800, Australia*
[3] *Energy Research Institute at Nanyang Technological University (ERI@N), Research Techno Plaza, X-Frontier Block Level 5, 50 Nanyang Drive, Singapore 637553, Singapore*
[4] *Nanyang Technological University, School of Materials Science and Engineering, 50 Nanyang Avenue, Singapore 639798, Singapore*

2.1.1 Introduction

The scientific interest raised by perovskite solar cells has resulted in an incessant increase of their power conversion efficiencies (PCEs). Since pioneering reports in 2012, the number of reports analyzing the fundamentals of perovskite solar cells has risen rapidly. Despite these efforts, basic perovskite solar cell working mechanisms are not completely established, and thus they remain a topic of research and discussion.

An understanding of the working mechanisms of the cell is key to identifying the physical processes limiting the photovoltaic performance of the device. This is the most effective route to improve the solar cell PCE, particularly when the quality of the devices is close to the optimal one. Accordingly, the ultimate goal must be identifying the factors determining relevant photovoltaic parameters which define the efficiency, namely, short circuit current (J_{sc}), open circuit potential (V_{oc}), and fill factor (FF). The high efficiency achieved by perovskite solar cells till date reflects the absence of a major deficiency related to any of these parameters, but further enhancements toward the Shockley–Queisser limit will require their individual analysis and improvement. Knowledge obtained from precedent solar cell technologies (from silicon solar cells, to dye-sensitized and organic solar cells) is not always directly applicable to their perovskite counterparts. From the early days, it was clear that many of the phenomena observed in perovskite-based devices were foreign to other photovoltaic technologies. These unconventional features of perovskite photovoltaics (such as current-voltage hysteresis or large dielectric constant, to name a few) also indicate unprecedented working mechanisms. Altogether, it necessitates fundamental studies to fully understand, exploit, and improve halide perovskite solar cells.

Halide Perovskites: Photovoltaics, Light Emitting Devices, and Beyond, First Edition.
Edited by Tze-Chien Sum and Nripan Mathews.

Due to the rapid development and potential low fabrication cost of perovskite solar cells, they are already a subject of commercialization efforts. However, certain issues presently hinder the commercialization of this technology, including thermal stability, ambient (particularly moisture) degradation, toxicity of the components, and scalability of the processing techniques. The solution to these challenges requires not only an important engineering approach but also a strong scientific approach, as a complete understanding of the working mechanisms is essential to propose successful tools to address the mentioned issues.

This chapter examines the updated knowledge on the working mechanisms of perovskite solar cells, with the focus on physical processes determining the photovoltaic performance. This includes charge generation (absorption of light and formation of electrons and holes), charge transport, charge carrier losses through recombination, and charge extraction; and examines the main parameters defining those processes. Finally, the ionic nature of metal halide perovskites is discussed, as well as its implications in the aforementioned processes and unconventional phenomena of the solar cells.

2.1.2 Charge Generation

Two of the main characteristics of perovskite solar cells, which define their uniqueness and partially explain their success, are their excellent absorption properties and low exciton binding energy. Light absorption is the first physical process in photovoltaic generation. In short, the active material is excited by a photon more energetic than its bandgap and generates an exciton or an electron–hole pair, as discussed here. The advantages of metal halide perovskites in this aspect are clear: (i) the relatively high extinction coefficient ($>10^4\,\text{cm}^{-1}$, higher than that for GaAs2 [1]) allows absorption of incident light with a very thin perovskite layer; (ii) the sharp optical absorption edge which reduces the energetic losses ($CH_3NH_3PbI_3$ displays an Urbach energy of 15 meV [2]); and (iii) a tunable bandgap achievable by compositional engineering [3], although the record perovskite solar cell efficiencies to date have been obtained with a bandgap slightly larger [4] (~1.6 eV) than the ideal one for photovoltaics [5] (~1.3 eV).

As a direct consequence of these properties, the most efficient perovskite solar cells reported use of an absorber layer in the 300–600 nm range, almost three orders of magnitude smaller than silicon solar cells [6]. The thinner films required for light absorption means shorter paths for charge transport, which results in a reduction in the possibilities of recombination, thus reducing the energetic losses and increasing the final voltage of the device. The sharp optical absorption onset, with a Urbach energy of 15 meV, is characterized by their purely exponential behavior over more than four orders of magnitude, with the absence of optically active deep states (Figure 2.1.1). The possibility of changing the perovskite bandgap by tuning its composition is an advantage for perovskite photovoltaics. The metal halide perovskites employed in the most efficient single-junction solar cells are based on variations of the original $CH_3NH_3PbI_3$, with a combination of cations at the $CH_3NH_3^+$ position (formamidinium [7], cesium [8], and even rubidium [9], among others) and iodide–bromide mixtures

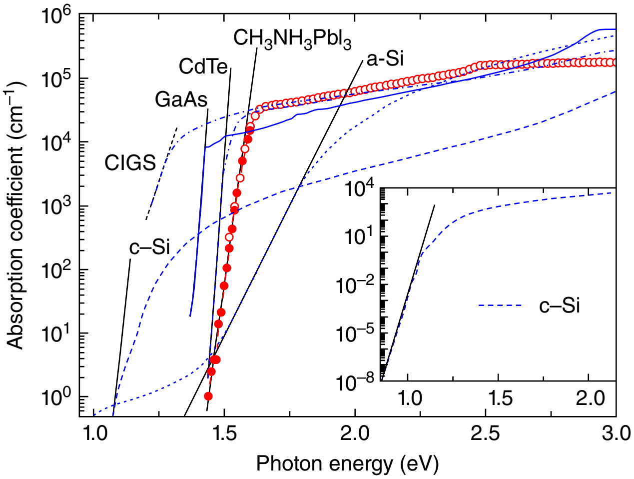

Figure 2.1.1 Effective absorption coefficient of a $CH_3NH_3PbI_3$ perovskite thin film compared to other typical photovoltaic materials, including amorphous silicon (a-Si), GaAs, CIGS, CdTe, and crystalline silicon (c-Si), all measured at room temperature with the slope of the Urbach tail indicated. The inset shows the data for c-Si down to low absorption values. Source: De Wolf et al. 2014 [2]. Reprinted with permission of American Chemical Society.

which result in a bandgap in the 1.5–1.7 eV range. As examples of perovskite tunability, the increase of the Br content results in a larger bandgap [10], which could be really attractive for multi-junction tandem applications if phase segregation issues are solved. Other strategies to reduce the bandgap include the (partial [11] or total [12]) substitution of the lead metal by tin, although in these systems reduced stability is a strong concern.

Organic and dye-sensitized solar cells, technologies that are often compared to perovskite photovoltaics, require an interface to dissociate the generated exciton/excited state. This is concomitant with an energetic price, which decreases the achievable open circuit voltage. The low exciton binding energy of perovskites, in contrast, results in a high population of both charge carriers (electrons and holes) within the same absorber material. This plays a key role in determining the working mechanism of perovskite solar cells, and is discussed later in the chapter. The splitting of the quasi-Fermi levels for electrons and holes within the absorber has implications on the transport, recombination, and extraction of charges. This is thus one of the main reasons for the high PCEs obtained with these materials, as it is possible to avoid V_{oc} limitations established by the contacts' energy levels. But let us first examine its underlying origin: what makes exciton binding energy so low in metal halide perovskites? The dielectric characteristics of a material is the primary factor determining the energy required to dissociate an exciton, as it is an estimate of its charge screening capability. In this sense, organic solar cells possess low dielectric constant and require an interface with an energy mismatch >0.3 eV in order to dissociate the generated exciton. Perovskites such as $CH_3NH_3PbI_3$ and $CH_3NH_3PbBr_3$ present unusually high dielectric constants [13] dependent on the illumination [14], which could also result in a polaronic behavior [15, 16].

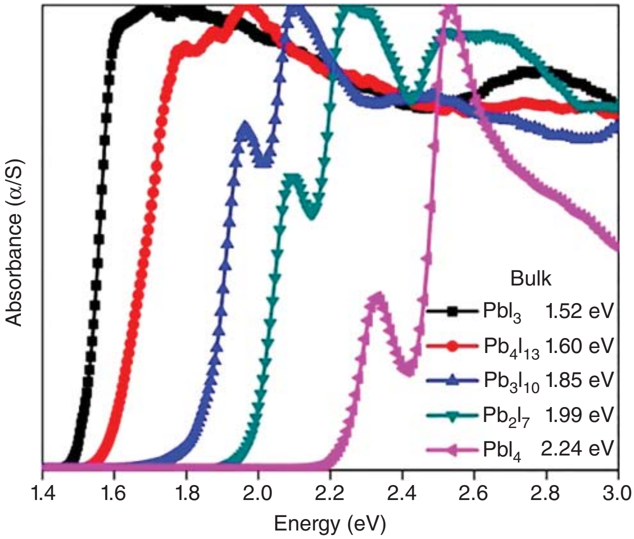

Figure 2.1.2 Optical absorbance of $(BA)_2(MA)_{n-1}Pb_nI_{3n+1}$ compounds displaying characteristic excitonic lower dimensional absorbance peaks. Source: Cao et al. 2015 [22]. Reproduced with permission of American Chemical Society.

As a result, Wannier–Mott excitons with a binding energy ~15 meV [17] have been reported for $CH_3NH_3PbBr_3$, whereas $CH_3NH_3PbI_3$ displays mostly an electronic behavior. For most intents and purposes, $CH_3NH_3PbI_3$ can be considered a non-excitonic material, as free charges are predominantly generated following light absorption in the structures employed in perovskite solar cells [18]. However, these materials are defined by an interplay between excitons and free carriers as both regimes are physically accessible by appropriately processing the compounds [19]. This is emphasized by a morphology-dependent exciton dissociation, as crystal sizes of ~1 μm display excitonic fingerprints in the transient absorption, while films with smaller grains showed purely electronic behavior. This trend is confirmed by the analysis of single crystals [20], which shows a size-dependent electronic or excitonic behavior.

The situation can be different for 2D or lower dimensionality perovskite films, where excitonic peaks, depending on the structure stack order (n), are evident in the absorption characteristics [21]. (Figure 2.1.2). This tunability of the excitonic behavior as a function of the film morphology, composition, and dimensionality is a great asset for perovskite optoelectronics, as similar materials can be modified to be employed in low exciton binding energy applications (such as photovoltaics) or high exciton binding applications ones (such as light emission) [3, 23].

2.1.3 Charge Transport

Once the electrons and holes are photogenerated in the perovskite, they have to arrive at the contacts to be extracted. This process is correlated to the charge-transport characteristics of the halide perovskite itself. In contrast to other photovoltaic systems, metal halide perovskites acting as absorbers in the usual thin-film solar cell configuration have to provide efficient transport for both electrons and holes. The outstanding PCE of metal halide perovskite solar cells is the result of, among other things, the exceptional charge-transport properties of the material, with long charge carrier diffusion lengths, L, of more than 5 μm, and an associated lifetime, τ, of $\sim$1 μs in both single-crystal and polycrystalline films [24, 25]. Such diffusion lengths assure the possibility of extracting the generated charge even in thicker films which absorb all the incident light. Metal halide perovskites' diffusion length values are orders of magnitude larger than those of most organic solution-processed materials (such as poly(3-hexylthiophene) (P3HT), phenyl-C_{61}-butyric acid methyl ester (PCBM)), in which diffusion lengths are typically lower than 10 nm [26].

More importantly, diffusion lengths for electrons and holes seem to be well balanced in perovskite solar cells [27], which is especially needed in thin-film solar cells to extract both carriers efficiently. Despite extensive characterization, the origin of these transport properties in metal halide perovskites is still a matter of scientific discussion. Mobility (μ) is the main parameter which determines the diffusion length, as $L = \sqrt{D\tau}$, where D is the diffusion coefficient defined as $D = \mu q/k_B T$ with q being the elementary charge, k_B the Boltzmann constant, and T the temperature. When perovskite mobilities are calculated theoretically, the values are high (comparable to those of crystalline inorganic semiconductors). Experimental values are, nonetheless, hard to obtain and not always coherent. While Hall-effect measurements yield relatively high mobility values (from 0.5 to 60 $\mathrm{cm^2\ V^{-1}\ s^{-1}}$ depending on the nature of the sample) [28], the effective carrier mobility in field-effect transistors (FETs) and diodes is much lower than expected [29] (Figure 2.1.3).

Indeed, as it usually happens with pure undoped band insulators, $CH_3NH_3PbI_3$ samples are highly resistive in the dark (with a typical sample resistance >100 GΩ). The low charge carrier density generally measured in the bulk of these materials, in the range of 10^{15}–10^{17} $\mathrm{cm^{-3}}$ for polycrystalline perovskite thin films and 10^{10} $\mathrm{cm^{-3}}$ for single crystals, results in a low dark conductivity [29].

In addition, the relatively low charge carrier density depicts a situation where the electric field can play an important role in charge extraction (unlike similar devices such as dye-sensitized solar cells, strongly dominated by charge diffusion). If the perovskite absorber is sandwiched between two doped contacts (n-type for the electron-extracting layer and p-type for the hole-extracting layer) in the solar cell, the band diagram of the system can then be approximated by a p-i-n model where the intrinsic perovskites homogeneously distributes the electric field (Figure 2.1.4). However, the presence of mobile ionic defects [30] as discussed in the last section of this chapter, is a key factor which has to be coupled to the aforementioned semiconductor properties when charge transport is discussed. Ions in perovskite, probably related to vacancies, are mobile charges which cannot be extracted through the contacts. As a consequence, redistributed upon the application of a voltage, the ions can determine the electric field within the perovskite absorber (Figure 2.1.4), even inverting the selectivity of the

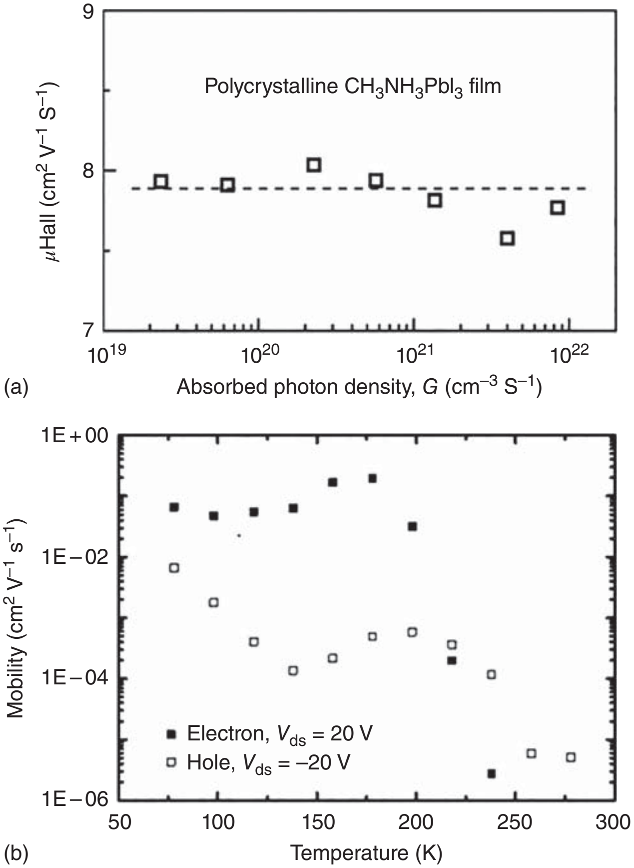

Figure 2.1.3 (a) Example of mobility measured at different photo-excitation densities for a polycrystalline $CH_3NH_3PbI_3$ 100-nm-thick film fabricated by vapor deposition. Source: Chen et al. 2016 [28]. (b) Temperature dependence of field-effect electron and hole mobilities of solution processed $CH_3NH_3PbI_3$ in a transistor configuration, extracted from the forward sweeping of transfer characteristics at $V_{ds} = 20$ V and $V_{ds} = -20$ V, respectively. Source: Chin et al. 2015 [29]. https://www.nature.com/articles/ncomms8383. Licensed Under CC BY 4.0.

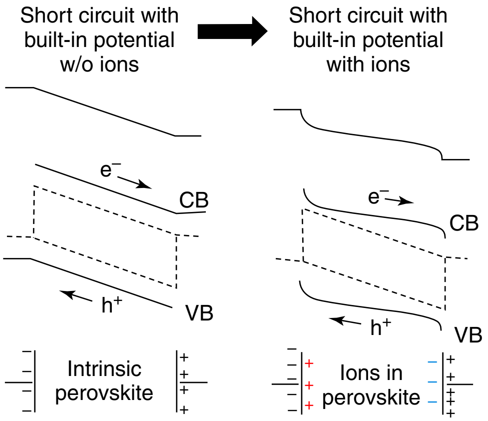

Figure 2.1.4 Schematic band diagram of a perovskite solar cell under illumination showing the screening effect of mobile ions (coded with + and − respectively). Quasi-Fermi levels are represented as dashed, CB = conduction band edge, VB = valence band edge. Source: Tress 2017 [30]. Reproduced with permission of American Chemical Society.

contacts in extreme cases [31]. As a consequence, the internal distribution of the electric field is an important factor for the charge transport of electrons and holes, which has thus to be considered in drift-diffusion models [32].

Another possible explanation connecting the large diffusion lengths and the moderate mobilities would be the presence of strong electron–phonon coupling, which would trigger polaronic-protected charge transport [15] even at room temperature. Polarons are quasi-particles formed by the interaction between the charge carriers and the material lattice. Perovskites' unusually high dielectric constant, discussed in the previous section, could form a particularly suitable system to screen the charge; which strongly relies on the crystallinity and stress state of the perovskite layer [33]. Although the temperature dependence of the conductivity could be an indication of polaron-dominated charge transport in $CH_3NH_3PbBr_3$ single crystals [28], further evidence is required to demonstrate this hypothesis.

These physical processes, which enable the outstanding transport properties of metal halide perovskites, are strongly grounded on the excellent crystallinity obtained from different fabrication routes (including low-temperature solution processes). The trap-density differences observed for single crystals [20, 24] (10^9–10^{10} cm^{-3} for $CH_3NH_3PbI_3$ and $CH_3NH_3PbBr_3$, comparable to those of the best intrinsic silicon and GaAs) and polycrystalline films ($\sim 10^{16}$ cm^{-3}), seem to indicate a significant concentration of traps in the grain boundaries. Following this approach, several studies have focused on increasing the grain size of the perovskite films as a route to improve the solar cell efficiency [34], justified as an improvement in grain-to-grain charge transport [32].

However, a combination of theoretical and experimental analysis pointed toward the intrinsic benignity of the defects [1], which would reduce the importance of a large grain size. Grain sizes >100 nm have actually been proved to have an insignificant role in the recombination [35]. Along the same lines, very high efficiency (>20%) perovskite solar cells have also been reported with grain size <10 nm, where the high FFs (>80%) indicate nearly optimal charge transport [36]. Further studies will be crucial to elucidate the main parameters governing the charge-transport processes, and correlate them to the film's structural and morphological characteristics as well as different fabrication routes.

2.1.4 Charge Recombination

The initial studies on metal halide perovskite–based solar cells had patches of perovskite crystals wetting the surface of TiO_2 mesoporous particles, and hole transport layer (HTL) infiltrated into the pores of the TiO_2. In this scenario, perovskite material injected electrons to TiO_2 and holes to the HTL. However, further works revealed unique properties for the hybrid perovskite materials. As previously discussed, the perovskite absorber does not necessarily require a nanostructured electron selective contact to store the photoexcited electrons in order to effectively extract the charges. Initial reports demonstrated that efficient solar cells could be achieved using electrically insulating mesoporous Al_2O_3 scaffold layers instead of mesoporous TiO_2, revealing that the perovskite could transport electrons by itself [37]. The planar perovskite structure arose after such a finding, with films over 500 nm in thickness able to efficiently separate and transport electrons and holes. This was possible thanks to the fast exciton dissociation, remarkably high charge diffusion lengths of perovskite and possibility of self-doping at the interface [38]. The unique working mechanisms of hybrid perovskite solar cells (PSC) also influence the way charge is lost by recombination. The recombination mechanisms in perovskite solar cells can be divided into three main groups; (i) through shunt paths directly contacting HTL and ETL (electron transport layer), (ii) recombination within the bulk of perovskite film, and (iii) at the perovskite/ETL or perovskite/HTL interface [39] (as depicted in Figure 2.1.5). Recombination of photogenerated charges competes with the charge extraction to external circuit; thus, the kinetics of these processes ultimately govern the overall photovoltaic conversion efficiency of the solar cells.

Charge recombination through shunt paths implies a direct electrical contact between the electron and hole extraction layers, akin to TiO_2 in contact with the electrolyte in dye sensitized solar cells (DSC). In the early days of PSC research, the fabrication methods of perovskite film could not always ensure complete coverage of the underlying material (commonly TiO_2 or poly(3, 4-ethylenedioxythiophene):polystyrene sulfonate (PEDOT:PSS)). Direct contact of ETL and HTL at perovskite pinholes was likely one of the major causes of charge loss by recombination, leading to the low performances achieved for PSC in early reports, specially reflected by low open circuit voltages, V_{oc} [40]. Several reports found that employing a "capping layer" of perovskite on top of the mesoporous TiO_2 dramatically enhanced the cell efficiency. Once film fabrication techniques improved and complete coverage was achieved for both planar and mesoporous devices, solar cell efficiencies were boosted over 15% and V_{oc} exceeded 1.1 V for $CH_3NH_3PbI_3$ cells [41]. Therefore, charge loss by recombination through shunt paths directly contacting ETL and HTL is

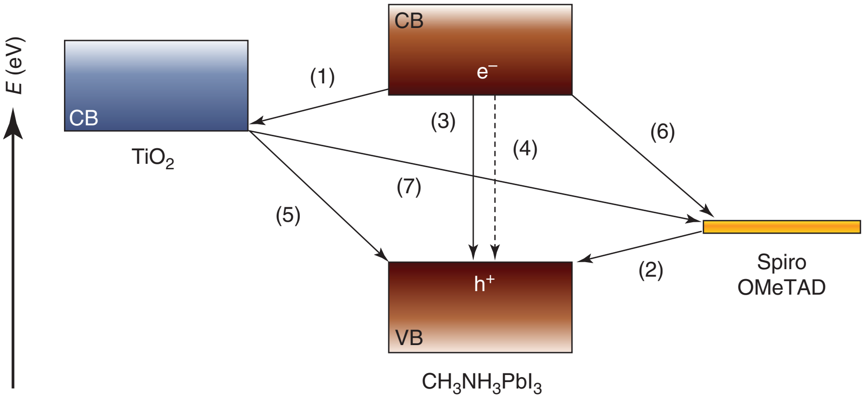

Figure 2.1.5 Schematic representation of possible recombination and charge transfer events occurring in a perovskite solar cell. Where (1) represents the electron injection to the TiO_2, (2) hole injection to the spiro-OMETAD, (3) the radiative and (4) non-radiative charge recombination within the perovskite layer, the interfacial recombination (5) with TiO_2 and (6) the spiro-OMeTAD and (7) the recombination through shunt paths directly contacting the selective layers.

negligible in current state-of-the-art high-performing perovskite solar cells. This leads to the conclusion that such charge loss is only dependent on the architecture or morphology of the layer, not on the material properties of the perovskite itself.

Bulk recombination, in contrast, accounts for electrons and holes recombining within the perovskite bulk, either band-to-band radiative recombination or non-radiative trap-assisted recombination. Therefore, this process will be determined by the traps present in the material, which will also define the loss rates. Reports have shown how the quality of the perovskite crystal lattice, such as ion vacancies or interstitials and the number of defects at the grain boundaries, is directly related to the number of trap states [42]. In a photoactive semiconductor, the band-to-band recombination can be termed as monomolecular (MR) and bimolecular (BR). MR takes place when either the electron (n_e) or the hole density (n_h) remains approximately constant and the recombination rate is proportional to the density of the minority carriers. This situation can take place, for example, in the presence of a large number of trapped electrons reducing n_e or on highly doped semiconductors. BR occurs when the density of both electrons and holes vary comparably and the recombination rate is proportional to n_e^2 (see Figure 2.1.6).

Transient photoluminescence (PL) techniques have been employed to reveal radiative recombination kinetics in pristine perovskite [43–45]. Despite their similarity to organic photovoltaic (OPV) materials, hybrid organic–inorganic perovskite crystals display very fast exciton dissociation into free charges. Thus, these charges are mainly lost by radiative recombination of electrons and holes rather than exciton relaxation [44]. In low-illumination conditions, where the electron population is less than the hole population (because some photoexcited electrons are trapped), the recombination is found to be MR [43]. When illumination is intense enough to fill all the trapped states, the recombination becomes BR with a PL power-law decay [43]. Similar MR and BR were found in the bulk and surface, respectively, of $CH_3NH_3PbBr_3$ and $CH_3NH_3PbI_3$ single crystals [46]. This was attributed to the increased number of defects in the single crystal surfaces compared to bulk, which can be extrapolated to grain

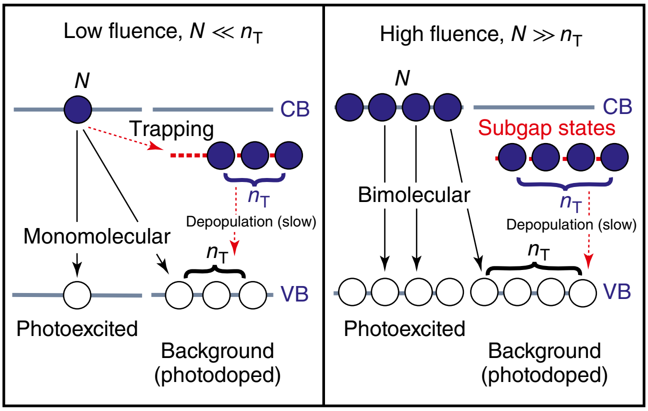

Figure 2.1.6 Mono and bimolecular recombination scheme. Reprinted with permission from Ref. [43].

boundaries and interfacial areas in actual PSC films. However, many of these fundamental studies have been carried out in isolated perovskite crystals or in thin films where photogenerated charges are not collected.

Non-radiative trap-assisted recombination may also play a role in the perovskite bulk. However, illumination is reported to induce the (reversible) formation of meta-stable deep-level trap states in the perovskite, which promotes bulk recombination in the long-term operation. Trap states seem to be mainly originated from lattice defects. Calculated energies for most of the common lattice defects such as halide vacancies are reported to be very shallow, close to the conduction or valence bands, thereby having a minimal effect on recombination. In devices, the perovskite/selective contact interfaces determine the performance of the solar cell (see Figure 2.1.7). Therefore, the role of interfacial recombination becomes a significant process to understand the photogenerated charge losses of the devices. Interestingly, recombination mechanisms were found to be influenced by the applied bias on perovskite solar cells [47]. As a consequence, the different operation conditions of a perovskite solar cell can determine the way charges recombine and, no less important, the location where recombination takes place. Recent studies have found that under low illumination intensities and when the internal electric field is minimized (voltages close to V_{oc}), the recombination is dominated by the bulk of the film [48]. However, for devices that have been polarized either under high illumination (photodoping) or by applying voltage (i.e. after measuring a j–V curve), the recombination occurs mainly at the interface [48]. This finding is linked to the fact that recombination is also time dependent and sensitive to the previous conditions and history of the device [43, 48].

For example, variation of V_{oc} or PL signal over timescales of seconds is often observed in perovskite solar cells, and such variation (increase or decay) differs depending on whether the device was biased or not prior to measurement [43, 48]. The most supported explanation for such phenomena is the ionic (vacancy) motion and accumulation at the interface inducing slow filling of distributed sub-gap trap states [43, 48], as discussed in the last section of this chapter. The presence of slow ionic transport and surface polarization has very important implications on the study of perovskite devices, because these changes cannot be separated from recombination kinetics [49]. Such

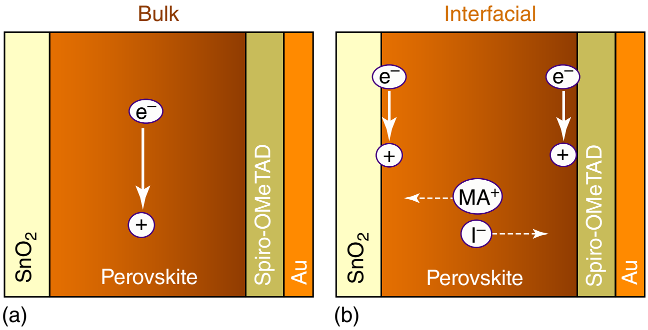

Figure 2.1.7 Changes from bulk to surface recombination.

interfacial recombination is dependent on both ionic motion and selective contact material, and has been proposed to be the cause of hysteresis [50]. Some publications reported the existence of a reverse injection after poling the device, which in the end is equivalent to recombination. Therefore, interfacial polarization, known, for example, in the giant switchable photovoltaic effect [31], directly affects the magnitude of interfacial recombination and is probably the most important mechanism governing the performance of the device.

The unique properties of perovskites, such as fast exciton dissociation and large diffusion lengths, together with the shallow trap states caused by impurities, reduces to a large extent the charge carrier loss within the perovskite bulk. Although it is still a controversial matter, mounting evidence points to the interface as a major cause of recombination. However, such recombination is largely affected by the interfacial polarization caused by ion/vacancy accumulation and is therefore difficult to quantify.

2.1.5 Charge Extraction/Injection: Interfacial Effects

All the working principles discussed up to this point of the chapter were strongly dependent on the perovskite film. However, the quality of the final device relies equally on the interfacial contacts with the charge extracting materials, following the notion "the interface is the device" [51]. After the absorption and charge transport, the final mechanisms required for the photovoltaic process is the extraction of the photogenerated charge. Thus, an optimal extracting interface should assure a minimal loss of voltage, current, and FF. In order to translate these requirements to physical processes, it is necessary to understand the particular role of the interfaces in perovskite solar cells.

An ideal selective contact should not absorb light, to avoid the reduction of light intensity in the perovskite. Similarly, there should not be energetic losses during the injection from the absorber (no interfacial recombination). While these contact materials have to be selective to allow the injection of only one kind of carrier, they also have to reduce the series resistance. Thus, this requires a balance between the intrinsic and doped nature of the semiconductor [39]. While these conditions define the ideal contact, any real material will introduce losses in the final photovoltaic performance, affecting J_{sc} (for example, by parasitic optical absorption), V_{oc} (with losses such as interfacial recombination) and FF (by the resistance of the material when extracting the photogenerated charge).

The initial evolution of perovskite solar cells relied on the charge extracting materials employed. The first ever devices employing $CH_3NH_3PbI_3$ and $CH_3NH_3PbBr_3$ as absorber already used nanoporous TiO_2 as electron extracting material; however, the photogenerated holes were extracted through a liquid electrolyte [52], as in standard dye-sensitized solar cells. These solar cells had two major differences compared to the current perovskite solar cells: on one hand, the solvent-based electrolyte compromised the stability of the system (lifetime < 10 minutes). On the other, the redox level pinned the hole quasi-Fermi level of the device, limiting the maximum achievable open circuit potential. In 2012, two works revolutionized the field using a solid-state hole-transporting material, spiro OMeTAD, in perovskite solar cells [40, 53]. These reports achieved PCEs close to 10% and V_{oc}s ~ 1 V, highlighting the importance of the contacts. After that, multiple configurations of perovskite solar cells have yielded high efficiencies, including C_{60} derivatives [54], Al_2O_3 [37], and ZnO [55], among others, for the electron extraction layers (both planar and mesoporous), as well as poly(triaryl amine) (PTAA) [35], CuSCN [56], NiO_x [57], carbon [58], etc. for the extraction of holes.

One of the first strategies proposed to improve the solar cell performance by interfacial tuning was the shift of the highest occupied molecular orbital (HOMO or valence band) of the hole-transporting material to increase the device V_{oc}. This approach is derived from the dye-sensitized solar cell system, where the hole quasi-Fermi level was pinned by a redox potential. However, metal halide perovskites possess low exciton binding energy which, as previously discussed, allows a quasi-Fermi level splitting within the absorber itself. As a consequence, as long as surface recombination is avoided, the energetics of the contacts does not influence V_{oc}, determined by the charge carrier concentration in the bulk. Therefore, shifting the HOMO of commonly used hole transport materials to higher binding energies is neither required nor a promising strategy to improve V_{oc}, as shown experimentally [59, 60], which justifies the large library of organic and inorganic materials successfully employed as charge collectors in perovskite solar cells. In contrast, the doping of the contact material can indeed affect the device performance through the achieved voltage, as it is related to the recombination losses at the interface [35].

This has strong implications in the charge extraction mechanisms of perovskite solar cells. For instance, unlike precedent solar cell technologies, V_{oc}s above the contacts' energetic levels difference (electron-transporting material conduction band and hole-transporting material valence band) were achievable since early reports [53]. Also derived from this idea, there are excellent results obtained through a reduction of interfacial (surface) recombination, a key parameter to consider for the contact material choice. Large bandgap intrinsic materials at the contact reduce the non-radiative recombination. Thus, the improvement of charge carrier selectivity of the contact results in a direct increase of the V_{oc} [36], similar to the use of buffer layers to reduce the recombination [54, 61].

The characteristics of the materials used as contacts in perovskite solar cells seem to be closely related to the uncommon features present in this kind of devices. Current-voltage hysteresis can be enhanced by the reduction of the electron-transporting material's conductivity, as this generates a charge carrier imbalance [62].

Further interface effects are evident in the internal electric field distribution. An accumulation region (usually attributed to positive charges) at the interface can define the field near the contact [63] (Figure 2.1.8). Despite the band distribution being still under scientific discussion, processes such as quantum tunneling could be necessary to understand the charge injection in this case [64]. Carrier accumulation has been characterized by a low-frequency capacitance, which can reach values as large as 10 mF cm^{-2} at one sun illumination in both methylammonium- and formamidinium-based devices [63, 65]. In these models, the charge accumulation contributes to the V_{oc} built up at the contact similarly to a standard dipolar effect, as the process is affected by slow mobile ion charges forming a double

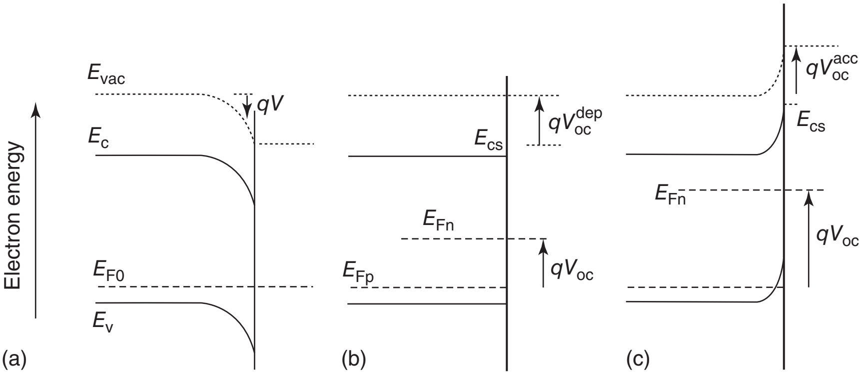

Figure 2.1.8 Schematic energy diagram for the perovskite/electron selective contact interface of a solar cell at open-circuit conditions. (a) Depletion layer at equilibrium. Generation of minority carriers produces flatband condition (b) and further accumulation (c).

layer at the interface. Although the accumulation effect seems independent of the contact employed, the associated charge dynamics varies with the employed material [66].

2.1.6 Ionic Mechanisms

The performance of perovskite solar cells is also dependent on the prior optical and electronic conditioning, an effect widely known as hysteresis which affects the shape of the j–V curves and, in a practical sense, determines the real performance of these types of solar cells [67, 68]. Time-dependent processes have also been observed like slow changes in device photocurrent, PL intensity, and V_{oc} in time scales of minutes [69, 70]. These processes are highly important as they are the foundation of transient characterization techniques such as PL decay, V_{oc} decay, intensity-modulated photovoltage spectroscopy/intensity-modulated photocurrent spectroscopy (IMVS/IMPS), or impedance spectroscopy (IS), from which the electronic charge transport and recombination is obtained, Thus, ion migration effects add an extra variable to consider. The general model to explain such slow processes is through time-varying quantities of charge accumulated at the perovskite interfaces, screening the internal electric field [31, 67, 71–73]. Several models have been proposed to explain the accumulation of charge by ferroelectric polarization, charge trapping or defect migration in the perovskite [68]. However, the polarization and trapping mechanisms would be intrinsically too fast to be the only cause of such processes in the scale of few seconds [69, 73, 74]. Evidence points to the slow motion of perovskite defects as the dominant mechanism causing hysteresis in the ABX_3 organic–inorganic perovskite. Halide anion (X) vacancies have shown the lowest formation energies, followed by the cation (A) and the metal (B) vacancies [71, 75]. Short circuit chronoamperometry measurements at different temperatures gave fitted values for activation energies of 0.6 eV, close to the activation energies calculated by discrete Fourier transform (DFT) for iodine vacancies [71, 73]. A large drift of iodine ions has been experimentally found in poling experiments evidenced by energy-dispersive X-ray (EDX) analyzer and by time-of-flight secondary ion mass spectrometry (ToF-SIMS) measurements [76, 77]. In the small scale, and within the operating voltage range of the solar cells, the halide vacancies migrate and accumulate in narrow Debye layers at the interfaces with selective contacts [31, 78]. Therefore, the timescales of ionic/vacancy migration/accumulation are consistent with the slow transient phenomena occurring in perovskite devices. However, a significant objection to this theory is that hysteresis can be effectively suppressed by modifying the perovskite composition or the selective contacts. By changing the selective contacts, a similar decrease in hysteresis was found, attributed to the control of trap density at the interface. PCBM was reported to passivate the grain boundaries of perovskite, either passivating the trapped states or blocking ion migration and thereby reducing the recombination causing hysteresis [79]. Recent works proposed that the effect of the PCBM is to reduce the effect of the ion accumulation at the interface by permeation between the small grains. These observations are contradictory to the theory that ion migration in the perovskite is the main cause of j–V hysteresis, and that it is more likely to be controlled by the choice of the contact material. However, theoretical simulations proposed that the process underlying hysteresis is a combination of both ionic migration and interfacial recombination via trapped states [80]. This effect was confirmed by some reports where they show through transient studies that hysteresis is only present where high rates of recombination exist at the perovskite/contact interface, whereas ionic migration exists in all devices with and without hysteresis. This is one of the most accurate models to describe the origin of the hysteretic effect independently of perovskite composition and device structure [50]. While ion migration in the timescales of 10^{-1}–100 seconds has been investigated to explain the hysteresis, the defects with higher formation energies will potentially affect the device in the long-term stability in timescales above 10^3 seconds [81]. Indeed, some works provide direct evidence of electric-field-induced ion migration within a perovskite solar cell device, where reversible PCE losses in timescales $>10^3$ seconds were attributed to asymmetrical accumulation of defects at both perovskite interfaces with selective contacts [77].

2.1.7 Concluding Remarks

The progress on perovskite solar cell has been characterized by fast and unexpected device performance improvements, but these have usually been driven by material or processing innovations. As a result, the link between the superb halide perovskite properties and the solar cell limiting processes is not completely defined yet, and even fundamental mechanisms determining the photovoltaic performance are currently under discussion. The recapitulation of the main steps required for the photovoltaic generation shows the gaps in the understanding of the working mechanisms. Some of the key open questions include the nature of the charge carrier transport, which shows signs of low mobility but high diffusion lengths; the main source of losses, either in the bulk or in the interfaces; and the role of mobile ions, which can affect the previous fundamental points and compromise long-term stability. These aspects will be crucial to fully understand the way perovskite solar cells work, a necessary step to use their full potential in an eventual commercialization.

References

1 Yin, W.J., Shi, T., and Yan, Y. (2014). *Adv. Mater.* 26: 4653.
2 De Wolf, S., Holovsky, J., Moon, S.-J. et al. (2014). *J. Phys. Chem. Lett.* 5: 1035.
3 Boix, P.P., Agarwala, S., Koh, T.M. et al. (2015). *J. Phys. Chem. Lett.* 6: 898.
4 Yang, W.S., Park, B.-W., Jung, E.H. et al. (2017). *Science* 356: 1376.
5 Shockley, W. and Queisser, H.J. (1961). *J. Appl. Phys.* 32: 510.
6 Yoshikawa, K., Kawasaki, H., Yoshida, W. et al. (2017). *Nat. Energy* 2: 17032.
7 (a) Koh, T.M., Fu, K., Fang, Y. et al. (2013). *J. Phys. Chem. C* 118: 16458.
(b) Lee, J.-W., Seol, D.-J., Cho, A.-N., and Park, N.-G. (2014). *Adv. Mater.* 26: 4991.
8 Saliba, M., Matsui, T., Seo, J.-Y. et al. (2016). *Energy Environ. Sci.* 9: 1989.
9 Saliba, M., Matsui, T., Domanski, K. et al. (2016). *Science* 354: 206.
10 Jeon, N.J., Noh, J.H., Yang, W.S. et al. (2015). *Nature* 517: 476.
11 Zhao, D., Yu, Y., Wang, C. et al. (2017). *Nat. Energy* 2: 17018.
12 Kumar, M.H., Dharani, S., Leong, W.L. et al. (2014). *Adv. Mater.* 26: 7122.
13 Tanaka, K., Takahashi, T., Ban, T. et al. (2003). *Solid State Commun.* 127: 619.
14 Juarez-Perez, E.J., Sanchez, R.S., Badia, L. et al. (2014). *J. Phys. Chem. Lett.* 5: 2390.
15 Brenner, T.M., Egger, D.A., Rappe, A.M. et al. (2015). *J. Phys. Chem. Lett.* 6: 4754.
16 Zhu, X.Y. and Podzorov, V. (2015). *J. Phys. Chem. Lett.* 23: 4758.
17 Tilchin, J., Dirin, D.N., Maikov, G.I. et al. (2016). *ACS Nano* 10: 6363.
18 D'Innocenzo, V., Grancini, G., Alcocer, M.J.P. et al. (2014). *Nat. Commun.* 5: 3586.
19 Grancini, G., Srimath Kandada, A.R., Frost, J.M. et al. (2015). *Nat. Photonics* 9: 695.
20 Dong, Q., Fang, Y., Shao, Y. et al. (2015). *Science* 347: 967.
21 Koh, T.M., Shanmugam, V., Schlipf, J. et al. (2016). *Adv. Mater.* 28: 3653.
22 Cao, D.H., Stoumpos, C.C., Farha, O.K. et al. (2015). *J. Am. Chem. Soc.* 137 (24): 7843.
23 Veldhuis, S.A., Boix, P.P., Yantara, N. et al. (2016). *Adv. Mater.* 28: 6804.
24 Shi, D., Adinolfi, V., Comin, R. et al. (2015). *Science* 347: 519.
25 Nie, W., Tsai, H., Asadpour, R. et al. (2015). *Science* 347: 522.
26 Beaujuge, P.M. and Fréchet, J.M.J. (2011). *J. Am. Chem. Soc.* 133: 20009.
27 Xing, G., Mathews, N., Sun, S. et al. (2013). *Science* 342: 344.
28 Chen, Y., Yi, H.T., Wu, X. et al. (2016). *Nat. Commun.* 7: 12253.
29 Chin, X.Y., Cortecchia, D., Yin, J. et al. (2015). *Nat. Commun.* 6: 7383.
30 Tress, W. (2017). *J. Phys. Chem. Lett.* 8: 3106.

31 Xiao, Z., Yuan, Y., Shao, Y. et al. (2014). *Nat. Mater.* 14: 193.

32 Correa-Baena, J.-P., Anaya, M., Lozano, G. et al. (2016). *Adv. Mater.* 28: 5031.

33 Feng, J. (2014). *APL Mater.* 2: 081801.

34 (a) Bi, Z., Liang, Z., Xu, X. et al. (2017). *Sol. Energy Mater. Sol. Cells* 162: 13. (b) Long, M., Zhang, T., Xu, W. et al. (2017). *Adv. Energy Mater.* 7: 1601882. (c) Yang, M., Zhang, T., Schulz, P. et al. *Nat. Commun.* 7: 2016, 12305.

35 Correa-Baena, J.-P., Tress, W., Domanski, K. et al. (2017). *Energy Environ. Sci.* 1: 556.

36 Momblona, C., Gil-Escrig, L.L., Bandiello, E. et al. (2016). *Energy Environ. Sci.* 9: 3456.

37 Lee, M.M., Teuscher, J., Miyasaka, T. et al. (2012). *Science* 338: 643.

38 Stranks, S.D., Eperon, G.E., Grancini, G. et al. (2013). *Science* 342: 341.

39 (a) Marchioro, A., Teuscher, J., Friedrich, D. et al. (2014). *Nat. Photonics* 8: 250.

40 (a) Salim, T., Sun, S., Abe, Y. et al. (2015). *J. Mater. Chem. A* 3: 8943. (b) Leijtens, T., Lauber, B., Eperon, G.E. et al. (2014). *J. Phys. Chem. Lett.* 5: 1096.

41 Liu, M., Johnston, M.B., and Snaith, H.J. (2013). *Nature* 501: 395.

42 Senocrate, A., Moudrakovski, I., Kim, G.Y. et al. (2017). *Angew. Chem. Int. Ed.* 56: 7755.

43 Stranks, S.D., Burlakov, V.M., Leijtens, T. et al. (2014). *Phys. Rev. Appl.* 2: 034007.

44 Yamada, Y., Nakamura, T., Endo, M. et al. (2014). *J. Am. Chem. Soc.* 136: 11610.

45 Johnston, M.B. and Herz, L.M. (2016). *Acc. Chem. Res.* 49: 146.

46 Wu, B., Nguyen, H.T., Ku, Z. et al. (2016). *Adv. Energy Mater.* 6: 1600551.

47 Yang, W., Yao, Y., and Wu, C.-Q. (2015). *J. Appl. Phys.* 117: 155504.

48 Correa-Baena, J.-P., Turren-Cruz, S.-H., Tress, W. et al. (2017). *ACS Energy Lett.* 2: 681.

49 (a) Bertoluzzi, L., Sanchez, R.S., Liu, L. et al. (2015). *Energy Environ. Sci.* 8: 910. (b) Gottesman, R. and Zaban, A. (2016). *Acc. Chem. Res.* 49: 320.

50 Calado, P., Telford, A.M., Bryant, D. et al. (2016). *Nat. Commun.* 7: 13831.

51 Editorial (2012). *Nat. Mater.* 11: 91.

52 (a) Kojima, A., Teshima, K., Shirai, Y., and Miyasaka, T. (2009). *J. Am. Chem. Soc.* 131: 6050. (b) Im, J.-H., Lee, C.-R., Lee, J.-W. et al. (2011). *Nanoscale* 3: 4088.

53 Ryu, S., Noh, J.H., Jeon, N.J. et al. (2014). *Energy Environ. Sci.* 7: 2614.

54 Lin, Y., Chen, B., Zhao, F. et al. (2017). *Adv. Mater.* 1700607.

55 Kumar, M.H., Yantara, N., Dharani, S. et al. (2013). *Chem. Commun.* 49: 11089.

56 Qin, P., Tanaka, S., Ito, S. et al. (2014). *Nat. Commun.* 5: 3834.

57 Jeng, J.-Y., Chen, K.-C., Chiang, T.-Y. et al. (2014). *Adv. Mater.* 26: 4107.

58 Ku, Z., Rong, Y., Xu, M. et al. (2013). *Sci. Rep.* 3: 3132.

59 Tress, W. (2017). *Adv. Energy Mater.* 7: 1602358.

60 Ravishankar et al. (2018). *Joule* 2: 788–798.

61 Tan, H., Jain, A., Voznyy, O. et al. (2017). *Science* 355: 722.

62 Wang, C., Xiao, C., Yu, Y. et al. (2017). *Adv. Energy Mater.* 1700414.

63 Zarazua, I., Bisquert, J., and Garcia-Belmonte, G. (2016). *J. Phys. Chem. Lett.* 7: 525.

64 Yan, K., Wei, Z., Zhang, T. et al. (2016). *Adv. Funct. Mater.* 26: 8545.

65 Zarazúa, I., Han, G., Boix, P.P. et al. (2016). *J. Phys. Chem. Lett.* doi: 10.1021/acs.jpclett.6b02193.

66 Gottesman, R., Lopez-Varo, P., Gouda, L. et al. (2016). *Chem* 1: 776.

67 Tress, W., Marinova, N., Moehl, T. et al. (2015). *Energy Environ. Sci.* 8: 995.

68 Snaith, H.J., Abate, A., Ball, J.M. et al. (2014). *J. Phys. Chem. Lett.* 5: 1511.

69 (a) O’Regan, B.C., Barnes, P.R.F., Li, X. et al. (2015). *J. Am. Chem. Soc.* 137: 5087. (b) Unger, E.L., Hoke, E.T., Bailie, C.D. et al. (2014). *Energy Environ. Sci.* 7: 3690.

70 Sanchez, R.S., Gonzalez-Pedro, V., Lee, J.-W. et al. (2014). *J. Phys. Chem. Lett.* 5: 2357.

71 Eames, C., Frost, J.M., Barnes, P.R.F. et al. (2015). *Nat. Commun.* 6: 7497.

72 (a) Richardson, G., O’Kane, S.E.J., Niemann, R.G. et al. (2016). *Energy Environ. Sci.* 9: 1476. (b) Yang, T.-Y., Gregori, G., Pellet, N. et al. (2015). *Angew. Chem. Int. Ed.* 54: 7905.

73 Meloni, S., Moehl, T., Tress, W. et al. (2016). *Nat. Commun.* 7: 10334.

74 (a) Coll, M., Gomez, A., Mas-Marza, E. et al. (2015). *J. Phys. Chem. Lett.* 6: 1408. (b) Leguy, A.M.A., Frost, J.M., McMahon, A.P. et al. (2015). *Nat. Commun.* 6: 7124.

75 (a) Yin, W.-J., Shi, T., and Yan, Y. (2014). *Appl. Phys. Lett.* 104: 063903. (b) Buin, A., Comin, R., Xu, J. et al. (2015). *Chem. Mater.* 27: 4405. (c) Azpiroz, J.M., Mosconi, E., Bisquert, J., and De Angelis, F. (2015). *Energy Environ. Sci.* 8: 2118. (d) Haruyama, J., Sodeyama, K., Han, L., and Tateyama, Y. (2015). *J. Am. Chem. Soc.* 137: 10048.

76 Yuan, Y., Wang, Q., Shao, Y. et al. (2016). *Adv. Energy Mater.* 6: 1501803.

77 Domanski, K., Roose, B., Matsui, T. et al. (2017). *Energy Environ. Sci.* 10: 604.

78 (a) Bergmann, V.W., Guo, Y., Tanaka, H. et al. (2016). *ACS Appl. Mater. Interfaces* 8: 19402. (b) Cao, R., Xu, F., Zhu, J. et al. (2016). *Adv. Energy Mater.* 6: 1600814.

79 Yuan, Y. and Huang, J. (2016). *Acc. Chem. Res.* 49: 286.

80 van Reenen, S., Kemerink, M., and Snaith, H.J. (2015). *J. Phys. Chem. Lett.* 6: 3808.

81 Kwon, K.C., Hong, K., Van Le, Q. et al. (2016). *Adv. Funct. Mater.* 26: 4213.

2.2

The Photophysics of Halide Perovskite Solar Cells

Mingjie Li, Bo Wu, and Tze-Chien Sum

Nanyang Technological University, Division of Physics and Applied Physics, School of Physical and Mathematical Sciences, 21 Nanyang Link, SPMS-PAP-03-05, Singapore 637371, Singapore

2.2.1 Introduction to Photophysics Studies of Halide Perovskites

The rapid transcendence of organic-inorganic lead halide perovskites to prominence is unprecedented in the annals of photovoltaic (PV) history. In less than a decade, the efficiencies of these amazing perovskite solar cells have bounded from a mere 3.8% in 2009 to 22.1% in 2016. Despite the great strides made with the device efficiency, the detailed understanding of halide perovskite's fundamental photophysics remains modest. To realize the full potential of these perovskite solar cells, both basic characterization and device optimization studies need to progress synchronously to gain a complete picture of their fundamental photophysical and optoelectronic properties. A wide array of optical spectroscopy techniques is available to the spectroscopist to characterize the optical properties and probe the charge dynamics of these materials and devices. These techniques range from the ubiquitous absorption spectroscopy to more sophisticated pump-probe techniques of transient absorption (TA), spectroscopy terahertz (THz) spectroscopy, and photoconductance spectroscopy. The operating principles of these techniques are not covered here, and the interested reader is directed to other excellent articles on them. In this chapter, we first discuss the basic optical properties of polycrystalline halide perovskite thin films, followed by the charge dynamics of these bare films and the interfacial charge-transfer mechanisms at the heterojunctions of perovskite solar cells. Lastly, we discuss the photophysical properties of perovskite single crystals (SCs) and their potential for perovskite optoelectronics.

Halide Perovskites: Photovoltaics, Light Emitting Devices, and Beyond, First Edition.
Edited by Tze-Chien Sum and Nripan Mathews.

2.2.2 Optical Properties of $CH_3NH_3PbI_3$ Polycrystalline Thin Films

2.2.2.1 Electronic Band Structure and Optical Transitions

The photophysics and charge carrier dynamics in semiconductors is highly dependent on their electronic band structures. We begin with considering the band structure of organic–inorganic lead halide perovskites (e.g. methylammonium lead iodide – $CH_3NH_3PbI_3$ or simply $MAPbI_3$ in short), which had been subjected to extensive theoretical calculations by many groups. Figure 2.2.1a shows the representative calculated band structure of cubic $MAPbI_3$ near the *R* point by the density functional theory (DFT) method with spin–orbit coupling included [3]. The cubic $MAPbI_3$ presents a direct bandgap where the valence band maximum (VBM) and conduction band minimum (CBM) occur at almost the same point in the Brillouin zone. Similarly, the tetragonal and orthorhombic phases of $MAPbI_3$ are also direct semiconductors with bandgaps comparable to the cubic phase. Despite the organic constituents, $MAPbI_3$ retains its inorganic semiconductor characteristics, with the CBM almost entirely composed of Pb p orbital with negligible coupling with I, while the VBM comprised the antibonding states derived from the hybridization of the I 5p- and Pb 6s states. The strong s–p antibonding coupling results in a small-hole effective mass which is comparable with the electron effective mass, making $MAPbI_3$-based perovskites an ideal candidate for thin-film p-i-n solar cells.

The optically allowed transitions ($E_{1/2,u} \rightarrow E_{1/2,g}$) at *R* represent the bandgap energy that is evident from the strong absorption onset at ~1.6 eV (see

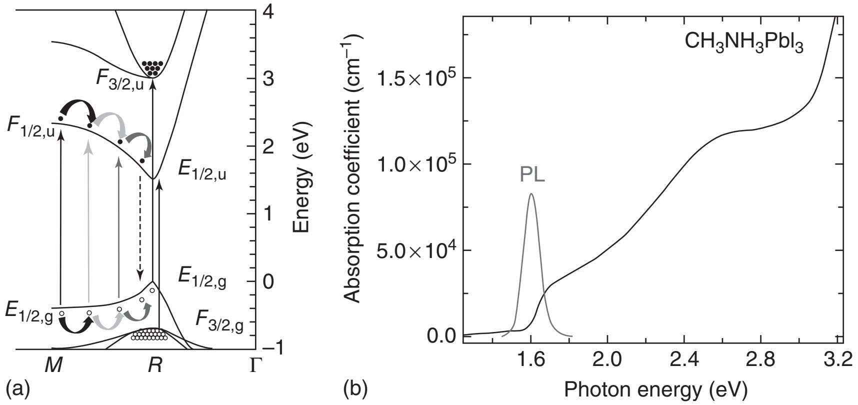

Figure 2.2.1 (a) Electronic band structure of cubic $MAPbI_3$ calculated from density functional theory with spin–orbit coupling [1]. Gray upward arrows indicate the allowed transitions in the visible range. The upward arrows at the *R* point represent the possible transitions corresponding to the higher absorption energies. (b) Room temperature absorption coefficient of polycrystalline $MAPbI_3$ thin film as a function of photon energy. Representative PL spectra at ~1.6 eV that arises from carrier recombination near the *R* valley (dashed line) in (a). Source: (a) Even et al. 2014 [1]. Copyright 2014. Reprinted with permission of American Chemical Society. (b) Xing et al. 2013 [2]. Copyright 2013. Reprinted with permission of the American Association for the Advancement of Science.

Figure 2.2.1b). $MAPbI_3$ also possesses a fairly large absorption coefficient ($>10^5$ cm^{-1} at ~2.5 eV or ~500 nm – see Figure 2.2.1b) [2], which is comparable to CdTe and GaAs and is approximately one order higher than crystalline Si. The charge carriers photoexcited by the wide range of visible light can subsequently relax into the R valley from the M point. These transitions would account for the absorption continuum for photon energies >1.6 eV band edge. Furthermore, Even et al. proposed that the absorption edge at ~2.6 eV arise from the optically allowed transitions at the R point, involving transitions from the deeper energy levels to the CBM or from the VBM to the higher energy states (see vertical arrows in Figure 2.2.1a). Eventually, the relaxation of carriers at the R valley from CBM to VBM would give rise to a photoluminescence (PL) peak near 1.6 eV.

2.2.2.2 Exciton Binding Energies and Photoexcited Species: Excitons Versus Free Carriers

Knowledge of the dominant photoexcited species in perovskites is essential for a clear understanding of the working principles of perovskite solar cells. One possible clue to whether the primary species is a free carrier or a bound electron–hole pair lies in the value of the exciton binding energy E_b. However, this is not entirely straightforward as a puzzling range of the exciton binding energies (E_b) soon emerged (i.e. <10 to ~50 meV) from the sustained efforts to identify the primary photoexcited species (excitons or free carriers) in $MAPbI_3$ [4–6]. These attempts are also greatly frustrated by the various experimental techniques used – ranging from optical absorption [7] and magnetoabsorption [8] to temperature-dependent PL [9, 10] and temperature-dependent absorption spectroscopy [4], etc., which contribute to the spread of exciton E_b. It is therefore difficult to conclude if the primary photoexcited species in these perovskites at room temperatures are excitons (insulating) or free carriers (conducting). $MAPbI_3$ differs from typical semiconductors such as CdS ($E_b \sim 26$ meV) which has dominating excitonic properties at room temperatures [11]. A coexistence of both species in thermal equilibrium at room temperatures seems plausible based on the E_b value alone. This coexistence picture is consistent with the findings of Vardeny's group, where evidence of both excitons and photogenerated carriers with an estimated branching ratio of 1 : 10 through pump-probe spectroscopy were presented [12].

Using femtosecond pumped transient THz spectroscopy, Sundstrom's group provided the first evidence that free charge carriers are generated within 2 ps in $MAPbI_3$ and $MAPbI_3$/me-Al_2O_3 thin films [13]. These findings concur with the Drude-like free-carrier responses from transient THz spectroscopy studies of perovskites by Herz's group [14]. Furthermore, the dominant free electron and free hole bimolecular recombination were evidenced by several groups [10, 15–17] over a wide range of photoexcited charge carrier concentration through ultrafast spectroscopy techniques (e.g. time-resolved THz, TA, and time-resolved photoluminescence (TRPL)). Direct measurements of the exciton binding energies using high magnetic fields eventually revealed binding energies <16 meV at low temperatures and a few milli-electron volts at room temperature (within the detection limits of the technique). Eventually, Petrozza's group [4] clearly showed that the grain size of the perovskite crystallites strongly affects the excitonic properties. The resulting surface-induced structural changes and doping could reduce the E_b. Hence, the broad spread of E_b found in the literature could be rationalized to be due to not only from the experimental uncertainties in the various measurement approaches, but, more importantly, from the strong dependence on the perovskite film processing (influencing the crystal size and morphology of solution-processed perovskites).

2.2.2.3 Carrier Diffusion Lengths, Carrier Mobilities, and Defects

Charge carrier transport is strongly affected by scattering from lattice defects and/or lattice vibrations in the absorber material. Generally, there is a higher degree of electronic disorder and defect states in low-temperature solution-processed semiconductors. Hence, the exciton or free electron–hole diffusion lengths in these semiconductors are typically limited to about 10 nm. Where such semiconductors are used as light absorbers, light absorption and charge carrier collection are usually decoupled in a bid to achieve high-efficiency PV cells. However, the impressive efficiency values demonstrated in a variety of PV architectures by low-temperature, solution-processed organic–inorganic halide perovskite materials seem to defy this traditional perception [18, 19].

The first reports on the long electron–hole diffusion lengths in $MAPbI_3$ and $MAPbI_{3-x}Cl_x$ perovskites were independently reported by Xing et al. [2] and Stranks et al. [20]. Both teams had utilized transient optical spectroscopy and selective extraction of the photoinduced electron or hole in $MAPbI_3$ with electron transport layers/hole transport layers (ETLs/HTLs) to elucidate balanced and long-range electron–hole diffusion lengths of at least 100 nm in polycrystalline $MAPbI_3$ (Figure 2.2.2). In addition, Stranks et al. measured electron–hole diffusion lengths of nearly one order of magnitude longer for $MAPbI_{3-x}Cl_x$ (i.e. >1 μm and balanced and correspondingly longer charge carrier lifetimes). Although the origins of this extended diffusion length were still unclear at that time, the charge diffusion lengths are highly sensitive to film-processing conditions even for the $MAPbI_{3-x}Cl_x$ films [21]. A minimum value of the diffusion length is necessary for obtaining an appreciable (>10%) power conversion in perovskite solar cells. It is presently unclear how organic or inorganic cation substitution or halide substitution/mixing affects the electron and hole diffusion lengths. Nonetheless, the ultimate value of the diffusion lengths is known to be defined by perovskite SCs, which were reported to be >10 μm and as long as 175 μm [22].

Related to the carrier diffusion lengths is the question about their charge carrier mobilities. With noncontact transient THz spectroscopy, Wehrenfennig et al. [14] reported the lower bounds for the high-frequency effective charge mobility of 11.6 $cm^2\ V^{-1}\ s^{-1}$ for $MAPbI_{3-x}Cl_x$ and 8 $cm^2\ V^{-1}\ s^{-1}$ for $MAPbI_3$ in polycrystalline samples that were spin coated on mesoporous Al_2O_3. The extracted mobility value is the sum of electron and hole mobilities. It is not possible to separate the respective contributions of the electrons and holes using this approach. With the same method, Ponseca et al. [13] reported charge carrier effective mobilities up to 25 $cm^2\ V^{-1}\ s^{-1}$ for solution-processed $MAPbI_3$ on an Al_2O_3 scaffold. Furthermore, through comparing the carrier mobilities with bare $MAPbI_3$ and $MAPbI_3$ on a TiO_2 scaffold, the electron and hole mobilities

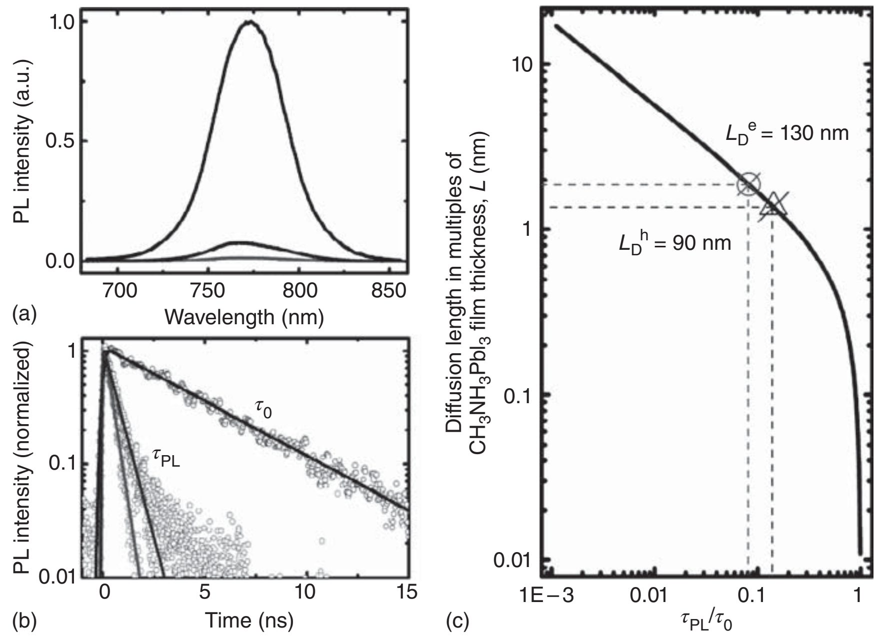

Figure 2.2.2 (a) Time-integrated PL spectra and (b) time-resolved PL decay transients measured at 760 ± 10 nm for quartz/$MAPbI_3$ (65 nm) (black), quartz/$MAPbI_3$ (65 nm)/PCBM (light gray), quartz/$MAPbI_3$ (65 nm)/spiro-OMeTAD (dark gray) films under vacuum after excitation at 600 nm (1 kHz, 150 fs, 1.3 mJ cm^{-2}). The solid lines in (b) are the single-exponential fits of the PL decay transients. a.u.: arbitrary units. (c) A plot of exciton diffusion length versus PL lifetime quenching ratios. The diffusion length is scaled in multiples of $MAPbI_3$ layer thickness ($L = 65$ nm). Source: Xing et al. 2013 [2]. Copyright 2013. Reprinted with permission of the American Association for the Advancement of Science.

are found to be relatively balanced up to the microsecond. In high-quality vapor-deposited $MAPbI_{3-x}Cl_x$ films, Wehrenfennig et al. [14] further reported that charge carrier mobilities ≥33 $cm^2\ V^{-1}\ s^{-1}$ could be achieved with these perovskites.

The first report on estimating the defect densities was by Xing et al. using a pump-fluence-dependent PL approach [23]. Briefly, the authors had considered an unknown (i) number of trapping pathways, each with their distinct trapping rates and trap densities. At low pump fluence where multiparticle recombination is suppressed, the photoexcited carriers relax via the band edge through spontaneous emission (with lifetime τ_0) or through trap-mediated pathways. The relaxation of the photogenerated charge carrier distribution via various trap-mediated non-radiative pathways (i.e. first term of Eq. (2.2.1)) and the radiative recombination (i.e. second term of Eq. (2.2.1)) can be described by the following differential equations:

$$\mathrm{d}n_{\mathrm{c}}(t)/\mathrm{d}t = -\sum_i a_i n_{\mathrm{c}}(t) n_{\mathrm{TP}}^i(t) - (n_{\mathrm{c}}(t)/\tau_0) \tag{2.2.1}$$

$$\mathrm{d}n_{\mathrm{TP}}^i(t)/\mathrm{d}t = -a_i n_{\mathrm{c}}(t) n_{\mathrm{TP}}^i(t) \tag{2.2.2}$$

where $n_{\mathrm{TP}}^i(t)$ is the distribution of the ith trap state or non-radiative pathway and a_i is the product of the trapping cross-section and the carrier velocity.

Whereupon, using the expression for the integrated band edge PL intensity ($I_{\mathrm{PL}} = k\int_0^{\infty} n_{\mathrm{c}}(t)/\tau_0\,\mathrm{d}t$, where k is a constant), the initial photogenerated charge carrier density $n_{\mathrm{c}}(0)$ can be obtained as

$$n_{\mathrm{c}}(0) = \sum_i n^i_{\mathrm{TP}}(0)(1 - \mathrm{e}^{-a_i \tau_0 I_{\mathrm{PL}}/k}) + I_{\mathrm{PL}}/k \tag{2.2.3}$$

Figure 2.2.3a shows a fit of the experimental data over the low pump fluence, which yields two distinct types of traps in $\mathrm{MAPbI_3}$ thin films – bulk traps (of trap density $n^{\mathrm{F}}_{\mathrm{TP}} \sim 5 \times 10^{16}\,\mathrm{cm^{-3}}$) with fast trapping times versus surface/interfacial traps (of trap density $n^{\mathrm{S}}_{\mathrm{TP}} \sim 1.6 \times 10^{17}\,\mathrm{cm^{-3}}$) with slow trapping times. These elucidated trap densities correlate well with a simple estimate of the total trap density (i.e. bulk and surface) obtained from the intersection of the linearly extrapolated PL intensity with that of the pump-fluence axis (i.e. $n^{0}_{\mathrm{TP}} \sim 2 \times 10^{17}\,\mathrm{cm^{-3}}$ – Figure 2.2.3b). This intersection represents the pump fluence needed to fill all the traps (i.e. the threshold trap pump fluence $P^{\mathrm{trap}}_{\mathrm{th}}$). Comparatively, the trap densities elucidated here are similar to defect densities in highly ordered organic crystals (10^{15}–10^{18} $\mathrm{cm^{-3}}$) [24] as well as that of solution-deposited, high-temperature-annealed Cu-In-Ga-S/Se (CIGS) chalcogenide layers (10^{16} $\mathrm{cm^{-3}}$) [25]; which are better than that of solution-processed organic thin films (10^{19} $\mathrm{cm^{-3}}$) [26]. For more details of this approach, the interested reader is directed to the supplementary information of Ref. [23]. The findings of this straightforward approach agree well with another more elaborate kinetic model approach [16] by Stranks et al. (i.e. accounting for exciton formation, exciton dissociation, exciton decay, and free electron trapping) that yielded a trap state density of 2.5×10^{16} $\mathrm{cm^{-3}}$.

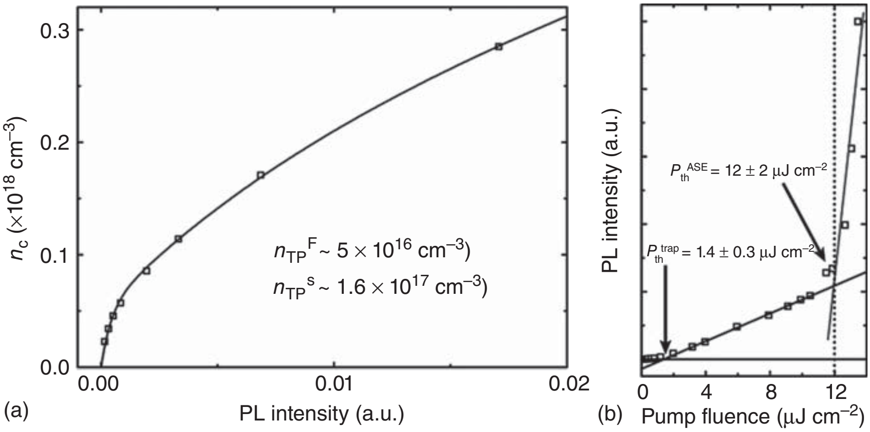

Figure 2.2.3 *Determination of the trap state densities.* (a) PL intensity as a function of photon-generated exciton density within the low pump-fluence range. The experimental data can be well fitted ($R^2 = 0.99$) with Eq. (2.2.3) for two types of trapping states. (b) PL intensity as a function of pump fluence. The arrows indicate the trap state saturation threshold fluence ($P^{\mathrm{trap}}_{\mathrm{th}}$) and the ASE threshold fluence ($P^{\mathrm{ASE}}_{\mathrm{th}}$). The dark gray and light gray lines represent the linear fits to experimental data in the two linear regimes of SE and ASE, respectively. The dashed vertical black line indicates the onset of ASE. Source: Xing et al. 2014 [23]. Copyright 2014. Reprinted with permission of Springer Nature.

Indeed, first-principles DFT calculations by Yan's group showed that $MAPbI_3$ possesses unusual defect properties (i.e. p-type V_{Pb} and n-type MA_i being the dominant defect) favorable for solar PV applications [27]. This suggests that $MAPbI_3$ thin film's conductivity can be tuned from intrinsic n-type to p-type by adjusting its preparation condition. Their calculations also reveal that defects such as MA_i, V_{Pb}, MA_{Pb}, I_i, V_I, and V_{MA} with low formation energies (<0.05 eV) yield shallow levels; while defects such as I_{Pb}, I_{MA}, Pb_i, and Pb_I with high formation energies create deep levels. The deep-level defects are the main source of non-radiative recombination. Defects with low formation energy may be formed in the mixed perovskite-based absorbers, or in the interfaces between the perovskite absorbers and contacts. These formation energies strongly suggest that $MAPbI_3$ intrinsically has a rather low non-radiative recombination rate and is consistent with the long electron–hole diffusion lengths. In view of the high solar cell efficiencies for $MAPbI_3$ thin films, it is unsurprising that the bulk defect densities are low.

2.2.2.4 Transient Spectral Features and Charge Dynamics

Femtosecond transient absorption (TA) spectroscopy is one of the most commonly used techniques to uncover the primary photophysical processes in $MAPbI_3$ perovskites. However, given that the organic component is highly sensitive to external environmental factors (i.e. humidity), sample handling, and fabrication steps, as well as experimental conditions during data acquisition, the observations of TA spectra need to be carefully interpreted.

Figure 2.2.4 shows the representative linear absorption and TA spectra of $CH_3NH_3PbI_3$ or ($MAPbI_3$). The latter were obtained with a commercial TA

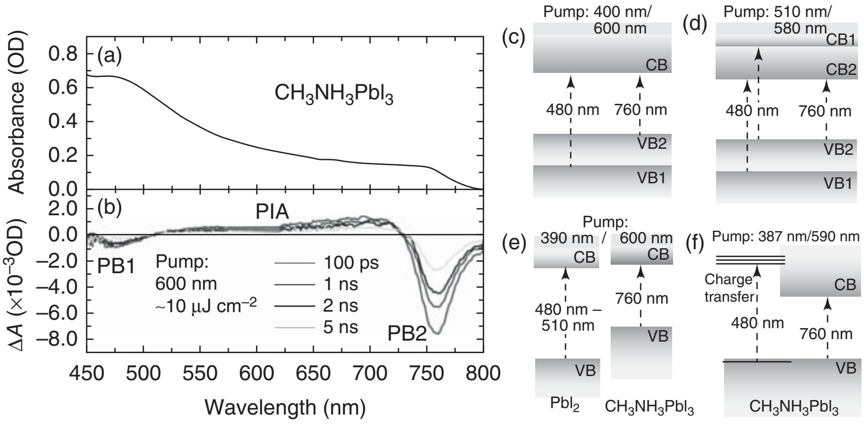

Figure 2.2.4 Representative linear absorption spectrum (a) of $CH_3NH_3PbI_3$ or ($MAPbI_3$) showing the absorption edges at ~480 and ~760 nm and its TA spectrum (b) showing the PB1, PB2, and PIA signatures at various probe delays. Schematic of PB1 (480 nm) and PB2 (760 nm) contributions from (c) dual valence band model [2] and (d) dual valence band and dual conduction band model [28] and overlapping signals from (e) PbI_2 [29] or from (f) iodoplumbate complexes [30]. Source: Sum et al. 2016 [31]. Copyright 2016. Reprinted with permission of American Chemical Society.

setup (HELIOS, Ultrafast Systems) using a pump of 600 nm and fluence of ~10 μJ cm^{-2}. There are two distinct negative ΔA valleys located at approximately 480 and 760 nm (simply termed PB1 and PB2, respectively) that originate from a combination of PB (photobleaching) and SE (stimulated emission) signals. A broad positive ΔA (or photoinduced absorption (PIA)) band spans over the 550–650-nm wavelengths, which is assigned to photoinduced refractive index changes [32]. The two PB signatures agree well with the two absorption edges present in the linear absorption spectrum previously assigned to excitonic transitions. Generally, there is broad agreement over the assignment of the band edge PB2 signal, but the origin of PB1 remains controversial. A detailed model that could account for all these spectral signatures is still lacking. Several interpretations have been proposed: (i) a dual valence band model [2], (ii) a dual conduction band and dual valence band model [28], (iii) overlapping contributions from PbI_2 impurities [29], and (iv) charge transfer of iodoplumbate complexes in the fully formed $MAPbI_3$ (or a dual excited state model) [30]. Recent first-principles band structure calculations have partly supported models (i) and (ii). For Figure 2.2.4c, photoexcitation with energy less than PB1 (i.e. with 600-nm pulses), the PB1 transition (480-nm transition) would correspond to the situation where only the CB is populated, hence the dual valence bands. On the other hand, under photoexcitation with energy less than PB1 (i.e. with 510- or 580-nm pulses), as shown in Figure 2.2.4d, the PB1 transition would correspond to situations where only the higher energy valence band (VB2) or the lowest energy conduction band (CB2) are populated, hence the dual conduction bands and dual valence bands. Detailed discussions of the VB/CB assignments in models (i) and (ii) can be found in the supplementary information of Ref. [2] and Chapter 5 of Ref. [28], respectively. Nevertheless, recent detailed TA studies of PbI_2 on TiO_2 by Flender et al. have shown that the bleaching at 500 nm is unlikely to be related to the plumbate possibly remaining in the perovskite samples, thus discounting model (iv) [33].

Although TA spectroscopy can provide considerable insights into the ground- and excited-state dynamics in $MAPbI_3$ films, it is important not to overgeneralize their findings to the actual performance of perovskite solar cells. The conditions in their device architectures are more complex than in neat films, where the morphology, series and shunt resistances, interfacial traps and band alignments, etc. can have a significant influence on the power conversion efficiency (PCE). There is a complex interplay of these factors in a real device, and these need not be reflected in the TA results of neat or heterojunction films. One should avoid extrapolating and drawing conclusions based on ultrafast optical spectroscopy (UOS) studies alone. UOS studies should be complemented with energetics investigation and materials and device characterization to gain a complete picture (see next section 2.2.3).

2.2.2.5 Photophysical Processes and Their Recombination Constants

A common approach to examine the recombination kinetics of thermalized photoexcited free electrons and holes through monomolecular and higher order processes can be described by the following rate equation:

$$\frac{\mathrm{d}n(t)}{\mathrm{d}t} = -k_1 n - k_2 n^2 - k_3 n^3 \tag{2.2.4}$$

where n is the photoexcited charge carrier density and t is time, k_1 is the monomolecular excitonic-type recombination or trap-mediated recombination constant, k_2 is the free carrier bimolecular recombination constant, and k_3 is the three-body Auger recombination constant. Global fitting the solutions to Eq. (2.2.4) to the time evolution of the carrier densities at different pump fluences measured by ultrafast spectroscopy techniques (e.g. from TRPL, TA, and time-resolved THz) such as those shown in Figure 2.2.1 will allow the different rate constants (k_1, k_2, k_3) to be extracted. The rate constants of various perovskite materials are summarized in Table 2.2.1.

Under low pump fluence excitation (e.g. AM1.5 illumination in solar cells), the photoinduced minority carrier concentration (10^{15}–10^{16} cm^{-3}) is smaller than the total majority carrier concentration (photoinduced + original doped). The first term in Eq. (2.2.4) will dominate the second term, and the carrier recombination kinetics is almost monomolecular in nature and exhibits a near monoexponential decay. Strong material dependencies can also be expected for trap-related recombination channels, because the nature of the traps varies according to film synthesis, processing, and the ensuing morphology. In fact, a wide range of monomolecular charge-carrier lifetimes ($1/k_1$) have been reported for $MAPbI_3$, $MAPbI_{3-x}Cl_x$, $FAPbI_3$, thin films, ranging from several nanoseconds to a few microseconds. Much research attention has been directed to the reduction of trap states density (i.e. k_1) in these thin films through optimizing the processing conditions and improving the morphologies.

At higher optical pump fluence, where photogenerated charge-carrier concentration is much higher than perovskite's trap states density, free electron–hole

Table 2.2.1 List of reported recombination constants for various halide perovskite thin films at room temperature.

	Recombination constants				
Thin film	**k_1 (μs^{-1})**	**$k_2 \times 10^{-10}$ (cm^3 s^{-1})**	**$k_3 \times 10^{-28}$ (cm^6 s^{-1})**	**Techniques**	**References**
$MAPbI_3$	15	0.6	1.6	THz	[34]
$MAPbI_3$	73	1.5	3.4	TA	[35]
$MAPbI_3$	18	1.7	—	TRPL	[17]
$MAPbBr_3$	27	4.9	13.5	TA	[35]
$FAPbI_3$	7	1.1	0.2	THz	[36]
$FAPbBr_3$	21	11	1.5	THz	[36]
$MASnI_3$	8	14	—	THz	[37]
$CsSnI_3$	720	100	—	TRPL	[38]

MA: methylammonium ($CH_3NH_3^+$) and FA: formamidinium ($HC(NH_2)_2^+$).

bimolecular recombination would dominate (i.e. the second term in Eq. (2.2.4). The charge-carrier kinetics as a function of pump fluence will follow a power-law-type decay. Such bimolecular decay kinetics will continue until the charge-carrier concentration falls below the trap states density. Upon which, the monomolecular-type decay will reappear and exhibit as a long exponential tail. In retrospect, the dominant bimolecular nature of the free electron–hole recombination in organic–inorganic lead halide perovskites at excitation fluence of tens of microjoules per square centimeter (or corresponding to carrier densities of $\sim 10^{18}$ cm^{-3}) is now firmly established. This is much larger than the typical PV regime of $\sim 10^{13}$–10^{15} cm^{-3}. Reported Auger rate constants k_3 vary in the range $0.2–14 \times 10^{-28}$ cm^6 s^{-1} for various solution-processed halide perovskite thin films (Table 2.2.1). Auger recombination is unlikely to play a dominant role in PV devices under standard solar illumination, although it may become relevant for the operation of concentrator-type perovskite PV devices. Nonetheless, Auger effects are still highly relevant in perovskite optical gain media/lasers that operate in the high charge-density regime.

Figure 2.2.5 shows a summative schematic of the key findings in seminal works of the dynamic interplay between the various photophysical processes and relaxation mechanisms in bare solution-processed MAPbI$_3$ perovskite thin films following photoexcitation [39]. Under low excitation fluence with carrier

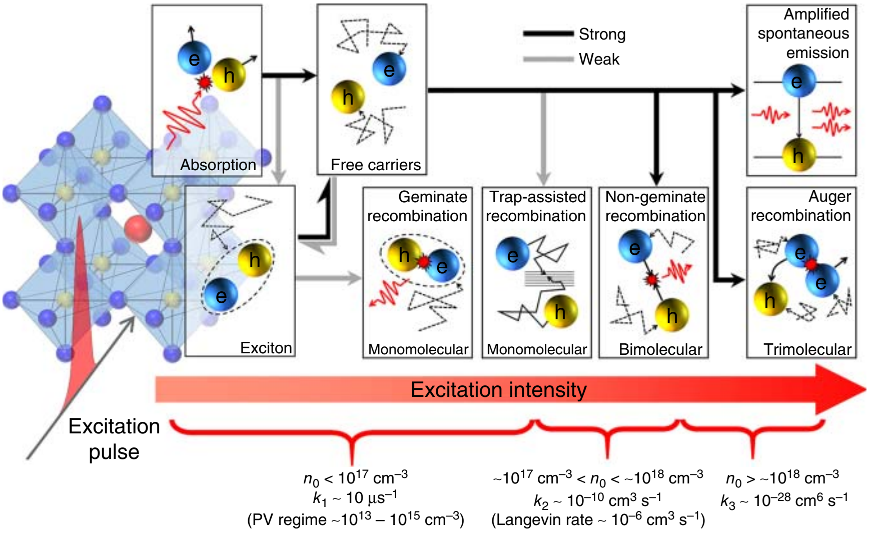

Figure 2.2.5 A schematic of the photophysical processes and loss mechanisms in perovskites following photoexcitation. Efficient (or strong) pathways and suppressed (or weak) pathways are denoted by the black and gray lines, respectively. Monomolecular recombination is charge carrier density independent, while bimolecular and Auger recombination are charge carrier density-dependent processes that would typically be present under high-intensity photoexcitation. In fact, under even higher photoexcitation densities, amplified spontaneous emission (ASE) will out-compete Auger recombination. However, under solar light intensities (low-intensity excitation), these latter processes will be strongly suppressed. Source: Sum et al. 2016 [31]. Copyright 2016. Reprinted with permission of American Chemical Society.

densities $n_0 \approx 10^{13}–10^{15}$ cm^{-3} (i.e. typical PV conditions), monomolecular processes like trap-assisted recombination or geminate recombination are found to be inefficient with low first-order recombination coefficients, $k_1 \approx 10\,\mu s^{-1}$ [14]. This observation agrees well with the relatively low trap densities (i.e. n_{trap} 10^{17} cm^{-3}) [40]. At higher $n_0 \approx 10^{16}–10^{18}$ cm^{-3}, multiparticle effects like non-geminate recombination (bimolecular) and Auger processes (trimolecular) become more important. The non-geminate recombination arises from the bimolecular recombination of two free charges; which is in contrast to the geminate recombination that originates from the monomolecular annihilation of two Coulombically bound charges. Surprisingly, their bimolecular recombination constants, $k_2 \approx 10^{-10}$ cm^3 s^{-1}, are approximately four orders lower [10, 14] than Langevin recombination rates for free electron–hole annihilation. However, their Auger rates are found to be large ($k_3 \approx 10^{-28}$ cm^6 s^{-1}) [14], and in the same order as strongly confined CdSe colloidal quantum dots [41]. Recent works reported that $MAPbI_3$ underwent strong band-filling effects [5, 15] and bandgap renormalization [32] at higher pump fluence. Depending on the film quality, amplified spontaneous emission (ASE) could even be realized at $n_0 \approx 10^{18}$ cm^{-3}, outcompeting the multiparticle processes. More exciting photophysics have also been uncovered recently: correlated electron–hole plasma over the PV and SE fluences [5], the slow hot-carrier cooling [2] arising from a hot phonon bottleneck effect [32, 42], the microstructure size dependence [43, 44] of the electron–hole interaction and their carrier lifetimes, and the photoinduced refractive index changes [32].

2.2.2.6 Hot Carriers in Perovskites

The previous section mainly discussed the carrier dynamics of thermalized carriers. In contrast, hot carriers refer to those initially generated carriers (i.e. electrons or holes in a Boltzmann distribution) that possess initial kinetic energies at least k_{BT} above the conduction (or valence) bands. The hot-carrier dynamics in perovskites have been investigated mainly using TA spectroscopy. Since the first report of slow hot-carrier cooling (~0.4 ps) in $MAPbI_3$ polycrystalline thin films by Xing et al. in 2013, Li et al. successfully slowed down the cooling by a further 2 orders in $MAPbBr_3$ nanocrystals (up to ~30 ps) and efficiently (~83% efficiency) extracted their hot carriers [45]. This later work aptly highlights the potential of perovskites for high-efficiency hot-carrier PVs, photocatalysis, and photodetectors. The long hot-carrier relaxation lifetime and increased hot-carrier diffusion coefficient are expected to give rise to long hot-carrier diffusion lengths. By imaging the charge transport using TA microscopy, a hot-carrier transport as long as ~600 nm within tens of picoseconds was directly visualized in $MAPbI_3$ thin films [46]. Such long hot-carrier transport will, in principle, enable hot-carrier PVs. Presently, the origins of slow hot carrier cooling in halide perovskite thin films are still under intense debate and have been attributed to various contributions such as large polaron screening effect [47], hot phonon effect [42], or acoustical-optical phonon upconversion [48]. Most recently, Sum's group elucidated a detailed fluence-dependent picture of the mechanisms of slow hot-carrier cooling in solution-processed $MAPbI_3$

thin films [49] using TA spectroscopy and correlating the measurements with detailed theoretical modeling and first-principles calculations. At moderate carrier concentrations (~10^{17}–10^{18} cm^{-3}), carrier cooling is mediated by polar Fröhlich electron–phonon interactions through zone-center delayed longitudinal optical (LO) phonon emissions (i.e. with a phonon lifetime of ~0.6 ± 0.1 ps) induced by the hot phonon bottleneck. The hot phonon effect arises from a large energy separation between the LO and longitudinal acoustic (LA) phonon branches, which suppresses the Klemens relaxation pathway essential for LO phonon decay. At high carrier concentrations (~10^{19} cm^{-3}), Auger heating further reduces the cooling rates. A clear understanding of these intrinsic photophysics is key to developing disruptive perovskite optoelectronic technologies.

2.2.2.7 Summary and Outlook

$CH_3NH_3PbI_3$ is now firmly established as the workhorse material in the perovskite field. However, its photophysical properties are highly sensitive to the processing and environmental factors. With the field progressing to newer halide perovskites (e.g. $CH_3NH_3Sn_{1-x}Pb_xI_3$, mixed $CH_3NH_3PbBr_3/HC(NH_2)_2PbI_3$), and lead-free systems (e.g. $CH_3NH_3SnI_3$), there is a greater urgency to thoroughly characterize and establish $CH_3NH_3PbI_3$ as the model system. One possibility for benchmarking among the various photophysics/photochemistry groups would be to perform round-robin studies of sealed standard $CH_3NH_3PbI_3$ (or $MAPbI_3$) films from leading materials laboratories. In the near future, UOS techniques, especially TAS, will continue to play a leading role in probing the photophysical mechanisms and charge dynamics in halide perovskites.

2.2.3 Energetics and Charge Dynamics at Perovskite Interfaces

2.2.3.1 Introduction

Our earlier discussion focused on the intrinsic photophysical properties of bare polycrystalline perovskite thin films. In the absence of any charge extraction heterojunctions, the photoexcited charges in the perovskite film eventually undergo recombination as the system relaxes back to its equilibrium state. In a typical perovskite solar cell, there are two essential interfaces (i.e. perovskite/HTL and perovskite/ETL) sandwiching the halide perovskite active layer to facilitate charge extraction to the electrodes. The presence of these charge transport layers would alter the relaxation pathways seen in the bare perovskite films. Inevitably, the energy-level alignments at these interfaces would strongly influence the charge-transfer dynamics. Herein, we examine some of these seminal developments from this perspective in perovskite solar cells.

2.2.3.2 Energetics at the Perovskite/Charge Transport Layer Interfaces

To facilitate hole transfer, the VBM of perovskite materials must be lower than that of the HTL (e.g. spiro-OMeTAD); and, conversely, to facilitate electron transfer, the CBM of perovskite materials must be higher than those of

ETL (e.g. TiO_2 or ZnO). Most papers simply assume that the energy levels of perovskite and the HTL/ETL are aligned from common vacuum levels, assuming that one is dealing with far apart isolated layers. This assumption need not be valid as Fermi-level pinning could also occur depending on the electronic interaction between the two layers and the position of the band onsets (or gap states) with respect to the vacuum level. Furthermore, interfacial states, interfacial dipoles, and band bending may also be present at the perovskite interface. Such interfacial electronic structures in perovskites would strongly influence the interfacial charge dynamics (e.g. barrier formation affecting the charge transfer); and the features of PV device operation (e.g. photocurrent generation and energy band offsets affecting the open-circuit voltages).

Photoelectron spectroscopy (PES) provides an important tool to investigate the interfacial energy alignment and electronic structure at material interfaces. The VBM and work function before and after interface formation can be precisely determined. Due to high surface sensitivity of the PES technique, the interface must be carefully prepared (e.g. by thermal deposition and transferred in situ or by spin coating in a glove box, followed by careful transfer in portable transfer capsules to the ultrahigh vacuum (UHV) PES chamber) to avoid external contaminants (such as water vapor and hydrocarbons) from the ambient. The first two PES studies on the energy-level alignment of perovskite/HTLs are by Schulz et al. [50] and Chen et al. [51]. The former investigated the energy-level alignments of $MAPbI_3$, $MAPbI_{3-x}Cl_x$, and $MAPbBr_3$ with spiro-OMeTAD using ultraviolet photoelectron spectroscopy (UPS) and inverse photoelectron spectroscopy (IPES). Their findings revealed a band bending of 0.1–0.3 eV for the spiro-OMeTAD layer. The latter study investigated the interfacial alignment between $MAPbI_3$ and CuPc (another HTL material) using X-ray photoelectron spectroscopy (XPS) and UPS, where a 0.3 eV band bending was found for the CuPc layer (Figure 2.2.6b). The band bending observed in these HTLs is a consequence of the Fermi-level alignment. As the work function of the HTL is smaller than that of the perovskite, charge transfer from the HTL to perovskite occurs as the two Fermi levels align. The reduction of the carriers at the surface of the HTL results in the bending of the bands upward at the interface to higher energies. This could be deleterious for the interfacial charge transfer, resulting in hole trapping and reducing the charge-transfer efficiency. Therefore, if the work function of the HTL can be slightly increased, the upward band bending (toward the interface) can be suppressed.

Conventional PES studies (with Al Kα ~ 1.486 keV photons) on the perovskite/ETL interface face inherent challenges from the sample preparation. For example, one would not be able to probe the interface of spin-coated perovskite on the TiO_2. To overcome this limitation, Lindblad et al. [52] utilized hard X-ray PES (with 4 keV photons) that yielded photoelectrons with a much longer inelastic mean free path to probe $MAPbI_3$ spin coated on mesoporous (me)-TiO_2 layers. They found the VBM of $MAPbI_3$ to be 2.1 eV higher than that of TiO_2. Based on the values of the optical band gaps for TiO_2 (3.2 eV) and $MAPbI_3$ (1.5 eV), they also deduced the CBM of $MAPbI_3$ to be ~0.4 eV higher than that of TiO_2. While this approach increased the sensitivity of the bulk energy levels of perovskite and TiO_2 and permits direct referencing between the bulk TiO_2 and perovskite, it is still not a direct probe of the interfacial energy alignment.

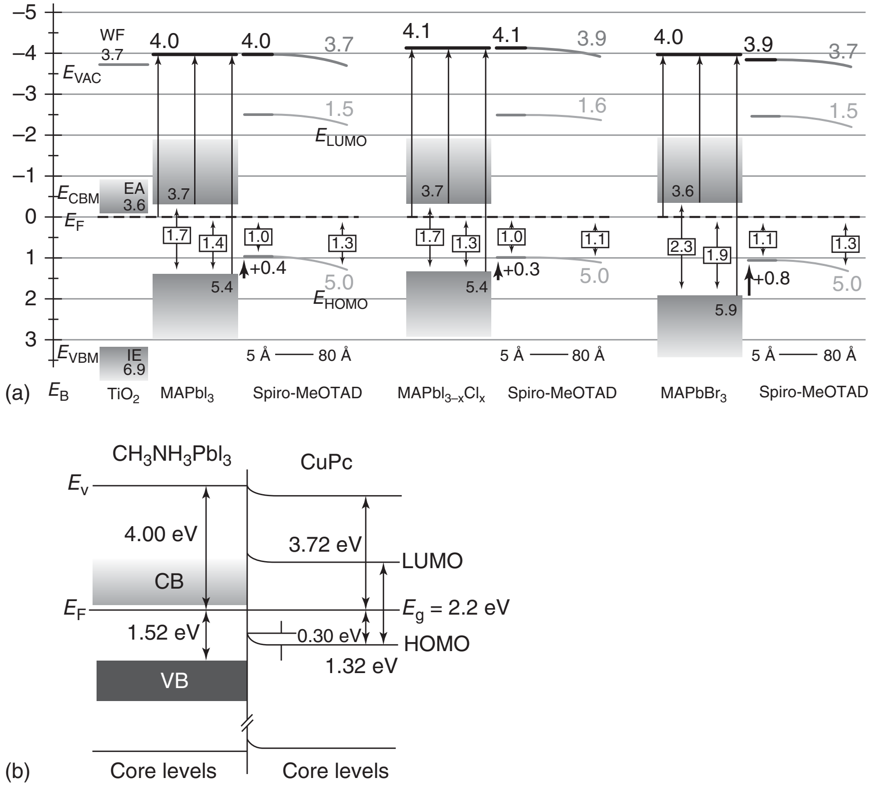

Figure 2.2.6 Energy-level alignment between perovskite and hole transport materials. (a) $MAPbI_3$, $MAPbI_{3-x}Cl_x$, and $MAPbBr_3$ aligned with spiro-MeOTAD. (b) $MAPbI_3$ aligned with CuPc where the CuPc energy levels bend down away from the interface. HOMO, highest occupied molecular orbital; LUMO, lowest unoccupied molecular orbital. Source: (a) Schulz et al. 2014 [50]. Copyright 2014. Reprinted with permission of Royal Society of Chemistry. (b) Chen et al. 2014 [51]. Copyright 2014. Reprinted with permission of American Physical Society.

A straightforward approach to study this interface with conventional PES would be to utilize in situ vapor deposition of perovskite materials on TiO_2 substrates.

The significance of investigating the interface band alignment is aptly highlighted in several works that reported strong dependence of perovskite's Fermi-level position on the underlying substrate [53, 54]. The substrate-type modulates the Fermi energy to VBM difference ($E_F - E_{VBM}$), thereby making the $MAPbI_3$ layer more n- or p-type. Typically, the VBM of $MAPbI_3$ is lowered to ~1.7 eV on n-type substrates such as ZnO, TiO_2, ZrO_2; while it can be significantly lowered to ~1.38 eV on PEDOT:PSS (poly(3,4-ethylenedioxythiophene) polystyrene sulfonate); ~1.0 eV on NiO_x and ~0.9 eV on Cu_2O [53]. Such tunability of the Fermi-level position and the majority carrier type with the substrate is believed to arise from the low density of intrinsic carriers (i.e. from unintentional dopants) and the low density of electronically active mid-gap bulk and interface defects (or otherwise E_F would be pinned) [54]. For future studies, it is extremely important to correlate these findings with interfacial charge-transfer studies and device characterization to fully understand the extent of the tunability to improve the performance of alternate inverted [55] or tandem [56] perovskite architectures.

2.2.3.3 Charge-Transfer Dynamics at the Perovskite/Charge-Transport Layer Interface

Using infrared TA spectroscopy and microwave photoconductivity, Moser in collaboration with Grätzel and coworkers performed the first study to probe the charge-transfer mechanism in perovskite solar cells (Figure 2.2.7). They found clear evidence of not only efficient hole injection from photoexcited $CH_3NH_3PbI_3$ into the HTL (spiro-OMeTAD) but also efficient electron injection from photoexcited $MAPbI_3$ into the ETL TiO_2; both processes occurring simultaneously over comparable ultrafast timescales within 3 ps [57]. Probing at 1.4 μm allowed the authors to directly observe the carrier's population decay within the perovskite itself (Figure 2.2.7b). Using TA spectroscopy, they demonstrated that the population of long-lived charges in $TiO_2/MAPbI_3$/HTM (hole transporting material) samples is higher than that in $Al_2O_3/MAPbI_3$/HTM samples (Figure 2.2.7b), which in turn indicated a more efficient charge separation in the former than in the later. It was revealed that the efficiency of charge extraction in a perovskite solar cell also depends on the ratio between charge recombination and charge separation rates. In this regard, Moser et al.'s findings showed that it is advantageous to use TiO_2 as the electron acceptor and transporter, together with an HTM in perovskite solar cells.

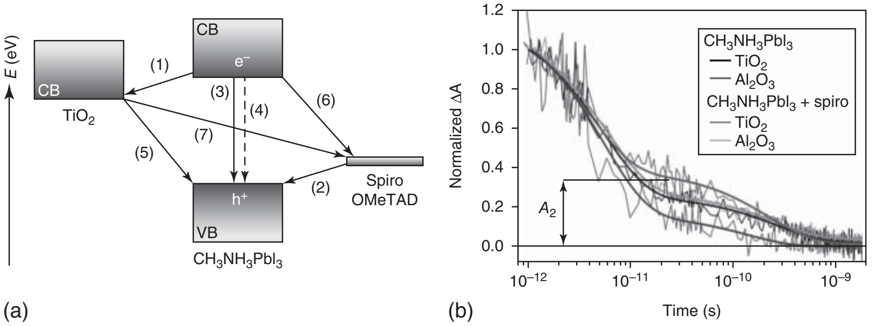

Figure 2.2.7 (a) Schematic diagram of energy levels and electron transfer processes in an HTM/perovskite/TiO_2 cell. (1) Electron injection; (2) hole injection; (3) radiative exciton recombination; (4) non-radiative exciton recombination; (5) back electron transfer at the TiO_2 surface; (6) back charge transfer at the HTM surface; (7) charge recombination at the TiO_2/HTM interface. (b) Transient absorption signals were measured at a probe wavelength of 1.4 μm following the femtosecond laser-pulsed excitation at 580 nm: $CH_3NH_3PbI_3$ (or $MAPbI_3$) on TiO_2 (black); $CH_3NH_3PbI_3$ on Al_2O_3 (dark gray – lower trace); $CH_3NH_3PbI_3$ and spiro-OMeTAD on TiO_2 (dark gray – upper trace); $CH_3NH_3PbI_3$ and spiro-OMeTAD on Al_2O_3 (light gray). Thick solid lines represent bi-exponential fits of experimental points starting at time $t = 1$ ps. A_2 represents the normalized absorbance change at 25 ps, used as a metric to compare the various samples. Source: Marchioro et al. 2014 [57]. Copyright 2014. Reprinted with permission of Springer Nature.

Although TiO_2 is the workhorse electron acceptor in perovskite PVs, a detailed understanding of the interfacial charge-transfer mechanisms at this heterojunction remains incomplete. In particular, there have been diverse conclusions about the charge-transfer times (i.e. spanning <1 ps to hundreds of picoseconds) and charge-transfer efficiencies have been obtained for the $MAPbX_3/TiO_2$ heterojunction (see summary in Table 2.2.2). The confusion could be partly traced to the mesoporous TiO_2 as the nanopores can greatly alter the perovskite's film morphology and crystallinity. Hence, systematic studies of the interfacial charge-transfer dynamics and comparison with other standard samples (e.g. perovskite/quartz, perovskite/Al_2O_3) are particularly difficult to achieve. Nevertheless, these diverse observations of the charge-transfer times together with evidence of carrier accumulation [63] in $MAPbI_3$ and anomalous $I-V$ hysteresis observed in $MAPbX_3/TiO_2$ heterojunction-based solar cells [64] indicate that the charge transfer at this interface may be more complex than was previously believed.

Through TRPL and TA spectroscopy, Xing et al. found that the electron transfer at the $MAPbI_3$/compact TiO_2 interface to be slower than that at the $MAPbI_3$/PCBM ([6,6]-phenyl-C-61-butyric acid methyl ester) interface [65]. These findings concur with those of Wojciechowski et al., who had also observed slow electron transfer at the $MAPbI_{3-x}Cl_x/TiO_2$ interface, in contrast to the effective quenching at the $MAPbI_{3-x}Cl_x$/PCBM or C_{60}-SAM (self-assembled monolayer) interfaces [66]. From the deficiency of surface organic cations (i.e. electron deficiency) in $MAPbI_3$ elucidated from XPS studies, Xing et al. deduced that the passivation of the surface states of $MAPbI_3$ and TiO_2 resulted in the formation of a strong interfacial dipole, which would function as an electron barrier at the $MAPbI_3/TiO_2$ interface. Consequently, this leads to PL intensity enhancement and PL lifetime lengthening for $MAPbI_3$ interfaced to compact TiO_2. This work aptly highlights the significance of complementary

Table 2.2.2 List of reported electron transfer times from perovskite to TiO_2.

Type of interface	Techniques	Charge-transfer time/ efficiency	References
$MAPbI_3$/me-TiO_2	TA	~3 ps	[57]
$MAPbI_3$/planar TiO_2	TA	39.9 ± 2.5 ps	[29]
$MAPbI_3$/me-TiO_2	TA	89.6 ± 12.5 ps	
$MAPbI_3$/me-TiO_2/planar TiO_2	TA	150.0 ± 17.6 ps	
$MAPbI_3$/me-TiO_2	TA	260–307 ps	[58]
$MAPbI_3$/me-TiO_2	TR-THz	<1 ps	[13]
$MAPbI_3$/me-TiO_2	TA	<200 fs	[59]
$MA_{(1-y)}FA_yPbI_xBr_{(3-x)}$/me-$TiO_2$	TA	~100 fs	[60]
$MAPbI_3/TiO_2$	DFT calculation	<100 fs	[61]
$MAPbI_3$/me-TiO_2/planar TiO_2	TRPL	Quenching efficiency 99%	[13]
$MAPbI_3$/planar TiO_2	PL	Quenching efficiency 47%	[62]

energetics and charge dynamics approach to tackle material interface problems. The presence of this interface is consistent with the observations of carrier accumulation [63] in $MAPbI_3$ from impendence spectroscopy and could possibly be one of the contributions to the anomalous $I-V$ hysteresis observed in $MAPbX_3/TiO_2$ heterojunction-based solar cells [64]. More recently, Nazeeruddin and coauthors reported an ultrafast interfacial electron injection from mixed-halide iodide–bromide perovskite $MA_{1-y}FA_yPbI_xBr_{3-x}$ into mesoporous TiO_2 within ~100 fs [60]. Such rapid electron transfer competes successfully with the electron–phonon energy relaxation inside the perovskite, demonstrating that hot charge carriers can be harvested before they thermalize, a potential way to break the Shockley–Queisser limit and boost the device efficiency. Further energetics and charge dynamics studies on other perovskite/ETL interfaces (e.g. $MAPbX_3/ZnO$) can be expected.

2.2.3.4 Summary and Outlook

Moving forward, it is important that charge dynamics studies at the perovskite/inorganic semiconductor interface should be accompanied by both energetics and physical studies to understand the intrinsic chemical and morphological nature of the surface where various defect types (e.g. surface traps, vacancies, etc.) and crystal sizes are inevitably present. The perovskite sample fabrication (i.e. single-step deposition, dual-deposition processing, and evaporation approach), processing (i.e. annealing temperatures and duration), and ambient conditions (i.e. the oxygen and moisture content in the glove box) all exert a profound influence on the perovskite film quality and its morphology and surface properties. Hence, the inclusion of XPS data of the perovskite surface in dynamics studies could help diagnose the surface chemical nature of the perovskite films made by various research groups, thereby permitting better comparison. Such standardization will become more important as surface engineering approaches are now becoming increasingly popular. Apart from energetics studies, careful control of the pump fluence in the dynamics studies is also important as the use of relatively high pump fluence would mask the effects of carrier accumulation (if a barrier is present) with a flood of photoexcited carriers. Similarly, use of pump energies far larger than the perovskite bandgap will generate a population of hot carriers that could overcome the barrier with hot-carrier transfer [65]. Any of these factors or a combination of them are likely to influence the interfacial charge-transfer times listed in Table 2.2.2, thus causing the spread. Further studies are needed to clarify this.

2.2.4 Toward Perovskite Single-Crystal Photovoltaics

Large-scale SCs typically possess fewer defects compared to polycrystalline or amorphous thin films. Hence, organic–inorganic halide perovskite SCs are expected to yield even better PV performances. Theoretical calculations have shown that efficiencies up to 25% can be obtained for large crystals (i.e. diameter > 10 μm), which is higher than those with smaller grain sizes [67]. A breakthrough in synthesizing large perovskite SCs using solution methods in 2015 has thrown them into the spotlight [22, 68–71]. Based on the historical developments for Si and GaAs solar cells, one can expect that perovskite PVs would soon embark on the same path toward single-crystalline solar cells. In this section, we focus on the photophysics of organic–inorganic halide perovskite SCs.

2.2.4.1 Absorption and Emission Properties

Unlike perovskite polycrystalline thin films, the absorption edge of perovskite SCs is usually extended. Figure 2.2.8a shows the typical absorption and emission profiles of $MAPbI_3$ SC, where its absorption edge is redshifted by around 0.1 eV (~50 nm) compared to the polycrystalline thin films (as shown in Figure 2.2.1) [22, 70]. The extended absorption, exhibiting a shoulder centered at around 800 nm, also contributes to the external quantum efficiency (EQE) of $MAPbI_3$ SC-based solar cells [22]. The extended absorption is possibly due to the weak absorption from the Urbach tail that only becomes pronounced in thick crystals. We note that this energy shift is also seen in the emission spectra. Using two-photon excitation, the bulk regions of the SC can be excited. Yamada et al.

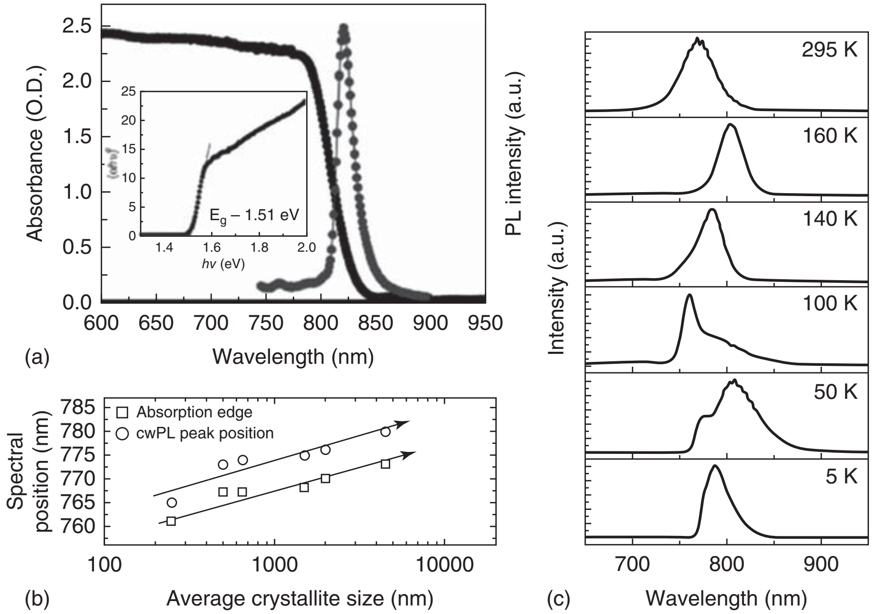

Figure 2.2.8 Absorption and PL properties of $MAPbI_3$ SCs. (a) Absorption and PL profile of a $MAPbI_3$ SC. (b) Grain-size-dependent PL energy shift. (c) Temperature-dependent $MAPbI_3$ SC PL profile change. Source: (a) Saidaminov et al. 2015 [70]. Copyright 2015. Reprinted with permission of Nature Publishing Group. (b) D'Innocenzo et al. 2014 [72]. Copyright 2014. Reprinted with permission of American Chemical Society. (c) Fang et al. 2015 [73]. Copyright 2015. Reprinted with permission of John Wiley & Sons.

found the PL peak of $MAPbI_3$ crystal to be around 812 nm, which is redshifted compared to polycrystalline thin films (~770–780 nm). One possibility for the emission redshift could be due to reabsorption [74]. As photons emitted in the interior pass through the thick crystal to the collection optics, the blue side of the spectrum becomes absorbed by the crystal. Such phenomenon usually happens in crystals with large band-to-band absorption and small Stokes shift [74]. The reabsorption will reshape the PL spectra, resulting in the redshift and narrowing of the spectrum. Another possibility for the emission redshift is that the bandgap energies of the $MAPbI_3$ polycrystalline thin film and SC are different. The difference could arise from the size effect. For example, $MAPbI_3$ perovskite in mesoporous TiO_2 matrix is found to have blueshifted absorption and PL spectra compared to polycrystalline thin films with relatively larger crystalline size [75]. As grain size decreases, the absorption edge and PL is found to continuously blueshift, while the linewidth is also simultaneously broadened (Figure 2.2.8b) [68, 72]. Smaller crystals may suffer from stronger inorganic cage deformation that compresses the lattice, resulting in an increased bandgap [68, 76]. These bandgap changes suggest a means of tuning the perovskite emission and broadening the light-harvesting spectrum by simply varying the crystal size [72].

Apart from tuning the bandgap, varying the crystal size also affects the nature of the primary photoexcited species – excitons versus free carriers (discussed earlier). The electron–hole interaction in hybrid perovskite system is sensitive to the microstructure of the material. Larger $MAPbI_3$ SCs show an excitonic transition at the absorption edge, which is absent in small crystals. It is speculated that the formation of excitonic transition in large crystals is related to the ordering of the system, particularly the orientational order of the organic cation (methylammonium, MA^+). The organic cation has a permanent dipole. If it can freely rotate, separation of electron–hole pairs is facilitated due to the increase of the low-frequency dielectric constant. However, in SCs, the rotational disorder of the cations is quenched. Thus, free carriers will thermalize and coalesce into forming excitons [43].

The emission spectra become more complicated at low temperatures when phase transitions occur (Figure 2.2.8c) [73]. Above the phase transition temperature (163 K for $MAPbI_3$), the PL spectrum shifts from 770 to 805 nm when the temperature drops, corresponding well with the absorption edge redshift and is attributed to the band-edge transition. Between 163 and 125 K, a blueshift of the PL peak occurs – opposite to the shift above 163 K. Below 100 K, a new band appears at ~805 nm and gradually dominates with lowering temperatures. Below the phase transition temperature, the PL spectra can be fitted using three Gaussian peaks. The high-energy peak (I) is assigned to free exciton (FE) emission, while the intermediate (II) and low (III) energy peaks are attributed to bound excitons (BEs). The BEs have long lifetimes and strong emission, possibly attributed to the localization caused by site distribution of the organic cations at low temperatures. For $MAPbBr_3$ SCs, hydrogen-like Wannier–Mott exciton emission was also observed. The first and second exciton transitions were found at 2.2558 and 2.2673 eV. According to the relation of the band-edge (E_g) and exciton binding energy (E_b): $E_n = E_g - E_b/n^2$, where $n = 1, 2, 3, \ldots$; an exciton binding energy of 15.9 meV was derived. Donor–acceptor (D–A) pair emission dictates the sub-bandgap emission band at low temperature [77]. With increasing excitation power, the D–A band does not increase in intensity, but instead shows a pronounced blueshift, corresponding to the increase of recombination events for close-by electron–hole pairs.

2.2.4.2 Surface Versus Bulk Optical Properties

In large semiconducting crystals, the surface and the bulk properties are usually distinct from each other. Surface defects and imperfections such as dangling bonds, dislocations, and chemical impurities adsorbed can result in very different optical and electronic properties at the surface compared to the bulk part. For example, moisture can cause a significant blueshift of $MAPbI_3$ SC emission from 796 to 770 nm [78]. Such a change is related to the surface-hydration-induced lattice expansion, which results in local stress and the surface reconstruction [79]. Distinct PL blueshift from the bulk to the surface was also observed when using one photon to excite the surface and two-photon excitation for the bulk [80]. However, reabsorption effects cannot be neglected here due to much deeper penetration depth with two-photon excitation. To further understand the surface defect properties and their effects, photocarrier dynamics with different surface passivation were also investigated. The passivation with an electron-rich ligand (hexylthiophene) was found to significantly improve $MAPbI_3$ SC emission intensity and carrier lifetime, while it also helps reduce the BE formation at low temperature. This implies that the electron-rich sulfur of the hexylthiophene donates its electrons to positively charged defects (likely to be iodide vacancies) at the surface of $MAPbI_3$ crystals.

Surface recombination occurring at the free surface or grain boundaries can also be a dominating factor limiting the device efficiency. This can result in a fast initial decay of the carrier density. For large crystals, their surfaces usually have much higher defect densities than those of the bulk in SC, thereby resulting in high surface recombination rates. The minority carrier lifetime can be expressed as

$$\frac{1}{\tau_{\text{minority}}} = \frac{1}{\tau_{\text{surface}}} + \frac{1}{\tau_{\text{radiative}}} + \frac{1}{\tau_{\text{defect}}} + \cdots \tag{2.2.5}$$

where $1/\tau_{\text{surface}}$, $1/\tau_{\text{radiative}}$, $1/\tau_{\text{defect}}$ are the surface, radiative, and bulk Shockley–Read–Hall (SRH) recombination rates, respectively; and higher order recombination is excluded in the expression. An important parameter to quantify the quality of a surface is the surface recombination velocity (SRV), which is defined by the ratio of the recombination rate per unit area (U_s) to the excess carrier concentration close to the surface (Δn):

$$S = \frac{U_s}{\Delta n} \tag{2.2.6}$$

Due to the presence of the surface recombination, the carrier dynamics of perovskite SC usually exhibits a bi-exponential decay manner. The initial fast decay with a lifetime of ~ns is attributed to the surface recombination, while the longer component is attributed to the bulk recombination lifetime [69, 81]. Quantification of the SRV is usually through TA spectroscopy or TRPL spectroscopy. For example, in $MAPbBr_3$ SCs, the SRV is around 3.4×10^3 cm s^{-1} (TA spectroscopy) and $\sim 6.7 \times 10^3$ cm s^{-1} (TRPL), while that for $MAPbI_3$ SCs is about half of the $MAPbBr_3$ values [80]. SRV as low as a few centimeters per second had been reported for $MAPbBr_3$ SC [82]. Surprisingly, the SRV of polycrystalline $MAPbI_3$ thin films (0.45×10^3 cm s^{-1}) was found to be more than six times lower than in the SCs (0.45×10^3 cm s^{-1}), possibly due to excess MA cations that passivate grain boundaries in the former. For SCs, a Pb^{2+}-rich environment was found instead [83]. We have to point out that in SCs or in polycrystalline thin films, the SRVs are generally a few orders lower than conventional non-passivated PV semiconductors such as GaAs, CdTe (10^5–10^6 cm s^{-1}). Considering that surface recombination occurs in an SRH-like trend, recombination via mid-gap traps created by surface defects will dominate and influence the SRV. In organic–inorganic halide perovskites, the defects at the grain boundaries or surfaces give rise to very few mid-gap states for recombination [84]. An empirical criterion to estimate the magnitude of SRV in semiconductors is to compare the position of the semiconductor band energy with the Fermi-level stabilization energy [85]. The Fermi-level stabilization energy (E_{FS}), also known as the neutral level, located at around 4.9 eV below the vacuum level, is the reference energy used to predict the dominant semiconductor native defects. For GaAs and CdTe, that E_{FS} lies near the middle of their bandgap, the SRVs are much higher ($>10^5$ cm s^{-1}), and therefore surface passivation is usually necessary [86]. For semiconductors such as InP as well as halide perovskites ($MAPbI_3$, $MAPbBr_3$), the E_{FS} lies either near the CBM or VBM, indicating that the native defects tend to form away from the mid-gap, and hence provide small SRV for $MAPbI_3$ ($\sim 10^3$ cm s^{-1}) and InP ($\sim 10^2$ cm s^{-1}) SCs [80, 87]. The SRV is so low in perovskite SCs that it indicates that surface passivation is unnecessary for optimizing the PV performance when grain sizes are larger than ~30 μm [81].

2.2.4.3 Carrier Lifetimes, Diffusion Lengths, and Diffusion Coefficients

With regards to PV application, apart from the earlier discussion, other key parameters include carrier lifetime τ (surface and bulk carrier lifetime), mobility μ, diffusion length L_D, and trap density n_t [69].

τ can be determined from the decay transients from TA spectroscopy or TRPL spectroscopy. For example, the dynamics of $MAPbX_3$ SCs usually show a bi-exponential decay [68, 69, 81]. A shorter decay time constant can be attributed to the lifetime at the surface part of the SC where surface recombination dominates. The longer component is due to the bulk carrier lifetime [81]. As shown in Figure 2.2.9a, the $MAPbI_3$ SC's surface carrier lifetime was measured to be ~18 ns, while the bulk lifetime was 570 ns – obtained using TA spectroscopy [70]. With other techniques, such as impedance spectroscopy and transient photovoltage measurements, the bulk carrier lifetime in $MAPbI_3$ SC is found to be as high as 82–95 μs [22].

μ is usually measured using space-charge-limited-current (SCLC), time-of-flight (ToF), Hall measurements, etc. High carrier mobilities were found for

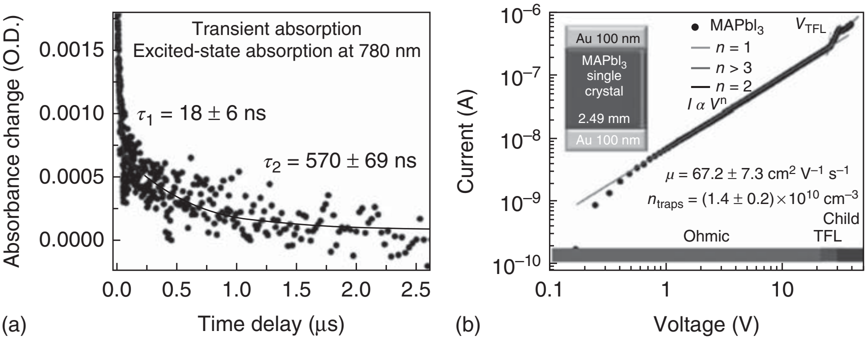

Figure 2.2.9 (a) Trap density of $MAPbI_3$ SC measured using trap-filled limit voltage. (b) Carrier lifetime measured using time-resolved PL spectroscopy. Source: Saidaminov et al. 2015 [70]. Copyright 2015. Reprinted with permission of Nature Publishing Group.

solution-processed $MAPbX_3$ SCs. For example, Dong et al. reported a hole mobility of $164 \pm 25\,\text{cm}^2\ \text{V}^{-1}\ \text{s}^{-1}$ and electron mobility of $24.8 \pm 4.1\,\text{cm}^2\ \text{V}^{-1}\ \text{s}^{-1}$ for $MAPbI_3$ using the SCLC and ToF techniques [22]. For $MAPbBr_3$, high carrier mobility of $115\,\text{cm}^2\ \text{V}^{-1}\ \text{s}^{-1}$ was also reported by Shi et al. using ToF measurements [69]. For $MAPbCl_3$, the carrier mobility is $42 \pm 9\,\text{cm}^2\ \text{V}^{-1}\ \text{s}^{-1}$ from SCLC measurements [71]. The carrier mobilities obtained for SCs are generally 1–2 orders higher than those for polycrystalline thin films.

L_D can be estimated from the expression:

$$L_D = \sqrt{D\tau} \tag{2.2.7}$$

where τ is the carrier lifetime and D is the diffusion coefficient that can be expressed using the following Einstein relation: $D = \mu V_t$, where μ is carrier mobility, V_t is the thermal energy. The diffusion length of $MAPbI_3$ SC is frequently reported to range from a few micrometers to hundreds of micrometers [22, 69]. Such a high carrier diffusion length implies that a perovskite SC-based PV device would be able to absorb all the above bandgap light and extract all the carriers generated simultaneously. The high carrier mobility and diffusion length is a result of the greatly reduced defect density in the bulk SC compared to the polycrystalline. As shown in Figure 2.2.9b, trap density estimated for $MAPbI_3$ SCs is on the order of $10^{10}\,\text{cm}^{-3}$ using trap-filled limit voltage (V_{TFL}), which is 5 orders lower than that of polycrystalline perovskite thin films measured using the same technique [22, 69].

2.2.4.4 Transient Spectral Features and Excitation Dynamics

The ability to interpret and discern the transient spectral features and excitation dynamics in perovskite SCs is key to understanding its full photophysics picture. A particularly problematic dilemma in the characterization of the large and thick perovskite SCs (several millimeters) is the limited penetration depth (of several 100 nm) for above bandgap photons via single-photon excitation. Two-photon excitation offers a viable solution. For example, it was reported that $MAPbBr_3$ SCs have two-photon absorption (TPA) coefficients of ~8.6 cm GW^{-1} at 800 nm excitation [88], which can result in a penetration depth of around 100 μm. Recently, Wu et al. utilized a combination of one-photon and two-photon excitation spectroscopy to elucidate a comprehensive photophysical picture of the surface and bulk regions of perovskite SCs.

Figure 2.2.10a shows the pseudo-color transient reflectivity (TR) spectra feature of a MAPbBr$_3$ SC with 400 nm excitation. Two anti-symmetric peaks were found centered around 2.3–2.4 eV (Figure 2.2.10b) [80, 81]. The shape of the TR spectra is consistent, except for the drop in magnitude with time. As organic–inorganic halide perovskites possess a large refractive index ($n \sim 2$–3), the TR is dominated by the refractive index change [32]:

$$\frac{\Delta R}{R} = \frac{4}{n(E)^2 - 1}\Delta n(E)$$

where $n(E)$ and $\Delta n(E)$ are the steady-state reflective index and reflective index change after excitation at photon energy E. The change of the refractive index is associated with a change of absorption coefficient $\Delta\alpha$, through the Kramers–Kronig relations:

$$\Delta n(E) = \frac{\hbar c}{\pi} P \int_0^{\infty} \frac{\Delta\alpha(E)}{E'^2 - E^2}\,\mathrm{d}E'$$

where c is the speed of light and P is the Cauchy principal integral.

Upon photoexcitation, the excitonic absorption peak and/or continuum bands are filled, leading to an absorption bleach at the probe wavelengths ($\Delta\alpha < 0$). Under low-fluence photoexcitation, the bleaching of the continuum band is negligible due to the low occupation probability. As shown in Figure 2.2.10b, the TR profile of MAPbBr$_3$ can be well fitted with an excitonic bleach at around 2.37 eV, confirming the validity of this interpretation. Due to the abrupt change in refractive index at the air/perovskite interface, the TR profile and dynamics are mainly from the very shallow surface region (~10 nm) [89]. With 400-nm excitation, the TR dynamics shown in Figure 2.2.10c originates from surface recombination dynamics and diffusion into the bulk. Hence, excitation wavelengths with different absorbing lengths will yield strikingly different TR dynamics due to the two varying contributions from surface recombination and diffusion [81].

On the other hand, if pump-probe spectroscopy is performed in transmission mode, no TA signal can be detected below 560 nm (2.22 eV) due to the strong absorption of the transmitted probe by the thick MAPbBr$_3$ SC (Figure 2.2.10d). The TA spectra show a negative change in transmission ($\Delta T < 0$) at wavelengths >620 nm. Also evident is an isosbestic point (occurring around 620 nm at 1 ps) that gradually blueshifts at longer delays, separating the $-\Delta T$ in the redder part of the spectrum from the $+\Delta T$ (or PB) in the bluer part. This $+\Delta T$ region is from the tail of the PB peak (arising from state-filling and SE following absorption of the pump beam). However, the PIA region ($-\Delta T$) that is present in SCs is absent in the TA spectrum of the polycrystalline thin film, indicating that it is a unique spectral feature of SCs. The PIA possibly arises from the transitions of the photoexcited species to higher excited states or sub-bandgap trap state absorption in the crystal, which is significant in thick crystals while being negligible in thin

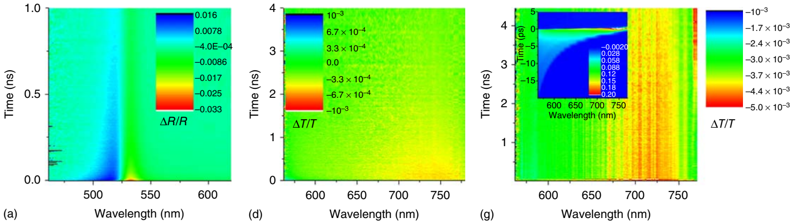

Figure 2.2.10 Femtoseconds to nanoseconds transient absorption of $MAPbBr_3$ single crystal. (a) The pseudocolor transient reflectivity (TR) profile of $MAPbBr_3$ with 400 nm excitation. (b) The TR profile (experimental result selected at 10 ps delay) (blue dot) and the fitted curve (blue solid) using surface exciton absorption (red line). (c) Normalized TR dynamics monitored at 532 nm and the fitted curves using model depicted in the text. (d) The pseudocolor transient absorption (TA) profile of $MAPbBr_3$ with 400 nm excitation. (e) TA profile of $MAPbBr_3$ SC at selected delays excited by 400 nm. (f) Normalized transient dynamics monitored at 700 nm for $MAPbBr_3$ SC with 400 nm excitation. (g) The pseudocolor TA profile of $MAPbBr_3$ with 800 nm excitation. Inset shows the zoom-in profile near time zero. (h) TA profile of $MAPbBr_3$ SC at selected delays excited by 800 nm. (i) Normalized transient dynamics monitored at 700 nm for $MAPbBr_3$ SC with 800 nm excitation. (The time zero has been shifted for better display.) The right side shows a schematic of the D-TPA and ND-TPA. Source: Wu et al. 2016 [80]. Copyright 2016. Reprinted with permission of John Wiley & Sons.

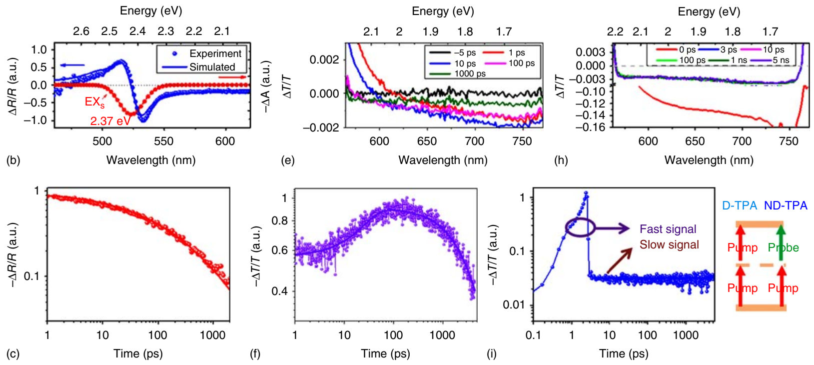

Figure 2.2.10 (*Continued*)

films. The fast blueshift of the isosbestic point and the disappearance of the PB band within 100 ps (Figure 2.2.10e) indicate that the excited species at the surface diffuses very efficiently into the bulk. The build-up time (~100 ps) of the PIA yields a diffusion length of 48 nm using the diffusion equation of $L = \sqrt{Dt}$. This value represents the average propagation distance of the excited species away from the surface photoexcited region into the bulk. The fitted PIA decay lifetime of ~3.8 ns (Figure 2.2.10f) is in between the value of the PL lifetimes of the true surface (~1 ns) and true bulk (~34 ns) values, constituting an average lifetime [80].

Figure 2.2.10g shows a pseudo-color TA profile of the SC with two-photon pumped (800 nm) excitation. In the first few picoseconds timescale, an ultrafast and strong PIA component appears immediately after excitation spanning the wavelength range of ~650–750 nm (Figure 2.2.10h). After the decay of this "ultrafast" component, a residue PIA component (slow) similar to that observed in 1PA excitation at long delays persists and does not show any decay within the 5 ns time window (Figure 2.2.10i). The ultrafast PIA component is an artifact that originates from the nondegenerate (ND)-2PA of the pump and probe – i.e. simultaneous absorption of a pump and a probe photon resulting in a TPA process. The "slow" component, on the other hand, is the "real" carrier relaxation dynamics following photoexcitation by degenerate (D)-2PA of the pump photons (Figure 2.2.10i schematic). The constant nonequilibrium $\Delta T/T$ signal over the 5 ns time window suggests the presence of a long-lived species in the bulk – in fact, its lifetime corresponds well with the bulk emission lifetime (30–40 ns) and is attributed to the bulk excitation recombination [80].

2.2.4.5 Recombination Constants in the Surface and Bulk Regions of Perovskite Single Crystals

Table 2.2.3 lists the recombination constants of several typical perovskite SCs. The monomolecular recombination coefficient (k_1) of SCs has been widely

Table 2.2.3 List of reported recombination constants for various halide perovskite single crystals at room temperature.

	Recombination constants			
Thin film	k_1 (μs^{-1})	$k_2 \times 10^{-10}$ (cm^3 s^{-1})	Techniques	References
$MAPbBr_3$	40	5.4	TRPL	[90]
$FAPbBr_3$	15	3.5	TRPL	[90]
$CsPbBr_3$	21	5.7	TRPL	[90]
$MAPbBr_3$	29	2.0	TRPL	[80]
$MAPbI_3$	0.7–0.8	0.38–0.82	(Micro-)TRPL	[91]
$MAPbBr_3$	2.5	2.0	(Micro-)TRPL	[91]

MA: methylammonium ($CH_3NH_3^+$) and FA: formamidinium ($HC(NH_2)_2^+$).

reported, corresponding to the inversion of the carrier lifetime under low fluence, as discussed. The SCs generally have a lower k_1 rate due to the presence of much lower trap density than do polycrystalline films. For example, the observed k_1 for $MAPbI_3$ SC is usually around 0.1–10 μs^{-1}, which is much lower compared to $MAPbI_3$ polycrystalline thin films with typical lifetimes of nanoseconds to microseconds (corresponding to a k_1 of $1–10^3$ μs^{-1}). Under high excitation densities, processes such as bimolecular and Auger recombination at the surface and bulk regions, as well as carrier diffusion would contribute to the observed decay dynamics and complicate the analysis. Hence, there have been few reports on the bimolecular and Auger recombination coefficients (k_2 and k_3). As Table 2.2.3 shows, the bimolecular recombination coefficients of lead bromide SCs are generally accepted on the order of 10^{-10} cm^3 s^{-1}, similar to that of polycrystalline thin films. Lead iodide SCs have a coefficient of around 10^{-11} cm^3 s^{-1}, which is slightly lower than polycrystalline thin films. Presently, there has been no report on the Auger recombination coefficients for SCs, which warrants further investigations.

Perovskite SCs are expected to have high potential application as PV materials. They possess many improved optoelectronic properties compared to their polycrystalline counterparts, such as much reduced trap density, lengthened carrier lifetime, improved diffusion length, reduced bandgap, etc. However, unlike polycrystalline thin films, perovskite SCs are relatively unexplored. For example, the bulk regions of the SCs still remain poorly understood compared to the surface part in spectroscopic characterization due to the limited above bandgap light penetration depth ($\sim 10^2$ nm). For example, photophysics properties such as exciton binding energy, PL quantum yield, bimolecular/Auger recombination coefficients, and hot-carrier relaxation are still unknown in the bulk. These bulk properties are very important, as they provide us an excellent platform to correlate with theoretical simulation and understand the intriguing fundamental properties. Meanwhile, developing a practical approach to synthesize thin SC films (e.g. ~1 μm thickness) should be the focus to boost the perovskite solar efficiency up to 25%.

2.2.5 Concluding Remarks

The rapid ascent of organic-inorganic lead halide perovskite to the world stage has presented both opportunities and challenges for the PV and materials characterization communities. With single-junction polycrystalline perovskite solar cells inching toward their Shockley–Queisser limits, one can look forward to the development of newer architectures like tandem and hot-carrier perovskite solar cells (or a combination of both) to breach that limit. Given the much better properties of perovskite SCs compared to their polycrystalline counterparts, one could also envisage new developments in that direction. However, a key challenge is to be able to grow large area and continuous SC thin films. Nonetheless, nondestructive and noncontact spectroscopy techniques will continue to play a vital role in understanding the photophysical properties, interfacial energetics, and charge-transfer mechanisms in these next-generation perovskite solar cells.

References

1 Even, J., Pedesseau, L., and Katan, C. (2014). *J. Phys. Chem. C* 118: 11566.

2 Xing, G.C., Mathews, N., Sun, S.Y. et al. (2013). *Science* 342: 344.

3 Even, J., Pedesseau, L., Katan, C. et al. (2015). *J. Phys. Chem. C* 119: 10161.

4 D'Innocenzo, V., Grancini, G., Alcocer, M.J.P. et al. (2014). *Nat. Commun.* 5: 3586.

5 Saba, M., Cadelano, M., Marongiu, D. et al. (2014). *Nat. Commun.* 5: 5049.

6 Sum, T.C., Chen, S., Xing, G.C. et al. (2015). *Nanotechnology* 26: 342001.

7 Koutselas, I.B., Ducasse, L., and Papavassiliou, G.C. (1996). *J. Phys. Condens. Matter* 8: 5953.

8 Hirasawa, M., Ishihara, T., Goto, T. et al. (1994). *Physica B* 201: 427.

9 Ishihara, T. (1994). *J. Lumin.* 60–61: 269.

10 Savenije, T.J., Ponseca, C.S., Kunneman, L. et al. (2014). *J. Phys. Chem. Lett.* 5: 2189.

11 Ip, K.M., Wang, C.R., Li, Q., and Hark, S.K. (2004). *Appl. Phys. Lett.* 84: 795.

12 Sheng, C.X., Zhang, C., Zhai, Y.X. et al. (2015). *Phys. Rev. Lett.* 114: 116601.

13 Ponseca, C.S., Savenije, T.J., Abdellah, M. et al. (2014). *J. Am. Chem. Soc.* 136: 5189.

14 Wehrenfennig, C., Eperon, G.E., Johnston, M.B. et al. (2014). *Adv. Mater.* 26: 1584.

15 Manser, J.S. and Kamat, P.V. (2014). *Nat. Photonics* 8: 737.

16 Stranks, S.D., Burlakov, V.M., Leijtens, T. et al. (2014). *Phys. Rev. Appl.* 2.

17 Yamada, Y., Nakamura, T., Endo, M. et al. (2014). *J. Am. Chem. Soc.* 136: 11610.

18 Lee, M.M., Teuscher, J., Miyasaka, T. et al. (2012). *Science* 338: 643.

19 (a) Burschka, J., Pellet, N., Moon, S.J. et al. (2013). *Nature* 499: 316. (b) Zhou, H.P., Chen, Q., Li, G. et al. (2014). *Science* 345: 542.

20 Stranks, S.D., Eperon, G.E., Grancini, G. et al. (2013). *Science* 342: 341.

21 Docampo, P., Hanusch, F.C., Stranks, S.D. et al. (2014). *Adv. Energy Mater.* 4.

22 Dong, Q.F., Fang, Y.J., Shao, Y.C. et al. (2015). *Science* 347: 967.

23 Xing, G., Mathews, N., Lim, S.S. et al. (2014). *Nat. Mater.* 13: 476.

24 Mehraeen, S., Coropceanu, V., and Bredas, J.L. (2013). *Phys. Rev. B* 87: 195209.

25 Graetzel, M., Janssen, R.A.J., Mitzi, D.B., and Sargent, E.H. (2012). *Nature* 488: 304.

26 Willa, K., Hausermann, R., Mathis, T. et al. (2013). *J. Appl. Phys.* 113: 133707.

27 Yin, W.-J., Shi, T., and Yan, Y. (2014). *Appl. Phys. Lett.* 104: 063903.

28 Marchioro, A. (2014). *Interfacial Charge Transfer Dynamics in SolidState Hybrid Organic- Inorganic Solar Cells*. Ph.D. Thesis. École polytechnique federale de Lausanne.

29 Wang, L.L., McCleese, C., Kovalsky, A. et al. (2014). *J. Am. Chem. Soc.* 136: 12205.

30 Stamplecoskie, K.G., Manser, J.S., and Kamat, P.V. (2015). *Energy Environ. Sci.* 8: 208.

31 Sum, T.C., Mathews, N., Xing, G. et al. (2016). *Acc. Chem. Res.* 49: 294.

32 Price, M.B., Butkus, J., Jellicoe, T.C. et al. (2015). *Nat. Commun.* 6.

33 Flender, O., Klein, J.R., Lenzer, T., and Oum, K. (2015). *Phys. Chem. Chem. Phys.* 17: 19238.

34 Milot, R.L., Eperon, G.E., Snaith, H.J. et al. (2015). *Adv. Funct. Mater.* 25: 6218.

35 Yang, Y., Yang, M.J., Li, Z. et al. (2015). *J. Phys. Chem. Lett.* 6: 4688.

36 Rehman, W., Milot, R.L., Eperon, G.E. et al. (2015). *Adv. Mater.* 27: 7938.

37 Noel, N.K., Stranks, S.D., Abate, A. et al. (2014). *Energy Environ. Sci.* 7: 3061.

38 Xing, G.C., Kumar, M.H., Chong, W.K. et al. (2016). *Adv. Mater.* 28: 8191.

39 Sum, T.C. and Mathews, N. (2014). *Energy Environ. Sci.* 7: 2518.

40 Yu, Z., You, S., Wang, C. et al. (2014). *J. Mater. Chem. A* 2: 9007.

41 Klimov, V.I., Mikhailovsky, A.A., McBranch, D.W. et al. (2000). *Science* 287: 1011.

42 Yang, Y., Ostrowski, D.P., France, R.M. et al. (2016). *Nat. Photonics* 10: 53.

43 Grancini, G., Kandada, A.R.S., Frost, J.M. et al. (2015). *Nat. Photonics* 9: 695.

44 deQuilettes, D.W., Vorpahl, S.M., Stranks, S.D. et al. (2015). *Science* 348: 683.

45 Li, M., Bhaumik, S., Goh, T.W. et al. (2017). *Nat. Commun.* 8: 14350.

46 Guo, Z., Wan, Y., Yang, M. et al. (2017). *Science* 356: 59.

47 Zhu, H., Miyata, K., Fu, Y. et al. (2016). *Science* 353: 1409.

48 Yang, J., Wen, X., Xia, H. et al. (2017). *Nat. Commun.* 8: 14120.

49 Fu, Q.X.J., Han, G., Wu, B. et al. *Nat. Commun.* doi: 10.1038/s41467-017-01360-3.

50 Schulz, P., Edri, E., Kirmayer, S. et al. (2014). *Energy Environ. Sci.* 7: 1377.

51 Chen, S., Goh, T.W., Sabba, D. et al. (2014). *APL Mater.* 2: 081512.

52 Lindblad, R., Bi, D., Park, B.-W. et al. (2014). *J. Phys. Chem. Lett.* 5: 648.

53 Miller, E.M., Zhao, Y., Mercado, C.C. et al. *Phys. Chem. Chem. Phys.* 16: 2014, 22122.

54 Schulz, P., Whittaker-Brooks, L.L., MacLeod, B.A. et al. (2015). *Adv. Mater. Interfaces* 2: 1400532.

55 Chen, W., Wu, Y., Liu, J. et al. (2015). *Energy Environ. Sci.* 8: 629.

56 Mailoa, J.P., Bailie, C.D., Johlin, E.C. et al. (2015). *Appl. Phys. Lett.* 106: 121105.

57 Marchioro, A., Teuscher, J., Friedrich, D. et al. (2014). *Nat. Photonics* 8: 250.

58 Zhu, Z.L., Ma, J.A., Wang, Z.L. et al. (2014). *J. Am. Chem. Soc.* 136: 3760.

59 Piatkowski, P., Cohen, B., Ramos, F.J. et al. (2015). *Phys. Chem. Chem. Phys.* 17: 14674.

60 Grancini, G., Viola, D., Lee, Y. et al. (2017). *ChemPhysChem* 18: 2381.

61 Long, R., Fang, W.H., and Prezhdo, O.V. (2017). *J. Phys. Chem. C* 121: 3797.

62 Docampo, P., Ball, J.M., Darwich, M. et al. (2013). *Nat. Commun.* 4: 2761.

63 Heo, J.H., Im, S.H., Noh, J.H. et al. (2013). *Nat. Photonics* 7: 487.

64 (a) Snaith, H.J., Abate, A., Ball, J.M. et al. (2014). *J. Phys. Chem. Lett.* 5: 1511. (b) Sanchez, R.S., Gonzalez-Pedro, V., Lee, J.W. et al. (2014). *J. Phys. Chem. Lett.* 5: 2357.

65 Xing, G.C., Wu, B., Chen, S. et al. (2015). *Small* 11: 3606.

66 Wojciechowski, K., Stranks, S.D., Abate, A. et al. (2014). *ACS Nano* 8: 12701.

67 Huang, J.S., Shao, Y.C., and Dong, Q.F. (2015). *J. Phys. Chem. Lett.* 6: 3218.

68 Nie, W.Y., Tsai, H.H., Asadpour, R. et al. (2015). *Science* 347: 522.

69 Shi, D., Adinolfi, V., Comin, R. et al. (2015). *Science* 347: 519.

70 Saidaminov, M.I., Abdelhady, A.L., Murali, B. et al. (2015). *Nat. Commun.* 6: 7586.

71 Maculan, G., Sheikh, A.D., Abdelhady, A.L. et al. (2015). *J. Phys. Chem. Lett.* 6: 3781.

72 D'Innocenzo, V., Kandada, A.R.S., De Bastiani, M. et al. (2014). *J. Am. Chem. Soc.* 136: 17730.

73 Fang, H.H., Raissa, R., Abdu-Aguye, M. et al. (2015). *Adv. Funct. Mater.* 25: 2378.

74 Yamada, Y., Yamada, T., Phuong, L.Q. et al. (2015). *J. Am. Chem. Soc.* 137: 10456.

75 Choi, J.J., Yang, X., Norman, Z.M. et al. (2014). *Nano Lett.* 14: 127.

76 Grancini, G., Marras, S., Prato, M. et al. (2014). *J. Phys. Chem. Lett.* 5: 3836.

77 Tilchin, J., Dirin, D.N., Maikov, G.I. et al. (2016). *ACS Nano* 10: 6363.

78 Grancini, G., D'Innocenzo, V., Dohner, E.R. et al. (2015). *Chem. Sci.* 6: 7305.

79 Murali, B., Dey, S., Abdelhady, A.L. et al. (2016). *ACS Energy Lett.* 1: 1119.

80 Wu, B., Nguyen, H.T., Ku, Z.L. et al. (2016). *Adv. Energy Mater.* 6: 1600551.

81 Yang, Y., Yan, Y., Yang, M.J. et al. (2015). *Nat. Commun.* 6.

82 Fang, H.H., Adjokatse, S., Wei, H.T. et al. (2016). *Sci. Adv.* 2: e1600534.

83 Yang, Y., Yang, M.J., Moore, D.T. et al. (2017). *Nat. Energy* 2: 16207.

84 (b) Kim, J., Lee, S.H., Lee, J.H., and Hong, K.H. (2014). *J. Phys. Chem. Lett.* 5: 1312.

85 Walukiewicz, W. (1989). *Appl. Phys. Lett.* 54: 2094.

86 (a) Kuciauskas, D., Kanevce, A., Dippo, P. et al. (2015). *IEEE J. Photovolt.* 5: 366. (b) Beck, S.M. and Wessel, J.E. (1987). *Appl. Phys. Lett.* 50: 149.

87 Rosenwaks, Y., Shapira, Y., and Huppert, D. (1992). *Phys. Rev. B* 45: 9108.

88 Walters, G., Sutherland, B.R., Hoogland, S. et al. (2015). *ACS Nano* 9: 9340.

89 (a) Tanaka, T., Harata, A., and Sawada, T. (1997). *J. Appl. Phys.* 82: 4033.
(b) Ahrenkiel, R.K. and Dashdorj, J. (2004). *J. Vac. Sci. Technol., B* 22: 2063.

90 Zhu, H., Trinh, M.T., Wang, J. et al. (2016). *Adv. Mater.* .

91 Tian, W.M., Zhao, C.Y., Leng, J. et al. (2015). *J. Am. Chem. Soc.* 137: 12458.

2.3

Charge-Selective Contact Materials for Perovskite Solar Cells (PSCs)

Peng Gao and Mohammad Khaja Nazeeruddin

Ecole Polytechnique Federale Lausanne, SCI-SB-MN, Rue de l'Industrie 17, Case postale 440, Sion 1951, Switzerland

High-efficiency perovskite solar cells (PSCs) are typically fabricated with an organometal halide perovskite–infiltrated mesostructure as light absorber and charge transporter, sandwiched between a p-type electron-blocking hole-selective layer hole transporting materials (HTM) and an n-type hole-blocking electron-selective layer electron transporting materials (ETM) [1–3]. During the early development stage of PSCs, researchers were puzzled by the situation that similar efficiencies can be obtained in devices employing completely different charge-selective contact materials, such as mesoporous TiO_2 [4], compact TiO_2 [5], mesoporous ZnO [6], or fullerene derivatives [7] as electron-selective materials; and spiro-OMeTAD [8], polytriarylamine (PTAA) [9], other molecular [10, 11] and polymeric materials [12], or even inorganic CuSCN [13] and NiO [14] as hole-selective materials. Although the organolead halide perovskites represented by methylammonium lead iodide ($CH_3NH_3PbI_3$) have been proved to be ambipolar semiconductors [15], devices with either no electron-selective materials [16] or hole-selective materials [17] were produced to give much lower photoconversion efficiency (PCE). Nowadays, it is generally accepted that both the electron- and hole-selective contact materials are critical to a high-performance perovskite photovoltaic (PV) device and only the selective contacts that allow an efficient charge separation can lead to the highest device performance [18]. These materials served to (i) tune the work function of the electrode to promote Ohmic contact at the absorber layer and electrode interface; (ii) determine the polarity of the device; (iii) improve the selectivity toward holes or electrons while blocking the other and minimizing charge carrier recombination at the interface; (iv) enhance light harvesting; and (v) improve device stability (Figure 2.3.1). In this regard, it is important to exploit their best candidates; and in this chapter, we attempt to give a systematic introduction about the choices of both electron- and hole-selective contact materials for efficient PSCs.

Halide Perovskites: Photovoltaics, Light Emitting Devices, and Beyond, First Edition.
Edited by Tze-Chien Sum and Nripan Mathews.

2.3.1 Hole-Selective Electron-Blocking Materials (HTMs)

An ideal HTM should meet some general requirements to work appropriately in PSCs, such as (i) good hole mobility, (ii) compatible HOMO (highest occupied molecular orbital) energy level, (iii) good solubility and film-forming properties, (iv) excellent thermal and photochemical stability, as well as (v) high cost performance. A huge number of HTMs have been synthesized for PSCs, which can be generally divided into organic and inorganic HTMs. The organic HTMs can be further categorized into three types: molecular HTMs, polymeric HTMs, and organometallic complexes, while the inorganic HTMs are mainly transition metal oxides, halides, etc. According to Figure 2.3.1, the open circuit voltage (V_{OC}) limit is imposed by the energetics level offset of the selective contact materials. Generally, most electron-selective contact materials have an electron affinity or conduction band (CB) energy of ~4 eV [19]. The ionization potential (IP) of the hole-selective contact materials vary significantly, and this has a direct effect on V_{OC}, providing all the rest conditions are the same. Figure 2.3.2b collates a large number (~85) of different HTMs and plots the relationship between IP and V_{OC}. Given the theoretical V_{OC} maximum of $CH_3NH_3PbI_3$ perovskite cells with optimized contacts is ~1.3 V, there is still considerable scope for improving the V_{OC} by optimizing the energetics of the contacts and transport layers.

2.3.1.1 Organic HTMs

2.3.1.1.1 Molecular HTMs

In a typical PSC, the most commonly used molecular hole-selective contact material is spiro-OMeTAD (**1**), which holds the record PCE (21.6%) of reported PSCs [21]. In the race toward achieving highly efficient and low-cost devices, various

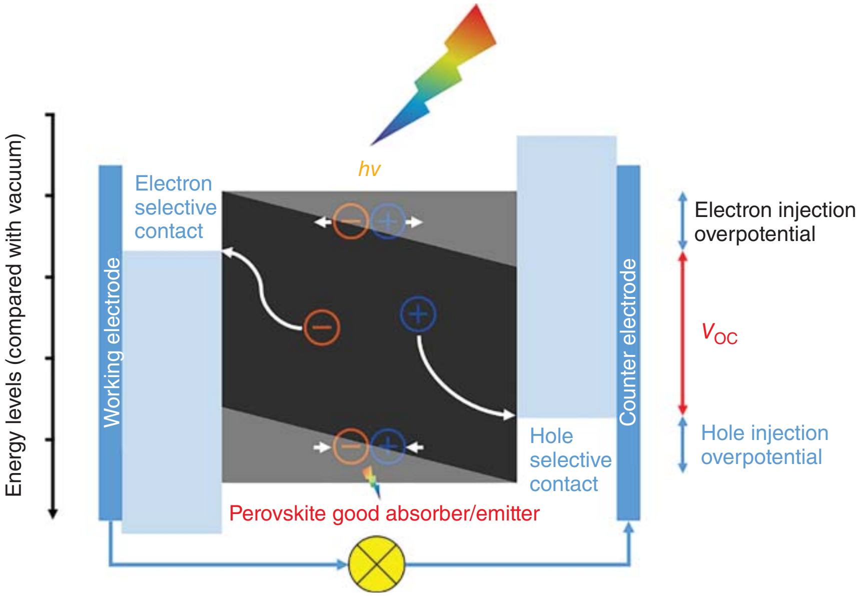

Figure 2.3.1 Working mechanism of a typical PSC with charge-selective contact materials.

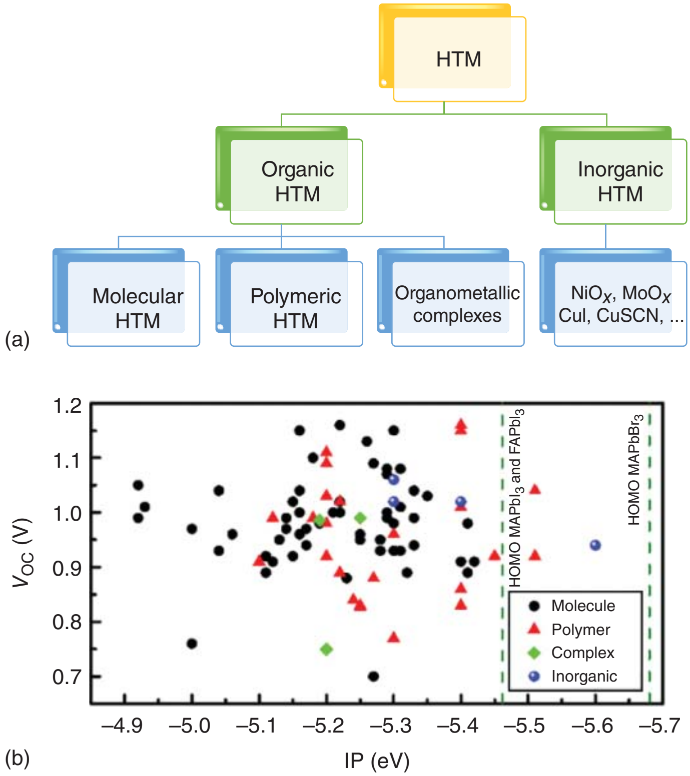

Figure 2.3.2 (a) Classification of hole-selective electron-blocking materials; (b) statistic distribution of V_{OC} versus ionization potential (IP), a survey of 85 reported high-efficiency perovskite solar cells [20].

molecular HTMs have been adopted, and some of them have a comparable PV performance to spiro-OMeTAD [20] (Figure 2.3.3).

A large group of new HTMs are designed to mimic the *spiro* structure of spiro-OMeTAD. Rakstys et al. reported a novel 9,9′-bifluorenylidene-based HTM (**2**, KR216), which has a pseudo *spiro* conformation and features straightforward synthesis from inexpensive starting materials [22]. The estimated price of **2** is around 50 times lower than that of commercial spiro-OMeTAD. A remarkable PCE of 17.8% was obtained for PSCs using KR216. Ganesan et al. developed a new spiro-type HTM, 4,4′,4″,4‴-(2H,2′H,4H,4′H-3,3′-spiro-bi[thieno[3,4-*b*][1,4]dioxepine]-6,6′,8,8′-tetrayl)tetrakis-(*N*,*N*-bis(4-methoxyphenyl)aniline) (**3**, PST1), via a facile synthetic route [10]. The PSC employing undoped **3** as the HTM layer exhibited a PCE of 12.7%, which is much higher than that of spiro-OMeTAD under the same conditions. Recently, our group synthesized a highly hindered dispiro-oxepine derivative as HTM (**4**), via a facile three-step synthetic route [23]. PSCs that employed **4** as HTM showed one of the highest power conversion efficiencies (PCEs) of 19.4% reported to date. The solid structure study by single crystallography indicated again that the π–π interaction is not a prerequisite for designing effective HTMs. PSCs with high PCEs above 19% have also been realized from the two new HTMs (**5** and **6**), which have less crowded aryl amine substitution [24, 25]. Especially, the HTM **5**–based devices compared favorably

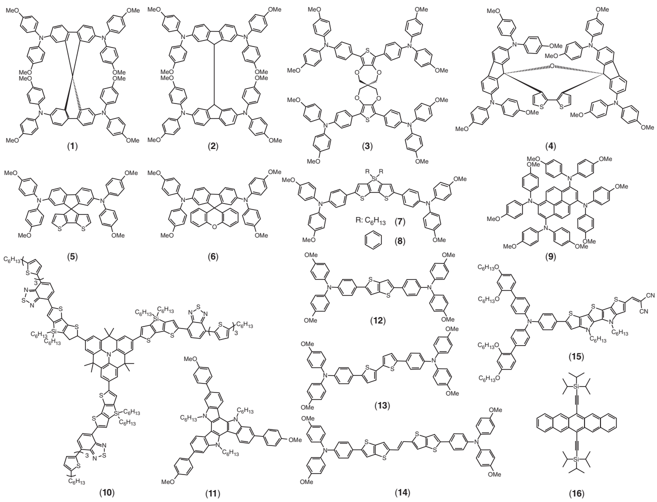

Figure 2.3.3 Chemical structures of selected molecular HTMs used in PSCs.

to spiro-OMeTAD in all performance tests, yielding PCEs up to 20.2%, which is one of the highest (uncertified) reported values for molecular HTMs. The laboratory synthesis costs of fluorene–dithiophene (FDT) are estimated to be ~60 US$ g^{-1}. This is about a fifth of the costs of purified spiro-OMeTAD (~500 US$ g^{-1}, high purity, Merck). Another spiro-type HTM (**7**, **8**) with silolothiophene-linked methoxy triphenylamines was made by Paek and coworkers and found to have a half-life of 6 K h, compared to 1 K h collected for the state-of-the-art PSCs using spiro-OMeTADs as HTMs [26].

Another type of HTMs features a C_4 or C_3 symmetric molecular geometry. Our group utilizing pyrene-core arylamine (**9**) demonstrated a PCE of 12.4% under 1 sun [27]. Paek and coworkers synthesized a donor–acceptor-type quinolizino acridine HTM (**10**), which possesses a well-matched HOMO level with $CH_3NH_3PbI_3$ (−5.23 versus −5.43 eV), and the highest PCE reported (12.8%) was achieved without any dopant and additive [28].

Rakstys et al. synthesized substituted triazatruxene and a remarkable PCE of 18.3% was obtained with the methoxyphenyl substituent (**11**), which is higher than that of spiro-OMeTAD under the same conditions [29].

Molecular HTMs can also be synthesized with donor–π–donor (D-π-D) or donor–π–acceptor (D-π-A) electronic structures. Paek et al. synthesized three new D–π–D-type HTMs (**12**,**13**,**14**), incorporating thiophene or thienothiophene with two electron-rich triphenyl amine (TPA) units [30]. The optimized devices of **14** exhibited an impressive PCE of 16.9% under standard global AM 1.5 illumination with minimized hysteretic behavior, which is comparable to devices using a state-of-the-art spiro-OMeTAD hole transport layer under similar conditions. On the other hand, Bi and coworkers reported a novel D–π–A molecular HTM [31] (**15**) incorporating *S*,*N*-heteropentacene as π-spacer, triarylamin as donor, and dicyanovinylene as acceptor. PSCs using **15** achieved similar excellent PCEs of up to 16.9% [32]. However, a much prominent *J*–*V* hysteresis phenomenon was observed, possibly due to the asymmetric electronic structure of the HTM.

Acenes are intrinsic p-type derivatives for semiconductors in optoelectrical devices. Their derivatives are potential HTM candidates as long as the energy level can be matched with that of perovskites. Rakstys and coworkers exploited TIPS-pentacene (**16**) as the HTM in $MAPbI_3$-based PSCs [33]. The best PCE was obtained with the HTM in its pristine form, while the use of additives decreased the PV performance, which was attributed to the formation of trap sites or a disorder in chain packing.

2.3.1.1.2 Polymeric HTMs

The advantage of using polymer HTMs over molecular counterparts is that the material cost can be reduced, as the concentration used is much lower yet form very good films. Poly(triaryl amine) (**17**, PTAA) is the most popular polymer HTM and has been tested by Heo and coworkers, which demonstrated 12% efficiency using $CH_3NH_3PbI_3$ perovskite light harvester (Figure 2.3.4) [34]. The highest PCE with this combination was just achieved by our group as 19.5% [35]. In 2014, Seok and coworkers recorded the highest certified PCE (16.2%) employing PTAA as the HTM [9]; an even higher certified PCE of 17.9% has also been demonstrated [36]. In the second year, the first certified 20.1% PCE was reported by the same group [1] (Figure 2.3.4).

The exploitation of poly(3-hexylthiophene-2,5-diyl) (**18**, P3HT) as the HTM was demonstrated by Abrusci et al. [37] and Heo et al. [34], where the PCEs of 3.8% and 6.7% were achieved, respectively. A remarkable improvement from 9.2% to 12.4% in the P3HT-based PSCs was observed after doping P3HT with bis(trifluoromethane)sulfonamide lithium salt (Li-TFSI) and 2,6-di-*tert*-butylpyridine (D-TBP) [38]. Another two TPA-based polymer HTMs were reported by Yang and coworkers [39] and Nazeeruddin and coworkers [40] by either copolymerize polyfluorene with TPA or homopolymerize TPA derivatives (**19** and **20**). Devices based on HTM **19** in mesoscopic PSCs based on $MAPbI_3$ absorber presented promising efficiencies (10.9–12.8%), which are comparable to the corresponding values for spiro-OMeTAD (9.8–13.6%). Furthermore, Qin et al. used S197 (**20**) to replace PTAA and a PCE of 12% was measured, which was similar to the reference device made from PTAA.

Donor–acceptor-conjugated polymers have the freedom of tuning their IP by varying the donor and acceptor moieties. Therefore, the prospect of having an even higher V_{OC} seems possible with the combination of $CH_3NH_3PbBr_3$ and HTMs with deeper HOMO levels. The first demonstration was realized by Cai et al. deploying diketopyrrolopyrrole (DPP)-based copolymer (**21**, PCBTDPP) [41]. The developed PSCs exhibited high V_{OC} of 1.16 V. This was supported with the work reported by Seok's group, where they demonstrated high V_{OC} of 1.4 V using a combination of triarylamine-based HTM similar to **19** and $CH_3NH_3PbBr_3$ absorber [42]. Other DPP-containing copolymer-based HTMs were also studied in mesoscopic $MAPbI_3$-based PSCs. Qiao and coworkers [43] exploited (**22**, PDPP3T) as HTM in mesoporous devices attaining a PCE of 12.3%. They highlighted that by avoiding the use of t-BP and lithium salts as p-dopants in the HTM gave an enhancement in the stability of the device. A similar stability was observed in the device based on **23** reported by Kwon et al., where an excellent long-term durability remained over 90% of their initial efficiencies after 1000 hours under a humidity of ≈20%, whereas spiro-OMeTAD-based devices only remained at ≈70% [44]. This excellent long-term durability of **23** should be probably attributed to the hydrophobic properties of such polymers, which prevents water penetration into the perovskite surface. Benzothiadiazole was also used as the acceptor in the D–A-conjugated polymer HTM. Seok and coworkers reported PCDTBT (**24**)-based PSCs but the performance of the device was relatively low with a PCE of 4.2% for **24** [34]. PEDOT:PSS (poly(3,4-ethylenedioxythiophene):polystyrene sulfonate, **25**) were tested extensively in the p–i–n PSC devices as the hole-selective contact devices. Recently, the PCE of such devices increased rapidly and was approaching 19% [45]. However, the acidity of such compounds poses a fundamental threat to the long-term stability of the devices.

2.3.1.1.3 Organometallic Complex HTMs

Phthalocyanines (Pcs) are mostly developed organometallic complex HTMs [46] (Figure 2.3.5). The tendency of Pcs to form aggregates on the metal oxide semiconductor surface is a blessing to use as HTMs to transport charges efficiently from the perovskite absorber [10, 31, 47]. In addition, Pcs are photochemically

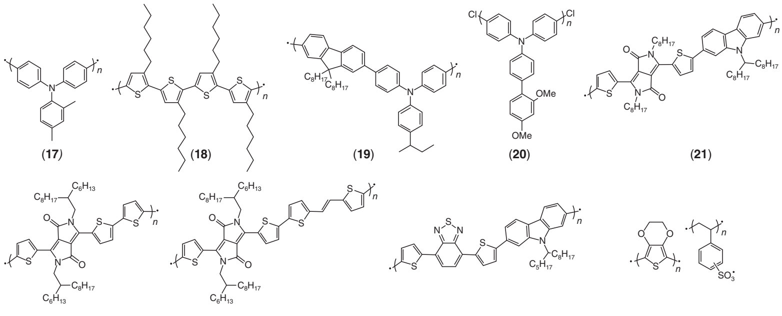

(17) (18) (19) (20) (21)

(22) (23) (24) (25)

Figure 2.3.4 Chemical structures of selected polymeric HTMs used in PSCs.

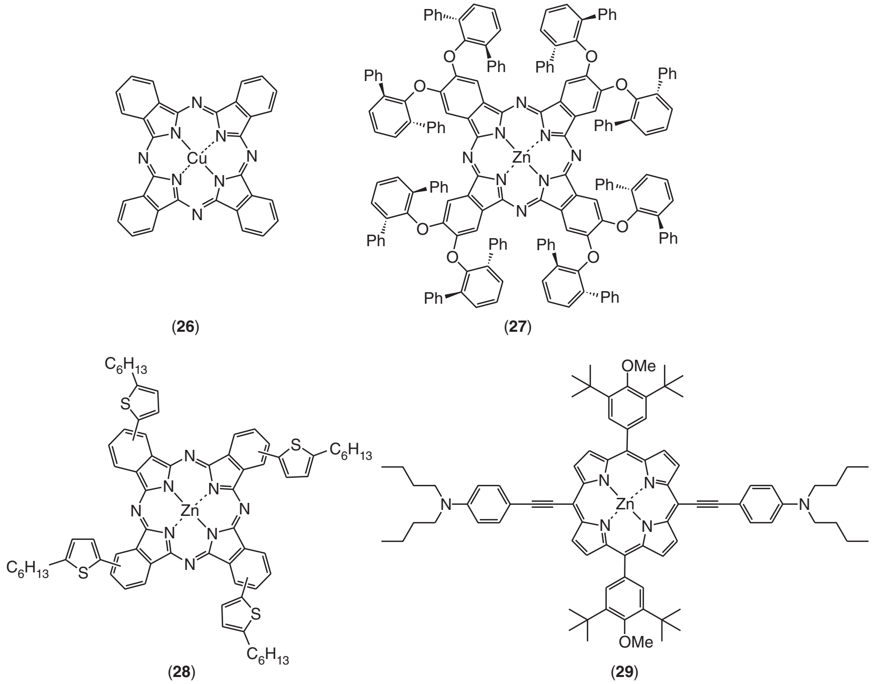

(**26**) (**27**) (**28**) (**29**)

Figure 2.3.5 Chemical structures of selected organometallic complex HTMs used in PSCs.

and electrochemically stable compounds, which add additional values for their use as HTMs. At the end of 2014, Kumar et al. reported the first non-substituted Cu(II)-phthalocyanine (**26**)-based HTM deposited by vacuum deposition for solid-state PSCs and a PCE of 5.0% was achieved [48]. Seok and coworkers used Cu(II) *tert*-butyl phthalocyanine as HTM and demonstrated the fabrication of compositive perovskite-based PSCs, which yielded an efficiency of 15.2% [49]. Zn(II)-phthalocyanine is another Pc analog and features more shifted absorption compared with Cu(II)-phthalocyanine in most common solvents [50]. Our group reported the first PSCs with easily soluble Zn(II) octa(2,6-diphenylphenoxy) phthalocyanine (**27**) and Zn(II) 5-hexyl-2-thiophene phthalocyanine (**28**) as the HTMs with a PCE of 6.7% and 12.3%, respectively [51, 52]. It was not until very recently that zinc porphyrin was used as HTMs in PSCs. The first report from Li et al. showed that zinc chlorophyll aggregates as efficient biocompatible dopant-free HTM for PSCs with a PCE of 11.44% [53]. One month later, Chou et al. reported the best-performing porphyrin-based solar cell with symmetric ethynylaniline-substituted porphyrins (**29**) as HTM giving a PCE of 16.60% [54].

2.3.1.2 Inorganic Hole-Selective Electron-Blocking Materials

Although the progress in inorganic HTMs is rather slow due to the limited selection of materials, their low cost and stability under ambient conditions

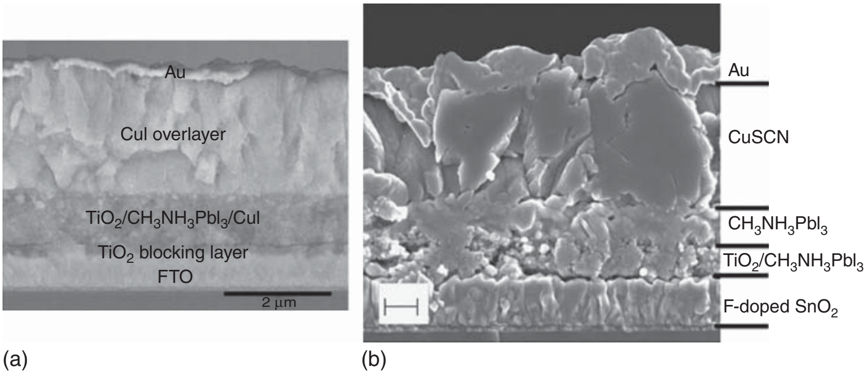

Figure 2.3.6 Scanning electron microscopic (SEM) cross-section images of solar cells employing (a) CuI and (b) CuSCN. Source: Qin et al. 2014 [56] and Christians et al. 2014 [57]. Reprinted with permission of Springer Nature.

verify why they are still competitive with organic HTMs. So far, inorganic semiconductor materials, such as CuI, CuSCN, NiO_x, VO_x, and MoO_x, have also been explored as hole-selective materials for use in perovskite-based solar cells [55]. In 2013, Kamat and coworkers demonstrated the first example using inorganic p-type copper(I) iodide (CuI)-based HTMs in $MAPbI_3$ PSCs, providing higher FF and better J_{SC} stability compared with those devices based on spiro-OMeTAD due to its higher electrical conductivity (Figure 2.3.6a) [57]. Nonetheless, the high recombination in the CuI layer limited the V_{OC}. Following another copper-based inorganic p-type hole conductor, copper thiocyanate (CuSCN) has also been actively studied and the highest PCE (12.4%) achieved after optimization of the perovskite morphology (Figure 2.3.6b) [56].

In another interesting report by Yang's group employing nickel oxide (NiO), a PCE of 9.11% has been reported; and a slight improvement was achieved by Wang and coworkers, with a PCE of 9.51% utilizing NiO as a hole-collecting electrode [58, 59]. Although the performance of the p-type semiconductor is less promising, the highest V_{OC} of about 1.05 V reported recently for NiO HTM is rather promising [60].

2.3.2 Electron-Selective Hole-Blocking Materials

In a typical PSCs, the electron-selective contact material (ETM) is responsible for selective extraction of electrons at the anode contact, adopted from dye-sensitized solar cells (DSSCs) and blocking holes from recombination with injected electrons. Similar to its counterpart HTM, the ETM can be divided into inorganic ETM, organic ETM, and composite ETM depending on the nature of the material. The lowest unoccupied molecular orbital (LUMO) or CB energy levels of some ETMs used in PSCs are shown in Figure 2.3.7b, which are crucial to the performance of the device.

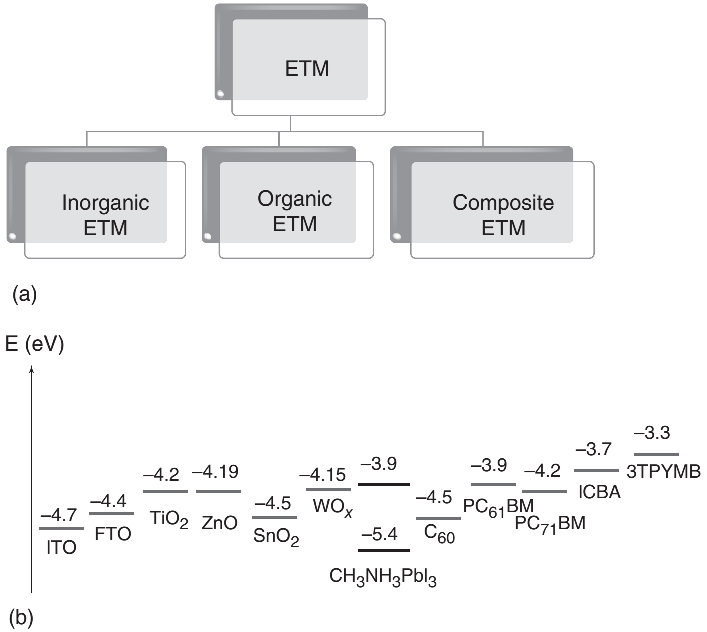

Figure 2.3.7 (a) Classification of electron-selective hole-blocking materials; (b) energy level diagram showing conduction band minimum/LUMO levels of various ETLs. Source: Yang et al. 2016 [19]. Reproduced with permission of Royal Society of Chemistry.

2.3.2.1 Inorganic Electron-Selective Hole-Blocking Materials

2.3.2.1.1 TiO_2

In a classic n–i–p device configuration, the most commonly used electron-selective contact materials is compact TiO_2 [61]. Some device configurations also include a thin mesoporous layer of TiO_2, which is infiltrated and capped with the perovskite absorber. This type of device structure holds so far the highest reported PCE of a PSC [21]. The metal oxide scaffold is believed to provide an effective n-doping in this infiltrated layer, likely resulting in a favorable n-type/intrinsic homojunction within the perovskite layer [62]. It was supposed that the effective n-doping may be due to under-coordinated halides acting as shallow electron donors on the crystal surface, or due to a surface charge effect of the mesoporous metal oxide. Our group recently found by focused ion beam energy dispersive X-ray (FIB-EDX) analysis in a cross-section of PSCs the nonuniform distribution of iodine element from mesoporous layer to capping layer [35].

In general, the compact TiO_2 blocking layer is deposited using a spin-coating technique or spray pyrolysis method. The deposition of mesoporous TiO_2 scaffold is now dominated by spin coating an organotitanium precursor, while the doctor blade technique derived from the DSSCs is used in rare cases. Optimal infiltration of the perovskite and HTM into the pores of the mesoporous TiO_2 is desirable for highly efficient devices. Kim et al. investigated the thickness dependence of device performance and found that as the TiO_2 thickness increases, the V_{OC} and FF values decrease significantly [63]. Our group reported on a $CH_3NH_3PbI_3/TiO_2$ heterojunction solar cell using anatase nanosheets with domain (001) facets as the ETM, with a side length of 30 nm and a thickness of 7 nm [17]. The constructed device demonstrated a moderate performance with J_{SC} of 16.1 mA cm^{-2}, V_{OC} of 0.631 V, and FF of 0.57 corresponding to 5.5% efficiency. The lower performance is arguably due to the absence of HTM in the device structure. Later, collaborative work between Park and Grätzel demonstrated high-performance PSCs based on 0.6 μm rutile TiO_2 nanorods along with $CH_3NH_3PbI_3$ perovskite nanodots (Figure 2.3.8) [64]. The rutile nanorods were successfully hydrothermally grown and the lengths were controllable via the reaction time. They reported that shorter rutile nanorods were remarkably better for the infiltration of HTMs compared to those with longer length. The device produces 9.4% efficiency along with J_{SC} of 15.6 mA cm^{-2}, V_{OC} of 0.955 V, and FF of 0.63.

Gao et al. initiated a work on a freestanding TiO_2 nanotube array film prepared by means of two-step anodization process and detached from the substrate by in situ field-assisted chemical dissolution and later transferred onto a fluorin-doped tin oxide (FTO) substrate which was covered by a TiO_2 blocking layer [65]. As comparison, the control device with TiO_2 nanoparticles (similar

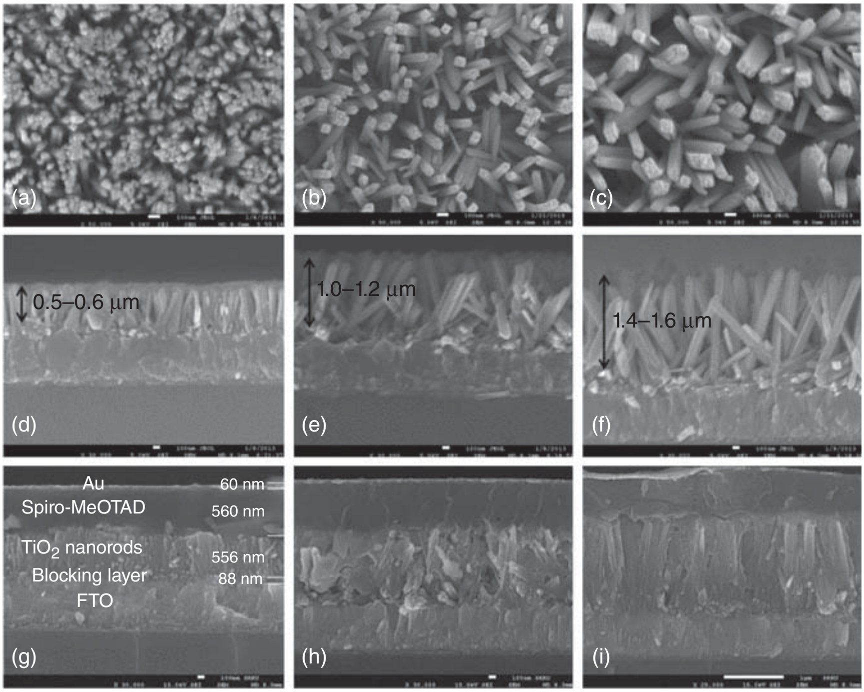

Figure 2.3.8 (a–c) Surface and (d–f) cross-sectional field-effect scanning electron microscopic (FESEM) images of rutile TiO_2 nanorods grown on FTO substrate. (g–i) Cross-sectional SEM images of solid-state DSSCs based on perovskite $CH_3NH_3PbI_3$-sensitized rutile TiO_2 nanorod photoanode, the spiro-MeOTAD hole transporting layer, and the Au cathode. Source: Kim et al. 2013 [64]. Reprinted with permission of American Chemical Society.

thickness) was also developed and they found that their proposed TiO_2 nanotube had a better absorption than with TiO_2 nanoparticles, most likely due to the improved light-trapping capability (Figure 2.3.9). Moreover, they also observed that the TiO_2 nanotube array presented a higher charge collection efficiency compared to that of TiO_2 nanoparticles. Their PSCs constructed with TiO_2 nanotubes yielded 6.25% efficiency with a J_{SC} of 17.9 mA cm^{-2}. These observations show that the improvement of TiO_2 nanotube PSCs was attributed to both the improved light harvesting and reduced carrier recombination.

Despite being widely used as ETM, TiO_2 also has some drawbacks which could possibly lead to Ohmic losses or nonideal space charge distribution with PSCs. Pathak et al. suggested that Al doping reduces the number of sub-bandgap states of TiO_2 (improving the V_{OC}) and greatly improves electron conductivity [66]. PSCs with 0.3 mol% Al-doping level produced 13.8% efficiency compared to those without doping of only 11.13%. Significant improvement in solar cells with doped TiO_2 was mainly due to the improved quantum efficiency leading to J_{SC} of 20 mA cm^{-2}. Prior to this study (Ref. [67]), Yang and colleagues reported yttrium-doped TiO_2 in the PSCs which led to 19.3% efficiency. Doped TiO_2 produced a better conductivity compared to undoped TiO_2 film (2×10^{-5} versus 6×10^{-6} S cm^{-1}), which was due to the improved carrier concentration as well as decreased series resistance in the device. It is worth noting that the conductivity of doped TiO_2 was similar to our frequently used HTM, spiro-OMeTAD, and 10 order of magnitudes higher compared with undoped TiO_2.

Our group also successfully investigated the use of Y^{3+}-substituted TiO_2 (0.5% Y-TiO_2) in PSCs comprising $CH_3NH_3PbI_3$ and spiro-OMeTAD (Figure 2.3.10) [68]. The doped devices produced 11.2% efficiency and observed

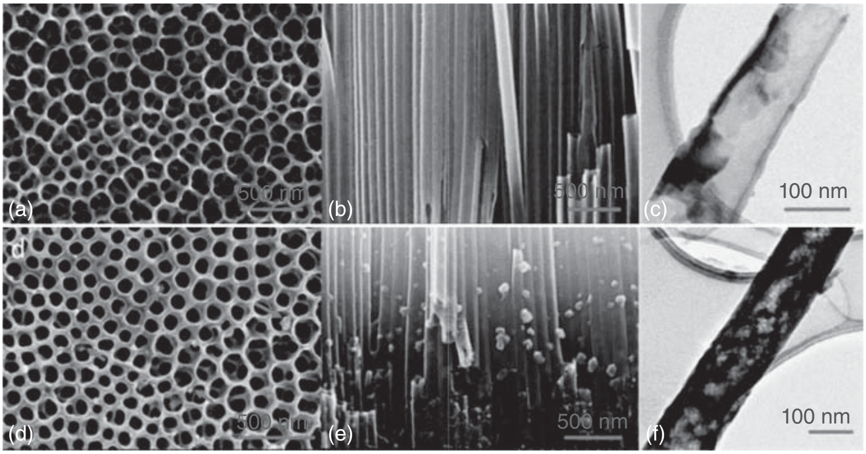

Figure 2.3.9 Morphology characterization of TiO_2 nanotubes before and after the perovskite dye deposition. (a–c) SEM images of the top view (a), the cross-section image (b), and the transmission electron microscopic (TEM) image (c) of pristine TiO_2; (d–f) SEM images of the top view (d), the cross-section image (e), and the TEM image (f) of TiO_2 nanotubes with $CH_3NH_3PbI_3$ deposition. Source: Gao et al. 2014 [65]. Reprinted with permission of Royal Society of Chemistry.

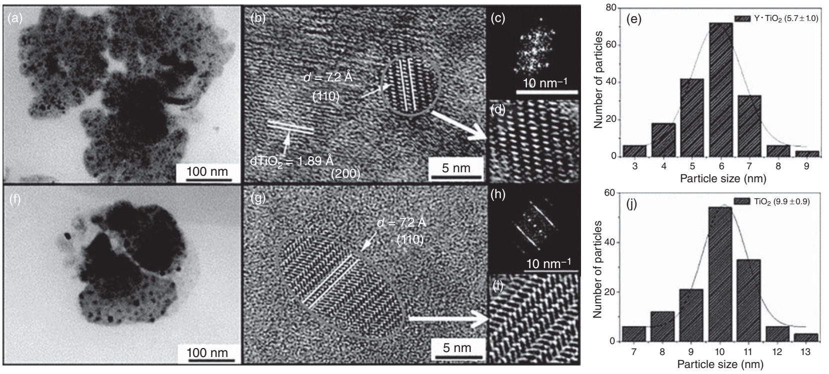

Figure 2.3.10 TEM analysis of 0.5%Y–$TiO_2/CH_3NH_3PbI_3$ and $TiO_2/CH_3NH_3PbI_3$ electrodes. (a–e) 0.5%Y-$TiO_2/CH_3NH_3PbI_3$ electrode and (f–j) $TiO_2/CH_3NH_3PbI_3$ electrode: (a, f) bright field transmission electron microscopy (BFTEM) micrographs; (b, g) high-resolution transmission electron microscopy (HRTEM) micrographs of dark-colored (encircled) individual nanoparticles deposited on TiO_2; (c, h) fast Fourier transform (FFT) patterns obtained from the corresponding HRTEM; (d, i) zoomed HRTEM showing prominent lattice fringes; (e, j) histograms showing particle size distribution. Source: Qin et al. 2014 [68]. Reprinted with permission of Royal Society of Chemistry.

15% enhancement in the J_{SC} compared with pristine TiO_2. The J_{SC} improvement was arguably because of the effect of Y^{3+} on the dimensions of perovskite nanoparticles formed on the semiconductor surface.

2.3.2.1.2 ZnO

Apart from TiO_2, there have been a lot of reports employing ZnO as a potential replacement to TiO_2 for PSCs due to its comparable energy levels and good transport properties (bulk mobility: 205–300 $cm^2\ V^{-1}\ s^{-1}$). Kumar et al. were among the first to employ the ZnO compact layer formed by electrodeposition technique and ZnO nanorods prepared by chemical bath deposition (Figure 2.3.11) [69]. The blocking-ZnO/ZnO nanorod-based PSCs documented 8.90% efficiency with astonishingly high J_{SC} of 16.98 mA cm^{-2} compared to the planar ZnO-based device with only 5.54% efficiency and a greatly lower J_{SC} of 11.27 mA cm^{-2}. In this study, they argued that the improved J_{SC} was due to better charge generation and collection efficiency because of the enhanced light scattering and larger heterojunction interface.

Park's group also reported on ZnO nanorods grown on the ZnO seed layer from solution to fabricate their $CH_3NH_3PbI_3$ PSCs (Figure 2.3.12) [70]. The lengths and diameters of ZnO nanorods were manipulated by precursor concentration as well as growth time. They were able to obtain 11.13% efficiency with J_{SC} of 20.08 mA cm^{-2}, V_{OC} of 0.991 V, and FF of 0.56. Their control devices with TiO_2 nanorods demonstrated a slightly less performance, with only 10.02% efficiency; and they attributed the decrease in device performance to a low V_{OC} (0.869 V). The slightly lower V_{OC} was due to the lower CB of TiO_2 with respect to ZnO nanorods as well as slower recombination properties.

Liu et al. independently demonstrated planar PSCs featuring ZnO nanoparticles [6]. They demonstrated the capability of ZnO nanoparticles under two different types of devices: rigid and flexible formats. A notable performance was demonstrated for the rigid format with 15.7% efficiency, while 10.2% efficiency was reported for flexible PSCs. The high performance of rigid solar cells was due to the unconstrained $CH_3NH_3PbI_3$ perovskite crystallite growth that took place in the absence of a mesoporous scaffold. However, ZnO suffers from the issue of chemical instability [71].

2.3.2.1.3 SnO_2

Recently, SnO_2 has emerged as another promising ETM with a high transparency and electron mobility (bulk mobility: 240 $cm^2\ V^{-1}\ s^{-1}$). Li et al. successfully utilized $TiCl_4$-treated SnO_2 nanoparticles as ETMs in PSCs and the efficiency of the device with SnO_2 films exceeded 10% [72]. Song et al. demonstrated that low-temperature-processed SnO_2 compact layer-based planar PSCs could achieve a high PCE of 13.0%, which is highly durable with exposure to the ambient air environment for 30 days [73]. Another low-temperature sol–gel-fabricated SnO_2 ETM was reported by Yang et al. An average efficiency of 16.02% was obtained without hysteresis [74]. Recently, Hagfeldt and coworkers used a 15-nm-thick SnO_2 as ETM processed by atomic layer deposition (ALD) technique [75]. They showed hysteresis-free, high-stabilized planar PSCs with a high voltage of 1.19 V.

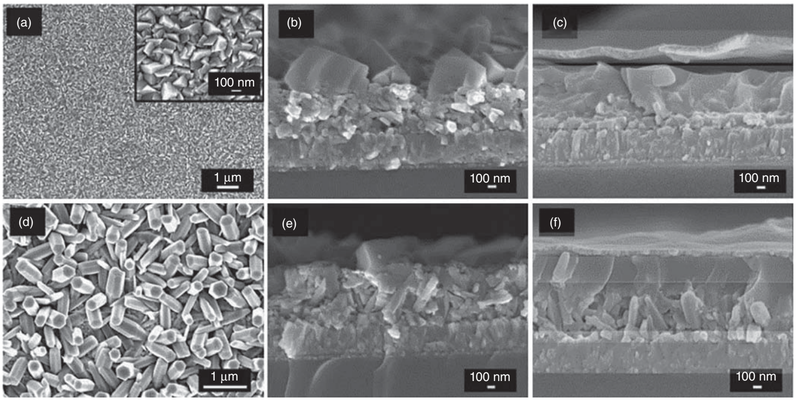

Figure 2.3.11 FESEM images of (a) top view of the ZnO compact layer electrodeposited on FTO (inset shows a high-resolution image); (b) cross-sectional view of perovskite islands on the ZnO compact layer; (c) cross-sectional view of the complete planar ZnO device; FTO, ZnO BL, perovskite + spiro, gold; (d) top view of ZnO nanorods grown on the ZnO compact layer on the FTO substrate; (e) cross-sectional view of perovskite islands on ZnO nanorods; and (f) cross-sectional view of the complete ZnO nanorod device; FTO, ZnO BL, ZnO nanorod + perovskite, spiro, gold. Source: Kumar et al. 2013 [69]. Reprinted with permission of Royal Society of Chemistry.

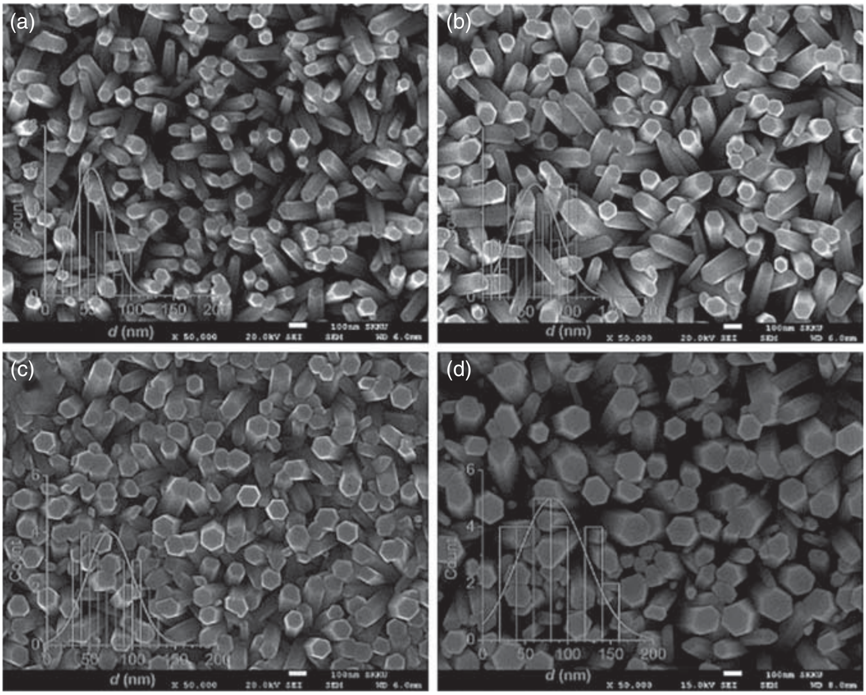

Figure 2.3.12 Surface SEM images of hexagonal ZnO nanorods grown at (a) 20 mM, (b) 25 mM, (c) 30 nM, and (d) 35 mM of the precursor solution containing equimolar zinc nitrate hexahydrate and hexamethylenetetramine. The ZnO seed layer–deposited FTO substrates were immersed in the precursor solution at 90 °C for 180 minutes. Insets represent distribution of diameters of ZnO nanorods. Reprinted with permission [70].

2.3.2.2 Organic Electron-Selective Hole-Blocking Materials

In contrast to the inorganic ETMs, a smaller variety of organic materials has been checked as an alternative electron-selective contact: 2,9-dimethyl-4,7-diphenyl-1,10-phenanthroline (BCP), C60, indene-C60 bisadduct (ICBA), phenyl-C61-butaric acid methyl ester (PCBM) are a few examples [19] (Figure 2.3.13). These ETMs are normally used in p–i–n structured PSC devices, where the perovskites are coated upon a p-type HTM (for example, PEDOT:PSS or nickel oxide) before the deposition of an electron-selective charge collection layer on top of the perovskite. It is worth mentioning that these so-called inverted PSCs with all organic contacts generally exhibit little hysteresis. The use of fullerene (C_{60}, **31**) and its derivatives was proposed by Jeng et al. [76]. Their device consists of ITO/PEDOT:PSS/$CH_3NH_3PbI_3$/C_{60}/BCP/Al. A thin bathocuproine (BCP, **30**) film functioned as a hole-blocking layer and they obtained 3.0% efficiency. When C_{60} was substituted with PCBM (**33**) and ICBA (**32**), the efficiency improved to 3.9% and 3.4%, respectively. The results suggest the existence of donor–acceptor interface at the $CH_3NH_3PbI_3$/fullerene heterojunction as well as the variation of device performance by acceptors of various LUMO levels. Snaith and collaborators constructed perovskite/PCBM flexible solar cells with

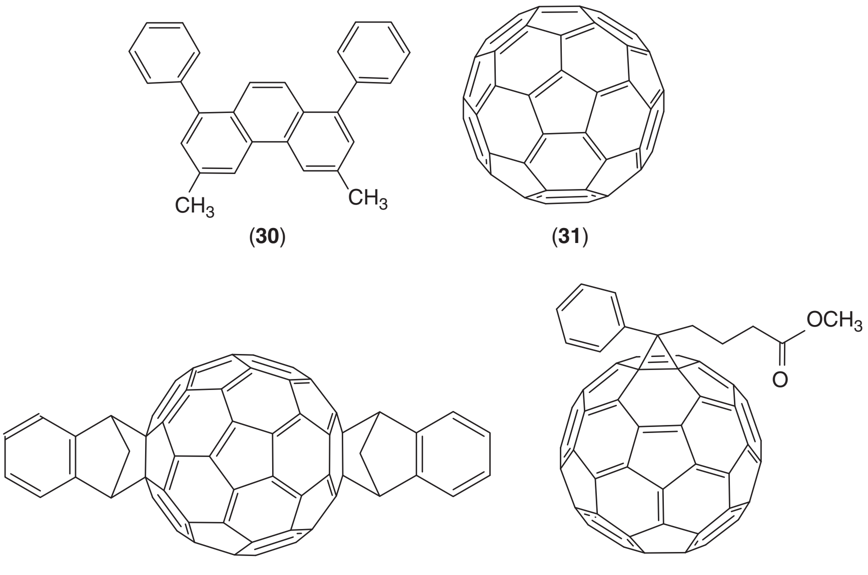

(30) (31) (32) (33)

Figure 2.3.13 Chemical structures of selected organic ETMs used in PSCs.

a conversion efficiency of 6% and later the performance was slightly improved to 7% by Bolink's group adopting similar device architecture [77].

2.3.2.3 Composite ETMs

In general, TiO_2 surfaces possess deep mid-gap states which enable non-radiative recombination channels at the perovskite interface that will eventually influence the device performance [78]. Hence, voluminous reports have been put forward to passivate surface traps of TiO_2 surface, for example, by introducing polar molecules [79], C_{60}-SAM (self-assembled monolayer) [37, 80], graphene quantum-dots [81–84], and antimony (III) sulfide (Sb_2S_3) [85]. It was found that the introduction of antimony (III) sulfide (Sb_2S_3) not only modified the TiO_2/perovskite interface but also enhanced the lifetime of the device even under continuous light illumination. From this study, Ito and coworkers believe that the light degradation takes place at the $TiO_2/CH_3NH_3PbI_3$ interface.

2.3.3 Conclusion

Nowadays, both n–i–p and p–i–n device structures are reported to give high-performance PSCs. In a p–i–n architecture, holes are extracted by the bottom electrode, transparent ITO or FTO in most cases, while electrons are extracted at the bottom electrode in the n–i–p architectures. The efficiency of the device is determined by the charge-selective contact materials. Hence, by introducing proper contact materials with good charge selectivity, one could potentially reduce interfacial charge recombination as well as increase device performance. In order to efficiently extract hole from the anode electrode, hole-selective materials should possess a suitable energy alignment with perovskite films. It is of importance that the CB or the LUMO of the HTMs should be high enough to efficiently block the back diffusion of electrons to the cathode electrode. Identical principles also apply to the electron-selective layers. It is desirable that selective contact materials have larger bandgaps than that of perovskite films to avoid the excitons from recombining at the electrode. Also, it is crucial to design and synthesize selective contact materials with high conductivity to reduce the series resistance of the PSCs. In the past few years, copious selective contact materials have been proposed. It has been observed that both selective contacts contribute to enhance the cell FF, while the hole-selective contact is mainly responsible for the high V_{OC} [86].

References

1 Yang, W.S., Noh, J.H., Jeon, N.J. et al. (2015). High-performance photovoltaic perovskite layers fabricated through intramolecular exchange. *Science* 348 (6240): 1234–1237.

2 Bi, D., Tress, W., Dar, M.I. et al. (2016). Efficient luminescent solar cells based on tailored mixed-cation perovskites. *Sci. Adv.* 2 (1): e1501170.

3 Gao, P., Grätzel, M., and Nazeeruddin, M.K. (2014). Organohalide lead perovskites for photovoltaic applications. *Energy Environ. Sci.* 7 (8): 2448.

4 Burschka, J., Pellet, N., Moon, S.-J. et al. (2013). Sequential deposition as a route to high-performance perovskite-sensitized solar cells. *Nature* 499 (7458): 316–319.

5 Liu, M., Johnston, M.B., and Snaith, H.J. (2013). Efficient planar heterojunction perovskite solar cells by vapour deposition. *Nature* 501 (7467): 395–398.

6 Liu, D. and Kelly, T.L. (2013). Perovskite solar cells with a planar heterojunction structure prepared using room-temperature solution processing techniques. *Nat. Photonics* 8 (2): 133–138.

7 Xiao, Z., Bi, C., Shao, Y. et al. (2014). Efficient, high yield perovskite photovoltaic devices grown by interdiffusion of solution-processed precursor stacking layers. *Energy Environ. Sci.* 7 (8): 2619.

8 Ko, H.-S., Lee, J.-W., and Park, N.-G. (2015). 15.76% efficiency perovskite solar cells prepared under high relative humidity: importance of PbI_2 morphology in two-step deposition of $CH_3NH_3PbI_3$. *J. Mater. Chem. A* 3 (16): 8808–8815.

9 Jeon, N.J., Noh, J.H., Kim, Y.C. et al. (2014). Solvent engineering for high-performance inorganic–organic hybrid perovskite solar cells. *Nat. Mater.* 13 (9): 897–903.

10 Ganesan, P., Fu, K., Gao, P. et al. (2015). A simple spiro-type hole transporting material for efficient perovskite solar cells. *Energy Environ. Sci.* 8 (7): 1986–1991.

11 Li, H., Fu, K., Hagfeldt, A. et al. (2014). A simple 3,4-ethylenedioxythiophene based hole-transporting material for perovskite solar cells. *Angew. Chem. Int. Ed.* 53 (16): 4085–4088.

12 Lin, Q., Armin, A., Nagiri, R.C.R. et al. (2014). Electro-optics of perovskite solar cells. *Nat. Photonics* 9 (2): 106–112.

13 Ye, S., Sun, W., Li, Y. et al. (2015). CuSCN-based inverted planar perovskite solar cell with an average PCE of 15.6%. *Nano Lett.* 15 (6): 3723–3728.

14 Xu, X., Liu, Z., Zuo, Z. et al. (2015). Hole selective NiO contact for efficient perovskite solar cells with carbon electrode. *Nano Lett.* 15 (4): 2402–2408.

15 Ball, J.M., Lee, M.M., Hey, A., and Snaith, H.J. (2013). Low-temperature processed meso-superstructured to thin-film perovskite solar cells. *Energy Environ. Sci.* 6 (6): 1739.

16 Liu, D., Yang, J., and Kelly, T.L. (2014). Compact layer free perovskite solar cells with 13.5% efficiency. *J. Am. Chem. Soc.* 136 (49): 17116–17122.

17 Etgar, L., Gao, P., Xue, Z. et al. (2012). Mesoscopic $CH_3NH_3PbI_3/TiO_2$ heterojunction solar cells. *J. Am. Chem. Soc.* 134 (42): 17396–17399.

18 Green, M.A. (2002). Photovoltaic principles. *Physica E* 14 (1–2): 11–17.

19 Yang, G., Tao, H., Qin, P. et al. (2016). Recent progress in electron transport layers for efficient perovskite solar cells. *J. Mater. Chem. A* 4 (11): 3970–3990.

20 Yu, Z. and Sun, L. (2015). Recent progress on hole-transporting materials for emerging organometal halide perovskite solar cells. *Adv. Energy Mater.* 5 (12): 1500213.

21 Bi, D., Yi, C., Luo, J. et al. (2016). Polymer-templated nucleation and crystal growth of perovskite films for solar cells with efficiency greater than 21%. *Nat. Energy* 1 (10): 16142.

22 Rakstys, K., Saliba, M., Gao, P. et al. (2016). Highly efficient perovskite solar cells employing an easily attainable bifluorenylidene-based hole-transporting material. *Angew. Chem. Int. Ed.* 55 (26): 7464–7468.

23 Rakstys, K., Paek, S., Sohail, M. et al. (2016). A highly hindered bithiophene-functionalized dispiro-oxepine derivative as an efficient hole transporting material for perovskite solar cells. *J. Mater. Chem. A* 4 (47): 18259–18264.

24 Saliba, M., Orlandi, S., Matsui, T. et al. (2016). A molecularly engineered hole-transporting material for efficient perovskite solar cells. *Nat. Energy* 1 (2): 15017.

25 Bi, D., Xu, B., Gao, P. et al. (2016). Facile synthesized organic hole transporting material for perovskite solar cell with efficiency of 19.8%. *Nano Energy* 23: 138–144.

26 Abate, A., Paek, S., Giordano, F. et al. (2015). Silolothiophene-linked triphenylamines as stable hole transporting materials for high efficiency perovskite solar cells. *Energy Environ. Sci.* 8 (10): 2946–2953.

27 Jeon, N.J., Lee, J., Noh, J.H. et al. (2013). Efficient inorganic–organic hybrid perovskite solar cells based on pyrene arylamine derivatives as hole-transporting materials. *J. Am. Chem. Soc.* 135 (51): 19087–19090.

28 Qin, P., Paek, S., Dar, M.I. et al. (2014). Perovskite solar cells with 12.8% efficiency by using conjugated quinolizino acridine based hole transporting material. *J. Am. Chem. Soc.* 136 (24): 8516–8519.

29 Rakstys, K., Abate, A., Dar, M.I. et al. (2015). Triazatruxene-based hole transporting materials for highly efficient perovskite solar cells. *J. Am. Chem. Soc.* 137 (51): 16172–16178.

30 Paek, S., Zimmermann, I., Gao, P. et al. (2016). Donor–π–donor type hole transporting materials: marked π-bridge effects on optoelectronic properties, solid-state structure, and perovskite solar cell efficiency. *Chem. Sci.* 7 (9): 6068–6075.

31 Paek, S., Rub, M.A., Choi, H. et al. (2016). A dual-functional asymmetric squaraine-based low band gap hole transporting material for efficient perovskite solar cells. *Nanoscale* 8 (12): 6335–6340.

32 Bi, D., Mishra, A., Gao, P. et al. (2016). High-efficiency perovskite solar cells employing a *S,N*-heteropentacene-based D–A hole-transport material. *ChemSusChem* 9 (5): 433–438.

33 Kazim, S., Ramos, F.J., Gao, P. et al. (2015). A dopant free linear acene derivative as a hole transport material for perovskite pigmented solar cells. *Energy Environ. Sci.* 8 (6): 1816–1823.

34 Heo, J.H., Im, S.H., Noh, J.H. et al. (2013). Efficient inorganic–organic hybrid heterojunction solar cells containing perovskite compound and polymeric hole conductors. *Nat. Photonics* 7 (6): 486–491.

35 Zhang, Y., Gao, P., Oveisi, E. et al. (2016). PbI_2-HMPA complex pretreatment for highly reproducible and efficient $CH_3NH_3PbI_3$ perovskite solar cells. *J. Am. Chem. Soc.* doi: 10.1021/jacs.6b08347.

36 Jeon, N.J., Noh, J.H., Yang, W.S. et al. (2015). Compositional engineering of perovskite materials for high-performance solar cells. *Nature* 517 (7535): 476–480.

37 Abrusci, A., Stranks, S.D., Docampo, P. et al. (2013). High-performance perovskite-polymer hybrid solar cells via electronic coupling with fullerene monolayers. *Nano Lett.* 13 (7): 3124–3128.

38 Guo, Y., Liu, C., Inoue, K. et al. (2014). Enhancement in the efficiency of an organic–inorganic hybrid solar cell with a doped P3HT hole-transporting layer on a void-free perovskite active layer. *J. Mater. Chem. A* 2 (34): 13827.

39 Zhu, Z., Bai, Y., Lee, H.K.H. et al. (2014). Polyfluorene derivatives are high-performance organic hole-transporting materials for inorganic−organic hybrid perovskite solar cells. *Adv. Funct. Mater.* 24 (46): 7357–7365.

40 Qin, P., Tetreault, N., Dar, M.I. et al. (2015). A novel oligomer as a hole transporting material for efficient perovskite solar cells. *Adv. Energy Mater.* 5 (2): 1400980.

41 Cai, B., Xing, Y., Yang, Z. et al. (2013). High performance hybrid solar cells sensitized by organolead halide perovskites. *Energy Environ. Sci.* 6 (5): 1480.

42 Ryu, S., Noh, J.H., Jeon, N.J. et al. (2014). Voltage output of efficient perovskite solar cells with high open-circuit voltage and fill factor. *Energy Environ. Sci.* 7 (8): 2614.

43 Dubey, A., Adhikari, N., Venkatesan, S. et al. (2016). Solution processed pristine PDPP3T polymer as hole transport layer for efficient perovskite solar cells with slower degradation. *Sol. Energy Mater. Sol. Cells* 145: 193–199.

44 Kwon, Y.S., Lim, J., Yun, H.-J. et al. (2014). A diketopyrrolopyrrole-containing hole transporting conjugated polymer for use in efficient stable organic–inorganic hybrid solar cells based on a perovskite. *Energy Environ. Sci.* 7 (4): 1454.

45 Nie, W., Tsai, H., Asadpour, R. et al. (2015). High-efficiency solution-processed perovskite solar cells with millimeter-scale grains. *Science* 347 (6221): 522–525.

46 Cho, K.T., Rakstys, K., Cavazzini, M. et al. (2016). Perovskite solar cells employing molecularly engineered Zn(II) phthalocyanines as hole-transporting materials. *Nano Energy* .

47 Liu, J., Wu, Y., Qin, C. et al. (2014). A dopant-free hole-transporting material for efficient and stable perovskite solar cells. *Energy Environ. Sci.* 7 (9): 2963.

48 Kumar, C.V., Sfyri, G., Raptis, D. et al. (2015). Perovskite solar cell with low cost Cu-phthalocyanine as hole transporting material. *RSC Adv.* 5 (5): 3786–3791.

49 Seo, J., Jeon, N.J., Yang, W.S. et al. (2015). Effective electron blocking of CuPC-doped spiro-OMeTAD for highly efficient inorganic–organic hybrid perovskite solar cells. *Adv. Energy Mater.* 5 (20): 1501320.

50 Ghani, F., Kristen, J., and Riegler, H. (2012). Solubility properties of unsubstituted metal phthalocyanines in different types of solvents. *J. Chem. Eng. Data* 57 (2): 439–449.

51 Javier Ramos, F., Ince, M., Urbani, M. et al. (2015). Non-aggregated Zn(ii)octa(2,6-diphenylphenoxy) phthalocyanine as a hole transporting material for efficient perovskite solar cells. *Dalton Trans.* 44 (23): 10847–10851.

52 Gao, P., Cho, K.T., Abate, A. et al. (2016). An efficient perovskite solar cell with symmetrical Zn(ii) phthalocyanine infiltrated buffering porous Al_2O_3 as the hybrid interfacial hole-transporting layer. *Phys. Chem. Chem. Phys.* 18 (39): 27083–27089.

53 Li, M., Li, Y., Sasaki, S. et al. (2016). Dopant-free zinc chlorophyll aggregates as an efficient biocompatible hole transporter for perovskite solar cells. *ChemSusChem* 9 (19): 2862–2869.

54 Chou, H.-H., Chiang, Y.-H., Li, M.-H. et al. (2016). Zinc porphyrin–ethynylaniline conjugates as novel hole-transporting materials for perovskite solar cells with power conversion efficiency of 16.6%. *ACS Energy Lett.* 1 (5): 956–962.

55 Xiao, M., Gao, M., Huang, F. et al. (2016). Efficient perovskite solar cells employing inorganic interlayers. *ChemNanoMat* 2 (3): 182–188.

56 Qin, P., Tanaka, S., Ito, S. et al. (2014). Inorganic hole conductor-based lead halide perovskite solar cells with 12.4% conversion efficiency. *Nat. Commun.* 5 (May): 1–6.

57 Christians, J.A., Fung, R.C.M., and Kamat, P.V. (2014). An inorganic hole conductor for organo-lead halide perovskite solar cells. Improved hole conductivity with copper iodide. *J. Am. Chem. Soc.* 136 (2): 758–764.

58 Zhu, Z., Bai, Y., Zhang, T. et al. (2014). High-performance hole-extraction layer of sol–gel-processed NiO nanocrystals for inverted planar perovskite solar cells. *Angew. Chem. Int. Ed.* 53 (46): 12571–12575.

59 Wang, K.-C., Jeng, J.-Y., Shen, P.-S. et al. (2014). p-Type mesoscopic nickel oxide/organometallic perovskite heterojunction solar cells. *Sci. Rep.* 4: 4756.

60 Hu, L., Peng, J., Wang, W. et al. (2014). Sequential deposition of $CH_3NH_3PbI_3$ on planar NiO film for efficient planar perovskite solar cells. *ACS Photonics* 1 (7): 547–553.

61 Park, N.-G. (2013). Organometal perovskite light absorbers toward a 20% efficiency low-cost solid-state mesoscopic solar cell. *J. Phys. Chem. Lett.* 4 (15): 2423–2429.

62 Leijtens, T., Stranks, S.D., Eperon, G.E. et al. (2014). Electronic properties of meso-superstructured and planar organometal halide perovskite films: charge trapping, photodoping, and carrier mobility. *ACS Nano* 8 (7): 7147–7155.

63 Kim, H.-S., Lee, C.-R., Im, J.-H. et al. (2012). Lead iodide perovskite sensitized all-solid-state submicron thin film mesoscopic solar cell with efficiency exceeding 9%. *Sci. Rep.* 2: 591.

64 Kim, H.-S., Lee, J.-W., Yantara, N. et al. (2013). High efficiency solid-state sensitized solar cell-based on submicrometer rutile TiO_2 nanorod and $CH_3NH_3PbI_3$ perovskite sensitizer. *Nano Lett.* 13 (6): 2412–2417.

65 Gao, X., Li, J., Baker, J. et al. (2014). Enhanced photovoltaic performance of perovskite $CH_3NH_3PbI_3$ solar cells with freestanding TiO_2 nanotube array films. *Chem. Commun.* 50 (48): 6368–6371.

66 Pathak, S.K., Abate, A., Ruckdeschel, P. et al. (2014). Performance and stability enhancement of dye-sensitized and perovskite solar cells by Al doping of TiO_2. *Adv. Funct. Mater.* 24 (38): 6046–6055.

67 Zhou, H., Chen, Q.Q., Li, G. et al. (2014). Interface engineering of highly efficient perovskite solar cells. *Science* 345 (6196): 542–546.

68 Qin, P., Domanski, A.L., Chandiran, A.K. et al. (2014). Yttrium-substituted nanocrystalline TiO_2 photoanodes for perovskite based heterojunction solar cells. *Nanoscale* 6 (3): 1508–1514.

69 Kumar, M.H., Yantara, N., Dharani, S. et al. (2013). Flexible, low-temperature, solution processed ZnO-based perovskite solid state solar cells. *Chem. Commun.* 49 (94): 11089.

70 Son, D.-Y., Im, J.-H., Kim, H.-S., and Park, N.-G. (2014). 11% efficient perovskite solar cell based on ZnO nanorods: an effective charge collection system. *J. Phys. Chem. C* 118 (30): 16567–16573.

71 Dong, X., Hu, H., Lin, B. et al. (2014). The effect of ALD-Zno layers on the formation of $CH_3NH_3PbI_3$ with different perovskite precursors and sintering temperatures. *Chem. Commun.* 50 (92): 14405–14408.

72 Li, Y., Zhu, J., Huang, Y. et al. (2015). Mesoporous SnO_2 nanoparticle films as electron-transporting material in perovskite solar cells. *RSC Adv.* 5 (36): 28424–28429.

73 Song, J., Zheng, E., Bian, J. et al. (2015). Low-temperature SnO_2-based electron selective contact for efficient and stable perovskite solar cells. *J. Mater. Chem. A* 3 (20): 10837–10844.

74 Ke, W., Fang, G., Liu, Q. et al. (2015). Low-temperature solution-processed tin oxide as an alternative electron transporting layer for efficient perovskite solar cells. *J. Am. Chem. Soc.* 137 (21): 6730–6733.

75 Correa Baena, J.P., Steier, L., Tress, W. et al. (2015). Highly efficient planar perovskite solar cells through band alignment engineering. *Energy Environ. Sci.* 8 (10): 2928–2934.

76 Jeng, J.-Y., Chiang, Y.-F., Lee, M.-H. et al. (2013). $CH_3NH_3PbI_3$ perovskite/fullerene planar-heterojunction hybrid solar cells. *Adv. Mater.* 25 (27): 3727–3732.

77 Malinkiewicz, O., Yella, A., Lee, Y.H. et al. (2014). Perovskite solar cells employing organic charge-transport layers. *Nat. Photonics* 8 (2): 128–132.

78 Nakamura, I., Negishi, N., Kutsuna, S. et al. (2000). Role of oxygen vacancy in the plasma-treated TiO_2 photocatalyst with visible light activity for NO removal. *J. Mol. Catal. A: Chem.* 161 (1–2): 205–212.

79 Ogomi, Y., Morita, A., Tsukamoto, S. et al. (2014). All-solid perovskite solar cells with HOCO-R-$NH_3^+I^-$ anchor-group inserted between porous titania and perovskite. *J. Phys. Chem. C* 118 (30): 16651–16659.

80 Wojciechowski, K., Stranks, S.D., Abate, A. et al. (2014). Heterojunction modification for highly efficient organic–inorganic perovskite solar cells. *ACS Nano* 8 (12): 12701–12709.

81 Zhu, Z., Ma, J., Wang, Z. et al. (2014). Efficiency enhancement of perovskite solar cells through fast electron extraction: the role of graphene quantum dots. *J. Am. Chem. Soc.* 136 (10): 3760–3763.

82 Liu, T., Kim, D., Han, H. et al. (2015). Fine-tuning optical and electronic properties of graphene oxide for highly efficient perovskite solar cells. *Nanoscale* 7 (24): 10708–10718.

83 Yeo, J.-S., Kang, R., Lee, S. et al. (2015). Highly efficient and stable planar perovskite solar cells with reduced graphene oxide nanosheets as electrode interlayer. *Nano Energy* 12: 96–104.

84 Wang, C., Tang, Y., Hu, Y. et al. (2015). Graphene/$SrTiO_3$ nanocomposites used as an effective electron-transporting layer for high-performance perovskite solar cells. *RSC Adv.* 5 (64): 52041–52047.

85 Ito, S., Tanaka, S., Manabe, K., and Nishino, H. (2014). Effects of surface blocking layer of Sb_2S_3 on nanocrystalline TiO_2 for $CH_3NH_3PbI_3$ perovskite solar cells. *J. Phys. Chem. C* 118 (30): 16995–17000.

86 Juarez-Perez, E.J., Wuβler, M., Fabregat-Santiago, F. et al. (2014). Role of the selective contacts in the performance of lead halide perovskite solar cells. *J. Phys. Chem. Lett.* 5 (4): 680–685.

2.4

Beyond Methylammonium Lead Iodide Perovskite

Teck M. Koh[1], *Biplab Ghosh*[2, 3], *Padinhare C. Harikesh*[2, 3], *Subodh Mhaisalkar*[1, 3], *and Nripan Mathews*[1, 3]

[1] *Energy Research Institute @ NTU (ERI@N), Research Techno Plaza, X-Frontier Block, Level 5, 50 Nanyang Drive, Singapore 637553, Singapore*
[2] *Nanyang Technological University, Interdisciplinary Graduate School, 50 Nanyang Avenue, Singapore 639798, Singapore*
[3] *Nanyang Technological University, School of Materials Science and Engineering, 50 Nanyang Avenue, Singapore 639798, Singapore*

2.4.1 Introduction: Beyond $CH_3NH_3PbI_3$

Lead (Pb)-based halide perovskites have revolutionized the photovoltaic (PV) research community with its rich structural diversity, unusual optoelectronic properties, defect-tolerant characteristics, and cheaper processing routes. However, concerns over the stability of the typical perovskite structures as well as the toxicity of the Pb within the perovskite have prompted investigations beyond $CH_3NH_3PbI_3$. This chapter discusses development of such novel Pb-based perovskites as well as the development of Pb-free alternatives.

2.4.1.1 Multidimensional Perovskites

In general, the typical halide perovskite is defined by the general formula AMX_3 (where A = Cs, $CH_3NH_3^+$ or MA^+, $HC(NH_2)_2^+$ or FA^+; M = Pb^{2+}, Sn^{2+}, Ge^{2+}, Cu^{2+}; and X = I^-, Br^-, Cl^-) [1]. Goldschmidt tolerance (t, Eq. (2.4.1)) and the octahedral (μ, Eq. (2.4.2)) factors are the tools that are commonly used to determine the structural stability of perovskites by considering the ionic radii of A^+, M^{2+}, and X^-. The equations are defined as follows [1], respectively:

$$t = \frac{R_A + R_X}{\sqrt{2}(R_M + R_X)} \tag{2.4.1}$$

$$\mu = \frac{R_M}{R_X} \tag{2.4.2}$$

where R_A, R_M, and R_X refer to the corresponding ionic radii. The majority of stable "three-dimensional" (3D) perovskites possess values of $0.8 < t < 0.9$ and $0.442 < \mu < 0.895$, with significant deviations that result in the edge-shared and

Halide Perovskites: Photovoltaics, Light Emitting Devices, and Beyond, First Edition.
Edited by Tze-Chien Sum and Nripan Mathews.

face-shared octahedral, instead of the pristine corner-shared structure of the classic AMX_3 perovskite [1, 2]. A number of organic ammonium cations that do not accommodate within the octahedral cavities in the 3D perovskite structure, on the other hand, adopt the "two-dimensional" (2D) perovskite slabs with corner-shared octahedra, and conform to the Ruddlesden–Popper formulae of $A_{n-1}A'_2M_nX_{3n+1}$, where A′ are typically bulkier organic ammonium cations [3, 4], whereas A, M, and X retain the same definitions. Consequently, along with the development of new organic cations, numerous perovskite materials with the general formulae $(RNH_3)_2(A)_{n-1}M_nX_{3n+1}$ ($n =$ integer) are now generally defined as 2D perovskites, while $(RNH_3)_2(A)_mM_mX_{3m+2}$ is categorized as a 1D perovskite, where RNH_3 is an aliphatic or aromatic alkylammonium cation [5]. Hence, these perovskites can be broadly classified as multidimensional perovskites (Figure 2.4.1a) [6], although the term 0D perovskites are strictly just molecular crystals and are not considered.

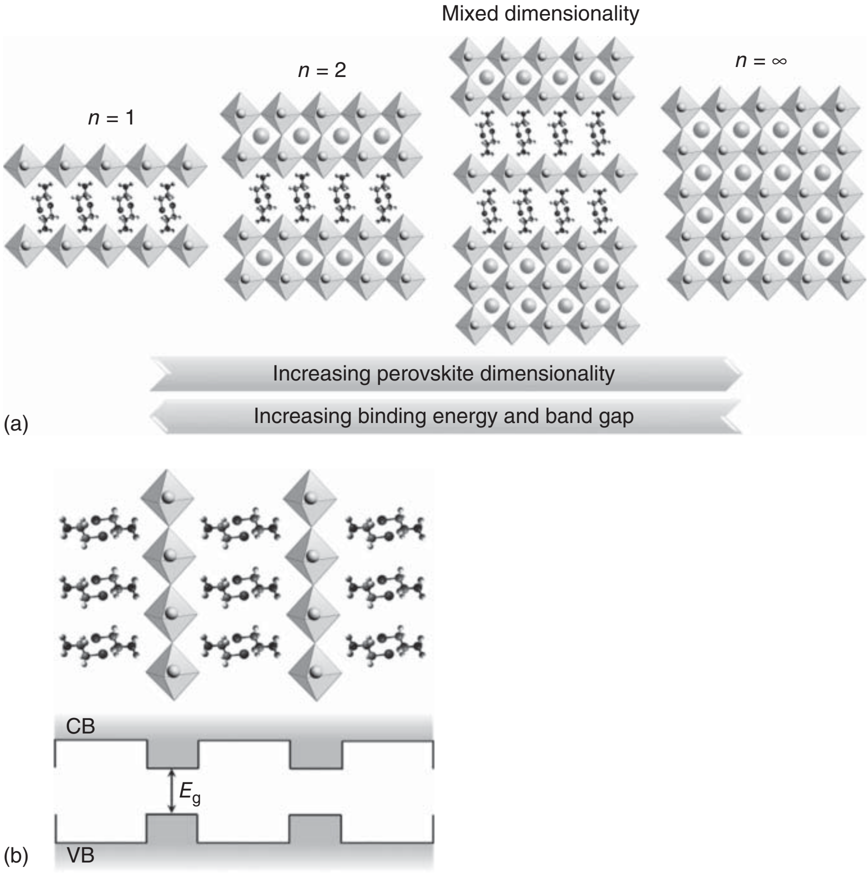

Figure 2.4.1 (a) Schematic illustration showing the crystalline structure of multidimensional perovskites, including 2D perovskites ($n = 1$ and 2, where n represents the metal halide lattices) and mixed-dimensional perovskites, and 3D perovskites ($n = \infty$). Source: Koh et al. 2016 [6]. Copyright 2016. Adapted from Wiley-VCH Verlag GmbH & Co. KGaA. (b) Schematic representation of the bandgap (E_g) between the conduction band and the valence band (CB and VB, respectively) in 2D perovskites. Layered perovskites form multiple quantum wells, in which the inorganic and organic layers act as "well" and "barrier," respectively.

The corner-shared PbX_6^{4-} octahedra layers accommodate larger cations and the energy difference between the ionic bonding in the inorganic layers and the van der Waals forces among the organic molecules lead to the formation of self-assembled layered perovskites that contain alternating organic and inorganic layers [7]. This unique configuration creates internal multiple quantum wells (Figure 2.4.1b) and displays interesting photophysical properties. For instance, the highest occupied molecular orbital–lowest unoccupied molecular orbital (HOMO–LUMO) energy gap of the organic ammonium cation is typically larger than the bandgap of the inorganic layers [8], and therefore the difference in the dielectric constants between these two layers creates periodic barriers and wells. Hence, these materials can be considered as containing a self-organized multiple-quantum-well structure. The strong tendency to form layered perovskites and the solubility of both starting components in the same solvent has permitted a facile and convenient spin-coating technique to deposit the thin films with homogeneous coverage on the substrate [9]. This controlled formation of layered structures has led to perovskites with larger cations and variable structures and sizes that alter the photophysical and electronic properties of these new semiconductors [10]. Adding to this versatility, mixed cations with different sizes can also form well-organized layered structures where the smaller cations occupy voids created by the corner-shared PbX_6^{4-} octahedral, while the larger cations cap the stacks of inorganic layers and interleave between the 2D nanosheets [3, 11, 12]. Some prototypical examples of mixed-dimensional perovskites are $(CH_3(CH_2)_3NH_3)_2(CH_3NH_3)_2Pb_3I_{10}$ and $(CH_3(CH_2)_3NH_3)_2(CH_3NH_3)_3Pb_4I_{13}$, which crystallized as well-organized layered structures [6]. The properties such as the bandgap, band energy levels, carrier binding energy, and charge transport, among others, can be easily tuned simply by varying the organic cations and the thickness of the inorganic layers [6].

2.4.1.2 Multidimensional Perovskite Photovoltaics

Tremendous effort has been placed in the conventional 3D perovskites ($MAPbI_3$, $FAPbI_3$, for example) for their solar cell applications; however, significantly less research studies were found in multidimensional perovskite PVs. Smith et al. reported the first multidimensional perovskite solar cells (PSCs) only in 2014 [13]. They presented the first single-crystal structure of an $n=3$ perovskite, $(PEA)_2(MA)_2[Pb_3I_{10}]$ (PEA^+ = phenethylammonium cation), derived from dark red crystals that were obtained from slow evaporation of a saturated perovskite solution. The pure $n=3$ perovskite single crystal can be grown; however, the spin-coated thin film from the lead precursor solution actually consisted of a mixture of different orders ($n=1$, 2, 3, 4, and 5) in the perovskite film due to the rapid and uncontrollable self-assembly process. These multidimensional perovskite-based PVs exhibit overall power conversion efficiency (PCE) of 4.73%, J_{sc} of 6.72 mA cm^{-2}, V_{oc} of 1.18 V, and fill factor (FF) of 0.60. Importantly, the V_{oc} value observed here is higher than that of $MAPbI_3$-based solar cells, which is probably due to its slightly larger bandgap. Despite the lower efficiencies, this multidimensional perovskite displays high moisture resistance even after storage for 46 days under 52% relative humidity (RH), whereas the $MAPbI_3$ thin film had turned from black to yellow under the same conditions (Figure 2.4.2a).

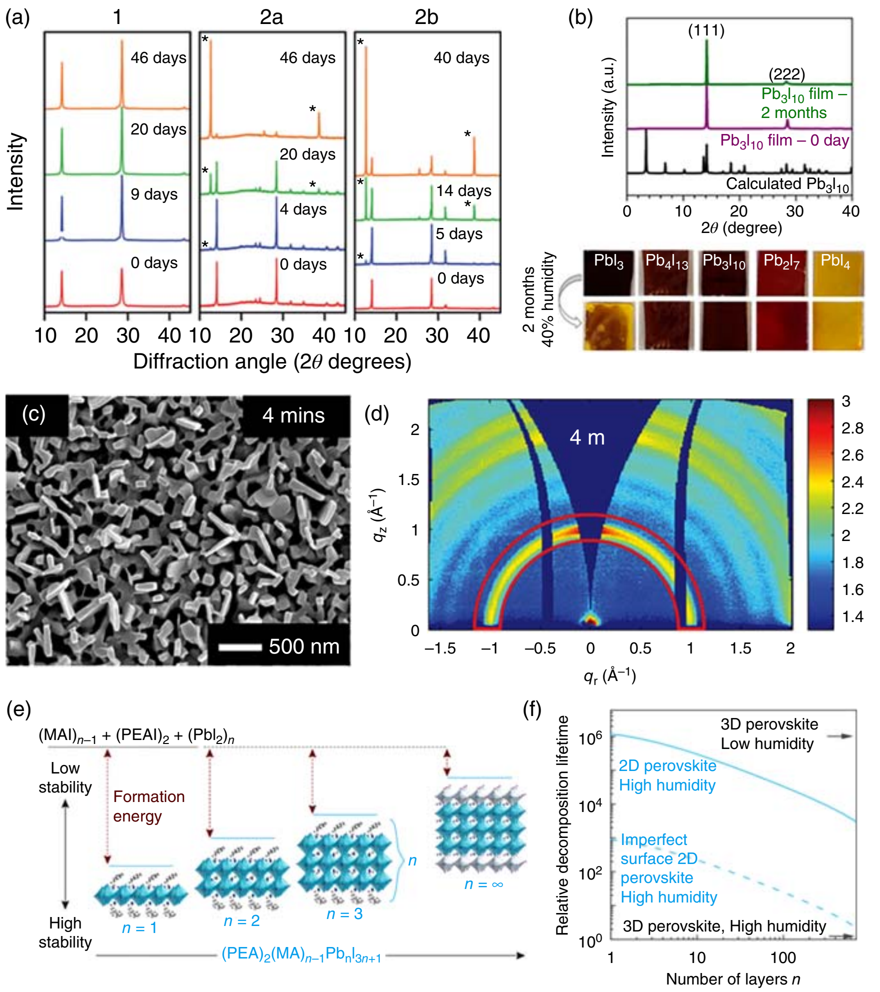

Figure 2.4.2 (a) Powder XRD patterns of films of $(PEA)_2(MA)_2Pb_3I_{10}$ (1), $MAPbI_3$ formed from PbI_2 (2a), and $MAPbI_3$ formed from $PbCl_2$ (2b), which were exposed to 52% RH. Films of 2a (15 minutes) and 2b (80 minutes) were annealed at 100 °C prior to humidity exposure. Asterisks denote the major reflections from PbI_2. Source: Smith et al. 2014 [13]. Copyright 2014. Adapted from American Chemical Society. (b) XRD patterns of fresh and aged (two months) $(BA)_2(MA)_2Pb_3I_{10}$ films. The images below are the five different perovskite films before and after exposure to humidity. Source: Cao et al. 2015 [14]. Copyright 2015. Adapted from Wiley-VCH Verlag GmbH & Co. KGaA. (c) Top-view field emission scanning electron microscopic (FESEM) images of nanostructures of $(IC_2H_4NH_3)_2(CH_3NH_3)_{n-1}Pb_nI_{3n+1}$ perovskites on top of mesoporous TiO_2 layer from two different dipping durations in the sequential technique. (d) 2D grazing-incidence wide-angle X-ray scattering (GIWAXS) data shown with a logarithmic false-color scale. The inhomogeneous intensity distribution of the ring at $q = 1$ Å^{-1} for the four minutes sample indicates preferentially oriented crystals. Source: Koh et al. 2016 [6]. Copyright 2016. Adapted from Wiley-VCH Verlag GmbH & Co. KGaA. (e) Unit cell structure and relative energetics of formation (i.e. stability) for $(C_8H_9NH_3)_2(CH_3NH_3)_{n-1}Pb_nI_{3n+1}$ with different values of n. (f) DFT calculations illustrating the relative formation energy of the 2D perovskites containing different values of n under different humidity environments. Source: Quan et al. 2016 [11]. Copyright 2016. Adapted with permission of American Chemical Society.

Almost a year later, a second demonstration of PSCs based on multidimensional perovskites was reported by Cao et al. [14]. They synthesized a series of homologous perovskites, $(BA)_2(MA)_{n-1}PbI_{3n+1}$ (BA = n-butylammonium cation) by incorporating bulkier primary organic ammonium cations, thus confining the perovskites into a layered structure. Similarly, these perovskite thin films also contained multiple orders of perovskites as the films were simply prepared by the single-step deposition method. The presence of mixed-dimensional perovskites cannot be realistically avoided with the fast and low-temperature self-assembly processes currently utilized. The highest recorded efficiency for these multidimensional perovskites was only 4.02% with $(BA)_2(MA)_2Pb_3I_{10}$, but the perovskite film possesses high ambient stability over two months (Figure 2.4.2b). Importantly, X-ray diffraction (XRD) analysis revealed that the lower dimensional perovskites ($n = 1$ and 2) tend to grow parallel to the substrate (along the (00k) and (0k0) plane), resulting in poorer charge transport in the (111) direction due to the intercalated insulating organic cation layers. Hence, stable and highly efficient multidimensional perovskites can be achieved in higher order 2D perovskites. Another key advantage of the multidimensional perovskites is their homogeneous coatings on the substrates, which were far superior to the 3D $MAPbI_3$ counterpart films, indicating the potential for facile processing in both laboratory-scale and large-scale fabrication.

The nanostructuring approach to direct the growth of multidimensional perovskites is an interesting strategy to solve the charge-transport challenges in multidimensional perovskites to create high-efficiency and stable PSCs [6]. The insulating organic layers present in the multidimensional perovskites tend to impede the vertical charge transport, and this challenge can be addressed by growing the perovskite perpendicular to the substrate. First, a pure 2D perovskite ($n = 1$) was deposited by spin coating the precursor solution containing a stoichiometric ratio of lead iodide (PbI_2) and iodoethylammonium iodide ($IC_2H_4NH_3I$). Subsequently, the substrate was immersed into a solution containing methylammonium iodide (CH_3NH_3I) for different dipping durations to increase the stacking order and convert it into a mixed-dimensional perovskite. Control of the dipping duration allows to tune the optical properties, direct the crystal growth perpendicular to the substrate, and hence improve the electrical properties (Figure 2.4.2c,d). This class of multidimensional perovskites exhibited good air stability and achieved over 9% PCE with a mixed-cation approach [6]. More importantly, the PV devices degrade at much slower rates compared to those with $MAPbI_3$ without any encapsulation under high RH (70–80%).

Increasing the number of stacked inorganic sheets could potentially alleviate the inferior charge transport in multidimensional PSCs. For instance, Quan et al. demonstrated the utilization of a relatively high order ($n = 60$) of multidimensional perovskites in PSCs, resulting in both high efficiency and stability (Figure 2.4.2e,f) [11]. The replacement of methyl ammonium iodide (MAI) with phenethylammonium iodide (PEAI) engenders higher stability owing to the latter's higher desorption energy and consequently slows down the decomposition of the perovskite film. By periodically examining the absorbance, transient photoluminescence (PL) decay, and structure (by XRD) of the perovskite films, the authors verified that the multidimensional perovskites with intercalated PEA cations possessed superior stability compared to the 3D perovskites under ambient atmospheres, likely due to the increased formation energy. The high-efficiency $MAPbI_3$ PSC (16.6%) deteriorated drastically to a PCE of less than 3% over eight weeks, whereas the multidimensional PVs remained stable at 11–13% PCE.

Bulkier and hydrophobic organic cations in multidimensional perovskites could strain the surface Pb—I bonds and repel water molecules from reactive sites in the perovskites, thereby promoting moisture resistance and prolonging the lifetime of the PSCs under ambient conditions [15]. Therefore, polymeric organic cations are also potential candidates in preparing multidimensional perovskites with high air stability. Yao et al. demonstrated the advantages of utilizing polyethylenimine hydriodide (PEI·HI) as intercalating organic cations

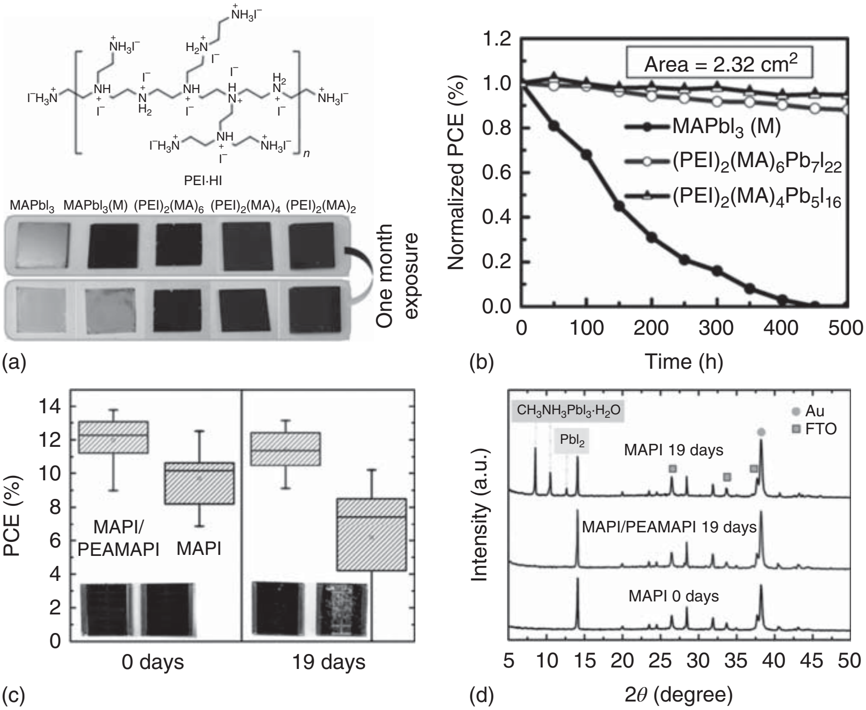

Figure 2.4.3 (a) Chemical structure of polyethylenimine hydriodide (PEI·HI) and the images of various perovskite films before and after exposure to 50% RH. (b) Stability of unsealed cells under simulated solar illumination (AM 1.5; 100 mW cm^{-2}) during a shelf-life investigation for 500 hours. Source: Yao et al. 2016 [16]. Copyright 2016. Adapted with permission of American Chemical Society. (c) Device stability test at 75% RH in air at room temperature for 19 days. Efficiency distribution for 20 $MAPbI_3/(PEA)_2(MA)_2Pb_3I_{10}$ and 20 $MAPbI_3$ devices before and after exposure to humidity. The insets show the corresponding photograph of a $MAPbI_3/(PEA)_2(MA)_2Pb_3I_{10}$ cell (left) compared to a $MAPbI_3$ control cell (right). (d) XRD patterns of an intact $MAPbI_3$ cell, a $MAPbI_3/(PEA)_2(MA)_2Pb_3I_{10}$ cell, and a $MAPbI_3$ cell upon exposure to moisture. Source: Hu et al. 2016 [17]. Copyright 2016. Adapted with permission of American Chemical Society.

in forming highly stable multidimensional perovskites (Figure 2.4.3a) [16]. High-quality pinhole-free perovskites containing polymeric cations are readily formed after the spin-coating process, thus minimizing the shunt paths for the leakage current and offer opportunities to manufacture scalable PSCs. The strong interaction between the polymeric organic–inorganic structures led to a lower bandgap compared to smaller molecular organic cations. The scaled-up PSCs (active area of 2.32 cm^{-2}) with polymer-based multidimensional perovskites exhibited PCEs exceeding 8% with excellent device lifetimes (Figure 2.4.3b).

Most recently, bilayer hybrid 2D/3D perovskites were adopted in another strategy to promote the ambient stability of the existing high-efficiency PSCs. Generally, these kinds of bilayer hybrid structures contain high-efficiency 3D perovskites on top of mesoporous TiO_2, while lower dimensional perovskites are placed on top to enhance the moisture resistance. Docampo and coworkers deposited layered perovskites, consisting of PEA^+ and MA^+, on top of $MAPbI_3$ and obtained PSCs with PCEs up to 16.8% with increased V_{oc} and FF [17]. The perovskites capped with lower dimensional perovskites exhibited average PCEs of 11.4% after exposure to 19 days in 75% RH, whereas pure 3D perovskite devices only retained average PCEs of 6.1% (Figure 2.4.3c,d). In summary, it is clear that utilization of the multidimensional approach in perovskite PVs has significantly improved its ambient stability. However, more research effort was expected to enhance the PV efficiency of multidimensional perovskite devices while attaining ambient stability.

2.4.2 Theoretical Calculations for Pb-Free Halide Perovskites

The concern of toxicity in typical $CH_3NH_3PbI_3$ PSC triggered the intensive research in looking for a replacement for Pb. In this section, a review of the theoretical calculations and experimental validation of lead-free halide perovskites and their solar cell applications are presented. However, it should be noted that the list of Pb-free halide perovskites is not exclusive, because with more computational power and better understanding of the materials physics, newer horizons are being unveiled rapidly.

2.4.2.1 $ASnX_3$ Perovskites: 3D Pb-Free Structures

Replacing Pb^{2+} with Sn^{2+} in the perovskite structure appeared to be most viable solution toward Pb-free perovskite for optoelectronic applications. Tin (Sn)-based halide perovskites with $ASnX_3$ (A = protonated cation, X = halogen element) structure is an interesting family of perovskite compounds that display temperature-dependent phase change, bandgap tunability, ferroelectricity, and excellent optoelectronic properties, as well as composition-dependent dimensionality [18–20]. Early studies include those by Lang et al. [21] who explored the electronic and optical properties of Sn- and Pb-based perovskites using standard density functional theory (DFT) and found that all these compounds possess a similar electronic structure, expecting similar electronic behavior. However, the inherent instability of Sn^{2+} cation in the atmospheric conditions leads to poor performance as solar cell absorber materials. Theoretical investigations on Sn-based inorganic halide perovskites had begun as early as the 1980s due to their interesting temperature-dependent phase transitions. Sn-based halide perovskites undergo several phase transitions from a high-temperature cubic phase toward a lower symmetry structure with decreasing temperature. These phase changes are associated with increasing packing density through distortion and rotation of SnX_6 octahedra, rather than a complete reordering of the atoms [22, 23]. Some earlier reports also claimed that the stereochemically active lone pair electron of tin had a key role to play in the distorted low-temperature phases [24]. Initially, the cubic $CsSnBr_3$ was thought to be semimetallic based on semiempirical extended Huckel theory (EHT) calculations [25]. Although this method is quite satisfactory for describing valence band structure, EHT performs poorly in describing the conduction band nature. Lefebvre et al. [26] performed band structure calculations based on the pseudopotential approach, which gives a better description of lowest conduction band along with valence electrons. Interestingly, they found $CsSnBr_3$ to be a zero-bandgap compound even without considering the spin-orbit coupling (SOC) effect. However, these results do not agree with experimental values. The bandgap problem was somewhat corrected by Bose et al. [27] when they performed a scalar-relativistic muffin-tin-orbital calculation based on local density approximation (LDA) within the framework of DFT and concluded that $CsSnBr_3$ is a narrow bandgap semiconductor with a direct bandgap of 0.26 eV. Considering the use of LDA, it can be fairly assumed that the original bandgap should be much higher than that. Their simulation also indicated that the valence band of $CsSnBr_3$ is a mixture of Sn 5s and Br 4p orbitals and the role of Cs^+ is negligible in the band edges. However, there was no change in the bandgap due to a low-temperature structural change in the perovskite. In 2008, Borriello et al. [23] performed *ab initio* calculations based on DFT using the generalized gradient approximation (GGA) for exchange correlation energy on several $ASnX_3$ compounds ($A = Cs$, CH_3NH_3, $NH_2CH{=}NH_2$, $X = Cl$, I). They have shown that in the high-temperature cubic phase, the A site cation has little role in determining the band edges of Sn-based halide perovskites. They concluded that the A site (organic or inorganic) cations mainly control the crystal structure of the perovskite, which has a drastic effect on the bandgap of the compound. For example, phase change in $CsSnI_3$ is associated with progressive tilting of SnI_6 octahedra along the ab-plane, without any observable change in Sn—I bond length or the angle (Figure 2.4.4a,b). Hence, all the phases of $CsSnI_3$ exhibit direct bandgap, which gradually increases with progressive tilting of the SnI_6 octahedra. Even replacing Cs^+ with MA or FO does not change the crystal symmetry at room temperature. On the other hand, the phase change in $CsSnCl_3$ is associated with the drastic change in the crystal structure, from a corner-sharing octahedral network (high-temperature cubic phase) to almost isolated edge-sharing octahedral chain network (low-temperature monoclinic phase), resulting in a much wider bandgap and an anisotropic valence band. Interestingly, the hybrid analogous $MASnCl_3$ preserves the corner-sharing octahedra even at low temperature, which is attributed to the steric interaction

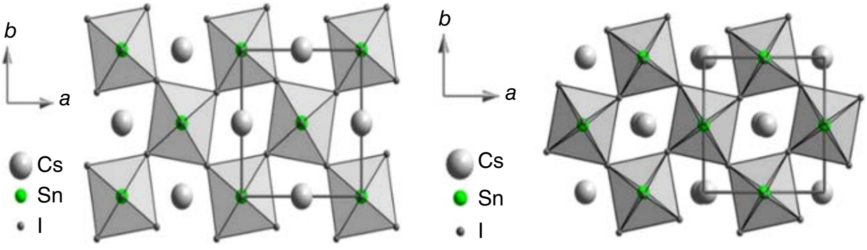

(a) Tetragonal phase (b) Orthorhombic phase

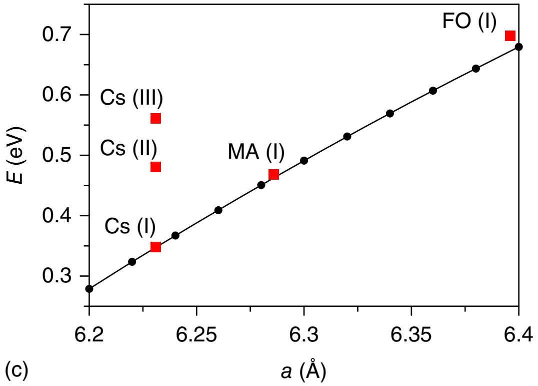

Figure 2.4.4 (a) A perspective of $CsSnI_3$ in the tetragonal phase and (b) orthorhombic phase, (c) The energy bandgap as a function of the cubic lattice *a*. The black circles represent the calculated band gap for a perfect cubic perovskite $CsSnI_3$ with different lattice parameters. The squares represent the bandgap of $CsSnI_3$ in the three phases, and the bandgap of $MASnI_3$ and of $FOSnI_3$ in the cubic phase. Source: Borriello et al. 2008 [23]. Copyright 2008. Adapted with permission of American Physical Society.

between the inorganic cage and larger organic cation. The role of the A site cation thus can be generalized only as the electron donor, as neither the organic nor inorganic cations play any role in the valence band maximum (VBM) or conduction band minimum (CBM). The change in bandgap can then be explained easily by the change in lattice constant originating from different cation sizes (Figure 2.4.4c).

After the emergence of PSC, Sn-based halide perovskites, especially $CsSnI_3$ and its hybrid compound $MASnI_3$ returned to the spotlight due to interesting optoelectronic properties such as p-type metallic conductivity and strong luminescence. As the standard DFT calculations are not reliable in predicting the bandgap of semiconductors, Huang and Lambrecht [28] reinvestigated the electronic structure of cubic phase $CsSnX_3$ (X = Cl, Br, I) using quasiparticle self-consistent GW (QSGW) method. In general, the QSGW method has been proved to be very accurate and reliable for describing the band structure and excited-state properties for weakly correlated systems. They found that the bandgap is essentially controlled by Sn s to I p covalent antibonding interaction which is expected to be weaker with increasing lattice constant, resulting in a wider bandgap with increasing cell volume. On the other hand, the bandgap is expected to increase from Cl to I due to lower energetic anion p levels. However, the opposing SOC effect in heavier halogen atoms further compensates the increase in bandgap, and the total effect on bandgap due to the change in halogen atoms is quite small. An interesting finding from their work is that the exciton binding energy of $CsSnI_3$ was found to be around 0.1 meV, which is two orders smaller than the experimentally reported value of 18 meV [29]. The authors argued that the reported value of exciton binding energy can only be interpreted as exciton linewidth or the energy of bound exciton, as the free exciton binding energy should be lower than that. Based on the band structure, the effective masses of hole and electrons were found to be small and decreased from Cl to I. However, nearly equal effective hole and electron mass failed to explain the p-type conductivity in $CsSnI_3$. Defect characteristics studies by Chung et al. [20] shed light on the origin of the p-type conductivity. The role of defects in the optoelectronic properties of the solution-processable semiconductor is crucial as the defects are in thermodynamic equilibrium with the constituents. The defect formation energy can be calculated using first-principles calculations based on the supercell approach. An excellent review on defect formation energy calculations can be found in Freysoldt et al. [30]. Figure 2.4.5 illustrates the intrinsic defect formation energy as a function of Fermi level in three different growth conditions. The p-type conductivity eventually arises from the Sn vacancies (V_{Sn}), which is the most favorable intrinsic defect in $CsSnI_3$. The strong luminescence at near-band edge can also be explained by the V_{Sn}-modulated defect centers. The presence of V_{Sn} as deep-level defects were also confirmed by Kumar et al. [31]. In addition to PV applications, Sn-based halide perovskite, especially formamidinium tin iodide ($FASnI_3$), has been shown to display excellent ferroelectric properties. Based on first-principles calculations, polarization of $FASnI_3$ can be changed depending upon the spatial arrangement of FA^+ cation [32].

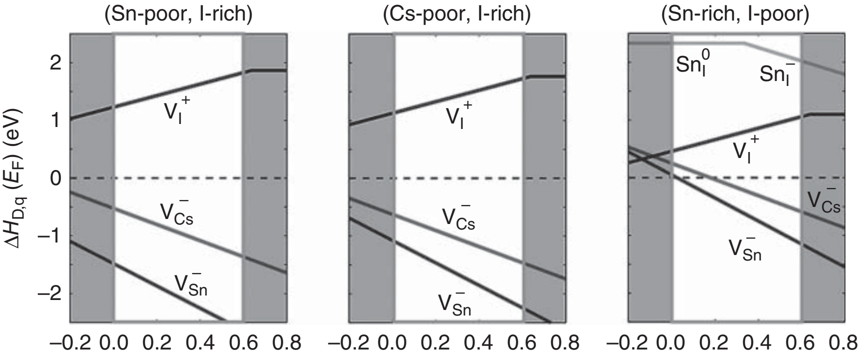

Figure 2.4.5 Calculated defect formation energies for V_{Sn}, V_{Cs}, Sn_I, and V_I in the cubic $CsSnI_3$. Charge state, q, is denoted by +, 0, and −. The energy level of the VBM is set to zero. The regions below VBM and above CBM are shaded in gray. The defect formation energies of Sn_I are higher than 2.5 eV in the Sn-poor, I-rich and the Cs-poor, I-rich conditions. Source: Chung et al. 2012 [20]. Copyright 2012. Adapted with permission of American Chemical Society.

2.4.2.2 A_2SnX_6 Perovskites: Metal-Deficient Structures

Although the electronic and optical properties of Sn-based halide perovskites are quite tempting, poor stability of Sn^{2+} limits the extensive applications. Sn^{2+} in perovskite structure can readily be oxidized into Sn^{4+}, which ushers in an alternate class of perovskites. The use of tetravalent Sn^{4+} to replace divalent Pb^{2+} results in a vacancy-ordered perovskite structure to maintain the charge balance (Figure 2.4.6). It can also be visualized as the ordered double perovskites with the general formula $A_2B'B''X_6$ in which one B-site cation is replaced with a vacancy ($A_2B\square X_6$). However, there is some ambiguity as to whether such simple ionic model can be applied for complex salts [22, 34]. From first-principles calculations, Sn 5s was found to be well below the Fermi level and the corresponding Bader charge analysis suggests the divalent nature of Sn [34, 35]. First-principles calculations based on the self-consistent, full-potential linearized augmented plane wave (LAPW) method within DFT, using the GGA-PBE (Perdew-Burke-Ernzerhof) for the exchange and correlation potential, resulted in a direct bandgap of ~1.3 eV, which is in excellent agreement with the experimental values [36]. It should be noted that the bandgap correction was done using the modified Becke–Johnson exchange potential. Later, Saparov et al. [37] reported an experimental bandgap of 1.6 eV and calculated bandgaps of 1.27 and 1.62 eV with (Heyd-Scuseria-Ernzerhof) HSE06 hybrid functional with 34% and 37% exchange, respectively. However, the use of SOC was not mentioned in the calculation. Maughan et al. [33] carried out electronic band structure calculations in a similar manner, but with explicit treatment of SOC and found a direct bandgap of 0.97 eV. Their GW0 calculation, which is more sophisticated than hybrid calculations, also indicated a bandgap of 0.88 eV. Hence, the experimental bandgap of 1.6 eV may be influenced by some secondary phase formation, which is quite common in complex perovskite semiconductors. Moving on from the bandgap discrepancy, the nature of charge carriers is also different between Cs_2SnI_6 and $CsSnI_3$, where the former shows n-type conductivity and the latter shows p-type. This could be explained by the defect characteristics. The formation energies of iodine vacancies are quite small

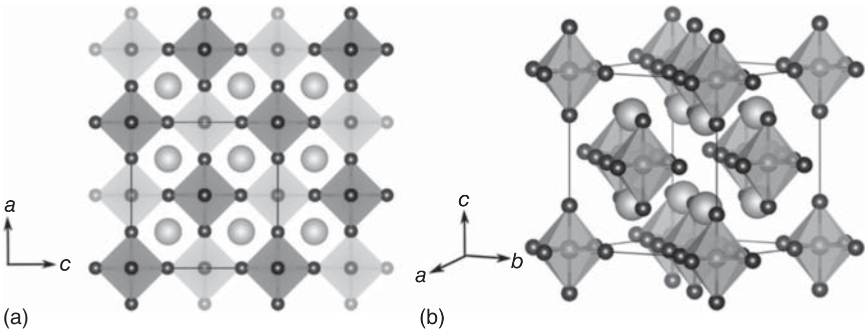

Figure 2.4.6 (a,b) Crystal structure of the vacancy-ordered double perovskites, Cs_2SnI_6. Source: Maughan et al. 2016 [33]. Copyright 2016. Adapted with permission of American Chemical Society.

(0.14–0.39 eV depending upon the chemical potential) and the 0/1 transition states are located just 0.07 eV below the VBM, which is most likely the source of n-type conductivities [33].

2.4.2.3 Germanium-Based Perovskites

Like Pb- and Sn-based halide perovskites, theoretical investigations on germanium (Ge)-based halide perovskites began even before the realization of their potential applications in PVs. Unlike Pb- and Sn-based halide perovskites, the smaller ionic radius of Ge^{2+} as well as the presence of stereochemically active $4s^2$ electron pair hinders the formation of stable cubic perovskites in room temperature. Hence, the GeX_6 octahedra is distorted drastically to form a pyramidal structure symmetry, which is expected to exhibit nonlinear optical properties. However, Ge-based perovskites also exhibit rich structural diversity depending on the temperature and protonated cation. For example, $CsGeI_3$ transforms from rhombohedral phase into cubic (Pmmm) symmetry above 290 °C. The band structure calculated by Li-Chuan et al. [38] following the standard DFT approach with LDA as exchange correlational functional shows similar orbital characteristics as that of Pb- or Sn-based halide perovskites. However, the bandgap seemed to be underestimated severely due to use of LDA. Follow-up calculations also reveal the increase in bandgap from I to Cl, which is in good agreement with the experimental trends [39]. However, the potential of Ge-based halide perovskites in solar cell absorber materials were not fully realized until Stoumpos et al. [40], and Krishnamoorthy et al. [19] synthesized organic-cation-based Ge iodide perovskites. Although the role of organic cation is limited to the crystal motif's formation as the interaction with inorganic network is negligible, the charge carrier properties among different hybrid Ge iodide perovskites vary significantly [41]. In comparison to Sn- or Pb-based halide perovskites, the values of effective mass are much higher for similar calculations, but comparable to other thin-film semiconductors. Sun et al. [42] studied the effect of systematic replacement of Pb^{2+} from $MAPbI_3$ with Ge^{2+} using DFT at different calculation levels. The incorporation of Ge^{2+} in place of Pb^{2+} displays gradual constriction in lattice constants and increase in lattice deformations. The change in bandgap is severely affected by the SOC effect for Pb^{2+}, while for the lighter Ge^{2+} the effect is minimal (Figure 2.4.7a). The optical absorption coefficients of mixed Pb/Ge perovskites calculated from first-principles calculations is projected to be higher than those of either $MAGeI_3$ or $MAPbI_3$. However, the change in orbital characteristics near the band edges is also minimal, except for a sharp increase of Ge p orbital in the CBM at the expense of Pb p orbital contribution. As for charge-transport properties, the change in average electron and hole effective masses are shown in Figure 2.4.7b. Among the studied Ge/Pb iodide perovskites, $MAGe_{0.75}Pb_{0.25}I_3$ shows best transport properties with nearly balanced electron and hole effective mass.

Nevertheless, the main challenge associated with Ge-based perovskites is its stability in ambient atmosphere. Ge-based perovskites readily decompose in the presence of ambient atmosphere. Sun et al. [43] investigated the effect of water (H_2O) molecule on the $MAGeI_3$ surface based on first-principles calculations.

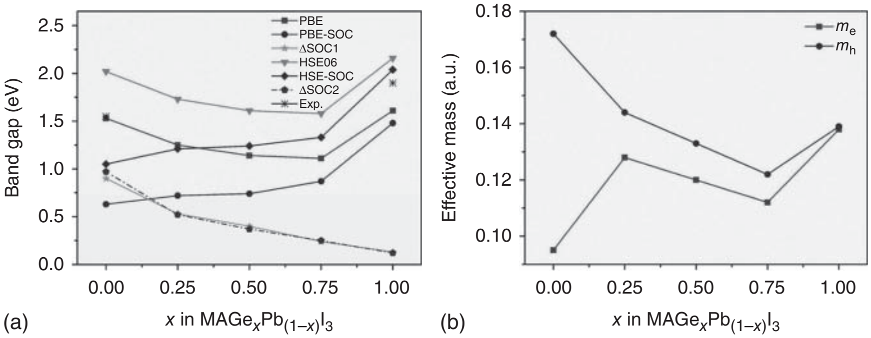

Figure 2.4.7 (a) Experimental and calculated bandgap trends with different methods. (b) The calculated average electron and hole effective masses of $MAGe_xPb_{(1-x)}I_3$ structures as a function of proportion x. The effective masses were calculated from HSE-SOC band structure. Source: Sum et al. 2016 [42]. Reproduced with permission of PCCP Owner Societies.

They found that H_2O molecules can easily diffuse through the surface of the $MAGeI_3$. The most stable surface of $MAGeI_3$ was found to be (101) plane, which is composed of Ge—I dangling bonds with iodine atoms exposed on the surface. The MA^+ cations reside inside the voids of the inorganic cage compensating the charge balance (Figure 2.4.8a). Initially, a single water molecule is adsorbed on the surface of $MAGeI_3$ through hydrogen bonding connected with O—(H_2O) and H with nearest MA^+ cation (region O in Figure 2.4.8a). Surprisingly, with increasing number of water molecule near the surface, the adsorption energy decreases from −0.1 eV for one H_2O molecule to a minimum of −0.27 eV for six water molecules. When the number of water molecules increases to more than six, the

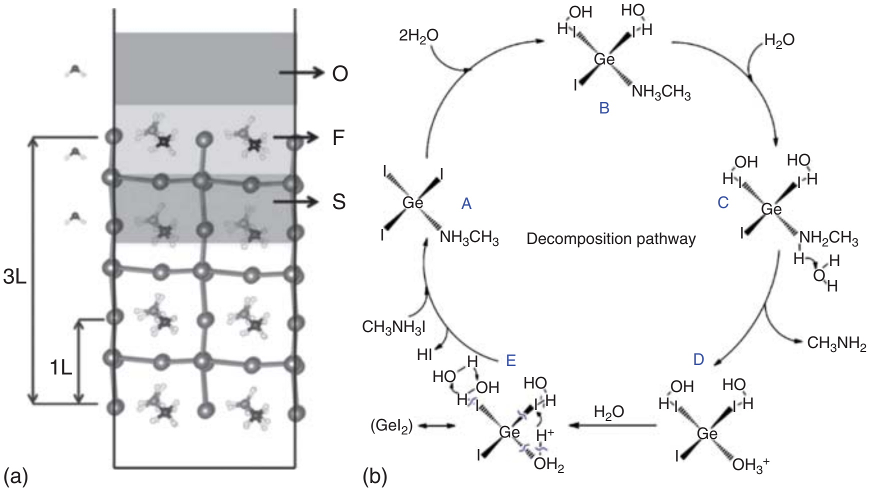

Figure 2.4.8 (a) The structure of the three-layer (101) $MAGeI_3$ surface slab with possible locations of adsorbed H_2O. (b) The decomposition pathway for one $MAGeI_3$ molecule under water attack. Source: Sun et al. 2016 [43]. Reproduced with permission of PCCP Owner Societies.

intermolecular hydrogen bonding becomes stronger, resulting in a decrease in the hydrogen bond strength between H_2O molecules and MA^+ cations of the perovskite, corresponding to a greater adsorption energy. However, to degrade the perovskite completely, the water molecule needs to diffuse first through the dangling bond region (region F in Figure 2.4.8a). The energy of one water molecule inside the dangling bond region was found to be much lower than the adsorption energy with an activation barrier as little as 0.09 eV. As a consequence, water molecules are most likely to stay inside that region and the adsorption on the surface can proceed in the forward direction easily. For further penetration inside the $MAGeI_3$ crystal, the water molecule then needs to pass through the I–Ge–I inorganic network (region S in Figure 2.4.6). The energy barrier for that transition state was found to be 0.43 eV, which is still quite small. Based on their calculation, the authors proposed the following mechanism (Figure 2.4.8b):

1. The degradation of $MAGeI_3$ starts as soon as the inorganic network of GeI_2 begins to be damaged by hydration of the phase.

   $$\mathrm{nMAGeI_3 + NH_2O \rightarrow (MAGeI_3)_{\mathit{n}} \cdot NH_2O \rightarrow (MA)_4GeI_6 \cdot 2H_2O}$$

   The hydrated phase exists for $N \leq 2$.
2. As soon as another water molecule is adsorbed, the perovskite surface starts degrading with release of CH_3NH_2 gas.

   $$\begin{aligned}&\mathrm{(MAGeI_3)_{\mathit{n}} \cdot NH_2O + H_2O \rightarrow (MA)_{\mathit{n}-1}(GeI_3)_{\mathit{n}} \cdot (H_2O)_{\mathit{m}} \cdot (H_3O^+)}\\&\quad \mathrm{+\, CH_3NH_2} \uparrow\end{aligned}$$

3. With increasing number of water molecules on the surface, the Ge—I bonds start to break due to stronger H-binding with I^- anion.
4. The new hydrate generated in step 2 will continue to degrade with the release of HI

   $$\begin{aligned}&\mathrm{(MA)_{\mathit{n}-1}(GeI_3)_{\mathit{n}}(H_2O)_{\mathit{m}} \cdot (H_3O^+) + H_2O \rightarrow HI + GeI_2}\\&\quad \mathrm{+\, (MAGeI_3)_{\mathit{n}-1} \cdot \mathit{m}'H_2O}\end{aligned}$$

5. In humid atmosphere, the continuous adsorption of the water molecule will continue the release of CH_3NH_2, resulting in the degradation of the perovskite.

2.4.2.4 Bismuth/Antimony-Based Perovskites

The excellent optoelectronic properties of lead-based halide perovskites is often linked with the presence of $6s^2$ lone pair electrons. Group 15 elements, especially Bi^{3+} and Sb^{3+}, also possess an electronic structure similar to that of Pb^{2+} due to which similar optoelectronic properties are expected. Since these elements exist in the stable +3 oxidation state, it is difficult to accommodate Bi^{3+} or Sb^{3+} inside the conventional AMX_3 perovskite structure. Previous studies on Bi/Sb-based ternary halide compounds had mostly focused on single-crystal properties, ferroelectricity, phase transformations, and nonlinear optical properties [44]. Recently, the interest in these compounds has been renewed due to their potential applications in PVs. The electronic structure calculations for Bi- and Sb-based ternary halides have shown remarkable similarities in band edge characteristics to that of Pb-based halide perovskites [45]. Contrary to conventional semiconductors such as Si or GaAs, the CBM and VBM of $[PbI_6]^{4-}$ cluster are antibonding in nature, contributed by the partially oxidized Pb^{2+} cation and Pb—I antibonding orbital, respectively [46]. For the Bi/Sb-based ternary halide perovskite, a similar VBM nature is expected due to lone pair $6s^2$ electrons [47]. The contribution of A^+ cation on VBM and CBM is also negligible as the band edges are formed by the Sb/Bi—I bonding. Analogous observations can also be found for conventional Pb-halide perovskites, where the influence of +1 cation is negligible on the VBM and CBM characteristics [48]. So the electronic structures of inorganic Bi/Sb-based ternary halides can represent the family justly. The valence band of $Cs_3Sb_2I_9$ is mainly contributed by the p orbital of I and partly by Sb(s). These antibonding characteristics of VBM are expected to suppress the valence-band-derived states such as cation vacancies. The nature of the CBM, on the other hand, is quite different and is dependent on the crystal structure (dimer or layered). For example, the electronic structure of $Cs_3Bi_2I_9$ and $Cs_3Sb_2I_9$ dimer phase exhibits remarkable similarities as both possess indirect bandgap and similar conduction band features. While conduction band is mostly Pb(p)/Sb(p) characteristics in Pb-based and Sb-based ternary halides (layered structure), respectively, a mixture of I(p) and Bi(p)/Sb(p) orbitals dominates the CBM of dimer $Cs_3Bi_2I_9/Cs_3Sb_2I_9$. The p-orbital characteristics of both valence and conduction bands lead to high joint density of states, resulting in an unusually large absorption coefficient for both Bi- and Sb-based ternary halides. Although the layered structure of $Cs_3Sb_2I_9$ is more promising in terms of optoelectronic properties than in its dimer structure, the latter is more favorable to form under normal processing conditions. However, one possible way to solve the problem is to replace Cs with smaller cations. For example, $Rb_3M_2I_9$ ($M = Sb^{3+}$, Bi^{3+}) essentially forms the layered structure even under normal processing conditions and exhibits better optoelectronic properties than the homologous dimer structure [49]. The electronic structure calculations further reveals a flat band structure for both the Sb- and Bi-based dimer phase, which can be attributed to the heavy effective mass of the carriers [47, 50]. In addition, Sb- and Bi-based ternary halide compounds have lower crystal symmetry as compared to Pb-based halide perovskite, which leads to anisotropic charge transfer. In addition, most of the intrinsic defects (except Cs vacancy and interstitial Cs) in $Cs_3Sb_2I_9$ form deep level states in the bandgap which can act as non-radiative recombination centers in optoelectronic applications. This could be explained on the basis of the orbital characteristics of the compound. The Sb p orbital is more localized than the Pb p orbital, resulting in stronger Sb p–I p antibonding than the Pb p–I p antibonding, which in turn implies that the energy difference between the anion's p orbital and the CBM is larger for $Cs_3Sb_2I_9$ than for $CH_3NH_3PbI_3$.This results in mid-bandgap states of the donor defects. On the other hand, weaker s–p antibonding coupling is the primary reason for deep acceptor defects. In addition to that, defect characteristics also reveal the transition from p-type conductivity to n-type conductivity when the crystal growth conditions can be tuned from I-rich/Sb-poor to Sb-rich/I-poor conditions.

2.4.2.5 Double Perovskites: Hybrid Binary Metal Structures

Instead of a single divalent element, one monovalent and one trivalent element can replace two Pb^{2+} from the halide perovskite structure. The idea of double perovskites is not new, with the analogous oxide structures having been examined for a long time. Such atomic transmutation has been successful in even thin-film solar cell application such as the copper zinc tin sulfide (CZTS) systems. Following a similar strategy, a Pb-free halide perovskite family with the formula $A_2M^+M^{3+}X_6$ has received attention among the halide PV community. Giorgi and Yamashita [51] studied the $MATl_{0.5}Bi_{0.5}I_3$ and $MAIn_{0.5}Bi_{0.5}I_3$ based on DFT calculations and found striking similarities in electronic structure with Pb-based halide perovskites. The bandgaps of the compounds are 1.68 and 1.03 eV, respectively, as per PBE/PAW (projector augmented wave)-level calculations. More recently, successful synthesis of $Cs_2AgBiBr_6$ and $Cs_2AgBiCl_6$ enabled detailed theoretical understanding of these types of materials [52, 53]. The bandgap of the Bi-based halide double perovskites are quite similar to lead-based halide perovskites, however indirect in nature [53]. The valence band is composed primarily of the halogen p orbital and the conduction band formed by the antibonding of Ag 5s and Bi 6p states. The main problem is the admixture of Ag d orbital in the valence band, which is partially responsible for the indirect bandgap. Later, Zhao et al. [54] identified 11 potential halide double perovskites based on first-principles calculations. For the M^{3+} cation, Bi^{3+} and Sb^{3+} cations were considered due to the similar electronic structure as that of Pb^{2+}. For the M^+ cation, they considered group IA (Na^+, K^+, Rb^+)/group IB (Cu^+, Ag^+, Au^+)/group IIIA (In^+, Tl^+) elements (Figure 2.4.9). They used four criteria to screen the perovskite compounds such as decomposition enthalpy (>0), bandgap (0.8–2 eV), effective mass ($<1.0\ m_0$), and exciton binding energy (<100 meV). Out of all the combinations, they successfully found 11 optimal halide double perovskite compounds such as $Cs_2CuSbCl_6$, $Cs_2CuSbBr_6$, $Cs_2CuBiBr_6$, $Cs_2AgSbBr_6$, Cs_2AgSbI_6, Cs_2AgBiI_6, $Cs_2AuSbCl_6$, $Cs_2AuBiCl_6$, $Cs_2AuBiBr_6$, $Cs_2InSbCl_6$, and $Cs_2InBiCl_6$. Among these compounds, the first nine compounds exhibit indirect bandgap, while the bandgaps of the two In^+ based double perovskites are direct in nature. In a similar manner, Pb^{2+} and two I^- can be transmuted into one M^{3+} and one Ch^{2-} (chalcogenide) anions, leading to $I–III–VI–VII_2$ structure. Sun et al. [55] calculated the electronic band structure of Bi- and Sb-based chalcogenide-halide perovskites and found that these compounds are promising PV materials in terms of bandgap. However, subsequent reports indicate that none of these materials are thermodynamically stable as they will be prone to decomposition into other binary or ternary phases [56].

2.4.3 Experimental Efforts in Pb-Free Perovskite Photovoltaics

Most of the efforts to replace lead in perovskite halides were focused on elements in the same group or adjacent groups such as Sn, Ge, Bi, and Sb assuming that

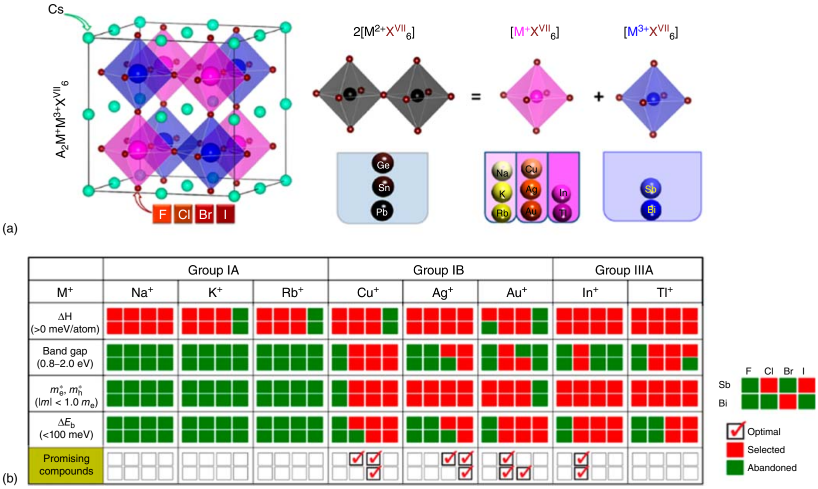

	Group IA			Group IB			Group IIIA	
M^+	Na^+	K^+	Rb^+	Cu^+	Ag^+	Au^+	In^+	Tl^+
ΔH (>0 meV/atom)	🟥🟥🟥🟥 🟥🟥🟥🟥	🟥🟥🟥🟩 🟥🟥🟥🟩	🟥🟥🟥🟩 🟥🟥🟥🟩	🟥🟥🟥🟩 🟥🟥🟥🟩	🟥🟥🟥🟥 🟥🟥🟥🟥	🟥🟥🟥🟩 🟩🟥🟥🟩	🟥🟥🟥🟥 🟥🟥🟥🟥	🟥🟥🟥🟥 🟥🟥🟥🟥
Band gap (0.8–2.0 eV)	🟩🟩🟩🟩 🟩🟩🟩🟩	🟩🟩🟩🟩 🟩🟩🟩🟩	🟩🟩🟩🟩 🟩🟩🟩🟩	🟩🟥🟥🟥 🟩🟥🟥🟥	🟩🟩🟥🟥 🟩🟩🟩🟥	🟩🟥🟩🟩 🟩🟥🟥🟩	🟩🟥🟩🟩 🟩🟥🟩🟩	🟩🟥🟥🟥 🟩🟥🟥🟩
m_e^*, m_h^* ($\|m\| < 1.0\ m_e$)	🟩🟩🟩🟩 🟩🟩🟩🟩	🟩🟩🟩🟩 🟩🟩🟩🟩	🟩🟩🟩🟩 🟩🟩🟩🟩	🟩🟥🟥🟥 🟩🟥🟥🟥	🟥🟥🟥🟥 🟥🟥🟥🟥	🟥🟥🟥🟩 🟥🟥🟥🟩	🟥🟥🟥🟥 🟥🟥🟥🟥	🟥🟥🟥🟥 🟥🟥🟥🟥
ΔE_b (<100 meV)	🟩🟩🟩🟩 🟩🟩🟩🟩	🟩🟩🟩🟩 🟩🟩🟩🟩	🟩🟩🟩🟩 🟩🟩🟩🟩	🟩🟥🟥🟥 🟩🟩🟥🟥	🟩🟩🟥🟥 🟩🟩🟩🟥	🟩🟥🟥🟥 🟩🟥🟥🟥	🟩🟥🟥🟥 🟩🟥🟥🟥	🟩🟩🟥🟥 🟩🟩🟥🟥
Promising compounds	☐☐☐☐ ☐☐☐☐	☐☐☐☐ ☐☐☐☐	☐☐☐☐ ☐☐☐☐	☐☑☑☐ ☐☐☑☐	☐☐☑☑ ☐☐☐☑	☐☑☐☐ ☐☑☑☐	☐☑☐☐ ☐☑☐☐	☐☐☐☐ ☐☐☐☐

	F	Cl	Br	I
Sb	🟩	🟥	🟩	🟥
Bi	🟩	🟩	🟥	🟩

☑ Optimal
🟥 Selected
🟩 Abandoned

Figure 2.4.9 (a) Space of candidate $A_2M^+M^{3+}X_6$ perovskites for materials screening: left panel shows adopted double-perovskite structure, and right panel shows schematic idea of atomic transmutation. (b) Materials screening process by considering gradually the properties relevant to photovoltaic performance, i.e. decomposition enthalpy (ΔH), bandgap, carrier effective masses (m_e*, m_h*), and exciton binding energy (ΔE_b). The red squares mean the materials passing the screening (selected) and the green ones mean not passing (abandoned). The optimal nontoxic $A_2M^+M^{3+}X_6$ perovskites satisfying all the criterions are marked with red checks. Source: Zhao et al. 2017 [54]. Copyright 2017. Adapted with permission of American Chemical Society.

similar electronic configurations will lead to similar optoelectronic properties. Suitable oxidation states, ionic sizes, and the presence of ns^2 electrons which result in the defect-tolerant properties of lead are the major criteria in the search for the replacements.

2.4.3.1 Sn^{2+} and Ge^{2+} as Replacements for Pb^{2+}

As discussed earlier, tin with an electronic configuration [Kr] $4d^{10}$ $5s^2$ $5p^2$ is very similar to lead and hence was considered first as its most potential replacement. The first report on tin-based perovskites in a solar cell was on $CH_3NH_3SnI_3$ with an efficiency of 6.4% [18a] formed by spin coating SnI_2 and CH_3NH_3I in dimethylformamide (DMF) in an inert atmosphere. The device exhibited a reasonable open circuit voltage of 0.88 V considering its low bandgap of 1.23 eV. However, these were very unstable in air due to oxidation of +2 Sn to +4 states, resulting in a large spread in the device efficiencies with much of the solar cells showing very low power conversion efficiencies. The presence of +4 Sn also resulted in variable self-doping of the material, resulting in a high hole-doping density of $\sim 10^{18}$ cm^{-3}. The recombination with these self-doped carriers limited the diffusion lengths to only 30 nm, significantly lower than $MAPbI_3$. It was suggested that reducing these background carriers could be an effective strategy to improve the performances by improving the diffusion lengths. Another interesting development in the area of Sn perovskites was the use of a mixed metal cation with lead ($CH_3NH_3Pb_{1-x}Sn_xI_3$) [57]. This resulted in anomalous behavior, with the mixed perovskite exhibiting a bandgap lower than either the pure Pb- or Sn-based perovskites, thus extending the absorption range to near infrared (1050 nm). In another work, the same group investigated the possibility of a mixed halide Sn perovskite – $MASnI_{3-x}Br_x$ [18b] – in order to tune the bandgap of the material. The highest power conversion efficiency realized was 5.73% for $CH_3NH_3SnIBr_2$.

The first report on fully inorganic Sn-based perovskite was on $CsSnI_3$ [31] with a power conversion efficiency of 2.02%. It was found that the pristine $CsSnI_3$ exhibited very poor PV performance due to the presence of Sn vacancies. These tin vacancies were passivated by addition of 20% SnF_2 to attain good PV performance. This was also reflected in the reduction of carrier density of 10^{19} cm^{-3} in pristine sample to 10^{17} cm^{-3} with 20% SnF_2 addition. The excess SnF_2 increases the Sn chemical potential, leading to increase in formation energy of Sn vacancies and a decreased concentration of these defects. The background carrier density of 10^{17} cm^{-3} is still very high compared to $CH_3NH_3PbI_3$ (with carrier densities of 10^9–10^{11} cm^{-3}), which could be the reason for the limited V_{oc} of 240 mV in the champion device. Higher open circuit voltages were obtained by opening up the bandgap through halide substitution, although power conversion efficiencies were still limited [58]. The bandgap of $CsSnI_{1-x}Br_x$ was tuned between 1.27 and 1.75 eV (Figure 2.4.10a) with a reduction in charge carrier densities to 6.3×10^{15} cm^{-3} for $CsSnIBr_2$. Another strategy to tune the bandgap of the Sn perovskite is to change the A cation. Formamidinium-based Sn perovskites crystallize in an orthorhombic (*Amm2*) crystal structure and exhibit a slightly higher bandgap of 1.41 eV, which is close to the optimum value for single-junction solar

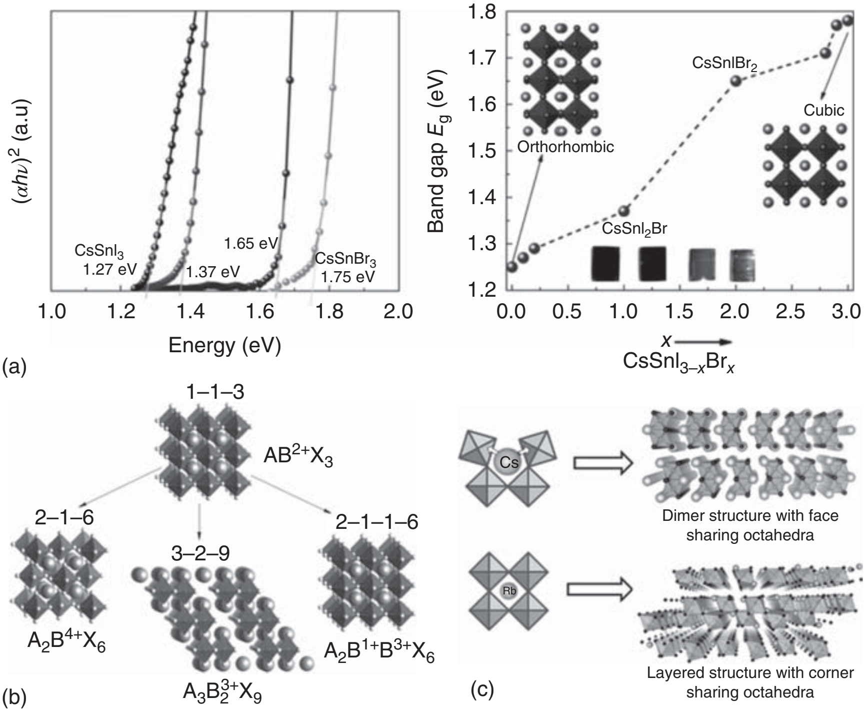

Figure 2.4.10 (a) Viability of tuning the bandgap of lead-free perovskites by anion mixing. Source: Sabba et al. 2015 [58]. Copyright 2015. Adapted with permission of American Chemical Society. (b) Strategies to develop lead-free halide perovskites. Source: Giustino and Snaith 2016 [59]. Copyright 2016. Adapted with permission of American Chemical Society. (c) Structural variants existing within the $A_3M_2X_9$ composition. Source: Harikesh et al. 2016 [49]. Copyright 2016. Adapted with permission of American Chemical Society.

cells. $FASnI_3$-based solar cells were fabricated with an efficiency of 2.1% [60] by again utilizing the SnF_2 addition to reduce tin vacancies. However, the low solubility of SnF_2 in DMF resulting in phase separation is a limiting factor to achieve higher voltage. Another report on the same material suggests that the solubility of SnF_2 in DMF can be improved by addition of pyrazine [61], which can form a complex with SnF_2. This avoids phase separation and yielded perovskite films with full coverage on TiO_2, improving the efficiency to 4.8%.There are also reports on Cs- and FA-based Sn perovskites on inverted architectures, albeit with lower efficiencies [62]. In addition to the challenges rendered by tin oxidation, morphology control of these tin halide perovskites is challenging. The rapid crystallization of the Sn perovskite with DMF as solvent limits the ability to form pinhole-free film by spin coating and limiting the open circuit voltage. A systematic study of various solvents (DMF, dimethyl sulfoxide (DMSO), *N*-methylpyrollidone (NMP)) suggested that DMSO could be a better alternative to the commonly used DMF [63] in obtaining higher quality films. The reason is the ability to coordinate strongly to the SnI_2, forming an adduct of formula $SnI_2{\cdot}3DMSO$. This adduct allows the MAI ions to react with SnI_2 in a controlled manner limited by the rate of DMSO removal to obtain controlled crystallization and uniform coverage.

Moving even further up in the group of the periodic table, the smaller Germanium was also investigated as a potential candidate to form perovskites with PV properties. $CsGeI_3$, $MAGeI_3$, and $FAGeI_3$ exhibit a bandgap of 1.63, 2.0, and 2.35 eV, respectively [64]. All of them crystallize in rhombohedral symmetry at room temperature. However, solar cells of $CsGeI_3$ and $MAGeI_3$ suffered from a very low V_{oc} of 74 and 150 mV, respectively, restricting the efficiencies to 0.11% and 0.2% only. Germanium is even more unstable compared to Sn and gets easily oxidized to the +4 state, which is the reason for the poor performance. The problem is aggravated by its poor solubility in polar solvents, which restricts good film formation.

Most of the research on lead replacement was focused on Sn or Ge in the same group. However, it is known that the inert pair effect responsible for the stability of the +2 state of lead reduces as we move up in the group. Thus, Sn^{2+} and Ge^{2+} are very unstable and gets oxidized to +4 ions. These +4 ions can act as traps leading to recombination and hence limit the performances. Furthermore, reports show that Sn perovskites can be even more toxic compared to lead due to its potential oxidation to the +4 oxidation state releasing HI into the environment [65]. This necessitated expanding the search to other group elements and other perovskite derivatives as well.

2.4.3.2 A_2SnX_6 as a Stable Alternative to $ASnX_3$

The use of tetravalent Sn is a strategy to enhance the stability of the Sn perovskite. However, a +4 Sn can only form compounds of structure A_2SnX_6, which is considered a 0D perovskite structure with isolated $(SnI_6)^{2-}$ octahedra (Figure 2.4.10b) [59]. There are several reports utilizing Cs_2SnI_6 as a hole-transporting material in dye-sensitized solar cells due to its exceptional p-type conductivity [36, 66]. However, the reports on the bandgap, carrier densities, mobility, and type of charge carriers are still inconclusive, as shown in Table 2.4.1. It is claimed that the pristine material is n-type and the reported p-type behavior is caused by doping with Sn^{2+}. Nevertheless, the optimum bandgap of 1.3–1.6 eV of the material makes it interesting as an absorber for solar cells. The only report (so far) of Cs_2SnI_6 as a solar cell absorber material is by utilizing ZnO nanorods as electron-transporting layer and

Table 2.4.1 Reported optoelectronic characteristics of Cs_2SnI_6.

References	Bandgap (eV)	Carrier density (cm^{-3})/type	Mobility ($cm^2\ V^{-1}\ s^{-1}$)
Lee et al. [36]	1.3 (direct)	1×10^{14} (n)	310
Lee et al. [36]	1.3 (direct)	1×10^{14} (p)	42
Saparov et al. [37]	1.6 (direct)	6×10^{16} (n)	2.9

poly(3-hexylthiophene-2,5-diyl) (P3HT) as hole transporting material (HTM) reaching an efficiency ~1% [67].

2.4.3.3 Cu^{2+}: an Alternative Divalent Metal Cation

If one excludes group 14 elements, the next alternatives are the transition metals due to their ability to form +2 oxidation states essential for AMX_3 halide perovskite structures. However, the small size of the transition metal cations limits their ability to form corner-sharing structures. Instead, most of them form linear chains of face-sharing octahedra which might seriously affect the charge transport in these class of compounds. In addition, most of the transition metal halides are moisture sensitive as well. However, one alternative is to form 2D perovskites of the structure A_2MX_4 exhibited by metal ions such as Cu^{2+}, Ni^{2+}, Co^{2+}, Fe^{2+}, etc. Some research groups have investigated 2D perovskites of Cu for application in solar cells due to their stable +2 oxidation state in aerobic environment and good absorption in visible region. A detailed analysis of the copper perovskites of the structure $(CH_3NH_3)_2CuCl_xBr_{4-x}$ revealed that the presence of Cl is essential to stabilize the system against copper reduction and enhance crystallization [1a]. In addition, changing the Br/Cl ratio helped tune the absorption within the visible to near-infrared range. However, the solar cells fabricated were limited by low V_{oc} and short circuit current densities. The low absorption coefficient and the heavy mass of the holes arising from the layered nature of the material were found to be the reasons for this poor performance. In addition, the paper also discussed the probability of Cu^+ formation, which could act as potential traps. Copper-based 2D perovskites of the structure: $(p\text{-}F\text{-}C_6H_5C_2H_4\text{-}NH_3)_2CuBr_4$, and $(CH_3(CH_2)_3NH_3)_2CuBr_4$ [68] were also demonstrated as solar cell absorbers albeit with very low efficiencies.

The poor performance of copper perovskites may also be due to the absence of the outer ns^2 electrons, which provide the defect tolerance and the dispersive valence band in case of lead. Thus, a more logical strategy is to search for compounds with outer ns^2 electrons. This necessitates looking for elements with other oxidation states as well rather than confining to +2.

2.4.3.4 Bi^{3+} and Sb^{3+}: Toward Trivalent Metal Cations

As discussed earlier, Bi^{3+} and Sb^{3+} which have electronic configuration similar to that of Pb^{2+} are other viable alternatives. The presence of ns^2 electrons must also equip them with the defect-tolerant property of lead. However, the +3 state constrains their ability to form a 3D corner-sharing perovskite structure. Instead, they form $A_3Sb_2X_9$ compounds with a dimer structure (with fused bi-octahedron) or a layered structure (with corner-sharing octahedron).The first report on bismuth-based perovskite was on $Cs_3Bi_2I_9$ with an efficiency of ~1% [69]. The material consisted of fused bi-octahedral $(Bi_2I_9)^{3-}$ clusters surrounded by Cs atoms. It is claimed to be nontoxic and was reported to be stable over a month, with no noticeable reduction in efficiency when stored at humidity less than 10%. The PL and PV performance of $MA_3Bi_2I_9$ was found to be very low compared to $Cs_3Bi_2I_9$ consistent with the other reports on $MA_3Bi_2I_9$ solar cells with a low efficiency of 0.19% [70]. $MA_3Bi_2I_9$ exhibited p-type conductivity with a carrier density of 10^{16} cm^{-3} and mobility of 1 cm^2 V^{-1} s^{-1}. This high background carrier density was suspected to have contributed to bulk recombination, leading to a low V_{oc} of 0.35 V. Other reports attribute the lower performance to poor morphology of the $MA_3Bi_2I_9$ layer, with the efficiency influenced by the underlying mesoporous TiO_2 layer [71]. The devices made on anatase TiO_2 mesoporous layer showed better performance than those on a mesoporous brookite TiO_2 layer or a planar architecture. A detailed material study on $MA_3Bi_2I_9$ [72] suggested that post treatment with pyridine can improve the PL lifetime of the material possibly by passivation of under-coordinated bismuth ions on the surface. A maximum PL lifetime of 0.76 ns was achieved, depending on the processing technique adopted. This is encouraging because materials with <1 ns lifetimes have been reported to achieve efficiencies close to 10% [73]. Interestingly, double perovskites of the formula $Cs_2AgBiBr_6$ exhibited extraordinary PL lifetimes of 660 ns, which are on par with $MAPbI_3$, substantiating the defect-tolerant property of bismuth. In addition, the compound was found to exhibit extraordinary stability in moisture and light exposure even after one month. However, the presence of Ag seriously inhibits the solution processability of the material. The potential of bismuth halides as potential replacement is also corroborated by the $AgBi_2I_7$ solar cells with efficiency of 1.22% [74] and BiI_3-based solar cells with efficiency of 0.3% [75, 76].

There are also reports of $A_3M_2X_9$ structures based on Sb as viable PV materials. However, the highest efficiency reported till date is only 0.5% with $MA_3Sb_2I_9$ as absorber [77]. It is claimed that the layered structure of $A_3Sb_2I_9$ should exhibit better optoelectronic properties compared to the dimer form from first-principles calculations [47]. However, the lack of solution processability of the structure is a bottleneck to its formation. In addition, the material is also susceptible to various defects which can induce deep traps, limiting the PV performance. A smaller cation like Rb was found to template the formation of the layered phase even via a solution process [49] (Figure 2.4.10c). However, the presence of deep defects possibly limited the device performance. Thus, a strict control over the stoichiometry using optimum fabrication conditions will be necessary to obtain good performance with these classes of compounds (Table 2.4.2).

2.4.4 Concluding Remarks and Outlook

The conventional highly efficient $MAPbI_3$ perovskite mainly suffers from moisture instability and bioaccumulative toxicity, which may eventually restrict the commercialization of this technology. The moisture stability issue in the current 3D $MAPbI_3$ perovskite would be addressed by utilizing multidimensional perovskites containing bulkier hydrophobic organic cations, avoiding contact between water molecules and perovskite surface. Although the moisture stability could be greatly enhanced, the potential drawback in multidimensional perovskites will be its charge transport within the perovskite due to the presence

Table 2.4.2 Highest reported photovoltaic characteristics of lead-free halides.

Material	Device architecture	η (%)	J_{sc} (mA cm^{-2})	V_{oc} (V)	FF
$MASnI_3$ [18a]	FTO/bl-TiO_2/TiO_2/$MASnI_3$/HTM/Au	6.4	16.8	0.88	0.42
$CsSnI_3$ [31]	FTO/bl-TiO_2/TiO_2/$CsSnI_3$/HTM/Au	2.02	22.7	0.24	0.37
$FASnI_3$ [61]	FTO/bl-TiO_2/TiO_2/$FASnI_3$/HTM/Au	4.8	23.7	0.32	0.63
Cs_2SnI_6 [67]	FTO/bl-ZnO/ZnO-NR/Cs_2SnI_6/P3HT/Ag	0.86	3.2	0.52	0.52
$MAGeI_3$ [64]	FTO/bl-TiO_2/TiO_2/$CsGeI_3$/HTM/Au	0.20	4.0	0.15	0.30
$Cs_3Bi_2I_9$ [69]	FTO/bl-TiO_2/TiO_2/$Cs_3Bi_2I_9$/HTM/Au	1.0	2.15	0.85	0.60
$MA_3Bi_2I_9$ [71]	FTO/bl-TiO_2/TiO_2/$MA_3Bi_2I_9$/HTM/Au	0.25	0.83	0.56	0.48
$AgBi_2I_7$ [74]	FTO/bl-TiO_2/TiO_2/$AgBi_2I_7$/P3HT/Au	1.22	3.3	0.56	0.67
Ag_2BiI_5 [78]	FTO/bl-TiO_2/TiO_2/Ag_2BiI_5/P3HT/Au	2.1	6.8	0.49	0.63
BiI_3 [76]	FTO/bl-TiO_2/TiO_2/BiI3/PIDT-DFBT/Au	0.32	1.7	0.42	0.45
$MA_3Sb_2I_9$ [77]	ITO/PEDOT:PSS/$MA_3Sb_2I_9$/$PC_{61}BM$/ZnO-NP/Al	0.49	1.0	0.89	0.55
$Rb_3Sb_2I_9$ [49]	FTO/bl-TiO_2/TiO_2/$Rb_3Sb_2I_9$/Poly-TPD/Au	0.66	2.11	0.55	0.57

FTO, fluorine doped tin oxide; ITO, indium tin oxide; NR, nanorod; PEDOT, poly(3,4-ethylenedioxythiophene); PSS, polystyrene sulfonate; NP, nanoparticle; TPD, [*N*,*N*′-bis(4-butylphenyl)-*N*,*N*′-bisphenylbenzidine].

of insulating organic layers. Future research on molecular and device engineering in improving ambient stability without inhibiting charge conduction in multidimensional perovskites will be the main challenge in this field. On the other hand, most of the efforts in looking for toxic Pb replacement were focused on the same group 14 elements (mainly Sn). However, Sn^{2+} may not be a viable alternative considering the instability of +2 cation and the associated toxicity. The focus of research has recently shifted to $A_3M_2X_9$ structures with +3 metal ions like Bi^{3+} and Sb^{3+}. However, the +3 oxidation state limits the formation of 3D corner-sharing structure and corresponding device performances. More environment-friendly Pb-free perovskites should be studied theoretically and experimentally in order to achieve a better fundamental understanding on optoelectronics, which helps in designing a good Pb-free perovskite for PVs. Thus, expanding the research to other halide structures based on these elements rather than confining to the perovskite structure may also prove to be a better strategy for further research.

References

1 (a) Cortecchia, D., Dewi, H.A., Yin, J. et al. (2016). *Inorg. Chem.* 55: 1044. (b) Egger, D.A., Rappe, A.M., and Kronik, L. (2016). *Acc. Chem. Res.* 49: 573. (c) Goldschmidt, V.M. (1926). *Naturwissenschaften* 14: 477.

2 Kim, H.S., Im, S.H., and Park, N.G. (2014). *J. Phys. Chem. C* 118: 5615.

3 Stoumpos, C.C., Cao, D.H., Clark, D.J. et al. (2016). *Chem. Mater.* 28: 2852.

4 (a) Beznosikov, B.V. and Aleksandrov, K.S. (2000). *Crystallogr. Rep.* 45: 792. (b) Ruddlesden, S.N. and Popper, P. (1958). *Acta Crystallogr.* 11: 54. (c) Schaak, R.E. and Mallouk, T.E. (2002). *Chem. Mater.* 14: 1455.

5 Gonzalez-Carrero, S., Galian, R.E., and Perez-Prieto, J. (2015). *Part. Part. Syst. Char.* 32: 709.

6 Koh, T.M., Shanmugam, V., Schlipf, J. et al. (2016). *Adv. Mater.* 28: 3653.

7 Liu, Y., Xiao, H., and Goddard, W.A. (2016). *Nano Lett.* 16: 3335.

8 Chondroudis, K. and Mitzi, D.B. (1999). *Chem. Mater.* 11: 3028.

9 Yuan, M., Quan, L.N., Comin, R. et al. (2016). *Nat. Nanotechnol.* doi: 10.1038/nnano.2016.110.

10 (a) Giovanni, D., Chong, W.K., Dewi, H.A. et al. (2016). *Sci. Adv.* 2: e1600477. (b) Chong, W.K., Thirumal, K., Giovanni, D. et al. (2016). *Phys. Chem. Chem. Phys.* 18: 14701.

11 Quan, L.N., Yuan, M., Comin, R. et al. (2016). *J. Am. Chem. Soc.* 138: 2649.

12 Yao, K., Wang, X., Li, F., and Zhou, L. (2015). *Chem. Commun.* 51: 15430.

13 Smith, I.C., Hoke, E.T., Solis-Ibarra, D. et al. (2014). *Angew. Chem. Int. Ed.* 53: 11232.

14 Cao, D.H., Stoumpos, C.C., Farha, O.K. et al. (2015). *J. Am. Chem. Soc.* 137: 7843.

15 Yang, S., Wang, Y., Liu, P. et al. (2016). *Nat. Energy* 1: 15016.

16 Yao, K., Wang, X., Xu, Y.-x. et al. (2016). *Chem. Mater.* 28: 3131.

17 Hu, Y., Schlipf, J., Wussler, M. et al. (2016). *ACS Nano* 10: 5999.

18 (a) Noel, N.K., Stranks, S.D., Abate, A. et al. (2014). *Energy Environ. Sci.* 7: 3061. (b) Hao, F., Stoumpos, C.C., Cao, D.H. et al. (2014). *Nat. Photonics* 8: 489. (c) Stoumpos, C.C., Malliakas, C.D., and Kanatzidis, M.G. (2013). *Inorg. Chem.* 52: 9019.

19 Krishnamoorthy, T., Ding, H., Yan, C. et al. (2015). *J. Mater. Chem. A* 3: 23829.

20 Chung, I., Song, J.-H., Im, J. et al. (2012). *J. Am. Chem. Soc.* 134: 8579.

21 Lang, L., Yang, J.-H., Liu, H.-R. et al. (2014). *Phys. Lett. A* 378: 290.

22 da Silva, E.L., Skelton, J.M., Parker, S.C., and Walsh, A. (2015). *Phys. Rev. B* 91: 144107.

23 Borriello, I., Cantele, G., and Ninno, D. (2008). *Phys. Rev. B* 77: 235214.

24 Atkins, P. (2010). *Shriver and Atkins' Inorganic Chemistry*. Oxford: Oxford University Press.

25 Parry, D.E., Tricker, M.J., and Donaldson, J.D. (1979). *J. Solid State Chem.* 28: 401.

26 Lefebvre, I., Lippens, P.E., Lannoo, M., and Allan, G. (1990). *Phys. Rev. B* 42: 9174.

27 Bose, S.K., Satpathy, S., and Jepsen, O. (1993). *Phys. Rev. B* 47: 4276.

28 Huang, L.-y. and Lambrecht, W.R.L. (2013). *Phys. Rev. B* 88: 165203.

29 Chen, Z., Yu, C., Shum, K. et al. (2012). *J. Lumin.* 132: 345.

30 Freysoldt, C., Grabowski, B., Hickel, T. et al. (2014). *Rev. Mod. Phys.* 86: 253.

31 Kumar, M.H., Dharani, S., Leong, W.L. et al. (2014). *Adv. Mater.* 26: 7122.

32 Stroppa, A., Di Sante, D., Barone, P. et al. (2014). *Nat. Commun.* 5: 5900.

33 Maughan, A.E., Ganose, A.M., Bordelon, M.M. et al. (2016). *J. Am. Chem. Soc.* 138: 8453.

34 Xiao, Z., Zhou, Y., Hosono, H., and Kamiya, T. (2015). *Phys. Chem. Chem. Phys.* 17: 18900.

35 Xiao, Z., Lei, H., Zhang, X. et al. (2015). *Bull. Chem. Soc. Jpn.* 88: 1250.

36 Lee, B., Stoumpos, C.C., Zhou, N. et al. (2014). *J. Am. Chem. Soc.* 136: 15379.

37 Saparov, B., Sun, J.-P., Meng, W. et al. (2016). *Chem. Mater.* 28: 2315.

38 Li-Chuan, T., Chen-Shiung, C., Li-Chuan, T., and Jung, Y.H. (2000). *J. Phys. Condens. Matter* 12: 9129.

39 Li-Chuan, T., Yia-Chung, C., Jung-Yau, H. et al. (2009). *Jpn. J. Appl. Phys.* 48: 112402.

40 Stoumpos, C.C., Frazer, L., Clark, D.J. et al. (2015). *J. Am. Chem. Soc.* 137: 6804.

41 Lu, X., Zhao, Z., Li, K. et al. (2016). *RSC Adv.* 6: 86976.

42 Sun, P.-P., Li, Q.-S., Feng, S., and Li, Z.-S. (2016). *Phys. Chem. Chem. Phys.* 18: 14408.

43 Sun, P.-P., Chi, W.-J., and Li, Z.-S. (2016). *Phys. Chem. Chem. Phys.* 18: 24526.

44 (a) Girnyk, I., Krupych, O., Martunyuk-Lototska, I. et al. *Ukr. J. Phys. Opt.* V4: 4. (b) Machulin, V., Motsnyi, F., Peresh, E.Y. et al. (2004). *Low Temp. Phys.* 30: 1283. (c) Motsnyi, F. (2010). Optical measurements of ferroelastics (Cs3Bi2I9): new phenomena and optical devices. Presented at 2010 International Conference on Advanced Optoelectronics and Lasers, Sevastopol, Ukraine, 10–14 Sept. 2010.

45 Lehner, A.J., Fabini, D.H., Evans, H.A. et al. (2015). *Chem. Mater.* 27: 7137.

46 Umebayashi, T., Asai, K., Kondo, T., and Nakao, A. (2003). *Phys. Rev. B* 67: 155405.

47 Saparov, B., Hong, F., Sun, J.-P. et al. (2015). *Chem. Mater.* 27: 5622.

48 Yin, W.-J., Yang, J.-H., Kang, J. et al. (2015). *J. Mater. Chem. A* 3: 8926.

49 Harikesh, P.C., Mulmudi, H.K., Ghosh, B. et al. (2016). *Chem. Mater.* 28: 7496.

50 Pazoki, M., Johansson, M.B., Zhu, H. et al. (2016). *J. Phys. Chem. C* 120: 29039.

51 Giorgi, G. and Yamashita, K. (2015). *Chem. Lett.* 44: 826.

52 (a) Slavney, A.H., Hu, T., Lindenberg, A.M., and Karunadasa, H.I. *J. Am. Chem. Soc.* 2016, 138: 2138. (b) Wei, F., Deng, Z., Sun, S. et al. (2017). *Chem. Mater.* 29: 1089. (c) Wei, F., Deng, Z., Sun, S. et al. (2016). *Mater. Horiz.* 3: 328.

53 McClure, E.T., Ball, M.R., Windl, W., and Woodward, P.M. (2016). *Chem. Mater.* 28: 1348.

54 Zhao, X.-G., Yang, J.-H., Fu, Y. et al. (2017). *J. Am. Chem. Soc.* 139: 2630.

55 Sun, Y.-Y., Shi, J., Lian, J. et al. (2016). *Nanoscale* 8: 6284.

56 Hong, F., Saparov, B., Meng, W. et al. (2016). *J. Phys. Chem. C* 120: 6435.

57 Hao, F., Stoumpos, C.C., Chang, R.P.H., and Kanatzidis, M.G. (2014). *J. Am. Chem. Soc.* 136: 8094.

58 Sabba, D., Mulmudi, H.K., Prabhakar, R.R. et al. (2015). *J. Phys. Chem. C* 119: 1763.

59 Giustino, F. and Snaith, H.J. (2016). *ACS Energy Lett.* 1: 1233.

60 Koh, T.M., Krishnamoorthy, T., Yantara, N. et al. (2015). *J. Mater. Chem. A* 3: 14996.

61 Lee, S.J., Shin, S.S., Kim, Y.C. et al. (2016). *J. Am. Chem. Soc.* 138: 3974.

62 (a) Zhang, M., Lyu, M., Yun, J.-H. et al. (2016). *Nano Res.* 9: 1570. (b) Marshall, K.P., Walton, R.I., and Hatton, R.A. (2015). *J. Mater. Chem. A* 3: 11631.

63 Hao, F., Stoumpos, C.C., Guo, P. et al. (2015). *J. Am. Chem. Soc.* 137: 11445.

64 Krishnamoorthy, T., Ding, H., Yan, C. et al. (2015). *J. Mater. Chem. A* 3: 23829.

65 Babayigit, A., Duy Thanh, D., Ethirajan, A. et al. (2016). *Sci. Rep.* 6: 18721.

66 Kaltzoglou, A., Antoniadou, M., Kontos, A.G. et al. (2016). *J. Phys. Chem. C* .

67 Qiu, X., Jiang, Y., Zhang, H. et al. (2016). *Phys. Status Solidi RRL* 10: 587–591.

68 Cui, X.-P., Jiang, K.-J., Huang, J.-H. et al. (2015). *Synth. Met.* 209: 247.

69 Park, B.W., Philippe, B., Zhang, X. et al. (2015). *Adv. Mater.* 27: 6806.

70 Lyu, M., Yun, J.-H., Cai, M. et al. (2016). *Nano Res.* 9: 692.

71 Singh, T., Kulkarni, A., Ikegami, M., and Miyasaka, T. (2016). *ACS Appl. Mater. Interfaces* 8: 14542–14547.

72 Hoye, R.L., Brandt, R.E., Osherov, A. et al. (2016). *Chem. Eur. J.* 22: 2605–2610.

73 Kranz, L., Gretener, C., Perrenoud, J. et al. (2014). *Adv. Energy Mater.* 4: 1301400.

74 Kim, Y., Yang, Z., Jain, A. et al. (2016). *Angew. Chem. Int. Ed.* 55: 9586.

75 Brandt, R.E., Kurchin, R.C., Hoye, R.L.Z. et al. (2015). *J. Phys. Chem. Lett.* 6: 4297.

76 Lehner, A.J., Wang, H., Fabini, D.H. et al. (2015). *Appl. Phys. Lett.* 107: 131109.

77 Hebig, J.-C., Kühn, I., Flohre, J., and Kirchartz, T. (2016). *ACS Energy Lett.* 1: 309–314.

78 Zhu, H., Pan, M., Johansson, M.B., and Johansson, E. (2017). *ChemSusChem* 10: 2592–2596.

2.5

Halide Perovskite Tandem Solar Cells

Teodor K. Todorov, Oki Gunawan, and Supratik Guha

IBM T.J. Watson Research Center,Department of Physical Science, 1101 Route 134 Kitchawan Road, Yorktown Heights, NY 10598, USA

2.5.1 Introduction

The current solar energy landscape is changing faster than ever. Commercial photovoltaic (PV) module prices are rapidly dropping, exceeding by far the targets of \$1/Wp that were considered aggressive even a few years ago [1]. Complete PV installations are attaining grid parity in many places – signaling the advent of a new era of consumer-driven renewable energy expansion. Land, inverters, frames, installation, and other auxiliary expenses today dominate PV system costs – consequently, the main cost-driving factor for solar energy becomes efficiency (typically 12–24% for commercial devices). Any gain in performance is therefore proportional to a price drop. However, neither crystalline silicon technology nor the continuously improving conventional thin-film technologies, including perovskites, are expected to reach eficiencies beyond the single-absorber Shockley–Queisser limit of 33% [2]. These technologies, which together account for almost all of the PV market, are based on single absorbers; and efficiencies beyond 30% so far have been accomplished only with tandem or multijunction devices comprising monolithically integrated and already highly efficient single juctions (more details on types of tandem devices are given later).

Many of the intriguing characteristics of perovskite materials that make them such an efficient PV absorber have been discussed elsewhere in this book. While achieving efficiencies that rival even the best commercial thin-film materials, two unique features of the perovskite materials make them particularly suited to efficient tandem devices. These are (i) high efficiency and a tunable bandgap between 1.48 and 2.3 eV and (ii) a low processing temperature (below 200 °C) which is crucial for preserving device integrity when building monolithic tandem cells. No other scaleable thin-film material to date possesses these characteristics that can bring high added value to many of the mainstream technologies already efficient at relatively low bandgap (e.g. crystalline silicon and copper–indium–gallium–selenide (CIGS)).

While the perovskite solar cells are very efficient, their long-term stability is of significant concern. Many factors have been shown to damage the perovskite

Halide Perovskites: Photovoltaics, Light Emitting Devices, and Beyond, First Edition.
Edited by Tze-Chien Sum and Nripan Mathews.

materials and devices including heat, ionic migration, and humidity, the last of which is likely the easiest to manage. Many efforts – some of which we review here – target minimizing performance deterioration and have shown initial promise. However, it is important to understand that until perovskites become capable of retaining their high performance for years under normal operation conditions, they cannot transition to large-scale manufacturing and may remain in the realm of exciting science.

2.5.2 Tandem Device Type and Performance Limitations

There are several energy loss factors in a real solar cell such as radiative recombination, relaxation, or thermalization to the band edges of above-the-bandgap photons, blackbody radiation, nonuniform solar spectrum, and various non-radiative recombination factors. A single-junction device has a maximum theoretical power conversion efficiency of 33.7% (at 1.34 eV bandgap, AM1.5G illumination). The majority of the losses are due to unabsorbed below-the-bandgap photons (~50%) and relaxation loss of the above-the-bandgap photons that are absorbed (~20%) [3]. These losses can be minimized in a tandem device solar cell that consists of a number of junctions with different bandgaps. The theoretical limit for a multijunction tandem solar cell can be calculated using a detailed balance limit calculation and yields 68.2% for an infinite multijunction solar cell [4] and 42% for a two-junction cell for 1 sun AM1.5G solar spectrum.

There are several types of tandem solar cells that have been studied in the literature that can be classified according to the number of junctions, their device materials, number of terminals, the number of transparent conducting electrode layers, and illumination type (e.g. direct illumination or spectrum-split illumination). In this chapter, we limit ourselves to a two-junction tandem cell. One useful classification scheme is to use a number of transparent conducting electrodes (TCEs) used in the device since this layer often imposes processing and performance bottlenecks. The TCE here includes transparent conducting oxides (TCOs) such as ZnO, ZnO:Al, In_2O_3:Sn, SnO_2:F, and other materials such as graphene, carbon nanotubes, and silver nanowires or thin metal films [5–8]. Another convenient classification scheme is to use a number of terminals. We classify tandem devices into the number of TCE layers involved and the number of terminals, as shown in Figure 2.5.1.

2.5.2.1 Single TCE/Two-Terminal (2-T) Monolithic Stack

This device consists of a monolithically integrated top and bottom cell with a single TCE layer on top and a recombination or tunneling layer in between. This configuration is attractive for commercial deployment due to its simplicity and compatibility with the series interconnect fabrication of standard modules. However, the performance is severely limited by two factors: (i) the current matching condition, i.e. the total current is limited by the junction with the lowest current

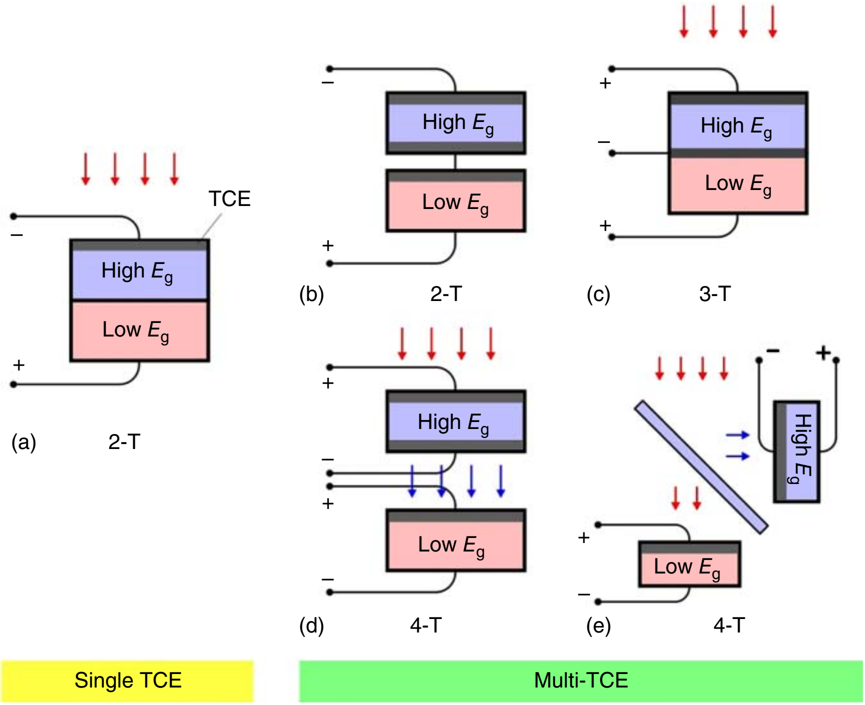

Figure 2.5.1 Classifications of two junction tandem solar cells based on the number of transparent conducting electrode (TCE) and contact terminals. (a) Single TCE: Single TCE, 2-T monolithic; and multi-TCE: multiple TCE layer. (b) 2-T mechanically stacked tandem. (c) 3-T monolithic tandem. (d) 4-T mechanically stacked tandem and (e) 4-T spectrum-split tandem. E_g is bandgap.

density, i.e. the top cell and (ii) fabrication, thermal processing, and choice of TCE layer constraint in monolithic tandem fabrication.

2.5.2.2 Multi-TCE/Two-Terminal (2-T) Mechanical Stack

The device consists of top and bottom cells that are serially connected and mechanically stacked on top of each other. This eliminates the need for the interfacial tunneling layer and the constraints of thermal processing – as both cells can be independently processed at their respective optimum condition. Unfortunately, this device requires three TCE layers (two of them for the top cell) and thus can result in severe optical losses.

2.5.2.3 Multi-TCE/Three-Terminal (3-T) Mechanical Stack

This device is essentially the same as the single TCE/two-terminal (2-T) device (monolithic stack) except there is a third terminal provided connecting the interfacial layer. The extra terminal relieves the device of the limiting current matching condition by adding a load resistor across either the top or the bottom junction.

This type of tandem is not common, but has been demonstrated in a-Si [9] and polymer solar cell [10].

2.5.2.4 Multi-TCE/Four-Terminal (4-T) Mechanical Stack

This is similar to the 2-T mechanical stack (Fig. 2.5.1b); however, each cell produces its own electrical output via two terminals and operates at its own maximum power point, thus producing a higher total output power. This type of perovskite tandem device has reached efficiencies of 26.4% [11, 12] and 22.1% [13] with perovskite-silicon and perovskite-CIGS tandems, respectively [8, 13].

2.5.2.5 Multi-TCE/Four-Terminal (4-T) Spectrum Split

Although similar to the previous four-terminal (4-T) device, a dichroic filter is used to split the light spectrum. This system only requires two TCE layers, thus reducing the optical loss. The disadvantages are the added cost of the filter, larger required space, and the extra complexity in the 4-T connection. This type of tandem has been demonstrated using perovskite and silicon heterojunction cells with a total projected efficiency of 28.0% [14].

To understand the impact of the different number of terminal configurations in a two-junction tandem cell, we can evaluate an idealized case of a tandem device consisting of a silicon bottom cell (E_g = 1.14 eV) and a top cell with a varying bandgap (E_{g_2}), as shown in Figure 2.5.2. Each cell operates at the Shockley–Queisser limit and we assume there are no parasitic losses such as optical losses (that reduce J_{sc}) of various layers except due to shadowing of the top cell or electrical resistive losses (that reduce fill factor (FF)). To account for the top cell shadowing loss, we assume 100% solar light absorption up to the band edge of the top cell.

The total theoretical efficiencies are calculated for each top cell bandgap for the case of 2-T and 4-T tandems. In the 4-T tandem device, each cell operates independently at its own maximum power point. As a result, it yields the highest

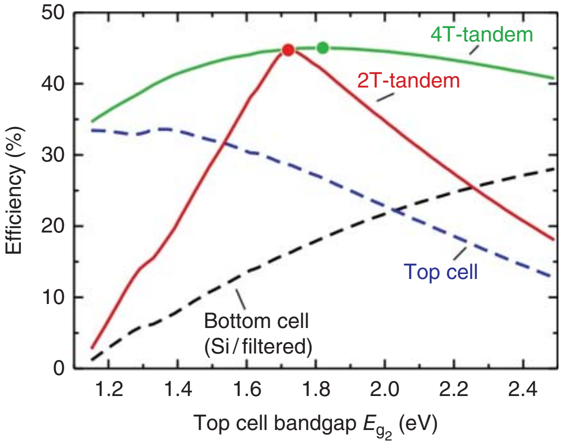

Figure 2.5.2 Idealized tandem cell efficiencies and the constituents as a function of top bandgap with different terminal connections. Source: Todorov et al. 2016 [15]. Reproduced with permission of Royal Society of Chemistry.

total efficiency of 45% at a top cell bandgap of 1.82 eV. In the 2-T tandem device, the current is limited by the cell with lower current (top cell) and the voltage is added in series. As a result, the efficiency profile strongly varies with respect to the top bandgap (E_{g_2}) with a peak performance of ~44% at $E_{g_2} = 1.72$ eV. Note that at this optimum bandgap, the 2-T tandem practically performs the same as the 4-T tandem, as both cells achieve the same current density (thus, there is no power loss due to current matching condition). A more detailed modeling in the Si-perovskite 2-T tandem cell yields an optimum bandgap value of 1.8 eV [15], not too far off from the 1.72 eV predicted via this simple model. We also observe that the optimum 2-T tandem cell performs at the same efficiency as the 4-T tandem counterpart, as it operates at a current matching condition. Furthermore, the maximum efficiency of the 2-T device (red dot) is almost the same as with the 4-T device (green dot).

A typical set of J–V curves of a CIGS-perovskite monolithic 2-T tandem cell is shown in Figure 2.5.3a together with the corresponding stand-alone bottom (CIGS) and top (perovskite) cell. We can also estimate the J–V curve of the tandem cell from the J–V characteristics of the top cell and the bottom cell *shadowed* with the top cell. This is plotted as a tandem (projected) curve (the dashed curve in Figure 2.5.3a). We note that the experimental tandem V_{oc} agrees well with the tandem (projected) V_{oc}, but the experimental J_{sc} is lower due to the use of aluminum TCE in the tandem cell (instead of the TCO/glass in the stand-alone perovskite device) [16].

A typical quantum efficiency (QE) loss analysis model in the tandem cell is shown in Figure 2.5.3b [16]. The perovskite (on top) contributes to short wavelength absorption (blue) in the range of 300–750 nm and the CIGS cell (at the bottom) contributes to the long wavelength absorption (red) to its band edge at ~1200 nm. Note that there is a small, residual QE response of the CIGS cell in

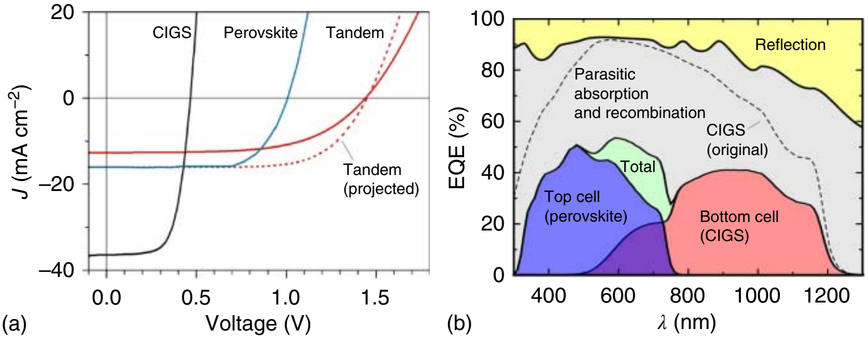

Figure 2.5.3 (a) J–V characteristics of a CIGS perovskite tandem cell and the stand-alone bottom and top cells (AM1.5G 1 sun). The dashed curve is the projected tandem J–V curve based on the bottom and top cell J–V. (b) Quantum efficiency loss model in a tandem perovskite-CIGS cell. The perovskite external quantum efficiency (EQE) is normalized to the measured tandem J_{sc} of 8.9 mA cm^{-2} [16]. The bottom cell (CIGS) EQE is measured on a stand-alone CIGS cell shadowed by the perovskite. The dashed curve is the EQE of the stand-alone CIGS cell. Source: Todorov et al. 2016 [16]. Reproduced with permission of John Wiley & Sons.

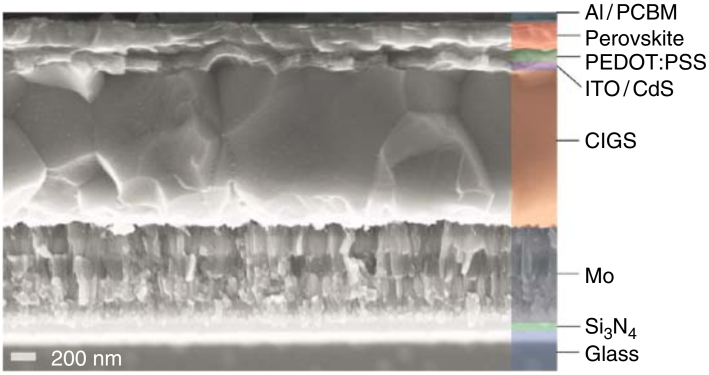

Figure 2.5.4 Cross-section scanning electron microscopic (SEM) image of the perovskite-CIGS tandem solar cell structure, Al/PCBM/perovskite/PEDOT:PSS/ITO/CdS/CIGS/Mo/Si_3N_4/glass. Source: Todorov et al. 2016 [15]. Reproduced with permission of Royal Society of Chemistry.

the perovskite absorption range from 500 to 750 nm due to the shadowing effect of the top cell. The total QE response of the tandem curve is shown as the green region. Another major absorption loss component (marked as a gray region) is due to the parasitic absorption at various additional layers such as the Al/PCBM layer on top of the perovskite; and poly(3,4-ethylenedioxythiophene) polystyrene sulfonate (PEDOT:PSS), CdS, indium tin oxide (ITO) in between the perovskite and the CIGS cells. Finally, there is reflection loss due to the top layer marked as the yellow region.

Here, we give an example of experimental device data used for the optimization of a monolithic tandem CIGS-perovskite monolithic tandem structure consisting of TCE/PCBM/perovskite/PEDOT:PSS/ITO/CdS/CIGS/Mo/Si_3N_4/glass (cross-section shown in Figure 2.5.4). [16]. Figure 2.5.5 shows device parameters of single-junction devices with varied bandgap perovskite absorbers as well as corresponding data points of low-bandgap (1.04 eV) CIGS solar cell shadowed by the perovskite. Increasing the perovskite bandgap results in increased light availability and, therefore, current of the shadowed cell, while the perovskite cell performance decreases at least in part due to narrower absorbed spectrum. The same figure shows the performance of the actual monolithic full tandem stacks fabricated with corresponding absorbers at the given bandgap showing a maximum at 1.72 eV, in close agreement with abovementioned calculations.

2.5.3 Perovskite Tandem Photovoltaic Device Research

The perovskites, as pointed out in the Introduction, successfully address two key challenges for single TCE solar cells: (i), achieving efficient high-bandgap top cells (especially difficult for inorganic PV materials such as CIGS) and (ii) avoiding processing incompatibilities such as junction deterioration resulting from high-temperature processes or other processes such as sputtering damage. Until recently no other PV devices, with the exception of III–V materials and

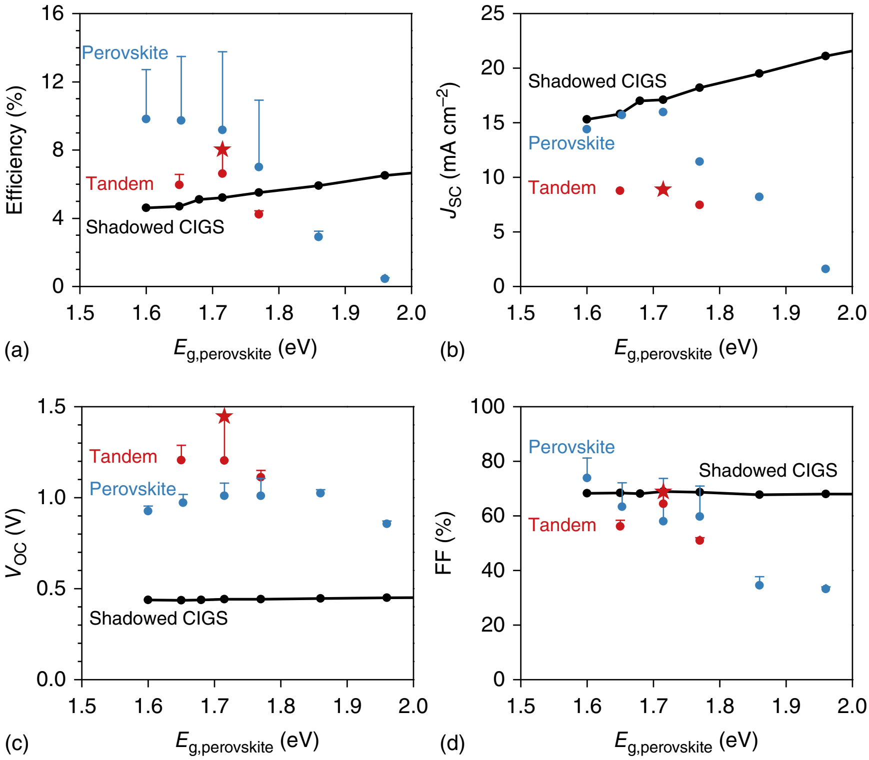

Figure 2.5.5 Empirical data from CIGS-perovskite tandem device optimization studies [16]. Photovoltaic device performance, (a) efficiency, (b) J_{sc}, (c) V_{oc}, and (d) FF, plotted against the perovskite bandgap (E_g, perovskite). Blue and red circles (bars) represent average values (the highest values) of individual perovskite devices and tandem devices, respectively. Black circles represent stand-alone CIGS devices shadowed by perovskite-coated glass filter. Black lines are guides to eye. The star point represent the champion tandem device. Source: Todorov et al. 2016 [16]. Reproduced with permission of John Wiley & Sons.

amorphous silicon have been able to combine these in an efficient device. For example, in chalcogenide solar cells such as CIGS and copper–zinc–tin–sulfide (CZTS), it is very difficult to achieve high efficiency at high bandgap due to significant V_{oc} deficit increase [17, 18]; and at the same time, the p–n junction starts deteriorating at temperatures exceeding 200 °C. This makes it extremely difficult to fabricate monolithic tandems, and most early demonstrations of CIGS tandem solar cells employed a multi-TCE/4-T configuration. Some examples include CIGS-CdTe [19], CIGS-dye-sensitized solar cell [20], CIGS-CGS [21], and CIGS-CIGS [22] cells with different ratios of In:Ga. The introduction of organic solar cells enabled the fabrication of devices at low processing temperatures, triggering a new wave of research on monolithic single TCE tandems. Organic layer transfer on CIGS yielded 3.7% efficiency [23]. Multiple examples of all-organic polymer tandem cell solar cells have also been reported, reaching efficiencies up to 11% [24–26]. As we see here, the unique processing advantages of perovskite solar cells not only allowed to fabricate tandem devices with other materials partners but also perovskite–perovskite tandems, reaching 18.1% efficiency in monolithic 2-T [27] and 21% in 4-T configuration [28].

The advent of perovskite PV with its unprecedented fast progress in solar cell efficiency demonstrations to over 20% in just a few years [29, 30], the highest reported 22.1% [31] through iodine management, triggered an interest in using this material for tandem architectures. The current literature data on perovskite tandem device achievements is summarized in Table 2.5.1. The materials and device versatility of these absorbers coupled with low-temperature processing conditions (from room temperature to 150 °C) opened an array of new opportunities for monolithic tandem solar cells. The possibility of depositing them in either p–n or n–p sequence and an easily tunable bandgap within the 1.48–2.3 eV range [12] makes them ideal for device engineering with precise optical and current matching [16]. The low processing temperature allows them to be used not only for perovskite-silicon monolithic tandems [8, 38] but also tandems with temperature-sensitive bottom cells such as chalcogenide CZTSSe [39] and CIGSSe [16] and even recently polymer and perovskite.

Of the many challenges related to building efficient perovskite tandem devices, a general one for all device architectures comes with the need to grow a TCE on top of a device already containing a perovskite layer. Standard TCE sputtering processes can produce thermal and plasma damage unless special precautions are used. Alternative TCE chemical vapor deposition (CVD) routes can cause even more severe thermal and chemical damage, and to date none has been successfully applied on a perovskite absorber.

Although multi-TCE devices are less suited for practical applications, these were instrumental for the rapid progress of the single TCE cells reviewed here. Isolated perovskite devices are more convenient for studying and optimizing the fabrication processes and achieving compatibility of different TCEs on the perovskite layers. Completely replacing the sputtered electrode with alternatives

Table 2.5.1 Examples of recent performance tandem perovskite devices.

Device type	Efficiency (%)	Fabrication sequence	References
All-perovskite stacked	20.3	Inverted	[32]
All-perovskite monolithic	17.0	Inverted	[32]
All-perovskite monolithic	10.8	Straight + inverted	[33]
CIGS-2-T monolithic	10.9	Inverted	[16]
CIGS-2-T stacked	18.5	Straight	[34]
CIGS-4-T stacked	20.7	Straight	[35]
CIGS-4-T stacked	22.1	Inverted	[13]
Si-4-T stacked	25.2	Straight	[12]
Si-4-T spectrum split	28.0	Straight	[14]
Si-2-T monolithic	19.9	Straight	[36]
Si-2-T monolithic	23.6	Inverted	[37]

such as silver nanowires has been one of the first successful TCE on perovskite fabrication approaches. It was employed for the first demonstrations in 4-T perovskite tandem devices that yielded efficiencies of 17% with Si and 18.6% with CIGS bottom devices [8].

The first reported monolithic perovskite tandem device (single TCE) employed a kesterite bottom cell with a semitransparent TCE composed of a thin aluminum layer. The high reflectivity and absorbance of aluminum only allowed a net optical transmission below 50%. A non-optimized bandgap further limited the conversion efficiency to 4.7%, which nevertheless was a record for any kind of chalcogenide monolithic tandem at the time [39]. This performance was soon improved to 10.9% with lower bandgap CIGS bottom cells (Figure 2.5.3), where the bandgap of the perovskite absorber was engineered in situ with the help of a proprietary vapor annealing tool with real-time spectroscopic capability [16]. A higher transmission TCE (75–85%) based on evaporated calcium coupled with a bathocuproine diffusion barrier was developed as well.

A different approach for depositing the TCE is a two-step method: the use of an initial non-sputtered oxide coating to protect the perovskite layer against a subsequent sputtering process of the high-quality layer. This approach been used extensively for demonstrating semitransparent cells with a double TCE for use in bifacial and tandem devices with the multi-TCE architecture. An efficiency of 20.5% was achieved with 4-T devices, employing an evaporated MoO_3 layer in combination with an amorphous In_2O_3:H layer on top of a low-bandgap CIGS absorber [40]. The use of lower temperature sputtering and less intense ion bombardment in comparison to standard ZnO:Al was also key for achieving this performance [40]. Ink-based coatings such as ITO nanoparticle buffer layers prior to depositing sputtered ITO is another approach to protect the sensitive perovskite device structure from sputter damage. This way, a 25% efficient 4-T device on silicon was achieved, showing for the first time the feasibility of achieving perovskite tandems with performance beyond this value.

Many examples of single TCE tandem devices with crystalline silicon bottom cells have been reported. Silicon p–n junctions are significantly more resilient to thermal damage than substrate chalcogenides, which expand the processing windows to n-type layers such as TiO_2. In addition, if no patterning for enhanced light trapping is applied, the monocrystalline silicon wafer is smoother than thin-film polycrystalline materials such as CIGS and CZTS, allowing the fabrication of high-quality spin-coated layers on top by spin coating, which is a preferred technique for fabricating many layers in the perovskite device including electron-selective layers, absorbers, and hole-selective layers.

Different strategies for nondestructive TCE have been demonstrated with monolithic silicon tandems. An early example used Ag-nanowire TCE deposited on top of the spiro-OMeTAD layer covering the perovskite, thus avoiding sputtering damage. The device also employed dense and mesoporous TiO_2 layers and reached efficiency of 13.7% [38]. Another way of protecting the underlying organic layers was shown with an evaporated MoO_3 layer before sputtering ITO on top of the device, achieving efficiency of 19.9% (18.1% stabilized). The hysteresis effect was minimized and stability was enhanced with SnO_2 electron-selective contacts [36]. Even higher performance was obtained by combining the protective effect of MoO_3 with hydrogenated In_2O_3:H and ITO [41], resulting in a monolithic perovskite tandem device with 21.2% efficiency. The current record of 23.6% efficient silicon-perovskite solar cell [37] (Figure 2.5.6) merges state-of-the-art developments across the fields of both perovskite and silicon devices to enable, at the same time, excellent light management and processing conditions for a high efficiency tandem with enhanced stability. The Si solar cell was optimized for the infrared spectrum and patterned only on the back, providing smooth front interface for perovskite deposition. For the perovskite cell, a reliable inorganic NiO_x hole-selective layer was used instead of PEDOT to achieve higher voltage and stability. Perovskite absorber with composition $Cs_{0.17}FA_{0.83}Pb(Br_{0.17}I_{0.83})_3$ benefited from improved stability due to Cs and formamidinium substitutions and increased bandgap due to Br substitution (1.63 eV). SnO_2–ZnO buffer on top of the PCBM (Phenyl-C61-butyric acid methyl ester) layer provided efficient electron extraction, minimal parasitic absorption, and protection during the sputtering of ITO transparent conducting layers (TCLs). The resultant device exhibited good stability during the 1000 hours damp heat test.

Depending on the type of bottom device, different charge recombination layers (CRLs) have been used. Inorganic bottom cells allowed for CRL similar to standard device elements with small modifications. One example is thin ITO used in chalcogenide monolithic tandems, where the standard underlying *i*-ZnO layer typically used in stand-alone devices was omitted due to the thermal degradation of the perovskite stack in its presence [16, 39]. Recent developments with other CRL prepared with soft processing conditions have allowed the fabrication of monolithic tandems with organic PV-perovskite and even pure perovskite–perovskite tandems. A 16% efficient tandem with low hysteresis employed graded CRL comprising C-60 derivative/Ag/MoO_3 that allowed depositing a polymer device on top of a perovskite solar cell [42]. The first demonstration of monolithic all perovskite–perovskite tandems was achieved with another CRL combination based on spiro-OMeTAD/PEDOT:PSS/PEI/PCBM:PEI [33]. The fabrication involved dry layer transfer for the PEDOT layer as well as careful selection of the processing steps to minimize the degradation of the underlying device structure. A pair of pure iodide (both low bandgap) cells reached remarkable additive V_{oc} of 1.89 V with efficiency of 7% [33]. Further development of this concept including bandgap optimization led to monolithic 2-T devices with 18.1% efficiency [27]. Perovskite–perovskite devices in 4-T configurations have reached 21% efficiency [28].

While the progress of perovskite solar cells has been spectacular in many respects, it is important to keep in mind some of the challenges that still keep this material from being considered as a serious manufacturable technology candidate. Significant instability with respect to humidity, elevated temperatures close to real operation conditions, as well as ionic migration are of serious concern [43]. The humidity sensitivity can be mitigated with proper packaging, although this can add to the cost. Particular instability was observed in high-bandgap materials employing mixed I-Br systems for bandgap adjustment [12, 44]. Formamidinium [45] and combinations of formamidinium and cesium

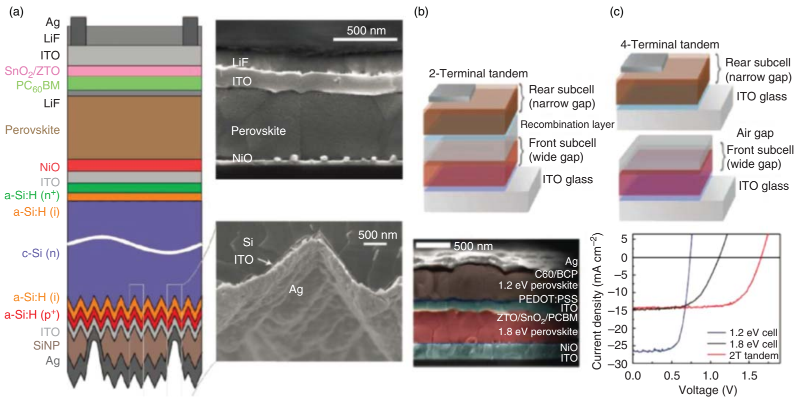

Figure 2.5.6 (a) Monolithic Si-perovskite tandem solar cell with 23.6% efficiency. Source: Bush et al. 2017 [37]. (Reproduced with permission of Springer Nature) and (b) All-perovskite 2-terminal tandem and its SEM cross section. (c) All-perovskite 4-terminal tandem and its JV characteristics. Source: Eperon et al. 2016 [32]. (Reproduced with permission of Science).

substitutions [12] have shown promising progress toward enhanced stability. Coupling the high-bandgap formamidinium bromide absorber with improved hole-transporting materials based on fluorene–dithiophene derivatives produced a remarkable V_{oc} of 1.47 V. The microstructural stability of perovskite interfaces under realistic operation conditions is the subject of a growing number of studies. For mitigation of metal-migration-induced degradation, Al_2O_3 nanoparticle layers and chromium diffusion barriers have been proposed [46, 47]. Other reports claim improved stability under ambient conditions via a variation in the rest of the device layers, for example, introducing double TiO_2-ZrO_2 and omitting the hole-transporting layer [48]. Before industry embraces any of the proposed perovskite device solutions, it will require extended testing and proof that the exciting high initial efficiency of these fascinating absorbers can be retained for a sufficient time (at least several years) under real operation conditions.

2.5.4 Conclusion and Outlook

Perovskite PV technology offers a unique combination of a high-efficiency, tunable bandgap within the optimal range for top cells in tandem stacks and processing conditions that are softer than any other material at this level of performance. Naturally, in just a couple of years, these solar cells have become one of the most popular partners for tandem device architectures, leading to significant progress with both multiterminal and the industry-preferred monolithic device configurations. With first demonstrations of efficiencies in the 25% range, further progress is just a matter of time. The development of nondestructive TCE and CRL formation techniques was key to preserve the fragile perovskite device structure and open multiple opportunities for device integration. The main challenge that lies ahead of this technology is the poor long-term stability of the perovskite solar cell. Promising first steps have been taken to address the device degradation, and success in this direction will be decisive for the future of perovskite tandem solar cells.

References

1 M. Woodhouse, R. Jones-Albertus, D. Feldman, R. Fu, K. Horowitz, D. Chung, D. Jordan, and S. Kurtz, *On the Path to SunShot: The Role of Advancements in Solar Photovoltaic Efficiency, Reliability, and Costs*, National Renewable Energy Laboratory, 2016.

2 Shockley, W. and Queisser, H.J. (1961). Detailed balance limit of efficiency of p–n junction solar cells. *J. Appl. Phys.* 32: 510.

3 Hirst, L.C. and Ekins-Daukes, N.J. (2011). Fundamental losses in solar cells. *Prog. Photovoltaics Res. Appl.* 19: 286.

4 De Vos, A. (1980). Detailed balance limit of the efficiency of tandem solar cells. *J. Phys. D: Appl. Phys.* 13: 839.

5 Wang, X., Zhi, L., and Mallen, K. (2008). Transparent, conductive graphene electrodes for dye-sensitized solar cells. *Nano Lett.* 8: 323.

6 Wu, Z. et al. (2004). Transparent, conductive carbon nanotube films. *Science* 305: 1273.

7 Du Pasquier, A., Unalan, H.E., Kanwal, A. et al. (2005). Conducting and transparent single-wall carbon nanotube electrodes for polymer-fullerene solar cells. *Appl. Phys. Lett.* 87: 203511.

8 Bailie, C.D. et al. (2015). Semi-transparent perovskite solar cells for tandems with silicon and CIGS. *Energy Environ. Sci.* 8: 956.

9 Tai, C.-H., Lin, C.-H., Wang, C.-M., and Lin, C.-C. (2011). Three-terminal amorphous silicon solar cells. *Int. J. Photoenergy* 2011: 813093.

10 Sista, S., Hong, Z., Park, M.H. et al. (2009). High-efficiency polymer tandem solar cells with three-terminal structure. *Adv. Mat.* 22: E77.

11 Duong, T. et al. (2017). Rubidium multication perovskite with optimized bandgap for perovskite-silicon tandem with over 26% efficiency. *Adv. Energy Mater.* 7: 1700228.

12 McMeekin, D.P. et al. (2016). A mixed-cation lead mixed-halide perovskite absorber for tandem solar cells. *Science* 351: 151.

13 Fu, F., Feurer, T., Weiss, T.P. et al. (2016). High-efficiency inverted semi-transparent planar perovskite solar cells in substrate configuration. *Nat. Energy* 2: 16190.

14 Uzu, H., Ichikawa, M., Hino, M. et al. (2015). High efficiency solar cells combining a perovskite and a silicon heterojunction solar cells via an optical splitting system. *Appl. Phys. Lett.* 106: 013506.

15 Todorov, T.K., Gunawan, O., and Guha, S. (2016). A road towards 25% efficiency and beyond: perovskite tandem solar cells. *Mol. Syst. Des. Eng.* 1: 370.

16 Todorov, T., Gershon, T., Gunawan, O. et al. (2016). Monolithic perovskite-CIGS tandem solar cells via *in situ* band gap engineering. *Adv. Energy Mater.* 5: 1500799.

17 Shafarman, W.N., Klenk, R., and McCandless, B.E. (1996). Device and material characterization of Cu(InGa)Se_2 solar cells with increasing band gap. *J. Appl. Phys.* 79: 7324.

18 Gunawan, O., Mitzi, D.B., and Gokmen, T. (2015). Device characteristics of hydrazine-processed CZTSSe. In: *Copper Zinc Tin Sulfide-Based Thin Film Solar Cells* (ed. K. Ito). Wiley.

19 Symko-Davies, M. and Noufi, R. (2005). Future in High-Performance PV: Polycrystalline Thin-Film Tandem Cells. Proceedings of the 20th European Photovoltaic Solar Energy Conference, Barcelona, Spain, June 6-10

20 Liska, P., Thampi, K.R., Grätzel, M. et al. (2006). Nanocrystalline dye-sensitized solar cell/copper indium gallium selenide thin-film tandem showing greater than 15% conversion efficiency. *Appl. Phys. Lett.* 88: 203103.

21 Nishiwaki, S., Siebentritt, S., and Walk, P. (2003). A stacked chalcopyrite thin-film tandem solar cell with 1.2 V open-circuit voltage. *Prog. Photovoltaics Res. Appl.* 11: 243.

22 Kaigawa, R., Funahashi, K., Fujie, R. et al. (2010). Tandem solar cells with $Cu(In,Ga)S_2$ top cells on ZnO coated substrates. *Sol. Energy Mater. Sol. Cells* 94: 1880.

23 Reinhard, M., Sonntag, P., Eckstein, R. et al. (2013). Monolithic hybrid tandem solar cells comprising copper indium gallium diselenide and organic subcells. *Appl. Phys. Lett.* 103: 143904.

24 You, J. et al. (2013). A polymer tandem solar cell with 10.6% power conversion efficiency. *Nat. Commun.* 4: 1446.

25 Chen, C.C., Chang, W.H., Yoshimura, K. et al. (2014). An efficient triple-junction polymer solar cell having a power conversion efficiency exceeding 11%. *Adv. Mat.* 26: 5670.

26 Zhou, H., Zhang, Y., Mai, C.K. et al. (2015). Polymer homo tandem solar cells with best efficiency of 11.3%. *Adv. Mat.* 27: 1767.

27 Forgács, D., Gil-Escrig, L., Pérez-Del-Rey, D. et al. (2017). Efficient monolithic perovskite/perovskite tandem solar cells. *Adv. Energy Mater.* 7: 1602121.

28 Zhao, D. et al. (2017). Low-bandgap mixed tin–lead iodide perovskite absorbers with long carrier lifetimes for all-perovskite tandem solar cells. *Nat. Energy* 2: 17018.

29 Liu, M., Johnston, M.B., and Snaith, H.J. (2013). Efficient planar heterojunction perovskite solar cells by vapour deposition. *Nature* 501: 395.

30 Jeon, N.J., Noh, J.H., Yang, W.S. et al. (2015). Compositional engineering of perovskite materials for high-performance solar cells. *Nature* 517: 476.

31 Yang, W.S. et al. (2017). Iodide management in formamidinium-lead-halide-based perovskite layers for efficient solar cells. *Science* 356: 1376.

32 Eperon, G.E. et al. (2016). Perovskite-perovskite tandem photovoltaics with optimized band gaps. *Science* 354: 861.

33 Jiang, F., Liu, T., Luo, B. et al. (2016). A two-terminal perovskite/perovskite tandem solar cell. *J. Mater. Chem. A* 4: 1208.

34 Uhl, A.R., Yang, Z., Jen, A.K.-Y., and Hillhouse, H.W. (2017). Solution-processed chalcopyrite–perovskite tandem solar cells in bandgap-matched two-and four-terminal architectures. *J. Mater. Chem. A* 5: 3214.

35 Guchhait, A., Dewi, H.A., Leow, S.W. et al. (2017). Over 20% efficient CIGS–perovskite tandem solar cells. *ACS Energy Lett.* 2: 807.

36 Albrecht, S. et al. (2016). Monolithic perovskite/silicon-heterojunction tandem solar cells processed at low temperature. *Energy Environ. Sci.* 9: 81.

37 Bush, K.A. et al. (2017). 23.6%-efficient monolithic perovskite/silicon tandem solar cells with improved stability. *Nat. Energy* 2: 17009.

38 Mailoa, J.P., Bailie, C.D., Johlin, E.C. et al. (2015). A 2-terminal perovskite/silicon multijunction solar cell enabled by a silicon tunnel junction. *Appl. Phys. Lett.* 106: 121105.

39 Todorov, T., Gershon, T., Gunawan, O. et al. (2014). Perovskite-kesterite monolithic tandem solar cells with high open-circuit voltage. *Appl. Phys. Lett.* 105: 173902.

40 Fu, F., Feurer, T., Jager, T. et al. (2015). Low-temperature-processed efficient semi-transparent planar perovskite solar cells for bifacial and tandem applications. *Nat. Commun.* 6: 8932.

41 Werner, J., Weng, C.-H., Walter, A. et al. (2016). Efficient monolithic perovskite/silicon tandem solar cell with cell area >1 cm^2. *J. Phys. Chem. Lett.* 7: 161.

42 Liu, Y., Renna, L.A., Bag, M. et al. (2016). High efficiency tandem thin-perovskite/polymer solar cells with a graded recombination layer. *ACS Appl. Mater. Interfaces* 8: 7070.

43 Guerrero, A., You, J., Aranda, C. et al. (2015). Interfacial degradation of planar lead halide perovskite solar cells. *ACS Nano* 10: 218.

44 Hoke, E.T., Slotcavage, D.J., Dohner, E.R. et al. (2015). Reversible photo-induced trap formation in mixed-halide hybrid perovskites for photovoltaics. *Chem. Sci.* 6: 613.

45 Eperon, G.E., Stranks, S.D., Menelaou, C. et al. (2014). Formamidinium lead trihalide: a broadly tunable perovskite for efficient planar heterojunction solar cells. *Energy Environ. Sci.* 7: 982.

46 Domanski, K., Correa-Baena, J.-P., Mine, N. et al. (2016). Not all that glitters is gold: metal migration-induced degradation in perovskite solar cells. *ACS Nano* 10: 6306.

47 Guarnera, S., Abate, A., Zhang, W. et al. (2015). Improving the long-term stability of perovskite solar cells with a porous Al_2O_3 buffer layer. *J. Phys. Chem. Lett.* 6: 432.

48 Mei, A. et al. (2014). A hole-conductor-free, fully printable mesoscopic perovskite solar cell with high stability. *Science* 345: 295.

Part III

Perovskite Light Emitting Devices

3.1

Perovskite Light-Emitting Devices – Fundamentals and Working Principles

Michele Sessolo, Maria-Grazia La-Placa, Laura Martínez-Sarti, and Henk J. Bolink

Universidad de Valencia, Instituto de Ciencia Molecular (ICMol), C/Catedrático José Beltrán 2, 46980 Paterna, Spain

Hybrid organic-inorganic lead halide perovskites (from now on referred to as hybrid perovskites) have been known since the past century [1, 2], but only recently they have emerged as a promising class of semiconducting materials. This renaissance is due to their extraordinary performances in solar cells where, in only few years of development, power conversion efficiencies (PCEs) exceeding 22% have been demonstrated [3, 4]. Ideally, the highest performing solar cells will operate in the radiative limit, where the absorbed photon flux is equal to the emitted flux, under open circuit conditions. This is because the electronic transitions governing radiative recombination are also responsible for light absorption. Therefore, light emission cannot be avoided and, in efficient solar cells, one should minimize the non-radiative recombination since it involves states which are not related to absorption. While this concept might sound counterintuitive, the optical reciprocity has been demonstrated to apply in a number of photovoltaic devices [5–10]. In fact, the external quantum efficiency for electroluminescence (EQE_{EL}) is a useful figure of merit for comparing the performance of photovoltaic devices, and it scales with the device efficiency (Figure 3.1.1) [9]. Interestingly, perovskite solar cells were found to have rather high EQE_{EL} when compared to other single-junction technologies [12, 13]. Recent measurements on cells employing a mixed cation/halide lead compound have shown that when the efficiency approaches that of inorganic semiconductors (>20%), the EQE_{EL} of perovskite also becomes increasingly high (0.5%) [11]. Hence, hybrid perovskites do emit light efficiently, and are promising candidates for future inexpensive light sources and phosphors. The research toward light-emitting diodes (LEDs) employing perovskites as the emitting material has already started, and the field is constantly growing as the physics behind perovskite electroluminescence is being unveiled [14–16]. The development of new perovskite emitters with fine-tuned properties, together with the well-established knowledge acquired for organic LEDs, can lead to the development of a new generation of potentially inexpensive light-emitting devices.

Halide Perovskites: Photovoltaics, Light Emitting Devices, and Beyond, First Edition.
Edited by Tze-Chien Sum and Nripan Mathews.

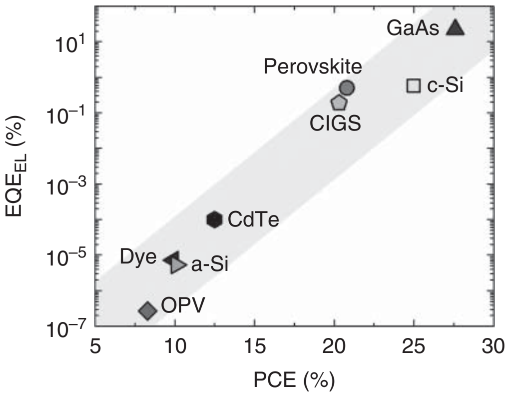

Figure 3.1.1 Relationship between the external quantum efficiency for the electroluminescence (EQE_{EL}) and the power conversion efficiency (PCE) of the most relevant single-junction photovoltaic devices. Source: Data are taken from Refs. [9, 11].

In order to develop efficient electroluminescent devices, a few general considerations must be taken into account. The EQE_{EL} can be conceptually expressed with a few terms describing the main processes taking place in LEDs:

$$EQE_{EL} = \eta_i \, \eta_{rad} \, \eta_{ext}$$

where η_i is the current injection efficiency, the fraction of the total diode current that recombines before reaching the contacts; η_{rad} is the radiative efficiency, the fraction of the charges recombining radiatively; η_{ext} is the extraction efficiency or outcoupling, the fraction of generated photons that get out of the device (and are not either reabsorbed or wave guided into the device). While the optimization of η_{ext} involves substantial device engineering, i.e. use of outcoupling structures and/or choice of low refractive index substrates, the other two components, η_i and η_{rad}, are more directly related to the materials aspect in the design of light-emitting devices. η_i can be optimized by ensuring ohmic contacts from the electrodes to the semiconductors and efficient charge transport within the device, potentially with a multilayer structure confining the electrons and holes to the emitting layer (choice of proper and complementary transport materials). Most importantly, one should enhance the photoluminescence quantum yield (PLQY) of the light-emitting semiconductor in order to enhance the radiative efficiency η_{rad}. In this chapter, we review the progress toward perovskite LEDs, highlighting the importance of developing high PLQY perovskite materials and their incorporation into optimized multilayer light-emitting devices.

3.1.1 Excitons, Free Carriers, and Trap States in Hybrid Perovskite Thin Films

The optical behavior of three-dimensional (3D) hybrid perovskites has been investigated mainly for the archetype compound methylammonium lead iodide ($MAPbI_3$), but certain properties can be generalized to the other commonly used compounds, such as $MAPbBr_3$ or $MAPbCl_3$, and even to their inorganic relatives, such as $CsPbBr_3$. What makes hybrid perovskites an exciting material

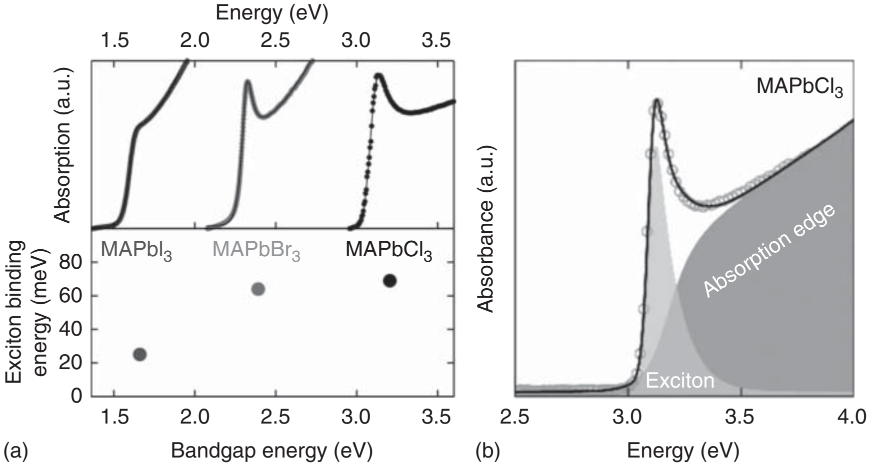

Figure 3.1.2 (a) Absorption spectra for lead halide perovskites at room temperature (top panel) with respective fits based on Elliott's formula (back lines). The bottom panel shows the exciton binding energy extracted from the fit as a function of the energy bandgap of the respective materials [19]. (b) Plot of the absorbance (symbols) of a MAPbCl$_3$ thin film as a function of energy with two-component (exciton and band-to-band absorption) fit overlaid [20].

for photovoltaics is their high absorption coefficient ($\varepsilon > 10^5$ cm^{-1}), comparable to those of inorganic semiconductors such as GaAs [17]. While MAPbI$_3$ has an absorption onset at about 1.6 eV (in the near-infrared, NIR), the bandgap (and hence the absorption/emission spectra) of the 3D perovskite family can be easily tuned by partial or complete halide exchange [18], with the pure MAPbBr$_3$ and MAPbCl$_3$ having a bandgap of approximately 2.3 and 3.1 eV, leading to absorption/emission in the green and blue spectral region, respectively (Figure 3.1.2). The control over the bandgap can be finely tuned all over the visible spectra using the mixed compounds MAPb(X$_n$Y$_{1-n}$)$_3$, where X and Y stand for I$^-$ and Br$^-$ or Br$^-$ and Cl$^-$. This feature is of obvious interest when designing LEDs and lasers.

From the absorption profiles of the three methylammonium (MA) halide perovskites (Figure 3.1.2a), one can note the presence of a peak at the absorption edge, increasing from iodide to bromide and chloride. As highlighted in Figure 3.1.2b in the case of MAPbCl$_3$, the absorption comprises two contributions, an excitonic peak at lower energies and an extended absorption edge representing the band-to-band electronic transitions [20, 21]. Exciton binding energies reported for MAPbI$_3$ are comparable to the thermal energy at room temperature ($k_B T = 25.6$ meV) [22–24]; hence, the photogenerated mobile charges will be mainly free carriers in an optoelectronic device. On the other hand, lead halide perovskites with Br or Cl anions display a more pronounced excitonic resonance even at room temperature (Figure 3.1.2a) [19]. This dual character of the excited states in hybrid perovskites has large implications in the design of LEDs, since the charge recombination dynamics of free carriers differ substantially from excitonic transitions.

Another interesting feature of hybrid perovskites is their characteristic photoluminescence (PL), consisting of a narrow band appearing just below the absorption edge. Importantly, some perovskite thin films do not show substantial PL at low excitation intensity [25], while emission can be progressively observed by increasing the excitation intensity. This phenomenon was first studied in solution-processed $MAPbI_3$ samples, where a PLQY as high as 70% was obtained at high excitation intensity ($>1\ W\ cm^{-2}$) [26]. The lower PLQY at low excitation is related to the presence of trap states; hence, the PL becomes dominant at high fluence after the defects are filled. Such trap states have been identified in $MAPbI_3$ thin films using ultraviolet photoelectron spectroscopy (UPS) [27]. With this technique, an additional density of states above the valence band maximum (VBM), extending toward the Fermi level was identified. These states were associated with charge carrier (hole) traps on the surfaces of the perovskite thin films. In another study, lasing at room temperature has been observed for $MAPbX_3$ ($X = I$, Br, Cl) perovskites [28]. Again, at low pump fluence, the PL intensity was observed to increase linearly with increasing pump fluence while the average transient PL lifetime was progressively decreasing. This same behavior was observed and analytically described by Stranks et al., who studied the temperature, fluence, and time dependence of the carrier recombination in $MAPbI_{3-x}Cl_x$ thin films [29]. They confirmed that the dominant species are free charges, at least at room temperature and low excitation fluence. Figure 3.1.3a shows the time-resolved PL decays at low temperature (190 K) as a function of excitation fluence. The fit agrees well with the experimental data and assumes a trap concentration that is temperature dependent. Most likely, these traps are associated with thermally activated point defects in the perovskite structures. Also, it is visible how the recombination becomes faster at higher excitation fluence, i.e. when the traps are filled. The authors described this behavior with the aid of the schematics in Figure 3.1.3b. At higher temperatures and/or lower excitation fluence (left panel), the photoexcited species are essentially free charges; and the free electrons are more probably trapped in defect sites, resulting in non-radiative decay. As the excited charge density increases and/or the temperature is reduced, the fractional time the charges are bound as excitons increases, and the density of available trap states is reduced. Hence, the competition for radiative decay increases with respect to charge trapping, leading to an augmented PLQY.

Another interesting optical property of hybrid perovskites is the temporally fluctuating PL, also known as blinking [29–31]. Nanocrystalline thin films of the $MAPbI_3$ and $MAPbBr_3$ possess highly spatially inhomogeneous and temporally fluctuating PL, as a consequence of the presence of very few either emitting or quenching sites per nanocrystal (NC). The nature of such quenching sites might be the same as that of the charge traps discussed before, and are likely to be formed at the NC boundaries, where the defect formation is most probable. Interestingly, the PL can be enhanced by light soaking in oxygen, and the timescale of the PL activation was found to be dependent on the crystal size [32]. The origin of PL enhancement was ascribed to a photochemical reaction involving oxygen, passivating deep traps that cause non-radiative recombination and the very low PLQY in perovskite thin films at low excitation intensity [33].

In the perspective of developing electroluminescent devices, the low PLQY generally observed in hybrid perovskites at low excitation intensity means that

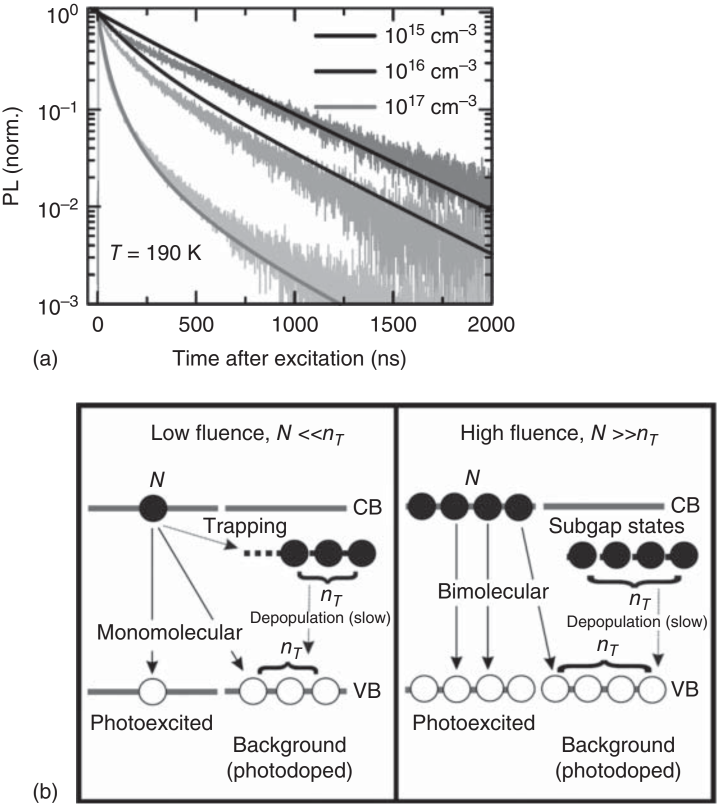

Figure 3.1.3 (a) PL decays detected at 780 nm from a $MAPbI_{3-x}Cl_x$ thin film at 190 K, following pulsed excitation (510 nm, 300-kHz repetition rate) with different initial photoexcitation densities. Solid lines are fits from the analytical model. (b) Schematic illustrating the recombination mechanisms at low (left) and high (right) excitation fluence [29].

high current densities would be needed in order to generate high luminance levels, leading to a decrease in the overall PCE of such devices. Hence, the development of strategies to substantially enhance the PL in hybrid perovskites is of primary importance. In analogy to inorganic semiconductors, the most promising strategy to promote radiative recombination, especially at low excitation intensity, is the spatial confinement of the charge carriers. In fact, NCs have much larger exciton binding energies compared to bulk and thin-film hybrid perovskites, which leads to higher PLQY [34]. In the following, we review the recent advances in the preparation of luminescent perovskite materials, and their incorporation into light-emitting devices.

3.1.2 Hybrid Perovskite Light-Emitting Diodes

As for perovskite solar cells, the embodiment and materials of perovskite LEDs are analogous to that of organic light-emitting diodes (OLEDs) [35–37]. They consist in multilayer devices grown on a transparent conductor and capped

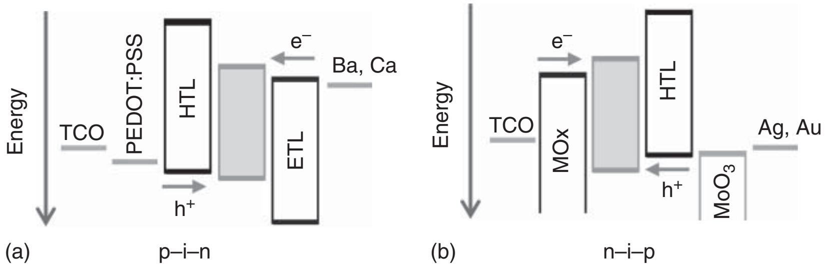

Figure 3.1.4 Schematic energy diagrams for (a) p–i–n and (b) n–i–p perovskite LEDs.

with a metal electrode, where the processes of charge injection, transport, and recombination are separated and optimized in each layer. Common transparent electrodes are transparent conductive oxides (TCOs) such as indium tin oxide (ITO) or fluorine-doped tin oxide (FTO), deposited on glass or plastic foils. The light-emitting layer (a perovskite film, in our case) is deposited from solution or by vacuum deposition and sandwiched between a hole transport layer (HTL) and an electron transport layer (ETL). Depending on whether the TCO is used as the anode (injection of holes) or the cathode (injection of electrons), the LEDs are named p–i–n or n–i–p, respectively. p–i–n LEDs (Figure 3.1.4a) are, in most cases, fully organic, and a thin film of poly(3,4-ethylenedioxythiophene) doped with polystyrene sulfonate (PEDOT:PSS) is used to smooth the ITO surface and enlarge its work function (WF). An HTL (also electron blocking) can be deposited on top, to ensure charge confinement within the light-emitting layer. The perovskite film is then deposited on top and coated with an ETL (also hole blocking) capped with a metal electrode. In p–i–n diodes, since electrons must be injected into the lowest unoccupied molecular orbital (LUMO) of the ETL material, the cathode must have a low WF; hence, Ba, Ca, or LiF/Al are frequently selected.

As mentioned before, n–i–p devices use an inverted structure (Figure 3.1.4b), commonly used in high-efficiency solar cells and also, to a minor extent, in OLEDs [14, 38]. In order to have efficient electron injection from the TCO to the perovskite, an n-type metal oxide (MOx, TiO_2, or ZnO) film is used. After deposition of the perovskite films, an organic HTL is deposited, occasionally in combination with a thin MoO_3 layer which ensures ohmic charge injection from the top anode into the organic semiconductors.

The most studied material for photovoltaic application, $MAPbI_3$, was among the first to be employed in LEDs. Infrared electroluminescence was obtained using an n–i–p architecture (ITO/TiO_2/Al_2O_3 (1 nm)/$MAPbI_3$/F8/MoO_3/Ag), where the thin Al_2O_3 was used to reduce charge back transfer from the perovskite to the TiO_2 ETL and the F8, poly(9,9′-dioctyl-fluorene), was used as the HTL [39]. Besides the achievement of radiance of 13.2 W sr^{-1} m^{-2} at a current density of 363 mA cm^{-2}, the EQE was rather low, 0.76%. In the same work, the authors showed also p–i–n LEDs, using the structure ITO/PEDOT:PSS/$MAPbBr_3$/F8/Ca/Ag device. Bright devices were obtained (360 cd m^{-2}), but the current density was rather high resulting in an EQE of 0.1%. The lower EQE observed for the green LED can be due to the energy mismatch for the hole injection from the

PEDOT:PSS HIL (−5.0/−5.2 eV) into the $MAPbBr_3$ valence band (−5.9 eV) [40]. Interestingly, the EQE was found to increase with increasing current density, demonstrating a need for high charge densities to achieve efficient radiative recombination [12, 39]. This is in agreement with the observations of high PLQY in perovskites at high excitation intensity. Several works explored the use of perovskite thin films in LEDs, either in p–i–n or n–i–p configurations, with encouraging results but showing low EQE [25, 41]. A series of studies explored the versatility of hybrid perovskites in terms of color tuning [20, 42]. By partially exchanging the halide, one can tune the electroluminescence spectra of the mixed compound $MAPb(I_{1-x}Br_x)_3$ from 770 to 780 nm ($x = 0$) to about 540 nm ($x = 1$), and from 540 to 410 nm for $MAPb(Br_{1-x}Cl_x)_3$ ($x = 0$ and 1, respectively) [43–45]. As mentioned before, an important characteristic of visible-emitting hybrid perovskites (such as $MAPbBr_3$, $MAPbCl_3$, and their mixed compounds) is their low-lying valence band (≤−5.9 eV). This is challenging for the development of efficient LEDs, hindering an efficient hole injection from common anode materials used in p–i–n devices (ITO, PEDOT:PSS, WF of −4.8/−5.2 eV). Kim et al. showed bright p–i–n perovskite LEDs with the structure ITO/ buffer hole-injection layer (Buf-HIL)/perovskite/TPBi/Al, where TPBi is the small molecule ETL 2,2′,2″-(1,3,5-benzinetriyl)-tris(1-phenyl-1-*H*-benzimidazole), and Buf-HIL is a modified PEDOT:PSS film [46]. By adding a perfluorinated polymeric acid (Nafion®) to the PEDOT:PSS suspension, the WF of the resulting Buf-HIL varies from about −5.2 to −6.0 eV (Figure 3.1.5a), essentially matching the perovskite valence band energy.

In this way, they obtained high luminance values independently on the type of perovskite used (Figure 3.1.5b). The device EQE was however still moderate, most likely due to an energy mismatch at the aluminum/TPBi interface. Analogously, in n–i–p devices, a barrier for the injection of electrons from the ZnO or TiO_2 conduction bands to the perovskite conduction band exists. In order to minimize it and promote charge injection and enhanced device performances, ethanolamine or polyethyleneimine (PEI) can be applied on top of the metal oxide surface (Figure 3.1.5c) [47, 48]. Rather high luminance values (20 000 cd m^{-2}, Figure 3.1.5d) and EQE up to 2% have been achieved through this method, indicating that, as for OLEDs, the energy barriers for the charge injection and transport have a large effect on the overall LED performances. Even though the achievement of an EQE of 2% is promising, it is still far from the maximum EQE value of around 20 as may be expected from the architecture of planar thin-film devices with an outcoupling efficiency (η_{ext}) of 0.2 [49]. Cho et al. recently developed hybrid green-emitting perovskite LEDs with exceptional current efficiency (>40 cd A^{-1}) and maximum EQE of 8.5% [50]. The PLQY of the $MAPbBr_3$ perovskite was enhanced by passivation of the perovskite with controlled excess of $PbBr_2$ precursor, and by blocking the perovskite crystal growth by anti-solvent treatment. With the latter method, the grain-size as well as the perovskite surface can be controlled in order to ensure homogeneity and high luminescence, resulting in PLQY of the films of 46%. Finally, efficient hole injection in p–i–n diodes was achieved by modifying the PEDOT:PSS with a perfluorinated polymer. Hence, the processes of charge injection, confinement into the active layer, and radiative recombination were separately optimized and

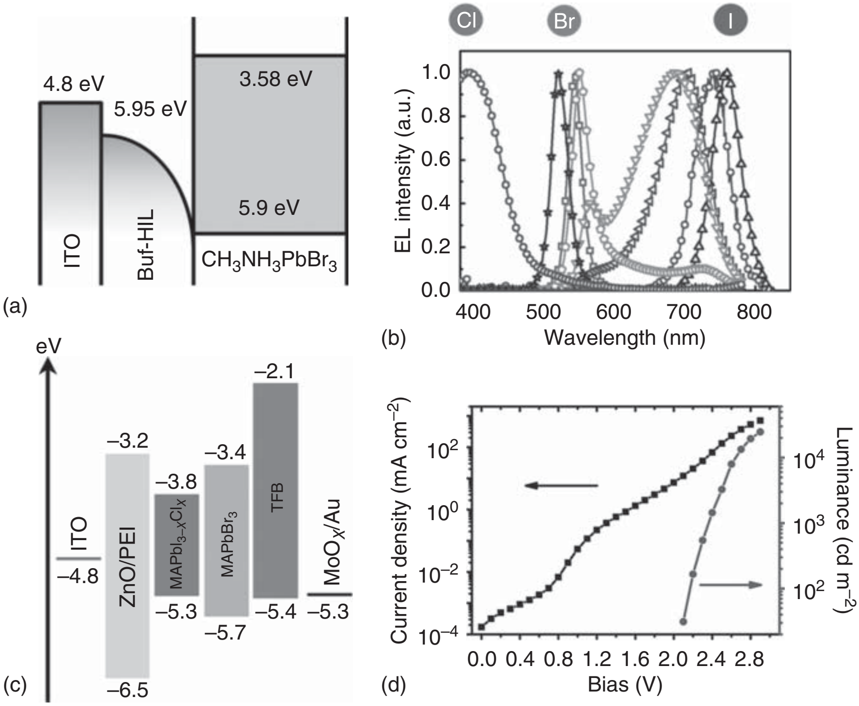

Figure 3.1.5 (a) Schematic energy-level diagram of ITO/Buf-HIL/MAPbBr$_3$ and (b) electroluminescence spectra obtained from a series of devices using Buf-HIL and mixed halide perovskites [46]. (c) Schematic energy-level diagram of an n–i–p device where the ZnO ETL was modified with a thin PEI film, and (d) corresponding optoelectronic characteristic where MAPbBr$_3$ is used as the emitter [47].

led to the first highly efficient perovskite LEDs to date. Alternative perovskite emitters that employ inorganic cations, such as Cs$^+$, have also been studied, in particular to enhance thermal stability of the devices. In fact, despite the remarkable performance of hybrid perovskite LEDs, their stability in high current density conditions remains a major concern. All-inorganic halide perovskites, such as the green-emitting compound CsPbBr$_3$, have been used as alternative emitters in LEDs [51]. Controlling and reducing the trap density in CsPbBr$_3$ films is key to enhance the LED performance. With this aim, it has been showed how the processing conditions (precursor concentration and ratio, use of additives) are crucial in determining the final film properties. Using CsBr-rich solutions, the trap density of solution-processed CsPbBr$_3$ films can be reduced, leading to increased luminescence (>400 cd m^{-2}) and decreased turn-on voltage (3 V) of the LEDs. Ling et al. found that by adding small amounts of poly(ethylene oxide) (PEO) into the precursor solutions, smooth and pinhole-free perovskite films with small crystal domains can be obtained [52]. When incorporated into LEDs, the CsPbBr$_3$:PEO layers lead to very high brightness (>50 000 cd m^{-2}), and EQE as high as 4.3%. This was achieved using high-conductive PEDOT:PSS formulations, and by capping the perovskite with a suitable ETL (TPBi). More recently, Zhang et al. demonstrated high-quality dense $CsPbBr_3$ perovskite thin films by incorporating a small amount of organic MA cation into the precursor solution, as well as using a hydrophilic insulating polymer interface layer on top of the ZnO ETL [53]. The latter was used to suppress the non-radiative recombination centers at the interfaces with the ZnO and in the perovskite film. By optimizing the relative concentration of Cs and MA, highly luminescent films of $Cs_{0.87}MA_{0.13}PbBr_3$ with PLQY exceeding 50% were obtained. When used in LEDs, these materials exhibited very intense and efficient electroluminescence, with peak brightness >90 000 cd m^{-2} and a peak EQE of 10.4%. The development of new perovskite emitters with improved optoelectronic and film-forming properties, together with a rational choice of the device structure and materials, can further expand the impact of hybrid perovskite to electroluminescent device applications. In particular, to substantially increase the EQE values in hybrid perovskite LEDs, the suppression of non-radiative recombination has to be pursued. Progress toward these materials is described in the next paragraphs.

3.1.3 Hybrid Perovskite Nanostructures and Nanoparticles

While the development of highly luminescent nanocrystalline perovskites is currently a trending topic, such materials were already studied almost 20 years ago. In particular, two-dimensional (2D) hybrid perovskites, layered compounds composed of a single layer of inorganic sheet alternated with organic ammonium cations, were observed to self-organize as NCs when synthesized in a polymer matrix [54, 55]. Importantly, the exciton binding energy and the PL intensity were observed to increase as a consequence of the dielectric confinement of the polymer. Later, but in a conceptually similar manner, $MAPbBr_3$ 3D perovskites were grown within a porous alumina scaffold [56]. The porous oxide acts as a template, limiting the growth of the $MAPbBr_3$ crystals, hence highly luminescent, green-emitting perovskite thin films were obtained. The same approach was recently used to obtain highly photoluminescent mixed Br/Cl perovskites (with tunable emission color) [57]. Several methods for the preparation of nanostructured perovskite films have been presented, using small-molecular-weight organic molecules [50, 58], polymer dielectrics [59], or metal oxide nanoparticle (NP) suspensions [60]. The advantage of using a templating material is to avoid the aggregation of the NCs in the solid state, which would strongly reduce the PLQY. In fact, by preparing perovskite–alumina composite thin films, PLQY values up to 40% have been obtained [60]. Also, the size and shape of the perovskite NC can be easily controlled by tuning the relative amount of matrix material and perovskite precursor used [58, 60]. Li et al. used a polyimide precursor (PIP) dielectric as the matrix to form perovskite crystals in thin films [61], with crystal size decreasing with increasing PIP concentration. The PIP-based film formed a pinhole-free charge-blocking layer, and was used as the emitting material in a p–i–n LED, with PEDOT:PSS and F8 as the hole- and

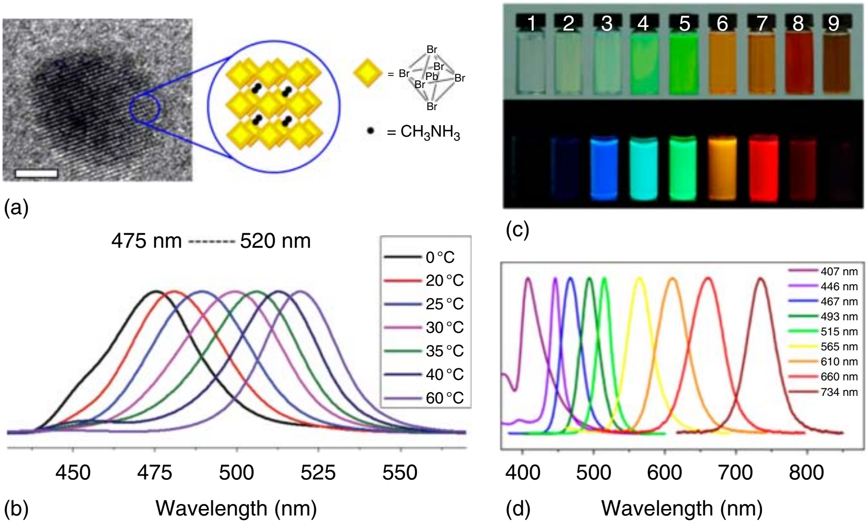

Figure 3.1.6 (a) High-resolution transmission electron microscopic (HRTEM) image of an isolated perovskite nanoparticle (scale bar 2 nm) and schematic representation of the $MAPbBr_3$ perovskite [24]. (b) PL spectra of $MAPbBr_3$ NPs depending on the NPs size (i.e. synthesis temperature) [63]. (c) Optical images of $MAPbX_3$ nanoparticles under ambient light and a 365-nm UV lamp, with (d) PL emission spectra for the same series of samples [64].

electron-injection layers, respectively. In this way, high current densities that are frequently observed in perovskite LEDs were avoided, leading to a substantial enhancement in the EQE, about 1.2%. Recently, blends of perovskite with organic semiconductors containing a phosphine oxide functionality, capable of efficiently passivating the perovskite surface, have been presented [62]. Besides the very high PLQY obtained (>85%), these materials behave poorly when incorporated into electroluminescent devices. A drawback of employing a dielectric or low-mobility matrix is the hindered charge transport through the film, which limits the application of these materials to optoelectronic devices. An alternative to obtain NCs is through direct colloidal synthesis. Schmidt et al. were the first to report the preparation of stable dispersions of 6-nm-sized $MAPbBr_3$ NPs, using a long chain ammonium cation as the capping ligand (Figure 3.1.6a) [24]. When casted as thin films, the perovskite NPs yielded a PLQY of about 20%, limited by the particle aggregation. These authors also demonstrated the first room-temperature-emitting perovskite-based LEDs. Using a complementary weak Lewis base ligand, passivating surface states, and reducing aggregations, thin films with PLQY exceeding 70% were obtained [65]. As opposed to inorganic semiconductors, where the emission spectra can be tuned all over the visible range simply by changing the particle size, the bandgap of perovskite NPs is weakly size dependent (Figure 3.1.6b) [63, 66]. Hence, the emission wavelength can be more conveniently tuned over the whole visible spectra by simple halide exchange (Figure 3.1.6c,d) [64]. The recent breakthroughs in the PLQY (>90%) [63] points to perovskite NPs as one of the most promising materials for light-emission applications.

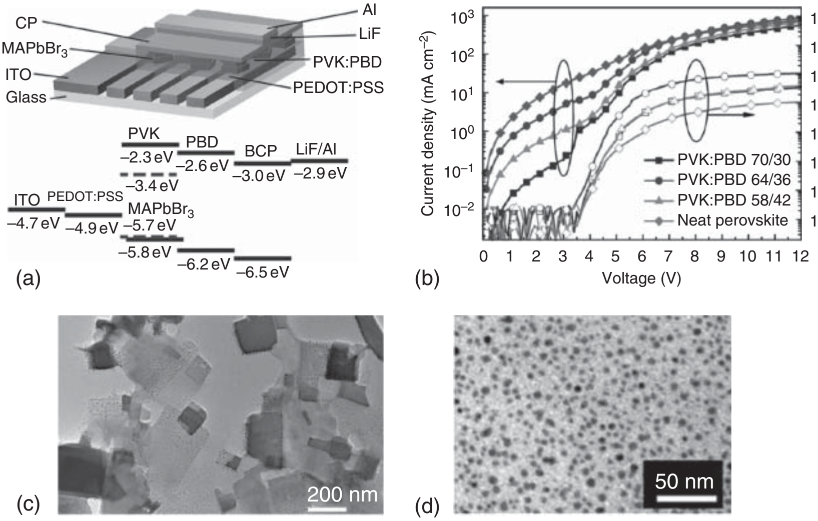

Figure 3.1.7 (a) Device architecture for a perovskite LED using $MAPbBr_3$ nanoplatelets as emitter, and flat-band energy level diagram for the materials used. (b) Current–voltage and brightness–voltage characteristics for the control device (neat perovskite without PVK:PBD) and devices with PVK:PBD (PBD is the ETL) [69]. (c) TEM image of colloidal $MAPbBr_3$ nanoplatelets and (d) of $MAPbBr_3$ QDs with diameter of 4.6 ± 1.1 nm [67].

LEDs employing perovskite NPs have indeed been demonstrated with encouraging results [24, 67, 68]. Ling et al. showed very bright LEDs using $MAPbBr_3$ nanoplatelets [69]. They used an organic multilayer structure and dispersed the perovskite in the hole-transporting poly(9-vinylcarbazole) (PVK), in a manner similar to the host–guest approach used in OLEDs (Figure 3.1.7a). They achieved luminance values exceeding 20 000 cd m^{-2} (Figure 3.1.7b), yet with an EQE of about 0.5%, as a consequence of the high current density flowing through the diode. They termed the structures observed by transmission electron microscopy (TEM, Figure 3.1.7c) as nanoplatelets, which are commonly observed during the synthesis of perovskite NPs. These nanoplatelets consist of large sheets of compounds embedding small NCs, and the latter determined the PL emission color [70]. In fact, as the synthesis uses both the MA and long chain ammonium cations, there is an inevitable competition between the formation of 3D and 2D nanostructures. By fine-tuning the synthetic conditions, however, it is possible to obtain pure monodisperse perovskite NCs (Figure 3.1.7d), which can be used in the preparation of colorful and bright LEDs, yet with a limited EQE [70–72].

Xing et al. synthesized colloidal perovskite $MAPbX_3$ (X = halides) NPs with amorphous structure, with emission covering the entire visible spectrum and with high PLQY [73]. The PLQY of $MAPbBr_3$ NPs was about 80%; on the contrary, lower PLQYs were obtained on Cl- and I-based perovskites. They observed that the integrated PL intensity of NP films increases exponentially with decreasing temperature, suggesting that nonradiative channels are responsible for the lower PLQY. Interestingly, the PL intensity of amorphous $MAPbBr_3$ NPs was found to be nearly independent of temperature, implying that nonradiative decay is insignificant. When applied in multilayer LEDs using a 20-nm-thick n-type-doped ETL, a maximum brightness of 3515 cd m^{-2} accompanied by a maximum EQE of 3.8% was obtained. Kim et al. reported highly efficient perovskite LEDs by employing $MAPbBr_3$ NPs with increasing dimensions and using a Buf-HIL, as previously described [74]. Perovskite NCs with a size exceeding the Bohr radius (i.e. 11–27 nm) showed the highest PLQE (>70%), while perovskite quantum dots (QDs) showed a gradually decreasing PLQE from ~65% for 5-nm QDs to ~62% for 3-nm QDs. They attributed this decrease to the increase in trap-assisted recombination of excitons at surface traps due to the larger surface-to-volume ratio in perovskite QDs. By using 30-nm-thick active NP layers, they achieved a maximum EQE of 5.1%, with sharp electroluminescence at about 1000 cd m^{-2}. Novel colloidal NCs based on alternative cations such as formamidinium (FA) or mixed MA/Cs are also being investigated [75, 76]. Besides their simplicity, however, typical synthesis methods for perovskite NCs have some drawbacks for device applications. Long and insulating ligands are required for the stability of colloidal NCs in solution, but they unavoidably hinder charge transport through the film. Moreover, it is difficult to obtain uniform and dense films from colloidal suspensions. In fact, they saturate at low concentration and undergo substantial aggregation during film formation. For this reason, Zhao et al. developed a method for preparing perovskite NC films in situ, by incorporating bulky organoammonium halides as additives to confine the crystal growth during film formation [77]. They applied this method to the preparation of nanocrystalline films of $MAPbI_3$ and $MAPbBr_3$, with an average crystal size of about 6 nm. These films showed significantly improved PLQY and led to an electroluminescence efficiency of 7.9% and 7.0%, hence being a promising alternative to colloidal perovskite systems for lighting applications.

3.1.3.1 Inorganic Cesium Lead Halide Quantum Dots

Practically, hybrid organic–inorganic perovskite nanostructures are rather unstable and cannot be easily synthetized with a narrow size distribution nor isolated in a single phase (for example, avoiding coexistence of 3D and 2D crystal structures) [78]. Probably as a result of this, several groups turned to the preparation of the analogous inorganic perovskites, where a Cs^+ cation replaces the MA without substantial changes in the structure. Cubic or orthorhombic $CsPbX_3$ NPs can be synthesized with a fine control over the size and shape, as clearly visible in Figure 3.1.8a–c. Importantly, they show enhanced optical properties compared to the hybrid perovskites, i.e. PLQY >90% and a narrow spectral width [79, 81, 82], a tunable bandgap (again, weakly due to size effect, easily modified by halide exchange, Figure 3.1.8d) [80, 83, 84], very small spectral variation, and enhanced stability due to the absence of organic cations in the perovskite [85–87].

As in the case of $MAPbX_3$, the high PLQY of $CsPbX_3$ QDs results from negligible electron- or hole-trapping pathways, when passivated with proper capping ligands [88]. The combination of enhanced optical properties and chemical stability makes $CsPbX_3$ QDs appealing as luminescent materials for lasing [86, 89, 90] and as phosphors to generate white light from UV- or blue-emitting inorganic LEDs. This is especially important for the blue-green spectral region, where more

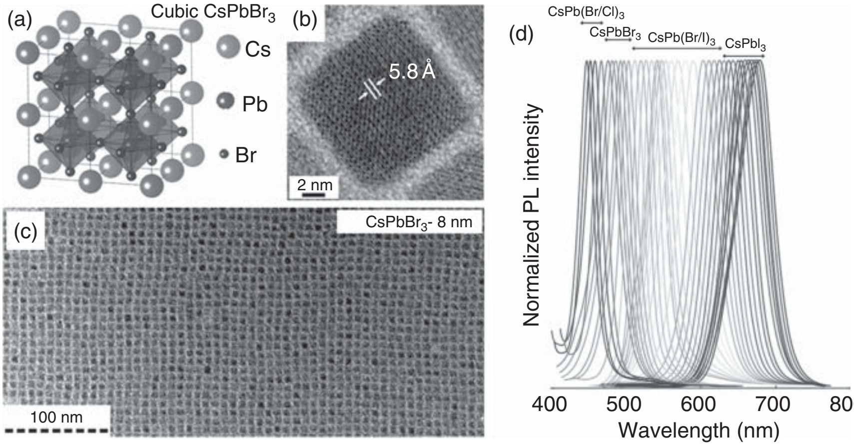

Figure 3.1.8 (a) Schematic of the cubic perovskite lattice and (b, c) typical transmission electron microscopy (TEM) images of monodisperse $CsPbBr_3$ NPs [79]. (d) Fluorescence spectra of $CsPbX_3$ NPs (X: Cl, Br, I and Cl/Br and Br/I mixed halide systems) spanning the whole visible spectral region, obtained by continuously varying the ratio between the lead and cesium sources in a droplet-based microfluidic platform [80].

traditional metal-chalcogenide-based QDs suffer from photodegradation [79]. Recently, their use in LEDs has also been investigated. Song et al. reported the preparation of LEDs based on all-inorganic cesium lead halide ($CsPbX_3$, X = Cl, Br, I) perovskite NCs [91]. They obtained high-quality perovskite QDs through hot-injecting cesium stearate into $PbBr_2$ solution, in the presence of alkylammonium ligands. The luminescence wavelength was tuned by both the size and halide composition of the QDs. Thanks to the good dispersity and the stability of the dispersions, homogeneous, pinhole-free, 10-nm-thick QD thin films could be obtained and used in LEDs. PEDOT:PSS was used in combination with a thin PVK film as the HTL, while TPBi capped with a LiF/Al cathode were used to inject electrons into the device. While rather high luminance was achieved (1000 cd m^{-2} for the green-emitting $CsPbBr_3$), the maximum EQE was low, about 0.1%, especially considering the high PLQY of the thin film used (>85%). Similar results were obtained for $CsPbBr_3$ NCs deposited onto an HTL modified with a perfluorinated polymer, used to enlarge the WF and hence match the perovskite valence band energy [92]. Most likely, beside the homogeneous morphology of the active layer used in these works, current recombination at either the hole- or the electron-transport interface can occur, limiting the device efficiency. To aliviate this, Li et al. used a short exposure to trimethylaluminum (TMA) vapors to cross-link the NCs, reducing the current tunneling through the active layer and allowing the deposition of subsequent charge-injection layers from the solution without damaging the perovskite film [93].

Using an n–i–p configuration with ZnO as the ETL and TFB (poly[(9,9-dioctylfluorenyl-2,7-diyl)-*co*-(4,4′-(*N*-(4-*sec*-butylphenyl))diphenylamine)]) as the HTL, a series of LEDs emitting different colors (from deep red for $CsPbI_3$ to sky blue for $CsPbBr_{1.5}Cl_{1.5}$) were obtained (Figure 3.1.9a). Importantly, the TMA cross-linking was found to have a substantial effect on the device performance,

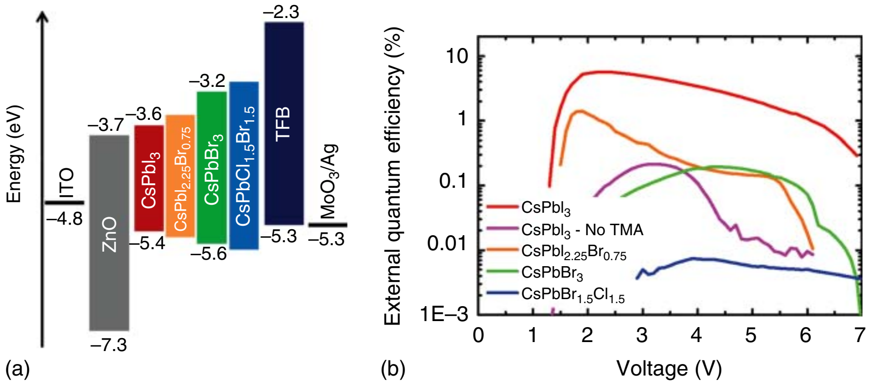

Figure 3.1.9 (a) Flat band energy diagram for the materials used in the preparation of CsPbX3 QDs LEDs and (b) EQE for the same device series. Note the effect of the QDs cross-linking on the device EQE (red and purple curve) [93].

lowering the overall current density and enhancing the radiative recombination by confining the charges in the active layer (Figure 3.1.9b). Through this method, very promising EQE as high as 5.7% was obtained for the $CsPbI_3$ QDs. On the other hand, at increasing bandgap (for blueshifted emission), the EQE was found to drop substantially, most likely due to a barrier for the hole injection at the TFB/perovskite interface (Figure 3.1.9a). In general, the surface chemistry of QDs is crucial for the electroluminescence efficiency. If, from one side, a high density of ligands is needed to provide sufficient surface passivation, they will also hinder an efficient charge transfer when deposited as a thin film. Pan et al. demonstrated stable films of $CsPbX_3$ QDs capped with di-dodecyl dimethyl ammonium bromide, a relatively short ligand that facilitates carrier transport in the film enabling the preparation of efficient LEDs [94]. The synthesis of these films includes an unconventional ligand-exchange strategy to avoid the degradation of the perovskite nanostructures. Besides the moderate luminance level obtained, the multilayer LEDs produced with $CsPbBr_3$ compounds showed high EQE of 3.0%. Furthermore, they applied the ligand-exchange strategy to mixed halide perovskite QDs, and fabricated blue LEDs with a promising maximum EQE 1.9%. Li et al. demonstrated highly efficient solution-processed LEDs by optimizing surface passivation and carrier transport via ligand density control [95]. A cyclic treatment on $CsPbBr_3$ QDs using hexane/ethyl acetate mixed solvent was used to remove excess ligand while maintaining the film luminescence and microstructure. By sandwiching these materials in between polyTPD and TPBi hole and ETLs, respectively, they obtained remarkable EQE exceeding 6%. Chiba et al. studied a series of solvent washing treatment to efficiently remove the ligand excess without altering the perovskite NP film properties [96]. LEDs based on $CsPbBr_3$ washed with butyl acetate exhibited a narrow EL spectrum with a high color purity (full width at half maximum (FWHM) of 17 nm) and a very low turn-on voltage (2.6 V). Importantly, the maximum EQE reached 8.73% at high luminance levels. A more simple but effective post-deposition treatment has been presented by Zhang et al., who were able to efficiently passivate the surface defects of mixed halide $CsPb(I/Br)_3$ NCs with PEI [97]. Using such well-passivated perovskite NC films in optimized LEDs employing both organic and metal oxide charge-transport layers, they obtained red electroluminescence with an EQE of 6.3%. In view of the encouraging performance, stability, and the enhanced optical properties, inorganic perovskite QDs appear to be among the most promising materials for the development of novel LEDs, phosphors, as well as optically and electrically pumped lasers.

3.1.3.2 Quasi-2D Hybrid Lead Halide Perovskites

Besides efficiency, a crucial factor for optoelectronic devices is the environmental stability and photostability under realistic operating conditions. This aspect has long be studied in perovskite photovoltaics, but applies also to LEDs, where the high current densities typically needed to achieve intense brightness cause a severe thermal stress to the emitting material itself. In contrast to their three-dimensional counterparts, layered two-dimensional perovskite films have shown promising stability, thanks to the use of larger and less reactive alkyl- and arylammonium cations. These same species, however, can hinder the out-of-plane charge transport when the organic and insulating layers are oriented parallel to the conducting substrate [98]. This issue has been recently circumvented by engineering perovskite films where the crystallographic planes of the lead halide component have a preferential out-of-plane alignment with respect to the substrate, facilitating charge transport. High photovoltaic PCE and long-term stability under standard operating conditions have been achieved with these materials [99, 100]. In those reports, the materials used are Ruddlesden–Popper layered perovskites with the general formula $(RNH_3)_2(A)_{n-1}Pb_nI_{3n+1}$, where RNH_3 is an alkylammonium cation (i.e. butylammonium) and A is the small intercalated cation (Cs^+, MA, FA, or their mixtures). The $RNH_3{}^+$ cations act as spacers between the inorganic layers $A_{n-1}PbI_{3n+1}$, whose thickness increases with increasing n (Figure 3.1.10a) [104]. For $n = 0$, the material is a pure two-dimensional perovskite formed by layers of lead halide octahedra separated by organic cations. On the contrary, when $n \rightarrow \infty$, the structure is a 3D perovskite analogous to those described in the previous paragraphs. This class of materials, also known as quasi-2D perovskites, gives an additional degree of freedom in the design/tuning of the optoelectronic property. In fact, the structure is that of a multiple quantum well, where the quantum confinement (and hence the bandgap of the semiconductor) depends on the thickness of the inorganic sheet (strictly defined by n) [105]. Byun et al. were the first to report electroluminescent devices from quasi-2D hybrid perovskites [106]. They studied the PL and electroluminescence of perovskite films prepared by mixing the 2D perovskite phenethylammonium lead bromide (PEA_2PbBr_4) with $MAPbBr_3$. They obtained very high PLQY (>40%) for the compound synthesized from PEA_2PbBr_4:$MAPbBr_3$ in 1 : 6 M ratio, due to the formation of smooth and uniform films with very small grain size. They ascribed the enhanced luminescence of the material to the coexistence of different quasi-2D structures ($1 < n < 4$), with an efficient energy transfer occurring from the crystals with larger bandgap to those with smaller bandgap.

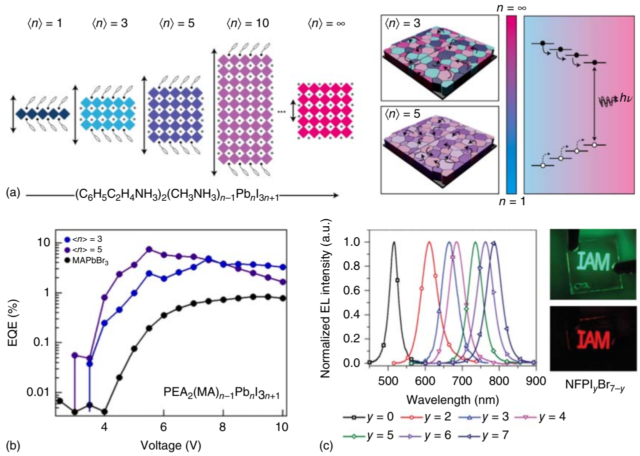

Figure 3.1.10 (a) Unit cell structure of $(PEA)_2(MA)_{n-1}Pb_nI_{3n+1}$ perovskites with different n values, showing the evolution of dimensionality from 2D ($n = 1$) to 3D ($n = \infty$). On the right, illustrations of the carrier transfer process in the same materials with $n = 3$ and $n = 5$, as well as scheme of the energy transfer across an inhomogeneous energy landscape, concentrating carriers to smallest bandgap emitters [101]. (b) EQE versus applied voltage characteristics of the LEDs employing different 3D and quasi-2D perovskite emitters [102]. (c) EL spectra of LEDs based on the quasi-2D perovskites employing 1-naphthylmethylammonium and formamidinium as the large and small cations, respectively. The fraction of iodide versus bromide is represented by y, which in turn modified the emission properties from the red to the green part of the visible spectrum (pictures of working LEDs on the left) [103].

These energy-transfer schemes have been confirmed by Yuan et al., who investigated the analogous iodide series $(PEA)_2(MA)_{n-1}Pb_nI_{3n+1}$ [101]. By means of transient absorption and time-resolved fluorescence spectroscopy, they demonstrated that such quasi-2D perovskite films are indeed inhomogeneous in terms of distribution of structures with different n value, and that carriers are rapidly transferred to the smaller bandgap emitters limiting non-radiative recombination (Figure 3.1.10a). This hypothesis is further confirmed by the fact that the steady-state PL spectrum of a quasi-2D perovskite film reflects the smallest bandgap component, and it is very often close in energy to the bulk 3D material. The performance of quasi-2D perovskite LEDs varies as a function of the n value, and intense NIR electroluminescence with a maximum 8.8% EQE was obtained for quasi-2D perovskite films with $n = 5$. The same group later extended this approach to green-emitting $(PEA)_2(MA)_{n-1}Pb_nBr_{3n+1}$ compounds [102]. By tuning the composition and the deposition parameters, they were able to modulate the domain distribution in the perovskite thin films, achieving PLQY in excess of 60%. When incorporated in simple multilayer devices employing PEDOT:PSS and TPBi as the HTL and the ETL, respectively, high EQEs (7.4%, Figure 3.1.10b) and high luminance (8400 cd m^{-2}) were obtained at low driving voltage. The same approach has also been applied to other quasi-2D systems varying the organic cations and the halide anions. Wang et al. prepared a series of compounds using an aromatic cation, 1-naphthylmethylammonium, and observed the presence of mixed energy gap perovskite structures, responsible for energy transfer and ultimately for the high PLQY (>60%) [103]. The rapid energy transfer process inhibits the exciton quenching effect observed in pure 2D and 3D perovskite thin films. Using PEI ethoxylated-modified zinc oxide as the ETL and TFB/MoO_3 as the hole-injection interface, they prepared LEDs with peak EQE of 11.7% at 2.6 V and a high radiance of around 82 W sr^{-1} m^{-2} at 3.6 V. They also demonstrated that the bandgap of quasi-2D perovskites can be tuned exactly as in their 3D counterparts by exchanging the halide component. LEDs can achieve narrow emission peaks at 736, 685, 664, 611 or 518 nm, when the quasi-2D perovskite films are produced using precursor solutions with various ratios of Br to I (Figure 3.1.10c). More recently, Xiao et al. reported a solution process to form highly uniform and ultrasmooth perovskite films with nanometer-sized grains that can be used in efficient LEDs [107]. The addition of n-butylammonium halides (BAX; X = I, Br) in the 3D perovskite precursor solution impedes the growth of 3D perovskite grains, starting a transition from 3D to layered (Ruddlesden–Popper) perovskite structures. In this way, the EQE of iodide-based perovskite LEDs increased from 1.0% to 10.4% due to the incorporation of BAI. Similarly, the EQE of lead bromide hybrid perovskite LEDs increased from 0.03% to 9.3% following the incorporation of BABr. In the latter green-emitting devices, the power and current efficiency reached 13.0 lm W^{-1} and 17.1 cd A^{-1}, respectively. In view of this, the recently developed quasi-2D perovskite LEDs are now at the forefront of perovskite-based electroluminescent devices, and have the potential to lead not only to efficient but also to very stable optoelectronic devices.

3.1.3.3 Final Considerations

Organic–inorganic (hybrid) and all-inorganic perovskites show optical and electronic properties with a potential for high impact in the development of future light sources. In view of the available literature, when developing perovskite LEDs, one should consider the following:

1) Non-radiative recombination losses must be minimized (the PLQY maximized), either by an effective passivation of traps in bulk perovskite thin films or through the use of nanostructures whose reduced size and surrounding ligands ensure high luminescence efficiency. The use of fast energy-transfer schemes to avoid defect-assisted recombination such as in quasi-2D perovskite is a recent and promising alternative.
2) The perovskite active layer is polycrystalline in nature; hence, the morphology has to be controlled in order to ensure smooth, homogeneous, and pinhole-free films. When using NPs, the same rule applies, and compact layers have to be produced in order to limit charge recombination at the interfaces.
3) The energy levels of perovskites differ sensibly from traditional organic semiconductors. In particular, the low-lying VBM (especially for wide bandgap materials) urges the use and development of HTLs with very large ionization energy, to minimize PCE losses. To a less extent, the same is true for the electron-injection interface. When all these requirements are met, LEDs with EQE comparable to the organic or even to inorganic counterpart can probably be achieved [15, 108, 109].

References

1 Remy, H. and Laves, G. (1933). *Ber. Dtsch. Chem. Ges. A, B* 66: 401–407.
2 Koppen, J., Hamersma, R., Lebesque, J.V., and Miedema, A.R. (1967). *Phys. Lett. A* 25: 376–377.
3 Yang, W.S., Noh, J.H., Jeon, N.J. et al. (2015). *Science* 348: 1234–1237.
4 Saliba, M., Matsui, T., Seo, J.-Y. et al. (2016). *Energy Environ. Sci.* 9: 1989–1997.
5 Kirchartz, T. and Rau, U. (2007). *J. Appl. Phys.* 102: 104510.
6 Kirchartz, T. and Rau, U. (2008). *Phys. Status Solidi A* 205: 2737–2751.
7 Kirchartz, T., Helbig, A., Reetz, W. et al. (2009). *Prog. Photovoltaics Res. Appl.* 17: 394–402.
8 Vandewal, K., Tvingstedt, K., Gadisa, A. et al. (2009). *Nat. Mater.* 8: 904–909.
9 Green, M.A. (2012). *Prog. Photovoltaics Res. Appl.* 20: 472–476.
10 Geisz, J.F., Steiner, M.A., García, I. et al. (2013). *Appl. Phys. Lett.* 103: 041118.
11 Bi, D., Tress, W., Dar, M.I. et al. (2016). *Sci. Adv.* 2: e1501170.
12 Tvingstedt, K., Malinkiewicz, O., Baumann, A. et al. (2014). *Sci. Rep.* 4: 6071.
13 Tress, W., Marinova, N., Inganäs, O. et al. (2015). *Adv. Energy Mater.* 5: 1400812.

14 Stranks, S.D. and Snaith, H.J. (2015). *Nat. Nanotechnol.* 10: 391–402.

15 Sutherland, B.R. and Sargent, E.H. (2016). *Nat. Photonics* 10: 295–302.

16 Chirvony, V.S., González-Carrero, S., Suárez, I. et al. (2017). *J. Phys. Chem. C* 121: 13381–13390.

17 Yin, W.-J., Shi, T., and Yan, Y. (2014). *Adv. Mater.* 26: 4653–4658.

18 Hoke, E.T., Slotcavage, D.J., Dohner, E.R. et al. (2015). *Chem. Sci.* 6: 613–617.

19 Saba, M., Quochi, F., Mura, A., and Bongiovanni, G. (2016). *Acc. Chem. Res.* 49: 166–173.

20 Comin, R., Walters, G., Thibau, E.S. et al. (2015). *J. Mater. Chem. C* 3: 8839–8843.

21 Saba, M., Cadelano, M., Marongiu, D. et al. (2014). *Nat. Commun.* 5: 5049.

22 Sun, S., Salim, T., Mathews, N. et al. (2014). *Energy Environ. Sci.* 7: 399–407.

23 D'Innocenzo, V., Grancini, G., Alcocer, M.J.P. et al. (2014). *Nat. Commun.* 5: 3586.

24 Schmidt, L.C., Pertegás, A., González-Carrero, S. et al. (2014). *J. Am. Chem. Soc.* 136: 850–853.

25 Gil-Escrig, L., Longo, G., Pertegás, A. et al. (2015). *Chem. Commun.* 51: 569–571.

26 Deschler, F., Price, M., Pathak, S. et al. (2014). *J. Phys. Chem. Lett.* 5: 1421–1426.

27 Wu, X., Trinh, M.T., Niesner, D. et al. (2015). *J. Am. Chem. Soc.* 137: 2089–2096.

28 Xing, G., Mathews, N., Lim, S.S. et al. (2014). *Nat. Mater.* 13: 476–480.

29 Stranks, S.D., Burlakov, V.M., Leijtens, T. et al. (2014). *Phys. Rev. Appl.* 2: 034007.

30 Tian, Y., Merdasa, A., Peter, M. et al. (2015). *Nano Lett.* 15: 1603–1608.

31 Wen, X., Ho-Baillie, A., Huang, S. et al. (2015). *Nano Lett.* 15: 4644–4649.

32 Tian, Y., Merdasa, A., Unger, E. et al. (2015). *J. Phys. Chem. Lett.* 6: 4171–4177.

33 Tian, Y., Peter, M., Unger, E. et al. (2015). *Phys. Chem. Chem. Phys.* 17: 24978–24987.

34 Zheng, K., Zhu, Q., Abdellah, M. et al. (2015). *J. Phys. Chem. Lett.* 6: 2969–2975.

35 D'Andrade, B.W. and Forrest, S.R. (2004). *Adv. Mater.* 16: 1585–1595.

36 Xiao, L., Chen, Z., Qu, B. et al. (2011). *Adv. Mater.* 23: 926–952.

37 Chiba, T., Pu, Y.-J., and Kido, J. (2015). *J. Mater. Chem. C* 3: 11567–11576.

38 Sessolo, M. and Bolink, H.J. (2011). *Adv. Mater.* 23: 1829–1845.

39 Tan, Z.-K., Moghaddam, R.S., Lai, M.L. et al. (2014). *Nat. Nanotechnol.* 9: 687–692.

40 Schulz, P., Edri, E., Kirmayer, S. et al. (2014). *Energy Environ. Sci.* 7: 1377–1381.

41 Jaramillo-Quintero, O.a., Sánchez, R.S., Rincón, M., and Mora-Sero, I. (2015). *J. Phys. Chem. Lett.* 6: 1883–1890.

42 Noh, J.H., Im, S.H., Heo, J.H. et al. (2013). *Nano Lett.* 13: 1764–1769.

43 Kumawat, N.K., Dey, A., Narasimhan, K.L., and Kabra, D. (2015). *ACS Photonics* 2: 349–354.

44 Kumawat, N.K., Dey, A., Kumar, A. et al. (2015). *ACS Appl. Mater. Interfaces* 7: 13119–13124.

45 Sadhanala, A., Ahmad, S., Zhao, B. et al. (2015). *Nano Lett.* 15: 6095–6101.

46 Kim, Y.-H., Cho, H., Heo, J.H. et al. (2015). *Adv. Mater.* 27: 1248–1254.

47 Wang, J., Wang, N., Jin, Y. et al. (2015). *Adv. Mater.* 27: 2311–2316.

48 Yu, J.C., Kim, D.B., Baek, G. et al. (2015). *Adv. Mater.* 27: 3492–3500.

49 Choy, W.C.H., Chan, W.K., and Yuan, Y. (2014). *Adv. Mater.* 26: 5368–5399.

50 Cho, H., Jeong, S.-H., Park, M.-H. et al. (2015). *Science* 350: 1222–1225.

51 Yantara, N., Bhaumik, S., Yan, F. et al. (2015). *J. Phys. Chem. Lett.* 6: 4360–4364.

52 Ling, Y., Tian, Y., Wang, X. et al. (2016). *Adv. Mater.* 28: 8983–8989.

53 Zhang, L., Yang, X., Jiang, Q. et al. (2017). *Nat. Commun.* 8: 15640.

54 Kitazawa, N. (1998). *J. Mater. Sci.* 33: 1441–1444.

55 Kitazawa, N. and Watanabe, Y. (2002). *J. Mater. Sci.* 37: 4845–4848.

56 Kojima, A., Ikegami, M., Teshima, K., and Miyasaka, T. (2012). *Chem. Lett.* 41: 397–399.

57 Zhang, M., Yu, H., Lyu, M. et al. (2014). *Chem. Commun.* 50: 11727–11730.

58 Di, D., Musselman, K.P., Li, G. et al. (2015). *J. Phys. Chem. Lett.* 6: 446–450.

59 Li, J., Bade, S.G.R., Shan, X., and Yu, Z. (2015). *Adv. Mater.* 27: 5196–5202.

60 Longo, G., Pertegas, A., Martinez-Sarti, L. et al. (2015). *J. Mater. Chem. C* 3: 11286–11289.

61 Li, G., Tan, Z.-K., Di, D. et al. (2015). *Nano Lett.* 15: 2640–2644.

62 Longo, G., La-Placa, M.-G., Sessolo, M., and Bolink, H.J. (2017). *ChemSusChem* 10: 3788–3793.

63 Huang, H., Susha, A.S., Kershaw, S.V. et al. (2015). *Adv. Sci.* 2: 1500194.

64 Zhang, F., Zhong, H., Chen, C. et al. (2015). *ACS Nano* 3: 4533–4542.

65 Gonzalez-Carrero, S., Galian, R.E., and Pérez-Prieto, J. (2015). *J. Mater. Chem. A* 3: 9187–9193.

66 Tyagi, P., Arveson, S.M., and Tisdale, W.A. (2015). *J. Phys. Chem. Lett.* 6: 1911–1916.

67 Huang, H., Zhao, F., Liu, L. et al. (2015). *ACS Appl. Mater. Interfaces* 7: 28128–28133.

68 Deng, W., Xu, X., Zhang, X. et al. (2016). *Adv. Funct. Mater.* 26: 4797–4802.

69 Ling, Y., Yuan, Z., Tian, Y. et al. (2016). *Adv. Mater.* 28: 305–311.

70 González-Carrero, S., Galian, R.E., and Pérez-Prieto, J. (2015). *Part. Part. Syst. Char.* 32: 709–720.

71 Sichert, J.A., Tong, Y., Mutz, N. et al. (2015). *Nano Lett.* 15: 6521–6527.

72 Gonzalez-Carrero, S., Espallargas, G.M., Galian, R.E., and Pérez-Prieto, J. (2015). *J. Mater. Chem. A* 3: 14039–14045.

73 Xing, J., Yan, F., Zhao, Y. et al. (2016). *ACS Nano* 10: 6623–6630.

74 Kim, Y.-H., Wolf, C., Kim, Y.-T. et al. (2017). *ACS Nano* 11: 6586–6593.

75 Perumal, A., Shendre, S., Li, M. et al. (2016). *Sci. Rep.* 6: 36733.

76 Xu, B., Wang, W., Zhang, X. et al. (2017). *J. Mater. Chem. C* 5: 6123–6128.

77 Zhao, L., Yeh, Y.-W., Tran, N.L. et al. (2017). *ACS Nano* 11: 3957–3964.

78 Vybornyi, O., Yakunin, S., and Kovalenko, M.V. (2016). *Nanoscale* 8: 6278–6283.

79 Protesescu, L., Yakunin, S., Bodnarchuk, M.I. et al. (2015). *Nano Lett.* 15: 3692–3696.

80 Lignos, I., Stavrakis, S., Nedelcu, G. et al. (2016). *Nano Lett.* 16: 1869–1877.

81 Swarnkar, A., Chulliyil, R., Ravi, V.K. et al. (2015). *Angew. Chem. Int. Ed.* 54: 15424–15428.

82 Li, X., Wu, Y., Zhang, S. et al. (2016). *Adv. Funct. Mater.* 26: 2435–2445.

83 Nedelcu, G., Protesescu, L., Yakunin, S. et al. (2015). *Nano Lett.* 15: 5635–5640.

84 Akkerman, Q.A., D'Innocenzo, V., Accornero, S. et al. (2015). *J. Am. Chem. Soc.* 137: 10276–10281.

85 Kim, Y., Yassitepe, E., Voznyy, O. et al. (2015). *ACS Appl. Mater. Interfaces* 7: 25007–25013.

86 Pan, J., Sarmah, S.P., Murali, B. et al. (2015). *J. Phys. Chem. Lett.* 6: 5027–5033.

87 De Roo, J., Ibáñez, M., Geiregat, P. et al. (2016). *ACS Nano* 10: 2071–2081.

88 Wu, K., Liang, G., Shang, Q. et al. (2015). *J. Am. Chem. Soc.* 137: 12792–12795.

89 Wang, Y., Li, X., Song, J. et al. (2015). *Adv. Mater.* 27: 7101–7108.

90 Yakunin, S., Protesescu, L., Krieg, F. et al. (2015). *Nat. Commun.* 6: 8056.

91 Song, J., Li, J., Li, X. et al. (2015). *Adv. Mater.* 27: 7162–7167.

92 Zhang, X., Lin, H., Huang, H. et al. (2016). *Nano Lett.* 16: 1415–1420.

93 Li, G., Rivarola, F.W.R., Davis, N.J.L.K. et al. (2016). *Adv. Mater.* 28: 3528–3534.

94 Pan, J., Quan, L.N., Zhao, Y. et al. (2016). *Adv. Mater.* 28: 8718–8725.

95 Li, J., Xu, L., Wang, T. et al. (2017). *Adv. Mater.* 29: 1603885.

96 Chiba, T., Hoshi, K., Pu, Y.-J. et al. (2017). *ACS Appl. Mater. Interfaces* 9: 18054–18060.

97 Zhang, X., Sun, C., Zhang, Y. et al. (2016). *J. Phys. Chem. Lett.* 7: 4602–4610.

98 Mitzi, D.B., Chondroudis, K., and Kagan, C.R. (2001). *IBM J. Res. Dev.* 45: 29–45.

99 Tsai, H., Nie, W., Blancon, J.C. et al. (2016). *Nature* 536: 312–317.

100 Wang, Z., Lin, Q., Chmiel, F.P. et al. (2017). *Nat. Energy* 2: 17135.

101 Yuan, M., Quan, L.N., Comin, R. et al. (2016). *Nat. Nanotechnol.* 11: 872–877.

102 Quan, L.N., Zhao, Y., García de Arquer, F.P. et al. (2017). *Nano Lett.* 17: 3701–3709.

103 Wang, N., Cheng, L., Ge, R. et al. (2016). *Nat. Photonics* 10: 699–704.

104 Stoumpos, C.C., Soe, C.M.M., Tsai, H. et al. (2017). *Chem* 2: 427–440.

105 Stoumpos, C.C., Cao, D.H., Clark, D.J. et al. (2016). *Chem. Mater.* 28: 2852–2867.

106 Byun, J., Cho, H., Wolf, C. et al. (2016). *Adv. Mater.* 28: 7515–7520.

107 Xiao, Z., Kerner, R.A., Zhao, L. et al. (2017). *Nat. Photonics* 11: 108–115.

108 Veldhuis, S.A., Boix, P.P., Yantara, N. et al. (2016). *Adv. Mater.* 28: 6804–6834.

109 Kim, Y.-H., Cho, H., and Lee, T.-W. (2016). *Proc. Natl. Acad. Sci. U.S.A.* 113: 11694–11702.

3.2

Toward Electrically Driven Perovskite Lasers – Prospects and Obstacles

Songtao Chen[1] *and Arto Nurmikko*[2]

[1] *Brown University, School of Engineering, 184 Hope Street, Providence, RI, 02912, USA*
[2] *Brown University, School of Engineering, Department of Physics, 184 Hope Street, Providence, RI 02912, USA*

3.2.1 Introduction

Synthesis of organic-inorganic halide perovskites by low-cost, solution-based methods has produced an abundance of basic science in the study of light–matter interaction of these newly emerging thin-film and lower dimensional optoelectronic materials. As noted elsewhere in this book, catalyzed by the surge of interest in the Pb-based perovskites and their recent remarkable demonstrations as high-efficiency (>20%) solar cells, solid thin-film perovskites are now subject also to intense scrutiny as possible photonic sources. At this writing (in 2016), one pending question is whether these organic–inorganic hybrid materials can be transformed to competitive high-performance light emitters to disrupt established photonics technologies such as inorganic and organic light-emitting diodes (LEDs) across the visible spectrum, and even more challenging, establish a footprint as useful semiconductor lasers. This chapter outlines both the opportunities and challenges ahead in gauging the prospects of organic-inorganic halide semiconductors as coherent light sources.

Semiconductor light emitters are part of everyday life and just one in the large family of highly developed commodity optoelectronics. Compact lasers form the backbone of fiber optic networks and optical storage devices such as DVDs, while LEDs have already transformed the world of lighting and displays. While LEDs have benefited from both inorganic and organic semiconductor heterostructures, the laser-based device technologies rely dominantly on inorganic III–V compounds, produced by sophisticated epitaxial single-crystal (SC) growth techniques based on molecular beam epitaxy (MBE) and metal–organic chemical vapor deposition (MOCVD). Diode lasers from milliwatt to kilowatt power outputs are off-the-shelf devices in multiple geometries ranging from vertical-cavity to wide-area edge-emitting configurations which are mass produced on large wafer scales. Whether directly or indirectly energized by electrical current injection, the electronically active elements in such laser devices typically consist of a very thin single quantum well (QW) or multiple QWs, about 10 nm each in thickness, that confine the motion of free Bloch-wave

Halide Perovskites: Photovoltaics, Light Emitting Devices, and Beyond, First Edition.
Edited by Tze-Chien Sum and Nripan Mathews.

electrons and holes to nearly two dimensions. Extraordinary performance has been achieved by further reduction in electronic state dimensionality and further enhancement of radiative optical cross-sections. One ultralow current threshold example is the InAs/GaAs materials system where random arrays of quantum dots (QDs), approximating zero-dimensionality in electron–hole (e-h) pair confinement, are formed within the layered device heterostructures by engineering the lattice mismatch strain [1, 2].

In addition to established SC epitaxial lower dimensional optoelectronic materials by MBE and MOCVD in the 1980s, synthesis of a wide range of potentially useful optical nanocrystal (NC) materials has been explored by remarkably simple yet creative routes via solution-based chemistry. This work initially produced a plethora of high quantum yield inorganic luminescent materials, specifically colloidal II–VI, III–V, and lead salt QD compounds. One concrete example of pragmatic success is the recent commercialization of colloidal CdSe-based QDs as full-color luminescent media in flat-panel TVs [3]. This list of inorganics has now been joined in the past few years by the organic-inorganic halide perovskite nano- and microcrystals which are the focus of this chapter. Enticingly, by continuous chemical compositional variation (as opposed to quantum confinement effects in inorganic QDs), the perovskite light emission (and absorption) can span the wavelength range from deep blue to the near infrared (NIR). Hence, an opportunity beckons: low-cost production of single thin-film material where the wavelength of light emission can be tuned seamlessly across a huge spectral range. To date, as reviewed here, early work on solid-state perovskite LEDs based on fine-grain polycrystalline films (ABX_3, A = Cs, CH_3NH_3, $CH(NH_2)_2$; B = Pb; X = Cl, Br, I) have shown encouraging initial laboratory demonstrations (N.B. we use the terms "LED" for perovskites in this chapter as synonymous with the term "electroluminescent devices," given that a number of the charge injection schemes experimented so far lack full microscopic understanding of charge transport in multilayer heterostructures which, by contrast, are well understood in SC pn-junction LEDs).

Moving the goalposts further, the question arises about the opportunities and challenges for full-color spectrum ultracompact coherent sources (high-performance lasers) in the perovskite material families. The internal radiative efficiencies of perovskite NCs can now exceed 90% across the range covering visible and NIR. Crucially, however, and posing challenges well above those of LED requirements, any functional semiconductor laser must be endowed with three critical attributes: (i) an electronic energy band structure compatible with formation of optical gain (amplification); (ii) a low-loss optical resonator for internal photon feedback; and (iii) means for energy-efficient external injection of e–h pairs into the optical gain volume to achieve the lowest possible excitation (current density) threshold for lasing. Beyond achieving high temporal and spatial coherence (monochromaticity and collimated laser beams, respectively), the laser devices must sustain operation without degradation for thousands of hours, say, in such applications as projection display technologies and biomedical spectroscopy.

We first review ongoing exploratory work on electroluminescent devices to understand the electrical injection process in perovskites. This is followed by sections which address the key elements required for a perovskite laser, with examples of contemporary research. Finally, we return to the question of development of the means for electrical injection for perovskite heterostructures in the high current density regime demanded by a diode laser.

3.2.2 Electrical Injection in Perovskite-Based Light-Emitting Diodes (LEDs)

The remarkable efficiencies demonstrated by prototype perovskite-based solar cells reflect the rapid improvements in material quality and thus suggest the potential for perovskite materials as competitive light emitters. Fundamentally, for useful LEDs, one requires a combination of large radiative cross-sections with the ability to efficiently inject e–h pairs into the active region within a heterostructure and the means to configure a device for efficient photon extraction. Practically, achieving long continuous-wave (CW) device lifetimes is of competitive essence. Compared to conventional MBE or MOCVD processing for current solid light devices, an electroluminescent perovskite device could provide an alternative via a solution-based, low-temperature process toward cost-effective optoelectronic applications. However, many basic research and practical obstacles must be overcome (the latter being large-scale fabrication and device lifetime) before perovskite LEDs can become competitive. For example, to reach performance of current inorganic LEDs, which can last brightly and continuously for years with a few tens of A cm^{-2} current density, innovations in the device designs, and particularly the protection and stabilization of perovskite materials, are essential steps to success. We next illustrate the recent work on electroluminescent perovskites focusing on the electrical injection part of perovskite LED devices while referring the reader to more comprehensive recent reviews in the literature [4, 5], and previous chapters in this book.

In spite of partially known details of their electronic states, approaches to design organic-inorganic perovskite LEDs [6–24] borrow from physical concepts of charge-transport and interband optical processes from both organic and inorganic semiconductor physics. This follows, in part, as their electron and hole wave functions may lie typically somewhere between Frenkel excitons in organics (molecular scale Bohr radii) and extended Block states (such as Wannier excitons in crystalline inorganics). Thus, the present prototype perovskite LED structure consists of an active light-generating perovskite layer (normally spin-casted from precursor solution), an n-type electron transport layer (ETL), a p-type hole transport layer (HTL) and external (hopefully Ohmic) metallic contacts. Under forward bias, electrons/holes are injected into the perovskite luminescent layer and radiatively recombined to spontaneously emit photons omnidirectionally. To achieve best working conditions, proper choices about the contacts and ETL/HTL are crucial to realize optimized band alignment. Suggested band alignment of perovskites and various ETLs and HTLs that have been used in reported perovskite LEDs are summarized in Figure 3.2.1a. We underscore that the various suggested band alignments in the literature (such as in Figure 3.2.1a) are based on assumed electronic band

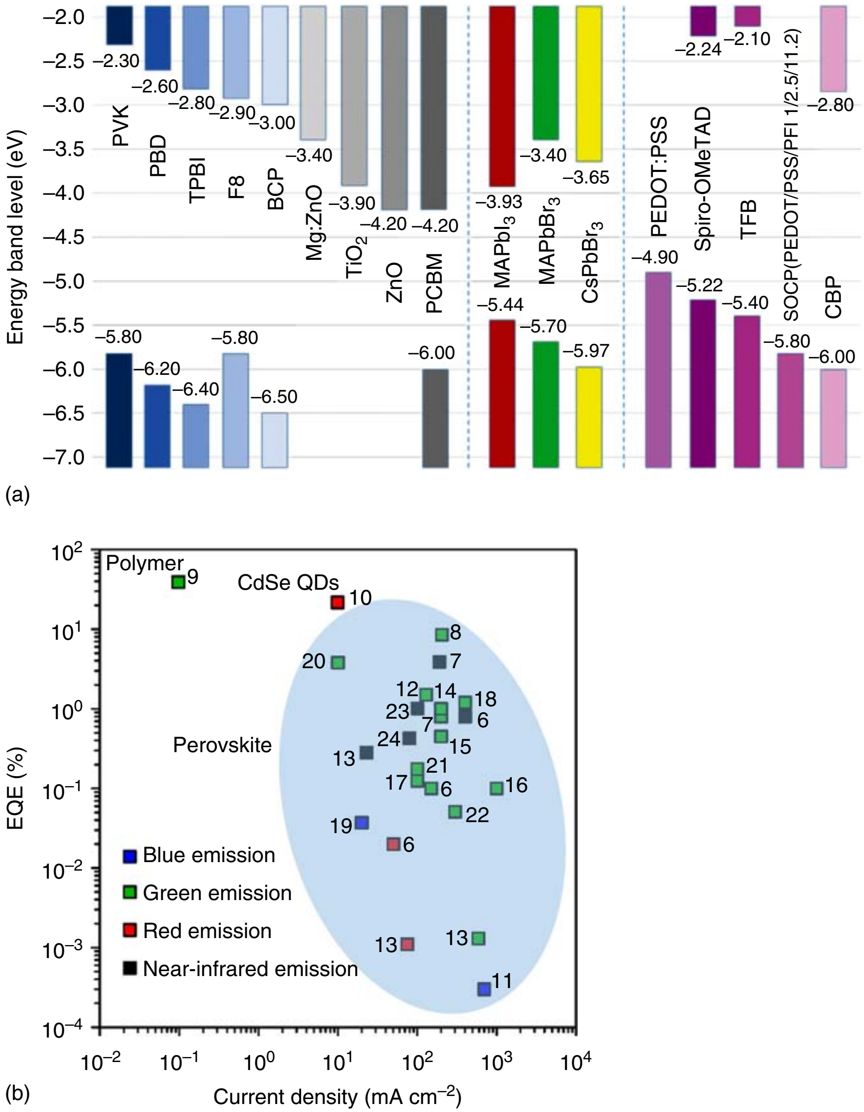

Figure 3.2.1 (a) Energy levels for different materials acting as ETLs (left), active perovskite solid-state films (middle), and HTLs (right) in perovskite LED structures. Source: Veldhuis et al. 2016 [4]. Copyright 2016. Reproduced with permission of Wiley-VCH. (b) Maximum external quantum efficiencies (EQEs) versus corresponding current density from reported perovskite LEDs. Polymer and CdSe QD LED devices are plotted for comparison. Numbers correspond to references.

edges that are derived from, e.g. work function or electron affinity data. Such data or computational estimates are based on electronic states relative to a vacuum interface and have been inaccurate as witnessed during the evolution of the III–V and II–VI inorganic semiconductor heterostructures 20–30 years ago. Realities of solid–solid material interfaces typically renormalize the actual band offsets and band lineups of those predicted from electron affinities due to complex atomic/molecular-level interactions at the interfaces.

Focusing on the microscopics of the electronic and photonic processes within the perovskite active layers within today's exploratory LEDs, one already identified intrinsic challenge is the presence of the non-radiative (three-body) Auger recombination process. The estimated and reported magnitudes of the Auger cross-sections for perovskites vary widely (>one order of magnitude) in the current literature. Relevant to higher injection levels, we note that as a three-particle inelastic scattering process, Auger rates increase nonlinearly with electron–hole pair densities (as $\sim n^3$ for the Bloch state wave functions in SC inorganic semiconductors where there is also an additional scaling factor through the bandgap energy, making smaller bandgap semiconductors more vulnerable). Thus, although the non-radiative Auger loss can be modest at low excitation levels, which is typically used in the LED devices, it affects demonstrably the performance of devices under higher level injections (e.g. to realize high-power perovskite LEDs), and is aggravated further when the carrier injection is imbalanced due to the imperfect transport layers and interfaces. In terms of external quantum efficiencies, the intrinsically rather high refractive index of perovskite thin films ($n = 2.2$–2.6 for bromide and iodide-based perovskites) needs to be dealt with for the development of efficient perovskite LEDs, to minimize the internally generated photon recapture within the active layer due to the total internal reflection (e.g. at the multiple interfaces of the enveloping injector structure). This photon recycling process was shown to be quite efficient in perovskite films [25], limiting the intrinsic external photoluminescence quantum efficiency of perovskite materials in the absence of light output coupling schemes.

Returning to the basic physics of spontaneous emission in perovskites, we note the following. If the radiative recombination processes in the organic-inorganic halide perovskites are closer to the Wannier than to the Frenkel exciton limits, available scaling rules suggest larger exciton binding energies yield increased recombination cross-sections (and help further confine the injected carriers in active layers). Results to date for the smallest bandgap iodide-based perovskites confirm that closely packed solid perovskite thin films may have an inherently low exciton binding energy [26], whereas the bromide-based larger gap materials show, e.g. clear bound exciton states in their room temperature films. Using a thinner perovskite active layer to mimic QWs can benefit carrier confinement, yet fabrication of ultrathin and continuous polycrystalline films remains challenging. In attempts to reduce the electronic state dimensionality, fabrication of perovskite nanoplatelets [27]/nanorods [28]/QDs [29] has been recently reported; however, the LED devices based on these newer forms of perovskites have failed to reach higher performance (e.g. higher injection current) than 3D perovskite solid film emitters. Due to current fabrication challenges, additional transport and photonic loss mechanisms (e.g. nonideal surface passivation, poor film quality, etc.) need to be addressed on the way to the next generation of lower dimension perovskite LEDs.

As a snapshot of ongoing progress, Figure 3.2.1b summarizes performance of some representative recent perovskite LED devices while focusing on metrics such as the maximum EQEs and corresponding current densities. Contemporary performance of small-molecule polymer [9] and II–VI CdSe QD [10] LEDs are also plotted for comparison. With a more mature material system and reasonably well-optimized carrier transport layers and interfaces, polymer and II–VI QD LEDs can now achieve EQE up to 20–40%, although both are still in research and development phase. For another important gauge of progress to date, we note that all the perovskite LED devices reported so far (to the best of our knowledge) show limit current density (~1 A cm^{-2}). Further increase of the current density will result in efficiency roll-off in the device performance and, given also the relatively high junction voltages, leads to rapid sample degradation, most likely due to internal heat generation in the active layer [6]. Indeed, thermal and chemical stability of perovskite materials are proved to be less competitive than conventional materials like polymer or II–VI QDs (let alone the epitaxial grown SC QWs). Beyond the optimization of carrier transport layers and interfaces in the device, further protection (i.e. hermetic sealing) and effective surface passivation of perovskite layers, as well as improving the film quality are essential for realizing robust perovskite LEDs, which also benefits perovskite solar cells and prospects for diode lasers. Especially for establishing credentials for a perovskite laser, considerable progress in ongoing and future research is imperative, to significantly increase robustness and capability to support much higher levels of current injection (probably starting at a minimum of ~100 A cm^{-2} to the kA cm^{-2} regime), while also satisfying the requirements for optical gain and fabrication of integrated optical resonators as described next. We return to the issues associated with electrical injection at the end of this chapter.

3.2.3 Optical Gain in Thin-film Solid-state Perovskites

Optical gain is fundamental for any laser, resulting from a population inversion (extreme nonthermal equilibrium) within a given set of electronic states. These states and gain dynamics are very well known in the inorganic III–Vs and II–VIs, while a corresponding picture is rather opaque in the perovskite latecomers in the visible and NIR. As for other solution-derived materials, and providing a possible guide to perovskites, literature reaching back 20 years shows that significant optical gain (in units of cm^{-1}) can be achieved in colloidal II–VI CdSe/CdS and related core–shell semiconductor QDs. One example of optical gain manifested through amplified spontaneous emission (ASE) is shown in Figure 3.2.2a–c. In the colloidal II–VI QDs, research initially focused on dissecting the role of various multiple exciton states as underpinning optical gain. From evidence that biexciton complexes were the main contributor to optical gain [30, 31], recent work on densely packed thin films has progressed to show that the so-called single exciton gain regime can be reached with the benefit of lower excitation levels for gain, thereby eliminating most of the non-radiative many-body Auger recombination [32–34]. Importantly, Wannier-type excitons in II–VI QDs are robust at room temperature, providing large optical oscillator strengths (and gain) across a narrow spectral resonance.

A new actor for solution-grown II–VI NCs has emerged in past years as a complement material for potential use for lasers in the visible, namely, so-called

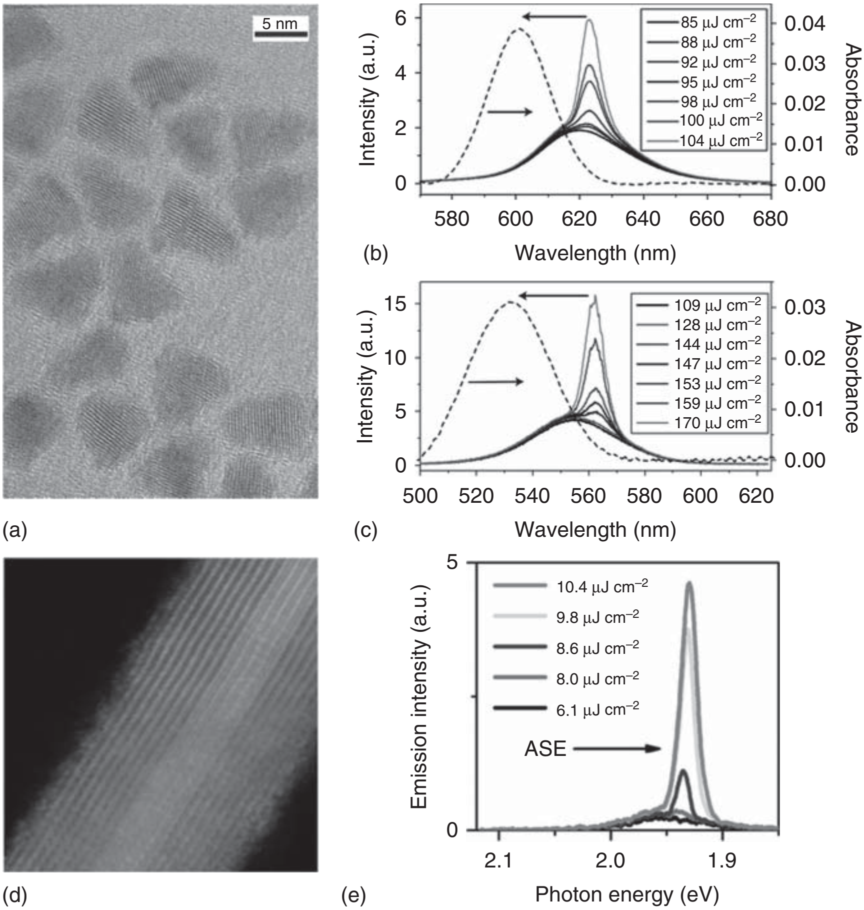

Figure 3.2.2 (a) TEM image of red colloidal CdSe/CdS QDs. (b, c) Spectral analysis of edge emission ASE, together with absorption peaks of the lowest exciton state for red and green colloidal QD films. The lowest exciton absorption peaks were isolated from full spectrum absorbance results. Source: (a–c) Dang et al. 2012 [32]. Copyright 2012. Reproduced with permission of Nature Publishing Group. (d) Cross-sectional TEM image of a CdS–CdSe–CdS single nanoplatelet, resolving individual atomic planes. (e) ASE from thin-film nanoplatelet ensembles at increasing levels of pulsed optical pumping energy density. Source: (d, e) She et al. 2014 [35]. Copyright 2014. Reproduced with permission of American Chemical Society.

QW nanoplatelets [36]. The nanoplatelet concept bridges the traditional epitaxial QW laser research (such as exploited in the first blue-green diode lasers in the 1990s [35, 39]) and established colloidal QD work. By adjusting growth conditions (whether in solution or vacuum deposition processes), ensembles of single platelets can be produced. In each platelet, the electronic states form a hybrid between the QWs and QDs for e–h pair confinement for enhancement of the exciton Coulomb interaction for gain [35, 39] (ASE example is shown in Figure 3.2.2d,e). Remarkably, even CW lasing from closely packed nanoplatelet thin films has been reported, suggesting a role for cooperative single-exciton effects across the platelet ensemble by dipolar coupling [40]. The question in case of the organic-inorganic halide perovskites is whether excitons or free electron–hole pairs (in interacting dense plasma), or a mixture of both, reflect the microscopics of gain with examples of experimental results discussed next.

For the solution-grown perovskites, the past years have witnessed multiple reports on stimulated emission, both in perovskite polycrystalline thin films [41, 42] and inorganic perovskite colloidal NCs [43]. In both cases, the implied optical gain can cover both NIR and visible spectra through chemical (compositional) tuning of the halide elements. Figure 3.2.3 summarizes some early results of such stimulated emission from compositionally varying perovskite thin films. Encouragingly, ASE can be observed at rather low threshold energy density albeit under transient (ultrashort) optical pumping conditions. The first reported value [41] of an ASE threshold of $10 \pm 2\,\mu\text{J cm}^{-2}$ (bulk equivalent carrier density $\rho = 1.7 \times 10^{18}$ cm^{-3}; assuming no non-radiative recombination in this extreme transient limit) is lower or comparable with state-of-the-art solution-processed II–VI colloidal QDs or nanoplatelets [32, 35]. The relatively low ASE threshold benefits from the large absorption coefficient of perovskite thin-film materials, low density of trap states and (in this case) modest Auger recombination rates. The low threshold energy density also assists the film to sustain the stimulated emission for 26 hours ($\sim 10^8$ laser shots) under continuous femtosecond ultrashort pulse pumping [41].

While the ASE experiments under extreme transient conditions (<1 ps) serve as useful prognosticators of perovskite light emitters, practical lasers require that optical gain is sustainable under longer pulse-pumping condition on the way toward fully CW operation. Reaching such steady-state regimes of operation adds additional factors of significance which must be characterized: (i) the need to quantify effects of competing Auger recombination at a given required e–h pair density and (ii) managing the significantly increased thermal load that the perovskite solid films must endure by incorporating effective heatsinking into the device structure. The latter is inherently challenging given the relatively low thermal conductivity of the fine-grain polycrystalline film structure typical of perovskite solution-originating solid thin films. While work is still in the embryonic stage, we note that ASE signals have been reported in a steady-state regime (using 300-ns-long pump pulses), from a $CH_3NH_3PbI_3$ solid thin film – but below 240 K [42] (Figure 3.2.4a). At room temperature, stimulated emission from perovskite solid films under such long pulse pumping is yet to be reported (at this writing). Examples of other ASE reports [41–50] (i.e. threshold energy density and corresponding excitation pulse duration) observed at room temperature are summarized in Figure 3.2.4b for comparison (as of mid-2016).

For thin films of high optical uniformity, optical gain coefficients are usually extracted by the variable stripe length (VSL) method as being practically the simplest [51]. Here, spontaneous emission photons are amplified through propagation along the stripe excited area, which benefits from vertical waveguide optical confinement by index contrast between the layers, and from lateral confinement due to self-induced index change in the electronically excited stripe medium. Above the threshold of ASE, net modal gain g_{mod} exceeds zero so that the amplified emission emerges from the stripe edge ($g_{\text{mod}} = \Gamma g_{\text{mat}} - \alpha$, where

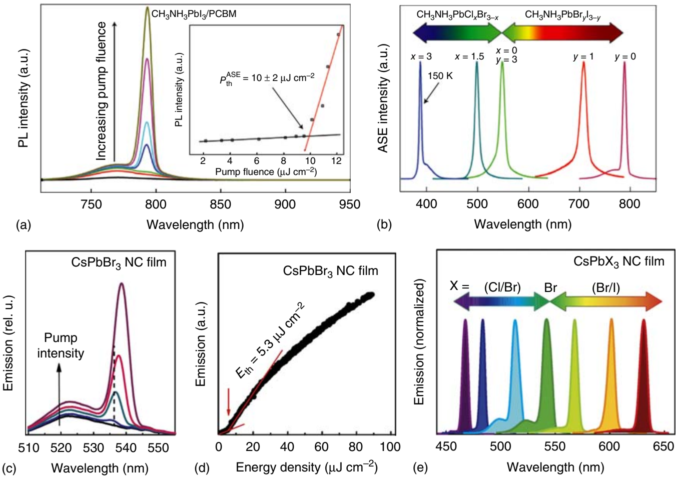

Figure 3.2.3 (a) The pump-fluence-dependent PL spectra and PL intensity (inset) of the quartz/$CH_3NH_3PbI_3$ (65 nm)/PCBM film structure. In the inset, the black and red lines represent the linear fits to experimental data in the two linear regimes of spontaneous emission and ASE, respectively. (b) Wide wavelength tunability of ASE wavelengths from solution-processed organic–inorganic halide perovskite films. Source: (a, b) Xing et al. 2014 [41]. Copyright 2014. Reproduced with permission of Springer Nature. (c) Pump-fluence dependence of the emission from a $CsPbBr_3$ NC film (pumping energy density range: 3–25 μJ cm^{-2}). (d) Threshold behavior for the intensity of the ASE band of the $CsPbBr_3$ NC film. (e) Spectral tunability of ASE via compositional modulation. Source: (c–e) Yakunin et al. 2015 [43]. Copyright 2015. Reproduced with permission of Springer Nature.

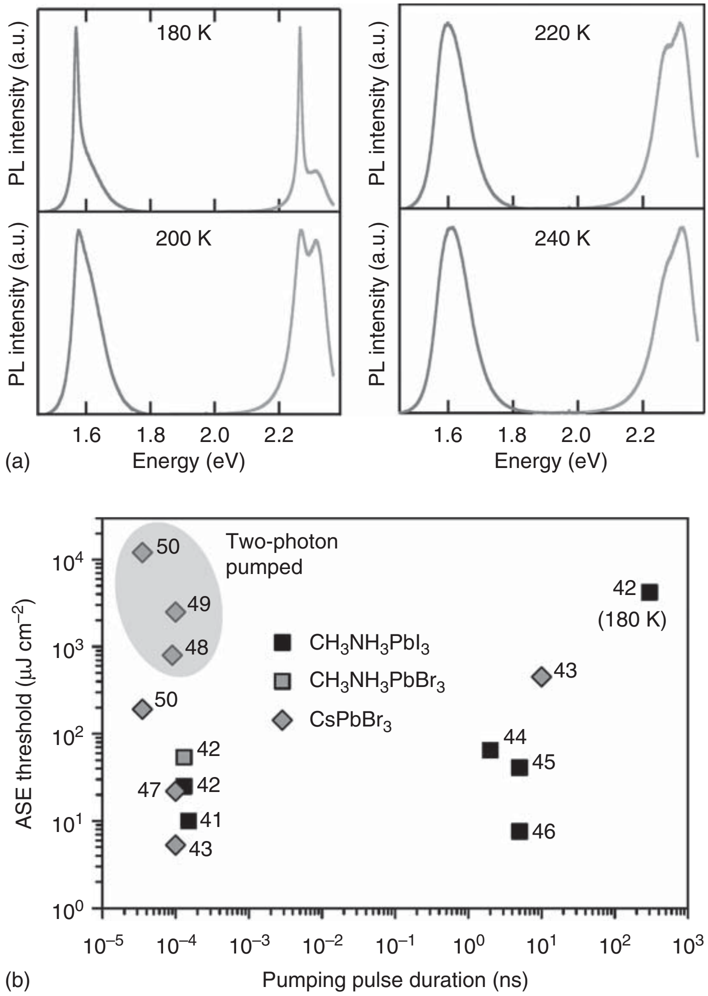

Figure 3.2.4 (a) Time-integrated photoluminescence spectra of $CH_3NH_3PbI_3$ (left, ~1.6 eV) and $CH_3NH_3PbBr_3$ (right, ~2.3 eV) perovskites at different temperatures; ASE occurred at cryogenic temperatures (180 K), but disappeared around 220 K. The photoluminescence was excited by 300-ns-long laser pulses with a repetition rate of 6 Hz and 2.35 eV photon energy. Source: Reproduced with permission [42]. Copyright 2015, WILEY-VCH. (b) Room temperature ASE threshold values of perovskite ($CH_3NH_3PbI_3$, $CH_3NH_3PbBr_3$, $CsPbBr_3$) thin films versus corresponding excitation pulse durations. Numbers indicate the corresponding references.

g_{mod} is the net modal gain, Γ is the optical confinement factor, g_{mat} is the material gain, and α is the optical loss). The telltale signature is a greatly narrowed emission spectrum and sharply increased output power. The significant refractive index contrast between perovskite thin films and typical cladding layers (i.e. quartz substrate, organic layer, air, etc.) generally results in rather large optical confinement ($\Gamma \approx 1$). Thus, the amount of net modal gain largely depends on the perovskite material gain and optical losses the photons experience during propagation within the film, both closely relate to the film quality.

Solution-grown perovskites appear usually as polycrystalline solid thin films where the single grain size ranges from a few tens to a few hundreds of nanometers. Thus, light scattering (Rayleigh–Mie range) can readily introduce unwanted or confounding optical losses and/or interference. For example, such random scattering, acting as random optical feedback, has led to early reports of so-called random lasing from perovskite films [52, 53]. While being important indicators of the presence of optical gain, random lasing offers few changes for harnessing coherent emission as well-defined laser beams. Obviously, a smaller grain (subwavelength size) perovskite film will experience less optical scattering for light amplification and emission, yet the higher density of grain surfaces and boundaries can also induce more non-radiative recombination. Optimized balance in this trade-off is apparently needed for best results of optical amplification and laser-like function of perovskite thin films (such trade-offs being much less critical in photovoltaics). By the VSL method, a rather large range of values for the net modal gain have been reported for organic-inorganic halide perovskites [41, 44, 54] (in the range of 40–250, 125, 12–27 cm^{-1}). Cesium lead halide perovskite NC thin films have been demonstrated as another efficient solution-processed gain medium; net modal gain values of 450 and 580 cm^{-1} were reported in this larger bandgap material [43, 48] at shorter visible wavelengths. Synthesis and fabrication efforts are ongoing to further reduce the grain size toward very small (<100 nm) perovskite grains in the fabrication of densely packed thin films to achieve a less polydisperse grain size distribution and to achieve commensurate increases in the modal gain.

At present, the electronic origin of optical gain in halide perovskites is considerably less transparent than for conventional III–V semiconductor lasers or, for that matter, in the colloidal II–VIs, mainly given the perovskites' incompletely understood electronic structure. Of obvious relevance also to the perovskite-based solar cells, focused research is needed particularly to model theoretically the lowest electronic excitations near the band-edge states. Experiments suggest that e–h pairs may have only a few meV exciton binding energy at room temperature [26] in the (NIR) iodide compounds so that free electron–hole Fermi-plasma-type recombination is more likely to account for the stimulated emission in these classes of organic-inorganic halide perovskite material [55]. As an example, for ASE in the lead halide perovskites, a predominant population of free carriers was generated at a carrier density $\rho < 10^{18}\ \text{cm}^{-3}$ (i.e. screening of excitons in the plasma state) [55]. At even higher densities ($\sim 10^{19}\ \text{cm}^{-3}$), which may be required for high-power laser operation whether optically or electrically pumped, the carrier dynamics enter a regime where added competition between bimolecular recombination and Auger process will occur. On the other hand, for cesium lead halide–based perovskite NCs with their larger bandgap and lower dielectric constant, excitonic gain has been speculated to be the origin of the stimulated emission, given the robust spectral fingerprints of bound excitons at room temperature [43, 47]. In principle, the optical gain cross-section benefits from Coulomb-bound states since oscillator strength is concentrated within a narrower energy range than for a Fermi gas. Overall, however, detailed spectroscopic studies of optical gain await further understanding of perovskite material gain for maximum exploitation in laser devices.

3.2.4 Integrating Optical Resonators and Perovskite Gain Media

Fundamental to making an electromagnetic oscillator, gain in the active medium must be combined with physical structures that provide closed-loop feedback for amplified photons with minimal losses in a laser. In the case of MBE/MOCVD-grown epitaxial QW and QD semiconductor lasers, microfabrication of optical cavities is inherently compatible with the layered heterostructures (whether as ridge-waveguide edge-emitting geometries or as vertical surface-emitting resonators). By contrast, this perovskite film extracted from solution-processed materials requires both innovation and process dexterity in microfabricating compact optical feedback structures from physically and chemically compatible materials and integrating those with the perovskite films. Most reports in the perovskite laser literatures (such as those cited earlier) have been content to express evidence for stimulated emission from ASE-based observations that report (i) spectral narrowing and (ii) change of slope in the input–output power characteristics across a threshold for onset of stimulated emission. As noted, there are also a number of instances where intrinsic or extrinsic microstructure features of the solution-processed films embed "accidental" optical resonators, whereby the radiation collected from the samples exhibits, e.g. whispering gallery modes (WGMs) or random lasing, or a mixture of the two. Such outcomes bypass an important practical issue, namely, the implementation of optical resonators whereby useful laser beams (i.e. spatially and temporally coherent cavity modes) are extracted from the devices. This particular aspect requires more attention of current perovskite laser research so that the claims of laser operation fully justify such an appellation – while accompanied by direct evidence of a spatially coherent device output.

Demonstrations of true laser-like devices are now emerging using thin films derived from solution-grown source materials. Both vertical cavity and distributed feedback (DFB) optically pumped lasers have been microfabricated [56–59]. The DFB-type Bragg-reflector cavities as well as the more advanced structures such as the recently demonstrated photonic crystals [60, 61] require that the thin films can be deposited from the solution conformally onto nonplanar, nanostructured patterned templates which embed an optical waveguide feedback structure, or by applying post-fabrication of resonator features after such deposition by employing lithographic and other micropatterning tools. Conformal deposition of perovskite films even on high-Q micro-ring [48] or spherical cavity microspheres [43, 44] have been demonstrated, although efficient coupling of coherent light out from such high-confinement photonic structures remains a generic challenge. A sampling of reported optical resonator/feedback structures for perovskite thin-film lasers are shown in Figure 3.2.5a–d. The threshold values for perovskite thin-film lasers [44, 48, 52, 53, 56–61] span the range of excitation energy densities from 1 to 100 μJ cm^{-2} under pulsed optical pumping conditions (summarized in Figure 3.2.5e). These laboratory results are encouraging at this early stage of perovskite laser development as the lasing threshold values are comparable to some of the best performance for other

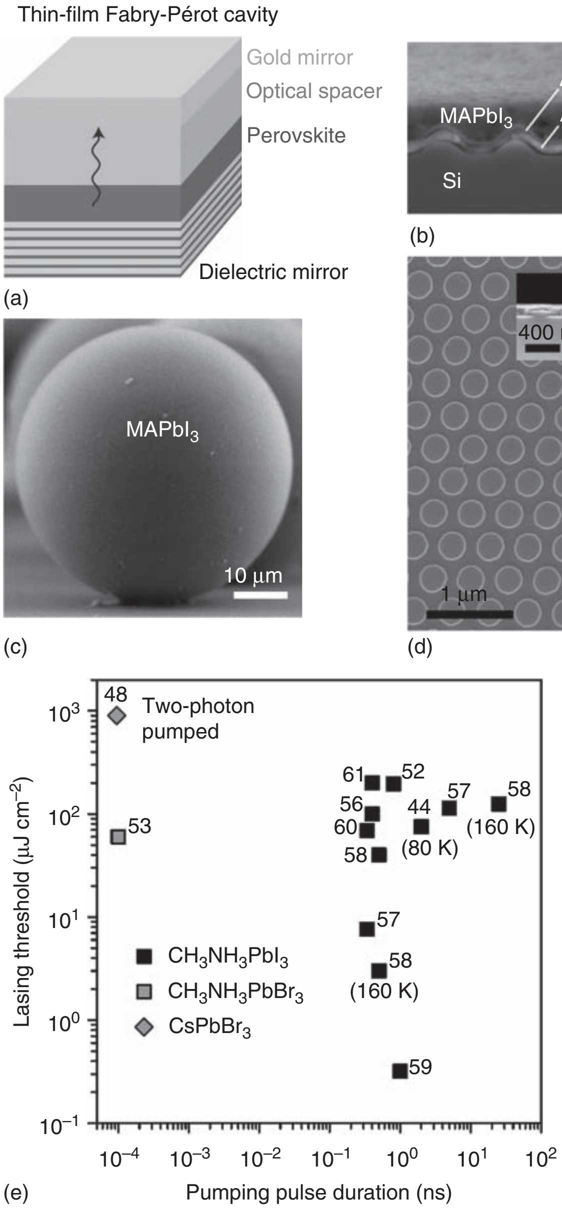

Figure 3.2.5 (a) Schematic of basic vertical cavity Fabry–Perot laser enclosing planar perovskite gain medium. Source: Reproduced with permission [5]. Copyright 2016, Nature Publishing Group. (b) Cross-sectional SEM image of one perovskite DFB laser structure. Source: Reproduced with permission [58]. Copyright 2016, American Chemical Society. (c) SEM image of a microsphere cavity coated with perovskite gain medium. Source: Reproduced with permission [44]. Copyright 2016, American Chemical Society. (d) Plan view SEM image of 2D photonic crystal nanostructure pattern. Inset shows cross-sectional SEM image of a perovskite film deposited on the photonic crystal pattern. Source: Reproduced with permission [60]. Copyright 2016, American Chemical Society. (e) Comparison of representative room temperature lasing thresholds of optically pumped pulsed perovskite ($CH_3NH_3PbI_3$, $CH_3NH_3PbBr_3$, $CsPbBr_3$) thin-film lasers versus corresponding excitation pulse durations. Numbers indicate corresponding references.

solution-processed materials, including polymers [62], colloidal II–VI QDs [32], and nanoplatelets [39] under similar optically pumped excitation conditions.

These examples illustrate that, in principle, the organic-inorganic halide perovskites possess an electronic structure and optical properties derived therefrom are attractive candidates as compact low-cost coherent light emitters. Further representative of current progress of work on advanced microcavities is shown in Figure 3.2.6 of a vertical-cavity surface-emitting laser ("PeVCSEL"), which lends itself to detailed photonic characterization while emitting spatially and temporally coherent well-defined modes. This device was achieved by constructing a monolithic high-Q planar PeVCSEL structure where a uniform 300-nm-thick perovskite solid film was sandwiched between two high-reflectivity ($R \approx 99.5\%$) distributed Bragg reflectors (DBRs). The DBRs, in turn, deployed gallium nitride semiconductor process innovations where nanoporous-GaN (NP-GaN) provided the low-index layers to a NP-GaN/GaN multilayer DBR stack. The low-loss photonic microcavity enabled low-threshold ($\sim$7.6 μJ cm^{-2}) single-mode laser operation at room temperature and allowed direct access to the study of perovskite gain dynamics and material robustness for future device development.

Ultimately, as noted, CW operation of a perovskite laser at room temperature will represent a key milestone and reality check. This milestone has not yet been achieved in perovskite laser devices even in the optically pumped case. At a cryogenic temperature (i.e. 160 K), perovskite thin-film steady-state lasing was shown with DFB grating structure under 25 ns pulse pumping [58]. Jia and his coauthors used sapphire and metal-coated silicon gratings structure as the optical resonator (Figure 3.2.5b), in an attempt to combine optical feedback with a highly thermally conductive cavity. At room temperature, lasing operation was observed with 5 ns pulse pumping in a vertical-cavity surface-emitting (VCSEL) structure [57]. This pumping condition likely places the laser into a quasi-steady-state regime as follows: at lasing threshold of $\sim$110 μJ cm^{-2} (carrier injection density $\rho \sim 1.4 \times 10^{18}$ cm^{-3}), the Auger recombination lifetime was estimated to be in the range of 1.4–4.2 ns depending on the range of different Auger rate constants $(1.3\text{–}4) \times 10^{-28}$ cm^6 s^{-1} reported [55, 63–65]. To enable further increase in the duty cycle (toward quasi-cw operation and beyond), there is much room for further reduction of optical losses and improvement of laser cavity Q-value (thus, lowering threshold gain needed for laser operation). In parallel, research into chemical/physical engineering of the thermal/chemical/photostability of perovskite thin films is essential for advancing proof-of-concept perovskite laser devices illustrated here.

Another approach for making perovskite optical resonators takes advantage of their direct SC synthesis in the form of nanowires [66–72] and nano/microplatelets [73–78]. Such solution or chemical vapor deposition (CVD)-grown structures can naturally form Fabry-Perot-type (Figure 3.2.7a) or WGM-type (Figure 3.2.7b,c) microcavities to provide built-in, total internal-reflection-enabled waveguided optical feedback. Efficient optical feedback of an SC cavity and the evidently low trap density in these types of nanomaterials have led to reports of ultralow lasing threshold of $\approx$0.22 μJ cm^{-2}, albeit under extreme transient conditions ($\sim$100 fs pulsed pumping) [66].

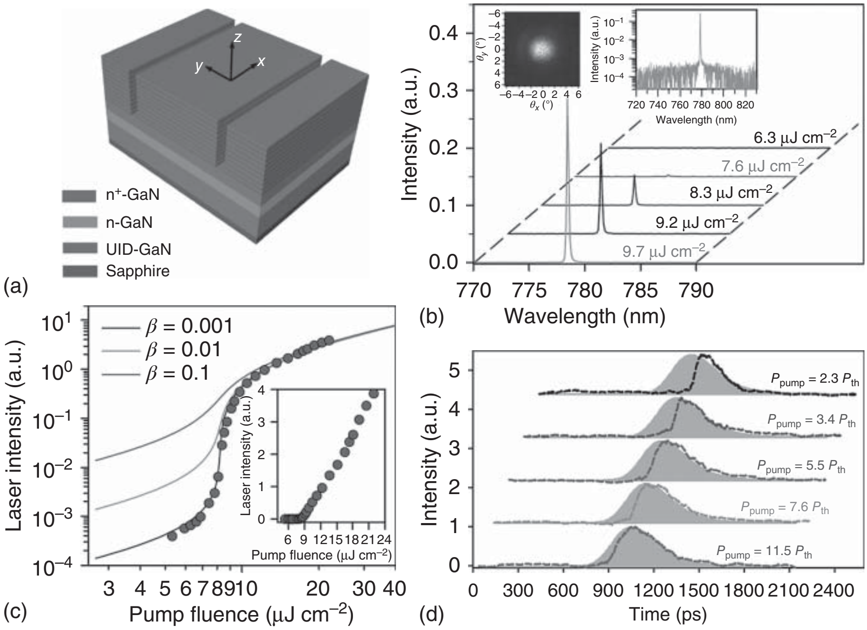

Figure 3.2.6 PeVCSEL laser characteristics under sub-ns pumping (from [57]). (a) Schematic structure of a GaN-based DBR. After epitaxial growth of 10 pairs λ/4 n^+-GaN/GaN stack, trench grooves were dry etched to expose the side walls of n^+-GaN layers. Electrochemical etching process was then used to convert n^+-GaN into NP-GaN laterally. (b) Spectrum (770–790 nm) evolution under different pump fluences. Spectrally coherent single-mode lasing peak at 778.4 nm with a FWHM of 0.24 nm was observed. Left inset shows the far-field pattern of the PeVCSEL laser. Well-defined output beam was emitted perpendicular to the device plane, consistent with spatial coherence and small divergence angle (<3°). Right inset shows the spectrum on logarithmic plot demonstrating single-mode operation (background suppression ratio > 20 dB). (c) Device output power with increasing pump fluences in log–log scale, showing the threshold region as the "kink" between two linear regimes of spontaneous emission and lasing, and yielding threshold energy density of $7.6 \pm 0.6\ \mu J\ cm^{-2}$. The solid lines are rate equation fittings, the best fit to the experiment data gives estimated value of spontaneous emission factor β (∼0.001) and cavity quality factor Q (∼1110). The fits to hypothetical β of 0.01 and 0.1 are also presented for comparison. Inset shows threshold knee behavior in L–L curve plotted on a linear scale. (d) High-speed time-resolved measurements of PeVCSEL lasing pulses (time referenced to pump pulses) at varying pump energy densities. The gray background shows the temporal shape of pump pulses (532 nm, 0.34 ns, 1 kHz). The amplitudes of both pump pulses and PeVCSEL laser output are normalized for ease of visual comparison.

As a practical matter, the random spatial distribution and orientation of these types of microstructures when distilled from the solution on a solid substrate poses a challenge of isolating and extracting "best" single devices, in addition to difficulties in providing for efficient laser light extraction/collection for useful purposes. Yet, by pre-patterning the single-layer h-BN with lithography and etching process, Liu et al. realized periodic growing of perovskite microplatelets [74] (Figure 3.2.7d) on a silicon substrate. Although evidence for phase-coherent laser emission from such a 2D perovskite microplatelet array is perhaps not yet

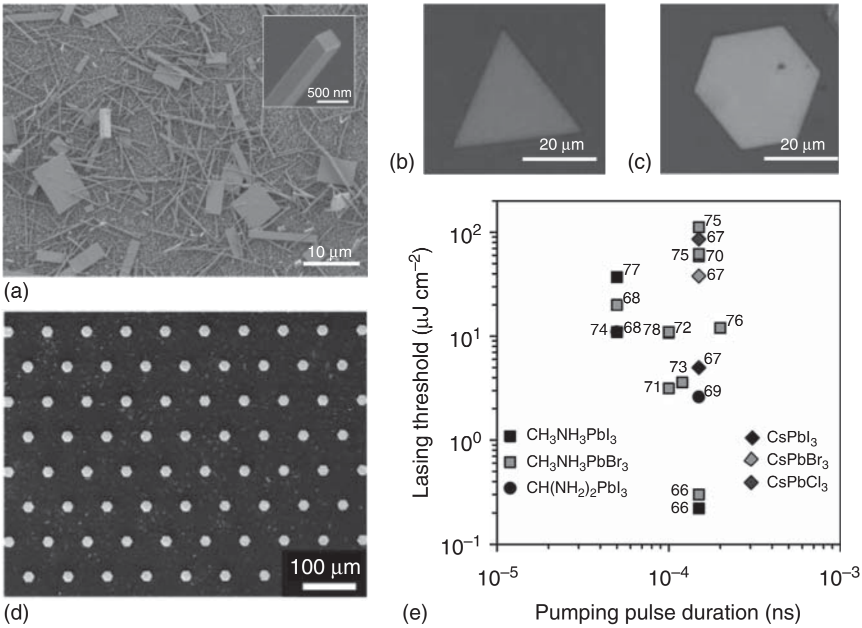

Figure 3.2.7 (a) SEM images of solution-grown mixture of $CH_3NH_3PbI_3$ nanostructures within a reaction time of 24 hours. Source: Reproduced with permission [66]. Copyright 2015, Nature Publishing Group. (b, c) Optical images of two typical CVD-grown $CH_3NH_3PbI_3$ nanoplatelets. Source: Reproduced with permission [77]. Copyright 2014, American Chemical Society. (d) SEM image of the as-prepared $CH_3NH_3PbI_3$ platelet 2-D array. The edge length of hexagonal platelet is ≈15 µm. Source: Reproduced with permission [74]. Copyright 2016, WILEY-VCH. (e) Room temperature lasing threshold values of perovskite single-crystal (nanowire/platelet) lasers versus corresponding excitation pulse durations. Numbers indicate corresponding references.

wholly unambiguous, this innovative synthesis/microfabrication approach may offer a pathway for useful outcome of the microplatelet material translational strategy. As a short summary, Figure 3.2.7e compares lasing threshold values of reported SC perovskite lasers, including their corresponding excitation pulse durations [66–78]. Compared with perovskite thin-film lasers, the early SC-based perovskite laser devices have slightly lower threshold energy density (using the ultrashort femtosecond pump pulses). On the other hand, the significantly higher surface-to-volume ratio in perovskite SC nanowires/platelets (versus the polycrystalline thin film) makes them more sensitive to temperature and environment due to exposed surfaces, and thus more vulnerable when exposed in ambient conditions without protective packaging. Similar to the field of nanowires and nanoplatelets as a whole, the perovskite structures such as in Figure 3.2.7a–d pose a downstream challenge of handling and development of techniques for electrical contacting on the microscale.

Returning to the question of perovskite material robustness relevant to laser conditions, we make the following observations. Similar to perovskite photovoltaics, yet even more acute is the question about photo- and thermal stability of the perovskites under the high electronic/photonic excitation densities typical in a laser. To date, device lifetimes on the order of a few hours have been demonstrated in perovskite lasers under continuous, but still under rather low-duty cycle-pulsed optical pumping [57, 60, 67, 69]. In the exploratory device configurations, such modest device lifetimes are attributed to irreversible degradation of the active perovskite media (solid thin films or nanowires) which is possibly driven by (i) elevated temperatures (say >150 °C) and/or (ii) chemical reaction with ambient oxygen and moisture. Based on experiments in both the transient and quasi-steady-state regimes with the corresponding experimentally determined threshold carrier densities in low-loss perovskite VCSELs, Chen et al. speculated that the threshold excitation power density needed for optically pumped CW laser operation [57], with excitation at $\lambda = 532$ nm for pure 300-nm-thick $CH_3NH_3PbI_3$ devices, would be approximately ~14 kW cm^{-2}, which corresponds to a current density of ~6.0 kA cm^{-2} when translated to equivalent electrical injection. On present evidence, given such threshold injection conditions, the thermal and chemical stability of the perovskite medium seems likely to be the most critical issue to be solved for realizing competitive perovskite laser devices in the future (versus commercial GaN/AlGaN, GaAs/InGaAs laser diodes with CW lifetimes in tens of thousands of hours). Improving the material stability through optimization of material synthesis, device fabrication, and hermetic protection from oxygen and moisture as well as innovative heat management at device level is required. Elsewhere, further improvements in the quality factor of low-loss optical resonators to effectively lower the lasing thresholds present opportunities for explorations in search of robust CW optically pumped devices at room temperature. If and when such a goal is reached, new application spaces for purely optically pumped devices can open up (from projection displays to spectroscopic sources), while paving the way toward electrically driven emitters.

3.2.5 The Way Forward Toward Electrical Injection

Although a high-charge-transfer efficiency electrical interface to the active optical medium is essential for photovoltaic applications by definition and is similarly critical for the ubiquitous diode lasers, we note that indirect excitation pathways are also widely used. One example is the green laser pointer (as a commodity item), the optoelectronic ecosystem of which employs an NIR diode laser to optically pump a YAG-based solid-state infrared (IR) laser whose emission, in the last step, is frequency doubled by nonlinear optical conversion. Such diode-pumped solid-state (DPSS) laser approaches might also be one outcome for perovskite laser devices, say, to produce multicolor optically pumped compact lasers. We have noted how the high absorption coefficients of perovskite materials makes optical pumping at this time the most efficient way to create population inversion in solution-derived perovskite thin films as per the abovementioned examples. As for compact optical pump sources for perovskite lasers, commercial electrical injected red (GaAsInP) and blue (GaN) diode laser with high wall-plug efficiencies (>20%) are readily available, which makes it possible to pursue “cold photon” pumping [79] for perovskite lasers near their effective bandgap to maximize the energetic efficiency in the process and minimize heat generation from electron–phonon coupling. An optical pumping solution for perovskite lasers might be thus technologically of value given the discrete gaps which exist today in covering the full visible spectrum continuously with a single material system (note also the “green-orange” gap which still persists between the wide bandgap InGaN/GaN diode lasers and those on the red and IR side based on III-As and III-P compounds).

Development of direct electrical/charge injection to the present perovskite materials for light emission, whether in pn-junction type of more circuitous electroluminescence routes, is a truly major challenge today at both the fundamental level (physics of interfaces and their realistic electronic structures) and practical level (materials science). This chapter has already briefly reviewed the current status of perovskite LEDs; for injection lasers, the requisite current densities are well above those reached by these initial LED demonstrations. One useful caution is to look back at the (still) enduring efforts to realize electrically driven lasing from solution-processed and/or soft non-perovskite materials. For example, although organic/polymer LEDs [80] and their optically pumped lasers [81] were realized in the early 1990s, organic semiconductors suffer from low damage threshold, have an intrinsically low carrier mobility due to their basic electronic transport mechanisms, and can exhibit prohibitive non-radiative losses from exciton–exciton annihilation at high carrier injection [82]. Elsewhere, efforts to parlay solution-gown inorganic II–VI colloidal QDs to lasers (in spite of excellent luminescence properties and LED demonstrations) suffer from fast Auger recombination if excited beyond the single exciton gain regime [32]. Recent II–VI colloidal QW-type nanoplatelet materials have, however, shown promise by optically pumped CW lasing at room temperature [40], but development of an electrical/charge-transport interface to these new materials remains largely unexplored. Coincidentally, though, the perovskite thin films possess comparable Auger lifetime and ASE threshold to those of the II–VI nanoplatelets, which together with large-gain cross-sections and free-carrier densities does suggest the potential for achieving CW laser operation at room temperature.

We noted earlier in this chapter how in spite of many innovative proposals and implementations of injection schemes, the maximum current densities to date have only achieved ~1 A cm^{-2}. In today’s perovskite LED device prototypes, higher injection current will result in output emission roll-off, possibly resulted from perovskite thin-film degradation because of the overheating problem [6]. By way of comparison, the record low-threshold current density achieved in any epitaxially grown laser diode appears to be that for strained InAs/GaAs QD device. Here, benefiting from the high degree of electron–hole pair confinement (quasi-zero-dimensional electronic density of states), exceptionally low background optical losses, high electronic mobility in SC III–Vs ($\sim 10^3$ cm^2 V^{-1} s^{-1}) and very low contact resistances ($<10^{-3}$ Ω cm^{-2}), a threshold current density on the order of 10 A cm^{-2} per QD layer has been achieved in a multi-QD-layered device [1]. While most low-power injection diode lasers operate with threshold current density in the range from $J = 100$–1000 A cm^{-2}, the InAs/GaAs QD case presents perhaps one example of an approach to realize low-threshold lasers if a number of additional material issues can be resolved (note the much higher extrapolated values of J from optical pumping results, e.g. in perovskite VCSELs). Importantly also, while the charge injection in the III–V epitaxial diode lasers are well understood, from metal contacts to cladding layers to capture of e–h pairs in target QWs or QDs, detailed physical mechanisms of electronic energy transfer to perovskite microcrystals by e–h injection remains opaque given the current multiple material integration in the heterogeneous hybrid organic-inorganic material LED devices such as those reviewed earlier.

The common additional challenge for perovskite lasers is to remain stable and withstand the considerable temperature increases, which in the active gain/recombination region in SC epitaxial diode lasers typically exceeds 100 °C (the so-called effective junction temperature). This necessitates skillful heat management for the perovskites such as injection schemes for "cold" carriers into the active region and improving the thermal conductivity of the active device volume to conduct lattice energy to external heatsinks. Strategies have been recently proposed for stabilizing the perovskite material, including incorporating cesium into the lattice [49, 67], varying the organic cation [83], using bifunctional alkylphosphonic cross-linking molecules [84] or using reduced-dimensionality perovskites (which have the added benefit of higher exciton binding energy) [85].

As for improving the charge injection from contacts and cladding layers, one example is offered from II–VI colloidal QD-LED literature where more sophisticated contact/injection schemes have been recently advanced [10, 86], including LEDs on flexible substrates [87]. We noted that perovskite LED structures are now achieving highest EQE of ~8.53% [8] by optimized perovskite thin films (smaller grain size and better passivation) and improvements in choice and synthesis of the adjacent carrier transport layers. It is important that more detailed microscopic-level models need to be developed through experiment and theory for electronic states and their band-edge lineups at heterojunctions to describe realistically the energetics of interfaces and the influence by intrinsic and extrinsic interface states (dipoles, defects, etc.). In case of perovskite solar cells, inorganic nanostructure materials (such as ZnO and NiO_x)-based ETLs and HTLs have been recently demonstrated [88], offering improved chemical stability versus organic injectors (by also giving better protection of the perovskite layer from ambient oxygen and moisture). Using these inorganic electron/hole injectors in electrically driven structures, possible enhancement of injection current (through carrier transport layers) and better thermal management can be expected. Embedding the optical resonator within a high-thermal-conductivity substrate [89] is an example of complementary strategy to mitigate the thermal stress on the perovskite gain medium. Next key milestones include demonstration of device longevity under continuous excitation while trying to work around device degradation by intrinsic mechanisms and extrinsic defects.

3.2.6 Summary

This chapter has offered readers a series of snapshots for the purpose of framing both the opportunities and difficulties ahead in parlaying the new organic-inorganic halide perovskite from their low-cost, high-throughput material base to technologically viable laser devices. From a broader optoelectronic device point of view, the intrinsic optical properties of these thin-film materials, readily distilled from precursor solutions, are very attractive, e.g. in their large radiative cross-sections. The absorptive and emissive properties across the visible range are comparable to or exceed those of established (III–V, II–VI, and IV–VI) inorganic and organic (small molecule and polymer) semiconductors. The relative ease of creating a palette of colors for light emission by modest variations in the chemical composition gives the perovskites a potentially competitive edge, provided that energetically effective excitation methods can be developed. This, in turn, requires (i) further understanding of the electronic structure of the perovskites for tailoring the composition and synthesis methods for optimization, e.g. optical gain; (ii) methods of integrating or embedding low-loss optical resonators within thin solid perovskite films; and (iii) assessing how and if laser operation by direct electrical (current) injection can be achieved at levels where these somewhat photo- and thermal-sensitive materials can maintain device functionality without degradation. In parallel, the field needs to identify additional unique spaces where existing inorganic/organic semiconductor lasers are unable to penetrate. Beyond laser projection applications [60], we may perhaps envision uses, e.g. in portable spectrometry by integrating such new sources for compact chemical luminescence assays to large-area (wallpaper) coherent arrays of laser emitters on curved and flexible surfaces, including holographic displays.

This work was supported by US AFOSR and US DOE.

References

1 Shimizu, H., Saravanan, S., Yoshida, J. et al. (2005). InAs quantum dot lasers with extremely low threshold current density. *Jpn. J. Appl. Phys.* 44: 1103–1104.

2 Telford, M. (2004). QD lasers go to market. *III-Vs Rev.* 17: 28–31.

3 Steckel, J. S., Ho, J. & Coe-Sullivan, S. (2014). Photon. *Spectra* http://go.nature.com/mMfCaf (September 2014).

4 Veldhuis, S.A., Boix, P.P., Yantara, N. et al. (2016). Perovskite materials for light-emitting diodes and lasers. *Adv. Mater.* 28: 6804–6834.

5 Sutherland, B.R. and Edward, H.S. (2016). Perovskite photonic sources. *Nat. Photonics* 10: 295–302.

6 Tan, Z.K., Moghaddam, R.S., Lai, M.L. et al. (2014). Bright light-emitting diodes based on organometal halide perovskite. *Nat. Nanotechnol.* 9: 687–692.

7 Wang, J., Wang, N., Jin, Y. et al. (2015). Interfacial control toward efficient and low-voltage perovskite light-emitting diodes. *Adv. Mater.* 27: 2311–2316.

8 Cho, H., Jeong, S.H., Park, M.H. et al. (2015). Overcoming the electroluminescence efficiency limitations of perovskite light-emitting diodes. *Science* 350: 1222–1225.

9 Aizawa, N., Pu, Y.J., Watanable, M. et al. (2014). Solution-processed multilayer small-molecule light-emitting devices with high-efficiency white-light emission. *Nat. Commun.* 5: 5756.

10 Dai, X., Zhang, Z., Jin, Y. et al. (2014). Solution-processed, high-performance light-emitting diodes based on quantum dots. *Nature* 515: 96–99.

11 Kumawat, N.K., Dey, A., Kumar, A. et al. (2015). Band gap tuning of $CH_3NH_3Pb(Br_{1-x}Cl_x)_3$ hybrid perovskite for blue electroluminescence. *ACS Appl. Mater. Interfaces* 7: 13119–13124.

12 Zhang, X., Lin, H., Huang, H. et al. (2016). Enhancing the brightness of cesium lead halide perovskite nanocrystal based green light-emitting devices through the interface engineering with perfluorinated ionomer. *Nano Lett.* 16: 1415–1420.

13 Kumawat, N.K., Dey, A., Narasimhan, K.L., and Kabra, D. (2015). Near infrared to visible electroluminescent diodes based on organometallic halide perovskites: structural and optical investigation. *ACS Photonics* 2: 349–354.

14 Li, G., Tan, Z.K., Di, D. et al. (2015). Efficient light-emitting diodes based on nanocrystalline perovskite in a dielectric polymer matrix. *Nano Lett.* 15: 2640–2644.

15 Ling, Y., Yuan, Z., Tian, Y. et al. (2016). Bright light-emitting diodes based on organometal halide perovskite nanoplatelets. *Adv. Mater.* 28: 305–311.

16 Yu, J.C., Kim, D.B., Jung, E.D. et al. (2016). High-performance perovskite light-emitting diodes *via* morphological control of perovskite films. *Nanoscale* 8: 7036–7042.

17 Kim, Y.H., Cho, H., Heo, J.H. et al. (2015). Multicolored organic/inorganic hybrid perovskite light-emitting diodes. *Adv. Mater.* 27: 1248–1254.

18 Bade, S.G.R., Li, J., Shan, X. et al. (2015). Fully printed halide perovskite light-emitting diodes with silver nanowire electrodes. *ACS Nano* 10: 1795–1801.

19 Liang, D., Peng, Y., Fu, Y. et al. (2016). Color-pure violet light-emitting diodes based on layered lead halide perovskite nanoplates. *ACS Nano* 10: 6897–6904.

20 Xing, J., Yan, F., Zhao, Y. et al. (2016). High-efficiency light-emitting diodes of organometal halide perovskite amorphous nanoparticles. *ACS Nano* 10: 6623–6630.

21 Song, J., Li, J., Li, X. et al. (2015). Quantum dot light-emitting diodes based on inorganic perovskite cesium lead halides ($CsPbX_3$). *Adv. Mater.* 27: 7162–7167.

22 Yu, J.C., Kim, D.B., Baek, G. et al. (2015). High-performance planar perovskite optoelectronic devices: a morphological and interfacial control by polar solvent treatment. *Adv. Mater.* 27: 3492–3500.

23 Yuan, M., Quan, L.N., Comin, R. et al. (2016). Perovskite energy funnels for efficient light-emitting diodes. *Nat. Nanotechnol.* 11: 872–877.

24 Jaramillo Quintero, O.A., Sanchez, R.S., Rincon, M., and Mora-Sero, I. (2015). Bright visible-infrared light emitting diodes based on hybrid halide perovskite with Spiro-OMeTAD as a hole-injecting layer. *J. Phys. Chem. Lett.* 6: 1883–1890.

25 Pazos-Outón, L.M., Szumilo, M., Lamboll, R. et al. (2016). Photon recycling in lead iodide perovskite solar cells. *Science* 351: 1430–1433.

26 Miyata, A., Mitioglu, A., Plochocka, P. et al. (2015). Direct measurement of the exciton binding energy and effective masses for charge carriers inorganic-inorganic tri-halide perovskites. *Nat. Phys.* 11: 582–587.

27 Sichert, J.A., Tong, Y., Mutz, N. et al. (2015). Quantum size effect in organometal halide perovskite nanoplatelets. *Nano Lett.* 15: 6521–6527.

28 Wong, A.B., Lai, M., Eaton, S. et al. (2015). Growth and anion exchange conversion of $CH_3NH_3PbX_3$ nanorod arrays for light-emitting diodes. *Nano Lett.* 15: 5519–5524.

29 Protesescu, L., Yakunin, S., Bodnarchuk, M.I. et al. (2015). Nanocrystals of cesium lead halide perovskites ($CsPbX_3$, X = Cl, Br, and I): novel optoelectronic materials showing bright emission with wide color gamut. *Nano Lett.* 15: 3692–3696.

30 Klimov, V.I., Mikhailovsky, A.A., McBranch, D.W. et al. (2000). Quantization of multiparticle Auger rates in semiconductor quantum dots. *Science* 287: 1011–1013.

31 Chan, Y., Caruge, J.M., Snee, P.T., and Bawendi, M.G. (2004). Multiexcitonic two-state lasing in a CdSe nanocrystal laser. *Appl. Phys. Lett.* 85: 2460.

32 Dang, C., Lee, J., Breen, C. et al. (2012). Red, green and blue lasing enabled by single-exciton gain in colloidal quantum dot films. *Nat. Nanotechnol.* 7: 335–339.

33 Klimov, V.I., Ivanov, S.A., Nanda, J. et al. (2007). Single-exciton optical gain in semiconductor nanocrystals. *Nature* 447: 441–446.

34 Dang, C. and Nurmikko, A. (2013). Beyond quantum dot LEDs: optical gain and laser action in red, green, and blue colors. *MRS Bull.* 38: 737–742.

35 She, C., Fedin, I., Dolzhnikov, D.S. et al. (2014). Low-threshold stimulated emission using colloidal quantum wells. *Nano Lett.* 14: 2772–2777.

36 Ithurria, S., Tessier, M.D., Mahler, B. et al. (2011). Colloidal nanoplatelets with two-dimensional electronic structure. *Nat. Mater.* 10: 936–941.

37 Haase, M.A., Qiu, J., DePuydt, J.M., and Cheng, H. (1991). Blue-green laser diodes. *Appl. Phys. Lett.* 59: 1272–1274.

38 Jeon, H., Ding, J., Patterson, W. et al. (1991). Blue-green injection laser diodes in (Zn, Cd) Se/ZnSe quantum wells. *Appl. Phys. Lett.* 59: 3619–3621.

39 Guzelturk, B., Kelestemur, Y., Olutas, M. et al. (2014). Amplified spontaneous emission and lasing in colloidal nanoplatelets. *ACS Nano* 8: 6599–6605.

40 Grim, J.Q., Christodoulou, S., Di Stasio, F. et al. (2014). Continuous-wave biexciton lasing at room temperature using solution-processed quantum wells. *Nat. Nanotechnol.* 9: 891–895.

41 Xing, G., Mathews, N., Lim, S.S. et al. (2014). Low-temperature solution-processed wavelength-tunable perovskites for lasing. *Nat. Mater.* 13: 476–480.

42 Cadelano, M., Sarritzu, V., Sestu, N. et al. (2015). Can trihalide lead perovskites support continuous wave lasing? *Adv. Opt. Mater.* 3: 1557–1564.

43 Yakunin, S., Protesescu, L., Krieg, F. et al. (2015). Low-threshold amplified spontaneous emission and lasing from colloidal nanocrystals of cesium lead halide perovskites. *Nat. Commun.* 6: 8056.

44 Sutherland, B.R., Hoogland, S., Adachi, M.M. et al. (2014). Conformal organohalide perovskites enable lasing on spherical resonators. *ACS Nano* 8: 10947–10952.

45 Yuan, F., Wu, Z., Dong, H. et al. (2015). Electric field-modulated amplified spontaneous emission in organo-lead halide perovskite $CH_3NH_3PbI_3$. *Appl. Phys. Lett.* 107: 261106.

46 Stranks, S.D., Wood, S.M., Wojciechowski, K. et al. (2015). Enhanced amplified spontaneous emission in perovskites using a flexible cholesteric liquid crystal reflector. *Nano Lett.* 15: 4935–4941.

47 Wang, Y., Li, X., Song, J. et al. (2015). All-inorganic colloidal perovskite quantum dots: a new class of lasing materials with favorable characteristics. *Adv. Mater.* 27: 7101–7108.

48 Xu, Y., Chen, Q., Zhang, C. et al. (2016). Two-photon-pumped perovskite semiconductor nanocrystal lasers. *J. Am. Chem. Soc.* 138: 3761–3768.

49 Wang, Y., Li, X., Zhao, X. et al. (2015). Nonlinear absorption and low-threshold multiphoton pumped stimulated emission from all-inorganic perovskite nanocrystals. *Nano Lett.* 16: 448–453.

50 Pan, J., Sarmah, S.P., Murali, B. et al. (2015). Air-stable surface-passivated perovskite quantum dots for ultra-robust, single-and two-photon-induced amplified spontaneous emission. *J. Phys. Chem. Lett.* 6: 5027–5033.

51 Shaklee, K.L. and Leheny, R.F. (1971). Direct determination of optical gain in semiconductor crystals. *Appl. Phys. Lett.* 18: 475–477.

52 Dhanker, R., Brigeman, A.N., Larsen, A.V. et al. (2014). Random lasing in organo-lead halide perovskite microcrystal networks. *Appl. Phys. Lett.* 105: 151112.

53 Liu, S., Sun, W., Li, J. et al. (2016). Random lasing actions in self-assembled perovskite nanoparticles. *Opt. Eng.* 55: 057102.

54 D'Innocenzo, V., Srimath Kandada, A.R., De Bastiani, M. et al. (2014). Tuning the light emission properties by band gap engineering in hybrid lead halide perovskite. *J. Am. Chem. Soc.* 136: 17730–17733.

55 Saba, M., Cadelano, M., Marongiu, D. et al. (2014). Correlated electron-hole plasma in organometal perovskites. *Nat. Commun.* 5: 5049.

56 Deschler, F., Price, M., Pathak, S. et al. (2014). High photoluminescence efficiency and optically pumped lasing in solution-processed mixed halide perovskite semiconductors. *J. Phys. Chem. Lett.* 5: 1421–1426.

57 Chen, S., Zhang, C., Lee, J. et al. (2017). High-Q, low-threshold monolithic perovskite thin-film vertical-cavity lasers. *Adv. Mater.* 29: 1604781.

58 Jia, Y., Kerner, R.A., Grede, A.J. et al. (2016). Diode-pumped organo-lead halide perovskite lasing in a metal-clad distributed feedback resonator. *Nano Lett.* 16: 4624–4629.

59 Saliba, M., Wood, S.M., Patel, J.B. et al. (2016). Structured organic–inorganic perovskite toward a distributed feedback laser. *Adv. Mater.* 28: 923–929.

60 Chen, S., Roh, K., Lee, J. et al. (2016). A photonic crystal laser from solution based organo-lead iodide perovskite thin films. *ACS Nano* 10: 3959–3967.

61 Cha, H., Bae, S., Lee, M., and Jeon, H. (2016). Two-dimensional photonic crystal bandedge laser with hybrid perovskite thin film for optical gain. *Appl. Phys. Lett.* 108: 181104.

62 Samuel, I., David, W., and Graham, A.T. (2007). Organic semiconductor lasers. *Chem. Rev.* 107: 1272–1295.

63 Wehrenfennig, C., Eperon, G.E., Johnston, M.B. et al. (2014). High charge carrier mobilities and lifetimes in organolead trihalide perovskites. *Adv. Mater.* 26: 1584–1589.

64 Milot, R.L., Eperon, G.E., Snaith, H.J. et al. (2015). Temperature dependent charge carrier dynamics in $CH_3NH_3PbI_3$ perovskite thin films. *Adv. Funct. Mater.* 25: 6218–6227.

65 Trinh, M.T., Wu, X., Niesner, D., and Zhu, X.Y. (2015). Many-body interactions in photo-excited lead iodide perovskite. *J. Mater. Chem. A.* 3: 9285–9290.

66 Zhu, H., Fu, Y., Meng, F. et al. (2015). Lead halide perovskite nanowire lasers with low lasing thresholds and high quality factors. *Nat. Mater.* 14: 636–642.

67 Eaton, S.W., Lai, M., Gibson, N.A. et al. (2016). Lasing in robust cesium lead halide perovskite nanowires. *Proc. Natl. Acad. Sci. U.S.A.* 113: 1993–1998.

68 Xing, J., Liu, X.F., Zhang, Q. et al. (2015). Vapor phase synthesis of organometal halide perovskite nanowires for tunable room-temperature nanolasers. *Nano Lett.* 15: 4571–4577.

69 Fu, Y., Zhu, H., Schrader, A.W. et al. (2016). Nanowire lasers of formamidinium lead halide perovskites and their stabilized alloys with improved stability. *Nano Lett.* 16: 1000–1008.

70 Li, Y.J., Lv, Y., Zou, C.L. et al. (2016). Output coupling of perovskite lasers from embedded nanoscale plasmonic waveguides. *J. Am. Chem. Soc.* 138: 2122–2125.

71 Gu, Z., Wang, K., Sun, W. et al. (2015). Two-photon pumped $CH_3NH_3PbBr_3$ perovskite microwire lasers. *Adv. Opt. Mater.* 4: 472–479.

72 Wang, K., Gu, Z., Liu, S. et al. (2016). Formation of single-mode laser in transverse plane of perovskite microwire *via* micromanipulation. *Opt. Lett.* 41: 555–558.

73 Liao, Q., Hu, K., Zhang, H. et al. (2015). Perovskite microdisk microlasers self-assembled from solution. *Adv. Mater.* 27: 3405–3410.

74 Liu, X., Niu, L., Wu, C. et al. (2016). Periodic organic–inorganic halide perovskite microplatelet arrays on silicon substrates for room-temperature lasing. *Adv. Sci.* 3: 1600137.

75 Zhang, W., Peng, L., Liu, J. et al. (2016). Controlling the cavity structures of two-photon-pumped perovskite microlasers. *Adv. Mater.* 28: 4040–4046.

76 Nguyen, V.C., Katsuki, H., Sasaki, F., and Yanagi, H. (2016). Optically pumped lasing in single crystals of organometal halide perovskites prepared by cast-capping method. *Appl. Phys. Lett.* 108: 261105.

77 Zhang, Q., Ha, S.T., Liu, X. et al. (2014). Room-temperature near-infrared high-Q perovskite whispering-gallery planar nanolasers. *Nano Lett.* 14: 5995–6001.

78 Sun, W., Wang, K., Gu, Z. et al. (2016). Tunable perovskite microdisk lasers. *Nanoscale* 8: 8717–8721.

79 Knox, W.H., Fork, R.L., Downer, M.C. et al. (1985). Femtosecond dynamics of resonantly excited excitons in room-temperature GaAs quantum wells. *Phys. Rev. Lett.* 54: 1306.

80 Burroughes, J.H., Bradley, D.D.C., Brown, A.R. et al. (1990). Light-emitting diodes based on conjugated polymers. *Nature* 347: 539–541.

81 Tessler, N., Denton, G.J., and Friend, R.H. (1996). Lasing from conjugated-polymer microcavities. *Nature* 382: 695–697.

82 Grivas, C. and Pollnau, M. (2012). Organic solid-state integrated amplifiers and lasers. *Laser Photonics Rev.* 6: 419–462.

83 McMeekin, D.P., Sadoughi, G., Rehman, W. et al. (2016). A mixed-cation lead mixed-halide perovskite absorber for tandem solar cells. *Science* 351: 151–155.

84 Li, X., Dar, M.I., Yi, C. et al. (2015). Improved performance and stability of perovskite solar cells by crystal crosslinking with alkylphosphonic acid ω-ammonium chlorides. *Nat. Chem.* 7: 703–711.

85 Quan, L.N., Yuan, M., Comin, R. et al. (2016). Ligand-stabilized reduced-dimensionality perovskites. *J. Am. Chem. Soc.* 138: 2649–2655.

86 Mashford, B.S., Stevenson, M., Popovic, Z. et al. (2013). High-efficiency quantum-dot light-emitting devices with enhanced charge injection. *Nat. Photonics* 7: 407–412.

87 Yang, X., Mutlugun, E., Dang, C. et al. (2014). Highly flexible, electrically driven, top-emitting, quantum dot light-emitting stickers. *ACS Nano* 8: 8224–8231.

88 You, J., Meng, L., Song, T.B. et al. (2016). Improved air stability of perovskite solar cells *via* solution-processed metal oxide transport layers. *Nat. Nanotechnol.* 11: 75–81.

89 Adachi, M.M., Fan, F., Sellan, D.P. et al. (2015). Microsecond-sustained lasing from colloidal quantum dot solids. *Nat. Commun.* 6: 8694.

Part IV

Beyond Perovskite Photovoltaics

4.1

Novel Spin Physics in Organic–Inorganic Perovskites

Chuang Zhang, Dali Sun, and Zeev V. Vardeny

University of Utah, Department of Physics and Astronomy, 201 James Fletcher Building, 115 South 1400 East, Salt Lake City, UT 84112, USA

4.1.1 Introduction

While the organic–inorganic hybrid perovskites such as $CH_3NH_3PbX_3$ (where X stands for halide) have achieved rapid progress in optoelectronic device applications that include solar cells [1–3] and light-emitting diodes (LEDs) [4, 5], the community has realized that another research topic in this field is interesting as well, namely, spin physics and spin-related devices of hybrid perovskites [6]. In this regard, it was not clear why the Pb atoms having large spin–orbit coupling (SOC) in the hybrid perovskite lattice are necessary to achieve photovoltaic (PV) solar cells with such high power conversion efficiency (PCE) of ~21% [7, 8]. One commonly accepted concept is that the strong SOC brought about by the Pb heavy atoms substantially affects the hybrid perovskite band structure [9], leading to small exciton binding energy and consequently to efficient photocarrier generation [10, 11]. In spite of the large SOC in the perovskites, the recent study of magnetic field effect (MFE) in $CH_3NH_3PbI_{3-x}Cl_x$ has proved that the concept of photogenerated spin ½ carrier pairs is still viable in the hybrid perovskites [12, 13].

Other magnet field studies have provided in-depth understanding; and consequently useful and important information about the electronic properties of hybrid perovskites such as exciton binding energy was obtained [14]. In addition, optical excitation and ultrafast transient dynamics of spin-polarized photocarriers have been also measured using the pump–probe correlation technique with 100 fs time resolution [15]. At the same time, additional spin-related phenomena (e.g. Rashba effect) have been theoretically predicted in the hybrid perovskites [16, 17], indicating that these materials may have promising spin-related applications. In general, it is believed that the hybrid perovskites would combine the advantages of both organics (such as low-temperature processability and chemical versatility) [18] and inorganics (such as strong SOC and long carrier diffusion length) [19, 20], thus providing novel possibilities for multifunctional spintronic devices.

Halide Perovskites: Photovoltaics, Light Emitting Devices, and Beyond, First Edition.
Edited by Tze-Chien Sum and Nripan Mathews.

In this chapter we review the first observations of MFE in the organic–inorganic hybrid perovskite system, and other related measurements such as field-induced polarization and ultrafast spectroscopy. We show that a combination of these three experiments leads to a reliable interpretation of the data, and deepens our understanding of the spin physics in this materials family. Finally, we introduce a novel perovskite-based optoelectronic-spintronic device to show the great potential of hybrid materials in spintronic applications.

4.1.2 Magnetic Field Effect (MFE) on Photocurrent (PC), Photoluminescence (PL), and Electroluminescence (EL)

The MFE technique has been a powerful tool for studying spin-dependent generation and recombination processes of spin ½ pair (SP) species in organic semiconductors [21–24]. The applied magnetic field, B, modulates the outcome physical quantity in the optoelectronic device, in the form of magneto-conductivity (MC) and magneto-photoconductivity (MPC) in organic PV cells [25, 26], magneto-electroluminescence (MEL) in organic LEDs [27, 28], and also magneto-photoluminescence (MPL) in pristine films [24]. This occurs since B changes the spin sublevel character in the SP manifold (such as the singlet and triplet shown in Figure 4.1.1); which, in turn, changes the inter-sublevel spin-mixing rates that consequently modulate their respective steady-state populations since the recombination is spin dependent. Because of different dissociation and recombination rates for the SP in the singlet and triplet spin configuration, the population change may modulate the photocurrent (PC) or/and photoluminescence/electroluminescence (PL/EL) emission intensity.

In general, the MFE requires the existence of SP species in which there is a spin-mixing activity among the spin sublevels. This may be provided by a number of spin interactions [29] such as the hyperfine interaction (HFI), SOC, exchange, and also the difference, Δg between the g-factor of the spin ½ electron and hole in the SP species that leads to different precession frequencies of their respective spins about the applied field [24, 26]. The perovskite polycrystalline films contain a disorder that depends on the employed growth technique [30], so the relatively long-lived electron–hole (e–h) pairs may still be formed preceding recombination. However, the large SOC in the lead halide perovskites caused by the heavy

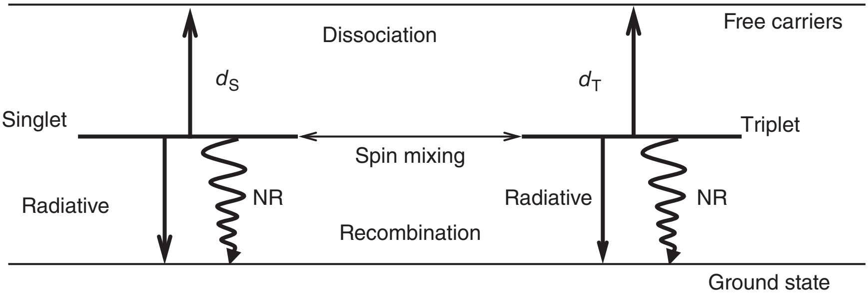

Figure 4.1.1 Illustration of MFE process based on spin mixing between spin ½ pairs.

atoms such as lead and halogen may significantly shorten the spin-lattice relaxation time, τ_{SL}, of the SP species, thereby diminishing the MFE, since the spin quantum number may not be preserved [31].

4.1.2.1 Observation of MFE in the $CH_3NH_3PbI_{3-x}Clx$ Films and Devices

In the case of solution-processed $CH_3NH_3PbI_{3-x}Cl_x$, which is the most widely used hybrid perovskite as the active layer in PV devices, it was not expected that MFE would be viable in these optoelectronic devices. Surprisingly, we measured significant MPC and MEL responses in hybrid perovskite-based devices, as well as MPL in thin films of these materials [12]. The $CH_3NH_3PbI_{3-x}Cl_x$ films and devices were fabricated using a standard spin-coating technique [32]. For the MFE investigations, the samples were transferred to a vacuum chamber that was placed in a magnetic field B, provided by a superconducting-type magnet with B up to ~1 T, or an electromagnet with B up to 200 mT. To observe MPC response, the short circuit photocurrent, J_{sc}, was measured at zero bias ($V_b = 0$) while sweeping B. MPC is thus defined as $\mathrm{MPC}(B) = [J_{sc}(B)/J_{sc}(0) - 1]$.

A typical PV cell (ITO/PEDOT:PSS/$CH_3NH_3PbI_{3-x}Cl_x$/PCBM/Al) was illuminated with two different lasers operating at 400 and 785 nm, respectively. When illuminated with above-gap excitation (400 nm), we obtained a broad magnetic response MPC(B) of ~0.45% (Figure 4.1.2a), which is in the form of a Lorentzian with half-width at half maximum (HWHM), $B_{1/2} \sim 325$ mT. No obvious MPC(B) response (<0.1%) was obtained using below-gap excitation, as shown in Figure 4.1.2b. This confirms that the MPC(B) with above-gap excitation is small but significant, showing that the concept of SPs in the $CH_3NH_3PbI_{3-x}Cl_x$ layer is still valid.

In such devices, MPC with above-gap illumination remains almost unchanged with varied excitation power (Figure 4.1.3a,b). It indicates that MPC is not limited by defects or traps; otherwise, it would have diminished at high excitation intensity. The linear dependence of PC on the excitation intensity also implies that carrier recombination kinetics is dominated by monomolecular process. MPC with below-gap excitation is always negligibly small in spite of laser power (Figure 4.1.3c), while the PC increases also linearly with the excitation intensity (Figure 4.1.3d). The linear increase of PC upon excitation intensity verifies the

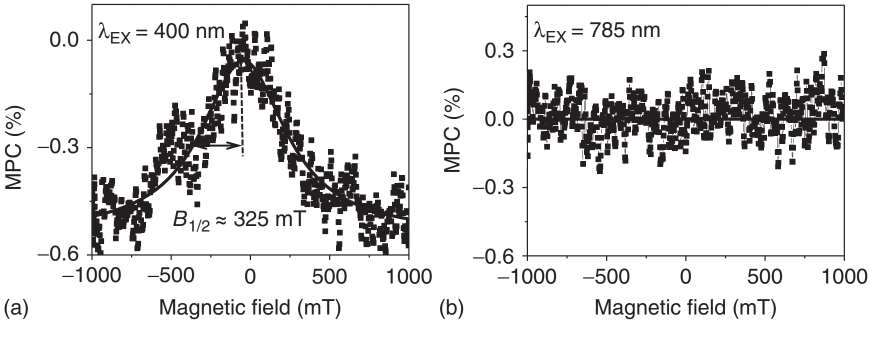

Figure 4.1.2 MPC(B) response in $CH_3NH_3PbI_{3-x}Cl_x$ PV cell with (a) above-gap (400 nm) and (b) below-gap (785 nm) excitations.

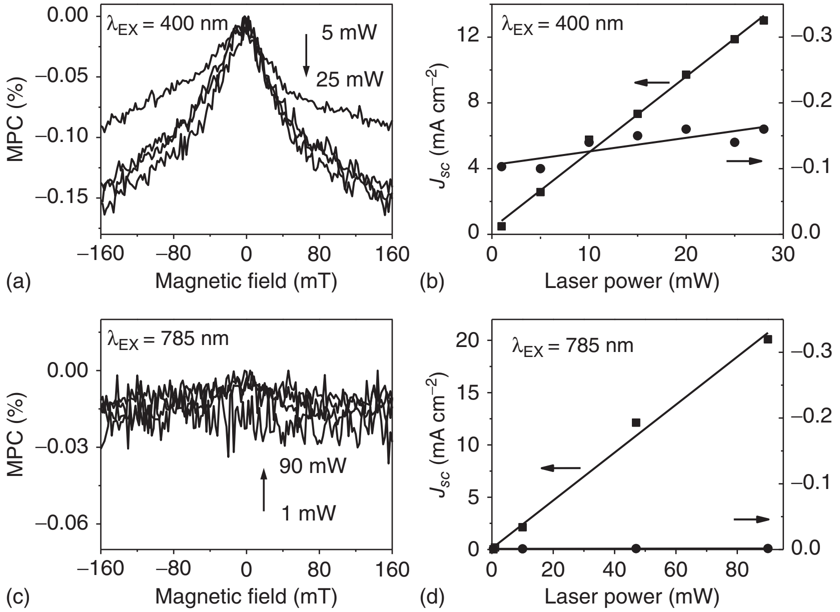

Figure 4.1.3 MPC(*B*) responses and intensity dependence of PC and MPC, respectively, with (a,b) above-gap and (c,d) below-gap excitations.

device quality of the solar cell [32], while the wavelength dependence shows that MPC is intrinsic of $CH_3NH_3PbI_{3-x}Cl_x$, rather than from the transport layers.

At forward bias, we obtained EL and also MEL response from the solar cell. Here, MEL is defined as MEL(B) = [EL(B)/EL(0) − 1] measured at a constant current density. As shown in Figure 4.1.4a, MEL(B) has the opposite polarity compared to that of MPC, and contains two components, broad $\mathrm{MEL_B}$ and narrow $\mathrm{MEL_N}$. $\mathrm{MEL_B}$ may originate from the field-induced change in the non-radiative channel, in which the carrier-exciton scattering is decreased and EL enhanced under applied field [33]. In contrast, $\mathrm{MEL_N}$ may be caused by field modulation of the radiative channel, where the field increases the population of singlet e–h pairs

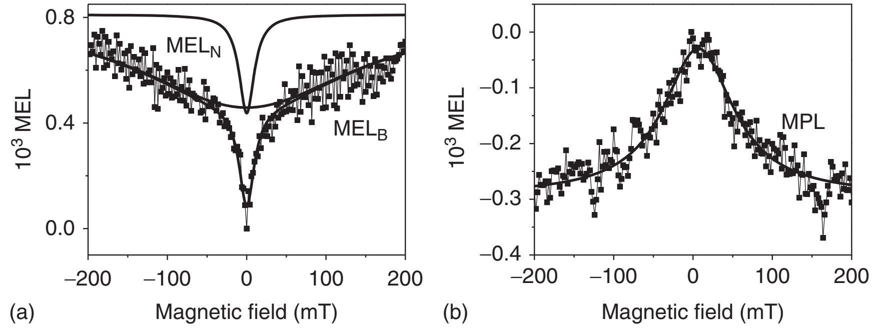

Figure 4.1.4 (a) MEL(*B*) response in the $CH_3NH_3PbI_{3-x}Cl_x$ PV cell. (b) MPL(*B*) response of a pristine film from the same fabrication procedure.

and luminescent excitons form. The MPL response in the pristine film grown under the same conditions, which is defined as $\mathrm{MPL}(B) = [\mathrm{PL}(B)/\mathrm{PL}(0) - 1]$, is relatively broad and negative (Figure 4.1.4b). The MPL response is similar to MPC but in contrast to MEL, indicating that the initial conditions of the born e–h pair are important to MFEs. While the photogenerated e–h pairs are born solely in the singlet configuration following photon absorption, the e–h pairs formed upon carrier injection have the initial triplet/singlet ratio of 3 : 1 [28].

4.1.2.2 MFE in Hybrid Perovskites; Morphology Dependence

The $CH_3NH_3PbI_{3-x}Cl_x$ active layer in the PV devices consists of many nanosized crystal domains, where the film morphology is crucial to carrier photogeneration and/or recombination processes [34]. The crystalline grain may localize the photogenerated carriers, and therefore the grain size may substantially affect the formation of SPs. By increasing the "post-annealing" temperature of the $CH_3NH_3PbI_{3-x}Cl_x$ layers, the grain size of the films decreases (Figure 4.1.5) [34]. The PV performance also largely depends on the perovskite morphology, in which PCE drops from 9.3% to 0.1% (Figure 4.1.6a) when the film changes morphology from that described in Figure 4.1.5a to that in Figure 4.1.5d.

Increased disorder in lesser quality perovskite layers evidently reduces the PV device efficiency, but, on the other hand enhances the EL emission intensity due to enhanced e–h radiative recombination rate. As shown in Figure 4.1.6b, the EL intensity from these devices varies more than three orders of magnitude at the same current injection. The "worst" solar cell is actually the "best" LED device, implying that the e–h pairs are more localized in more disordered films, and thus enhance luminescence through the radiative channel [5]. Surprisingly, we obtained MPC response in all four devices described in Figure 4.1.5, which shows an interesting revolution in the shape of MPC(B) curves. As indicated in Figure 4.1.6c,d, MPC(B) is larger and narrower in better LED-like devices.

The LED-like device (Device 4 in Figure 4.1.6) is based on a more disordered perovskite layer showing substantially less photocurrent (smaller J_{sc}). MPC(B) response (Figure 4.1.7a) still shows a broad $\mathrm{MPC_B}$; however, the overall response is dominated by a narrow component, $\mathrm{MPC_N}$ of ~1.8% with $B_{1/2} \sim 16$ mT. $\mathrm{MPC_N}$ should originate from more tightly bound SPs in the

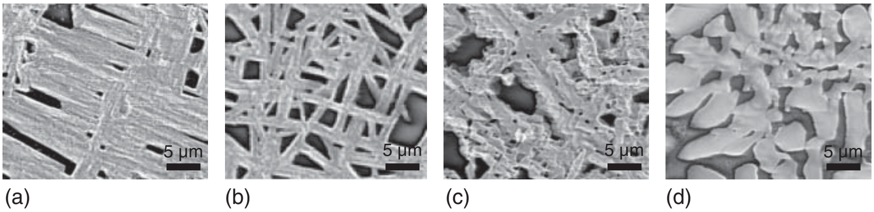

Figure 4.1.5 Scanning electron microscope (SEM) images of $CH_3NH_3PbI_{3-x}Cl_x$ films annealed at temperature, T, of (a) 90 °C, (b) 110 °C, (c) 120 °C, and (d) 130 °C, respectively, showing the change that occurs in the film morphology and grain size with annealing temperature.

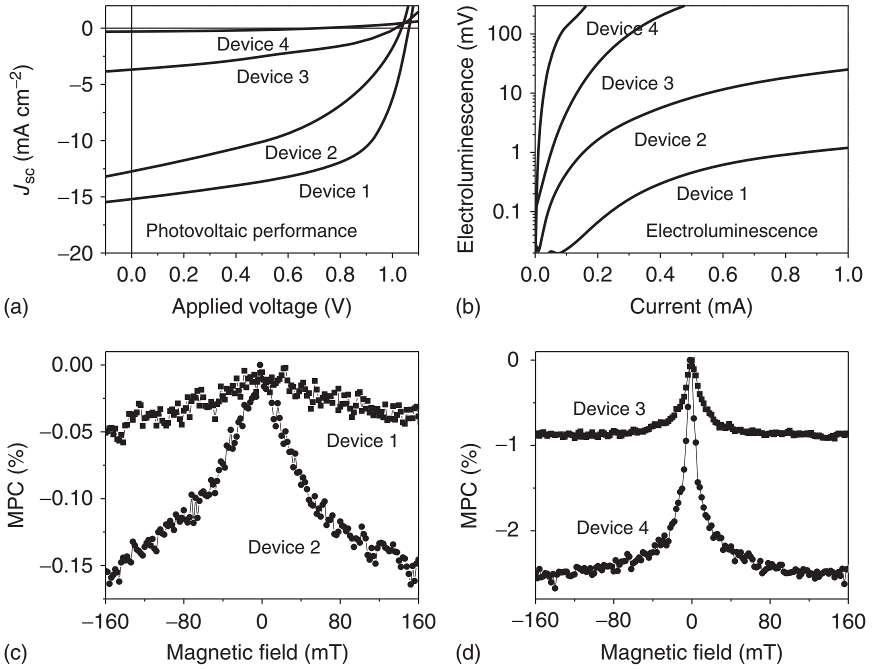

Figure 4.1.6 (a) Photovoltaic performance, (b) EL characteristics, and (c,d) MPC(*B*) response in various $CH_3NH_3PbI_{3-x}Cl_x$ devices. Devices 1–4 correspond to the films shown in Figure 4.1.5a–d, respectively.

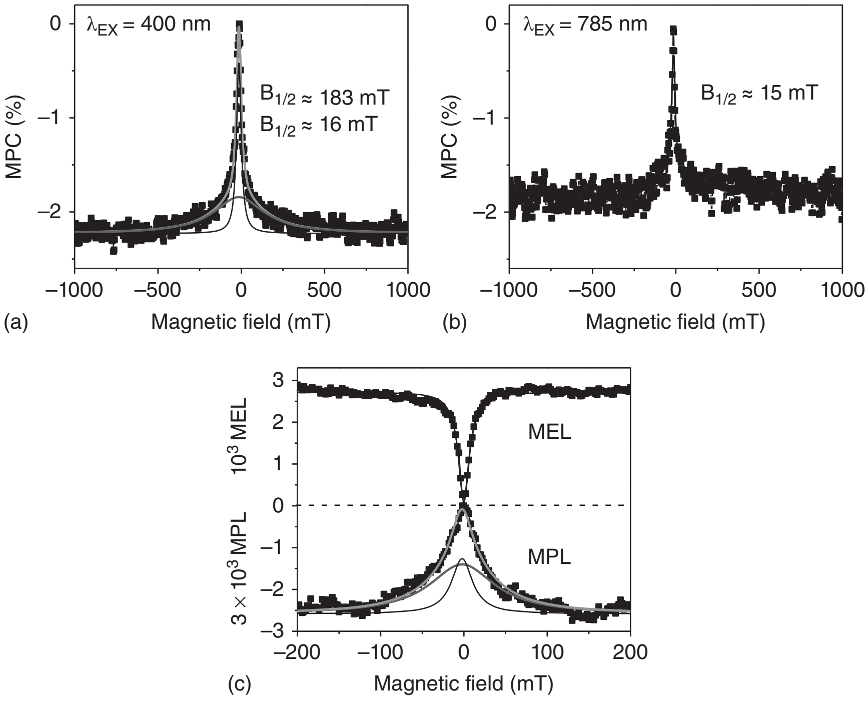

Figure 4.1.7 MPC(*B*) response with (a) above-gap and (b) below-gap excitations in an LED-like device based on $CH_3NH_3PbI_{3-x}Cl_x$. (c) MEL(*B*) and MPL(*B*) responses in the same device.

disordered $CH_3NH_3PbI_{3-x}Cl_x$ active layer. More interestingly, MPC_B and MPC_N responses show different dependencies on the excitation wavelength. Similar to that in the solar cell, the MPC_B in this device also disappears with below-gap excitation (Figure 4.1.7b). In sharp contrast, MPC_N remains almost unchanged with below-gap excitation, indicating that the traps that form the band tail are less important in this case.

The enhanced charge recombination leads to brighter EL emission from this device. In addition, the MEL(B) shows a similar but more pronounced narrow component MEL_N, as shown in Figure 4.1.7c. It should be noted that MEL(B) still has opposite polarity compared to MPC(B), because the enhanced recombination at $B > 0$ reduces PC but increases EL. The MPL response was also observed from the more disordered film, same as the active layer in the LED-like device. A narrow component MPL_N appears, and makes the response larger and much narrower than that in the $CH_3NH_3PbI_{3-x}Cl_x$ film used for the PV device (Figure 4.1.4b), following the same trend as MPC.

The PC is low in the LED-like device, presumably because the bimolecular recombination becomes more significant. To verify this assumption, we measured the excitation intensity dependence of both PC and MPC responses, as displayed in Figure 4.1.8a,b. The sublinear increase of PC starts at an intermediate laser power, indicating the bimolecular kinetics of e–h carrier recombination in this perovskite layer. The MPC response, however, shows an increase only at very low laser power, after which it becomes nearly constant along with the PC saturation at higher excitation intensity. This indicates that the photoexcited e–h pairs and their MFE are inherent for the $CH_3NH_3PbI_{3-x}Cl_x$, rather than depending on the type of recombination kinetics in the device. Otherwise, the MPC response would continuously increase even after the PC saturates at higher excitation power.

Hsiao et al. also reported independently the MPL and MPC in hybrid perovskite materials and devices [13]. Interestingly, they observed a strong dependence of MPL on the laser power (Figure 4.1.9a), where the MPL increases and becomes narrower at high excitation intensity. In parallel, the PL intensity showed a superlinear increase with the light intensity (Figure 4.1.9b), which agrees with the sublinear change of PC in the LED-like device.

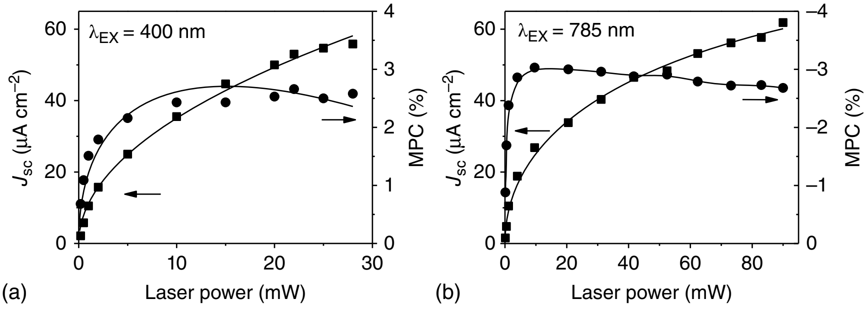

Figure 4.1.8 The excitation intensity dependence of PC and MPC in the $CH_3NH_3PbI_{3-x}Cl_x$ LED-like device with (a) above-gap and (b) below-gap excitations.

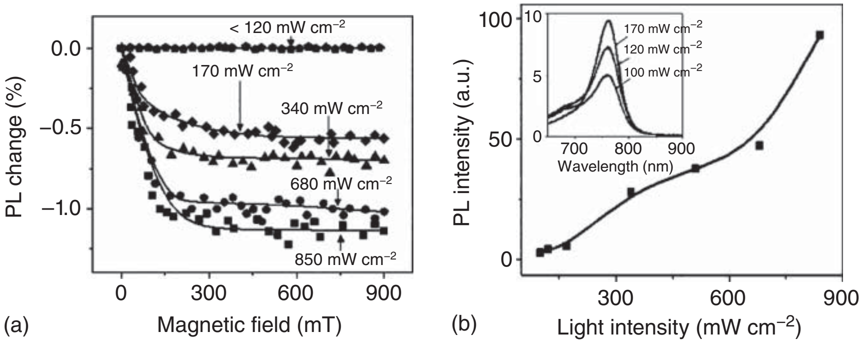

Figure 4.1.9 The excitation intensity dependence of (a) PL and (b) MPL in the hybrid perovskite, excited with a 532-nm laser. Source: Hsiao et al. 2015 [13]. Copyright 2015. Reproduced with permission of John Wiley & Sons.

We conclude from this survey that (i) MFEs do exist in the hybrid perovskite, although the spin relaxation is expected to be very fast due to the SOC in these materials and (ii) MFE response is complicated, since its field response varies with the film morphology, light excitation, etc. It is thus important to investigate the underlying mechanism of the MFE in hybrid perovskites, which may not only explain the efficient spin-mixing process under the conditions of high SOC strength but may also show the unique spin-related properties of these hybrid semiconductors.

4.1.2.3 The "Universal" Plot and the Spin-mixing Process via Δ*g* of Electrons and Holes

In analyzing the variation of the obtained MFE response in a number of devices and films, we have realized that the larger the magnetic field effect amplitude, A(MFE), the broader is the MFE(B) response, as measured by $B_{1/2}$, namely, the field at HWHM of the response. We summarize this surprising finding in a "universal plot" of A(MFE) versus $1/\mathrm{B}_{1/2}$ for all measured MPC and MPL responses, as shown in Figure 4.1.10a,b. It is seen that A(MFE) depends linearly on $1/B_{1/2}$ for both MPC and MPL, which, however, have different slopes. First, the existence of a "universal plot" shows that the various MFEs are intrinsic to the perovskite material; since the response is universal, namely, it depends on some internal parameter rather than varies arbitrarily among the devices and films. Secondly, it can be concluded that both A(MFE) and $B_{1/2}$ should be correlated and depend on the same internal parameter. The underlying mechanism for this correlation needs to be found by analyzing the underlying mechanism for the MFE(B) response, which can be achieved by knowing the spin-mixing mechanism as follows.

We note that $B_{1/2}$ of the broad $\mathrm{MPC_B}(B)$ (Figure 4.1.2a) component is much broader than the HFI strength, which is typically ~5 mT in the organics; therefore, this spin-mixing mechanism may be discarded in explaining the MFE in the perovskites. Also, the exchange interaction, J, in the e–h SP species

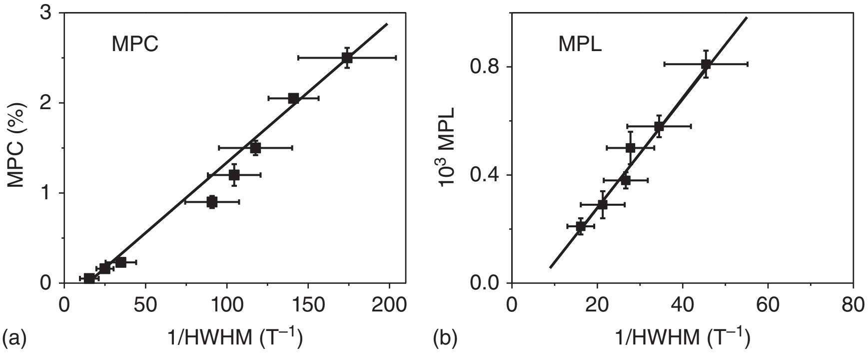

Figure 4.1.10 The universal plots of (a) MPC(B) and (b) MPL(B) amplitude versus the inverse of their response width.

should be small since the electrons and holes in the perovskites are known to be delocalized. Surprisingly, we found that MPC$_N$(B) response becomes narrower at low temperatures, which is very different from the MC(B) response of organic light-emitting diode (OLED) devices (such as MEH-PPV), where the HFI is dominated [24]. We thus discard as well the HFI in determining the MPC$_N$(B) component response. We conclude that another spin-mixing mechanism should be considered to explain the MFE in the hybrid perovskite system.

For SP species that are composed of two spin ½ partners with different g-factors, a known spin-mixing mechanism that is more efficient at higher fields is the so-called Δg mechanism [24, 26, 29], where Δg is the difference in the g-factor of the two spin ½ particles that constitute the SP species. The Δg mechanism has been considered for MPC in organic PV cells (where Δg is merely $\sim 10^{-3}$). From semiclassical consideration, for $B \neq 0$ the nonidentical precession rates of the two individual spins in the SP species result in intersystem crossing from overall spin singlet, S, to the T_0 triplet state, and vice versa, at a rate: $\Delta\omega_p = \mu_B \Delta g B/\hbar$ (Figure 4.1.11a). However, if Δg is small, then the time, $\tau_{ST} = 1/(2\Delta\omega_p)$ required for the S–T_0 transformation is way too long compared to τ_{SL}. In this case, spin decoherence occurs (Figure 4.1.11b), and consequently the MFE diminishes.

According to the "Δg mechanism," the MFE(B) response was found to have a Lorentzian shape with HWHM, $B_0 = \hbar/(2\mu_B \Delta g \tau)$, where τ is an average lifetime of the SP species [26]. In addition, if $\tau < \sim\tau_{SL}$, then the MFE value is proportional to the multiplication of a "decreasing factor," DF = $[1 - \exp(-\tau/\tau_{SL})]$ and a constant, $C = (1 - \chi)/(3 + \chi)$, where χ is the "symmetry breaking" ratio between S and T_0 spin configuration, namely, d_T/d_S (dissociation) for MPC and r_T/r_S (recombination) for MPL. Therefore, larger MFE amplitude is expected for e–h pairs with longer lifetime τ. From this analysis we see that both MFE amplitude, A(MFE) (via DF), and width, B_0 (via the coefficient $\Delta g \tau$), are related to the SP lifetime τ. Solving for τ in the DF and B_0 terms, we can eliminate it, and find for small A(MFE) and constant τ_{SL} that in fact A(MFE) $\sim C/B_0$. This shows that a plot of A(MFE) versus $1/B_0$ should be linear with a slope that is proportional to C.

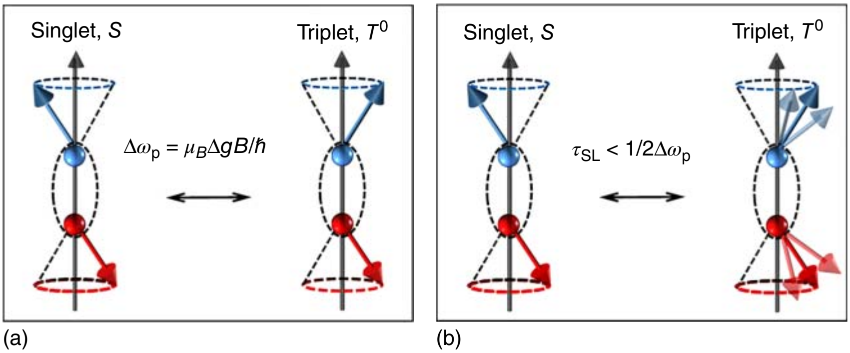

Figure 4.1.11 Illustration of (a) Δg spin-mixing mechanism and (b) the competition between spin mixing and spin relaxation within a spin-pair composed of spin ½ electron (upper arrow) and hole (lower arrow).

In Sections 4.1.2 and 4.1.3, we focus on the determination of these two factors, namely, Δg and τ using two experimental methods, which are the magnetic-field-induced circularly polarized emission technique and picosecond pump–probe spectroscopy.

4.1.3 High Magnetic Field Optical Phenomena

4.1.3.1 Direct Measurement of Δg by Field-Induced Circularly Polarized Emission

Using band theory calculation that includes e–e interaction and SOC, it was found that the holes in the valence band (VB) of $CH_3NH_3PbI_{3-x}Cl_x$ are quasi-particles with angular momentum eigenvalue $j = ½$, whereas the electrons in the conduction band (CB) have $j = 3/2$ [35]. The description of e–h pairs, excitons, and PL emission in this case is quite complicated. However, a simpler description of the e–h PL emission in III–V semiconductors (such as GaAs) [36, 37] that circumvents the difficulties of dealing with quasi-particles having $j > 1/2$, such as the electrons in the hybrid perovskites, has been advanced [38]. In this model, it is assumed that the "correlated" e–h pairs are still composed of electron and hole quasi-particles with spin ½, except that their g-value is very different from the g-value of free electron, g_e (= 2.002). In this approximation, the strong SOC influences the e–h g-values, but the generalized electron and hole have still angular momentum (or spin) ½.

In this simplified model, the internal e–h exchange coupling is very weak so that the effective e–h spin manifold still contains four uncorrelated levels, similar to regular e–h pairs, in which optical transitions may occur with $\Delta m = 0, \pm 1$ leading to PL emission (Figure 4.1.12a). When applying a magnetic field B, the electron and hole quasi-particles are each subjected to a different Zeeman interaction, and therefore the combined e–h energy level, E, that determines the PL emission

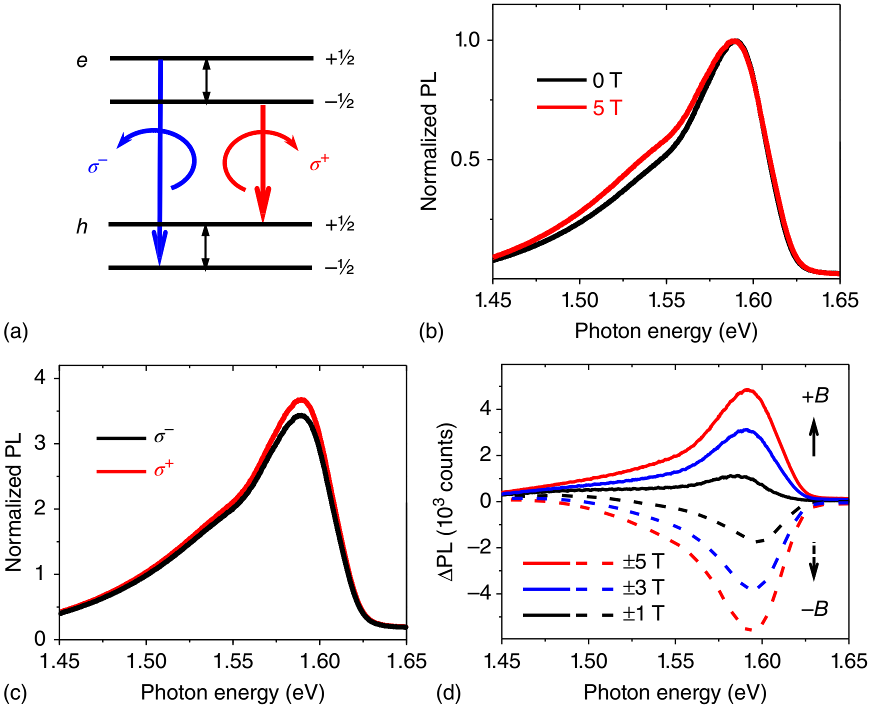

Figure 4.1.12 (a) Illustration of spin-sublevels in an e–h pair upon Zeeman splitting under external magnetic field. (b) Unpolarized PL spectra of $CH_3NH_3PbI_3$ at $B = 0$ T and $B = 5$ T, respectively. (c) PL spectra of right, σ^+ and left, σ^- circular polarized emission at $B = 5$ T from a pristine film. (d) The calculated difference, ΔPL, between σ^+ and σ^- emission spectra at fields ranging between −5 and 5 T.

wavelength broadens and shifts according to the equation [39]:

$$E^{(\pm)} = E_0 \pm ½\Delta g \mu_B B + c_0 B^2 \tag{4.1.1}$$

where c_0 is referred to as the "diamagnetic coefficient" of the e–h pairs. Therefore, upon a strong magnetic field, the PL emission should both broaden (Δg effect) and redshift (c_0 contribution). By comparing the PL spectra at zero field and $B = 5$ T (Figure 4.1.12b), we can clearly see the obvious broadening as well as the slight redshift with applied B field. However, it is difficult to determine Δg from the broadening because the PL emission band here is not sufficiently sharp.

We therefore measured the field-induced circular polarization (FICPO) effect from the perovskite PL emission in the Faraday configuration, which could help us determine the Δg factor. At low temperature, where the thermal energy is comparable to the Zeeman splitting, the four-spin sublevel populations obey the Boltzmann distribution at thermal equilibrium if the spin relaxation time is shorter than the SP lifetime. Two of these four optical transitions are circularly polarized since $\Delta m = \pm 1$, whereas the other two are unpolarized having $\Delta m = 0$ (Figure 4.1.12a). This yields unequal PL intensities in the two circular polarization directions related with $\Delta m = \pm 1$ that results in an overall circularly polarized emission under high magnetic field (Figure 4.1.12c). By comparing the right (σ^+) and left (σ^-) circularly polarized PL emission components, we obtained a PL polarization difference, $\Delta\text{PL} = (\sigma^+ - \sigma^-)$, which increases with the field B; moreover, ΔPL sense changes with $\boldsymbol{B}$ direction (Figure 4.1.12d).

The PL circular polarization P is defined as $P = (\sigma^+ - \sigma^-)/(\sigma^+ + \sigma^-)$. As shown in Figure 4.1.13a, we found that P increases approximately linear with B. The unequal $\Delta m = \pm 1$ transition intensities at field B in thermal equilibrium can be readily calculated using the Boltzmann distribution statistics. In this case, we get for the linear (unsaturated) regime:

$$P = \Delta g \mu_B B / 4 k_B T \tag{4.1.2}$$

where T is the sample local temperature. We also plotted P versus T at a fixed field, $B = 5$ T, as shown in Figure 4.1.13b. This dependence is nonlinear, since P is inversely proportional to T (inset in Figure 4.1.13b). Therefore, by fitting both curves with Eq. (4.1.2), we extracted $\Delta g \sim 0.65$ for the e–h spin pairs in the hybrid perovskite materials, which is over two orders of magnitude larger than that in organic semiconductors [24].

The circular polarization P should also depend on a "limiting factor," $\text{LF} = \exp(-\tau_{SL}/\tau)$, which limits the maximum population on the lowest spin-sublevels under thermal equilibrium since not all photoexcitations reach thermal equilibrium. At an even higher magnetic field, a saturation of P is expected and should be used to determine the LF value. The "$\Delta g \sim 0.65$" actually contains the LF "$\exp(-\tau_{SL}/\tau)$" term, which could not be further extracted from the linear regime of P versus B. Considering τ_{SL} is short in the hybrid perovskites due to the strong SOC, we believe the estimation of the Δg factor is still a good approximation, although the "real" Δg factor might be even larger for $CH_3NH_3PbI_3$. This also implies that ultrahigh magnetic field measurements of FICPO should be performed for further studying Δg in the hybrid perovskite materials.

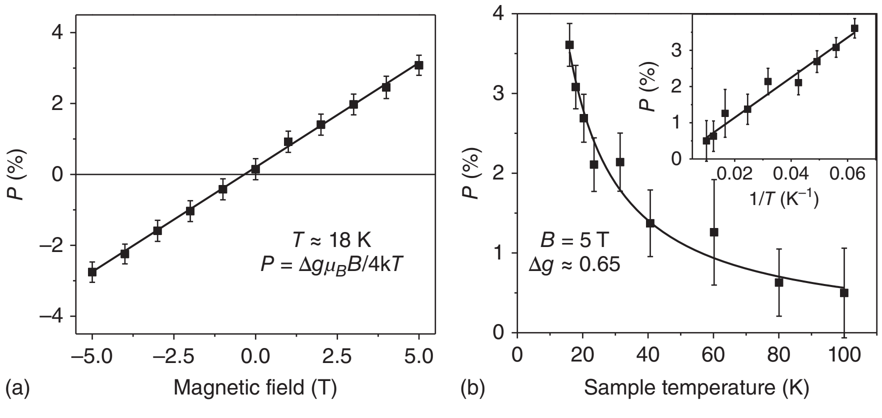

Figure 4.1.13 Circular polarization of PL versus (a) magnetic field B and (b) as a function of the sample temperature, T.

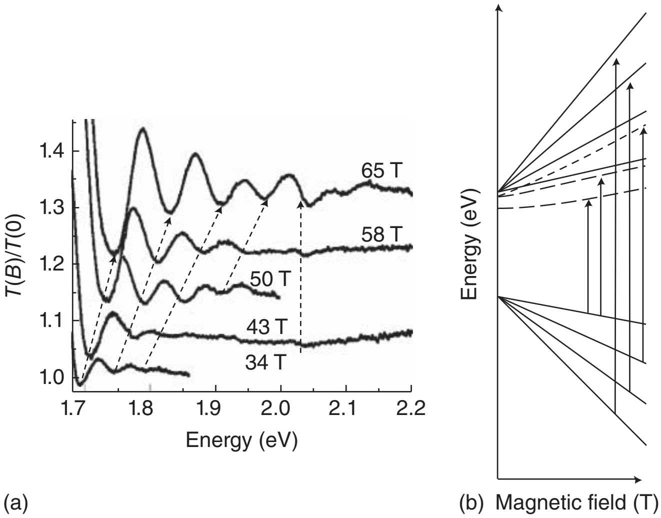

Figure 4.1.14 (a) Magneto-absorption (the ratio of the high-field spectra to zero field) of a $CH_3NH_3PbI_3$ polycrystalline film up to 65 T. (b) Energy levels and transitions between the free-electron and hole levels (solid lines) and the excitonic transitions (dashed lines). Source: Miyata et al. 2015 [14]. Copyright 2015. Reproduced with permission of Springer Nature.

4.1.3.2 Magneto-absorption Spectroscopy at Ultrahigh Magnetic Field

Recently, Miyata et al. measured the absorption spectrum of $CH_3NH_3PbI_3$ perovskite under ultrahigh magnetic field to directly determine the exciton binding in this compound [14]. As shown in Figure 4.1.14a, the resonant absorptions are minima in the ratio of transmission $T(B)/T(0)$, and a clear sequence of well-resolved Landau level transitions (Figure 4.1.14b) develop in magnetic fields of 34–65 T. The exciton binding energy, namely, the energy difference between excitonic and interband free-carrier transitions, was thus determined to be ~16 meV at low temperatures in the orthorhombic phase, and even smaller at room temperature in the cubic phase of this compound. This work may explain the high efficiency of photocarrier generation in solar cells based on $CH_3NH_3PbI_3$ perovskite.

4.1.4 Spin-Polarized Carrier Dynamics

4.1.4.1 Direct Measurement of Spin-pair Lifetime by Picosecond Pump–Probe Spectroscopy

The SP lifetimes in the $CH_3NH_3PbI_{3-x}Cl_x$ material can be measured directly using the pump/probe photomodulation (PM) spectroscopy on pristine films [40]. For this measurement, the pump photon wavelength was set at 400 nm (800 nm) that is above-gap (below-gap) excitation, similar to the laser wavelengths used for the MPC measurements mentioned. As shown in Figure 4.1.15a, the entire PM spectrum in the spectral range 1.6–2.2 eV shares the same decay dynamics, indicating that it originates from the same photogenerated e–h pair species. The PM spectra excited at 400 and 800 nm are very similar (Figure 4.1.15a,b). However, the PM decay dynamics generated at these two wavelengths is quite different, and strongly depends on the excitation wavelength (Figure 4.1.15c).

The transient dynamics excited above-gap could be fit with a double exponential decay that corresponds to two lifetimes (short and long) of ~22 and ~465 ps, respectively; whereas only the long decay of ~505 ps was observed with below-gap excitation. These lifetimes agree very well with the interpretation of MPC(B) response using the Δg mechanism, where the broad $\mathrm{MPC_B}$ corresponds to short-lived e–h pairs and only exists with the above-gap excitation. In comparison, the long-lived e–h pairs result in a more pronounced and narrower $\mathrm{MPC_N}$ response which is independent of the excitation wavelength.

To better correlate the e–h lifetime, τ and the MFE line shape (A(MFE) and $B_{1/2}$), we measured the PM dynamics and MPL on a series of $\mathrm{CH_3NH_3PbI_{3-x}Cl_x}$ films grown under different conditions (see also Figure 4.1.5). As shown in Figure 4.1.16a, the e–h pair lifetime becomes longer in the less crystalline film,

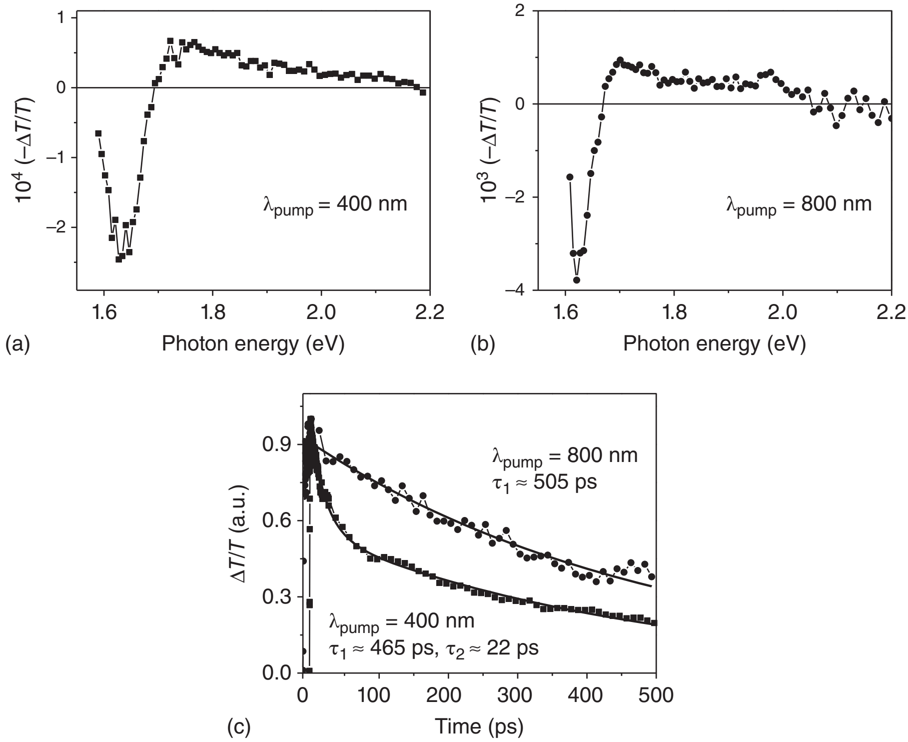

Figure 4.1.15 PM spectra from a $\mathrm{CH_3NH_3PbI_{3-x}Cl_x}$ film with excitation at (a) 400 nm and (b) 800 nm. (c) Corresponding decay dynamics of the PM spectra.

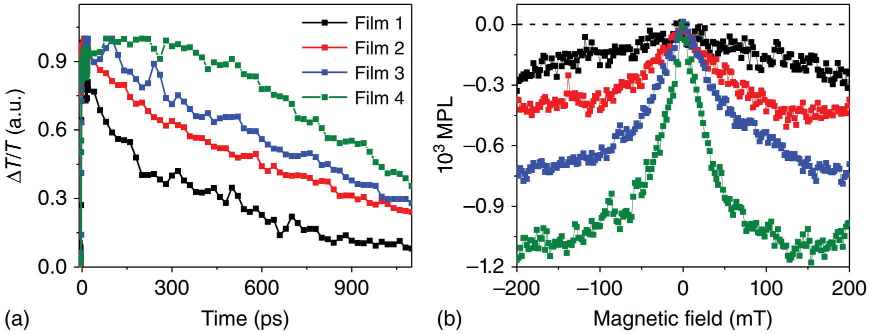

Figure 4.1.16 (a) PM dynamics and (b) MPL(B) response in various $CH_3NH_3PbI_{3-x}Cl_x$ films.

and the decay could be fit with an exponential function to obtain an average lifetime τ. The corresponding MPL(B) response shows a gradual change in both amplitude and width (A(MFE) and $B_{1/2}$, Figure 4.1.16b), similar to MPC(B) (Figure 4.1.6c,d). As is clearly evident from the figure, the longer the τ, the stronger and narrower is the MPL(B) response. This "control experiment" validates our interpretation that MFE in the perovskites is due to the Δg mechanism, where its field response is governed by the SP lifetime τ.

4.1.4.2 Determination of Spin Relaxation Time from Circular Pump–Probe Technique

By incorporating circular polarization in the pump–probe measurement, Giovanni et al. demonstrated the photogeneration of highly polarized carriers, and studied the spin dynamics of these polarized carriers [15]. As shown in Figure 4.1.17a, an initial degree of polarization (difference between σ^+ and σ^-) was photogenerated even at room temperature using the σ^+ pump excitation on the $CH_3NH_3PbI_3$ film, and the polarized carrier populations gradually disappeared within the time scale of picosecond. By cooling the sample down to 77 K, both the initial polarization and spin relaxation lifetime of photocarriers were significantly increased, as illustrated in Figure 4.1.17b.

Through the analysis based on a simple two-level system model, the electron spin decays on a much longer time scale of 7 ± 1 ps compared to that of the holes 1.1 ± 0.1 ps at low temperature (Figure 4.1.17c). The spin lifetime shows an obvious but weak dependence on temperature, which might be attributed to the spin relaxation through impurities and grain boundaries scattering. A much slower spin relaxation (over 100 ps) would be possible in a higher quality film with larger gains at lower temperature (for example, $T = 4$ K).

4.1.5 Conclusion and Outlook

Following the huge interest in perovskite solar cells, investigations of spin-related properties of these materials have begun during the past year. Within such a

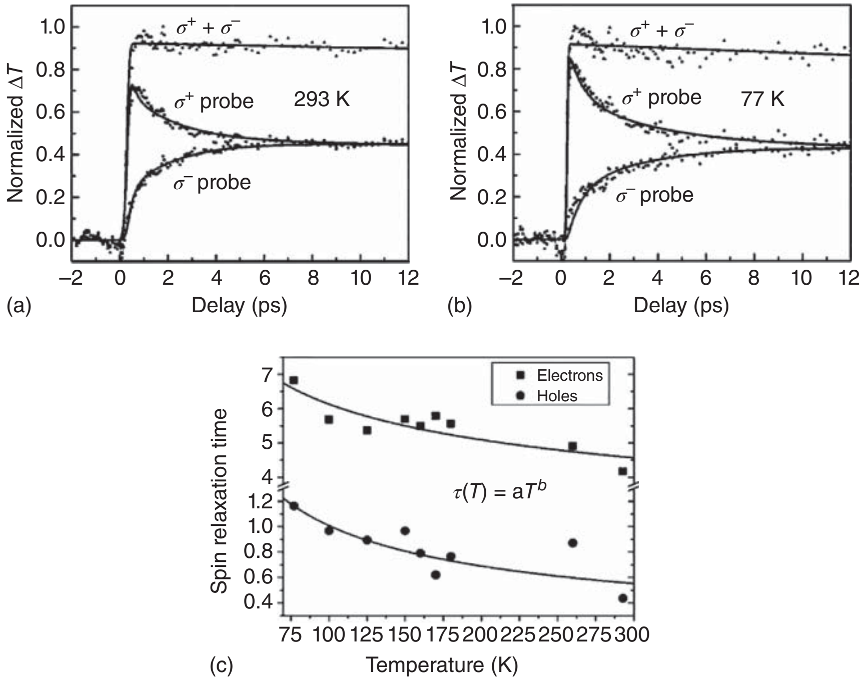

Figure 4.1.17 Normalized circular pump–probe picoseconds decay dynamics at (a) room temperature (293 K) and (b) low temperature (77 K). (c) The spin relaxation time versus temperature of electrons and holes. Source: Giovanni et al. 2015 [15]. Copyright 2015. Reproduced with permission of American Chemical Society.

short time, significant achievements have been made, which include (i) the observation/interpretation of MFEs in films and optoelectronic devices; (ii) the optical spectroscopy under high magnetic field where Landau levels dominate; and (iii) the spin-polarized carrier transient dynamics measurements. Many other important works, both theoretical and experimental, have been also reported recently [41–44]. They are related (but not limited) to the predication of spin-related phenomena, the demonstration of spin injection/manipulation, and fabrication of spintronic devices based on the hybrid perovskite materials. To give a specific example, we present here a “hybrid” optoelectronic–spintronics (O-S) device, which contains a hybrid perovskite LED device coupled to an inorganic spin valve (SV) [45, 46]. Their combination results in two new magneto-optoelectronic functionalities. These are light-controlled magneto-resistance and magnetically modulated EL colors, as illustrated in Figure 4.1.18.

Under light illumination, the device perovskite component acts as an optical-responsive electrical source that drives the composite circuit; in this case, the MPC amplitude increases up to two orders of magnitudes depending on the excitation intensity (Figure 4.1.19a). This ties together the photoresponsive resistance and the magnetic-responsive resistance, and demonstrates a novel approach to optical/magnetic-dual sensors in spintronic logic circuits. Using

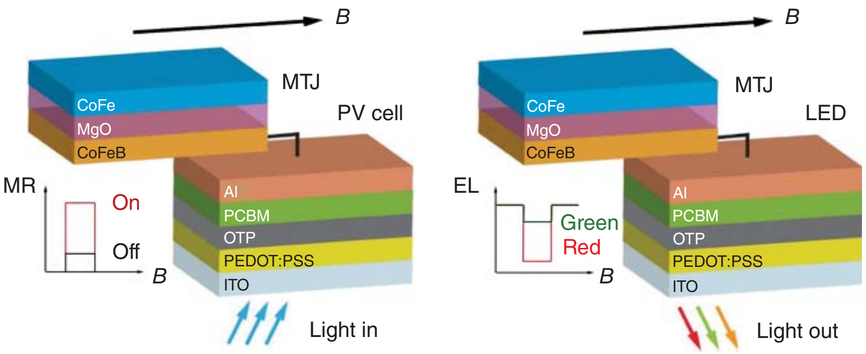

Figure 4.1.18 Illustration of the hybrid optoelectronic-spintronics devices based on hybrid perovskite materials.

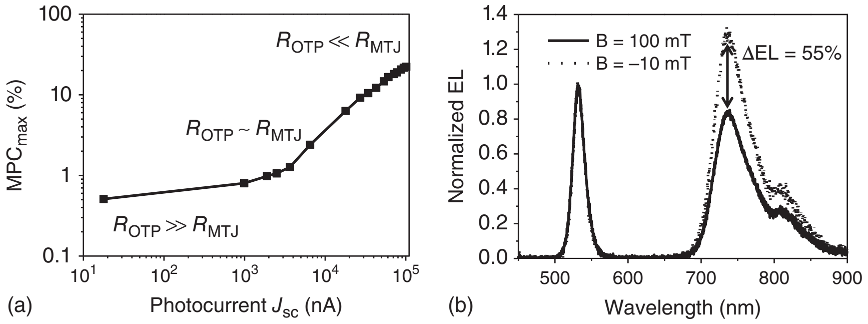

Figure 4.1.19 Tunable (a) MPC amplitude and (b) EL color from the perovskite O-S device.

the SV component to control the EL emission of the O-S device, a color change could be realized using two distinct perovskite LEDs (e.g. $CH_3NH_3PbI_3$ and $CH_3NH_3PbBr_3$) that is generated by applying a moderately weak magnetic field, as shown in Figure 4.1.19b. This capability in perovskite-based O-S devices may lead to unique potential applications in magnetically controlled display.

The study of spin physics has been rapidly developed in the organic–inorganic perovskite family, but still is considered to be in its infancy. Considering the vast number of compounds that may be synthesized in the hybrid perovskite family, we believe a lot of work needs be done to provide a more accurate overall picture of the spin physics in these hybrid semiconductors. For instance, the SOC strength could be varied by changing the chemical composition, such as using Sn-based materials [47]. Moreover, hybrid perovskites having organic cations with longer tails may result in a two-dimensional layered structure of the organic–inorganic hybrids, leading to quantum confinement of carriers within the inorganic layer, and thus to excitons with large binding energy [48]. We believe these semiconducting hybrids would not only bring elegant resolution in solar cells but also change the concepts of the research community in many aspects, similar to what the organic semiconductor counterparts have done in the past few decades [49, 50].

Acknowledgements

We acknowledge Dr. C.-X. Sheng at Nanjing University of Science and Technology, Ms Y. Zhai at University of Utah, and Drs. K. Mielczarek and A. Zakhidov at University of Texas at Dallas for their collaboration in this project. This work was supported by the DOE grant No. DE-FG02-04ER46109, and the Utah NSF-Materials Research Science and Engineering Centers (MRSEC) program DMR 1121252.

References

1 Kojima, A., Teshima, K., Shirai, Y., and Miyasaka, T. (2009). Organometal halide perovskites as visible-light sensitizers for photovoltaic cells. *J. Am. Chem. Soc.* 131: 6050–6051.
2 Liu, M., Johnston, M.B., and Snaith, H.J. (2013). Efficient planar heterojunction perovskite solar cells by vapour deposition. *Nature* 501: 395–398.
3 Burschka, J., Pellet, N., Moon, S.-J. et al. (2013). Sequential deposition as a route to high-performance perovskite-sensitized solar cells. *Nature* 499: 316–319.
4 Tan, Z.-K., Moghaddam, R.S., Lai, M.L. et al. (2014). Bright light-emitting diodes based on organometal halide perovskite. *Nat. Nanotechnol.* 9: 687–692.
5 Cho, H., Jeong, S.-H., Park, M.-H. et al. (2015). Overcoming the electroluminescence efficiency limitations of perovskite light-emitting diodes. *Science* 350: 1222–1225.
6 APS March Meeting (2016). Focus – Session X8: organic inorganic perovskite spintronics. https://meetings.aps.org/Meeting/MAR16/Session/X8.
7 Hao, F., Stoumpos, C.C., Cao, D.H. et al. (2014). Lead-free solid-state organic–inorganic halide perovskite solar cells. *Nat. Photonics* 8: 489–494.
8 Bi, D., Tress, W., Dar, M.I. et al. (2016). Efficient luminescent solar cells based on tailored mixed-cation perovskites. *Sci. Adv.* 2: e1501170.
9 Even, J., Pedesseau, L., Jancu, J.-M., and Katan, C. (2013). Importance of spin–orbit coupling in hybrid organic/inorganic perovskites for photovoltaic applications. *J. Phys. Chem. Lett.* 4: 2999–3005.
10 D'Innocenzo, V., Grancini, G., Alcocer, M.J.P. et al. (2014). Excitons versus free charges in organo-lead tri-halide perovskites. *Nat. Commun.* 5: 3586.
11 Xing, G., Mathews, N., Sun, S. et al. (2013). Long-range balanced electron- and hole-transport lengths in organic–inorganic $CH_3NH_3PbI_3$. *Science* 342: 344–347.
12 Zhang, C., Sun, D., Sheng, C.X. et al. (2015). Magnetic field effects in hybrid perovskite devices. *Nat. Phys.* 11: 427–434.
13 Hsiao, Y.-C., Wu, T., Li, M., and Hu, B. (2015). Magneto-optical studies on spin-dependent charge recombination and dissociation in perovskite solar cells. *Adv. Mater.* 27: 2899–2906.
14 Miyata, A., Mitioglu, A., Plochocka, P. et al. (2015). Direct measurement of the exciton binding energy and effective masses for charge carriers in organic–inorganic tri-halide perovskites. *Nat. Phys.* 11: 582–587.

15 Giovanni, D., Ma, H., Chua, J. et al. (2015). Highly spin-polarized carrier dynamics and ultralarge photoinduced magnetization in $CH_3NH_3PbI_3$ perovskite thin films. *Nano Lett.* 15: 1553–1558.

16 Kim, M., Im, J., Freeman, A.J. et al. (2014). Switchable $S = 1/2$ and $J = 1/2$ Rashba bands in ferroelectric halide perovskites. *PNAS* 111: 6900–6904.

17 Kepenekian, M., Robles, R., Katan, C. et al. (2015). Rashba and Dresselhaus effects in hybrid organic–inorganic perovskites: from basics to devices. *ACS Nano* 9: 11557–11567.

18 Saparov, B. and Mitzi, D.B. (2016). Organic–inorganic perovskites: structural versatility for functional materials design. *Chem. Rev.* 116: 4558–4596.

19 Stranks, S.D., Eperon, G.E., Grancini, G. et al. (2013). Electron–hole diffusion lengths exceeding 1 micrometer in an organometal trihalide perovskite absorber. *Science* 342: 341–344.

20 Dong, Q., Fang, Y., Shao, Y. et al. (2015). Electron–hole diffusion lengths >175 μm in solution-grown $CH_3NH_3PbI_3$ single crystals. *Science* 347: 967–970.

21 Sun, D., Ehrenfreund, E., and Vardeny, Z.V. (2014). The first decade of organic spintronics research. *Chem. Commun.* 50: 1781–1793.

22 Hu, B., Yan, L., and Shao, M. (2009). Magnetic-field effects in organic semiconducting materials and devices. *Adv. Mater.* 21: 1500–1516.

23 Bloom, F.L., Wagemans, W., Kemerink, M., and Koopmans, B. (2007). Separating positive and negative magnetoresistance in organic semiconductor devices. *Phys. Rev. Lett.* 99: 257201.

24 (a) Gautam, B.R., Nguyen, T.D., Ehrenfreund, E., and Vardeny, Z.V. (2012). Magnetic field effect on excited-state spectroscopies of π-conjugated polymer films. *Phys. Rev. B* 85: 205207. (b) also see Gautam, B.R. (2013). Magnetic field effect in organic films and devices. Doctoral Dissertation. The University of Utah.

25 Zhang, Y., Basel, T.P., Gautam, B.R. et al. (2012). Spin-enhanced organic bulk heterojunction photovoltaic solar cells. *Nat. Commun.* 3: 1043.

26 Devir-Wolfman, A.H., Khachatryan, B., Gautam, B.R. et al. (2014). Short-lived charge-transfer excitons in organic photovoltaic cells studied by high-field magneto-photocurrent. *Nat. Commun.* 5: 4529.

27 Hu, B. and Wu, Y. (2007). Tuning magnetoresistance between positive and negative values in organic semiconductors. *Nat. Mater.* 6: 985–991.

28 Wang, J., Chepelianskii, A., Gao, F., and Greenham, N.C. (2012). Control of exciton spin statistics through spin polarization in organic optoelectronic devices. *Nat. Commun.* 3: 1191.

29 Steiner, U.E. and Ulrich, T. (1989). Magnetic field effects in chemical kinetics and related phenomena. *Chem. Rev.* 89: 51–147.

30 Brenner, T.M., Egger, D.A., Kronik, L. et al. (2016). Hybrid organic–inorganic perovskites: low-cost semiconductors with intriguing charge-transport properties. *Nat. Rev. Mater.* 1: 15007.

31 Elliott, R.J. (1954). Theory of the effect of spin-orbit coupling on magnetic resonance in some semiconductors. *Phys. Rev.* 96: 266.

32 You, J., Hong, Z., Yang, Y. et al. (2014). Low-temperature solution-processed perovskite solar cells with high efficiency and flexibility. *ACS Nano* 8: 1674–1680.

33 Baldo, M.A., Adachi, C., and Forrest, S.R. (2000). Transient analysis of organic electrophosphorescence. II. Transient analysis of triplet–triplet annihilation. *Phys. Rev. B* 62: 10967–10977.

34 Dualeh, A., Tétreault, N., Moehl, T. et al. (2014). Effect of annealing temperature on film morphology of organic–inorganic hybrid pervoskite solid-state solar cells. *Adv. Funct. Mater.* 24: 3250–3258.

35 Tanaka, K., Takahashi, T., Ban, T. et al. (2003). Comparative study on the excitons in lead-halide-based perovskite-type crystals $CH_3NH_3PbBr_3$ $CH_3NH_3PbI_3$. *Solid State Commun.* 127: 619–623.

36 Nam, S., Reynolds, D., Litton, C. et al. (1976). Free-exciton energy spectrum in GaAs. *Phys. Rev. B* 13: 761.

37 Sandoval, M.T., da Silva, A.F., Silva, E.d.A.e., and La Rocca, G. (2012). Mesoscopic spin-orbit effect in the semiconductor nanostructure electron *g* factor. *Phys. Rev. B* 86: 195302.

38 Van Bree, J., Silov, A.Y., Koenraad, P. et al. (2012). *g* factors and diamagnetic coefficients of electrons, holes, and excitons in InAs/InP quantum dots. *Phys. Rev. B* 85: 165323.

39 Hirasawa, M., Ishihara, T., Goto, T. et al. (1994). Magnetoabsorption of the lowest exciton in perovskite-type compound $(CH_3NH_3)PbI_3$. *Physica B* 201: 427–430.

40 Zhai, Y., Sheng, C.X., Zhang, C., and Vardeny, Z.V. (2016). Ultrafast spectroscopy of photoexcitations in organometal trihalide perovskites. *Adv. Funct. Mater.* 26: 1617–1627.

41 Li, J. and Haney, P.M. (2016). Optical spintronics in organic–inorganic perovskite photovoltaics. *Phys. Rev. B* 93: 155432.

42 Zheng, F., Tan, L.Z., Liu, S., and Rappe, A.M. (2015). Rashba spin–orbit coupling enhanced carrier lifetime in $CH_3NH_3PbI_3$. *Nano Lett.* 15: 7794–7800.

43 Xu, Q., Liu, E., Qin, S. et al. (2014). Spin transport in $CH_3NH_3PbI_3$. *J. Phys. D: Appl. Phys.* 47: 405002.

44 Zhu, K., Chen, J., Fan, Q. et al. (2015). Magnetoresistance of $(CH_3NH_3)PbI_3$-Coated $La_{0.67}Sr_{0.33}MnO_3$ granular composites. *IEEE Trans. Magn.* 51: 1–4.

45 Sun, D., Basel, T.P., Gautam, B.R. et al. (2013). Room-temperature magnetically modulated electroluminescence from hybrid organic/inorganic spintronics devices. *Appl. Phys. Lett.* 103: 042411.

46 Sun, D., Basel, T.P., Gautam, B.R. et al. (2014). Giant magneto-electroluminescence from hybrid spin-organic light emitting diodes. *SPIN* 4: 1450002.

47 Stroppa, A., Di Sante, D., Barone, P. et al. (2014). Tunable ferroelectric polarization and its interplay with spin–orbit coupling in tin iodide perovskites. *Nat. Commun.* 5: 5900.

48 Papavassiliou, G.C. (1997). Three-and low-dimensional inorganic semiconductors. *Prog. Solid State Chem.* 25: 125–270.

49 Xiong, Z.H., Wu, D., Valy Vardeny, Z., and Shi, J. (2004). Giant magnetoresistance in organic spin-valves. *Nature* 427: 821–824.

50 Sun, D., van Schooten, K.J., Kavand, M. et al. (2016). Inverse spin Hall effect from pulsed spin current in organic semiconductors with tunable spin-orbit coupling. *Nat. Mater.* doi: 10.1038/nmat4618.

4.2

Perovskite Solar Cells for Photoelectrochemical Water Splitting and CO_2 Reduction

Gurudayal[1, 2, 3], *Joel Ager*[1, 2, 3, 4], *and Nripan Mathews*[5]

[1] *Joint Center for Artificial Photosynthesis, Lawrence Berkeley National Laboratory, 1 Cyclotron Road, Berkeley, CA 94720, USA*
[2] *Chemical Sciences Division, Lawrence Berkeley National Laboratory, 1 Cyclotron Road, Berkeley, CA 94720, USA*
[3] *Department of Materials Science and Engineering, University of California Berkeley, Berkeley, CA 94720, USA*
[4] *Materials Sciences Division, Lawrence Berkeley National Laboratory, 1 Cyclotron Road, Berkeley, CA 94720, USA*
[5] *Nanyang Technological University, Materials Science and Engineering, Block N4.1, 50 Nanyang Avenue, Singapore, 639798 Singapore*

4.2.1 Introduction

Rapid economic and demographic changes continue to increase the world's dependence on fossil fuels as an energy source. Urbanization and further increase in population will serve to accelerate the trend. Fossil fuels meet more than 80% of the total primary energy demand and generate over 90% of the primary greenhouse gases: (CO_2), methane (CH_4) and nitrous oxide (N_2O) [1]. The current atmospheric CO_2 level is more than 400 ppm, which is significantly higher compared to pre-industrial times, and continues to rise [2]. In principle, energy provided by the sun has the potential to meet our energy demand. However, it is a significant technological challenge to convert and store solar energy by efficient and cost effective methods on a large scale. While conversion of solar light to power via photovoltaic panels has grown rapidly, the temporal intermittency of the source, as well as its uneven geographical distribution, will ultimately limit its ability to displace fossil fuels.

Storing solar energy in the form of fuels would be advantageous and environmentally friendly, if it could be done efficiently [3, 4]. Photoelectrochemical (PEC) water splitting is inspired from the natural photosynthesis process in plants, where solar energy is captured and converted into hydrocarbons, glucose, and oxygen [5, 6]. Indeed, there is considerable research effort into "artificial photosynthesis," or PEC methods to convert solar energy to chemical fuels such as hydrogen and hydrocarbons [6, 7]. Considering the case of hydrogen, it can be generated by splitting of water by reaction (4.2.1).

$$2H_2O + \text{Light} \rightarrow 2H_2 + O_2 \quad E = 1.23\,\text{V versus RHE} \tag{4.2.1}$$

Halide Perovskites: Photovoltaics, Light Emitting Devices, and Beyond, First Edition.
Edited by Tze-Chien Sum and Nripan Mathews.

The half reactions are

$$H_2O + \text{Light} \rightarrow 2H^+ + \frac{1}{2}O_2 + 2e^- \quad (4.2.2a)$$

$$2H^+ + 2e^- \rightarrow H_2 \quad (4.2.2b)$$

The overall ΔE^0 is 1.23 eV, while an overpotential (0.4–0.6 eV) is required to overcome the thermodynamic and recombination losses associated with the reaction [8–11]. Hydrogen is an attractive fuel because it has high gravimetric energy density, nearly three times that of gasoline [12]. PEC generated hydrogen can be utilized as an energy source by converting it to electricity in a fuel cell [13, 14]. However, generating such chemical potential difference by solar absorption in a single semiconductor photoelectrode is challenging. At least two semiconductors in tandem with complimentary absorption spectrum and appropriate conduction and valence band positions with respect to water redox levels are required to efficiently harvest the solar energy and drive water-splitting reaction [15, 16].

Carbon dioxide (CO_2) is an alarming greenhouse gas and anthropogenic increases in its concentration are the major driver for global warming. To conserve environmental stability, CO_2 produced on Earth should balance consumption. Sustainable CO_2 reduction to form fuels would thus be able to tackle two environmental challenges concurrently. CO_2 conversion can be achieved by electrochemical and PEC reactions. However, CO_2 capture, conversion, and utilization requires high energy, appropriate selective catalysts that make this reaction more challenging. Electrochemical CO_2 reduction involves multi-electron transfer and can produce either gaseous (CO, CH_4, C_2H_4) or liquid fuels (HCOOH, CH_3OH, CH_3CH_2OH, etc.) The thermodynamic electrochemical half-reactions of CO_2 reduction with their standard electrode potentials are as follows:

$$CO_2 + 4H^+ + 4e^- \rightarrow C + 2H_2O \quad E_0 = 0.210\,\text{V versus SHE} \quad (4.2.3)$$

$$CO_2 + 2H^+ + 2e^- \rightarrow CO + H_2O \quad E_o = -0.103\,\text{V versus SHE} \quad (4.2.4)$$

$$CO_2 + 8H^+ + 8e^- \rightarrow CH_4 + 2H_2O \quad E_o = 0.169\,\text{V versus SHE} \quad (4.2.5)$$

$$2CO_2 + 12H^+ + 12e^- \rightarrow C_2H_4 + 4H_2O \quad E_o = 0.079\,\text{V versus SHE} \quad (4.2.6)$$

$$CO_2 + H^+ + 2e^- \rightarrow HCOO^- \quad E_o = -0.225\,\text{V versus SHE} \quad (4.2.7)$$

$$CO_2 + 2H^+ + 2e^- \rightarrow HCOOH \quad E_o = -0.250\,\text{V versus SHE} \quad (4.2.8)$$

$$CO_2 + 6H^+ + 6e^- \rightarrow CH_3OH + H_2O \quad E_o = 0.016\,\text{V versus SHE} \quad (4.2.9)$$

$$CO_2 + 12H^+ + 2e^- \rightarrow CH_3CH_2OH + 3H_2O \quad E_o = 0.084\,\text{V versus SHE} \quad (4.2.10)$$

When coupled to reaction (4.2.2a), which will yield a source of electrons via oxidation of water, it is possible to imagine the use of reactions (4.2.3)–(4.2.10) as a sustainable method to reduce CO_2 to fuels. It is to be noted that the all the reactions are within 225 mV of the potential for H_2 evolution reaction (HER) (4.2.2a), which is 0 V versus SHE at standard conditions. Thus, HER competes with the CO_2 reduction reaction (CO_2RR) in aqueous solution.

4.2.1.1 Photoelectrochemical Generation of H_2

Hydrogen generation from PEC cells through water splitting is a well-established concept [5, 8, 13]. However, primary challenges include improvement of the water splitting efficiency and stability [11, 17, 18]. In a water splitting PEC cell, water molecules are broken into hydrogen at the cathode/semiconductor photocathode and oxygen at the anode/semiconductor photoanode. When a semiconducting photo-electrode is immersed in an electrolyte solution, charge transfer occurs between the semiconducting electrode and the electrolyte until the equilibrium condition is achieved (Figure 4.2.1) [19, 20]. For an n-type semiconductor, typically upward band bending occurs at the surface of electrode

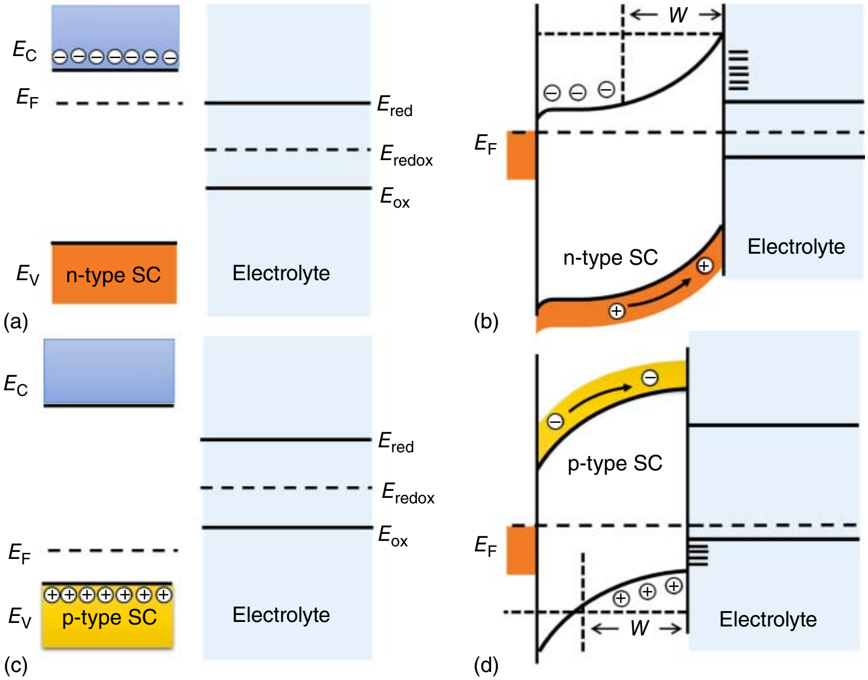

Figure 4.2.1 (a) The isolated energy band diagram of the n-type semiconductor and the electrolyte. (b) The equilibrated energy band diagram and the formation of space charge layer in n-type semiconductor when it is immersed in to the electrolyte. (c) The remote energy band diagram of the p-type semiconductor and the electrolyte. (d) The equilibrated energy band diagram and the formation of space charge layer in p-type semiconductor when it is immersed in to the electrolyte.

to match the Fermi level of the semiconductor and the redox level of the electrolyte. Similarly, downward band bending occurs at the surface of the electrode to match the Fermi level of a p-type semiconductor and the redox level of the electrolyte. A depletion layer or a space-charge layer exists at the interface of the semiconductor and electrolyte. Under illumination, the electric field in the space charge layer is useful for the separation of photo-generated electron and hole pairs. Figure 4.2.1 shows the energy levels of isolated and submerged n/p-type semiconducting photo-electrodes and the redox potentials of the redox species in the electrolyte. The overall water splitting reaction, water reduction and oxidation driven by photo-generated electron and holes are represented by the following reaction schematic; [15, 21]Although there has been significant development to make efficient PEC cells for hydrogen production, there still exists a big gap between the achieved and theoretically predicted efficiencies of PEC cells [11, 16, 22, 23].

4.2.1.2 PEC Electrode Materials

It remains a challenge to find a material, which can oxidize and reduce water without any external bias [24]. PEC electrode materials should have good aqueous stability, appropriate band levels with respect to water redox levels, high optical absorption in visible range and good electrical properties [25]. Many semiconducting materials for solar water splitting have been explored, but either the position of conduction and valence band are not favorable for both water reduction and oxidation potential simultaneously, or the ones that do have too large a bandgap to generate effective photocurrents (Figure 4.2.2) [27]. Metal oxides are relevant for PEC water splitting, mainly due to their semiconducting properties, stability in aqueous solutions and reasonably low cost [20, 26–29]. However, most

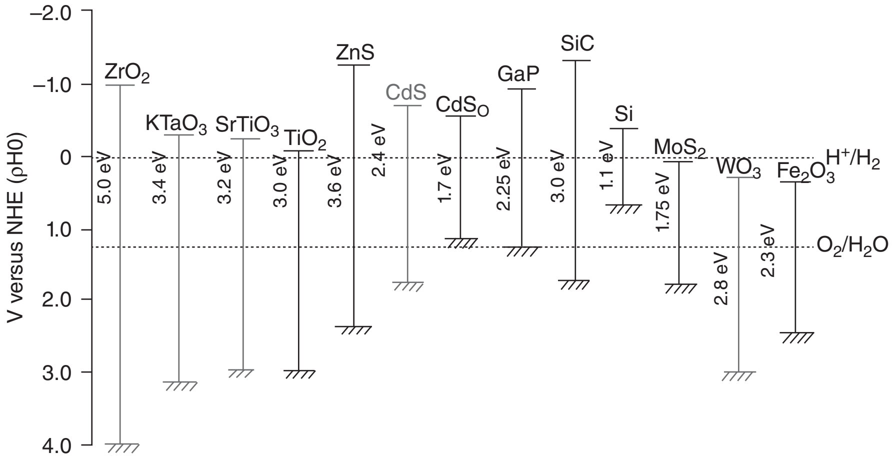

Figure 4.2.2 The band edge positions of different photoelectrodes with water oxidation/reduction potential. Source: Kudo and Miseki 2009 [26]. Reprinted with permission of Royal Society of Chemistry.

of metal oxides have wide energy band gap and poor semiconducting properties in comparison with traditional III–V semiconductors and Silicon [21, 28].

Among all metal oxide semiconductor oxides, TiO_2 has attracted much attention owing to its band levels, but high-energy band gap and inefficient absorption of sunlight spectrum has limited its performance [30, 31]. To tackle this problem, dyes with high visible light absorption capability, were utilized with limited success [31, 32]. Bismuth vanadate ($BiVO_4$) is another material explored for PEC water splitting, however its solar to hydrogen (STH) efficiency is limited by its band gap (2.4 eV), and poor stability [33, 34]. There have been major developments in the preparation of oxynitride materials (TaON and Ta_3N_5), which have an optimum energy band gap and can drive both water oxidation and reduction but the reported quantum efficiency (~5–6%) is still low [35]. Out of the various candidates explored, the most promising stable photocurrents reported to date was achieved using Iron (III) oxide, i.e. Fe_2O_3 or hematite [21, 36]. Iron (III) oxide shows largely favorable properties for water-splitting; however has an unfavorable conduction band level to reduce water necessitating the application of an external bias [37].

In addition to the challenges of stability, poor energy level alignment of the photoelectrodes with respect to water redox levels, the energy required for water splitting is significantly higher than the thermodynamic potential (1.23 eV) because of loss processes within the PEC cell. Furthermore, additional voltage is required to overcome the overpotentials resulting from the kinetic barriers of the intermediate species involved in the water oxidation and reduction mechanisms. The four-electron process for the oxygen evolution reaction (OER) demands even higher overpotential (0.3–0.5 eV) for a reasonable current density (~10 mA cm^{-2}). Accordingly, a single photo-absorbing material is not enough to generate the required photopotential to split water without an external bias.

In the following section, we discuss the approach to combine materials in a PEC cell and fabricate a tandem cell. Here, we distinguish a few commonly used approaches for bias free water splitting [38].

4.2.2 Tandem Configurations

Tandem approaches for STH conversion have been reviewed recently [18, 39, 40]. There are a number of demonstrations of overall water splitting tandem cells with decent STH conversion efficiency reported from different groups [16, 24, 40–44].

In tandem cell configurations (PEC cell-photovoltaic and photoanode–photocathode), the total photovoltage is produced by complementary optical absorption in two or more photoabsorbers connected in series to split water efficiently (Figure 4.2.3) [15, 16, 24, 44–46]. Whereas the most simplest and reliable approach is electrochemical-photovoltaic (EC-PV) configuration (Figure 4.2.3c). Additionally, it is hard to realize a single photoelectrode or photoanode–photocathode system to perform both OER and HER in the same pH electrolyte solution. For PEC-PV configuration, the photovoltage outputs of the sub-cells are crucial, especially the photovoltage generated by traditional solar cells, i.e. silicon, thin film chalcogenides is not enough to drive water

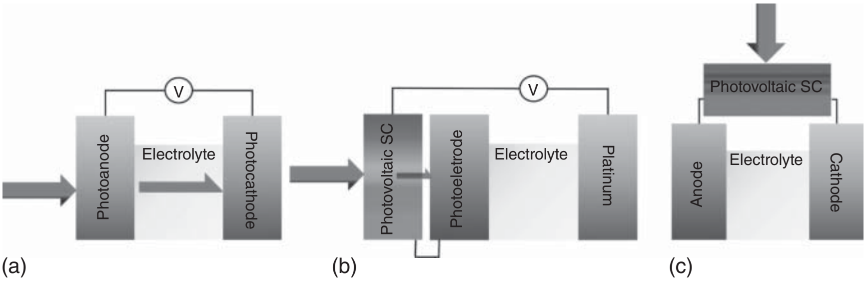

Figure 4.2.3 Tandem cell configurations, (a) photoanode–photocathode system, (b) photoelectrode-PV configuration, and (c) photovoltaic-electrocatalyst structure.

splitting reaction [24, 45, 47]. In this context, the relatively large open circuit voltages of the halide perovskite solar cells have made them attractive candidates as the photovoltaic components of solar fuel devices [16, 41, 42, 44]. The multiple light absorber tandem PEC systems can easily harvest a significant portion of the solar spectrum and generate enough voltage to overcome the overpotential and thermodynamical potential for water splitting. In the subsequent sections, different systems using multi photoabsorbers will be deliberated. Finally, a balance between the system complexity, cost, and STH conversion efficiency will be discussed.

For large scale applications, a PEC device should cost less than US$ 160 per m^2 with a STH efficiency of 10% [4]. To achieve this target, a PEC cell must be composed of abundant environment friendly materials combined with facile, cost-effective and scalable fabrication techniques to meet the high throughputs required of the PEC device [4, 44].

4.2.2.1 Photoanode–Photocathode Strategy

The photoanode–photocathode tandem devices drive two separate water redox half-reactions in a PEC cell. The p-type photocathode/n-type photoanode tandem system is the simplest and straightforward in terms of materials availability, fabrication cost and synthesis. The photoelectrodes can be either fabricated separately and subsequently wired to each other; or fabricated on the same substrate with local interconnects. The typical energy band diagram of photoanode–photocathode tandem system is shown in Figure 4.2.4. In addition to appropriate conduction and valence band edges to the water redox levels, the materials must have complimentary absorption spectra as well. However, this approach is under-explored in literature due to the additional challenge of driving both the water redox reactions at the same pH electrolyte solution. This challenge necessitates the development of robust protection layers. Most importantly, the energy band alignment of photoelectrodes is critical to achieve a notable STH efficiency. Turner et al. showed the importance of band alignment by fabricating a device of $GaInP_2$ ($E_g \sim 1.83$ eV) photocathodes in tandem with either WO_3 or Fe_2O_3 photoanodes under light illumination (more than 200 mW cm^{-2}) [48, 49]. Whereas, the $WO_3/GaInP_2$ tandem produced a

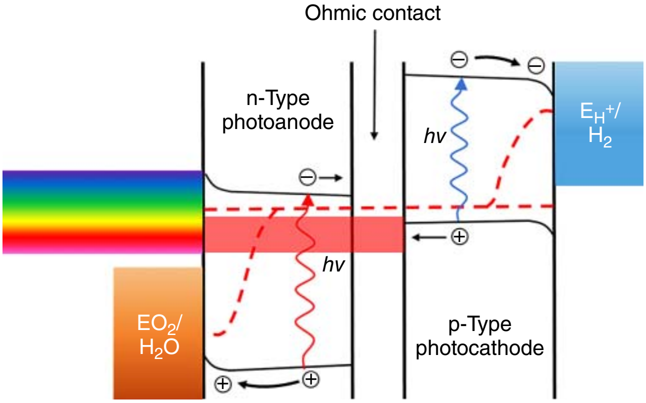

Figure 4.2.4 The schematic of energy band diagram of a photoanode–photocathode tandem cell.

detectable photocurrent 20 μA cm^{-2}, the Fe_2O_3/$GaInP_2$ tandem system produced negligible photocurrent even at 10 sun illumination because of mismatch of the conduction band minimum of the Fe_2O_3 thin film and the valence band maxima of $GaInP_2$ (Figure 4.2.5a,b). Gopal et al. demonstrated a tandem cell with improper band alignment, fabricated by a p-type Cu–Ti–O nanotube array photocathode in series with n-type TiO_2 photoanode [51]. This tandem configuration shows a small STH efficiency of 0.3%, which is because of similar absorption spectra of both materials [51]. Lai et al. investigated TiNi treated p-type Si photocathode/TiCo coated WO_3 photoanode and TiNi treated p-type Si/TiCo coated $BiVO_4$ photoanode PEC tandem systems for unassisted water splitting [52]. TiNi treated p-Si photocathode and TiCo coated $BiVO_4$ photoanode achieved unassisted water splitting STH efficiency of 0.05%, whereas the p-TiNi/Si photocathode and TiNi/WO_3 photoanode did not show any activity. This was the result of the 0.3 V higher CB position of $BiVO_4$ compared to WO_3, which might change the absorption spectrum matching and generate higher photovoltage and operating photocurrent [52].

There are also additional factors that need to be considered beyond band alignment. Nozik et al. fabricated an n-TiO_2/p-GaP tandem cell, which shows both hydrogen and oxygen evolution without an external bias voltage. However, the high internal series resistance limited the STH efficiency to 0.25% at zero bias. The device stability was also poor due to oxide layer formation on the surface of the p-GaP [19]. Liu et al. demonstrated a photoanode–photocathode tandem system of n-type TiO_2/p-type Si for unassisted water splitting that achieved a STH conversion efficiency 0.12% [53]. Again, the limited STH efficiency was due to the high-energy band gap of TiO_2 and ohmic losses in the device. Ding et al. demonstrated a FeOOH overlayer coated $BiVO_4$ photoanode and Pt treated Si photocathode tandem cell, where both the photoelectrodes are parallelly illuminated and exhibited a STH efficiency of 2.5% [54, 55]. A $BiVO_4$/Cu_2O tandem cell fabricated by Bornoz et al. showed a maximum STH efficiency of 0.5% (Figure 4.2.5c,d) despite a high theoretical STH efficiency of 8%

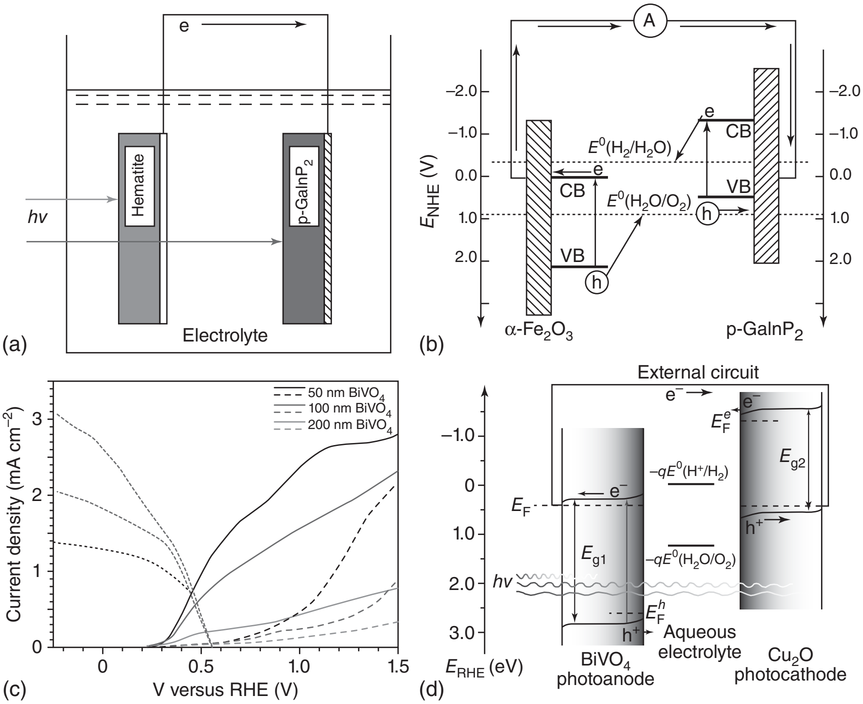

Figure 4.2.5 (a) Schematic of hematite and GanInP$_2$ tandem cell. (b) Energy diagram of a hematite photoanode and GanInP$_2$ photocathode tandem cell for unassisted water splitting. Source: Wang et al. 2008 [49]. Copyright 2008. Reprinted with permission of ELECTROCHEMICAL SOCIETY, INC. (c) J–V curves for the CoPi/BiVO$_4$ photoanodes and Cu$_2$O photocathode under simulated solar illumination (100 mW cm^{-2}). (d) Energy diagram of a BiVO$_4$ photoanode and Cu$_2$O photocathode tandem cell for unassisted water splitting. Source: Bornoz et al. 2014 [50]. Copyright 2014. Reprinted with permission of Royal Society of Chemistry.

with the rear Cu$_2$O photocathode expected to absorb all photons of wavelengths between 500 and 620 nm [50]. A p-type CaFe$_2$O$_4$ photocathode in tandem with n-type TiO$_2$ (parallel configuration) to generate an operating current density of 110 μA cm^{-2} in 0.1 M NaOH electrolyte solution [56]. This device was unstable and the Faradaic efficiency for gas evolution was observed to be only 12%, which is uncertain. Jang et al. showed PEC tandem cells comprising a NiFeOx overlayer coated hematite photoanode and a p-type Si photocathode in tandem, with STH efficiency of 0.91% (Figure 4.2.6a–c). Kim et al., reported another tandem configuration of a Pt/CdS/CuGa$_3$Se$_5$/(Ag,Cu)GaSe$_2$ photocathode and NiOOH/FeOOH/Mo doped BiVO$_4$ photoanode, which exhibit a STH conversion efficiency of 0.67% (Figure 4.2.6d–f) [57].

Although theoretical estimations predict an achievable STH efficiency of 29.7% from this configuration, practical demonstrations have been very disappointing [39]. Challenges include the lack of materials with suitable band gap, energy level positions and slow redox kinetics associated with systems explored so far.

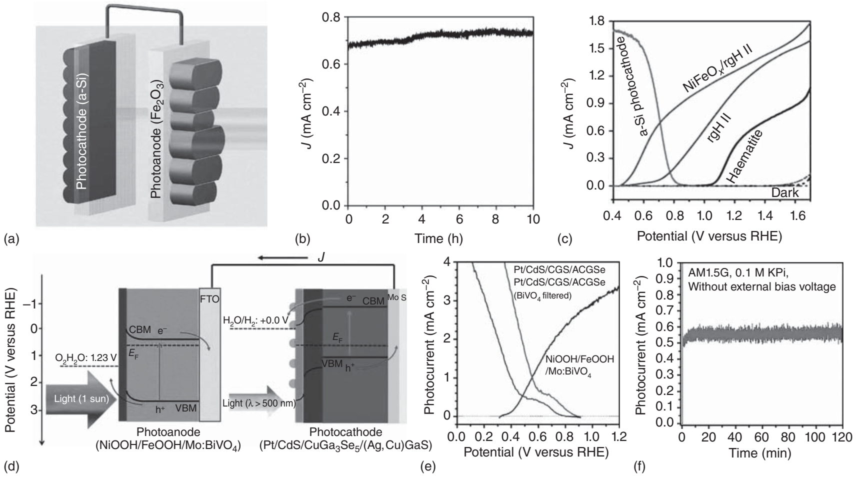

Figure 4.2.6 (a) Schematic of a photoanode–photocathode tandem cell with an amorphous Si photocathode and hematite photoanode. (b) Stability curve of a-Si–hematite tandem cell and (c) J–V curves of hematite coated with an OER catalyst (NiFeOx). Source: Jang et al. 2015 [55]. Copyright 2015. Reproduced with permission of John Wiley & Sons. (d) Schematic of NiOOH/FeOOH/Mo:BiVO$_4$ photoanode and Pt/CdS/CGS/(Ag,Cu)GaSe$_2$ photocathode tandem cell for overall water splitting. (e) J–V curves of photoanode (NiOOH/FeOOH/Mo:BiVO$_4$) and photocathode (Pt/CdS/CGS/GaSe$_2$) against applied potential for parallel and tandem scheme. (f) Stability curve for the tandem PEC cell. Source: Kim et al. 2016 [57]. Copyright 2016. Reproduced with permission of John Wiley & Sons.

4.2.2.2 PEC-PV Tandem System

The PEC-PV tandem approach is more advantageous than PEC alone because a single photoabsorber is unable to produce the required photovoltage to drive the water splitting reaction. This approach has been explored widely in literature, and involves either a photoanode or a photocathode connected in series (wired or stacked) with a single or multi-junction solar cell. The photoelectrode and photovoltaic solar cells with complimentary absorption spectra connected in series generates enough photovoltage to exceed the overpotential and thermodynamic potential necessary to drive water splitting. The contact between the photoelectrode and PV can be performed via a conducting metal wire or a transparent conductive oxide for wireless monolithic configurations [16, 42]. The wired configuration is convenient for assembling the components, whereas the wireless monolithic configuration is more appropriate for scalable development. Unfortunately, many of the wireless devices reported till date suffered from the stability issues [22].

A well noted PEC-PV configuration was implemented by Turner et al., consisted of a monolithic epitaxially grown III–V semiconductor system with a GaAs pn-junction coupled to a $GaInP_2$ photocathode. This device exhibited an impressive STH conversion efficiency of 12.5%, however the system suffered from stability issues due to corrosion of the $GaInP_2$ photocathode in contact with the aqueous electrolyte solution [22]. An additional drawback of this system is the high costs associated with its fabrication. Many tandem illumination configurations have been reported with similar performance and better light harvesting utilizing dye sensitized solar cells (DSSCs). While designing a tandem system for efficient water splitting, the choice of the photoelectrodes is critical. Park's group improved the STH efficiency of an integrated WO_3/DSSC to approximately 2.1% using a mesoporous WO_3 photoanode in 1 M H_2SO_4 electrolyte [58]. Gratzel's group demonstrated a simple yet cost effective DSSC-WO_3 and DSSC-Fe_2O_3 PEC-PV tandem cell with a STH efficiency of 3.1% and 1.7% respectively [24]. Furthermore, Shin and Park reported a transparent TiO_2 nanotube photoanode loaded with CdS/CdSe particles, with an STH efficiency of 2.1% STH efficiency [59]. Shi et al. also demonstrated a FeOOH/NiOOH $BiVO_4$/mesoporous WO_3 photoanodes and a DSSC PV in tandem configuration, which shows a 5.7% STH efficiency [59]. This PEC-PV tandem cell was assembled through a transparent double-sided conductive glass substrate in a wireless configuration [59]. The introduction of $BiVO_4$ improved solar light harvesting in the visible range compared to the WO_3 photoanode, while the water redox kinetics could be further enhanced with the loading of a co-catalyst (FeOOH/NiOOH). Fatwa et al. fabricated tandem devices using gradient-doped $BiVO_4$ integrated with double-junction amorphous Si PV cells in wired or wireless configurations, which reached 5.2% and 4.9% STH efficiency, respectively [45, 60].

Multijunction PV cells were heavily utilized for light harvesting compared with single PV cells in PEC-PV tandem cells. Due to the low open circuit voltages of conventional photovoltaic systems (Si, CuInGaS/Se), many of the tandem designs have required the series integration of several solar cells to generate the photopotential required for splitting water [24, 34, 45, 47]. These complicated approaches require a careful balance of the optical absorption and photocurrent generation within each solar cell to drive the overall reaction efficiently. Moreover, such architectures should also balance performance against fabrication complexity in order to allow for economical solar hydrogen production. Perovskite solar cells are revolutionary due to their facile fabrication, their high open circuit voltage (1.1–1.4 V) which is advantageous to drive solar assisted water splitting reaction with a single photoabsorber. The superb light-harvesting characteristics of perovskite materials in the solar-cell research field have led to a rapid increase in power conversion efficiency [44, 61].

In 2013, we have successfully demonstrated a $CH_3NH_3PbI_3$ ($E_g = 1.55$ eV) perovskite PV cell in a PEC/PV tandem cell with a Fe_2O_3 photoanode for unassisted water splitting, resulting in a 2.4% STH efficiency in 1 M NaOH electrolyte [42]. Our PEC-PV tandem device contained a single perovskite solar cell and a Mn-doped hematite photoanode, as shown in Figure 4.2.7. However, the PEC-PV tandem device still suffers from poor overall photocurrent density due to the low photocurrents produced by the thin Fe_2O_3 photoanode even after Mn doping. Kim et al. demonstrated a cobalt carbonate (Co–Ci) catalyst modified $BiVO_4$ photoanode with a single $CH_3NH_3PbI_3$ perovskite solar cell. This photoanode/perovskite tandem cell was encapsulated by epoxy for protection against corrosion and shown in Figure 4.2.8 [16]. This device exhibited a STH efficiency of 4.3% in wire configuration and 3.0% in wireless configuration, with an excellent stability of 10 hours [16]. Kamat's group successfully fabricated a $CH_3NH_3PbI_3$ perovskite solar-cell based PEC-PV tandem cell using $BiVO_4$ photoanode, which yielded 2.5% STH efficiency (Figure 4.2.9) [43]. A similar demonstration of perovskite solar cell and $TiO_2/BiVO_4$ photoanode tandem cell with a STH efficiency of 1.24% [62]. Dias et al. demonstrated a perovskite $CH_3NH_3PbI_3$-PEC tandem cell with an STH η of 2.5% [46], whereas the PEC cell consisting a p-type Cu_2O photocathode and IrO_2 anode. The transparency of Cu_2O photocathode was optimized by a thin gold underlayer, Cu_2O has a larger bandgap (2.1 eV) and was utilized as a top absorber component,

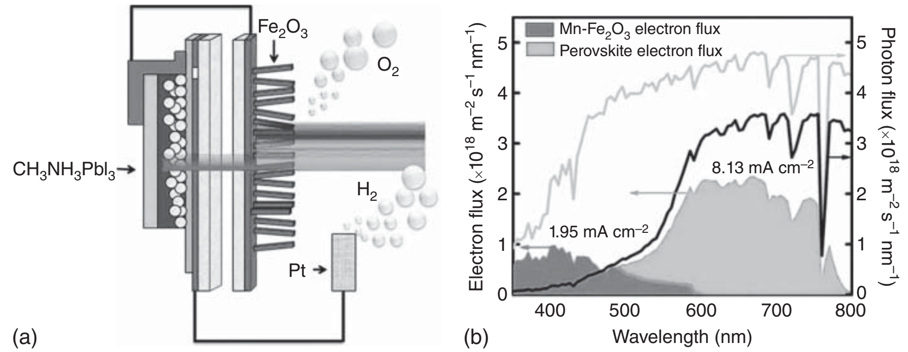

Figure 4.2.7 Hybrid photovoltaic and photoelectrosynthetic approach of Guru et al. for overall water splitting with an efficiency of 2.4%. A $CH_3NH_3PbI_3$ cells was used to bias an oxygen evolving Fe_2O_3 photoanode. Source: Gurudayal et al. 2015 [42]. Copyright 2015. Reproduced with permission of American Chemical Society.

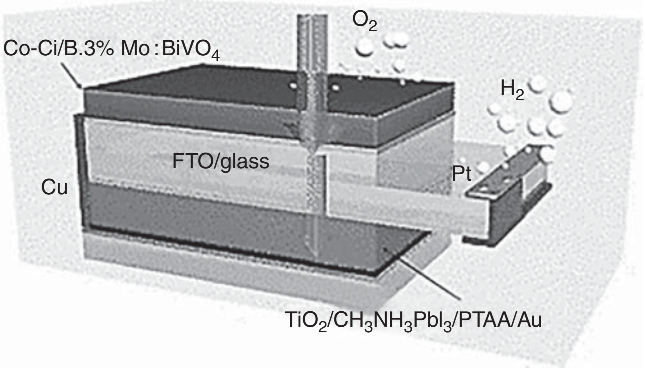

Figure 4.2.8 Wireless photoelectrosynthetic approach of Kim et al. 100 for overall water splitting with an efficiency of 3%. A $CH_3NH_3PbI_3$ cell was used in optical and electrical series with a Mo-doped $BiVO_4$ photoanode. Source: Kim et al. 2015 [16]. Copyright 2015. Reproduced with permission of American Chemical Society.

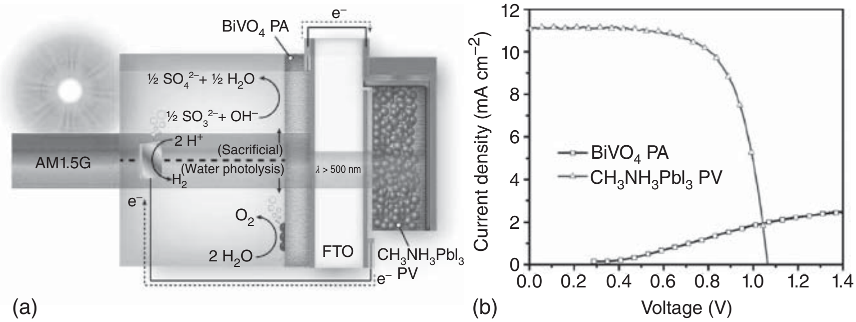

Figure 4.2.9 (a) Schematic diagram of the tandem $CoPi/BiVO_4$–$CH_3NH_3PbI_3$ device for solar water splitting, (b) Load curve of the J–V characteristics of $CoPi/BiVO_4$ photoanode and $CH_3NH_3PbI_3$ solar cell in 1 M KPi solution under 1 sun. Source: Chen et al. 2015 [43]. Copyright 2015. Reproduced with permission of American Chemical society.

whereas the $CH_3NH_3PbI_3$ was used as a bottom absorber. Other notable work include an inverted PEC-PV tandem cell configuration, where a perovskite large band gap $CH_3NH_3PbBr_3$ ($E_g = 2.3$ eV) PV cell was placed in tandem with a smaller bandgap $CuIn_xGa_{1-x}Se_2$ layer ($E_g = 1.1$ eV) which functioned as the photocathode [41]. This device exhibits an STH efficiency of 6.3% due to the proper energy band gap alignment, which enabled efficient harvesting of the solar spectrum. However, the $CH_3NH_3PbI_3$ solar cell tandem device showed only 2.6% STH efficiency, which is due to the high optical absorption of the $CH_3NH_3PbI_3$ in comparison of $CH_3NH_3PbBr_3$. The inverted PEC-PV tandem cell has the potential to further improve the STH efficiency, when it's in tandem with small energy band gap photoelectrodes [41]. A great advantage of using halide perovskites is its bandgap tunability (1.1–2.3 eV), which allows compatibility with a wide variety of photoelectrodes. However, the perovskite solar cell must be immersed in a water electrolyte, which induces an inherent stability problem. As a result, these perovskite-based PEC-PV tandem devices without protection layer cannot be operated for longer period of time. The numerous demonstrations of perovskite PV-PEC tandem devices and their comparison to other configurations is illustrated in Figure 4.2.10.

4.2.2.3 Photovoltaic-Electrocatalyst (PV-EC) Structure

PV-EC is the simplest configuration and has the highest potential for commercialization. In this approach, the water splitting anode and cathode is connected with a multijunction solar cell or a few solar cells in series to split water without an external bias. However, efficient, stable and economical friendly electrode materials need to be employed which can split water with minimum overpotential. Early approaches utilized multi-junctions Si, III–V, and DSSC PV based tandem devices. Those devices are complex in terms of number of solar cell used and poor STH efficiencies. Yamada et al. demonstrated a triple junction Si wired with a Co–Mo cathode and FeNiO anode durable for more than 18 hours and achieved STH η of approximately 2.5% [66]. Yamane et al. utilized a tandem configuration consisting of a multi-junction Si based PV cell and an electrolyzer with RuO_2 anode and Pt cathode, which exhibited an STH efficiency of 2.3% [67]. Reece et al. demonstrated higher STH efficiency of 4.7% by using a triple-junction a-Si PV cell and an electrolyzer containing NiMoZn based cathode and cobalt oxide based anode [64]. Cox et al., designed a tandem cell with a triple-junction a-Si PV cell integrated with an NiMoZn cathode and an NiBi anode with a notable STH efficiency of 10% [9b]. May et al. demonstrated a III–V based tandem device, in which a GaInP/GaInAs

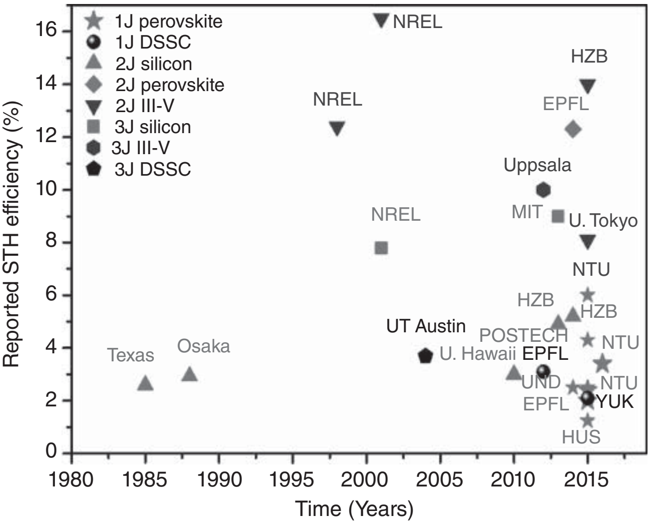

Figure 4.2.10 Selected reported solar to hydrogen (STH) conversion efficiencies of PV-PEC configuration under 1 sun illumination conditions. All STH efficiencies are as reported here the original publications [9b, 10, 16, 22, 34, 41, 42, 44–47, 59, 62–65].

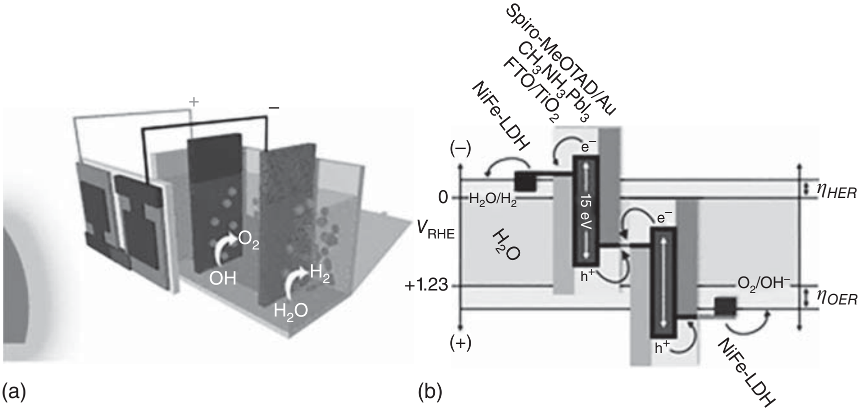

Figure 4.2.11 Photovoltaic-electrosynthetic approach of Luo et al. for overall water splitting with an efficiency of 12.3%. Two side-by-side $CH_3NH_3PbI_2$ cells were used; they were wired to NiFe hydrogen and oxygen evolution catalysts. Source: Luo et al. 2014 [44]. Copyright 2014. Reproduced with permission of The American Association for the Advancement of Science.

photovoltaics connected in series with Rh and RuO_2 based electrodes with a STH efficiency of 14% [68]. Rau et al. substituted the Rh/RhO_2 electrolyzer with a proton exchange membrane (PEM) electrolyzer, while using GaInP/GaInAs photovoltaics. This configuration exhibited even higher STH efficiency of 16.8% [69]. Licht et al. reported an exceptional PV-EC tandem device by combining a III–V PV with an electrolyzer containing RuO_2 anode and Pt cathode in 1 M $HClO_4$ electrolyte with a notable STH efficiency of 18.3% under 1 sun illumination [70]. Verlage et al. fabricated a monolithic wireless tandem device consisting of an $NiMo/GaAs/GaInP_2/TiO_2/Ni$ structure for sustained unassisted solar driven overall water splitting with STH efficiency of 8.6% [65]. A III–V based tandem device with an extraordinary STH efficiency of 30% was achieved utilizing two polymer electrolyte membrane electrolyzers in tandem with a triple-junction InGaP/GaAs/GaInNAsSb solar cell [71].

More recently, perovskite PV cells have been utilized in PV-EC tandem configurations due to their high open circuit potential and simple solution processed fabrication technique. A highly efficient and low-cost water splitting device by using a double-junction perovskite ($CH_3NH_3PbI_3$) PV cell and a bifunctional earth-abundant NiFe layered double hydroxide catalyst was reported by Gratzel's group, as shown in Figure 4.2.11. The STH efficiency reached 12.3% [44].

Rashid bin et al, demonstrated a bifunctional metal free nitrogen doped reduced graphene oxide/nitrogen doped carbon nanotube (NrGO/NCNT) hybrid electrocatalyst for HER and OER in an alkaline electrolyte (1 M KOH) in tandem with perovskite solar cell for the overall water splitting. This system exhibits a STH conversion efficiency of 9.02% (Figure 4.2.12) [72]. The high activity and bifunctional nature of their catalyst was attributed to the nitrogen doping.

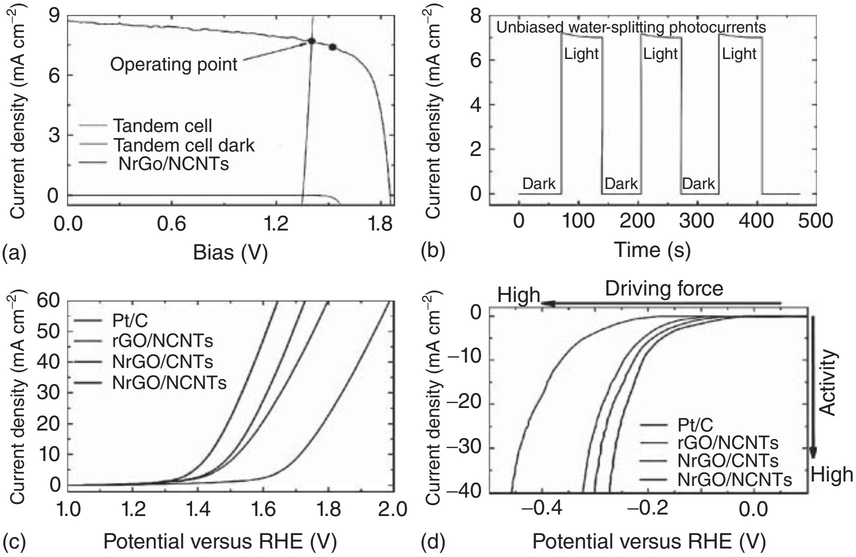

Figure 4.2.12 (a) Load curve analysis shows the operating point of a PEC cell as the intersection of the J–V curve of the hybrid tandem perovskite solar cell and the J–V curve of the electrocatalysts. (b) Current density–time curve of the integrated PEC water splitting without external bias under chopped illumination AM 1.5G 100 mW cm^{-2}. (c) OER characteristics of different electrocatalysts in a three-electrode configuration. (d) HER curves comparing their electrocatalytic activity in a three-electrode configuration in a 1M KOH electrolyte. Source: Bin et al. 2016 [72]. Copyright 2016. Reprinted with the permission of Royal Society of Chemistry.

4.2.3 EC/PEC-PV Approach for CO_2 Reduction

Photo/electrochemical CO_2 reduction reaction is even more challenging than the water splitting reaction due to the multiple electrons requirement to produce hydrocarbons and oxygenates and high overpotential due to kinetic losses. Different type of catalysts such as metals, semiconducting photoelectrodes, metal complexes, molecular catalysts have been discovered to perform the CO_2 reduction reaction. There have been a few reports of solar driven CO_2 reduction with solar to fuel efficiencies in the 1–5% range; in all cases, $2e^-$ products like CO or formate were produced. For CO_2 reduction reaction, a minimum of 3–4 V is required, which corresponds to six to eight silicon solar cells. Perovskite solar cells would help to reduce the complexity and fabrication cost of CO_2 reduction tandem cell due to its high open circuit voltage. Schreier et al. reported CO_2 reduction utilizing three perovskite solar cells integrated with an IrO_2 anode and an Au cathode, which achieved 7% solar-to-CO conversion efficiency (Figure 4.2.13) [73].

Recently, Jeong Jang reported an Au/ZnO/ZnTe/CdTe core–shell nanorod array photocathode, cobalt–bicarbonate anode and a $CH_3NH_3PbI_3$ perovskite solar cell in tandem for solar assisted CO_2 reduction [74]. This device harvested light efficiently, as the photocathode absorbed the higher energy photons (>2.14 eV), while the perovskite solar cell absorbed the lower energy photons

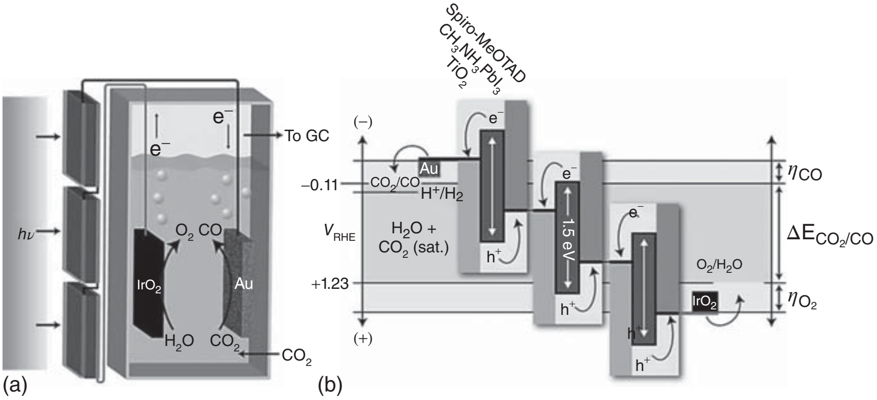

Figure 4.2.13 (a) Schematic of a triple junction perovskite solar cell with FeNiOx bifunctioanal layer electrocatalyst for solar assisted overall water splitting, (b) Thin film Photovoltaic-electrosynthetic approach of Scheier et al. for solar-driven CO_2 reduction. Three side-by-side $CH_3NH_3PbI_2$ cells were used; they were wired to an Au cathode for reduction of CO_2 to CO and to an IrO_2 anode for water oxidation. Source: Schreier et al. 2015 [73]. Copyright 2015. Reproduced with permission of Nature Publishing Group.

(>1.5 eV). However this device only showed a nominal solar to CO conversion efficiency of 0.35% and a solar to fuel conversion efficiency exceeding 0.43% including H_2 (Figure 4.2.14). The device performance was reduced by nearly 30% within three hours [74].

4.2.4 Concluding Remarks and Outlook

Artificial photosynthesis incorporating PEC methods to convert solar energy to chemical fuels such as hydrogen and hydrocarbons is an area of research that have been driven steadily by developments in earth abundant absorber materials, efficient catalysts and new device configurations/structures. Due to the seemingly insurmountable challenge of driving the chemical reactions utilizing the photovoltage from a single optical absorber, various tandem configurations would remain a focus of the field for unassisted water splitting/CO_2 reduction reactions. The advantages of halide perovskite for driving such reactions are clear-facile cost-effective fabrication, band gap tunability and high photovoltages. Despite the technological and scientific richness of configurations that include photocathodes, photoanodes-economical reasons may dictate that photovoltaic driven electrocatalytic devices would be the closest to reality. Such configurations would take advantages of the drastic cost reductions achieved in the photovoltaic industry. Again, perovskites with their printability, low constituent costs could be a major player. Further developments in the perovskite driven PEC arena would have to focus on improving the stability of both the halide perovskite photovoltaics as well as the catalytic electrodes.

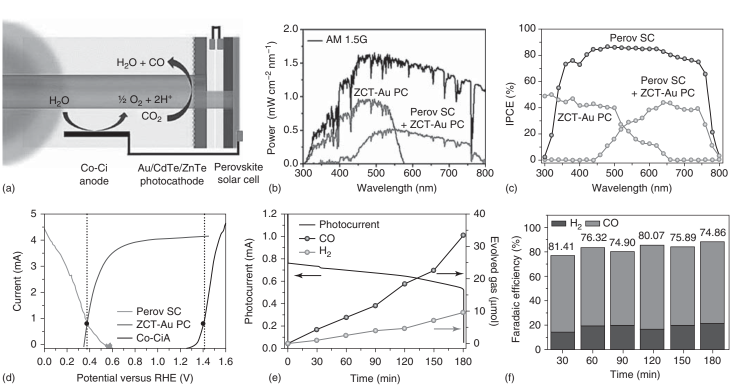

Figure 4.2.14 (a) Schematic of a tandem cell comprising of ZnO/ZnTe/CdTe-Au NR photocathode, cobalt bicarbonate (Co–Ci) and perovskite solar cell for photoelectrochemical CO_2 reduction. (b) Incident photons of AM 1.5G spectrum by two light absorbers. (c) IPCE responses of photocathode, perovskite solar cell, and the tandem device. The IPCE of photocathode was measured at −0.11 VRHE. (d) J–V curves of ZCT-Au photocathode and Co–Ci anode measured in three-electrode configuration with overlaid response of the solar cell in the stacked tandem device. (e) Chronoamperometry and time-profiled production of CO and H_2 for three hours in the tandem device. (f) Faradaic efficiencies of CO and H_2 during three hours in the tandem cell with a CO_2-saturated $KHCO_3$ electrolyte under simulated 1 sun illumination. Source: Jang et al. 2016 [74]. Copyright 2016. Reprinted with permission of American Chemical Society.

References

1 (a) MacKay, D.J.C. (2013). *Philos. Trans. R. Soc. London, Ser. A* 371: 20110431. (b) International Energy Agency (IEA) (2015); (c) BP Energy Outlook, BP (2016); (d) Renewable Energy Policy Network For 21st Century (2015).

2 (a) Scripps Institution of Oceanography US San Diago (2015). (b) Solomon, S., Plattner, G.-K., Knutti, R., and Friedlingstein, P. (2009). *Proc. Natl. Acad. Sci.* 106: 1704.

3 (a) Tachibana, Y., Vayssieres, L., and Durrant, J.R. (2012). *Nat. Photonics* 6: 511. (b) Walter, M.G., Warren, E.L., McKone, J.R. et al. (2010). *Chem. Rev.* 110: 6446.

4 Keable, J. and Holcroft, B. (2012). Economic and business perspectives. In: *Photoelectrochemical Hydrogen Production* (ed. R. van de Krol and M. Grätzel), 277. Boston, MA: Springer.

5 Barber, J. (2009). *Chem. Soc. Rev.* 38: 185.

6 Listorti, A., Durrant, J., and Barber, J. (2009). *Nat. Mater.* 8: 929.

7 Liu, C., Colón, B.C., Ziesack, M. et al. (2016). *Science* 352: 1210.

8 Bak, T., Nowotny, J., Rekas, M., and Sorrell, C.C. (2002). *Int. J. Hydrogen Energy* 27: 991.

9 (a) Gamelin, D.R. (2012). *Nat. Chem.* 4: 965. (b) Cox, C.R., Lee, J.Z., Nocera, D.G., and Buonassisi, T. (2014). *Proc. Natl. Acad. Sci. U.S.A.* 111: 14057. (c) Doscher, H., Geisz, J.F., Deutsch, T.G., and Turner, J.A. (2014). *Energy Environ. Sci.* 7: 2951.

10 Jacobsson, T.J., Fjallstrom, V., Sahlberg, M. et al. (2013). *Energy Environ. Sci.* 6: 3676.

11 Ronge, J., Bosserez, T., Martel, D. et al. (2014). *Chem. Soc. Rev.* 43: 7963.

12 Crabtree, G.W., Dresselhaus, M.S., and Buchanan, M.V. (2004). *Phys. Today* 57: 39.

13 Grätzel, M. (2001). *Nature* 414: 338.

14 Butler, M.A. and Ginley, D.S. (1980). *J. Mater. Sci.* 15: 1.

15 Brillet, J., Cornuz, M., Formal, F.L. et al. (2010). *J. Mater. Res.* 25: 17.

16 Kim, J.H., Jo, Y., Kim, J.H. et al. (2015). *ACS Nano* 9: 11820.

17 Chen, Z., Jaramillo, T.F., Deutsch, T.G. et al. (2010). *J. Mater. Res.* 25: 3.

18 Ager, J.W., Shaner, M.R., Walczak, K.A. et al. (2015). *Energy Environ. Sci.* 8: 2811.

19 Nozik, A.J. (1976). *Appl. Phys. Lett.* 29: 150.

20 Peter, L.M. (1990). *Chem. Rev.* 90: 753.

21 Bassi, P.S., Gurudayal, Wong, L.H., and Barber, J. (2014). *Phys. Chem. Chem. Phys.* 16: 11834.

22 Khaselev, O. and Turner, J.A. (1998). *Science* 280: 425.

23 (a) Turner, J.A. (2004). *Science* 305: 972. (b) Dotan, H., Mathews, N., Hisatomi, T. et al. (2014). *J. Phys. Chem. Lett.* 5: 3330.

24 Brillet, J., Yum, J.-H., Cornuz, M. et al. (2012). *Nat. Photonics* 6: 824.

25 (a) Bolton, J.R. (1996). *Sol. Energy* 57: 37. (b) Singh, A. and Spiccia, L. (2013). *Coord. Chem. Rev.* 257: 2419.

26 Kudo, A. and Miseki, Y. (2009). *Chem. Soc. Rev.* 38: 253.

27 Lin, Y., Yuan, G., Liu, R. et al. (2011). *Chem. Phys. Lett.* 507: 209.

28 Alexander, B.D., Kulesza, P.J., Rutkowska, I. et al. (2008). *J. Mater. Chem.* 18: 2298.

29 Chen, X., Shen, S., Guo, L., and Mao, S.S. (2010). *Chem. Rev.* 110: 6503.

30 Kavan, L. and Grätzel, M. (1995). *Electrochim. Acta* 40: 643.

31 Park, J.H. and Bard, A.J. (2005). *Electrochem. Solid-State Lett.* 8: G371.

32 (a) Shin, K., Yoo, J.-B., and Park, J.H. (2013). *J. Power Sources* 225: 263. (b) Cherepy, N.J., Smestad, G.P., Grätzel, M., and Zhang, J.Z. (1997). *J. Phys. Chem. B* 101: 9342. (c) Kroeze, J.E., Savenije, T.J., and Warman, J.M. (2004). *J. Am. Chem. Soc.* 126: 7608.

33 (a) Gonçalves, R.H., Leite, L.D.T., and Leite, E.R. (2012). *ChemSusChem* 5: 2341. (b) Pihosh, Y., Turkevych, I., Mawatari, K. et al. (2014). *Small* 10: 3692. (c) Shaner, M.R., Fountaine, K.T., Ardo, S. et al. (2014). *Energy Environ. Sci.* 7: 779. (d) Pihosh, Y., Turkevych, I., Mawatari, K. et al. (2015). *Sci. Rep.* 5: 11141.

34 Coridan, R.H., Shaner, M., Wiggenhorn, C. et al. (2013). *J. Phys. Chem. C* 117: 6949.

35 Maeda, K. and Domen, K. (2011). *MRS Bull.* 36: 25.

36 (a) Kennedy, J.H. and Frese, K.W. Jr. (1978). *J. Electrochem. Soc.* 125: 709. (b) Le Formal, F., Tetreault, N., Cornuz, M. et al. (2011). *Chem. Sci.* 2: 737. (c) Ling, Y., Wang, G., Wheeler, D.A. et al. (2011). *Nano Lett.* 11: 2119. (d) Zhang, P., Kleiman-Shwarsctein, A., Hu, Y.-S. et al. (2011). *Energy Environ. Sci.* 4: 1020. (e) Liao, P. and Carter, E.A. (2012). *J. Appl. Phys.* 112: 013701. (f) Peter, L.M., Wijayantha, K.G.U., and Tahir, A.A. (2012). *Faraday Discuss.* 155: 309. (g) Warren, S.C., Voïtchovsky, K., Dotan, H. et al. (2013). *Nat. Mater.* 12: 842.

37 (a) Gurudayal, Chee, P.M., Boix, P.P. et al. (2015). *ACS Appl. Mater. Interfaces* 7: 6852. (b) Gurudayal, Chiam, S.Y., Kumar, M.H. et al. (2014). *ACS Appl. Mater. Interfaces* 6: 5852.

38 Nielander, A.C., Shaner, M.R., Papadantonakis, K.M. et al. (2015). *Energy Environ. Sci.* 8: 16.

39 Hu, S., Xiang, C., Haussener, S. et al. (2013). *Energy Environ. Sci.* 6: 2984.

40 Zhang, K., Ma, M., Li, P. et al. (2016). *Adv. Energy Mater.* 6: 1600602.

41 Luo, J., Li, Z., Nishiwaki, S. et al. (2015). *Adv. Energy Mater.* 5: 1501520.

42 Gurudayal, Sabba, D., Kumar, M.H. et al. (2015). *Nano Lett.* 15: 3833.

43 Chen, Y.-S., Manser, J.S., and Kamat, P.V. (2015). *J. Am. Chem. Soc.* 137: 974.

44 Luo, J., Im, J.-H., Mayer, M.T. et al. (2014). *Science* 345: 1593.

45 Abdi, F.F., Han, L., Smets, A.H.M. et al. (2013). *Nat. Commun.* 4.

46 Dias, P., Schreier, M., Tilley, S.D. et al. (2015). *Adv. Energy Mater.* 5: 1501537.

47 Chae, S.Y., Park, S.J., Joo, O.-S. et al. (2016). *Sol. Energy* 135: 821.

48 Wang, H. and Turner, J.A. (2010). *J. Electrochem. Soc.* 157: F173.

49 Wang, H., Deutsch, T., and Turner, J.A. (2008). *J. Electrochem. Soc.* 155: F91.

50 Bornoz, P., Abdi, F.F., Tilley, S.D. et al. (2014). *J. Phys. Chem. C* 118: 16959.

51 Mor, G.K., Varghese, O.K., Wilke, R.H.T. et al. (2008). *Nano Lett.* 8: 1906.

52 Lai, Y.-H., Palm, D.W., and Reisner, E. (2015). *Adv. Energy Mater.* 5: 1501668.

53 Liu, C., Tang, J., Chen, H.M. et al. (2013). *Nano Lett.* 13: 2989.

54 Ding, C., Qin, W., Wang, N. et al. (2014). *Phys. Chem. Chem. Phys.* 16: 15608.

55 Jang, J.-W., Du, C., Ye, Y. et al. (2015). *Nat. Commun.* 6: 7447.
56 Ida, S., Yamada, K., Matsunaga, T. et al. (2010). *J. Am. Chem. Soc.* 132: 17343.
57 Kim, J.H., Kaneko, H., Minegishi, T. et al. (2016). *ChemSusChem* 9: 61.
58 Kim, J.K., Shin, K., Cho, S.M. et al. (2011). *Energy Environ. Sci.* 4: 1465.
59 Shi, X., Zhang, K., Shin, K. et al. (2015). *Nano Energy* 13: 182.
60 Han, L., Abdi, F.F., van de Krol, R. et al. (2014). *ChemSusChem* 7: 2832.
61 (a) Xing, G., Mathews, N., Sun, S. et al. (2013). *Science* 342: 344. (b) Bi, D., Gao, P., Scopelliti, R. et al. (2016). *Adv. Mater.* 28: 2910.
62 Zhang, X., Zhang, B., Cao, K. et al. (2015). *J. Mater. Chem. A* 3: 21630.
63 Park, J.H. and Bard, A.J. (2006). *Electrochem. Solid-State Lett.* 9: E5.
64 Reece, S.Y., Hamel, J.A., Sung, K. et al. (2011). *Science* 334: 645.
65 Verlage, E., Hu, S., Liu, R. et al. (2015). *Energy Environ. Sci.* 8: 3166.
66 Yamada, Y., Matsuki, N., Ohmori, T. et al. (2003). *Int. J. Hydrogen Energy* 28: 1167.
67 Yamane, S., Kato, N., Kojima, S. et al. (2009). *J. Phys. Chem. C* 113: 14575.
68 May, M.M., Lewerenz, H.-J., Lackner, D. et al. (2015). *Nat. Commun.* 6: 8286.
69 Rau, S., Vierrath, S., Ohlmann, J. et al. (2014). *Energy Technol.* 2: 43.
70 Licht, S., Wang, B., Mukerji, S. et al. (2000). *J. Phys. Chem. B* 104: 8920.
71 Jia, J., Seitz, L.C., Benck, J.D. et al. (2016). *Nat. Commun.* 7: 13237.
72 Bin, A.R., Yusoff, M., and Jang, J. (2016). *Chem. Commun.* 52: 5824.
73 Schreier, M., Curvat, L., Giordano, F. et al. (2015). *Nat. Commun.* 6: 7326.
74 Jang, Y.J., Jeong, I., Lee, J. et al. (2016). *ACS Nano* 10: 6980.

Index

Halide Perovskites: Photovoltaics, Light Emitting Devices, and Beyond, First Edition.
Edited by Tze-Chien Sum and Nripan Mathews.